FRONTIERS IN MATERIALS: RISING STARS 2020

EDITED BY: Anastasiia O. Krushynska, Amy Sarah Gandy, Miriam Navlani-García, David Salinas Torres, Chang-Mou Wu, Jong-Seok Oh and Federico Carosio

PUBLISHED IN: Frontiers in Materials

frontiers Research Topics

ISSN 1664-8714
ISBN 978-2-88966-950-9
DOI 10.3389/978-2-88966-950-9

About Frontiers

Frontiers is more than just an open-access publisher of scholarly articles: it is a pioneering approach to the world of academia, radically improving the way scholarly research is managed. The grand vision of Frontiers is a world where all people have an equal opportunity to seek, share and generate knowledge. Frontiers provides immediate and permanent online open access to all its publications, but this alone is not enough to realize our grand goals.

Frontiers Journal Series

The Frontiers Journal Series is a multi-tier and interdisciplinary set of open-access, online journals, promising a paradigm shift from the current review, selection and dissemination processes in academic publishing. All Frontiers journals are driven by researchers for researchers; therefore, they constitute a service to the scholarly community. At the same time, the Frontiers Journal Series operates on a revolutionary invention, the tiered publishing system, initially addressing specific communities of scholars, and gradually climbing up to broader public understanding, thus serving the interests of the lay society, too.

Dedication to Quality

Each Frontiers article is a landmark of the highest quality, thanks to genuinely collaborative interactions between authors and review editors, who include some of the world's best academicians. Research must be certified by peers before entering a stream of knowledge that may eventually reach the public - and shape society; therefore, Frontiers only applies the most rigorous and unbiased reviews.
Frontiers revolutionizes research publishing by freely delivering the most outstanding research, evaluated with no bias from both the academic and social point of view. By applying the most advanced information technologies, Frontiers is catapulting scholarly publishing into a new generation.

What are Frontiers Research Topics?

Frontiers Research Topics are very popular trademarks of the Frontiers Journals Series: they are collections of at least ten articles, all centered on a particular subject. With their unique mix of varied contributions from Original Research to Review Articles, Frontiers Research Topics unify the most influential researchers, the latest key findings and historical advances in a hot research area! Find out more on how to host your own Frontiers Research Topic or contribute to one as an author by contacting the Frontiers Editorial Office: frontiersin.org/about/contact

FRONTIERS IN MATERIALS: RISING STARS 2020

Topic Editors:
Anastasiia O. Krushynska, University of Groningen, Netherlands
Amy Sarah Gandy, The University of Sheffield, United Kingdom
Miriam Navlani-García, University of Alicante, Spain
David Salinas Torres, University of Alicante, Spain
Chang-Mou Wu, National Taiwan University of Science and Technology, Taiwan
Jong-Seok Oh, Kongju National University, South Korea
Federico Carosio, Politecnico di Torino, Italy

Cover image: 24Novembers/Shutterstock.com

The *Frontiers in Materials* Editorial Office team are delighted to present the second edition of the "Rising Stars" article collection, "Frontiers in Materials: Rising Stars 2020", showcasing the high-quality work of internationally recognized researchers in the early stages of their independent careers.

All Rising Star researchers featured within this collection were individually nominated by the Topic Editors in recognition of their potential to influence the future directions of their respective fields. The work presented here highlights the diversity of research performed across the entire breadth of the materials science and engineering field and presents advances in theory, experimentation, and methodology with applications for solving compelling problems.

This Editorial features the corresponding author(s) of each paper published within this important collection, ordered by section alphabetically, highlighting them as the great researchers of the future.

The *Frontiers in Materials* Editorial Office team would like to thank each researcher who contributed their work to this collection. We would also like to personally thank the Topic Editors for their exemplary leadership of this article collection; their strong support and passion for this important, community-driven collection has ensured its success and global impact.

Emily Young
Journal Development Manager

Topic Editors

Anastasiia O. Krushynska

Dr. Anastasiia Krushynska is an assistant professor at Engineering and Technology Institute Groningen, the University of Groningen, the Netherlands, and a former Marie Sklodowska-Curie Researcher at the University of Torino, Italy. Her research interests are in Wave Dynamics, Acoustics, and Advanced Materials. She has published about 35 papers in leading international journals, including Physical Review Letters, Applied Physics Letters, Journal of Mechanics and Physics of Solids, and the New Journals of Physics, with some of them highlighted in the news. She serves as an associate editor in two journals and a reviewer for more than 35 journals, three international conferences, and three funding agencies.

Amy Sarah Gandy

Dr. Amy Sarah Gandy is a Senior Lecturer in Nuclear Materials Engineering in the Department of Materials Science and Engineering at the University of Sheffield, United Kingdom. She was awarded an MPhys in Physics and Space Technology from the University of Salford, United Kingdom, and holds a Ph.D. in Physics and Materials Science from the University of Salford and the University of Poitiers, France. Her research focuses on determining radiation-induced damage and recovery mechanisms and gas bubble formation in alloys and poly-crystalline oxide-based materials for nuclear fission and fusion, and she leads an international collaboration between UK and Indian researchers to develop radiation-damage-resistant alloys for advanced nuclear systems. Her research group is currently developing reduced-activation compositionally complex alloys for plasma-facing components and lithium-containing ceramics, which are candidates for tritium breeder materials for fusion technology. Amy also works in collaboration with the Culham Centre for Fusion Energy (CCFE) and National Nuclear Laboratory (NNL).

Miriam Navlani-García

Dr. Miriam Navlani-García is a Distinguished Researcher at the Inorganic Chemistry Department and the Institute of Material Science of the University of Alicante. From this university, she received a degree in Chemistry (2008) and achieved her Ph.D. in Material Science. She moved to Osaka University, Japan, as an Assistant Professor in the Division of Materials and Manufacturing Science (2015–2017). After that, she was awarded a JSPS Postdoctoral Fellowship for Research in Japan (Standard) by the Japan Society for the Promotion of Science (2017–2018). She was awarded a Postdoctoral Grant for researchers with an international profile [GenT Plan (Talent Generation)]. Her research interests are mainly focused on the design and development of nano-sized materials for environmental and catalytic applications, such as hydrogen production from hydrogen carrier molecules and CO_2 valorization.

David Salinas Torres

Dr. Salinas-Torres is a researcher at the Institute of Materials Science of the University of Alicante (UA). He obtained a BSc. in Chemistry (2008) and a Ph.D. in Material Science (2014) at the UA. He was awarded a BeIPD-COFUND fellowship at the Université de Liège (2015–2017), where he developed a project related to energy storage devices. Then, he moved to Osaka University as an Assistant Professor, where he subsequently became a JSPS fellow. He is currently a "Juan de la Cierva" postdoctoral fellow, and his work is focused on energy applications based on carbon materials.

Chang-Mou Wu

Prof. Chang-Mou Wu is a Professor of Materials Science and Engineering at Taiwan University of Science and Technology, Taiwan. He received his Ph.D. degree in Materials Science and Engineering from the National Sun Yet-Sen University, Taiwan, in 1999. During his Ph.D. study, he also worked as a guest researcher at IVW, Kaiserslautern University, Germany. He has subsequently worked as a scientist at research institutes (Academia Sinica and ChungShan Institute of Science and Technology) and in the industry (Optimax). In 2007, he started his teaching and researching career at FengChia University. His current research interests are functional organic/inorganic nanocomposite and nanocomposites for Piezo/Pyro/Triboelectric Nanogenerators.

Jong-Seok Oh

Dr. Jong-Seok Oh received his B.S. degree, MS degree, and Ph.D. degrees in Mechanical Engineering from Inha University in 2009, 2011, and 2015, respectively. He is currently an Assistant Professor at Kongju National University. His research interests are robust controller design and control of various systems using smart actuators, such as magnetorheological (MR), electrorheological (ER) fluid, and piezo actuators.

Federico Carosio

Prof. Federico Carosio achieved his Ph.D. (2012) in Materials Science and Technology at Politecnico di Torino with his thesis: "Layer by Layer assembly of nanostructured coatings for flame retardancy and barrier properties". At present, he is an Associate Professor at the Department of Applied Science and Technology of Politecnico di Torino, Italy. His research is focused on polymers and nanostructures, smart fibers and textiles, and nanocellulose-based materials (thin films and foams) with particular attention to their flame retardancy properties achieved through water-based deposition techniques. He has co-authored more than 70 scientific papers (total citations: 5065, H-index 39, source google scholar) published in international peer-review journals, and he has attended several national and international congresses and workshops.

Citation: Krushynska, A. O., Gandy, A. S., Navlani-García, M., Torres, D. S., Wu, C.-M., Oh, J.-S., Carosio, F., eds. (2021). Frontiers in Materials: Rising Stars 2020. Lausanne: Frontiers Media SA. doi: 10.3389/978-2-88966-950-9

Table of Contents

SMART MATERIALS

STRUCTURAL MATERIALS

Carbon-Based Materials

José Rodríguez-Mirasol

Prof. José Rodríguez-Mirasol is a Professor of Chemical Engineering at the University of Málaga and has focused his research interest on the valorization of biomass and industrial waste by thermochemical processes within the framework of sustainability, contributing to the advancement of knowledge of the biorefinery processes in producing biofuels and chemicals of industrial interest. He also has conducted research on the synthesis of advanced materials of scientific and technical relevance in adsorption and heterogeneous catalytic processes for environmental and energy applications by use of electrospinning/electrospray and liquid-phase impregnation techniques. He has also been a visiting scientific researcher at Pennsylvania State University and the Delft University of Technology.

María José Valero-Romero

Dr. María Jose Valero Romero obtained her MSc in Chemical Engineering in 2009 at the University of Malaga and her Ph.D. in Chemical Engineering at the same university in 2015 (with her thesis, "Carbon-based catalysts for oxidation and alcohol dehydration reactions"). During her Ph.D. studies, she had two short research stays (in 2012 and 2014) at the Catalysis Engineering (CE) group at Delft University of Technology (the Netherlands), working on the research project of Fischer-Tropsch synthesis. In 2015, she joined back at CE group as a postdoctoral researcher, firstly with a private contract financed by Shell Global Solutions (Towards Heterogeneous Hydroformylation Catalysts) and later within a European project (EU Horizon 2020): "Adaptable Reactors for Resource- and Energy-Efficient Methane Valorisation", ADREM. In May 2018, she came back as a postdoctoral researcher for the TERMA group with a research award granted by UMA (I Plan Propio).

frontiers in Materials

REVIEW
published: 04 February 2021
doi: 10.3389/fmats.2020.617432

Carbon-Based Materials as Catalyst Supports for Fischer–Tropsch Synthesis: A Review

María José Valero-Romero, Miguel Ángel Rodríguez-Cano, José Palomo, José Rodríguez-Mirasol* and Tomás Cordero*

Departamento de Ingeniería Química, Facultad de Ciencias, Universidad de Málaga, Andalucía Tech, Málaga, Spain

The use of carbon-based materials as catalyst supports for Fischer–Tropsch synthesis (FTS) is thoroughly reviewed. The main factors to consider when using a carbonaceous catalyst support for FTS are first discussed. Then, the most relevant and recent literature on the topic from the last 2 decades is reviewed, classifying the different examples according to the carbon structure and shape. Some aspects such as the carbon textural properties, carbon support modification (functionalization and doping), catalyst preparation methods, metal particle size and location, catalyst stability and reducibility, the use of promoters, and the catalyst performance for FTS are summarized and discussed. Finally, the main conclusions, advantages, limitations, and perspectives of using carbon catalyst supports for FTS are outlined.

Keywords: Fischer-Tropsch synthesis, synthesis gas (syngas), catalysts, carbon supports, catalytic performance

OPEN ACCESS

Edited by:
David Salinas Torres, University of Alicante, Spain

Reviewed by:
Dong Hyun Chun, Korea Institute of Energy Research, South Korea
Vladimir Mordkovich, Technological Institute for Superhard and Novel Carbon Materials, Russia

****Correspondence:***
María José Valero-Romero
mjvalero@uma.es
José Rodríguez-Mirasol
mirasol@uma.es

Specialty section:
This article was submitted to Carbon-Based Materials, a section of the journal Frontiers in Materials

Received: *14 October 2020*
Accepted: *30 November 2020*
Published: *04 February 2021*

Citation:
Valero-Romero MJ, Rodríguez-Cano MÁ, Palomo J, Rodríguez-Mirasol J and Cordero T (2021) Carbon-Based Materials as Catalyst Supports for Fischer–Tropsch Synthesis: A Review. Front. Mater. 7:617432. doi: 10.3389/fmats.2020.617432

INTRODUCTION

Hydrocarbons are the most widely used chemicals and fuels and are the main driving force of occidental social well-being. The major part of hydrocarbons on earth are produced from crude oil, which provide approximately 33% of the current world's primary energy requirements, followed by coal (27%) and natural gas (24%). In the past 10 years, oil consumption has grown globally by an average of 1.1% (1.1 million barrels per day), Asia being the region that has shown the highest growth, where coal consumption is still dominant. Furthermore, the global proved oil reserves account only for around 45 years at the current consumption ratio, whereas the estimates of the extent of available reserves of natural gas and coal seem to be around 50 and 132 years, respectively (BP Statistical Review, 2020). Therefore, the growing global demand for crude oil, together with its fast depletion rate, and the implementation of a more stringent environmental legislation on liquid fuels boost the use of alternative and sustainable hydrocarbon sources.

In this sense, Fischer–Tropsch synthesis (FTS) is an alternative industrial process for the production of clean liquid fuels and value-added chemicals from synthesis gas (a mixture of CO and H_2), which can be derived from nonpetroleum feedstocks including natural gas, coal, and renewable biomass (mainly, lignocellulosic biomass) (Noureldin et al., 2014; Ren et al., 2019). Depending on the feedstock, the process is referred to as GTL (gas-to-liquid), CTL (coal-to-liquid), or BTL (biomass-to-liquid). Nowadays, there are large commercial FTS plants operating worldwide that produce liquid fuels and hydrocarbons from syngas obtained by partial oxidation and steam reforming of natural gas and by coal gasification (Lappas and Heracleous, 2016). However, the vast majority of BTL schemes, which uses syngas from gasification of biomass, are in the pilot or demonstration phase. The development of a commercial BTL process seems to be hindered due to the limited commercial experience in biomass gasification and its integration with fuel production

processes and to the high capital costs associated to the BTL technology (Lappas and Heracleous, 2016).

Transition metals are used in FTS process due to their considerable activity. Among them, Fe and Co are the only industrially relevant catalysts that are currently commercially used in FTS. The choice of catalyst depends primarily on the FTS operating mode: (1) the so-called low-temperature Fischer–Tropsch synthesis (LT-FTS) and (2) high-temperature Fischer–Tropsch synthesis (HT-FTS) (Steynberg, 2004). In the former case, at LT-FTS conditions (200–240°C), mostly long-chain paraffins (wax) are produced over either Fe- or Co-based catalysts. This wax is afterward (hydro) cracked in the desired product spectrum (Luque et al., 2012). On the other hand, the use of Fe-based catalysts at HT-FTS conditions (300–350°C) is typically aimed to produce short-chain unsaturated hydrocarbons, olefins (Fischer–Tropsch to olefins, FTOs), and oxygenates (Torres Galvis et al., 2012b). Furthermore, high selectivities toward gasoline-range hydrocarbons can be produced using Fe at HT-FTS conditions (Steynberg et al., 1999).

Moreover, the choice of metal also depends on the feedstock used for the FTS. When high-purity syngas is used, Co-based catalysts are preferred because of their higher intrinsic activity for FTS and higher selectivity toward linear products than those of Fe (at similar conditions). Moreover, Co-based catalysts present a low activity toward water-gas shift (WGS) and a high hydrogenation activity, therefore produce less unsaturated hydrocarbons and oxygenates, while having a higher catalyst stability (Munirathinam et al., 2018). Therefore, cobalt-based catalyst is the choice when using syngas with a $H_2/CO \geq 2$, as that produced from natural gas as feedstock (Aasberg-Petersen et al., 2004). On the other hand, iron-based catalysts are cheaper and widely available compared with Co-based catalysts and present a high flexibility in terms of operating conditions and poisoning, being their use possible at different temperatures and H_2/CO molar ratios (Abelló, S., and Montané, D. (2011). Exploring Iron-based Multifunctional Catalysts for Fischer-Tropsch Synthesis: A Review. ChemSusChem 4, 1538-1556). This flexibility for different H_2/CO ratios is of great interest when using syngas derived from biomass or coal gasification, which present H_2/CO molar ratios lower than 2 (Lappas and Heracleous, 2016). This is related to the high WGS activity of Fe-based catalysts, which could compensate the lack of hydrogen until reaching the stoichiometric proportions required for the FT reaction (Sartipi et al., 2014).

Supported catalysts for FTS have been extensively studied in academia, in spite of only Co-supported catalysts have been used up to know at industrial scale in the LT-FTS (Luque et al., 2012). In this sense, FT catalyst structure and performance are highly influenced by the catalyst support. Conventional inorganic materials such as Al_2O_3, SiO_2, TiO_2, and zeolites have been frequently studied to disperse and stabilize both Fe and Co catalyst nanoparticles (Sun et al., 2000; Prieto et al., 2009; Sartipi et al., 2014; Abrokwah et al., 2019). Unfortunately, highly dispersed cobalt and iron nanoparticles can interact with the metal oxide support during the thermal activation treatments (high-temperature calcination and/or reduction), resulting in formation of cobalt and iron-supported mixed compounds (i.e., cobalt and iron silicates in the case of Co/SiO_2 and Fe/SiO_2 catalysts, respectively), which are hardly reducible and therefore nonactive in the FTS reaction (Lund and Dumesic, 1981; Tauster et al., 1981; Munirathinam et al., 2018). In order to tackle this issue, the use of more inert materials, such as carbon-containing supports, has been proposed. Carbon-based materials have been reported to minimize the metal-support interactions because of their inert nature, high surface area and tunable porous texture, and surface chemistry. The high thermal conductivity of carbon materials is an additional advantage of carbon-based supports for FTS catalysts, which favors the catalyst heat-transfer properties during the highly exothermic FTS reaction (Chin et al., 2005; Asalieva et al., 2020). Thus, carbon-based materials have been successfully applied as catalyst supports for FTS (Xiong et al., 2010; Moussa et al., 2014; Dlamini et al., 2020), but only in the area of research because they have not yet been used at an industrial level, as it has been already mentioned.

Figure 1 shows the evolution of the number of research papers published regarding the use of carbon-based materials as catalyst supports for FTS. We have selected for the present work 164 research papers reported in scientific journals of high impact (80% Q1) indexed in JCR in the areas of knowledge of Chemistry, Chemical Engineering, Environmental Engineering, and Materials Technology, between 2004 and 2020. Approximately, 25% of the studies related to catalysts for FTS are devoted to catalyst supported on carbon materials and 35% of these research studies have been reported in the last 3 years, which highlight the potential interest in this topic. Accordingly, 67.3% of the research papers correspond to carbon-supported Co catalysts, 32.7% to Fe-related catalysts, and 2.5% to Ru catalysts. Ru has been less investigated due to the high metal costs and, therefore, to the greatest difficulties of implementation in industrial applications. Furthermore, the most active area of research along the past 2 decades has been in activated carbons (AC, 15%) and in multiwall carbon nanotubes and nanofibers (CNTs and CNFs, respectively, 42%). More recently, there has been an increasing interest in the use of new carbon materials with uniform structures for FTS process, such as ordered mesoporous carbons (OMC), carbon spheres (CS), and graphene. A considerable increasing number of studies have also investigated the use of carbon/oxide hybrid supports (i.e., C/Al_2O_3, C/SiO_2, and C/HZSM-5), and, very recently, Metal Organic Frameworks-derived catalysts. In the latter case, the thermal decomposition in inert conditions of Co- and Fe-containing MOFs, namely, the MOF-mediated synthesis technique, resulted in carbon-doped Co and Fe metal catalysts with very interesting results for FTS (Santos et al., 2015; Otun et al., 2020). **Figure 2** summarizes the different carbon support materials reported in the literature for FTS catalysts classified according to the carbon structure and morphology.

Herein, we have summarized the most relevant and recent advances in conversion of syngas to hydrocarbons by FTS using heterogeneous catalysts supported on different carbon-based materials (AC, OMC, CNTs, CNFs, CSs, and graphene) reported during the last 2 decades. We first bring to the attention of the reader important characteristics to take into

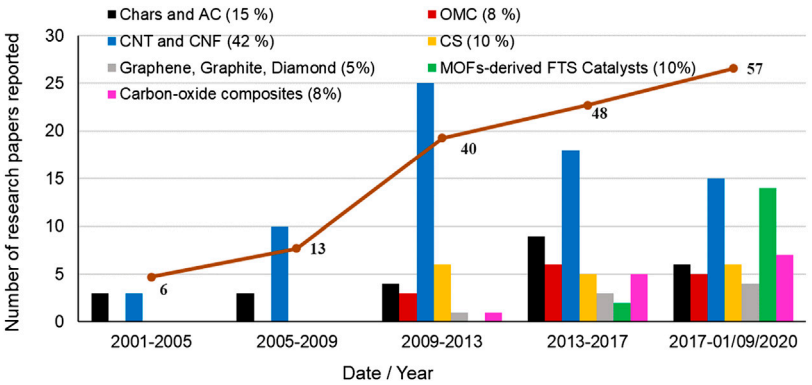

FIGURE 1 | Evolution of the literature reported for different carbon-based supports for FT catalysts in the last 2 decades. The values in parenthesis in the legend indicate the percentage of research papers dedicated to each carbon support. Source: Scopus.

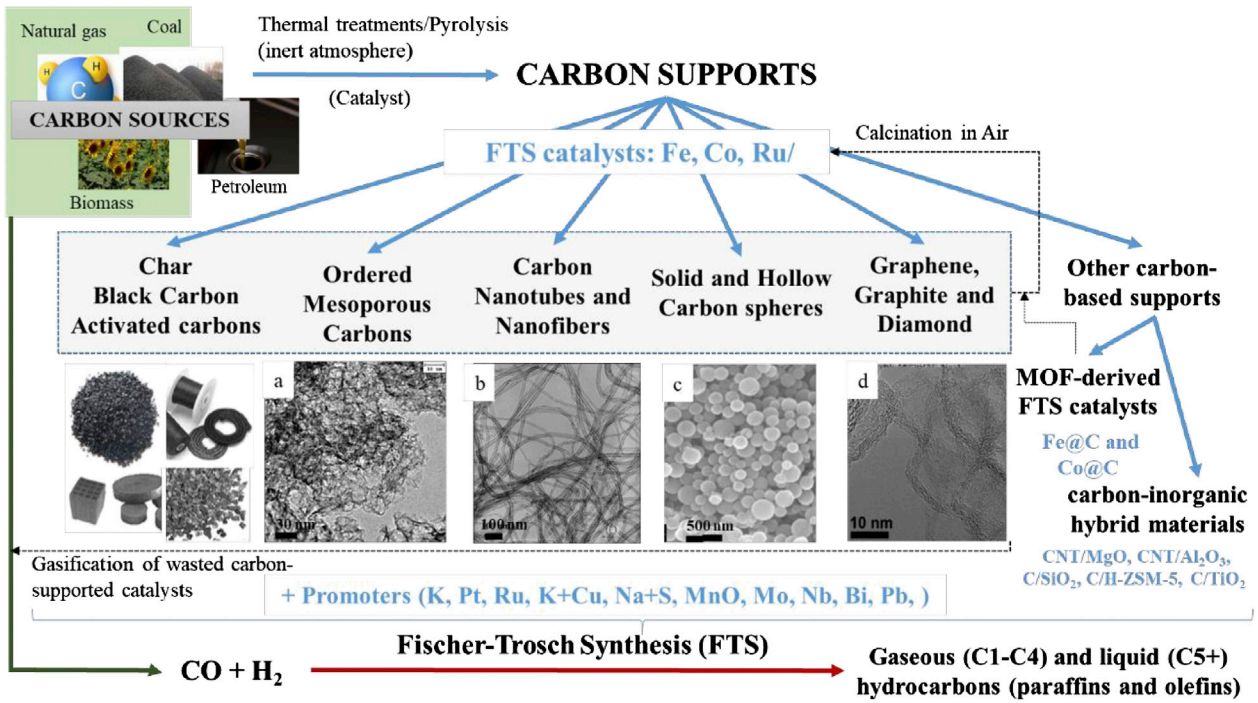

FIGURE 2 | Carbon-based supports for FT catalysts. TEM images A, B and D are adapted from (A) Valero-Romero, M.J., Márquez-Franco, E.M., Bedia, J., Rodríguez-Mirasol, J., and Cordero, T. Hierarchical porous carbons by liquid phase impregnation of zeolite templates with lignin solution. Microporous and Mesoporous Materials, 2014, 196, 68-78; (B) Serp, P., Corrias, M., and Kalck, P. Carbon nanotubes and nanofibers in catalysis. Applied Catalysis A: General, 2003, 253, 337-358; and (C) Chernyak, S.A., Stolbov, D.N., Ivanov, A.S., Klokov, S.V., Egorova, T.B., Maslakov, K.I., Eliseev, O.L., Maximov, V.V., Savilov, S.V. and Lunin, V.V. Effect of type and localization of nitrogen in graphene nanoflake support on structure and catalytic performance of Co-based Fischer-Tropsch catalysts. Catalysis Today, 2020, 357, 193-202. Copyrights 2014, 2003, and 2019, respectively, with permission from Elsevier. TEM image C was derived from (Valero-Romero et al., 2014).

account in the use of carbon materials in catalysis, particularly for the FTS process. Afterward, the different examples from the literature are thoroughly reviewed and discussed by classifying the carbon-based supports according to their properties, structure, and morphology. Otun et al. (2020) have recently reported a review on the use of MOF-derived catalysts in the FTS process. It is also to be noted that several important reviews have appeared on carbon supports for FTS catalysts in the last decade (Yang et al., 2011; Xiong et al., 2015; Ahn et al., 2016). However, this review focusses on the general relationship between the carbon catalysts properties, structure, and morphology and the catalytic performance in the FTS process from the most relevant and recent literature, with special emphasis in some catalyst aspects, such as pore structure, carbon support modification (functionalization and doping), catalyst preparation methods, catalyst stability, reducibility, metal particle size, and location

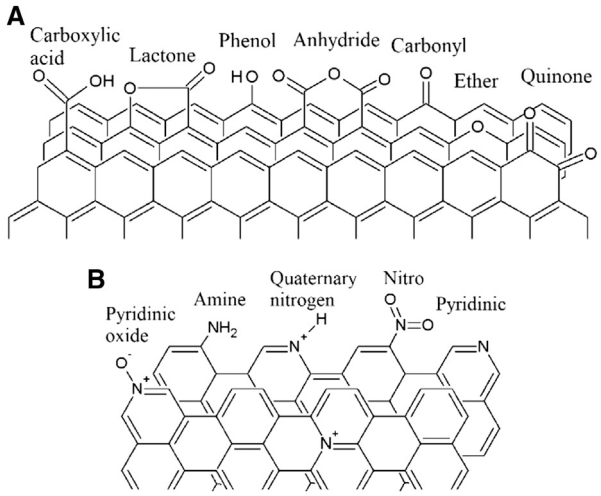

FIGURE 3 | Carbon surface oxygen **(A)** and nitrogen functional groups **(B)**.

and the use of metal promoters. Furthermore, the FTS catalyst performance in terms of FTS activity (CO conversion, metal-time yield (MTY), and turnover frequency (TOF)) and hydrocarbons selectivity is also tabulated for all the carbon-based supports (**Supplementary Tables S1–S7**), compared and deeply discussed. Finally, in the conclusions, some challenges and future perspectives about the industrial feasibility of carbon-based supported FT catalysts are also considered.

GENERAL CONSIDERATIONS ABOUT THE USE OF CARBON MATERIALS AS FT CATALYST SUPPORTS

The interest in carbon-based supports for catalytic applications relies on the great advantages it exhibits, such as good thermal conductivity, high specific surface area, and high thermal and chemical stability under middle operation conditions. On the other hand, in the case that biomass or lignocellulosic residues are used as carbon precursors, it would result in an additional advantage from the economic and environmental points of view (Rosas et al., 2010; Moulefera et al., 2020). Another remarkable feature that carbon supports possess is the possibility of tailoring both their porous structure and surface chemistry, not only during the preparation procedure, but also by further modification *via* different chemical and thermal treatments, which allow bonding extra heteroatoms on their surfaces, such as oxygen and nitrogen surface groups (Figueiredo et al., 1999; Xiong et al., 2014b). **Figure 3** shows typical oxygen (**Figure 3A**) and nitrogen surface groups (**Figure 3B**) on the carbon surface. The nature and concentration of functional groups on the surface of carbon materials have a significant influence on the catalyst dispersion and reducibility given that these surface groups act as anchoring sites for the active phase of supported catalysts and even they can be also the active sites for specific catalytic reactions. Oxygen functional groups are the most important in this context, as they can be formed spontaneously by exposure to the atmosphere or can be further generated or modified by oxidative and/or thermal treatments, in the liquid phase ($(NH_4)_2S_2O_8$, HNO_3, H_2O_2) (Moreno-Castilla et al., 1995; Moreno-Castilla et al., 2000; Palomo et al., 2017), or in the gas phase (O_2, O_3, N_2O, and HNO_3 vapor) (Figueiredo et al., 1999; Valero-Romero et al., 2017). Nevertheless, such treatments, particularly those under severe oxidizing conditions, may cause the partial destruction of the pore structure of the carbon material due to their gasification to CO_2 (and CO).

Regarding the preparation of catalysts for the FTS, it has been reported that metal-support interactions play a crucial role on the activity of the catalysts (Xiong et al., 2015). The main goal of any catalyst support is to enhance metal dispersion, giving rise a higher number of active sites on the catalyst surface as compared to the unsupported catalyst. Due to their inertness nature, especially when they are prepared at high carbonization temperatures, carbon materials produce low interactions with the FT metal-supported catalyst, which was investigated for the first time by Jung et al. (1982). Since then, many publications can be found in the literature on this issue, most of them dealing with the reduction of the metal-support interactions (Hernández Mejía et al., 2018; Van Deelen et al., 2019) and with the possibility of achieving a relatively low metal particle size (Bezemer et al., 2006a). However, these weak metal-support interactions are not always beneficial from the catalytic viewpoint. Metal sintering can also take place under reaction conditions, resulting in the loss of catalytic activity (De Smit and Weckhuysen, 2008). In order to overcome this metal sintering process and to achieve a higher metal dispersion values, several authors studied the modification of the carbon surface with oxygen and nitrogen surface groups, where the FT metal catalyst can be bonded during the impregnation stage (Xiong et al., 2010; Xiong et al., 2014a; Xiong et al., 2014b; Chernyak et al., 2016).

Another important issue relies on the maximum temperature at which carbon supports are stable under the operating conditions required for the FTS process. HT-FTS is usually carried out at 340°C. However, the conditions for iron/cobalt reduction usually require a higher temperature, above 350°C, under hydrogen flow (Chen et al., 2018). On this regard, several authors have observed the evolution of methane during the reduction treatment from 350°C (Bezemer et al., 2006b; Fu et al., 2014b; Valero-Romero et al., 2016). The chemical and thermal stability of a particular carbon-based catalyst depends on several aspects, such as the metal content. Therefore, catalyst stability measurements during reduction for each individual carbon-based catalyst should be addressed in order to determine the optimum reduction temperature.

On the other hand, the use of carbon materials as support of iron catalysts for FTS seems to be beneficial due to the easier formation of iron carbide species, which have been claimed to be the active phases for this reaction (Chen et al., 2008; Wezendonk et al., 2018). On the contrary, the formation of carbides has been reported to be not useful for cobalt FTS catalysts, where the active

TABLE 1 | Textural parameter range values and metal content range for Fe- and Co-supported carbon catalysts used in FTS.

Carbon support	*Co or Fe* wt%	S_{BET}	Total pore volumen cm^3/g	Average pore diameter nm
Activated carbons	10–20	476–990	0.29–0.7	1.1–5.4
Ordered mesoporus carbons	10–20	350–1,326	0.48–1.32	2.5–6.8
Carbon nanotubes and nanofibers	10–20	72–255	0.14–0.67	3.4–17.3
Carbon nanofibers	7.5–14.5	169–300	0.29–0.37	4.8–7.6
Carbon spheres (HTC)	5–15.4	350–465	0.21–0.59	2.8–9.1
Graphene	5–15	250–700	0.9–1.5	n.d.

phase is metallic cobalt. In this line, the formation of cobalt carbides has been reported to lower the catalytic performance of FTS catalysts, giving rise to high amounts of methane (Mohandas et al., 2011). However, carbon materials can be used as support of cobalt catalysts if harsh preparation conditions responsible for the formation of cobalt carbides are avoided.

High pore volume and high mean pore size have been reported to be important parameters to control metal particle size and dispersion on carbon materials for the FTS process (Ahn et al., 2016). A carbon support with a well-developed mesoporous and macroporous structure would have excellent advantages in FT reaction, because larger pores benefit the diffusion of the reactants and hydrocarbon products to and from the catalytic active reaction sites, respectively, thus, enhancing the production for longer hydrocarbon chains.

Finally, another interesting issue to take into account when carbon-based supports are used in the FTS process is the possibility of recovering the metal phase after aging or deactivation of the catalytic system under FTS conditions by a simple combustion or gasification of the carbon support. This type of active phase recovering would also result in a negligible net increase of CO_2 to the atmosphere in the case that renewable biomass had been used as the carbon source in the catalyst preparation, contributing to the reduction of greenhouse gas emissions. In addition to this, the spent (aging or deactivated) catalysts and/or mixtures of residual lignocellulosic biomass and spent catalysts could be used as feedstock in the gasification reactor for the production of syngas for the FTS (**Figure 2**).

CARBON-BASED MATERIALS USED AS CATALYST SUPPORTS FOR FTS

Catalysts Supported on Activated Carbons

The earlier studies on carbon-supported catalysts for the FTS process focused on the use of AC, black carbon, and glassy carbon as supports. These works were dedicated to study how to achieve small metal particles, and hence a high metal dispersion, and to study the metal-support interactions (Xiong et al., 2015). In the last years, however, ACs have been mostly studied as model catalyst supports for the FTS reaction, with the purpose of analyzing the effect of the carbon nature and porous texture as compared with other supports and with the aim of analyzing the effect of metal promoters on the FTS catalyst performance.

The preparation of AC can be achieved using several kinds of lignocellulosic waste as carbon precursor and by different chemical and/or physical activation processes, giving rise to carbon materials possessing different porous textures and surface chemistry. In this sense, a particular surface chemistry can be achieved by choosing the proper activation process (Rodríguez-Reinoso and Molina-Sabio, 1992; Rosas et al., 2008; Rosas et al., 2010). According to the literature, most of the ACs used for research as FTS catalyst supports were mainly commercial (purchased), with coconut shell or almond being the most commonly used carbon precursors, and as for the catalyst preparation method, incipient wetness impregnation (IWI) was commonly selected. In general, Co- and Fe-supported AC catalysts were characterized by a high BET surface area and pore volume and by a high contribution of microporosity (pores <2 nm). **Table 1** shows the textural parameter range values of different carbon-supported catalysts for the FTS process from the literature reviewed in the present work, and **Table 2** summarizes the FTS performance for the most relevant Fe- and Co-supported AC catalysts and their metal loading, and when a metal promoter is used, its loading is also shown. In addition to this, further details are reported in the supporting information file (**Supplementary Table S1**) as their metal particle size, C_2-C_4 olefin/paraffin ratio (O/P), and α value obtained from FTS.

Effect of Metal-Support Interactions and Activated Carbon Porous Texture on FTS

Activated carbon has been used as a model catalyst support in order to study the influence of metal-support interactions on the FTS catalyst performance. In this line, Cheng et al. (2014) studied the preparation of iron catalyst supported on silica and on different carbon-based materials. α-Fe_2O_3 was the main iron phase on silica supports, whereas magnetite (Fe_3O_4) and/or maghemite (γ-Fe_2O_3) were mainly present on the carbon supports. The presence of partially reduced iron oxides was related to the carboreduction of iron oxides during the iron nitrate precursor decomposition stage. These authors also found a higher carburization extent for the carbon-based iron catalysts as compared to the silica-supported counterparts during a CO activation stage. The higher activity found for the carbon-supported catalysts was attributed to the presence of iron carbide-magnetite composites. Among the carbon-based catalysts, the one prepared using AC as support presented the second highest

TABLE 2 | Summary of FTS performance of cobalt and iron catalysts supported on AC.

No.	Catalyst	*Co or Fe wt%*	Promoter *wt%*	T °C	P bar	H_2/CO	SV $m^3kg_{cat}^{-1}$ h^{-1}	MTY[a]	TOF 10^{-3} s^{-1}	X_{CO} %	S/ % C_1	C_{2-4}	C_{5+}	Ref.
1	Fe/AC	10	n.d.[b]	300	20	2.1	16	43.97	n.d.	64	7.8	38.5	53.7	Cheng et al., (2014)
2	15.7Fe/AC	15.7	n.d.	300	20.68	0.9	3	n.d.	n.d.	96.9	34.4	19.1	16.5	Ma et al., (2007)
3	15.7Fe/0.9K/AC	15.7	0.9	280	20.68	0.9	3	n.d.	n.d.	85.7	8.6	34.9	56.5	Ma et al. (2007)
4	Kn/Fe/AC	12.5	1.06	240	20	2	16	25.57	n.d.	62	9.2	18.8	72.1	hernavskii et al. (2018)
5	Fe/Kn/AC	8.5	0.9	240	20	2	16	52.88	n.d.	87.2	9.7	20	70.3	Chernavskii et al., (2018)
6	15Co/AC	15	0	230	20	2	0.5	n.d.		29.7	25	14.6	60.4	Chen et al. (2012)
7	15Co/MC	15	0	230	20	2	0.5	n.d.	9.4	73.1	19.1	10.1	70.8	Chen et al. (2012)
8	4Zr-10Co/AC	12.5	Zr: 4	250	25	2	500 h^{-1}	n.d.	n.d.	86.4	14.2	14.8	71	Wang et al. (2008)
9	0.2La4Zr-10Co/AC	14	Zr: 4 La: 0.2	250	25	2	500 h^{-1}	n.d.	n.d.	92.3	11.5	13.8	74.7	Wang et al. (2008)
10	30Co/AC-2	30	n.d.	260	5	2	8	n.d.	n.d.	100	54.4	20.7	24	Jiang et al. (2020)
11	30Co0.4Na/AC-2	30	0.4	260	5	2	8	n.d.	n.d.	98.7	49.9	16	34.1	Jiang et al. (2020)
12	30Co10Mn/AC-2	30	10	260	5	2	8	n.d.	n.d.	83.3	15.3	20.7	63.9	Jiang et al. (2020)
13	30Co10Mn0.4Na/AC-2	30	Mn: 10 Na:0.4	260	5	2	8	n.d.	n.d.	73.8	14.2	28.4	57.4	Jiang et al. (2020)

[a]*Metal-time yield (10^{-5} mol_{CO} $g_{Co,Fe}^{-1}s^{-1}$).*
[b]*n.d.: not determined.*

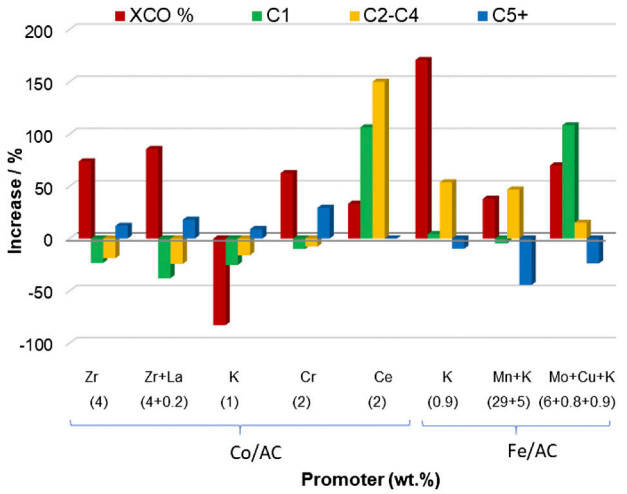

FIGURE 4 | Increase in CO conversion (except for Ce and Mo+Cu+K, that is syngas conversion) and in selectivity to C_1, C_2-C_4, and C_{5+} hydrocarbons values for different promoted Co/AC and Fe/AC catalysts compared to the ones of the unpromoted counterpart. The title in the *x*-axis indicates the promoter and its concentration in *wt*%. Data are adapted from refs. (Ma et al., 2004; Ma et al., 2006; Ma et al., 2007; Wang et al., 2008; Chen et al., 2012; Tian et al., 2017; Zhao et al., 2019). Reaction conditions: Zr and Zr+La, 250°C, 25 bar, H_2/CO = 2, 500 h^{-1}; K, 230°C, 20 bar, H_2/CO = 2, 0.5 m^3 kg^{-1} h^{-1}; Cr, 220°C, 30 bar, H_2/CO = 2, 2,000 h^{-1}; Ce, 240°C, 24 bar, H_2/CO = 2, 650 h^{-1}; K, 280°C, 20 bar, H_2/CO = 0.9, 3 m^3 kg^{-1} h^{-1}; Mn+K, 320°C, 20 bar, H_2/CO = 1, 3,000 h^{-1}; and Mo+Cu+K, 320°C, 20 bar, H_2/CO = 0.9, 3 m^3 kg^{-1} h^{-1}.

activity, being only surpassed by the one prepared using carbon nanotubes as support. The Fe/AC catalyst showed a CO conversion of 64%, with high selectivity to C_{5+} hydrocarbons (53.7%) (entry 1, **Table 2**) and a relatively high O/P ratio, 1.2. Similar conclusions were found by Jiang et al. (2017), who also compared the preparation of iron catalysts on ACs and different inorganic supports.

Fischer–Tropsch reaction is structure sensitive, being the conversion and the product distribution affected by the particle size of the active phase and by the porous texture of the support. On this issue, Fu et al. (2014b) studied the effect of pore size on the activity of cobalt-based catalysts supported on ACs and CNTs for FTS. The extent of reduction of Co/AC catalyst was the lowest, presumably due to the higher metal-support interactions, which gave rise to the lowest CO conversion value. In addition, this catalyst presented the highest and the lowest selectivity to methane and to C_{5+}, respectively. These catalytic features were justified based on the presence of a narrow microporosity and a low cobalt particle size, which resulted into a higher diffusion rate for H_2 as compared to CO, resulting in a high H_2/CO ratio inside the pores. Likewise, Chen et al. (2012) compared two AC supports with different average pore sizes (5.2 vs 2.5 nm). The catalytic results were in line with the findings reported by Fu et al. (2014b). The mesoporous carbon-based catalyst (15Co/MC) presented more than twice the CO conversion value than the one of the microporous carbon-based catalyst (15Co/AC), 73.1% vs 29.7%, respectively (entries 6 and 7, **Table 2**). In addition, the former presented a higher selectivity to C_{5+} hydrocarbons and a lower selectivity to methane.

Effect of Metal Promoters on FTS

The most commonly used promoters for Fe/AC catalysts are K, Mn, and Mo. On the other hand, K, Zr, Ce, Cr, Na, and Mn have been studied as catalyst promoters for Co/AC catalysts. **Figure 4** represents the increase in the CO conversion and selectivity to the main reaction products values for some Co- and Fe-supported catalyst on AC in comparison with those for the unpromoted counterpart.

Effect of Promoters in Iron-Based Catalysts

Some authors have reported an enhancement of CO conversion under certain K promotion amounts in Fe/AC catalysts. For

example, Ma et al. (2007) observed that a K content of 0.9 *wt*% produced an improvement of CO conversion as compared to the unpromoted catalyst (entries 2 and 3, **Table 2**). The selectivity to CO_2 was also increased with K promotion, due to the enhancement effect of K over the WGS reaction. Additionally, methane selectivity was reduced, whereas longer chain hydrocarbons were formed. Furthermore, the O/P ratio was also increased from 0.1 to 5 for C_2-C_4 short hydrocarbons. In this line, Chernavskii et al. (2018) observed that the catalyst prepared by first loading iron and then potassium as promoter showed a CO conversion value of 62%. However, when following a reverse sequence order for metal deposition (first K, then Fe), the CO conversion value reached a value of 87.2% (entries 4 and 5, **Table 2**). These differences in CO conversion were attributed to the magnetite particle size formed in each catalyst. The authors claimed that the alkalinization of the AC, prior to iron impregnation, increased the number of oxygen-containing groups on the AC surface, giving rise to the formation of more nucleation centers for Fe^{3+} ions and consequently, smaller magnetite particles were formed when K was firstly loaded on the AC.

Ma et al. (2006) studied the effect of Mo loading (6 and 12 *wt*%) on the properties and the catalytic performance of Fe-Cu-K-supported AC catalysts. The addition of Mo significantly inhibited iron reduction, which was attributed to the existence of iron-molybdenum mixed oxides, which were more difficult to reduce. Promotion with 6 *wt*% Mo showed a lower initial syngas conversion value (58%), which increased with time-on-stream up to 81% and remained unaltered for more than 80 h, which was attributed to the Mo capability of inhibiting iron sintering (Zhao et al., 1994). The addition of Mo also increased the selectivity to methane and C_2-C_4 hydrocarbons, lowered the selectivity to C_{5+}, and reduced the O/P ratio (**Figure 4**).

Tian et al. (2017) studied the effect of Mn as promoter for Fe/AC catalysts. Prior to iron impregnation, the AC support was oxidized with $KMnO_4$. During the $KMnO_4$ treatment, a redox reaction between the carbon surface and the $KMnO_4$ occurred, yielding a uniform MnO_2 layer covering the surface of the AC-oxygenated surface groups. Additionally, K was deposited on the carbon surface. The presence of K and Mn in the catalysts resulted in an enhancement of the CO conversion value (37%, with respect to that of the unpromoted catalyst) (**Figure 4**). Furthermore, the selectivity to main reaction products were also affected by the promoters, being observed an increase of a 46% in the C_2-C_4 selectivity and a decrease of a 44% in the C_{5+} selectivity, with respect to those of the unpromoted catalyst. In addition, the O/P ratio outstandingly increased from 0.65 for the unpromoted catalyst to 4.88 for the promoted one. The promotion effect of Mn was associated to the synergistic effect of MnO and Hägg carbides in enhancing CO adsorption and dissociation and K helped to form iron carbides on the AC surface.

In summing up, K promotion of Fe-based catalysts resulted in the increase of the CO conversion, when it was loaded in certain controlled amounts, and an enhancement of the activity for WGS. Additionally, the olefin/paraffin ratio and the C_{5+} selectivity values were increased. Mn and K promotion enhanced the CO conversion value and gave rise to a higher C_2-C_4 olefin production. On the other hand, the addition of Mo as a promoter has been shown to lower the initial activity but also to enhance the catalyst stability.

Effect of Promoters in Cobalt-Based Catalysts

Ma et al. (2004) studied the effect of Zr, K, and Ce as promoters for Co/AC catalysts. K acted as a strong poison for the catalyst, decreasing syngas conversion and methane selectivity, as compared to the unpromoted catalyst (**Figure 4**), which was attributed to the possible coverage of cobalt active sites by K. On the contrary, both Zr and Ce had a positive impact in the catalytic activity. Zr promoted CO conversion without largely modifying the hydrocarbon selectivity values and the activity for WGS. Ce enhanced both syngas conversion and activity for WGS and increased the methane and C_2-C_4 selectivity values. The positive effects of Zr and Ce as promoters were attributed to the improvements found in cobalt dispersion and to the enhanced interaction between cobalt and the oxygen surface groups resulting from the addition of Zr and Ce to the AC.

Based on these results, Wang et al. (2008) conducted an in-deep research focused on studying the effect of lanthanum in Zr-promoted Co/AC catalysts. The active phase of the catalysts was composed by 10 *wt*% Co, 4 *wt*% Zr, and different amounts of La. The presence of La in the catalyst increased the cobalt reducibility at low La loadings. However, La was detrimental at higher loadings. The CO conversion value increased from 86.4 to 92.3% when the content of La increased from 0 to 0.2% (entries 8 and 9, **Table 2**) and the C_{5+} selectivity was higher compared to the unpromoted catalyst.

Promotion of Co/AC catalysts with Cr (0–5*wt*%) resulted in the reduction of the cobalt species crystal size, excepting for the highest Cr content (Zhao et al., 2019). Additionally, the extent of reduction of the catalyst was also enhanced by the presence of Cr. Structural analyses of the active sites showed that the presence of Cr suppressed the formation of cobalt carbides. The reaction results showed an increase in both the CO conversion and the selectivity to C_{5+} values for a Cr content of 2% (**Figure 4**). Furthermore, the O/P ratio was lower after Cr promotion. The authors attributed these catalytic features to the higher H_2-rich surface environment caused by Cr promotion in the catalyst, which facilitated the α-hydrogen addition step and suppressed the β-hydride elimination and CO insertion steps, simultaneously.

Jiang et al. (2020) studied the promotion effect of Mn and Na on Co/AC catalysts. The unpromoted catalyst showed a CO conversion of 100% with a very high selectivity to methane (54.4%). Na promotion slightly decreased the CO conversion and methane selectivity values (98.7 and 49.9%, respectively). On the other hand, the presence of Mn slightly decreased the CO conversion value to 83.3% and noticeably the methane selectivity to 15.3%. The simultaneous presence of Mn and Na in the catalyst further reduced the CO conversion value from 83.3 to 73.8% as compared to the one for the catalyst just promoted with Mn (entries 10–13, **Table 2**). Furthermore, the O/P ratio experienced a noticeable increase, from 0.65 for the catalyst promoted with Mn to 1.54, when using together Na and Mn as promoters. Another feature observed in this work was the

capacity of Na to enhance the WGS reaction activity in cobalt catalysts.

Catalysts Supported on Ordered Mesoporous Carbons

The presence of narrow micropores in ACs resulted in internal diffusion limitations for reagents and products when they were used as catalyst supports for the FT process (Chen et al., 2012; Fu et al., 2013; Fu et al., 2014b). To overcome this problem, the use of carbons with a wider porous structure, such as ordered mesoporous carbons (OMCs), has been studied. Co and Fe supported on OMCs are characterized by exhibiting an ordered and well-defined mesoporous texture, with a large pore volume and average pore diameter in the range of 2–6 nm (**Table 1**). The preparation of OMCs can be carried out by two approaches: (1) the hard-template method, in which an inorganic material, such as SBA-15, is used as template of a carbon source, and then it is removed by HF/NaOH treatments. (2) The soft-template method, so-called solvent induced self-assembly (EISA), which involves the use of an organic directing agent, such as Pluoric F127. In this case, the template is removed during the carbonization step. **Supplementary Table S2** summarizes the FTS performance for the most relevant Fe and Co/OMC catalysts.

Effect of the OMC Preparation: The Hard-Template Method

Knox et al. (1986) were pioneers in reporting the preparation of OMCs by the hard-template method. Among the reported OMC, CMK-3, a hexagonally structured OMC, is the most commonly used OMC support for FTS catalysts. This material was first synthetized by Jun et al. (2000), using SBA-15 as the hard template and sucrose and H_2SO_4 in water solution as the carbon source.

For example, Oschatz et al. (2016b) prepared OMC-supported iron catalysts, using CMK-3. The active phase (Fe, Na, and S) loading was carried out by IWI. Afterward, the catalysts were stabilized at different temperatures. Hematite nanoparticles were found for calcination temperatures up to 500°C. Above this temperature, iron carbide species and metallic iron were found. Additionally, iron particles wrapped by a graphite shell forming core-shell structures were found at temperatures above 800°C, which lowered the catalytic activity. The lowest selectivity to methane and the highest selectivity to C_2-C_4, 13.4 and 59.5%, respectively, were achieved for the catalyst carbonized at 500°C (entry 1, **Supplementary Table S2**). An outstanding O/P ratio value of 10 was attributed to the efficient promotion of the catalyst with S.

Likewise, Kang et al. (2017) studied the preparation of iron catalyst for FTS using CMK-3 as support. In this case, metal loading was carried out by directly grounding the CMK-3 support with iron nitrate (in a physical mixture). The catalyst was stabilized under CO atmosphere. Uniformly distributed Fe_5C_2 nanoparticles were found in the pore system of the CMK-3. After a long induction period, the catalyst reached a 91.4% steady-state CO conversion value. The product distribution remained unaltered during the induction period, showing selectivity values to CH_4, C_2-C_4, and C_{5+} of 23.3, 68.3, and 8.3%, respectively (entry 2, **Supplementary Table S2**).

Co-supported CMK-3 catalysts were also studied by Fu et al. (2013) and Li et al. (2019). The loading of cobalt (20%) was carried out by ultrasonication-assisted IWI followed by stabilization at 200°C (Fu et al., 2013) and 350°C (Li et al., 2019). The average pore size of the catalyst was smaller for the sample treated at the highest temperature. However, similar CoO_x crystallite sizes were found for both catalysts. The CO conversion values were also very similar for both catalysts. Nevertheless, the catalyst carbonized at 200°C (Fu et al., 2013) yielded a higher production of diesel range hydrocarbons than gasoline ones, 48 vs 35%, whereas the catalyst stabilized at 350°C (Li et al., 2019) presented a higher selectivity to hydrocarbons in the gasoline range (entries 10 and 11, **Supplementary Table S2**).

Zhao et al. (2020) studied the preparation of OMC-supported cobalt catalysts. In this case, for the preparation of the OMC support, SBA-16 was used as the hard template and furfuryl alcohol (FA) and oxalic acid in ethanol solution were used as carbon source. After a carbonization stage, HF was used to eliminate the silica template and cobalt loading was carried out by IWI using cobalt nitrate. The CoO crystallite size slightly increased with increasing the support carbonization temperature due to the diminishment of the metal-support interactions. The catalyst presenting the highest catalytic activity was the one prepared using the OMC carbonized at the highest temperature (1,300°C), due to lower cobalt support-interactions and higher reducibility of the cobalt species. This catalyst showed a CO conversion value of 49.7% and a selectivity to C_{5+} hydrocarbons of 74% (entry 12, **Supplementary Table S2**).

Effect of the OMC Preparation: The Soft-Template Method

Liu et al. (2017) studied the preparation of OMC-based cobalt FTS catalysts in a single step using Pluoric F127 as directing agent, resorcinol and formaldehyde as carbon sources, and cobalt nitrate as metal precursor. FTS experiments showed a CO conversion value of 30.2%, with selectivity values to methane and to C_{5+} hydrocarbons of 15.2 and 81.5%, respectively (entry 13, **Supplementary Table S2**). The catalytic activity reported in this study is lower than those reported by other studies working under similar operation conditions (Fu et al., 2013; Li et al., 2019; Zhao et al., 2020). A possible explanation to this lower catalytic performance reported by Liu et al. (2017) could be the relatively high cobalt particle size and the lack of accessibility to these cobalt particles due to the deep embedment in the carbon support during the synthesis procedure.

Tailoring OMC Supports for Controlling Metal Crystallite Size

Metal particle size is a highly important Fischer–Tropsch catalyst feature, and thus, different catalyst synthesis strategies have been proposed to control the size of the active phase on OMC supports.

Yang et al. (2012) carried out a study dedicated to control the cobalt particle size in OMC-supported FTS catalysts by the modification of the OCM synthesis procedure. For this aim, different amounts of FA (carbon source) were introduced in

SBA-15 (hard template). Cobalt loading was carried out by IWI using cobalt nitrate. The average size of the cobalt particles on the catalyst increased with increasing the FA content. Additionally, the allocation of the cobalt particles was shifted to the outer surface when increasing the FA content. The highest activity was achieved for the catalysts prepared using a 50% FA (CO conversion value of 45.07%, with methane, C_2-C_4, and C_{5+} selectivity values of 24.6%, 11.31%, and 64.09%, respectively), entry 14, **Supplementary Table S2**.

More recently, Yang et al. (2014) carried out a study to control the cobalt particle size of FTS catalysts using an N-doped OMC as catalyst support. Nitrogen incorporation was carried out by a postsynthetic route using cyanamide. The metal loading was carried out by IWI using cobalt nitrate in acetone solution. The authors found that the higher the N content in the support, the smaller the cobalt particle size. This fact was associated to the capacity of N of improving dispersion of cobalt metal species and forming more uniform particles. The TOF values and the catalytic activity increased with increasing the cobalt particle size up to a 10 nm. Above this value, the TOF remained constant, but a decrease in the catalytic activity was observed.

Likewise, Sun et al. (2012) investigated the preparation of OMC-supported catalysts with different iron crystallite sizes for the FTS reaction. The preparation of the OMC-based catalysts was carried out using Pluronic F127 as directing agent, resol as carbon source, and iron nitrate as metal precursor. Different amounts of a chelating agent, acetylacetone, were used with the aim of controlling the metal particle size. The iron particle sizes were reduced when increasing the acetylacetone content. The catalyst presenting the smallest iron particle size (8.3 nm) showed the highest CO conversion value (90.1%), with a low selectivity to CO_2 (13.3%) and very high selectivity to C_{5+} hydrocarbons (>68%) (entry 3, **Supplementary Table S2**).

Cheng et al. (2014) controlled the iron particle size by varying solvent (water or acetone) used for the metal impregnation process. The catalyst prepared using water as iron nitrate solvent showed an average crystallite size four times larger than the one prepared using ethanol as solvent. The catalytic results were in line with those reported by Sun et al. (2012), being observed a higher CO conversion for the catalyst presenting a smaller iron particle size (49.7% and 38.5% for the catalysts prepared with ethanol and water, as impregnation solvent, respectively), entries 4 and 5, **Supplementary Table S2**.

Effect of Metal Promoters on FTS

The use of promoter has been also studied in OMC-supported Fischer–Tropsch catalysts. Cheng et al. (2015) reported that the use of Na as catalyst promoter reduced the average iron phase crystallite size. The reaction results showed that the presence of Na reduced the CO conversion value. However, a selectivity to C_{5+} up to 78.9% was obtained for a Na to Fe molar ratio of 0.3 (entries 6 and 7, **Supplementary Table S2**). Na promotion also increased the C_2-C_4 O/P ratio more than five times the value of the unpromoted catalyst. Similarly, Oschatz et al. (2016a) studied the effect of Na and S as promoters on Fe/OMC catalysts. The reaction results showed that CO conversion was lower for the Na-promoted catalyst than for the Na-S-promoted one. Additionally, the simultaneous presence of Na and S enhanced the selectivity to C_2-C_4 as compared to that of the Na-promoted catalyst (entries 8 and 9, **Supplementary Table S2**). The O/P ratio showed an outstanding value of 10 in both promoted catalysts studied.

Catalysts Supported on Carbon Nanotubes and Carbon Nanofibers

Typically, multiwall carbon nanotubes or carbon nanotubes (MWCNTs or CNTs) and carbon nanofibers (CNFs) are grown by the decomposition of carbon-containing compounds on a metal catalyst particle. By modifying the carbon source, as well as the chemical composition and morphology of the catalyst, it is possible to synthesize CNTs and CNFs with variable crystallinity degrees, sizes, and shapes. The main difference between nanotubes and nanofibers consists in the presence of a hollow cavity for CNTs. Single-wall carbon nanotubes (SWCNTs) are ideally made of a perfect graphene sheet rolled up into a cylinder and closed by two caps (semifullerenes), whereas MWCNTs are formed by concentric SWCNTs with increasing diameter. On the other hand, CNFs are made of domains of sp carbon atoms (graphene-like layers) bounded by sp^3 carbons or other terminal atoms or groups of atoms (Serp et al., 2003).

Typically, Co- and Fe-supported CNTs used in FTS have total surface areas ranging between 70 and 255 m^2/g (**Table 1**). The pores in these structures can vary from inner hollow cavities with diameters within the micropore range (less than 2 nm) and mesopore range (between 3 and 6 nm) to aggregated pores (>15 and up to 40 nm) in a larger extent, which are formed by interaction of isolated MWCNTs. The length of these structures can range from few microns to several millimeters. Furthermore, the external diameter of the MWCNT can reach 100 nm (Yang et al., 2001). In the case of Co- and Fe-supported CNFs, the surface area can range between 170 and 300 m^2/g, no micropores are found, and the mesopore volume ranges between 0.5 and 2 cm^3/g (De Jong and Geus, 2000). The external diameters of CNF are generally higher than the ones presented by nanotubes and can reach 500 nm (Serp et al., 2003). The detailed similarities and differences in adsorption, electronic, thermal, and mechanical properties, and growth mechanisms of CNTs and CNFs have been extensively reviewed (De Jong and Geus, 2000; Serp et al., 2003; Lehman et al., 2011).

Given that CNTs and CNFs are relatively inert materials, it is necessary to modify their nature by introducing surface functional groups in order to attain high stabilization and dispersion of the metal particles on their surface. In addition to this, these materials have been considered as model supports in the FTS reaction process. Therefore, the effect of CNT and CNF functionalization, catalyst preparation methods, metal particle size, pore size, pore confinement, and the incorporation of metal promoters on the catalysts structure and FTS performance have been investigated.

Effect of CNT and CNF Functionalization and Thermal Treatments

Several studies have been dedicated to study the surface functionalization of CNTs either by introduction of oxygen or

TABLE 3 | FT performance of unpromoted Co and Fe catalysts supported on CNTs and CNFs after different catalyst preparation methods.

No.	Catalyst	Catalyst preparation method	*Co or Fe wt%*	T°C	P bar	H_2/CO $m^3kg_{cat}^{-1}$ h^{-1}	SV	MTY[a]	TOF 10^{-3} s^{-1}	X_{CO} %	S/ % C_1	C_{2-4}	C_{5+}	Ref.
1	IWN13	IWI, water	13	210	35	2	n.d.[c]	4.35	22.5	66	n.d.	n.d.	81.7	Bezemer et al. (2006a)
2	IEN8	IWI, ethanol	7.5	210	35	2	n.d.	3.7	13.5	65	n.d.	n.d.	76.1	Bezemer et al. (2006a)
3	Co/CNT-IM	IWI	13.2	225	8	2	3,840 h^{-1}	n.d.	n.d.	25.9	30.6	n.d.	62.1	Xiong et al. (2011)
4	Co/CNT-DP	HDP	4.3	225	8	2	3,842 h^{-1}	n.d.	n.d.	9.9	23.5	4.4	72.1	Xiong et al. (2011)
5	Co/CNT-IWI	IWI	17.65	200	10	2	1,066 h^{-1}	n.d.	n.d.	65	30.5	22.5	45	Almkhelfe et al. (2018)
6	Co/CNT-F	Fenton	15.7	200	10	2	1,066 h^{-1}	n.d.	n.d.	80	9.4	18.4	70.2	Almkhelfe et al. (2018)
7	cs_Co^{100}/CNT	Colloidal synthesis	10	220	1	2	2002 h^{-1}	4.85	n.d.	2.47	39.5	34.5	26	Ismail et al. (2019)
8	ci_Co^{100}/CNT	IWI	10	220	1	2	2003 h^{-1}	4.22	n.d.	1.47	37	27	36	Ismail et al. (2019)
9	Co800	IWI-TT-800°C[b]	10.7	240	20	2	5	11.6	100	66.7	28.9	n.d.	61	Chernyak et al. (2020)
10	Co/RCR	Reduction-carburization-reduction	8.3	220	10	2	2	0.32	n.d.	n.d.	4.3	2.6	93.2	Ghogia et al. (2020)
11	hcp-Co/CNF	Thermal decomposition	6.2	220	10	2	2	0.67	5.3	n.d.	3.9	2.3	93.8	Ghogia et al. (2020)
12	fcc-Co/CNF	Thermal decomposition	8.3	220	10	2	2	0.53	3.4	n.d.	5	2.7	92.3	Ghogia et al. (2020)
	Fe/CNT-IW	IWI	12.1	270	8	2	2,120 h^{-1}	37.2	n.d.	80	14.6	42.1	43.3	Bahome et al. (2005)
14	Fe/CNT-DPU	HDP (urea)	10.5	270	8	2	2,120 h^{-1}	46.9	n.d.	76.7	15.4	39.8	44.7	Bahome et al. (2005)
15	Fe/CNT-IWI	IWI	18.47	250	10	2	1,066 h^{-1}	n.d.	n.d.	57	42	10	37.5	Almkhelfe et al. (2018)
16	Fe/CNT-F	Fenton	16.35	250	10	2	1,066 h^{-1}	n.d.	n.d.	68	12.5	21.6	62.9	Almkhelfe et al. (2018)
17	Fe800	IWI-TT-800°C[b]	10.4	300	20	1	5	20.3	0.9	71.4	6.2	10.3	57.3	Chernyak et al. (2020)
18	Fe-*in*-CNT	WI	10	270	51	2	20	n.d.	n.d.	40	12	41	29	Chen et al. (2008)
19	Fe-*out*-CNT	WI	10	270	51	2	20	n.d.	n.d.	29	15	54	19	Chen et al. (2008)
20	Fe/CNT-in	IWI	10.2	350	20	1	17	28	436	14.4	34.2	50.8	15	Gu et al. (2019)
21	Fe/CNT-out	IWI	10.3	350	20	1	17	16	403	24.8	28.5	50.7	20.8	Gu et al. (2019)

[a]*Metal-time yield (10^{-5} mol_{CO} $g_{Co,Fe}^{-1}s^{-1}$).*
[b]*Thermal treatment in inert conditions (TT).*
[c]*n.d.: not determined.*

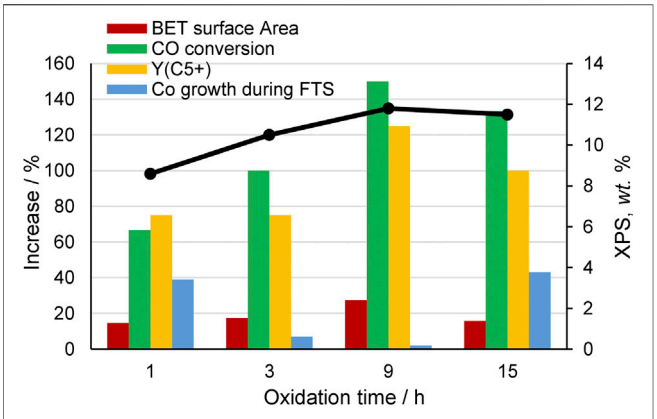

FIGURE 5 | Amount of oxygen measured by XPS and increase of BET surface area, CO conversion, C_{5+} yield, and Co particle growth during FTS for Co/CNT catalysts when CNTs were oxidized with HNO_3 for 1, 3, 9, and 15 h with respect to the catalyst supported on pristine CNTs. Data were adapted from ref. (Chernyak et al., 2016).

nitrogen surface groups and the influence of these groups on the structure and the catalytic performance of CNF- and CNT-supported FT catalysts. **Table S3** summarizes the most relevant results regarding the FT performance of unpromoted Co and Fe catalysts supported on CNTs and CNFs after different functionalization pretreatment conditions. In most cases, the optimum catalyst observed from each study is tabulated when different oxidizing conditions are studied. For example, Chernyak et al. (2016) investigated the CNT oxidation prior to Co impregnation by a treatment with ~70 *wt*% HNO_3 for different reaction times and tested them in FTS at 190°C, 1 bar, H_2/CO of 2 and space velocity (SV) of 2.2 $m^3kg_{cat}^{-1}h^{-1}$. **Figure 5** compares the results of the cobalt catalyst pretreated in acid for 1, 3, 9, and 15 h with respect to the untreated Co/CNT catalyst. Optimal oxidation conditions were found after 9 h of acid reaction, resulting in Co/CNTs with the highest porous development, oxygen content, and an optimal cobalt particle size of 4.2 nm was obtained after catalyst impregnation and activation, which also presented the highest FTS activity, C_{5+} hydrocarbons yield, and lower Co sintering during FTS. These results are in line with the research of Trépanier et al. (2009b) who investigated different nitric acid pretreatment temperatures (entries 1–3, **Supplementary Table S3**). The most severe acid-treatment conditions (15 h) produced the deterioration of the CNT material, resulting in a significant decrease of the BET surface area, which is in line with other studies (Fu et al., 2014a; Nakhaei Pour et al., 2018). The catalytic activity was also maximized for Co and Ru catalysts supported on oxidized CNTs with optimal HNO_3 concentrations of 70 and 68 *wt*%, respectively (Kang et al., 2009; Vosoughi et al., 2016) (entries 5 and 14, **Supplementary Table S3**). Likewise, pretreatment of CNTs with H_2O_2 (Nakhaei Pour et al., 2018) and H_2O_2 + O_3 (Karimi et al., 2014) yielded Co/CNT catalysts with higher FTS activity, higher selectivity to C_{5+} hydrocarbon fraction, and high stability compared to the untreated catalyst. Optimal preparation conditions were investigated for oxidizing CNTs for cobalt catalyst preparation with H_2O_2 and sonicated *via* a pulsing method (entry 6, **Supplementary Table S3**) (Nakhaei Pour et al., 2018). It appeared that sonication in a short time (10 s) resulted in Co/FCNTs-10 catalyst with a remarkably narrow cobalt particle size distribution.

On the other hand, Eschemann et al. (2015) reported that CNT oxidation adversely influenced the FT performance of the Co/CNT catalysts, with significantly lower cobalt-time yields (CoTYs) and C_{5+} selectivity for the cobalt catalyst pretreated in acid for LT-FTS. They ascribed the different catalytic performance to an increase in hexagonal-close-packed crystal structured (hcp-Co) on pristine CNTs compared to the surface-oxidized CNTs. Hcp-Co phase has been experimentally confirmed to be more active and selective to C_{5+} than the cubic Ghogia et al. (2020). Likewise, more recently, Van Deelen et al. (2020) reported a negative effect on the catalytic performance of presynthesized 6 nm colloidal CoO nanocrystals supported on oxidized CNTs tested under similar FTS conditions (entries 10 and 11, **Supplementary Table S3**). The different catalytic performance was ascribed to the low crystalline metallic Co content on oxidized CNTs than on pristine CNTs.

In addition, it has been reported that the nature of oxygen functional groups on CNTs and CNFs can be modified by the application of different thermal treatments. In this regard, Chernyak et al. (2016) investigated the thermal stability of surface functional groups on oxygen-functionalized CNTs after different thermal treatment conditions and stages (catalyst carbonization, catalyst activation or reduction, and FTS reaction). They observed that most of the carboxylic groups decomposed in the first stage carried out at 400°C, whereas a decrease in content of all oxygen functional groups was mainly observed after the catalyst reduction stage at 400°C, specially due to the decomposition of hydroxyl and ether groups. Only the more thermally stable oxygen surface groups, such as quinones and phenols, remained stable on the support surface after 70 h of FTS reaction at 190°C, 1 bar, H_2/CO of 2 and SV of 2.2 $m^3kg_{cat}^{-1}h^{-1}$. The authors highlighted that these oxygen surface groups together with the CNT defects and the CNT surface geometry effects might have prevented Co from sintering during the catalytic reaction, given that the catalysts were not deactivated with time-on-stream. In contrast, nitrogen groups were significantly more stable upon heating. Thermal treatment of nitrogen-containing CNTs at 600°C only caused a minor loss of pyridine and quaternary type nitrogen groups Kundu et al. (2010).

Xing et al. (2013) compared the FTS performance of Co-based catalysts supported on oxidized and thermally treated CNTs in inert atmosphere at 450, 650, and 900°C. The results of the FTS reaction revealed that the oxidized Co/CNT catalysts treated at 650°C (Co/CNTs-650) presented the highest CO conversion (89.3%), the lowest CH_4 selectivity (8.4%), and the highest C_{5+} hydrocarbon selectivity (83.7%) among all the tested catalysts (entry 12 and 13, **Supplementary Table S3**). They claimed that it was possible to partially remove the oxygen-containing functional groups from the surface of CNTs by controlling the thermal treatment temperature, while keeping the integrity of inner CNT walls and thus controlling the preferential encapsulation of cobalt

clusters (80% for Co/CNTs-650) with optimal size (5–10 nm) inside the CNTs.

The role of oxygen- and nitrogen-functionalized CNTs as supports for Fe-based FTS catalytic systems was also investigated. Malek Abbaslou et al. (2009) studied the acid treatment (35 *wt*% HNO_3) of CNTs with different BET surface areas at 25 and 110°C. These materials were used as support for the preparation of Fe-based catalysts for FTS. The resultant Fe/CNT catalysts revealed that the more severe the acid-treatment temperature and the higher BET surface area (46 m^2/g for Fe/ha-lsa-C and 200 m^2/g Fe/ha-hsa-C) of the CNT-supported Fe catalysts, the higher the activity, stability, and selectivity to C_{5+} hydrocarbons of the catalysts (entries 16 and 17, **Supplementary Table S3**).

Schulte et al. (2012) compared N-doped CNTs (N-CNTs) with conventional oxygen-functionalized CNTs as supports for iron catalyst for FTS. The supports were pretreated by gas phase NH_3 or HNO_3 vapor, respectively. They observed that doping CNTs with nitrogen enhanced Fe species dispersion and, as a result, an almost two-fold higher FT activity was found for Fe supported on the N-doped CNT (20Fe/N-CNT) as compared to the one of Fe supported on the oxidized CNT (20Fe/O-CNT) (entries 19 and 20, **Supplementary Table S3**). They suggested that high electric conductivity and good metal dispersion ability were the main advantages for the N-NCT support. These results were later supported by Chew et al. (2016).

On this context, Xiong et al. (2014a) reported a novel approach to prepare N-CNTs by a postdoping method in which acetonitrile was passed over CNTs at 700 and 900°C, and N atoms were homogeneously deposited on the CNT surface (so that the resulting N-CNTs contained 1.75 *wt*% N). The N-CNTs were later treated with HNO_3 prior to iron deposition. The resulting catalysts were tested in the HT-FTS reaction (entry 18, **Supplementary Table S3**). The surface N was in the form of pyridinic, quaternary, and pyridinic oxide type nitrogen. They observed that the Fe/N-CNT catalysts were more difficult to reduce than the corresponding Fe/CNT catalysts due to the prefunctionalization with nitrogen atoms. However, the Fe/N-CNT catalysts showed superior FTS activity when comparing with that of Fe/CNT catalysts. Therefore, N-doping seems to have a very positive effect on the FT catalyst performance, being it even superior than those results obtained for oxidized CNTs as supports of FT catalysts. In fact, as it can be observed in **Supplement Table S3**, Fe supported on N-doped CNTs presents the highest metal-time yield (MTY) operating at HT-FTS conditions.

Effect of Catalyst Preparation Methods

Various catalyst preparation methods to support FT catalysts on CNTs have been investigated and compared, including IWI, wetness impregnation (WI), homogeneous deposition-precipitation (HDP), colloidal synthesis technique, and most recently, a modified photo-Fenton process. Among of all of them, the standard IWI method is the most frequently used for fundamental studies. **Table 3** compares the FT catalytic performance of the most relevant unpromoted Co and Fe catalysts supported on CNTs and CNFs prepared using different catalysts preparation methods. Further details are reported in the supporting information file (**Supplement Table S4**) as the prefunctionalization method, metal particle size, C_2-C_4 O/P ratio and α value obtained from FTS. For example, it was found that using ethanol as a solvent for cobalt impregnation on oxidized CNTs and untreated CNTs showed a superior FTS activity as compared to those prepared from an aqueous solution and propanol (entries 1–2, **Table 3**) (Bezemer et al., 2006a; Eschemann et al., 2015). Eschemann et al. (2015) emphasized that choosing ethanol as solvent and an appropriate drying procedure reduced the average cobalt cluster size on the CNT surface and improved the metal dispersion.

The comparison of Co/CNT prepared by IWI (Co/CNT-IM) and the HDP method (Co/CNT-DP), using urea as the precipitation agent, showed that the catalysts prepared by IWI were 2.6 times more active, which was attributed to lower cobalt particle size and improved metal dispersion on the latter case (entries 3 and 4, **Table 3**) (Xiong et al., 2011).

Recently, Almkhelfe et al. (2018) investigated Co and Fe catalysts prepared in a single step by a modified photo-Fenton process without the need of a prefunctionalization stage, which showed higher CO conversion, selectivity to C_{5+} hydrocarbons, and an improved catalyst stability compared to those of the catalysts prepared *via* IWI at low FTS reaction temperatures (200 and 250°C for Co- and Fe-based catalysts, respectively, 10 bar and H_2/CO of 2). The main cause of the outstanding behavior for the photo-Fenton-prepared catalysts was the higher metal dispersion and optimal catalyst particle sizes with a narrow particle size distribution. In particular, the Co/CNT catalysts prepared from the photo-Fenton approach showed a CO conversion of 80% and a selectivity for liquid hydrocarbons of 70%, which is among the highest values reported for FTS (entry 6, **Table 3**).

Ismail et al. (2019) investigated the FT catalyst performance of Co/CNT catalysts prepared by a colloidal synthesis process (cs_Co_{100}/CNT) and IWI (ci_Co_{100}/CNT). It was found that the colloidally synthesized Co catalysts showed higher catalytic activity, higher selectivity toward C_2-C_4 fraction, and lower selectivity to C_{5+} hydrocarbons than the Co/CNT catalysts prepared by IWI at 1 bar and 220°C (entries 7 and 8, **Table 3**). Nevertheless, colloidally synthesized cobalt catalysts were previously reported to have a very high selectivity to long hydrocarbon chain at higher reaction pressure (20 bar and 220°C), given that high-pressure conditions promote C_{5+} product formation (Trépanier et al., 2010; Van Deelen et al., 2018).

The modification of the Co and Fe/CNT FTS catalysts by thermal treatments was also investigated. Chernyak et al. (2020) studied the effect of sintering temperature (800–1,200°C) on the structure and FTS catalytic performance of Co and Fe CNT-supported catalyst prepared by IWI *via* the spark plasma sintering approach (Co800 and Fe800, entries 9 and 17, **Table 3**). The sintered catalysts presented higher activity and selectivity to C_{5+} liquid hydrocarbons during FTS, as compared to those nonthermally treated catalysts and without the application of a prereduction step. The main reason was the presence of carbon-encapsulated metallic nanoparticles embedded in the CNT

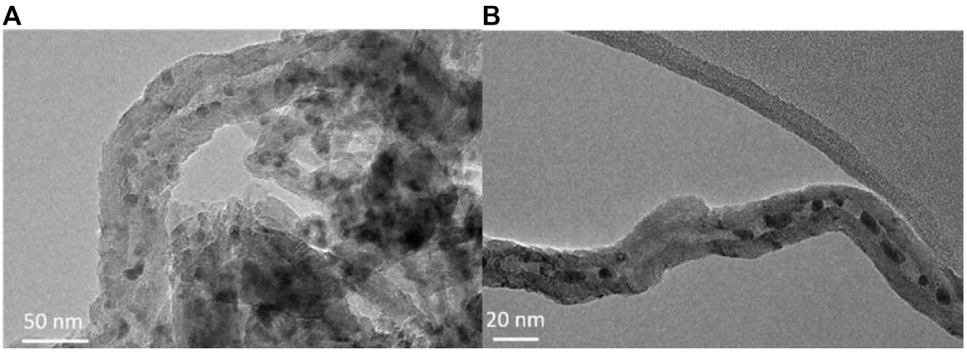

FIGURE 6 | TEM images of the fresh confined and nonconfined Fe catalysts: **(A)** Fe/CNT-out, **(B)** Fe/CNT-in. Reprinted from Gu et al., 2019, B., He, S., Peron, D.V., Strossi Pedrolo, D.R., Moldovan, S., Ribeiro, M.C., Lobato, B., Chernavskii, P.A., Ordomsky, V.V., and Khodakov, A.Y. Synergy of nanoconfinement and promotion in the design of efficient supported iron catalysts for direct olefin synthesis from syngas. Journal of Catalysis, 2019, 376, 1-16, copyright 2019, with permission from Elsevier.

framework. In the case of the sintered Fe/CNT catalyst, the close contact between the metallic site and the carbon material after the sintering approach facilitated the formation of the active iron carbide phase. It should be also highlighted the calculated TOF values for Co800 (0.10 s^{-1}) and for Fe800 (~1.0 s^{-1}), which were remarkably high as compared to other unpromoted FTS catalysts.

In a recent work, the controlled synthesis of cobalt catalyst with single hcp-Co supported on CNF was carried out through the controlled formation of a CoO oxide precursor, followed by a reduction step (entry 11, **Table 3**). Compared to the conventional reduction-carburization-reduction (RCR) process (entry 10, **Table 3**), this method improved Co particle dispersion and LT-FTS activity by avoiding sintering of the nanoparticles after reduction. Furthermore, this catalyst was catalytically stable for 400 h at the operation conditions studied (Lyu et al., 2019).

Effect of Pore Size

CNT pore confinement of the FT active phase and the effect of the support pore size have also shown to influence the activity and selectivity of the catalysts for FTS. As aforementioned, the pore size of the CNTs can be associated to both the inner diameter of the tube or to aggregated pores caused by CNT interaction.

On this context, Fu et al. (2014b) studied Co/CNT catalysts prepared by IWI with different CNT outer diameters (<8, 20–30, and 30–60). It was found that larger CNT outer diameters resulted in the formation of bigger Co_3O_4 crystallites and greater reducibility, but the larger sizes also resulted in less Co dispersion. The catalyst with larger outer diameters of 30–60 nm and pore sizes displayed higher TOF and selectivity to C_{5+} hydrocarbons, which was due to the suitable particle sizes and the better crystallized graphitic structure for the support with larger pore sizes, which promoted CO conversion. These results are in line with the observations by Xie et al. (2012) about the FTS performance of Co/CNT catalysts with different outer diameters. In contrast, Zhang et al. (2009) observed that the diameter of carbon nanotubes seemed to have negligible impact on the FTS performance of Co/CNT catalysts.

The effects of pore diameters of Fe catalysts supported on CNT on the FTS reaction rates and product selectivity were also studied. Abbaslou et al. (2010) showed that both the selectivity to C_{5+} hydrocarbons and the CO conversion were improved for Fe/CNT catalysts with the narrower pore structure. Deposition of iron inside the nanotubes (~80% according to the TEM images) with narrower pore structure resulted in smaller metal particle size (12 nm compared to 17 nm of Fe/wp-CNT catalyst with wider pore structure) and better metal dispersion. These features conferred the catalyst a better extent of reduction and an improved catalytic performance.

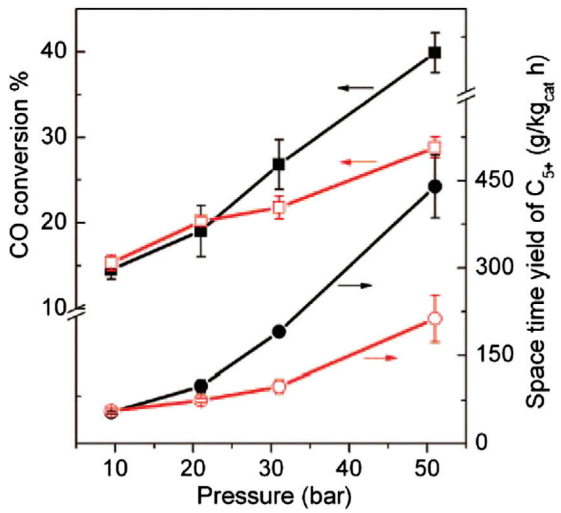

FIGURE 7 | FTS activity of Fe-*in*-CNT (filled symbols) and Fe-*out*-CNT (open symbols) at 270°C as a function of pressure. Square symbols represent CO conversion and circles the space-time yield of C_{5+} hydrocarbons. Reprinted with permission from (Chen, W., Fan, Z., Pan, X., and Bao, X. Effect of confinement in carbon nanotubes on the activity of Fischer-Tropsch iron catalyst. J Am Chem Soc, 2008, 130, 9414-9419.). Copyright 2008, American Chemical Society.

Effect of Catalyst Pore Confinement

In general, metal catalysts encapsulated inside CNTs are obtained by direct incorporation during the pyrolysis of precursor mixtures, such as ferroceneacetylene (Karmakar et al., 2004),

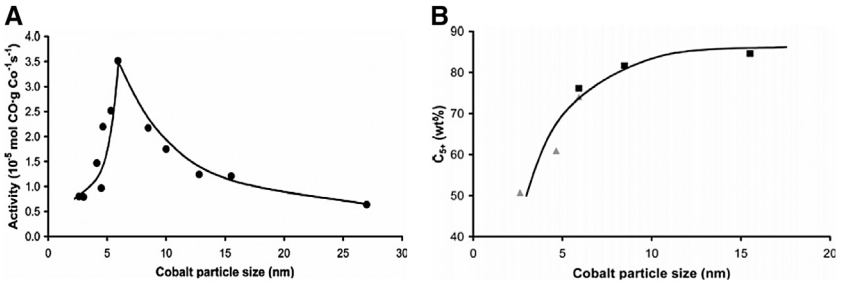

FIGURE 8 | The influence of cobalt particle size on **(A)** FT synthesis activity normalized to cobalt loading (220°C, H2/CO = 2, 1 bar) and **(B)** the C_{5+} selectivity measured at 35 bar, data markers in black at 210°C and in gray at 250°C. Figure reprinted with permission from (Bezemer, G.L., Bitter, J.H., Kuipers, H.P.C.E., Oosterbeek, H., Holewijn, J.E., Xu, X., Kapteijn, F., Van Dillen, A.J., and De Jong, K.P. Cobalt Particle Size Effects in the Fischer-Tropsch Reaction Studied with Carbon Nanofiber Supported Catalysts. Journal of the American Chemical Society. 2006, 128, 3956-3964). Copyright 2006, American Chemical Society.

by metal deposition on CNTs with opened tips after a strong-acid pretreatment (Chen et al., 2008) or by a two-step IWI methods, first with an aqueous solution and later with the metal precursor solution (Abbaslou et al., 2009). **Figure 6** shows TEM images of confined and nonconfined Fe catalysts.

The research group of professor Bao Xinhe (Chen et al., 2006; Chen et al., 2007; Chen et al., 2008) evidenced that iron species located inside the CNT tubes (Fe-*in*-CNT) had better reducibility and tended to form a more active iron carbide phase under reaction conditions than iron located outside the CNT channels (Fe-*out*-CNT). This caused a remarkable enhanced activity in LT-FTS and the favored formation of C_{5+} hydrocarbons working from 20 to 50 bar at 270°C and H_2/CO of 2 (entries 18–19, **Table 3**). This has been recently supported by Gu et al. (2019). **Figure 7** shows the catalytic performance of the Fe-*in*-CNT and Fe-*out*-CNT catalysts during FTS as a function of the pressure reported by Chen et al. (2008). This behavior was attributed to the modified redox properties of the confined iron catalysts and to the trapping effect of the reaction intermediates inside the CNTs, which was suggested to increase their contact time with iron catalysts, favoring the growth of longer chain hydrocarbons.

Several authors also investigated the confinement effect of cobalt particles inside CNT on the FTS catalyst performance. Tavasoli et al. (2010) confirmed that encapsulation of the Co catalytic sites inside the CNTs resulted in lower rates of sintering of the Co nanoparticles as compared with the particles located on the outer layer of the CNTs. Furthermore, Xie et al. (2012) and Fu et al. (2014b) agreed that the FTS activity and the selectivity to C_{5+} hydrocarbons was improved over the catalysts with most of the Co nanoparticles located inside the CNT due to the enhanced catalyst reducibility and to the favorable chain growth of the intermediates formed inside the tubes.

Effect of Metal Particle Size

Professor De Jong and co-workers reported the influence of both metallic cobalt and iron carbide particle size of graphitic CNFs (Co/CNFs and Fe/CNFs) as support for the FTS reaction under 1 and 35 bar (Bezemer et al., 2006a; Torres Galvis et al., 2012a). In this regard, Bezemer et al. (2006a) found that the surface-specific activity (apparent TOF) in the FT reaction was independent of cobalt particle size for unpromoted cobalt catalysts with sizes larger than 6 nm at 1 bar or 8 nm at 35 bar (220°C, H_2/CO = 2) [11]. The authors attributed the lower TOF values of the catalysts with Co particles smaller than 6 nm as the result of a significant increase in the CH_x intermediates residence time combined with a decrease of the CH_x coverage and, among others, to the presence of irreversible bonded CO molecules on smaller particles, which causes partial blockage of the Co surface (Den Breejen et al., 2009). These results have been later supported for Co/AC, Co/CNT, Co/CNF, Co/CSs, and Co-MOFMS catalysts (Xiong et al., 2011; Fu et al., 2014b; Luo et al., 2019).

On the other hand, both the activity and the selectivity of the CNF-supported cobalt catalysts were strongly influenced by the catalysts with smaller cobalt particle sizes. **Figure 8** shows the CoTY (**Figure 8A**) and the selectivity to C_{5+} hydrocarbons (**Figure 8B**) for Co supported on CNF as a function of the cobalt particle size at 35 bar (Bezemer et al., 2006a). It was found a volcano-like curve for the CoTY as a function of the cobalt particle size with a maximum CoTY at 5–6 nm. Furthermore, the selectivity to C_{5+} hydrocarbons increased with the cobalt particle size up to 15 nm, whereas the opposite trend was observed for the production of methane. The higher selectivity to methane of small Co particles was mainly attributed to their higher hydrogen coverage. A similar result for a Co/CNF catalyst was reported by Den Breejen et al. (2010). They agreed that the increase of the cobalt particle size positively affected the selectivity to C_{5+} hydrocarbons, especially for particle sizes lower than 8 nm. In addition, the selectivity to C_{5+} was constant for Co particle size from 8 to 15 nm. A similar positive relationship between cobalt particle size (<45 nm in diameter) and C_{5+} selectivity on Co/CNTs, Co/carbon-sphere, and Co-derived MOF catalysts was also reported (Xiong et al., 2011; Luo et al., 2019).

Torres Galvis et al. (2012a) investigated the influence of the Fe carbide particle size of CNF-supported catalysts. The TOF based on the initial activity of unpromoted catalysts increases 6–8 times at 1 bar (350°C, H_2/CO = 1) when the average iron carbide particle size decreased from 7 to 2 nm, whereas the selectivity

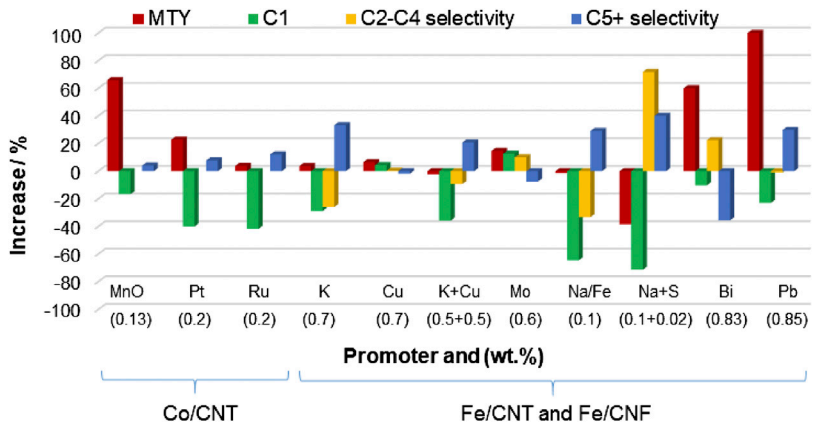

FIGURE 9 | Increase in metal-time yield and C_1, C_2-C_4, and in selectivity to C_{5+} hydrocarbons for different promoted Co- and Fe-supported catalysts on CNFs and CNTs compared to those of the unpromoted counterpart. The title in the *x*-axis indicates the promoter and its concentration in *wt*%. Data are adapted from refs. (Bahome et al., 2005; Bezemer et al., 2006b; Malek Abbaslou et al., 2011; Zhang et al., 2011; Cheng et al., 2015; Xie et al., 2016; Gu et al., 2018). Reaction conditions: MnO-, Pt-, or RuCo/CNT (H_2/CO = 2, 220°C, 20 bar), K- and/or Cu-Fe/CNT (H_2/CO = 2, 275°C, 8 bar), Mo-Fe/CNT (H_2/CO = 1, 275°C, 20 bar), Na-Fe/CNT (H_2/CO = 2, 300°C, 20 bar), Na and S-Fe/CNT (H_2/CO = 1, 340°C, 20 bar), and Bi- or Pb-Fe/CNF (H_2/CO = 1, 350°C, 10 bar).

to methane and lower olefins remained constant. On the other hand, Ru nanoparticles supported on CNTs, AC, and graphite have been also studied. Kang et al. (2009) reported that Ru nanoparticles supported on carbon nanotubes with a mean particle size of 7 nm, exhibited the highest selectivity toward C_{10}-C_{20} (60%) and TOF for CO conversion at 260°C, 20 bar and H_2/CO = 1.

Cobalt and Iron Bimetallic Catalysts and Effect of Promoters on Fischer–Tropsch Synthesis

The combination of cobalt and iron in a bimetallic-supported catalyst has been investigated in the last years. This interest stems from the prediction that the simultaneous use of CoFe bimetallic catalysts will give rise to a "synergistic" effect between the two active phases on the FT process. However, the studies reported on these bimetallic catalytic systems are a bit contradictory. In addition to this, optimization of Co-, Fe-, and CoFe-supported CNT and CNF catalysts for FTS process, especially related to product selectivity, can be addressed by catalyst promotion. Among various promoters, MnO and noble metals such as Pt and Ru have been incorporated to cobalt-supported CNF and CNT catalysts, whereas K, Cu, Mo, Na, S, Bi, and Pb have been added to Fe/CNFs and Fe/CNTs catalysts. **Figure 9** represents the increase in CO conversion and selectivity to C_2-C_4 and C_{5+} products for different promoted Co and Fe catalysts supported on CNFs and CNTs compared to those of the unpromoted counterpart, whereas **Supplementary Table S5** summarizes the FTS performance of bimetallic and promoted cobalt and iron catalysts supported on CNTs and CNFs.

Tavasoli et al. (2009) conducted some studies on CoFe/CNT catalysts and found that cobalt catalyst with 0.5 *wt*% of Fe increased the CO conversion with minor modifications of the selectivity to C_{5+} hydrocarbons during LT-FTS (entry 1, **Supplementary Table S5**). However, incorporation of 4 *wt*% of iron to the bimetallic catalyst resulted in a decrease of the catalyst activity and selectivity to C_{5+} hydrocarbon, whereas the alcohol selectivity notably increased. This behavior was attributed to the formation of Co-Fe alloys. Contrary to this, another study found that cobalt and iron supported on CNFs with a metal loading of 10 *wt*% Co and 5 *wt*% Fe (10Co5Fe/CNF), tested at 250°C and H_2/CO of 2, presented the highest yield to long-chain hydrocarbons, with minor selectivity to methane and carbon dioxide (Díaz et al., 2014). These studies agreed that the incorporation of iron to cobalt catalysts improved the dispersion of cobalt on the support and facilitated the reduction of iron species to the metallic form. In a recent study, Ismail et al. (2019) found that colloidally synthesized bimetallic $Co_{50}Fe_{50}$/CNT catalyst had considerably higher FT activity than the monometallic iron catalyst prepared by the same method and similar to the monometallic cobalt one under atmospheric pressure, 220°C and H_2/CO of 2. Furthermore, a significant selectivity to C_{5+} hydrocarbon and lower selectivity to CH_4 were obtained for the bimetallic catalyst. The authors attributed this behavior to the role of iron enhancing the distribution of cobalt species over the carbon support, in line with the aforementioned studies, and to the presence of Co-Fe alloys.

Several authors have investigated the incorporation of Pt and Ru promoters to the Co/CNT catalytic system and tested their performance in LT-FTS. Promotion with 0.2 *wt*% of Pt or Ru resulted in a significantly enhanced cobalt catalyst reduction and slight increase in the CoTY and C_{5+} hydrocarbon selectivity (82.5% for RuCo/CNTs and 79.2 for PtCo/CNTs) with respect to the unpromoted catalysts, **Figure 9** and entries 5 and 6 in **Supplementary Table S5** (Zhang et al., 2011). Similar conclusions were obtained by Trépanier et al. (2009a) for the 0.5 *wt*% Ru-promoted Co/CNT catalyst and significant C_{5+} hydrocarbon selectivity of 77% was also obtained (entry 7, **Supplementary Table S5**). Recently, the comparison of

Co-Ru/CNT catalyst (4 *wt*% Ru) prepared by the chemical reduction method and IWI showed that the Co-Ru/CNT catalysts synthesized by the reduction technique (entry 8, **Supplementary Table S5**) increased the FTS rate by 11% and the C_{5+} selectivity by 16% when compared to that obtained through the impregnation method. Moreover, these Ru-promoted catalysts outperform the unpromoted catalyst. The different in the performance of the catalysts was attributed to the different crystallite sizes and the catalyst reduction enhancement for the Ru-promoted catalysts (Shariati et al., 2019).

The research group of professor De Jong investigated the influence of MnO on Co/CNT catalysts under LT-FTS conditions (Bezemer et al., 2005; Bezemer et al., 2006b). MnO was reported to favorably affect both activity and selectivity to C_{5+} hydrocarbons, depending on concentration and reaction conditions. They concluded that the CoTY increased c.a. 65% and the C_{5+} selectivity increased c.a. 4% with respect to the unpromoted catalyst after incorporation of 0.13 *wt*% MnO (**Figure 9**). The promoter effect was suggested to originate from a lower degree of cobalt reduction and moderation of hydrogenation reactions. On this research line, Liu and Li (2020), based on a computational study, have recently proposed a promising and novel Co/Mn bimetallic center supported on N-doped CNTs as an efficient FTS catalytic system for the production of long-chain hydrocarbons.

0.7 *wt*% K-promoted Fe/CNT catalysts decreased the catalyst reducibility, decreased FT rate, increased the yield of CO_2 and C_2 olefins, and reduced the methane selectivity, when compared with unpromoted catalysts (Bahome et al., 2005; Trépanier et al., 2009a). However, promotion with 0.7 *wt*% Cu did not greatly influence the FT product selectivity (**Figure 9** and entries 10–11, **Supplementary Table S5**). In other work, a synthesized K-doped MnO_2-coated CNT composite was used to support iron catalysts (7.9 *wt*% Fe, 15.7 *wt*% Mn, and 1.9 *wt*% K) (Wang et al., 2015). It was found a remarkable selectivity to C_2-C_4 olefins (50.3%) and higher CO conversion than FeMnK/CNT catalyst prepared by the coimpregnation method using CNTs as support. This was associated to the small-sized and narrow nanoparticle distribution, high dispersion of the promoters, and the weak metal-support interaction.

Combined promotion of Fe/CNF catalysts with 0.1 *wt*% Na and 0.2 *wt*% S was shown to improve the selectivity to light olefins at low conversions operating at HT-FTS conditions (**Figure 9** and entry 15, **Supplementary Table S5**) (Xie et al., 2016). The comparison with the unpromoted Fe/CNF revealed a notable enhanced iron carburization and higher initial catalytic activities over the promoted iron catalysts with Na and S.

More recently, professor Khodakov and collaborators (Gu et al., 2018; Gu et al., 2019) found extremely strong promotion effect of Bi and Pb on the catalytic performance of Fe/CNT catalysts. Compared to the unpromoted catalysts, a significant increase in FT reaction rate and a higher selectivity to the C_2-C_4 olefins (55–60%) at 10 bar were obtained (**Figure 9** and entries 16 and 17, **Supplementary Table S5**). The promoting effects of Bi and Pb on iron catalysts have been reinforced by their preferential localization at the surface of iron carbide nanoparticles leading to the formation of core-shell structures. Furthermore, the presence of Bi enhanced the catalyst reducibility and facilitated carburization of iron nanoparticles. For example, the FeTY was 82×10^{-5} mol_{CO} g_{Fe}^{-1} s^{-1} for the FePb/CNT-*in* catalyst at 350°C, total syngas pressure of 10 bar, and SV of 17 m^3 kg^{-1} h^{-1}, which is one of the best results for unpromoted and promoted iron-based FTS catalysts available so far in the literature.

To sum up, from **Figure 8**, it can be concluded that promotion with MnO to Co/CNTs catalysts produced a very significant increase of CoTY with respect to the unpromoted catalyst, whereas promotion of Bi and Pb enhanced considerably the FeTY in Fe/CNT catalysts. Regarding the selectivity values, it should be remarked that promotion with K+Cu and Na enhanced selectively C_{5+} formation over Fe/CNT catalytic systems with respect to the unpromoted catalysts compared under very similar FeTY values.

Catalysts Supported on Carbon Spheres

Since the discovery of buckminsterfullerenes, spherically shaped carbons or carbon spheres (CSs) are receiving great attention from the scientific community (Ugarte, 1992). The preparation of CSs is usually accomplished by two major approaches. On the one hand, the chemical vapor deposition (CVD) method involves high-temperature decomposition of a carbon-based material under inert atmosphere, typically in the absence of a catalyst (Serp et al., 2001). This noncatalytic synthesis procedure allows the direct preparation of CSs with low surface areas (<10 m^2/g) and high purity (Xiong et al., 2011; Yang et al., 2014). The surface of theses CSs prepared by CVD is composed of graphitic layers/flakes with sizes ranging from 1 to 10 nm (Xiong et al., 2011), which can be arranged in different structures, forming concentric, radial, or random configurations (Serp et al., 2001). They are reported to be good model catalyst supports in FTS (Xiong et al., 2010). On the other hand, hydrothermal carbonization (HTC) process, where a carbon source (i.e., sucrose, glucose, and resorcinol) is hydrothermally treated between 80 and 250°C in an autoclave reactor, has been also proposed for the preparation of these shaped carbons (Hu et al., 2010). Compared to other preparation routes, the HTC process has some advantages, including low toxicological impact of materials and processes, easy instrumentation and techniques, the use of renewable sources, and a high energy and atom economy. Carbon spheres prepared by the HTC approach are characterized by a hydrophobic core and a hydrophilic shell with abundant surface OH and C=O groups. These CSs usually have intrinsic porous structures with controllable morphology and surface functionality. Furthermore, coupling either hard- or soft-templating effect with the HTC process has shown interesting results in the preparation of hollow carbon spheres (HCSs). The textural parameter range of typical Fe- and Co-supported CSs used in the FTS reaction are shown in **Table 1**. The BET surface area for the Fe- and Co-supported CSs prepared *via* the HTC approach can vary between 143 and 465 m^2/g, whereas the total pore volume can vary between 0.2 and 0.59 cm^3/g (Cheng et al., 2019; Phaahlamohlaka et al., 2020). **Supplementary Table S6** summarizes the FTS performance of Fe- and Co-supported CS catalysts.

The effect of support pretreatment, catalyst preparation methods, and promoters on the FTS performance of Fe- and

Co-supported CSs have been investigated. In the case that hollow carbon spheres (HCSs) were used as supports, the effect of catalyst confinement was studied.

Effect of Support Functionalization and FT Catalyst Preparation Methods

CSs prepared by the CVD process are characterized for exhibiting a high carbon purity and an inert surface chemistry. In order to achieve a high metal dispersion when using these carbon materials as catalyst supports, CSs have to be functionalized with different oxygen and/or nitrogen surface groups. On the contrary, CSs obtained by the HTC approach usually do not require functionalization due to their hydrophilic shell with abundant oxygen functional groups.

Yu et al. (2010) were pioneers in reporting the use of iron-containing CSs in the FTS process. The authors reported a one-stage route for the preparation of Fe_xO_y@C spheres embedded with highly dispersed iron oxide nanoparticles by the hydrothermal treatment of a glucose solution mixed with iron nitrate under mild conditions. A steady-state CO conversion of 76% and a selectivity to C_{5+} hydrocarbons of 60% were obtained. In particular, the selectivity values to C_{5+} hydrocarbons are even better than the values reported for unpromoted iron catalysts, including Fe-*in*-CNT and Fe-*out*-CNT catalysts tested under similar FTS conditions (at 270°C, 20 bar and H_2/CO of 1) (**Table 3**). The remarkable catalytic activity and stability was associated to the favorable formation of iron carbides during H_2 activation, which were embedded into the carbonaceous matrix.

Professor Coville and collaborators (Xiong et al., 2010; Xiong et al., 2011) carried out a comprehensive study on the prefunctionalization treatments (with HNO_3 or $KMnO_4$) and preparation catalyst methods (IWI and HDP) of CS-supported Fe and Co catalysts. The higher the HNO_3 treatment temperature (up to 90°C), the higher degree of functionalization and metal dispersion achieved in the final catalysts. They observed that in both cases, for Fe- and Co-supported CSs, the catalysts prepared using iron/cobalt nitrate and the HDP method using urea as precipitation agent (Fe/CSs-C-DP and Co/CS-C-DP) showed the highest MTY for the FTS reaction among the different catalysts prepared, which was attributed to the smallest average metal particle size and highest metal dispersion (entries 2 and 13, **Supplementary Table S6**). Functionalization using nitric acid or $KMnO_4$ showed comparable catalytic activity and C_{5+} hydrocarbon selectivity.

More recently, Kuang et al. (2019) prepared Co/CS catalysts by thermal decomposition (TD), IWI, and ultrasonic impregnation (UI) methods. The preparation of the CS support was carried out by the hydrothermal approach using an aqueous glucose solution followed by carbonization at 800°C in N_2. The catalyst prepared by the TD method (CoO/C-TD) presented the highest metal dispersion and, as consequence, remarkably higher CO conversion (21%) and selectivity to C_{5+} hydrocarbons (81.9%) during LT-FTS.

Regarding the use of N-doped CSs as supports, Xiong et al. (2014b) investigated Fe-supported N-doped CS catalysts for HT-FTS prepared by different strategies. It was suggested that the presence of pyrrolic and pyridinic N atoms is essential in anchoring and stabilizing Fe atoms to the carbon surface, whereas quaternary N atoms play a minor role. Among all of them, the Fe-supported N-doped CSs *via* CVD of a mixture of acetylene and CH_3CN in a vertical furnace (Fe/NCS_{ver}) had the highest N content (4 *wt*%, mainly pyrrolic and pyridinic N atoms) and well-dispersed Fe oxide particles on the N-doped CSs. Therefore, Fe/NCS_{ve} catalyst exhibited the highest FT activity and selectivity to C_{5+} hydrocarbons (entry 3, **Supplementary Table S6**).

More recently, Cheng et al. (2019) studied the preparation of N-doped CSs using biomolecule dopamine as carbon and nitrogen sources and they are used as supports for cobalt catalyst. In line with the observations reported by Xiong et al. (2014b), the sample with the highest content of pyrrolic N and smallest cobalt particle size (that pretreated at 500°C, Co/NCS-500) exhibited the highest CO conversion and C_{5+} hydrocarbon selectivity under LT-FTS reaction (entries 14 and 15, **Supplementary Table S6**).

Cobalt and Iron Bimetallic Catalysts and Effect of Promoters

Dlamini et al. (2015) prepared a series of Fe-Co bimetallic-supported CS catalysts and investigated their use in the FTS reaction. The addition of small amounts of Fe to Co-based catalyst resulted in an enhancement of the CO conversion, being its maximum for the catalyst containing 0.5 *wt*% Fe and 9.5 *wt*% Co (entry 17, **Supplementary Table S6**). Fe/Co alloy formation was detected upon reduction above 450°C, but its relative amount was not correlated with higher C_{5+} selectivity. The bimetallic catalysts with iron content higher than 2 *wt*% showed the highest C_{5+} selectivity (87%) at a CO conversion of 21%.

Zhang et al. (2015) carried out a deep study on the effect of different promoters (Na, K, Mn, and Zn) over Fe-supported CSs prepared through one pot solvothermal method and their use in the FTS process. The catalytic experiments showed that K, Na, and Zn promotion resulted in an enhancement of the CO conversion values as compared to that of the unpromoted catalyst. However, Mn promotion resulted in the decrease of the CO conversion. The FTS results revealed that Na was the one enhancing the catalytic performance to the most. Na promotion strongly decreased the methane generation, producing more C_{5+} hydrocarbons and enhancing the O/P ratio.

In this line, K- and Mn-promoted Fe-supported spherical mesoporous carbons (Fe/SMCs) were reported by Chen et al. (2018). These authors prepared spherical mesoporous carbons by a SiO_2 template assisted sol–gel procedure in water-in-oil emulsions, using resorcinol and formaldehyde as carbon sources. High iron loadings were achieved (30–50 *wt*%), and the BET surface area was very high (397 m^2/g for an iron loading of 40 *wt*%). 2.5 *wt*% K promotion decreased the FeTY and TOF values, whereas the presence of 5 *wt*% of Mn enhanced them. CO_2 generation was diminished by the presence of Mn but enhanced by K.

The favorable effect of alkali (Na, Li, and K) promotion over iron-based CS catalysts for the HT-FTS reaction was reported by Ma et al. (2020). In this study, the promoted iron-containing CSs were prepared though a one-step hydrothermal synthesis. The

reaction results showed an improvement in the CO conversions and in the O/P ratios for all the promoted catalysts compared to the unpromoted one. Here, Na was the promoter enhancing the CO conversion value to the most, which is in agreement to the work reported by Zhang et al. (2015). The presence of the metal promoters increased the selectivity to C_{5+} hydrocarbons following the order: Na > K > Li. A further study on the effect of Na content revealed that the CO conversion value was maximum for a Na load of 1 *wt*%, whereas the highest selectivity to C_{5+} hydrocarbons was achieved for the catalyst with 2 *wt*% of Na.

To sum up, alkali metals result in the enhancement of the CO conversion, the olefin/paraffin ratio, and the C_{5+} selectivity values when they are used as promoters in Fe/CS catalysts. However, in the case of cobalt-based catalysts, K promotion resulted in the decrease of the catalytic activity. On the other hand, Mn has been shown as a useful promoter for olefin generation purposes in Fe-supported CS catalysts.

Hollow Carbon Spheres as Catalyst Supports

CNTs as support for FT catalysts have the advantage of allocating the catalytic active phase either inside or outside the nanotube. This phenomenology was also studied with HCSs. HCSs used as supports for FTS catalysts were prepared by coating a carbon precursor onto either SiO_2 (Phaahlamohlaka et al., 2017; Teng et al., 2018) or polystyrene (Phaahlamohlaka et al., 2020) spheres as hard and soft templates, respectively, followed by a pyrolysis stage and removal of the template. The SiO_2 template spheres were removed by NaOH or HF treatments, whereas polystyrene was easily removed by heat treatment under an inert environment.

For example, Phaahlamohlaka et al. (2017) and Phaahlamohlaka et al. (2020) prepared Co-supported mesoporous hollow carbon spheres (MHCSs) promoted with ruthenium and both Co and Ru nanoparticles where located either outside or inside the MHCSs. The promoted catalysts exhibited higher FTS activity compared to the unpromoted counterparts, which was attributed to a hydrogen spillover effect from Ru to Co that enhanced cobalt oxide reducibility. When Co and Ru nanoparticles were located inside the MHCSs (CoRu@HCS), higher selectivity to methane and lower selectivity to C_{5+} hydrocarbons were obtained (entry 17, **Supplementary Table S6**). The authors attributed these differences to the confinement effect of the Co and Ru nanoparticles inside the hollow carbon structure, which gave rise to a hydrogen richer environment, which favored methane formation.

In other work, Teng et al. (2018) reported a highly efficient Fe-contained hollow CS catalyst with highly dispersed Fe_2C sites embedded within the carbon matrix and successfully tested it in the HT-FTS reaction. SiO_2 spheres were used as hard templates with different diameter sizes (150 and 260 nm) and resorcinol and formaldehyde as carbon sources. Iron loading was carried out prior to the pyrolysis of the polymer at different temperatures (500, 600, and 700°C) under N_2 flow, followed by etching the template. Lower carbon thickness and higher iron particle size was evidenced from TEM when increasing the pyrolysis temperature. It was found that the catalyst calcinated at 600°C exhibited the highest selectivity to lower olefins (30.1% in a CO_2-free basis) and the highest O/P ratio (4.8). Additionally, they found a higher methane formation and lower O/P ratio when using the larger template, which was also associated to the H_2 enrichment effect taking place inside the hollow structure of the catalyst, being it higher when increasing the cavity size of the CS catalyst.

Catalysts Supported on Graphene, Graphite, and Diamond

Graphene is formed by one or several layers (3 to <10) of sp^2-hybridized carbon films forming a two-dimensional (2D) crystal, which is considered as the basic building block for carbon materials of different dimensionalities, such as fullerenes (0D), nanotubes and nanofibers (1D), or graphite (3D) (Geim and Novoselov, 2007). Graphite consists of van der Waals coupled graphene layers, which can be stacked slightly differently and either alpha (hexagonal) or beta (rhombohedral) graphite forms can be formed (Lipson and Stokes, 1942). On the other hand, diamond is a crystalline carbon material formed by sp^3 hybridized carbon atoms. **Figure 10** shows a schematic crystal structure of graphene, graphite, and diamond and (**Supplementary Table S7**) the FTS performance of FT catalysts supported on these carbon materials.

To the best of our knowledge, there is only one work of Co-loaded powdered oxidized diamond catalyst tested in the FTS reaction (Honsho et al., 2012). The authors used a commercial powdered diamond having a surface area of 24 m^2/g, which was oxidized in air prior to cobalt deposition by IWI. The catalysts showed a high CO conversion of 44.5% and selectivity to C_{5+} hydrocarbons of 62.7%. This CO conversion was significantly higher than those obtained for Co-loaded on SiO_2 (38.4%), AC (12.2%), and powdered oxidized graphite catalysts (2.8%) with higher surface areas. The weaker interaction between the O-DIA surface and cobalt oxide contributed to the better FTS results.

Regarding the use of graphene as supports for FTS catalysts, Moussa et al. (2014) investigated the chemical reduction of graphene oxide in water in the presence of nitrates of iron and potassium under microwave irradiation resulting in $Fe_{15}K_5$-G catalyst (15 *wt*% of Fe and 5 *wt*% of K). It should be highlighted that graphene oxide does not require a prefunctionalization of the support due to the presence of epoxy groups on the surface, which act as anchoring sites for the metal catalysts. The FTS catalyst was tested under HT-FTS and compared with K-promoted Fe/CNT catalyst. It was observed that the graphene oxide-supported catalyst exhibited an excellent stability, recyclability, the highest CO conversion (73.5%), and selectivity to C_{8+} hydrocarbons (86.7%). The authors attributed the good FTS performance of the $Fe_{15}K_5$-G catalyst to the presence or defects within the graphene lattice, which acted as favorable nucleation sites to anchor the metal nanoparticles.

Karimi et al. (2015a) and Karimi et al. (2015b) performed a comparative study of 15Co/graphene (602 m^2/g) and 15Co/CNT (372 m^2/g) catalysts for the FTS reaction. Prior to catalyst preparation by IWI, both supports were treated

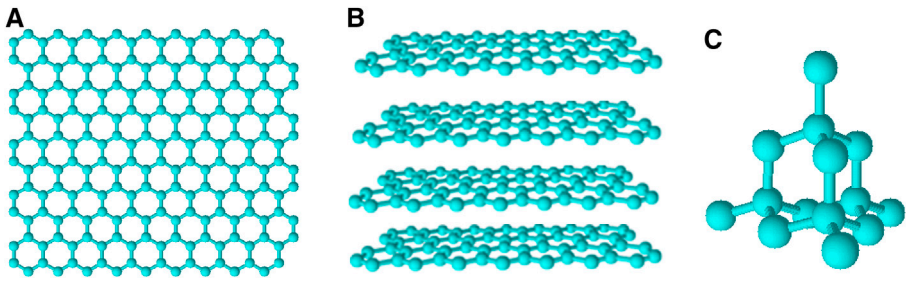

FIGURE 10 | Crystal structure of **(A)** graphene, **(B)** graphite, and **(C)** diamond crystal unit.

with HNO_3. The FTS rate and CO conversion percentage obtained by 15Co/graphene were significantly larger than that obtained using 15Co/CNT catalyst. The selectivity to C_{5+} hydrocarbons was also higher for 15Co/graphene (87.1%) than for 15Co/CNTs (83.9%) at isoconversion conditions (around 60% of CO conversion). In addition, the CO conversion dropped only by 22% over 15Co/graphene after 480 h, whereas it dropped by 34% for the 15Co/CNT catalyst, which was caused in both cases by cobalt sintering. Therefore, in this study, Co-supported graphene outperformed to Co-supported CNTs catalyst under the preparation and reaction conditions used.

In this line, Hajjar et al. (2017) compared the FTS performance of cobalt catalysts supported on graphene oxide and nanoporous graphene with BET surface areas of 290 and 700 m^2/g, respectively. The nanoporous graphene material was first oxidized in a mixture of sulfuric and nitric acids. As aforementioned, graphene oxide did not require functionalization. The resulting catalysts (15Co/GO and 15Co/NPG) were evaluated in the FTS reaction. The carbon nanostructured graphene-based catalysts exhibited higher CO conversion of around 65% and lower deactivation rate compared to 15Co/GO. Moreover, the selectivity to C_{5+} hydrocarbon was also significantly higher when using Co/NPG (87.4%), which was evident from the higher surface area and pore volume.

More recently, Chernyak et al. (2019) reported oxidized and N-doped graphene nanoflakes (GNFs) as supports for Co-based FT catalysts. In this work, pristine and N-doped GNFs were prepared by pyrolysis of hexane and acetonitrile, respectively. The oxidized derivatives were obtained after an HNO_3 treatment, and the Co-supported catalysts were prepared by the WI method, resulting in Co-supported GNFox (Co/GNFox) and Co-supported N-doped GNFox (Co/N-GNFox) having BET surface areas of 250 and 415 m^2/g, respectively. The introduction of acetonitrile at the pyrolysis stage led to the formation of predominantly bulk-distributed pyridine and graphitic nitrogen species, and the nitric acid oxidation of this material introduced the pyridone/pyrrolidone groups on the surface of the support. The catalysts were tested in the FTS reaction (entries 5 and 6, **Supplementary Table S7**). Interestingly, greatly higher TOF and selectivity to short-chain hydrocarbons (C_2-C_4) were obtained for Co/N-GNFox, whereas higher CO conversion and CH_4 selectivity was obtained for Co/GNFox. The presence of smaller cobalt oxide crystallites found in Co/N-GNFox and the higher resistance to particle sintering during catalyst activation could explain these results. However, their C_{5+} selectivity values were quite low (20–43%) due to the presence of very narrow pores on these samples (less than 1 nm), which hindered CO diffusion and increased H_2 intrapore concentration.

On the other hand, a high surface area graphite material (399 m^2/g) has been used as support of cesium-promoted Ru catalysts and tested for FT reaction (entries 8 and 9, **Supplementary Table S7**). In this work, Eslava et al. (2018) claimed that the presence of Cs_2O in the catalysts prepared with $CSNO_3$ as promoter precursor was responsible of a high selectivity to CO_2 during reaction, whereas the WGS reaction, and hence the CO_2 selectively, significantly decreased using CsCl.

ANALYZING THE EFFECT OF CARBON SUPPORT STRUCTURE ON FISCHER–TROPSCH SYNTHESIS CATALYST PERFORMANCE

It has been observed that the reducibility of Co- and Fe-based catalysts is improved on carbon-based supports compared to that of oxide materials. However, the preparation of highly dispersed and stable catalysts still requires at least of intermediate interactions between the carbon support surface and the metal precursor. Modification of surface chemical properties of inert (or highly ordered) carbon-based materials, especially those prepared at high carbonization temperatures and/or from CVD of a carbon precursor, such as of CNTs, CNFs, CSs, graphite, and graphene, by introduction of oxygen and nitrogen functional groups, was found to be essential to increase their ability to stably anchor the active metal species for the FTS. Consequently, an additional prefunctionalization step prior to the catalyst preparation resulted in an increase of metal dispersion and stability on the carbon surface, positively affecting the activity of the catalyst in this reaction. On the other hand, amorphous carbons such as ACs, OMCs, and CSs, which are usually prepared at lower carbonization temperatures (especially those obtained by the HTC approach), are characterized by the presence of abundant surface oxygen functional groups. These oxygen surface groups are mainly originated from the biomass source (biomass residues in the case of ACs or isolated carbohydrates in the case of OMCs and CSs) used as carbon precursor. Therefore,

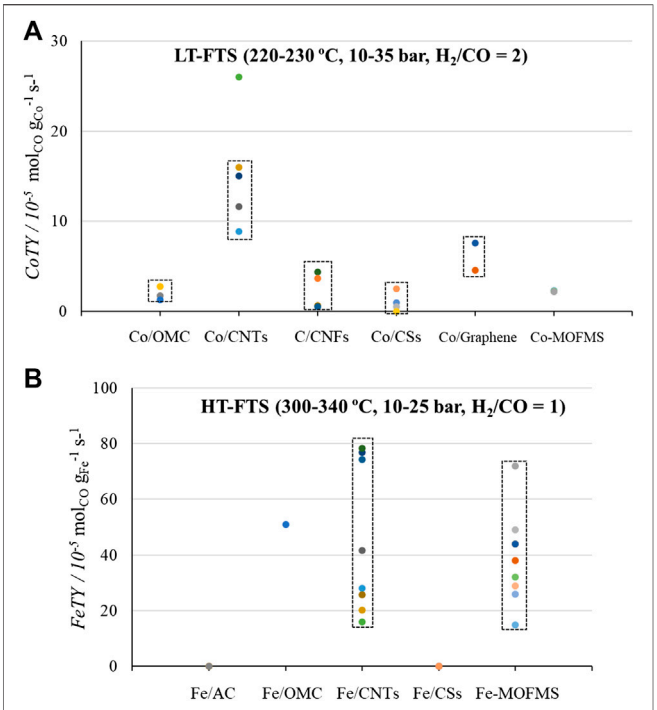

FIGURE 11 | Effect of carbon support structure for **(A)** Co catalysts on CoTY at LT-FTS reaction conditions (220–230°C, 10–20 bar, H2/CO = 2) and for **(B)** Fe catalysts on FeTY at HT-FTS reaction conditions (300–350°C, 10–20 bar, H_2/CO = 1). The data presented in the Figure can be found in the supplementary material (**Supplementary Tables S1–S7**). The data for Fe- and Co-derived MOFs catalysts are adapted from Otun et al. (2020).

these carbon supports did not require of a carbon surface functionalization stage. Furthermore, the use of activation agents and porous inorganic templates in the preparation of ACs and OMCs, respectively, together with the lower carbonization temperatures mostly used in the preparation of these carbon materials produced carbon supports with high BET surface areas, pore volumes, and oxygen surface groups, as shown for Co- and Fe-supported AC and OMC catalysts in **Table 1**. Undoubtedly, the metal loading and catalyst preparation procedure also influenced the textural characteristics and surface chemistry of the resultant catalysts, blocking part of support porosity and creating specific oxygen surface groups.

To compare the effect of carbon support structure of Co- and Fe-based catalysts on their activity for the FTS reaction, the weight specific activity (cobalt- and iron-time yield, CoTY and FeTY, respectively) and surface-specific activity (turnover frequency, TOF) were plotted for each type of carbon-based supported catalyst under similar reaction condition range, and the results are shown in **Figure 11** and **Supplementary Figure S1**, respectively.

Clearly, a strong dependence of the FTS catalytic activity on carbon-based support structure has been observed. It is noteworthy that both the CoTY and TOF are similar for Co-based catalysts. However, the lack of TOF values (or data to be able to calculate these values) reported for Fe-based catalysts does not make comparison between these two activity indicators possible. In general, the highest CoTY values are obtained for Co-supported CNTs, followed by Co/graphene and Co/CNFs (**Figure 11A**). The better crystallized graphitic structure in CNTs, which facilitate the electron transfer between the cobalt metal and CO molecules and highly stable cobalt nanoparticles, mainly dispersed inside the tubes, has been reported to be responsible of their higher catalytic performance (Pan and Bao, 2011; Fu et al., 2013; Xiao et al., 2015). A comparative study of the catalytic behavior of cobalt catalyst supported on graphene and on CNT for the FTS showed that the use of graphene increased the rate by 22%, shifted the product distribution to long-chain hydrocarbons, and exhibited higher stability when compared to CNT, at 220°C, 18 bar, and a H_2/CO ratio of 2 (Karimi et al., 2015a; Karimi et al., 2015b). These properties were attributed to a better dispersion of cobalt clusters and to an increase in the degree of reduction of Co at relatively lower temperatures in the graphene-supported catalyst. Nevertheless, the TOF values reported in this work for Co-supported on graphene and CNTs (38.6 and 35.1 s^{-1}, respectively) were quite far from the range of TOF values ($25\cdot\times\ 10^{-3}$–$160\cdot\times\ 10^{-3}\ s^{-1}$) reported for Co/CNTs under similar reaction conditions (**Supplementary Figure S1A**). In this sense, the poorly crystallized graphitic (amorphous) structure of ACs and OMCs does not seem to be a favorable characteristic for a catalyst support in FTS (Zaman et al., 2009; Fu et al., 2013).

Nevertheless, the unique (meso-) porous structure of the different carbon supports has been suggested to provide geometric constraints that allow controlling the product distribution through the shape selective role of the catalytic system. Particularly, the special confinement effect of CNTs was reported to restrict cobalt particle sintering during catalyst activation and FTS reaction conditions. As compared in **Table 1**, CNTs had the maximum pore (tube) diameter and most of the metal particles are usually inside the pores (tubes). Therefore, the reaction intermediates formed inside the pores can contact the metal active site for longer time, promoting the formation of long-chain hydrocarbons. Furthermore, the high length-to-diameter ratio in CNTs and CNFs confers them a high external surface area that together with the absence of microporosity significantly reduces the mass transfer limitations compared to those of the traditional microporous activated carbons (Abbaslou et al., 2010). Contrary to this, the confinement of cobalt catalyst inside hollow carbon spheres resulted in higher selectivity to methane associated to an H_2 enrichment effect inside the hollow carbon structure (Phaahlamohlaka et al., 2017; Phaahlamohlaka et al., 2020). Comparatively, the microporous structure in ACs is claimed to result in a higher selectivity to methane and a higher light hydrocarbon fraction, which was attributed to the high specific surface area of these carbon supports, leading to smaller cobalt particle sizes and diffusion limitations for CO as compared to that of H_2 (resulting in a higher H_2/CO ratio inside the pores) (Zaman et al., 2009; Fu et al., 2013). Similar results were recently reported for Co supported on oxidized and N-doped graphene nanoflakes with narrow pores (Chernyak et al., 2019). However, the wider pore sizes in OMC-supported catalysts leaded to improved catalyst mass transfer properties and

higher selectivity to long-chain hydrocarbons compared to those of AC-supported catalysts (**Supplementary Tables S1, S2**).

Regarding the use of Fe-supported catalysts, both Fe/CNTs and Fe-MOFMS catalysts present high and similar FeTY values (**Figure 11B**). It has been observed along the reported literature that the proximity between carbon and supported iron particles can facilitate the formation of iron carbides, thus leading to a higher concentration of the iron carbide active phase on the catalyst surface, giving rise to a high selectivity to C_{5+} hydrocarbons (Chen et al., 2008; Santos et al., 2015). The Fe nanoparticle confinement in CNTs seems to be an ideal condition for the successful formation of the active iron carbide species. This fact can explain the high FeTY obtained for these catalytic systems. Furthermore, the restricted iron sintering of the iron carbide nanoparticles confined and/or embedded in the carbon matrix in these carbon structures also confers a high catalyst stability. In this regard, it was suggested (Cheng et al., 2014) that the confinement of iron nanoparticles inside the CNT with unique electronic properties presents a more relevant impact on the preparation of more active, selective, and stable FT catalysts than that of iron dispersion.

In line with these observations, iron and cobalt nanoparticles highly dispersed and embedded in CSs and OMCs have been prepared in a single step *via* the hydrothermal synthesis of a mixture of the carbon and the metal precursors. According to this catalyst preparation procedure, the close contact between iron and the carbon can facilitate the easy formation of the active iron carbide phase during the subsequent carbonization stage and in the FTS reaction conditions, resulting in catalysts with a high FTS activity and stability (Yu et al., 2010; Sun et al., 2012; Teng et al., 2018). Contrary to this, a detrimental effect was observed for the case of Co-based catalysts with Co nanoparticles embedded in the carbon matrix, as that reported for Co/OMCs, due to the fact that the metallic cobalt surface is the active phase for Co-based catalysts in FTS reaction. Thus, when Co particles are surrounded by the carbonaceous matrix, a large part of the cobalt active sites are blocked, being deactivated (Liu et al., 2017).

Concerning the use of metal promoters, several authors observed that metal promotion effect is also dependent on the support structure. Nevertheless, the comparison of metal promotion on different carbon-supported catalysts has not been well investigated, which makes difficult the discussion of the effect of metal promotion on different carbon-supported catalysts on FTS performance. For example, sodium promotion was more pronounced on Fe/CNTs as compared to that on Fe/OMC, due to the presence of iron carbide species stabilized by encapsulation in the carbon matrix of the Fe/CNT catalytic system (Cheng et al., 2015). Therefore, higher selectivity values to both light and long-chain olefins were observed for Na-promoted Fe/CNT catalysts when compared to those of Fe/OMC. Likewise, it was found that the iron reducibility and carbidization proceeded much easier for iron species confined inside CNTs and promoted with Bi and Pb, which resulted in an increase in FeTY and in a higher selectivity to light olefins (around 40% at 10 bar and 60% at 1 bar, 350°C and $H_2/CO = 1$), as compared to those of the promoted and nonconfined catalysts (Gu et al., 2019). This behavior was attributed to the closer contact of the promoters with Fe inside the tubes due to the nanoconfinement effect. The use of carbon-based supports derived from lignocellulosic biomass in FTS has been less studied. Moreover, the presence of inorganic species in biomass-derived carbon supports might play an important role in enhancing the activity in FTS. Such studies would help to identify suitable biomass sources and natural and cheap promoters from the extensive and heterogeneous diversity of the biomass materials.

Another important aspect related to FT synthesis, which has not been so widely discussed in the literature, is the high exothermicity of the process in relation to heat removal and reactor temperature control. Highly exothermic reactions, such as those of the FTS, usually present important heat-transfer problems, giving rise to hotspots in chemical reactors that may damage the catalysts. In this line, it has been reported that local overheats in Co-based catalytic bed results in the increase of methane selectivity and in an acceleration of catalyst deactivation (Visconti et al., 2011; Fratalocchi et al., 2018). Conventional pelletized catalysts, which usually involve the use of alumina or silica as catalyst support, present certain limitations in relation to heat removal under FT synthesis reaction conditions (Asalieva et al., 2020). In order to tackle this issue, several approaches such as the use of monolithic (Visconti et al., 2011) or foam (Lacroix et al., 2011) structured catalysts and the operation in microchannel reactors (Holmen et al., 2013) have been explored.

The use of carbon materials has been also reported to be a feasible solution to overcome heat-transfer problems in FT reactors. Chin et al. (2005) reported the preparation of microstructured Co-Re catalysts based on aligned multiwall carbon nanotube arrays supported on FeCrAlY foam. A four times higher catalytic activity was obtained for the carbon-containing microstructured catalyst as compared to the one of an engineered catalyst structure without the carbon nanotube arrays. This difference was attributed to the superior thermal conductivity for the carbon-containing microstructured catalyst, which resulted in a higher mass and heat transfer and in an improved reactor temperature control, being it possible to operate at higher temperatures without methane selectivity runaway. In this context, professor Holmen and collaborators have intensively worked on the use of different monolithic/microstructured reactors using carbon-based catalysts (Zarubova et al., 2011; Holmen et al., 2013). They reported the preparation of Co catalysts supported on hierarchically structured carbon nanofibers (CNFs)/carbon felt composites. These materials showed enhanced heat and mass transfer and provided a relatively uniform temperature profile inside the reactor. Similarly, the addition of exfoliated graphite to pelletized Co-based catalysts resulted in a 30 times higher thermal conductivity for the catalytic bed than that of the catalyst without any additives and gave rise to an enhanced catalytic performance (Asalieva et al., 2020).

In the light of all the aforementioned results, one can conclude that carbon materials exhibit a huge potential not only in terms of reducing metal-support interactions and providing a high metal dispersion and FTS catalyst activity, but also for the enhancement of the heat and mass transfer inside the reactor, allowing for a

better reactor temperature control and a higher catalytic performance.

CONCLUSIONS, CHALLENGES, AND FUTURE PERSPECTIVES

Fischer–Tropsch synthesis (FTS) is an important industrial process in the transformation of nonpetroleum carbon resources, including natural gas, coal, and lignocellulosic biomass into clean hydrocarbon fuels and valuable chemicals. The FTS catalysts are required to be preferably supported, and carbon-based materials have been recognized as an interesting alternative to conventional metal oxides. In this review, we have described the use of different carbon-based materials as supports for Co, Fe, and in a lesser extent Ru-based FT catalysts (promoted and unpromoted) over the past 2 decades, including activated carbons (ACs), ordered mesoporous carbons (OMCs), carbon nanotubes and nanofibers (CNTs and CNFs), carbon spheres (CSs), diamond, grapheme, and graphite. Some general conclusions can be drawn from these studies: (1) the carbon surface modification (functionalization and doping) with oxygen and nitrogen functional groups, especially in the case of carbon supports prepared at high carbonization temperature, is crucial to produce catalysts with a high dispersion, FTS activity, stability, and enhanced selectivity; (2) the extent of reduction of FT metal-carbon catalysts is generally high due to the low metal-support interactions; (3) the proximity between carbon and supported iron can facilitate the formation of the active iron carbides, thus leading to a higher concentration of active sites on the catalyst surface; (4) the morphology and structure of the carbon are crucial aspects to modify the metal-support interactions, the metal dispersion, the particle size, and hence, their performance in the FTS process. Specifically, metal catalyst confinement inside the pores of CNTs has shown an outstanding behavior as compared to those of catalytic systems presenting metal nanoparticles supported on the outer CNT surface; (5) larger pores in the support, as those in CNTs, OMCs, and mesoporous carbon spheres, resulted in larger metal phase crystallites formed inside and, thus, higher metal reducibility and lower metal dispersion, enhancing, on the other hand, the hydrocarbon diffusion and the formation of long-chain hydrocarbons; (6) an optimum metal promoter loading and a close proximity between the promoter and the FT metal catalyst seem to be essential factors to increase the FT catalyst reducibility and, thus, to improve the FTS activity and selectivity; (7) it has been demonstrated that the carbon support improves the catalyst heat-transfer properties during the highly exothermic FTS reaction and, thus, the catalytic performance.

However, there are also some challenges to be addressed and future perspectives regarding the use of carbon-based materials as FTS catalyst supports from an industrial-scale point of view. One of these issues is the low density and, in some cases, the insufficient mechanical strength of carbon-based materials. Most of FT reactors used in industry are fixed-bed reactors and slurry reactors. When using a fixed-bed reactor, the catalyst requires to have an appropriate size and shape and therefore they need to be pelletized in order to facilitate intraparticle mass transfer and avoid high-pressure drops. In case of using a slurry reactor, problems derived from the catalyst abrasion and product-catalyst separation are remarkable. Carbon-supported catalysts have been less evaluated on a slurry reactor, and these issues need to be investigated.

One important disadvantage is related to the high costs of the nanostructured carbon materials as compared to conventional oxide supports, typically used in the FTS process. Although the industrial production of CNTs, CNFs, and AC is currently not an issue, the production of metal-doped carbons is currently not available on a large industrial scale. Furthermore, in most of the cases, petroleum-derived carbon sources are used for the preparation of the carbon-based materials. Only in the case of ACs, the use of biomassic sources has been explored as raw material. Nevertheless, most of the catalysts studied have been prepared using commercially available AC supports. Much research is still necessary in this direction. In this sense, renewable biomass residues, besides being used for the production of liquid fuels *via* gasification and further conversion of the produced syngas, could be used for the production of the FT catalyst supports, resulting in both a positive environmental and an economic impact. By this way, it would be possible to minimize greenhouse gas emissions and to achieve a significant reduction of fossil fuel dependency. On this context, the simulation of syngas from the gasification of biomass as feedstock to the FTS reactor operating at both low- and high-temperature (LT-FTS and LT-FTS) processes, using carbon-based catalyst supports, has not been explored in detailed. Therefore, process intensification and catalyst engineering are both crucial steps necessary to be investigated and optimized for the successful implementation of the biomass-to-liquid technology and the use of carbon-based catalyst supports for FTS at large scale.

AUTHOR CONTRIBUTIONS

JR-M and TC conceived and designed the structure of the review. MV-R, MR-C, and JP contributed with the literature analysis, illustrations, and writing the manuscript. All authors contributed to the manuscript revision and approved the submitted version.

ACKNOWLEDGMENTS

The authors acknowledge the Spanish Ministry of Science, Innovation, and Universities (MICIU) and FEDER (Project RTI2018-097555-B-I00) and Junta de Andalucía (Project UMA18-FEDERJA-110). MJVR acknowledges MICIU for her Juan de la Cierva-Incorporación postdoctoral fellowship (IJC2019-041222-I), and MARC thanks MICIU for his FPU predoctoral fellowship (FPU18/02796).

SUPPLEMENTARY MATERIAL

The Supplementary Material for this article can be found online at: https://www.frontiersin.org/articles/10.3389/fmats.2020.617432/full#supplementary-material.

REFERENCES

Aasberg-Petersen, K., Christensen, T. S., Dybkjaer, I., Sehested, J., Østberg, M., Coertzen, R. M., et al. (2004). Chapter 4-Synthesis gas production for FT synthesis. *Stud. Surf. Sci. Catal.* 152, 258–405. doi:10.1016/S0167-2991(04)80461-0

Abbaslou, R. M. M., Soltan, J., and Dalai, A. K. (2010). Effects of nanotubes pore size on the catalytic performances of iron catalysts supported on carbon nanotubes for Fischer–Tropsch synthesis. *Appl. Catal. Gen.* 379, 129–134. doi:10.1016/j.apcata.2010.03.006

Abbaslou, R. M. M., Tavassoli, A., Soltan, J., and Dalai, A. K. (2009). Iron catalysts supported on carbon nanotubes for Fischer–Tropsch synthesis: effect of catalytic site position. *Appl. Catal. Gen.* 367, 47–52. doi:10.1016/j.apcata.2009.07.025

Abrokwah, R. Y., Rahman, M. M., Deshmane, V. G., and Kuila, D. (2019). Effect of titania support on Fischer-Tropsch synthesis using cobalt, iron, and ruthenium catalysts in silicon-microchannel microreactor. *Molecular Catalysis*. 478, 110566. doi:10.1016/j.mcat.2019.110566

Ahn, C.-I., Park, Y. M., Cho, J. M., Lee, D. H., Chung, C.-H., Cho, B. G., et al. (2016). Fischer-trospch synthesis on ordered mesoporous cobalt-based catalysts with compact multichannel fixed-bed reactor application: a review. *Catal. Surv. Asia*. 20, 210–230. doi:10.1007/s10563-016-9219-5

Almkhelfe, H., Li, X., Thapa, P., Hohn, K. L., and Amama, P. B. (2018). Carbon nanotube-supported catalysts prepared by a modified photo-Fenton process for Fischer–Tropsch synthesis. *J. Catal.* 361, 278–289. doi:10.1016/j.jcat.2018.02.009

Asalieva, E., Sineva, L., Sinichkina, S., Solomonik, I., Gryaznov, K., Pushina, E., et al. (2020). Exfoliated graphite as a heat-conductive frame for a new pelletized Fischer–Tropsch synthesis catalyst. *Appl. Catal. Gen.* 601, 117639. doi:10.1016/j.apcata.2020.117639

Bahome, M. C., Jewell, L. L., Hildebrandt, D., Glasser, D., and Coville, N. J. (2005). Fischer–Tropsch synthesis over iron catalysts supported on carbon nanotubes. *Appl. Catal. Gen.* 287, 60–67. doi:10.1016/j.apcata.2005.03.029

Bezemer, G. L., Bitter, J. H., Kuipers, H. P., Oosterbeek, H., Holewijn, J. E., Xu, X., et al. (2006a). Cobalt particle size effects in the Fischer-Tropsch reaction studied with carbon nanofiber supported catalysts. *J. Am. Chem. Soc.* 128, 3956–3964. doi:10.1021/ja058282w

Bezemer, G. L., Falke, U., Van Dillen, A. J., and De Jong, K. P. (2005). Cobalt on carbon nanofiber catalysts: auspicious system for study of manganese promotion in Fischer-Tropsch catalysis. *Chem. Commun.* 731–733. doi:10.1039/b414788j

Bezemer, G. L., Radstake, P. B., Falke, U., Oosterbeek, H., Kuipers, H. P. C. E., Van Dillen, A. J., et al. (2006b). Investigation of promoter effects of manganese oxide on carbon nanofiber-supported cobalt catalysts for Fischer–Tropsch synthesis. *J. Catal.* 237, 152–161. doi:10.1016/j.jcat.2005.10.031

Chen, L., Song, G., Fu, Y., and Shen, J. (2012). The effects of promoters of K and Zr on the mesoporous carbon supported cobalt catalysts for Fischer-Tropsch synthesis. *J. Colloid Interface Sci.* 368, 456–461. doi:10.1016/j.jcis.2011.11.030

Chen, Q., Liu, G., Ding, S., Chanmiya Sheikh, M., Long, D., Yoneyama, Y., et al. (2018). Design of ultra-active iron-based Fischer-Tropsch synthesis catalysts over spherical mesoporous carbon with developed porosity. *Chem. Eng. J.* 334, 714–724. doi:10.1016/j.cej.2017.10.093

Chen, W., Fan, Z., Pan, X., and Bao, X. (2008). Effect of confinement in carbon nanotubes on the activity of Fischer-Tropsch iron catalyst. *J. Am. Chem. Soc.* 130, 9414–9419. doi:10.1021/ja8008192

Chen, W., Pan, X., and Bao, X. (2007). Tuning of redox properties of iron and iron oxides via encapsulation within carbon nanotubes. *J. Am. Chem. Soc.* 129, 7421–7426. doi:10.1021/ja0713072

Chen, W., Pan, X., Willinger, M. G., Su, D. S., and Bao, X. (2006). Facile autoreduction of iron oxide/carbon nanotube encapsulates. *J. Am. Chem. Soc.* 128, 3136–3137. doi:10.1021/ja056721l

Cheng, K., Ordomsky, V. V., Legras, B., Virginie, M., Paul, S., Wang, Y., et al. (2015). Sodium-promoted iron catalysts prepared on different supports for high temperature Fischer–Tropsch synthesis. *Appl. Catal. Gen.* 502, 204–214. doi:10.1016/j.apcata.2015.06.010

Cheng, K., Ordomsky, V. V., Virginie, M., Legras, B., Chernavskii, P. A., Kazak, V. O., et al. (2014). Support effects in high temperature Fischer-Tropsch synthesis on iron catalysts. *Appl. Catal. Gen.* 488, 66–77. doi:10.1016/j.apcata.2014.09.033

Cheng, Q., Zhao, N., Lyu, S., Tian, Y., Gao, F., Dong, L., et al. (2019). Tuning interaction between cobalt catalysts and nitrogen dopants in carbon nanospheres to promote Fischer-Tropsch synthesis. *Appl. Catal. B Environ.* 248, 73–83. doi:10.1016/j.apcatb.2019.02.024

Chernavskii, P. A., Pankina, G. V., Kazantsev, R. V., and Eliseev, O. L. (2018). Potassium as a structural promoter for an iron/activated carbon catalyst: unusual effect of component deposition order on magnetite particle size and catalytic behavior in Fischer–Tropsch synthesis. *ChemCatChem.* 10, 1313–1320. doi:10.1002/cctc.201701818

Chernyak, S. A., Ivanov, A. S., Maksimov, S. V., Maslakov, K. I., Isaikina, O. Y., Chernavskii, P. A., et al. (2020). Fischer-Tropsch synthesis over carbon-encapsulated cobalt and iron nanoparticles embedded in 3D-framework of carbon nanotubes. *J. Catal.* 389, 270–284. doi:10.1016/j.jcat.2020.06.011

Chernyak, S. A., Stolbov, D. N., Ivanov, A. S., Klokov, S. V., Egorova, T. B., Maslakov, K. I., et al. (2019). Effect of type and localization of nitrogen in graphene nanoflake support on structure and catalytic performance of Co-based Fischer-Tropsch catalysts. *Catal. Today*. 357, 193–202. doi:10.1016/j.cattod.2019.02.044

Chernyak, S. A., Suslova, E. V., Ivanov, A. S., Egorov, A. V., Maslakov, K. I., Savilov, S. V., et al. (2016). Co catalysts supported on oxidized CNTs: evolution of structure during preparation, reduction and catalytic test in Fischer-Tropsch synthesis. *Appl. Catal. Gen.* 523, 221–229. doi:10.1016/j.apcata.2016.06.012

Chew, L. M., Xia, W., Düdder, H., Weide, P., Ruland, H., and Muhler, M. (2016). On the role of the stability of functional groups in multi-walled carbon nanotubes applied as support in iron-based high-temperature Fischer–Tropsch synthesis. *Catal. Today* 270, 85–92. doi:10.1016/j.cattod.2015.09.023

Chin, Y.-H., Hu, J., Cao, C., Gao, Y., and Wang, Y. (2005). Preparation of a novel structured catalyst based on aligned carbon nanotube arrays for a microchannel Fischer-Tropsch synthesis reactor. *Catal. Today* 110, 47–52. doi:10.1016/j.cattod.2005.09.007

De Jong, K. P., and Geus, J. W. (2000). Carbon nanofibers: catalytic synthesis and applications. *Catal. Rev.* 42, 481–510. doi:10.1081/CR-100101954

De Smit, E., and Weckhuysen, B. M. (2008). The renaissance of iron-based Fischer-Tropsch synthesis: on the multifaceted catalyst deactivation behaviour. *Chem. Soc. Rev.* 37, 2758–2781. doi:10.1039/b805427d

Den Breejen, J. P., Radstake, P. B., Bezemer, G. L., Bitter, J. H., Frøseth, V., Holmen, A., et al. (2009). On the origin of the cobalt particle size effects in Fischer-Tropsch catalysis. *J. Am. Chem. Soc.* 131, 7197–7203. doi:10.1021/ja901006x

Den Breejen, J. P., Sietsma, J. R. A., Friedrich, H., Bitter, J. H., and De Jong, K. P. (2010). Design of supported cobalt catalysts with maximum activity for the Fischer–Tropsch synthesis. *J. Catal.* 270, 146–152. doi:10.1016/j.jcat.2009.12.015

Díaz, J. A., Akhavan, H., Romero, A., Garcia-Minguillan, A. M., Romero, R., Giroir-Fendler, A., et al. (2014). Cobalt and iron supported on carbon nanofibers as catalysts for Fischer–Tropsch synthesis. *Fuel Process. Technol.* 128, 417–424. doi:10.1016/j.fuproc.2014.08.005

Dlamini, M. W., Kumi, D. O., Phaahlamohlaka, T. N., Lyadov, A. S., Billing, D. G., Jewell, L. L., et al. (2015). Carbon spheres prepared by hydrothermal synthesis—a support for bimetallic iron cobalt Fischer–Tropsch catalysts. *ChemCatChem.* 7, 3000–3011. doi:10.1002/cctc.201500334

Dlamini, M. W., Phaahlamohlaka, T. N., Kumi, D. O., Forbes, R., Jewell, L. L., and Coville, N. J. (2020). Post doped nitrogen-decorated hollow carbon spheres as a support for Co Fischer-Tropsch catalysts. *Catal. Today* 342, 99–110.

Eschemann, T. O., Lamme, W. S., Manchester, R. L., Parmentier, T. E., Cognigni, A., Rønning, M., et al. (2015). Effect of support surface treatment on the synthesis, structure, and performance of Co/CNT Fischer–Tropsch catalysts. *J. Catal.* 328, 130–138. doi:10.1016/j.jcat.2014.12.010

Eslava, J. L., Fernández-García, M., Guerrero-Ruiz, A., Iglesias Juez, A., and Rodríguez-Ramos, I. (2018). Effect of different promoter precursors in a model Ru-Cs/graphite system on the catalytic selectivity for Fischer-Tropsch reaction. *App. Surf. Sci.* 328, 130–138. doi:10.1016/j.apsusc.2018.03.207

Figueiredo, J. L., Pereira, M. F. R., Freitas, M. M. A., and Órfão, J. J. M. (1999). Modification of the surface chemistry of activated carbons. *Carbon* 37, 1379–1389. doi:10.1016/S0008-6223(98)00333-9

Fratalocchi, L., Visconti, C. G., Groppi, G., Lietti, L., and Tronconi, E. (2018). Intensifying heat transfer in Fischer-Tropsch tubular reactors through the adoption of conductive packed foams. *Chem. Eng. J* 349, 829–837. doi:10.1016/j.cej.2018.05.108

Fu, T., Jiang, Y., Lv, J., and Li, Z. (2013). Effect of carbon support on Fischer–Tropsch synthesis activity and product distribution over Co-based catalysts. *Fuel Process. Technol.* 110, 141–149. doi:10.1016/j.fuproc.2012.12.006

Fu, T., Liu, R., Lv, J., and Li, Z. (2014a). Influence of acid treatment on N-doped multi-walled carbon nanotube supports for Fischer–Tropsch performance on cobalt catalyst. *Fuel Process. Technol.* 122, 49–57. doi:10.1016/j.fuproc.2014.01.016

Fu, T., Lv, J., and Li, Z. (2014b). Effect of carbon porosity and cobalt particle size on the catalytic performance of carbon supported cobalt Fischer–Tropsch catalysts. *Ind. Eng. Chem. Res.* 53, 1342–1350. doi:10.1021/ie402128y

Geim, A. K., and Novoselov, K. S. (2007). The rise of graphene. *Nat. Mater* 6, 183–191. doi:10.1038/nmat1849

Ghogia, A. C., Cayez, S., Machado, B. F., Nzihou, A., Serp, P., Soulantica, K., et al. (2020). Hydrogen spillover in the Fischer-Tropsch synthesis on carbon-supported cobalt catalysts. *ChemCatChem.* 12, 1117–1128. doi:10.1002/cctc.201901934

Gu, B., He, S., Peron, D. V., Strossi Pedrolo, D. R., Moldovan, S., Ribeiro, M. C., et al. (2019). Synergy of nanoconfinement and promotion in the design of efficient supported iron catalysts for direct olefin synthesis from syngas. *J. Catal.* 376, 1–16. doi:10.1016/j.jcat.2019.06.035

Gu, B., Ordomsky, V. V., Bahri, M., Ersen, O., Chernavskii, P. A., Filimonov, D., et al. (2018). Effects of the promotion with bismuth and lead on direct synthesis of light olefins from syngas over carbon nanotube supported iron catalysts. *Appl. Catal. B Environ* 234, 153–166. doi:10.1016/j.apcatb.2018.04.025

Hajjar, Z., Doroudian Rad, M., and Soltanali, S. (2017). Novel Co/graphene oxide and Co/nanoporous graphene catalysts for Fischer–Tropsch reaction. *Res. Chem. Intermed* 43, 1341–1353. doi:10.1007/s11164-016-2701-x

Hernández Mejía, C., Van Deelen, T. W., and De Jong, K. P. (2018). Activity enhancement of cobalt catalysts by tuning metal-support interactions. *Nat. Commun.* 9, 4459. doi:10.1038/s41467-018-06903-w

Holmen, A., Venvik, H. J., Myrstad, R., Zhu, J., and Chen, D. (2013). Monolithic, microchannel and carbon nanofibers/carbon felt reactors for syngas conversion by Fischer-Tropsch synthesis. *Catal. Today* 216, 150–157. doi:10.1016/j.cattod.2013.06.006

Honsho, T.-O., Kitano, T., Miyake, T., and Suzuki, T. (2012). Fischer–Tropsch synthesis over Co-loaded oxidized diamond catalyst. *Fuel* 94, 170–177. doi:10.1016/j.fuel.2011.08.045

Hu, B., Wang, K., Wu, L., Yu, S. H., Antonietti, M., and Titirici, M. M. (2010). Engineering carbon materials from the hydrothermal carbonization process of biomass. *Adv Mater Weinheim* 22, 813–828. doi:10.1002/adma.200902812

Ismail, A. S. M., Casavola, M., Liu, B., Gloter, A., Van Deelen, T. W., Versluijs, M., et al. (2019). Atomic-scale investigation of the structural and electronic properties of cobalt–iron bimetallic Fischer–Tropsch catalysts. *ACS Catal.* 9, 7998–8011. doi:10.1021/acscatal.8b04334

Jiang, F., Wang, S., Zheng, J., Liu, B., Xu, Y., and Liu, X. (2020). Fischer-Tropsch synthesis to lower α-olefins over cobalt-based catalysts: dependence of the promotional effect of promoter on supports. *Catal. Today*. doi:10.1016/j.cattod.2020.03.051

Jiang, F., Zhang, M., Liu, B., Xu, Y., and Liu, X. (2017). Insights into the influence of support and potassium or sulfur promoter on iron-based Fischer–Tropsch synthesis: understanding the control of catalytic activity, selectivity to lower olefins, and catalyst deactivation. *Catalysis Science & Technology* 7, 1245–1265. doi:10.1039/C7CY00048K

Jun, S., Joo, S. H., Ryoo, R., Kruk, M., Jaroniec, M., Liu, Z., et al. (2000). Synthesis of new, nanoporous carbon with hexagonally ordered mesostructure. *J. Am. Chem. Soc.* 122, 10712–10713. doi:10.1021/ja002261e

Jung, H. J., Walker, P. L., and Vannice, A. (1982). CO hydrogenation over well-dispersed carbon-supported iron catalysts. *J. Catal.* 75, 416–422. doi:10.1016/0021-9517(82)90223-8

Kang, J., Zhang, S., Zhang, Q., and Wang, Y. (2009). Ruthenium nanoparticles supported on carbon nanotubes as efficient catalysts for selective conversion of synthesis gas to diesel fuel. *Angew Chem. Int. Ed. Engl.* 48, 2565–2568. doi:10.1002/anie.200805715

Kang, S. W., Kim, K., Chun, D. H., Yang, J.-I., Lee, H.-T., Jung, H., et al. (2017). High-performance Fe5C2@CMK-3 nanocatalyst for selective and high-yield production of gasoline-range hydrocarbons. *J. Catal.* 349, 66–74. doi:10.1016/j.jcat.2017.03.004

Karimi, A., Nasernejad, B., Rashidi, A. M., Tavasoli, A., and Pourkhalil, M. (2014). Functional group effect on carbon nanotube (CNT)-supported cobalt catalysts in Fischer–Tropsch synthesis activity, selectivity and stability. *Fuel* 117, 1045–1051. doi:10.1016/j.fuel.2013.10.014

Karimi, S., Tavasoli, A., Mortazavi, Y., and Karimi, A. (2015a). Cobalt supported on Graphene – a promising novel Fischer–Tropsch synthesis catalyst. *Appl. Catal. Gen.* 499, 188–196. doi:10.1016/j.apcata.2015.04.024

Karimi, S., Tavasoli, A., Mortazavi, Y., and Karimi, A. (2015b). Enhancement of cobalt catalyst stability in Fischer–Tropsch synthesis using graphene nanosheets as catalyst support. *Chem. Eng. Res. Des.* 104, 713–722. doi:10.1016/j.cherd.2015.10.016

Karmakar, S., Sharma, S. M., Teredesai, P. V., and Sood, A. K. (2004). Pressure-induced phase transitions in iron-filled carbon nanotubes: X-ray diffraction studies. *Phys. Rev. B* 69, 165414.

Knox, J. H., Kaur, B., and Millward, G. R. (1986). Structure and performance of porous graphitic carbon in liquid chromatography. *J. Chromatogr. A* 352, 3–25. doi:10.1016/S0021-9673(01)83368-9

Kuang, T., Lyu, S., Liu, S., Zhang, Y., Li, J., Wang, G., et al. (2019). Controlled synthesis of cobalt nanocrystals on the carbon spheres for enhancing Fischer–Tropsch synthesis performance. *J. Energy Chem.* 33, 67–73. doi:10.1016/j.jechem.2018.08.012

Kundu, S., Xia, W., Busser, W., Becker, M., Schmidt, D. A., Havenith, M., et al. (2010). The formation of nitrogen-containing functional groups on carbon nanotube surfaces: a quantitative XPS and TPD study. *Phys. Chem. Chem. Phys.* 12, 4351–4359. doi:10.1039/b923651a

Lacroix, M., Dreibine, L., De Tymowski, B., Vigneron, F., Edouard, D., Bégin, D., et al. (2011). Silicon carbide foam composite containing cobalt as a highly selective and re-usable Fischer–Tropsch synthesis catalyst. *Appl. Catal. Gen.* 397, 62–72. doi:10.1016/j.apcata.2011.02.012

Lappas, A., and Heracleous, E. (2016). "18-Production of biofuels via Fischer–Tropsch synthesis: biomass-to-liquids," in *Handbook of Biofuels Production*. Editors R. Luque, C.S.K. Lin, K. Wilson, and J. Clark Second Edition (Cambridge, United Kingdom: Woodhead Publishing), 549–593.

Lehman, J. H., Terrones, M., Mansfield, E., Hurst, K. E., and Meunier, V. (2011). Evaluating the characteristics of multiwall carbon nanotubes. *Carbon* 49, 2581–2602. doi:10.1016/j.carbon.2011.03.028

Li, X., Nisa, M. U., Chen, Y., and Li, Z. (2019). Co-based catalysts supported on silica and carbon materials: effect of support property on cobalt species and Fischer–Tropsch synthesis performance. *Ind. Eng. Chem. Res.* 58, 3459–3467. doi:10.1021/acs.iecr.8b05451

Lipson, H., and Stokes, A. R. (1942). A new structure of carbon. *Nature* 149, 328. doi:10.1038/149328a0

Liu, C.-Y., and Li, E. Y. (2020). C–C coupling reactions promoted by CNT-supported bimetallic center in Fischer–Tropsch synthesis. *Sustainable Energy & Fuels* 4, 2638–2644. doi:10.1039/C9SE01289C

Liu, J., Wang, Z., Yan, X., and Jian, P. (2017). Metallic cobalt nanoparticles imbedded into ordered mesoporous carbon: a non-precious metal catalyst with excellent hydrogenation performance. *J. Colloid Interface Sci.* 505, 789–795. doi:10.1016/j.jcis.2017.06.081

Lund, C. R. F., and Dumesic, J. A. (1981). Strong oxide-oxide interactions in silica-supported magnetite catalysts. 1. X-ray diffraction and Mossbauer spectroscopy evidence for interaction. *J. Phys. Chem.* 85, 3175–3180. doi:10.1021/j150621a034

Luo, Q.-X., Guo, L.-P., Yao, S.-Y., Bao, J., Liu, Z.-T., and Liu, Z.-W. (2019). Cobalt nanoparticles confined in carbon matrix for probing the size dependence in Fischer-Tropsch synthesis. *J. Catal.* 369, 143–156. doi:10.1016/j.jcat.2018.11.002

Luque, R., De La Osa, A. R., Campelo, J. M., Romero, A. A., Valverde, J. L., and Sanchez, P. (2012). Design and development of catalysts for Biomass-To-Liquid-Fischer–Tropsch (BTL-FT) processes for biofuels production. *Energy Environ. Sci.* 5, 5186–5202. doi:10.1039/c1ee02238e

Lyu, S., Peng, B., Kuang, T., Rappé, K. G., Zhang, Y., Li, J., et al. (2019). Supported cobalt nanoparticles with a single active phase for Fischer–Tropsch synthesis. *ACS Applied Nano Materials* 2, 2266–2272. doi:10.1021/acsanm.9b00187

Ma, G., Xu, Y., Wang, J., Bai, J., Du, Y., Zhang, J., et al. (2020). An Na-modified Fe@C core–shell catalyst for the enhanced production of gasoline-range hydrocarbons via Fischer–Tropsch synthesis. *RSC Adv.* 10, 10723–10730. doi:10.1039/D0RA01036G

Ma, W.-P., Ding, Y.-J., and Lin, L.-W. (2004). Fischer–Tropsch synthesis over activated-carbon-supported cobalt Catalysts: effect of Co loading and promoters on catalyst performance. *Ind. Eng. Chem. Res.* 43, 2391–2398. doi:10.1021/ie034116q

Ma, W., Kugler, E. L., and Dadyburjor, D. B. (2007). Potassium effects on activated-carbon-supported iron catalysts for Fischer–Tropsch synthesis. *Energy Fuels* 21, 1832–1842. doi:10.1021/ef060654e

Ma, W., Kugler, E. L., Wright, J., and Dadyburjor, D. B. (2006). Mo–Fe catalysts supported on activated carbon for synthesis of liquid fuels by the Fischer–Tropsch Process: effect of Mo addition on reducibility, activity, and hydrocarbon selectivity. *Energy Fuels* 20, 2299–2307. doi:10.1021/ef0602372

Malek Abbaslou, R. M., Soltan, J., and Dalai, A. K. (2011). Iron catalyst supported on carbon nanotubes for Fischer–Tropsch synthesis: effects of Mo promotion. *Fuel* 90, 1139–1144. doi:10.1016/j.fuel.2010.10.044

Malek Abbaslou, R. M., Tavasoli, A., and Dalai, A. K. (2009). Effect of pre-treatment on physico-chemical properties and stability of carbon nanotubes supported iron Fischer–Tropsch catalysts. *Appl. Catal. Gen.* 355, 33–41. doi:10.1016/j.apcata.2008.11.023

Mohandas, J. C., Gnanamani, M. K., Jacobs, G., Ma, W., Ji, Y., Khalid, S., et al. (2011). Fischer–tropsch synthesis: characterization and reaction testing of cobalt carbide. *ACS Catal.* 1, 1581–1588. doi:10.1021/cs200236q

Moreno-Castilla, C., Ferro-Garcia, M. A., Joly, J. P., Bautista-Toledo, I., Carrasco-Marin, F., and Rivera-Utrilla, J. (1995). Activated carbon surface modifications by nitric acid, hydrogen peroxide, and ammonium peroxydisulfate treatments. *Langmuir* 11, 4386–4392. doi:10.1021/la00011a035

Moreno-Castilla, C., López-Ramón, M. V., and Carrasco-MarıfN, F. (2000). Changes in surface chemistry of activated carbons by wet oxidation. *Carbon* 38, 1995–2001. doi:10.1016/S0008-6223(00)00048-8

Moulefera, I., García-Mateos, F. J., Benyoucef, A., Rosas, J. M., Rodríguez-Mirasol, J. M., and Cordero, T. (2020). Effect of Co-solution of carbon precursor and activating agent on the textural properties of highly porous activated carbon obtained by chemical activation of lignin with H3PO4. *Front. Mater.* 7, 153–545. doi:10.3389/fmats.2020.00153

Moussa, S. O., Panchakarla, L. S., Ho, M. Q., and El-Shall, M. S. (2014). Graphene-supported, iron-based nanoparticles for catalytic production of liquid hydrocarbons from synthesis gas: the role of the graphene support in comparison with carbon nanotubes. *ACS Catal.* 4, 535–545. doi:10.1021/cs4010198

Munirathinam, R., Pham Minh, D., and Nzihou, A. (2018). Effect of the support and its surface modifications in cobalt-based Fischer–Tropsch synthesis. *Ind. Eng. Chem. Res.* 57, 16137–16161. doi:10.1021/acs.iecr.8b03850

Nakhaei Pour, A., Housaindokht, M. R., and Kamali Shahri, S. M. (2018). Fischer–tropsch synthesis over cobalt/CNTs catalysts: functionalized support and catalyst preparation effect on activity and kinetic parameters. *Ind. Eng. Chem. Res.* 57, 13639–13649. doi:10.1021/acs.iecr.8b02485

Noureldin, M. M. B., Elbashir, N. O., and El-Halwagi, M. M. (2014). Optimization and selection of reforming approaches for syngas generation from natural/shale gas. *Ind. Eng. Chem. Res.* 53, 1841–1855. doi:10.1021/ie402382w

Oschatz, M., Lamme, W. S., Xie, J., Dugulan, A. I., and De Jong, K. P. (2016a). Ordered mesoporous materials as supports for stable iron catalysts in the Fischer–Tropsch synthesis of lower olefins. *ChemCatChem.* 8, 2846–2852. doi:10.1002/cctc.201600492

Oschatz, M., Van Deelen, T. W., Weber, J. L., Lamme, W. S., Wang, G., Goderis, B., et al. (2016b). Effects of calcination and activation conditions on ordered mesoporous carbon supported iron catalysts for production of lower olefins from synthesis gas. *Catalysis Science & Technology* 6, 8464–8473. doi:10.1039/C6CY01251E

Otun, K. O., Liu, X., and Hildebrandt, D. (2020). Metal-organic framework (MOF)-derived catalysts for Fischer-Tropsch synthesis: recent progress and future perspectives. *J. Energy Chem.* 51, 230–245. doi:10.1016/j.jechem.2020.03.062

Palomo, J., Ternero-Hidalgo, J. J., Rosas, J. M., Rodríguez-Mirasol, J., and Cordero, T. (2017). Selective nitrogen functionalization of phosphorus-containing activated carbons. *Fuel Process. Technol.* 156, 438–445. doi:10.1016/j.fuproc.2016.10.006

Pan, X., and Bao, X. (2011). The effects of confinement inside carbon nanotubes on catalysis. *Acc. Chem. Res.* 44, 553–562. doi:10.1021/ar100160t

Phaahlamohlaka, T. N., Dlamini, M. W., Kumi, D. O., Forbes, R., Jewell, L. L., and Coville, N. J. (2020). Co inside hollow carbon spheres as a Fischer-Tropsch catalyst: spillover effects from Ru placed inside and outside the HCS. *Appl. Catal. Gen.* 599, 117617. doi:10.1016/j.apcata.2020.117617

Phaahlamohlaka, T. N., Kumi, D. O., Dlamini, M. W., Forbes, R., Jewell, L. L., Billing, D. G., et al. (2017). Effects of Co and Ru intimacy in Fischer–Tropsch catalysts using hollow carbon sphere supports: assessment of the hydrogen spillover processes. *ACS Catal.* 7, 1568–1578. doi:10.1021/acscatal.6b03102

Prieto, G., Martínez, A., Concepción, P., and Moreno-Tost, R. (2009). Cobalt particle size effects in Fischer–Tropsch synthesis: structural and *in situ* spectroscopic characterisation on reverse micelle-synthesised Co/ITQ-2 model catalysts. *J. Catal.* 266, 129–144. doi:10.1016/j.jcat.2009.06.001

Ren, J., Cao, J.-P., Zhao, X.-Y., Yang, F.-L., and Wei, X.-Y. (2019). Recent advances in syngas production from biomass catalytic gasification: a critical review on reactors, catalysts, catalytic mechanisms and mathematical models. *Renew. Sustain. Energy Rev.* 116, 109426. doi:10.1016/j.rser.2019.109426

Rodríguez-Reinoso, F., and Molina-Sabio, M. (1992). Activated carbons from lignocellulosic materials by chemical and/or physical activation: an overview. *Carbon* 30, 1111–1118. doi:10.1016/0008-6223(92)90143-K

Rosas, J. M., Bedia, J., Rodríguez-Mirasol, J., and Cordero, T. (2010). On the preparation and characterization of chars and activated carbons from orange skin. *Fuel Process. Technol.* 91, 1345–1354. doi:10.1016/j.fuproc.2010.05.006

Rosas, J. M., Bedia, J., Rodríguez-Mirasol, J., and Cordero, T. (2008). Preparation of hemp-derived activated carbon monoliths. Adsorption of water vapor. *Ind. Eng. Chem. Res.* 47, 1288–1296. doi:10.1021/ie070924w

Santos, V. P., Wezendonk, T. A., Jaén, J. J., Dugulan, A. I., Nasalevich, M. A., Islam, H. U., et al. (2015). Metal organic framework-mediated synthesis of highly active and stable Fischer-Tropsch catalysts. *Nat. Commun.* 6, 6451. doi:10.1038/ncomms7451

Sartipi, S., Makkee, M., Kapteijn, F., and Gascon, J. (2014). Catalysis engineering of bifunctional solids for the one-step synthesis of liquid fuels from syngas: a review. *Catalysis Science & Technology* 4, 893–907. doi:10.1039/C3CY01021J

Schulte, H. J., Graf, B., Xia, W., and Muhler, M. (2012). Nitrogen- and oxygen-functionalized multiwalled carbon nanotubes used as support in iron-catalyzed, high-temperature Fischer–Tropsch synthesis. *ChemCatChem.* 4, 350–355. doi:10.1002/cctc.201100275

Serp, P., Corrias, M., and Kalck, P. (2003). Carbon nanotubes and nanofibers in catalysis. *Appl. Catal. Gen.* 253, 337–358. doi:10.1016/S0926-860X(03)00549-0

Serp, P., Feurer, R., Kalck, P., Kihn, Y., Faria, J. L., and Figueiredo, J. L. (2001). A chemical vapour deposition process for the production of carbon nanospheres. *Carbon* 39, 621–626. doi:10.1016/S0008-6223(00)00324-9

Shariati, J., Haghtalab, A., and Mosayebi, A. (2019). Fischer–Tropsch synthesis using Co and Co-Ru bifunctional nanocatalyst supported on carbon nanotube prepared via chemical reduction method. *J. Energy Chem.* 28, 9–22. doi:10.1016/j.jechem.2017.10.001

Steynberg, A. P. (2004). "Chapter 1-introduction to Fischer-Tropsch technology," in *Studies in Surface Science and Catalysis*. Editors A. Steynberg and M. Dry (Amsterdam, Netherlands: Elsevier), 1–63.

Steynberg, A. P., Espinoza, R. L., Jager, B., and Vosloo, A. C. (1999). High temperature Fischer–Tropsch synthesis in commercial practice. *Appl. Catal. Gen.* 186, 41–54. doi:10.1016/S0926-860X(99)00163-5

Sun, S., Tsubaki, N., and Fujimoto, K. (2000). The reaction performances and characterization of Fischer–Tropsch synthesis Co/SiO2 catalysts prepared from mixed cobalt salts. *Appl. Catal. Gen.* 202, 121–131. doi:10.1016/S0926-860X(00)00455-5

Sun, Z., Sun, B., Qiao, M., Wei, J., Yue, Q., Wang, C., et al. (2012). A general chelate-assisted co-assembly to metallic nanoparticles-incorporated ordered mesoporous carbon catalysts for Fischer-Tropsch synthesis. *J. Am. Chem. Soc.* 134, 17653–17660. doi:10.1021/ja306913x

Tauster, S. J., Fung, S. C., Baker, R. T., and Horsley, J. A. (1981). Strong interactions in supported-metal catalysts. *Science* 211, 1121–1125. doi:10.1126/science.211.4487.1121

Tavasoli, A., Trépanier, M., Dalai, A. K., and Abatzoglou, N. (2010). Effects of confinement in carbon nanotubes on the activity, selectivity, and lifetime of Fischer–Tropsch Co/carbon nanotube catalysts. *J. Chem. Eng. Data* 55, 2757–2763. doi:10.1021/je900984c

Tavasoli, A., Trépanier, M., Malek Abbaslou, R. M., Dalai, A. K., and Abatzoglou, N. (2009). Fischer–Tropsch synthesis on mono- and bimetallic Co and Fe catalysts supported on carbon nanotubes. *Fuel Process. Technol.* 90, 1486–1494. doi:10.1016/j.fuproc.2009.07.007

Teng, X., Huang, S., Wang, J., Wang, H., Zhao, Q., Yuan, Y., et al. (2018). Fabrication of Fe2C embedded in hollow carbon spheres: a high-performance and stable catalyst for Fischer-Tropsch synthesis. *ChemCatChem.* 10, 3883–3891. doi:10.1002/cctc.201800488

Tian, Z., Wang, C., Si, Z., Ma, L., Chen, L., Liu, Q., et al. (2017). Fischer-Tropsch synthesis to light olefins over iron-based catalysts supported on KMnO4 modified activated carbon by a facile method. *Appl. Catal. Gen.* 541, 50–59. doi:10.1016/j.apcata.2017.05.001

Torres Galvis, H. M., Bitter, J. H., Davidian, T., Ruitenbeek, M., Dugulan, A. I., and De Jong, K. P. (2012a). Iron particle size effects for direct production of lower olefins from synthesis gas. *J. Am. Chem. Soc.* 134, 16207–16215. doi:10.1021/ja304958u

Torres Galvis, H. M., Bitter, J. H., Khare, C. B., Ruitenbeek, M., Dugulan, A. I., and De Jong, K. P. (2012b). Supported iron nanoparticles as catalysts for sustainable production of lower olefins. *Science* 335, 835–838. doi:10.1126/science.1215614

Trépanier, M., Dalai, A. K., and Abatzoglou, N. (2010). Synthesis of CNT-supported cobalt nanoparticle catalysts using a microemulsion technique: role of nanoparticle size on reducibility, activity and selectivity in Fischer–Tropsch reactions. *Appl. Catal. Gen.* 374, 79–86. doi:10.1016/j.apcata.2009.11.029

Trépanier, M., Tavasoli, A., Dalai, A. K., and Abatzoglou, N. (2009a). Co, Ru and K loadings effects on the activity and selectivity of carbon nanotubes supported cobalt catalyst in Fischer–Tropsch synthesis. *Appl. Catal. Gen.* 353, 193–202. doi:10.1016/j.apcata.2008.10.061

Trépanier, M., Tavasoli, A., Dalai, A. K., and Abatzoglou, N. (2009b). Fischer–Tropsch synthesis over carbon nanotubes supported cobalt catalysts in a fixed bed reactor: influence of acid treatment. *Fuel Process. Technol.* 90, 367–374. doi:10.1016/j.fuproc.2008.10.012

Ugarte, D. (1992). Curling and closure of graphitic networks under electron-beam irradiation. *Nature* 359, 707–797. doi:10.1038/359707a0

Valero-Romero, M. J., Cabrera-Molina, A., Guerrero-Pérez, M. O., Rodríguez-Mirasol, J., and Cordero, T. (2014). Carbon materials as template for the preparation of mixed oxides with controlled morphology and porous structure. *Catal. Today* 227, 233–241. doi:10.1016/j.cattod.2013.10.093

Valero-Romero, M. J., García-Mateos, F. J., Rodríguez-Mirasol, J., and Cordero, T. (2017). Role of surface phosphorus complexes on the oxidation of porous carbons. *Fuel Process. Technol.* 157, 116–126. doi:10.1016/j.fuproc.2016.11.014

Valero-Romero, M. J., Márquez-Franco, E. M., Bedia, J., Rodríguez-Mirasol, J., and Cordero, T. (2014b). Hierarchical porous carbons by liquid phase impregnation of zeolite templates with lignin solution. *Microporous Mesoporous Mater* 196, 68–78. doi:10.1016/j.micromeso.2014.04.055

Valero-Romero, M. J., Sartipi, S., Sun, X., Rodríguez-Mirasol, J., Cordero, T., Kapteijn, F., et al. (2016). Carbon/H-ZSM-5 composites as supports for bi-functional Fischer–Tropsch synthesis catalysts. *Catalysis Science & Technology* 6, 2633–2646. doi:10.1039/C5CY01942G

Van Deelen, T. W., Hernández Mejía, C., and De Jong, K. P. (2019). Control of metal-support interactions in heterogeneous catalysts to enhance activity and selectivity. *Nature Catalysis* 2, 955–970. doi:10.1038/s41929-019-0364-x

Van Deelen, T. W., Yoshida, H., Oord, R., Zečević, J., Weckhuysen, B. M., and De Jong, K. P. (2020). Cobalt nanocrystals on carbon nanotubes in the Fischer-Tropsch synthesis: impact of support oxidation. *Appl. Catal. Gen.* 593, 117441. doi:10.1016/j.apcata.2020.117441

Visconti, C. G., Tronconi, E., Groppi, G., Lietti, L., Iovane, M., Rossini, S., et al. (2011). Monolithic catalysts with high thermal conductivity for the Fischer–Tropsch synthesis in tubular reactors. *Chem. Eng. J* 171, 1294–1307. doi:10.1016/j.cej.2011.05.014

Vosoughi, V., Badoga, S., Dalai, A. K., and Abatzoglou, N. (2016). Effect of pretreatment on physicochemical properties and performance of multiwalled carbon nanotube supported cobalt catalyst for Fischer–Tropsch synthesis. *Ind. Eng. Chem. Res.* 55, 6049–6059. doi:10.1021/acs.iecr.5b04381

Wang, D., Zhou, X., Ji, J., Duan, X., Qian, G., Zhou, X., et al. (2015). Modified carbon nanotubes by KMnO4 supported iron Fischer–Tropsch catalyst for the direct conversion of syngas to lower olefins. *J. Mater. Chem.* 3, 4560–4567.

Wang, T., Ding, Y., Lü, Y., Zhu, H., and Lin, L. (2008). Influence of lanthanum on the performance of Zr-Co/activated carbon catalysts in Fischer-Tropsch synthesis. *J. Nat. Gas Chem.* 17, 153–158. doi:10.1016/S1003-9953(08)60043-2

Wezendonk, T. A., Sun, X., Dugulan, A. I., Van Hoof, A. J. F., Hensen, E. J. M., Kapteijn, F., et al. (2018). Controlled formation of iron carbides and their performance in Fischer-Tropsch synthesis. *J. Catal.* 362, 106–117. doi:10.1016/j.jcat.2018.03.034

Xiao, J., Pan, X., Guo, S., Ren, P., and Bao, X. (2015). Toward fundamentals of confined catalysis in carbon nanotubes. *J. Am. Chem. Soc.* 137, 477–482. doi:10.1021/ja511498s

Xie, J., Torres Galvis, H. M., Koeken, A. C., Kirilin, A., Dugulan, A. I., Ruitenbeek, M., et al. (2016). Size and promoter effects on stability of carbon-nanofiber-supported iron-based Fischer-Tropsch catalysts. *ACS Catal.* 6, 4017–4024. doi:10.1021/acscatal.6b00321

Xie, W., Zhang, Y., Liew, K., and Li, J. (2012). Effect of catalyst confinement and pore size on Fischer-Tropsch synthesis over cobalt supported on carbon nanotubes. *Sci. China Chem.* 55, 1811–1818. doi:10.1007/s11426-012-4727-2

Xing, C., Yang, G., Wang, D., Zeng, C., Jin, Y., Yang, R., et al. (2013). Controllable encapsulation of cobalt clusters inside carbon nanotubes as effective catalysts for Fischer–Tropsch synthesis. *Catal. Today* 215, 24–28. doi:10.1016/j.cattod.2013.02.018

Xiong, H., Jewell, L. L., and Coville, N. J. (2015). Shaped carbons as supports for the catalytic conversion of syngas to clean fuels. *ACS Catal.* 5, 2640–2658. doi:10.1021/acscatal.5b00090

Xiong, H., Motchelaho, M. a. M., Moyo, M., Jewell, L. L., and Coville, N. J. (2011). Correlating the preparation and performance of cobalt catalysts supported on carbon nanotubes and carbon spheres in the Fischer–Tropsch synthesis. *J. Catal.* 278, 26–40. doi:10.1016/j.jcat.2010.11.010

Xiong, H., Motchelaho, M. A., Moyo, M., Jewell, L. L., and Coville, N. J. (2014a). Fischer–Tropsch synthesis: iron-based catalysts supported on nitrogen-doped carbon nanotubes synthesized by post-doping. *Appl. Catal. Gen.* 482, 377–386. doi:10.1016/j.apcata.2014.06.019

Xiong, H., Moyo, M., Motchelaho, M. a. M., Jewell, L. L., and Coville, N. J. (2010). Fischer–Tropsch synthesis over model iron catalysts supported on carbon spheres: the effect of iron precursor, support pretreatment, catalyst preparation method and promoters. *Appl. Catal. Gen.* 388, 168–178. doi:10.1016/j.apcata.2010.08.039

Xiong, H., Moyo, M., Motchelaho, M. A., Tetana, Z. N., Dube, S. M. A., Jewell, L. L., et al. (2014b). Fischer–Tropsch synthesis: iron catalysts supported on N-doped carbon spheres prepared by chemical vapor deposition and hydrothermal approaches. *J. Catal.* 311, 80–87. doi:10.1016/j.jcat.2013.11.007

Yang, Q.-H., Hou, P.-X., Bai, S., Wang, M.-Z., and Cheng, H.-M. (2001). Adsorption and capillarity of nitrogen in aggregated multi-walled carbon nanotubes. *Chem. Phys. Lett.* 345, 18–24. doi:10.1016/S0009-2614(01)00848-X

Yang, Y., Chiang, K., and Burke, N. (2011). Porous carbon-supported catalysts for energy and environmental applications: a short review. *Catal. Today* 178, 197–205. doi:10.1016/j.cattod.2011.08.028

Yang, Y., Jia, L., Hou, B., Li, D., Wang, J., and Sun, Y. (2014). The effect of nitrogen on the autoreduction of cobalt nanoparticles supported on nitrogen-doped ordered mesoporous carbon for the Fischer–Tropsch synthesis. *ChemCatChem.* 6, 319–327. doi:10.1002/cctc.201300897

Yang, Y., Jia, L., Meng, Y., Hou, B., Li, D., and Sun, Y. (2012). Fischer–tropsch synthesis over ordered mesoporous carbon supported cobalt catalysts: the role of amount of carbon precursor in catalytic performance. *Catal. Lett.* 142, 195–204. doi:10.1007/s10562-011-0747-3

Yu, G., Sun, B., Pei, Y., Xie, S., Yan, S., Qiao, M., et al. (2010). Fe(x)O(y)@C spheres as an excellent catalyst for Fischer-Tropsch synthesis. *J. Am. Chem. Soc.* 132, 935–937. doi:10.1021/ja906370b

Zaman, M., Khodadi, A., and Mortazavi, Y. (2009). Fischer–Tropsch synthesis over cobalt dispersed on carbon nanotubes-based supports and activated carbon. *Fuel Process. Technol.* 90, 1214–1219. doi:10.1016/j.fuproc.2009.05.026

Zarubova, S., Rane, S., Yang, J., Yu, Y., Zhu, Y., Chen, D., et al. (2011). Fischer-Tropsch synthesis on hierarchically structured cobalt nanoparticle/carbon nanofiber/carbon felt composites. *ChemSusChem.* 4, 935–942. doi:10.1002/cssc.201100046

Zhang, H., Chu, W., Zou, C., Huang, Z., Ye, Z., and Zhu, L. (2011). Promotion effects of platinum and ruthenium on carbon nanotube supported cobalt catalysts for Fischer–Tropsch synthesis. *Catal. Lett.* 141, 438–444. doi:10.1007/s10562-010-0536-4

Zhang, H., Lancelot, C., Chu, W., Hong, J., Khodakov, A. Y., Chernavskii, P. A., et al. (2009). The nature of cobalt species in carbon nanotubes and their

catalytic performance in Fischer–Tropsch reaction. *J. Mater. Chem.* 19, 9241–9249. doi:10.1039/B911355J

Zhang, Y., Ma, L., Tu, J., Wang, T., and Li, X. (2015). One-pot synthesis of promoted porous iron-based microspheres and its Fischer–Tropsch performance. *Appl. Catal. Gen.* 499, 139–145. doi:10.1016/j.apcata.2015.04.017

Zhao, J. M., Feng, Z., Huggins, F. E., Shah, N., Huffman, G. P., and Wender, I. (1994). Role of molybdenum at the iron oxide surface. *J. Catal.* 148, 194–197. doi:10.1006/jcat.1994.1200

Zhao, Y., Huang, S., Wei, L., Zhang, Y., Lin, A., Liu, C., et al. (2020). Highly dispersed CoO on graphitic mesoporous carbon as an efficient catalyst for Fischer–Tropsch synthesis. *Ind. Eng. Chem. Res.* 59, 3279–3286. doi:10.1021/acs.iecr.9b06041

Zhao, Z., Lu, W., Feng, C., Chen, X., Zhu, H., Yang, R., et al. (2019). Increasing the activity and selectivity of Co-based FTS catalysts supported by carbon materials for direct synthesis of clean fuels by the addition of chromium. *J. Catal.* 370, 251–264. doi:10.1016/j.jcat.2018.12.022

Conflict of Interest: The authors declare that the research was conducted in the absence of any commercial or financial relationships that could be construed as a potential conflict of interest.

Ceramics and Glass

Gabriela Grzybek

Dr. Gabriela Grzybek defended her doctoral dissertation, titled "Modified spinel catalysts for low temperature N2O decomposition", at Jagiellonian University in 2012. She is presently an Assistant Professor of Faculty of Chemistry at Jagiellonian University in Krakow, Poland. She is a member of the Materials and Surface Chemistry Group. Her research interests are focused on the preparation and characterization of metal oxide materials and their use as catalysts in environmental protection [e.g., N2O decomposition, hydrogen production via steam reforming of (bio)ethanol, and soot oxidation] applications. Gabriela has published more than 30 articles in high-quality international peer-reviewed journals and holds four patents.

Kinga Góra-Marek

Prof. Kinga Góra-Marek is an Associate Professor at Jagiellonian University in Kraków, Poland. She is the Head of the Infrared Spectroscopy Laboratory. Her research focuses on IR spectroscopy, catalysis, and zeolites.

frontiers in Materials

ORIGINAL RESEARCH
published: 16 November 2020
doi: 10.3389/fmats.2020.597528

Bioethanol Steam Reforming over Cobalt-Containing USY and ZSM-5 Commercial Zeolite Catalysts

Gabriela Grzybek[1], Magdalena Greluk[2], Karolina Tarach[1], Kamila Pyra[1], Grzegorz Słowik[2], Marek Rotko[2] and Kinga Góra-Marek[1]*

[1]Faculty of Chemistry, Jagiellonian University, Krakow, Poland, [2]Faculty of Chemistry, University of Maria Curie-Sklodowska, Lublin, Poland

The ethanol steam reforming (ESR) process over cobalt-based zeolitic catalysts, differing significantly in the structure, was comprehensively examined. The cobalt spinel phase (10 wt%) was deposited on the surface of USY and ZSM-5 zeolites (Si/Al ratio of 31). The catalysts were characterized in terms of their chemical (ICP) and phase composition (XRD), textural properties (low-temperature N_2 adsorption), morphology (STEM/EDX), and reducibility (H_2-TPR). The aforementioned characteristics were supplemented by the catalysts' acidity and redox properties investigations (quantitative FT-IR studies of pyridine and carbon monoxide adsorption). Catalysts' activity was evaluated in the ESR process at 500°C for various ethanol/water mixtures. Both catalysts exhibited 100% ethanol conversion, whereas their selectivity toward H_2, CO_2, and C_2H_4 strongly depended on the applied ethanol-to-water molar ratio. Comparable selectivities observed for the 1 : 4 ratio were improved for the 1 : 9 ratio for both catalysts, as expected. For the ratio of 1 : 12, the significant difference in the reaction paths (the ethanol dehydration for CoUSY and the ethanol steam reforming for CoZSM-5) was explained by the cobalt reoxidation process facilitated by water molecules for the CoUSY. The superior overall performance of the CoZSM-5 catalyst in the ESR process, in comparison to CoUSY, also results from its almost three times enhanced accessibility of the cobalt species, as confirmed by the quantitative FT-IR studies of CO sorption. The microscopic studies also indicated a better dispersion of the cobalt phase supported on the ZSM-5 support. Thus, the structure of ZSM-5 zeolite assures higher cobalt active phase dispersion being more beneficial for the ESR process.

Keywords: cobalt catalyst, zeolite Y, zeolite ZSM-5, ethanol steam reforming, catalyst acidity

OPEN ACCESS

Edited by:
Miriam Navlani-García, University of Alicante, Spain

Reviewed by:
Maria A. Goula, Western Macedonia University of Applied Science, Greece
Martin Charles Wilding, Sheffield Hallam University, United Kingdom

****Correspondence:***
Gabriela Grzybek
g.grzybek@uj.edu.pl

Specialty section:
This article was submitted to Ceramics and Glass, a section of the journal Frontiers in Materials

Received: *24 August 2020*
Accepted: *08 October 2020*
Published: *16 November 2020*

Citation:
Grzybek G, Greluk M, Tarach K, Pyra K, Słowik G, Rotko M and Góra-Marek K (2020) Bioethanol Steam Reforming over Cobalt-Containing USY and ZSM-5 Commercial Zeolite Catalysts. Front. Mater. 7:597528. doi: 10.3389/fmats.2020.597528

INTRODUCTION

Hydrogen-derived energy sources are a sustainable and environmentally friendly alternative to the utilization of fossil fuels, for which the availability of reserves is subject to high uncertainty. This, combined with the negative impact of their combustion on the environment, grows the global interest in the development of renewable energy sources intensively. Paying attention to hydrogen as a green energy carrier is a derivative of its possible application in internal combustion engines or fuel cells for efficient electricity generation (Bion et al., 2010; Sekine et al., 2014; Ogo et al., 2015; Zanchet et al., 2015; Ogo and Sekine, 2020). Hydrogen is expected to become the main energy source and

long-term replacement for natural gas shortly. Nevertheless, the current hydrogen production relies heavily on the steam reforming of natural gas, coal, or light hydrocarbons. Consequently, the extensive use of hydrogen as a renewable and clean (CO_2-neutral) energy source is still a challenge and remains intensive research (Maggio et al., 1998; Armor, 1999; Alberton et al., 2007; Contreras et al., 2014; Lang et al., 2015). In light of the above, the conversion of biomass to ethanol and its use in the steam reforming to produce hydrogen constitutes an important research path in recent years (Ni et al., 2007).

The ethanol steam reforming process (ESR), defined by **Eq. 1**, is an endothermic reaction occurring at the temperature range of 400–800°C (Chica, 2013).

$$C_2H_5OH + 3H_2O \rightarrow 6H_2 + 2CO_2 \quad (1)$$

The high efficiency of hydrogen production with $H_2O/C_2H_5OH = 6$ and at low operating temperatures is highly desired. This reaction is, however, accompanied by parallel side reactions as decomposition, dehydration, dehydrogenation, hydrogenolysis, methanation, water-gas shift reaction, Boudart reaction, and finally coke formation (Haryanto et al., 2005; Mattos and Noronha, 2005; Vaidya and Rodrigues, 2006). The aforementioned side processes are the source of undesirable by-products such as C_2H_4, CO, CH_4, CH_3CHO, and $(CH_3)_2CO$. Among them, the most undesired path is the ethanol conversion to ethylene as the latter is easily transformed into the carbonaceous deposit. The ethanol dehydration to ethylene is undergone in the presence of acid sites (Tarach et al., 2016; Gołąbek et al., 2018). Therefore, the relative share of individual side reactions strongly depends on the acid/redox characteristic of the catalyst, but also on the applied reaction variables (e.g., temperature, $EtOH/H_2O$ ratio, and contact time).

Among catalysts considered for the steam reforming of ethanol, the oxide-supported noble metals (Rh, Ru, Pt, Ir, and Au) showed superior activity and stability (Freni, 2001; Breen et al., 2002; Liguras et al., 2003; Deluga et al., 2004; Sheng et al., 2004; Wanat et al., 2004; Mattos and Noronha, 2005; Hsiao et al., 2007; Ogo and Sekine, 2020). High cost limits their industrial application, and interest shifts to catalysts based on nonnoble metals such as Cu, Ni, and Co, of which cobalt-based catalysts seem to be the most promising systems (Freni et al., 2003; Comas et al., 2004; Kaddouri and Mazzocchia, 2004; Llorca et al., 2004; Benito et al., 2005; Frusteri et al., 2006; Song et al., 2007; Torres et al., 2007; Zhang et al., 2007; Contreras et al., 2014; Hou et al., 2015; Chen et al., 2020). A major role in the course of the ESR process over the cobalt catalysts is played by the cobalt oxidation state. However, the role of various Co species is still under debate. The highest activity is usually associated with the presence of both metallic Co^0 and Co^{2+} sites (Mattos et al., 2012; Zanchet et al., 2015; Sohn et al., 2016; Passos et al., 2017; Sohn et al., 2017). The DFT calculations implied that the C-C bond scission is favored on the Co^0 sites, while the water activation and the acetate species formation preferably occur on the Co^{2+} sites (Li and Wang, 2018; Li et al., 2019). The acetate pathway is thus preferred over the catalysts containing both these sites (Co^0 and Co^{2+}). The rapid reaction between the acetate species and water to form CO_x and H_2, without the involvement of the CH_4 formation, is responsible for the high performance of the Co-based catalysts in the ESR process (Sekine et al., 2014; Ogo et al., 2015; Ogo and Sekine, 2020). In turn, Inokawa et al. (2010) reported the rapid C_2H_4 production by ethanol dehydration in the presence of transition Co^{2+} and Ni^{2+} cations in the zeolites Y.

The main drawback of using the nonnoble metal catalysts, including those based on cobalt, is their rapid deactivation under reaction conditions. Both sintering and coke formation can, however, be limited by selecting appropriate support. The influence of the oxide-support on the catalyst activity in the ESR process was documented for several materials such as Al_2O_3, SiO_2, ZrO_2, Nb_2O_5, MgO, and CeO_2 (Llorca et al., 2002; Frusteri et al., 2004; Benito et al., 2005; Frusteri et al., 2006; Contreras et al., 2014; Riani et al., 2020). The role of support is to enhance the dispersion of the metallic active phase by metal-support interaction leading to an improvement of catalytic performance as well as to a reduction of carbon species forming during the process. High surface area and the porous structure can both assure high dispersion of metallic species and increase their resistance against sintering (Llorca et al., 2002; Da Costa-Serra et al., 2010). Thus, the zeolites with a microporous system of channels and cages typically offering high thermal stability and surface area around 400–800 m^2g^{-1} seem to be attractive candidates for supporting the metal-originating species (Campos-Skrobot et al., 2008; Chica and Sayas, 2009; Da Costa-Serra and Chica, 2011; Inokawa et al., 2011; Calles et al., 2020; Wang et al., 2020).

The early report on Cu-zeolites used for the ESR process can be found in 2001 (Łaniecki, 2001), whereas those concerning the catalytic steam reforming of ethanol started to appear in the 1990s (García and Laborde, 1991; Haga et al., 1997; Trimm, 1999). The role of zeolites as supports was raised again in the work of Campos-Skrobot et al. (2008). The Rh catalyst supported on the NaY zeolite allowed achieving the 68% yield of H_2. Vizcaino et al. reported Cu–Ni-based catalyst supported on nanocrystalline ZSM-5 zeolites for the ESR; however, the optimal identified operating temperature was 600°C (Vizcaíno et al., 2007). Chica et al. (Chica and Sayas, 2009; Da Costa-Serra and Chica, 2011) have proposed the use of delaminated pure silica ITQ-2 and ITQ-18 zeolites as a highly active and stable catalyst for the ESR process. Nevertheless, the cost-effective materials are still in high demand for industrial applications.

Thus, the present paper focuses on the use of commercially available ZSM-5 and USY zeolites as supports for Co-catalysts. Both applied zeolites are used as catalysts in the most important conversion processes used in petroleum refineries (fluid catalytic cracking). Both offer the three-dimensional porous network with interconnected channels varying in size; slightly larger pores openings are found in the USY zeolite than in the ZSM-5 and high thermal stability. As the acidic function of zeolites is responsible for the undesirable dehydration of ethanol, leading to coke formation, the high Si/Al ratio zeolites were selected.

Since the ethanol-to-water ratio is a key factor in the ESR reaction, the catalysts were extensively tested at variable water content ($EtOH/H_2O$ equal to 1 : 4, 1 : 9, and 1 : 12). Although the reaction stoichiometry determines the ethanol-to-steam (EtOH/

H_2O) molar ratio of 1 : 3, the use of excess water is advisable because bioethanol produced renewable in the fermentation process of biomass is a mixture of ethanol and water with a molar ratio of 1 : 7 to 1 : 13. Hence, it is advantageous to use bioethanol directly, i.e., without an energy-consuming ethanol distillation process, as this allows the final fuel cost to be minimized (Ni et al., 2007; Subramani and Song, 2007; Llorca et al., 2013; Bineli et al., 2016; Ghasemzadeh et al., 2019). Moreover, the excess water favors the water-gas shift reaction which is particularly important because it converts CO to CO_2 and H_2 products (Subramani and Song, 2007; Bineli et al., 2016; Zhurka et al., 2018). Therefore, to maximize the amount of H_2 produced, it is essential to ensure a sufficient supply of water (Comas et al., 2004; Ni et al., 2007; Ghasemzadeh et al., 2019). Furthermore, it is also well known that carbon formation can be minimized by gasification with steam, which means that the excess of water allows for reducing the formation of carbon deposits (Comas et al., 2004; Bineli et al., 2016).

The co-modified zeolitic catalysts (CoUSY and CoZSM-5) were thoroughly characterized by means of XRD, TEM/EDX, TPR, and FT-IR sorption studies to define the effect of the co-moieties dispersion and metal-support interactions on their catalytic performance in the ESR process carried out at variable water content.

EXPERIMENTAL

Materials

The super dealuminated ultrastabilized zeolite H-SDUSY (Si/Al = 31, CBV 760, labeled USY) was purchased from the Zeolyst Company. In turn, the proton form of the zeolite ZSM-5 (Si/Al = 31) was obtained by converting the ammonium form (Zeolyst, CBV 5524G) by calcination at 500°C for 2 h with a rate of 2°C/min. The cobalt in the amount of 10 wt% was introduced onto the surface of both zeolites by incipient wetness impregnation method from aqueous solution of cobalt(II) nitrate(V) (Aldrich). The final materials were dried at RT and then calcined under the condition indicated above.

Catalysts Characterization

The Si/Al ratio in the studied zeolites was verified using a Perkin Elmer Optima 2100DV ICP-OES spectrometer. Powder X-ray diffraction spectra were obtained using a Rigaku Multiflex diffractometer using Cu Kα radiation (40 kV, 40 mA). The diffractograms were recorded in the 2θ angle range of 10–50° (step size of 0.02° and the accumulation time of 3 s).

The texture of the native and Co-loaded zeolites was analyzed by N_2-physisorption at −196°C using a Quantachrome Autosorb-1-MP gas sorption instrument. Before the measurement, the sample was outgassed under a high vacuum at 350°C for 16 h. The micropore volume was calculated using the t-plot method, while the Brunauer–Emmet–Teller method together with Rouquerol et al. (2007) recommendations was applied to calculate the apparent specific surface area. The pore volume values were derived from the Barrett–Joyner–Halenda model using the adsorption branch (Barrett et al., 1951).

The morphology and cobalt phase dispersion, as well as phase composition of the fresh catalysts, were studied using the electron microscope, Titan G2 60–300 kV (FEI Company) with an accelerating voltage of the electron beam equal to 300 kV (the details of sample preparation, apparatus, and the experimental procedure described elsewhere (Słowik et al., 2016; Grzybek et al., 2020)). The mapping was carried out in the STEM mode by collecting point by point EDS spectrum of each of the corresponding pixels in the map. The collected maps were presented in the form of a matrix of pixels with the color mapped significant element and the intensity corresponding to the percentage of each element. Phase separation in the cobalt-based catalysts was performed with the FFT by using masking available in the Gatan DigitalMicrograph software package.

The acidic properties of examined samples were assessed from quantitative FT-IR studies of pyridine (Py, ≥99.8%, Sigma-Aldrich) adsorption. Before the measurements, the catalysts in the form of pellets were evacuated *in situ* in a quartz IR cell at 500°C under the pressure of 10^{-6} mbar for 1 h. The first step of the pyridine adsorption quantitative procedure was the neutralization of all acid sites at 130°C with the Py vapor under static conditions. Afterward, the nonchemisorbed Py molecules share was removed by the evacuation at the same temperature and the spectrum was collected. The intensities of the Py bands at 1545 cm^{-1} (pyridinium ions, PyH^+) and at 1,450 cm^{-1} (Py coordinatively bonded to Lewis sites, PyL) were used to calculate the concentration of the acid sites. The following values of the absorption coefficients 0.07 $cm^2 \cdot \mu mol^{-1}$ for the 1545 cm^{-1} band of PyH^+ and 0.10 $cm^2 \cdot \mu mol^{-1}$ for the 1,450 cm^{-1} band of PyL were applied. In addition, the sorption of carbon monoxide (Linde Gas Poland, 99.95%), being a probe molecule differentiating the nature of the cobalt moieties, was performed. The sorption of the small doses of CO was carried out at −100°C up to the total saturation of all the electron acceptor acid sites, which was manifested by the maximum intensities of the bands in the 2,300–2,180 cm^{-1}. All the spectra presented in this work were recorded by gathering 300 scans with a resolution of 2 cm^{-1} on a Vertex 70 spectrometer (Bruker) equipped with an MCT detector.

The temperature-programmed reduction (H_2-TPR) of tested catalytic materials was carried out in the AutoChem II 2920 analyzer (Micromeritics, United States) with the linear temperature increase (10°C/min) from room temperature to 900°C. A reducing mixture (5 vol% of H_2 in Ar) was supplied into the quartz reactor (filled with 50 mg of a catalyst sample) at a rate of 30 cm^3/min. The consumption of hydrogen was measured by an early calibrated thermal conductivity detector after removing water with a freezing trap.

Catalysts Performance in the Ethanol Steam Reforming Reaction

The activity and selectivity of cobalt-containing zeolite catalysts in the ESR reaction were determined in a continuous fixed-bed quartz reactor (Microactivity Reference unit, PID Eng & Tech.) at 500°C. To avoid the hot spot, 100 mg of catalyst (0.15–0.3 mm) was diluted with quartz grains. The catalyst prior to the reaction

was reduced in hydrogen at 550°C for 1 h. The EtOH/H_2O mixture with a molar ratio of 1 : 12, 1 : 9, or 1 : 4 was fed from a pressurized container using a mass controller (Bronkhorst) to an evaporator maintained at 150°C. In order to obtain a constant ethanol concentration of around 7.7 mol% for each molar ratio, the reactant vapors were fed to the reactor at a flow rate of 100 ml min^{-1} without diluting with any inert gas for the molar ratio of 1 : 12, at a flow rate of 77 ml min^{-1} diluted with argon with the flow rate of 23 ml min^{-1} for the molar ratio of 1 : 9, and at a flow rate of 38.5 ml min^{-1} diluted with argon with the flow rate of 61.5 ml min^{-1} for the molar ratio of 1 : 4. The analysis of feed composition (all in the gas phase) was carried out online by means of two gas chromatographs (Bruker 450-GC and Bruker 430-GC). Details on the chromatography equipment have been previously reported elsewhere (Greluk et al., 2020a; Greluk et al., 2020b).

The conversion of ethanol (X_{EtOH}) and the selectivity to carbon-containing products (X_{CP}) were determined from

$$X_{EtOH} = \frac{C^{in}_{EtOH} - C^{out}_{EtOH}}{C^{in}_{EtOH}} \times 100\% \quad (2)$$

$$X_{CP} = \frac{n_i C^{out}_i}{\sum n_i C^{out}_i} \times 100\% \quad (3)$$

where C^{in}_{EtOH} is the molar concentration of ethanol in the reaction mixture (mol%); C^{out}_{EtOH} is the molar concentration of ethanol in the postreaction mixture (mol%); C^{out}_i is the molar concentration of carbon-containing product in the postreaction mixture (mol %); n_i is the number of carbon atoms in carbon-containing molecule of the reaction product.

The selectivity of hydrogen formation was calculated from

$$H_2 selectivity = \frac{C^{out}_{H_2}}{C^{out}_{H_2} + 2 \times C^{out}_{CH_4} + 2 \times C^{out}_{C_2H_4} + 2 \times C^{out}_{CH_3CHO} + 3 \times C^{out}_{(CH_3)_2CO}} \times 100\% \quad (4)$$

where C^{out} is the molar concentration of the hydrogen-containing products in the postreaction mixture (mol%).

RESULTS AND DISCUSSION

Physicochemical Characterization

The Si/Al ratio of the reference zeolite supports, CoUSY and CoZSM-5 cobalt catalysts, determined by ICP, was found to be equal to 31 for each sample. From the X-ray diffractograms collected in **Figure 1**, it can be inferred that there was almost no change in the crystal structure of USY zeolite or ZSM-5 zeolite after the cobalt addition. Both, positions and intensities of the diffraction lines representative of the FAU and MFI structure, respectively, remained practically unaffected. Moreover, the additional low-intensity lines (marked by *) at 2θ equal to 31.2 and 36.9 in the diffraction patterns of CoUSY and CoZSM-5 catalysts were identified as corresponding to the (220) and (311) reflection planes of Co_3O_4 (ICSD 69378), respectively. The minor share of the cobalt phase in the registered diffractograms indicates its effective distribution in the as-prepared materials.

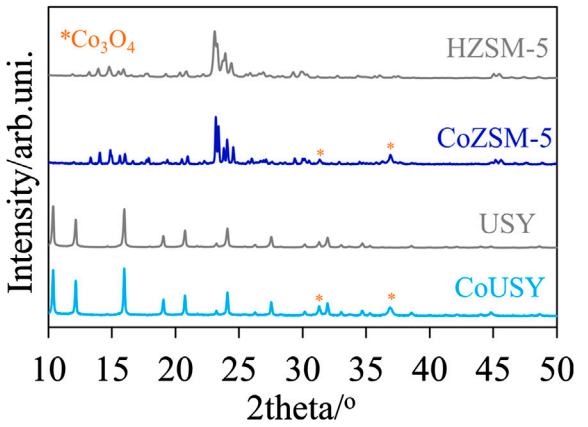

FIGURE 1 | XRD patterns of the CoUSY and CoZSM-5 catalysts as well as reference zeolite supports.

The chemical and structural characterization of the studied materials was complemented by the textural and morphological analysis. In general, the textural properties of both zeolite supports after impregnation with cobalt have been maintained (**Table 1**). Surprisingly, their microporosity did not decrease, indicating that the entire spinel cobalt phase covered the outside of the zeolite support grains and did not plug the micropores of the zeolites. On the other hand, the detected growth in the mesopore surface area (S_{meso}) (for the CoUSY catalyst) and mesopore volumes (V_{meso}) (for the CoUSY and CoZSM-5 catalysts) indicates a slight contribution of the cobalt spinel nanocrystals, located on the external surface of the zeolite grains, to the development of the catalyst mesoporosity.

The mentioned external location of the spinel cobalt phase was confirmed by the microscopic observations (**Figure 2**). HRTEM images of both CoUSY and CoZSM-5 samples (**Figures 2A$_1$–A$_2$,B$_1$–B$_2$**) show supports' particles with various shapes (mainly like a rectangle or coffin-shaped for the ZSM-5). On the external surface of the zeolite crystals, the cobalt species (dark places) are dispersed (**Figures 2A$_3$,B$_3$** and **3A,B$_1$**). Yet, the dispersion of the cobalt phase differs significantly for studied catalysts. The cobalt phase is forming on the USY zeolite surface large flattened agglomerates (**Figure 2A$_2$**), while in the case of the CoZSM-5 sample, a significant amount of small cobalt phase crystallites is present (**Figure 2B$_2$**). Phase identification of the CoUSY and CoZSM-5 catalysts, which was obtained based on the HRTEM images (**Figures 3A$_1$,B$_1$**) and FFT (Fast Fourier

TABLE 1 | Textural properties (from low-temperature N_2 physisorption) of the studied cobalt catalysts and reference zeolites.

Sample	S_{BET}/ $m^2.g^{-1}$	S_{micro}/ $m^2.g^{-1}$	S_{meso}/ $m^2.g^{-1}$	V_{micro}/ $cm^3.g^{-1}$	V_{meso}/ $cm^3.g^{-1}$
HZSM-5	380	340	40	0.15	0.07
CoZSM-5	385	350	36	0.15	0.10
USY	765	670	95	0.33	0.20
CoUSY	813	725	202	0.30	0.28

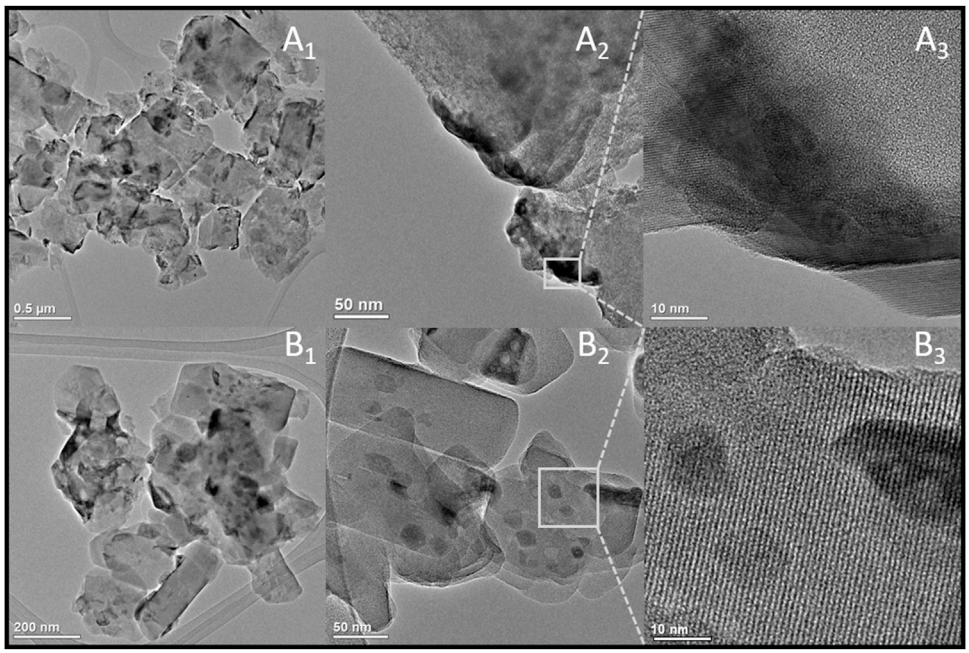

FIGURE 2 | HRTEM characteristics of the CoUSY **(A_1–A_5)** and CoZSM-5 **(B_1–B_5)** samples.

Transform) (**Figures 3A_2,B_2**), indicates that cobalt is present in the form of Co3O4 spinel in both samples. In the case of the CoUSY sample, it is confirmed by the following interplanar distances determined based on FFT: 2.44, 1.85, and 1.55 and corresponding to the lattice plane (311), (331), and (511), respectively, whereas the following interplanar distances and corresponding lattice planes were obtained for the CoZSM-5 catalyst: 2.85, 2.44 Å, and (220) and (311), respectively.

The local EDX analysis let us expose differences in the cobalt phase dispersion in the catalysts studied. As shown in **Figure 4**, the materials differ significantly in terms of the spinel crystallites' shape and size. In the case of CoUSY, the cobalt phase is mainly present in the form of flattened, long (100–200 nm) grains, while in the case of CoZSM-5, apart from such large crystallites, the small crystallites with sizes in the range of 10–100 nm are highly populated.

Acidic Properties (FT-IR Studies of Pyridine and CO Sorption)

The cobalt catalysts and reference zeolite supports were thoroughly characterized in respect to the nature, number, distribution, and strength of their acid sites by the FT-IR spectroscopy using pyridine and CO probe molecules. The results of pyridine sorption studies provided information on the total number of Brønsted (B) and Lewis (L) acid sites. In turn, the CO sorption studies enabled us to distinguish between Lewis acid sites of different origin and strength, which is documented by the various positions of the bands of CO interacting with them. For both used zeolite supports, the IR spectra of pyridine sorption (**Figure 5**) show the presence of the band at 1545 cm^{-1} and two bands at 1,445 and 1,455 cm^{-1}, corresponding to Py interacting with protonic and Lewis acid sites, respectively. The cobalt spinel deposition led to the generation of a significant number of Lewis acid sites of the strength different than found for protonic forms, giving an intense peak at 1,450 cm^{-1}. On the other hand, a noticeable decrease in the intensity of PyH^+ ions band upon cobalt deposition results from the replacement of the H^+ in exchangeable positions with the cobalt cations.

The concentration of the B and L acid sites in studied materials determined by pyridine is summarized in **Table 2**. The total acidity being the sum of Brønsted and Lewis sites corresponds well to the Al concentration determined from ICP analysis for the ZSM-5 zeolite. Still, it is significantly lower (about 24%) for the USY zeolite. Due to the framework geometry, the location of some H^+ in sodalite cages or hexagonal prisms make them inaccessible for pyridine molecule. Also, the copresence of nonacidic extraframework aluminum species cannot be excluded. Assuming that the impregnation procedure with the cobalt(II) salt solution did not affect the concentration of aluminum-originated Lewis sites, the enhancement in the amount of Lewis sites after Co-deposition was explicitly ascribed to cobalt(II) ions ($Co_{(Py)}$). In other words, the latter parameter was defined as the difference between the number of Lewis sites in the cobalt zeolite catalysts and corresponding proton zeolite forms (**Table 2**). The Py sorption studies revealed more than twice the concentration of Co-originated Lewis sites for the catalyst based on ZSM-5 zeolite support, demonstrating much better accessibility of the cobalt sites in this matrix. Worse accessibility of cobalt species in the CoUSY zeolite catalyst in combination with diffusion effects may affect

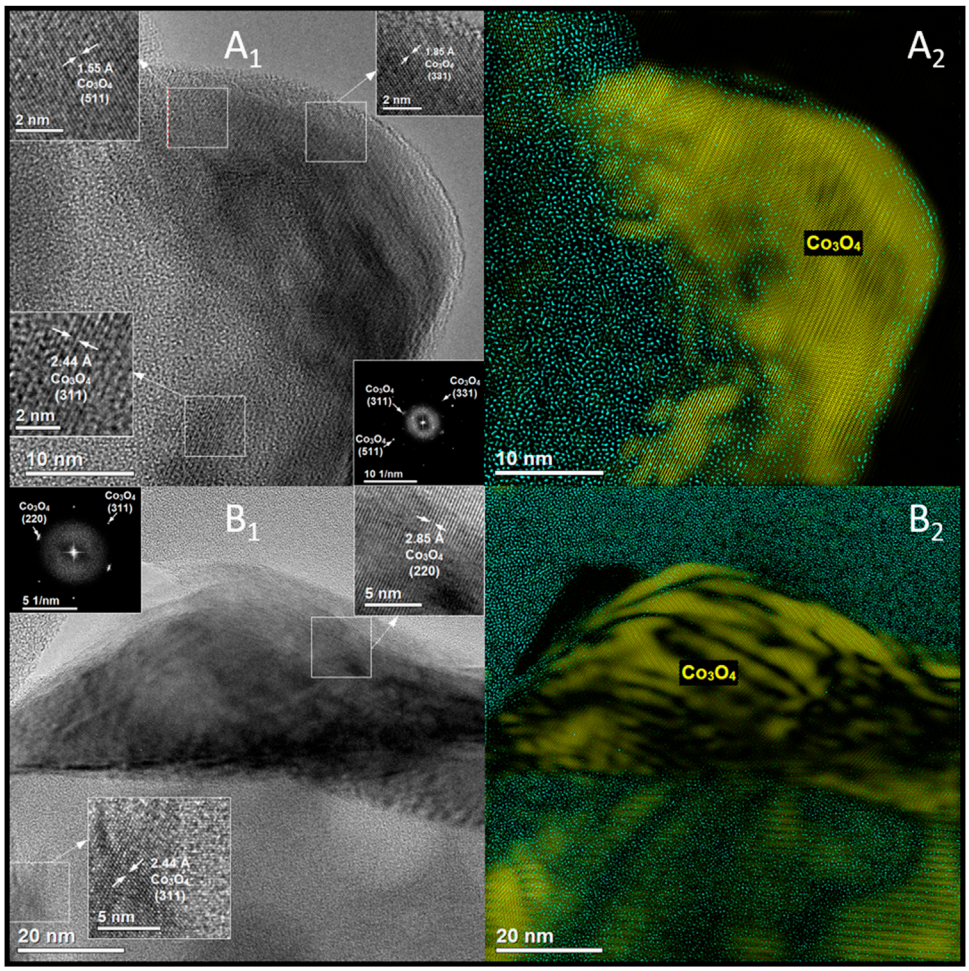

FIGURE 3 | HRTEM images together with FFT and phase identification of the CoUSY **(A_1,A_2)** and CoZSM-5 **(B_1,B_2)** samples.

the efficiency of the ESR reaction, providing premises for better performance of the CoZSM-5 catalyst.

The spectra of CO adsorbed on the zeolite supports (H-forms) and cobalt-containing catalysts are presented in **Figure 6**. The only band results from CO bonded to the Brønsted acid sites of H-zeolites is located at the frequency of 2,179 and 2,175 cm^{-1}, for USY and H-ZSM-5, respectively. No band in the frequency range of 2,300–2,180 cm^{-1} suggests no presence of Lewis electron acceptor sites. However, the presented above results of pyridine sorption studies indicate the presence of a small number of Lewis centers in H-zeolites (**Figure 5**). This discrepancy between the data obtained from CO and Py sorption can easily be explained by a significant difference in the basicity of probe molecules. The lower basicity of CO causes that the Lewis centers with low acidic strength will not be detectable by this probe (gas basicity of 898.1 for Py vs. 402.2 kJ/mol for CO) (Hunter and Lias, 1998).

In the case of cobalt-modified zeolites, the CO sorption studies indicated that the introduction of cobalt generates a significant number of Lewis sites. According to literature reports (Góra-Marek et al., 2007 and references therein), the appearance of bands in the range of 2,193–2,180 cm^{-1} is associated with the binding of the CO molecule by cobalt oxide centers. The higher CO band frequency observed in the CoUSY catalyst in comparison to CoZSM-5 is indicative of the stronger electron acceptor properties of the cobalt sites binding the CO molecule in the former. It is consistent with the TPR results presented further (**Figure 7**). In turn, the CO bands at 2,215 cm^{-1} (CoUSY) and 2,206 cm^{-1} (CoZSM-5) can be attributed to CO molecules coordinated to isolated cobalt(II) ions located in the exchangeable positions. As in the case of cobalt oxide-like centers, the higher frequency of Co^{2+} monocarbonyl band for the CoUSY catalyst points to stronger electron acceptor properties of its Co^{2+} ions.

Based on the methodology of quantitative measurement developed for cobalt sites in zeolites (Góra-Marek et al., 2009), the concentrations of isolated cobalt ions and cobalt ions in oxide forms were determined (**Table 2**). In general, there are similar trends for the CO and Py sorption studies: higher cobalt sites concentration was determined for the CoZSM-5 catalyst. However, the total number of cobalt sites from Py sorption studies is ca. twice of the one from CO

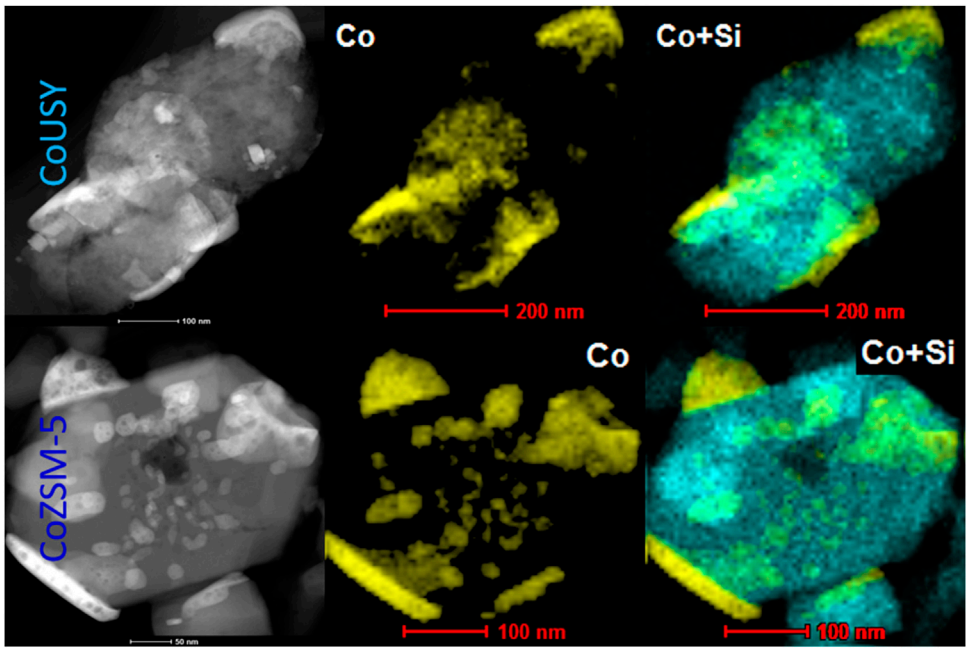

FIGURE 4 | HAADF/STEM images along with EDX maps of Co (yellow) and Si (blue) distributions in the CoUSY and CoZSM-5 catalysts.

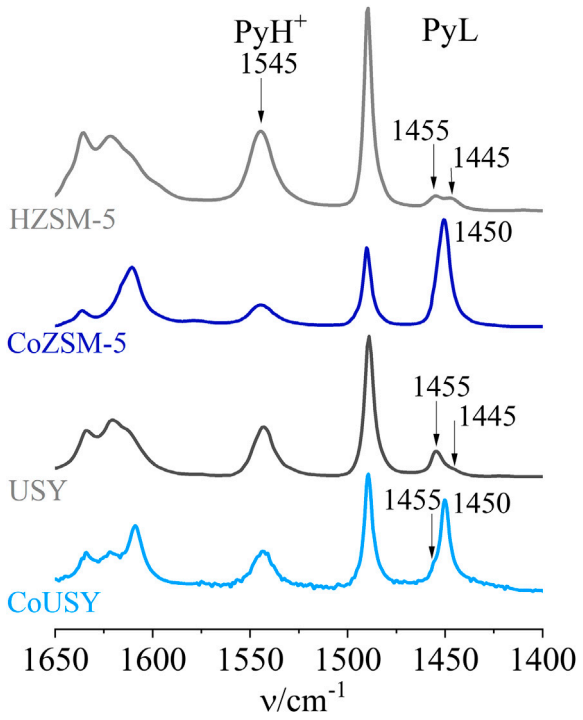

FIGURE 5 | IR spectra of pyridine sorption for the CoUSY and CoZSM-5 catalysts juxtaposed with the spectra of reference zeolite supports.

TABLE 2 | The content of Al, Brønsted (B), and Lewis (L) acid sites, in studied samples (Co-catalysts and reference zeolites) together with the content of Co species such as Co^{2+} ions and oxide-like cobalt forms (OLC) in the CoZSM-5 and Co-USY catalysts.

Sample	Al[a]	B[b]	L[b]	B + L[b]	Co-originated Lewis acid sites			
					$Co_{(Py)}$[b]	$Co^{2+}_{(CO)}$[c]	$OLC_{(CO)}$[c]	$(Co^{2+} + OLC)_{(CO)}$[c]
	μmol·g^{-1}				μmol·g^{-1}			
HZSM-5	472	445	70	515	—	—	—	—
CoZSM-5	472	247	328	575	258	62	77	139
USY	486	282	86	368	—	—	—	—
CoUSY	486	215	200	415	114	34	15	49

[a]*The concentration of Al from ICP analysis.*
[b]*The concentration of Brønsted (B) and Lewis (L) acid sites determined by FT-IR studies of pyridine adsorption.*
[c]*The concentration of Co^{2+} ions and oxide-like cobalt forms (OLC) determined by CO adsorption FT-IR studies (Góra-Marek et al., 2009).*

sorption studies. As mentioned above, it may be a consequence of a significant difference in the basicity of both probe molecules. The presented data revealed about two times higher total concentration of cobalt sites (Co^{2+} +OLC) capable of binding the pyridine molecule and almost three times higher total concentration of cobalt sites (Co^{2+} +OLC) capable of binding the CO molecule for the CoZSM-5 catalyst. Also, the greater preponderance of cobalt species concentration determined from CO sorption studies is probably a result of the limited accessibility of these species for a much bigger pyridine molecule. Thus, a fraction of Co sites in the CoZSM-5 catalyst detectable by CO may not be reached by the pyridine molecule. Assuming that only oxide-like cobalt forms are reduced to metallic Co^0, the CoZSM-5 catalyst provides nearly five times higher the number of

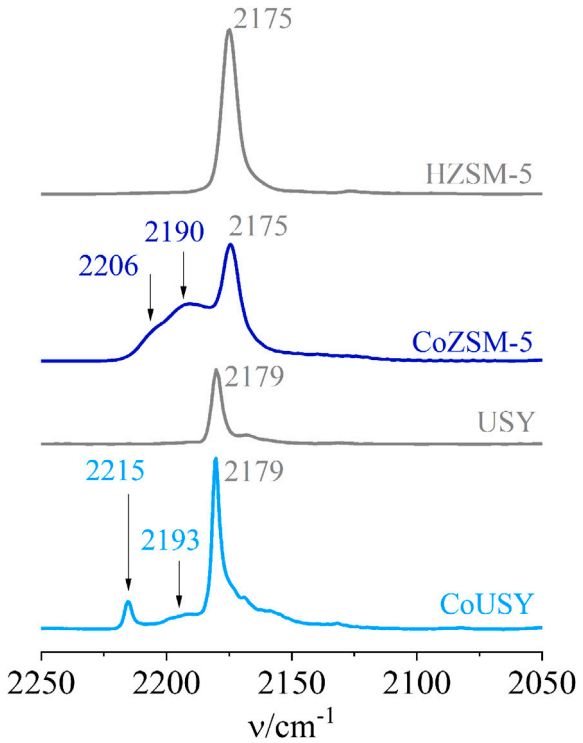

FIGURE 6 | IR spectra of CO sorption for the CoUSY and CoZSM-5 catalysts as well as reference zeolite supports.

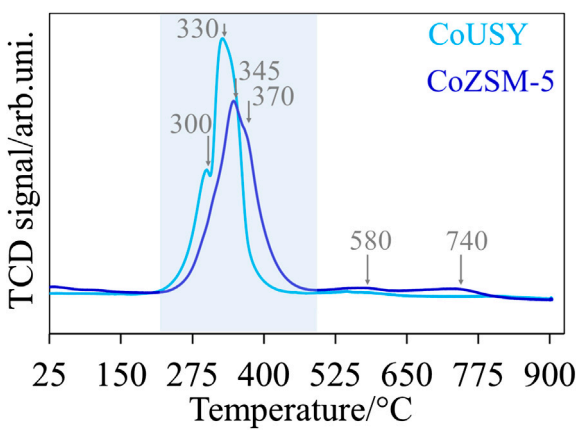

FIGURE 7 | H_2-TPR profiles of the CoUSY and CoZSM-5 catalysts.

metallic cobalt sites, i.e., the ESR process active sites, giving a premise to expect its better catalytic activity.

For both cobalt catalysts, the TPR profiles, collected in **Figure 7**, show two main reduction peaks in the temperature range of about 200–480°C, attributed to the reduction of cobalt oxide species (Grzybek et al., 2017) located on the external zeolite surface. These peaks centered at 300 and 330°C for the CoUSY catalyst are shifted toward the higher temperatures for CoZSM-5, to 345 and 370°C, respectively. This confirms the stronger electron acceptor properties of the CoUSY catalyst. Moreover, for the CoZSM-5 catalyst, additional low-intensity peaks at around 580 and 740°C can be noticed. Their presence is, most likely, related to the reduction of Co^{2+} in charge-compensating positions of the ZSM-5. It is further accompanied by a slight increase in the hydrogen consumption from 1.726 (for CoUSY) to 1.926 mmol H2/g (for CoZSM-5). The absence of these high-temperature peaks in the case of the CoUSY catalyst indicates the presence of a fraction of irreducible Co^{2+} ions, which does not participate in the ethanol steam reforming (Da Cruz et al., 1998; Wang et al., 2000). The presence of these irreducible ions is detected indirectly as the drop in the concentration of Brønsted acid sites after cobalt deposition (Py sorption IR studies).

The hydrogen consumption determined from the TPR profiles corresponds to approximately 76 and 85% of the total cobalt (10 wt%) contained in the CoUSY and CoZSM-5 catalysts, respectively, which indicates the presence of 24 and 15% of the irreducible cobalt species accordingly. On the other hand, the number of cobalt species determined by CO adsorption IR studies constitutes ca. 2.9 and 8.2% of that determined by H_2-TPR studies, indicating only partial accessibility of cobalt species. A significant share of cobalt, being enclosed inside the cobalt nanograins, is inaccessible for the CO probe molecule. Nevertheless, the amount of cobalt accessible in CoZSM-5 is almost 2.5 times higher than in CoUSY, which is consistent with the microscopic observations.

Catalysts Activity and Selectivity in the Ethanol Steam Reforming Process

The performance of the studied cobalt-containing in the ESR process carried out for ethanol-to-water molar ratio of 1 : 4, 1 : 9, and 1 : 12 is compared in **8** and **9**. The selectivity to the most important products, i.e., H_2, CO_2, and C_2H_4, is presented in **Figure 8**, while the residual products are presented in **Figure 9**. For both catalysts, the complete ethanol conversion (X_{EtOH} = 100%) is observed for 21 h of long time-on-stream tests for each studied ratio of 1 : 4, 1 : 9, and 1 : 12 (data not shown). The preliminary variability of the selectivity to reaction products over time results from the initial carbon deposition on the surface of the catalyst during side reactions. The selectivity of most of the products stabilized after about 6 h. After 21 h of the ESR reaction over the CoUSY catalyst, ca. 60%, 70%, and 30% of H_2 and ca. 25%, 35%, and 10% of CO_2 were produced at the EtOH/H_2O molar ratio of 1 : 4, 1 : 9, and 1 : 12, respectively (**Figure 10**). It means that the optimum the EtOH/H_2O molar ratio, which allows achieving the highest selectivity to two most desirable products of the ESR reaction, H_2, and CO_2, over the CoUSY catalyst is 1 : 9 (**Figure 10**). Surprisingly, the least amount of these products was formed not at the lowest water content (EtOH/H_2O molar ratio of 1 : 4) but the highest one (EtOH/H_2O molar ratio of 1 : 12). Regardless of the EtOH/H_2O molar ratio, CO selectivity was only ca. 5% after 21 h of the ESR reaction. It suggests that most of CO, occurring at the beginning of the process, was converted into CO_2 through the water-gas shift reaction (**Eq. 5**):

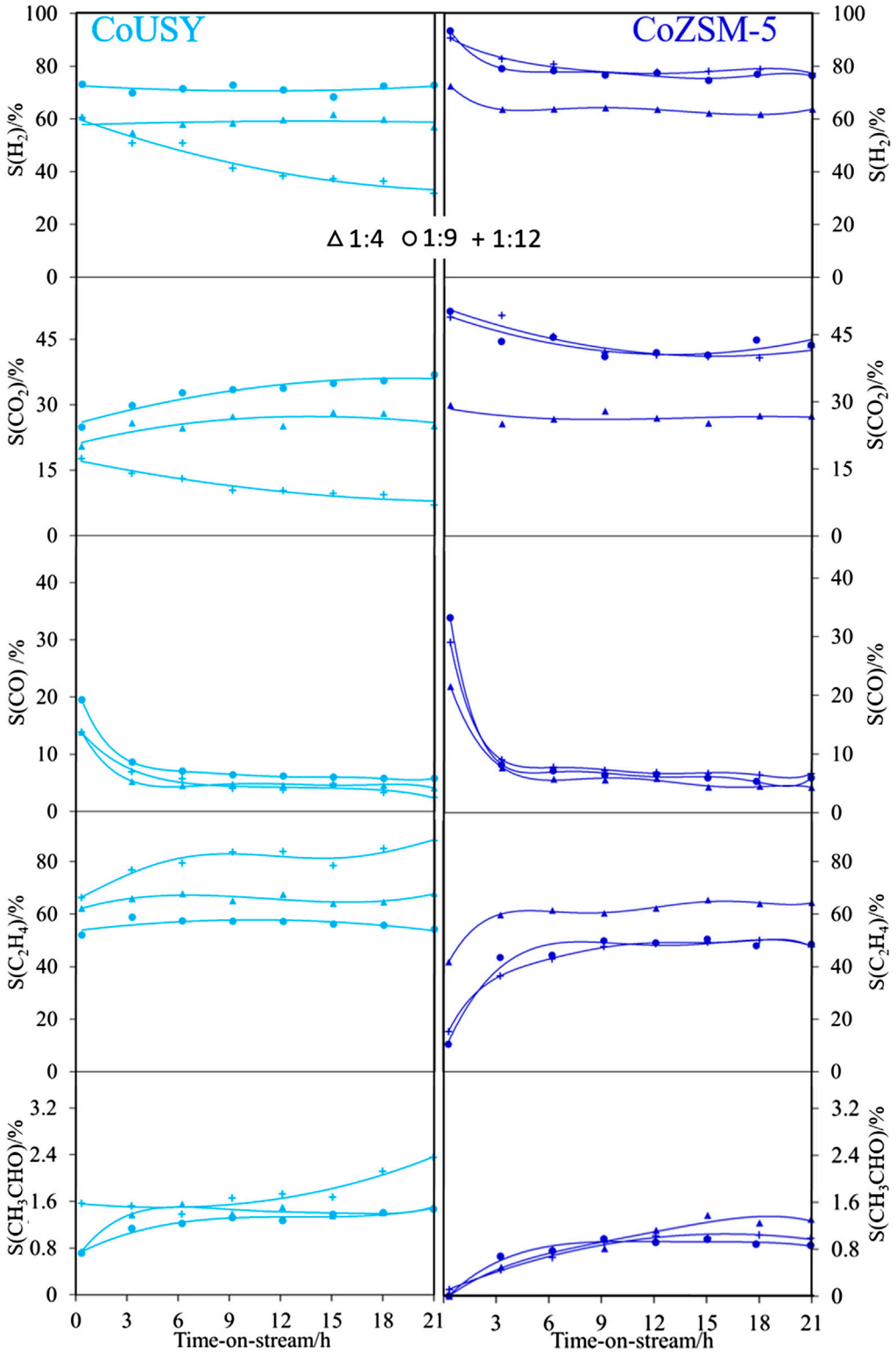

FIGURE 8 | Selectivity to the main products of the ESR process at 500°C for reaction mixtures with ethanol-to-water ratio of 1 : 4 (Δ), 1 : 9 (o), and 1 : 12 (+) for the CoUSY **(left column)** and CoZSM-5 **(right column)** catalysts.

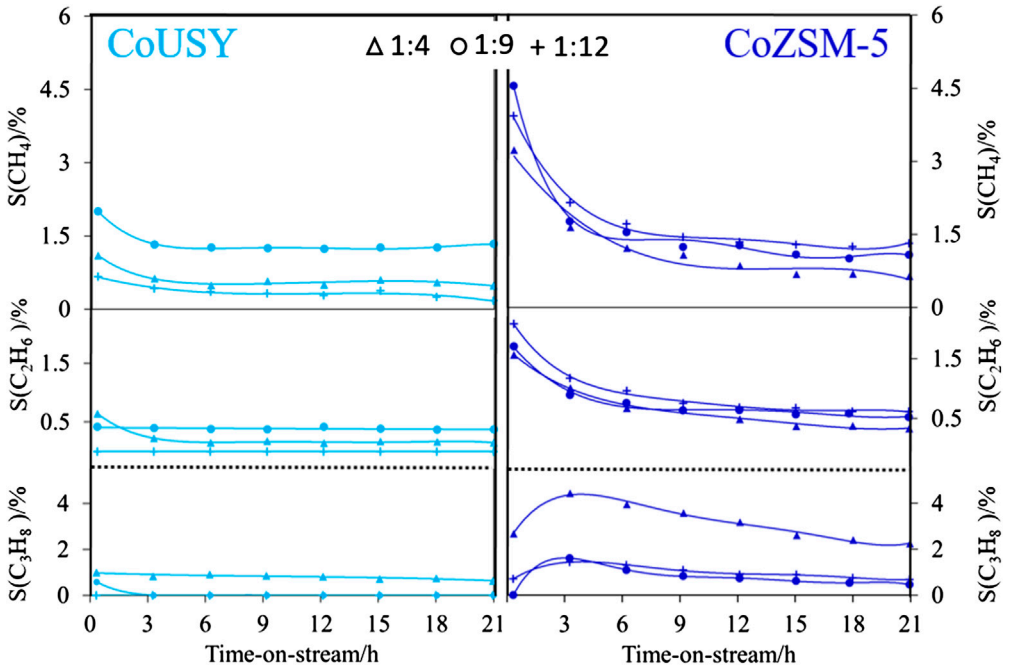

FIGURE 9 | Selectivity to residual products of the ESR process at 540°C for reaction mixtures with ethanol-to-water ratio of 1 : 4 (Δ), 1 : 9 (o), and 1 : 12 (+) for CoUSY **(left column)** and CoZSM-5 **(right column)** catalysts.

$$CO + H_2O \rightarrow CO_2 + H_2 \quad (5)$$

At the same time, the formation of C2 products (C_2H_4 and CH_3CHO) was the highest for the highest studied excess of water (EtOH/H_2O molar ratio of 1 : 12). Whereas the selectivity to CH_3CHO in the presence of the CoUSY catalyst is rather low at each studied EtOH/H_2O molar ratio (ca. 1.5% for 1 : 4 and 1 : 9 and ca. 2.5% for 1 : 12 after 21 h of the ESR), the number of C_2H_4 formed over this catalyst was significant (ca. 68%, 55%, and 88% for the EtOH/H_2O molar ratio of 1 : 4, 1 : 9, and 1 : 12, respectively). It indicates that ethanol dehydration to C_2H_4 (**Eq. 6**) was a dominant reaction while its dehydrogenation occurred to a lesser extent (**Eq. 7**):

$$C_2H_5OH \rightarrow C_2H_4 + H_2O \quad (6)$$

$$C_2H_5OH \rightarrow CH_3CHO + H_2 \quad (7)$$

Other hydrocarbons were produced over the CoUSY under the ESR conditions in much smaller quantities regardless of the EtOH/H_2O molar ratio (**Figure 9**). After 21 h of the ESR reaction, less than 1.5% of CH_4 and traces of C_2H_6 and C_3H_8 were detected. The formation of CH_4 can be ascribed to the direct decomposition of ethanol (**Eq. 8**) or acetaldehyde (**Eq. 9**), while C_2H_6 and C_3H_8 products probably resulted from the consecutive reactions of C_2H_4.

$$C_2H_5OH \rightarrow CH_4 + CO + H_2 \quad (8)$$

$$CH_3CHO \rightarrow CH_4 + CO \quad (9)$$

In the case of the CoZSM-5 catalyst, the increase of water content in the reaction mixture caused the enhancement of the process selectivity. After 21 h of the ESR reaction, selectivity to both H_2 and CO_2 increased from 64 to 77% and from 27 to 43%, respectively, with the change in EtOH/H_2O molar ratio from 1 : 4 to both 1 : 9 and 1 : 12 (**8** and **10**). After 21 h, also a similar amount of C_2H_4 (ca. 48%) was produced over the CoZSM-5 at both EtOH/H_2O molar ratios of 1 : 9 and 1 : 12, whereas selectivity to this product in the ESR reaction carried out at much lower water content (EtOH/H_2O molar ratio of 1 : 4) was much higher and equaled to ca. 64%. Similarly to results obtained for the CoUSY catalyst, the EtOH/H_2O molar ratio did not influence CO selectivity (ca. 6% for all EtOH/H_2O molar ratio after 21 h of ESR reaction). Other products, CH_3CHO (**Figure 8**), and hydrocarbons, CH_4, C_2H_6, and C_3H_8 (**Figure 9**), were detected in the presence of the CoZSM-5 catalyst in small quantities or even at trace level. Therefore, for both catalysts, the optimum EtOH/H_2O molar ratio, which allows achieving the highest selectivity to two main products of ESR reaction, was found to be 1:9. Still, more H_2 and CO_2 and fewer C_2H_4 were produced over the CoZSM-5 catalyst due to the better dispersion of the cobalt species. In turn, the influence of water (EtOH/H_2O equal to 1 : 12) observed for investigated catalysts was attributed to the water impact on the oxidation state of cobalt species. As reported by Varga et al. (2015) for the cobalt/ceria and rhodium-cobalt/ceria catalysts, the excess water can reoxidize the cobalt under reforming conditions. The authors reported that reoxidation occurs through the formation of water-induced Co oxides under the reforming condition. And since the Co^0/Co^{2+} ratio plays an important role in the catalyst activity in the ESR process (Ávila-Neto et al., 2013; Passos et al., 2014), the reoxidation appears to be of great importance. Thus, when the molar ratio of EtOH/H_2O is 1 : 12, the Co clusters may be

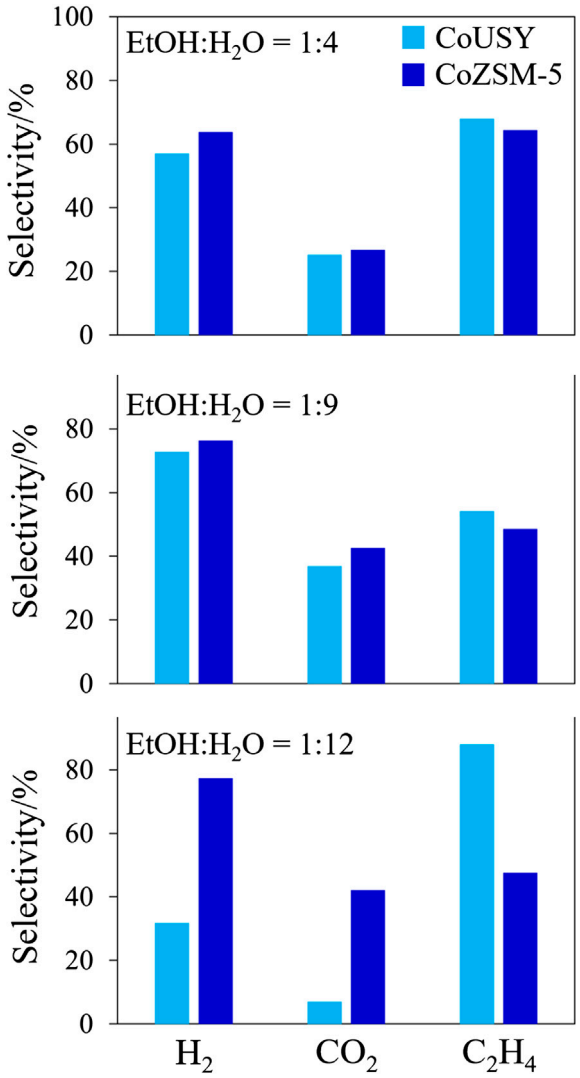

FIGURE 10 | The comparison of the selectivity to H_2, CO_2, and C_2H_4 products at the 21st hour of the ESR process at 500°C under various conditions (ethanol-to-water molar ratio of 1 : 4, 1 : 9, and 1 : 12).

disrupted due to strong interactions with water, and the reoxidation process can be more pronounced. The above combined with a higher starting share of Co^{2+} in CoUSY may lead to the dominance of the nonmetallic cobalt fraction in this catalyst and consequently to a reduction of hydrogen and CO_2 formation with a simultaneous increase in the formation of C_2H_4. This stays in good agreement with the report of Inokawa et al. (2010). The rapid C_2H_4 production by ethanol dehydration in the presence of transition Ni^{2+} and Co^{2+} cations in the zeolite Y was ascribed to both the interaction of metal cations with the OH groups of ethanol molecules and the appearance of additional H^+ by the dissociation of water molecules coordinated to cations. Indeed, at high water loading ($EtOH/H_2O$ equal to 1 : 12), nonreduced Co^{2+} cations (see TPR part) withdrawn from sodalite cages and hexagonal prisms can participate in both the binding of ethanol molecules and the hydrolysis process leading to the appearance of an additional number of protons as well. Consequently, the migration of cobalt cation and subsequent hydrolysis process together with reoxidation of metallic cobalt strongly affected the zeolite CoUSY activity. The partial dealumination of the zeolite can be also considered. The formation of extraframework aluminum species can be associated with the insertion of Al^{3+} cations into the Co_3O_4 matrix and progressive formation of the $Co_{3-x}Al_xO_4$ spinel. The ethanol conversion depends on the number of exposed cobalt active sites; thus, the formation of mixed spinel would perturb this number significantly.

CONCLUSIONS

The co-modified USY and ZSM-5 zeolite materials (Si/Al ratio of 31) were synthesized, characterized in terms of the chemical and phase composition, morphology, porosity, reducibility, and acidity, and evaluated in the ESR process at 500°C for various $EtOH/H_2O$ ratios (1 : 4; 1 : 9; and 1 : 12). The undisturbed micropore volume of zeolitic supports followed by a slight enhancement of their mesopore surface areas indicated the effective distribution of the Co_3O_4 phase (10 wt%) in the as-prepared materials. The detailed microscopic studies, together with the quantitative FT-IR studies of Py and CO sorption, confirmed the high dispersion of cobalt species, with the advantage of the CoZSM-5 catalyst with its better availability of cobalt species. Both catalysts showed 100% ethanol conversion, while their selectivity toward products such as H_2, CO_2, C_2H_4, and CH_4 strongly depended on the water content, showing the 1 : 9 ratio as the most effective one. The superior selectivity and stability of the CoZSM-5 catalyst, compared to CoUSY, resulted from enhanced accessibility of cobalt species. In addition, the negative effect of excess water (the $EtOH/H_2O$ molar ratio of 1 : 12) observed for the CoUSY catalyst (significant decrease in selectivity to H_2 and CO_2 and a significant increase to C_2H_4 in comparison for the 1 : 4 ratio) was explained based on the reoxidation of cobalt metallic species.

Since the structure of the zeolite support determines the cobalt active phase dispersion, strongly influencing its performance in the ESR process, it seems interesting to conduct a broader comparison of cobalt catalysts deposited on different zeolite supports in the next step.

DATA AVAILABILITY STATEMENT

The original contributions presented in the study are included in the article/supplementary materials, further inquiries can be directed to the corresponding author/s.

AUTHOR CONTRIBUTIONS

GG and KG were the originators of the concept and planned and supervised the experiments. KP and KT undertook the modification and characterization of materials with the FT-IR of probe molecules studies and assisted in their interpretation. MG planned and carried

out the catalytic testing and assisted in their interpretation. GS carried out the STEM measurements. MR carried out the H_2-TPR testing. GG wrote and edited the final article. All authors have read and agreed to the published version of the article.

FUNDING

This work was financed by Grant No. 2015/18/E/ST4/00191 from the National Science Centre, Poland.

REFERENCES

Ávila-Neto, C. N., Zanchet, D., Hori, C. E., Ribeiro, R. U., and Bueno, J. M. C. (2013). Interplay between particle size, composition, and structure of MgAl2O4-supported Co-Cu catalysts and their influence on carbon accumulation during steam reforming of ethanol. *J. Catal.* 307, 222–237. doi:0.1016/j.jcat.2013.07.025

Alberton, A. L., Souza, M. M. V. M., and Schmal, M. (2007). Carbon formation and its influence on ethanol steam reforming over Ni/Al2O3 catalysts. *Catal. Today.* 123, 257–264. doi:10.1016/j.cattod.2007.01.062

Armor, J. N. (1999). Striving for catalytically green processes in the 21st century. *Appl. Catal. Gen.* 189, 153–162. doi:10.1016/S0926-860X(99)00273-2

Barrett, E. P., Joyner, L. G., and Halenda, P. P. (1951). The determination of pore volume and area distributions in porous substances. I. Computations from nitrogen isotherms. *J. Am. Chem. Soc.* 73, 373–380. doi:10.1021/ja01145a126

Benito, M., Sanz, J. L., Isabel, R., Padilla, R., Arjona, R., and Daza, L. (2005). Bio-ethanol steam reforming: insights on the mechanism for hydrogen production. *J. Power Sources.* 151, 11–17. doi:10.1016/j.jpowsour.2005.02.046

Bineli, A., Tasic, M., and Filho, R. (2016). Catalytic steam reforming of ethanol for hydrogen production: brief status. *Chem. Ind. Chem. Eng. Q.* 22, 327–332. doi:10.2298/CICEQ160216017B

Bion, N., Epron, F., and Duprez, D. (2010). Bioethanol reforming for H2 production. *Catalysis.* 22, 1–55. doi:10.1039/9781847559630-00001

Breen, J. P., Burch, R., and Coleman, H. M. (2002). Metal-catalysed steam reforming of ethanol in the production of hydrogen for fuel cell applications. *Appl. Catal. B Environ.* 39, 65–74. doi:10.1016/S0926-3373(02)00075-9

Calles, J. A., Carrero, A., Vizcaıno, A. J., and Megia, P. J. (2020). Agglomerated Co e Cr/SBA-15 catalysts for hydrogen production through acetic acid steam reforming. *Int. J. Hydrog. Energy.* 45, 15941–15950. doi:10.1016/j.ijhydene.2019.05.237

Campos-Skrobot, F. C., Rizzo-Domingues, R. C. P., Fernandes-Machado, N. R. C., and Cantão, M. P. (2008). Novel zeolite-supported rhodium catalysts for ethanol steam reforming. *J. Power Sources.* 183, 713–716. doi:10.1016/j.jpowsour.2008.05.066

Chen, D., Liu, C., Mao, Y., Wang, W., and Li, T. (2020). Efficient hydrogen production from ethanol steam reforming over layer-controlled graphene-encapsulated Ni catalysts. *J. Clean. Prod.* 252, 119907. doi:10.1016/j.jclepro.2019.119907

Chica, A. (2013). Zeolites: promised materials for the sustainable production of hydrogen. *ISRN Chem. Eng.* 2013, 1–19. doi:10.1155/2013/907425

Chica, A., and Sayas, S. (2009). Effective and stable bioethanol steam reforming catalyst based on Ni and Co supported on all-silica delaminated ITQ-2 zeolite. *Catal. Today.* 146, 37–43. doi:10.1016/j.cattod.2008.12.024

Comas, J., Marino, F., Laborde, M., and Amadeo, N. (2004). Bio-ethanol steam reforming on Ni/Al_2O_3 catalyst. *Chem. Eng. J.* 98, 61–68. doi:10.1016/S1385-8947(03)00186-4

Contreras, J. L., Salmones, J., Colín-Luna, J. A., Nuño, L., Quintana, B., Córdova, I., et al. (2014). Catalysts for H_2 production using the ethanol steam reforming (a review). *Int. J. Hydrog. Energy.* 39, 18835–18853. doi:10.1016/j.ijhydene.2014.08.072

Da Costa-Serra, J. F., and Chica, A. (2011). Bioethanol steam reforming on Co/ITQ-18 catalyst: effect of the crystalline structure of the delaminated zeolite ITQ-18. *Int. J. Hydrog. Energy.* 36, 3862–3869. doi:0.1016/j.ijhydene.2010.12.094

Da Costa-Serra, J. F., Guil-López, R., and Chica, A. (2010). Co/ZnO and Ni/ZnO catalysts for hydrogen production by bioethanol steam reforming. Influence of ZnO support morphology on the catalytic properties of Co and Ni active phases. *Int. J. Hydrog. Energy.* 35, 6709–6716. doi:10.1016/j.ijhydene.2010.04.013

Da Cruz, R. S., Mascarenhas, A. J. S., and Andrade, H. M. C. (1998). Co-ZSM-5 catalysts for N_2O decomposition. *Appl. Catal. B Environ.* 18, 223–231. doi:10.1016/S0926-3373(98)00042-3

Deluga, G. A., Salge, J. R., Schmidt, L. D., and Verykios, X. E. (2004). Renewable hydrogen from ethanol by autothermal reforming. *Science.* 303, 993–997. doi:10.1126/science.1093045

Freni, S. (2001). Rh based catalysts for indirect internal reforming ethanol applications in molten carbonate fuel cells. *J. Power Sources.* 94, 14–19. doi:10.1016/S0378-7753(00)00593-0

Freni, S., Cavallaro, S., Mondello, N., Spadaro, L., and Frusteri, F. (2003). Production of hydrogen for MC fuel cell by steam reforming of ethanol over MgO supported Ni and Co catalysts. *Catal. Commun.* 4, 259–268. doi:10.1016/S1566-7367(03)00051-7

Frusteri, F., Freni, S., Chiodo, V., Donato, S., Bonura, G., and Cavallaro, S. (2006). Steam and auto-thermal reforming of bio-ethanol over MgO and CeO_2 Ni supported catalysts. *Int. J. Hydrog. Energy.* 31, 2193–2199. doi:10.1016/j.ijhydene.2006.02.024

Frusteri, F., Freni, S., Chiodo, V., Spadaro, L., Di Blasi, O., Bonura, G., et al. (2004). Steam reforming of bio-ethanol on alkali-doped Ni/MgO catalysts: hydrogen production for MC fuel cell. *Appl. Catal. Gen.* 270, 1–7. doi:10.1016/j.apcata.2004.03.052

García, E. Y., and Laborde, M. A. (1991). Hydrogen production by the steam reforming of ethanol: thermodynamic analysis. *Int. J. Hydrog. Energy.* 16, 307–312. doi:10.1016/0360-3199(95)00030-H

Góra-Marek, K., Gil, B., and Datka, J. (2009). Quantitative IR studies of the concentration of Co^{2+} and Co^{3+} sites in zeolites CoZSM-5 and CoFER. *Appl. Catal. Gen.* 353, 117–122. doi:10.1016/j.apcata.2008.10.034

Góra-Marek, K., Gil, B., Śliwa, M., and Datka, J. (2007). An IR spectroscopy study of Co sites in zeolites CoZSM-5. *Appl. Catal. Gen.* 330, 33–42. doi:10.1016/j.apcata.2007.06.033

Ghasemzadeh, K., Jalilnejad, E., and Tilebon, S. M. S. (2019). "Chapter 12 - hydrogen production technologies from ethanol,"in *Ethanol: science and engineering.*. Amsterdam, Netherlands: Elsevier. doi:10.1016/B978-0-12-811458-2.00012-2

Gołąbek, K., Tarach, K. A., Filek, U., and Góra-Marek, K. (2018). Ethylene formation by dehydration of ethanol over medium pore zeolites. *Spectrochim. Acta Part A Mol. Biomol. Spectrosc.* 192, 464–472. doi:10.1016/j.saa.2017.11.049

Greluk, M., Rotko, M., and Turczyniak-Surdacka, S. (2020a). Comparison of catalytic performance and coking resistant behaviors of cobalt- and nickel based catalyst with different Co/Ce and Ni/Ce molar ratio under SRE conditions. *Appl. Catal. A Gen.* 590, 117334. doi:10.1016/j.apcata.2019.117334

Greluk, M., Rotko, M., and Turczyniak-Surdacka, S. (2020b). Enhanced catalytic performance of La_2O_3 promoted Co/CeO_2 and Ni/CeO_2 catalysts for effective hydrogen production by ethanol steam reforming. *Renew. Energy.* 155, 378–395. doi:10.1016/j.renene.2020.03.117

Grzybek, G., Ciura, K., Wójcik, S., Gryboś, J., Indyka, P., Inger, M., et al. (2017). On the selection of the best polymorph of Al_2O_3 carriers for supported cobalt nano-spinel catalysts for N_2O abatement: an interplay between preferable surface spreading and damaging active phase-support interaction. *Catal. Sci. Technol.* 7, 5723–5732. doi:10.1039/c7cy01575e

Grzybek, G., Greluk, M., Indyka, P., Góra-Marek, K., Legutko, P., Słowik, G., et al. (2020). Cobalt catalyst for steam reforming of ethanol–Insights into the promotional role of potassium. *Int. J. Hydrog. Energy.* 5, 22658–22673. doi:10.1016/j.ijhydene.2020.06.037

Haga, F., Nakajima, T., Miya, H., and Mishima, S. (1997). Catalytic properties of supported cobalt catalysts or steam reforming of ethanol. *Catal. Lett.* 48, 223–227. doi:10.1023/a:1019039407126

Haryanto, A., Fernando, S., Murali, N., and Adhikari, S. (2005). Current status of hydrogen production techniques by steam reforming of ethanol: a review. *Energy Fuels.* 19, 2098–2106. doi:10.1021/ef0500538

Hou, T., Zhang, S., Chen, Y., Wang, D., and Cai, W. (2015). Hydrogen production from ethanol reforming: catalysts and reaction mechanism. *Renew. Sustain. Energy Rev.* 44, 132–148. doi:10.1016/j.rser.2014.12.023

Hsiao, W. I., Lin, Y. S., Chen, Y. C., and Lee, C. S. (2007). The effect of the morphology of nanocrystalline CeO_2 on ethanol reforming. *Chem. Phys. Lett.* 441, 294–299. doi:10.1016/j.cplett.2007.05.024

Hunter, E. P. L., and Lias, S. G. (1998). Evaluated gas phase basicities and proton affinity of molecules: an update. *J. Phys. Chem. Ref. Data.* 27, 413–656. doi:10.1063/1.556018

Inokawa, H., Nishimoto, S., Kameshima, Y., and Miyake, M. (2010). Difference in the catalytic activity of transition metals and their cations loaded in zeolite for ethanol steam reforming. *Int. J. Hydrog. Energy.* 35, 11719–11724. doi:10.1016/j.ijhydene.2010.08.092

Inokawa, H., Nishimoto, S., Kameshima, Y., and Miyake, M. (2011). Promotion of H_2 production from ethanol steam reforming by zeolite basicity. *Int. J. Hydrog. Energy.* 36, 15195–15202. doi:10.1016/j.ijhydene.2011.08.099

Kaddouri, A., and Mazzocchia, C. (2004). A study of the influence of the synthesis conditions upon the catalytic properties of Co/SiO_2 or Co/Al_2O_3 catalysts used for ethanol steam reforming. *Catal. Commun.* 5, 339–345. doi:10.1016/j.catcom.2004.03.008

Lang, L., Zhao, S., Yin, X., Yang, W., and Wu, C. (2015). Catalytic activities of K-modified zeolite ZSM-5 supported rhodium catalysts in low-temperature steam reforming of bioethanol. *Int. J. Hydrog. Energy.* 40, 9924–9934. doi:10.1016/j.ijhydene.2015.06.016

Łaniecki, M. (2001). "24-P-23-Cu-Y zeolite catalysts for methanol and ethanol steam reforming," In *Studies in surface science and catalysis.*. Editors J. V. A. Galarneau, F. Di Renzo, and F. Fajula (Amsterdam, Netherlands: Elsevier B.V.), 276. doi:10.1016/S0167-2991(01)81605-0

Li, M. R., and Wang, G. C. (2018). The mechanism of ethanol steam reforming on the Co^0 and Co^{2+} sites: a DFT study. *J. Catal.* 365, 391–404. doi:10.1016/j.jcat.2018.07.002

Li, X., Zheng, Z., Wang, S., Sun, C., Dai, R., Wu, X., et al. (2019). Preparation and characterization of core–shell composite zeolite BEA@MFI and their catalytic properties in ESR. *Catal. Lett.* 149, 766–777. doi:10.1007/s10562-018-2638-3

Liguras, D. K., Kondarides, D. I., and Verykios, X. E. (2003). Production of hydrogen for fuel cells by steam reforming of ethanol over supported noble metal catalysts. *Appl. Catal. B Environ.* 43, 345–354. doi:10.1016/S0926-3373(02)00327-2

Llorca, J., Corberán, V. C., Divins, N. J., Fraile, R. O., and Taboada, E. (2013). "Hydrogen from bioethanol," in *Renewable hydrogen technologies.*. Editors L. M. Gandía, G. Arzamendi, and P. M. Diéguez (Amsterdam, Netherlands: Elsevier). doi:10.1016/S0926-3373(02)00327-2

Llorca, J., Homs, N., Sales, J., Fierro, J. L. G., and De La Piscina, P. R. (2004). Effect of sodium addition on the performance of Co-ZnO-based catalysts for hydrogen production from bioethanol. *J. Catal.* 222, 470–480. doi:10.1016/j.jcat.2003.12.008

Llorca, J., Homs, N., Sales, J., and Ramírez de la Piscina, P. (2002). Efficient production of hydrogen over supported cobalt catalysts from ethanol steam reforming. *J. Catal.* 209, 306–317. doi:10.1006/jcat.2002.3643

Maggio, G., Freni, S., and Cavallaro, S. (1998). Light alcohols/methane fuelled molten carbonate fuel cells: a comparative study. *J. Power Sources.* 74, 17–23. doi:10.1016/S0378-7753(98)00003-2

Mattos, L. V., Jacobs, G., Davis, B. H., and Noronha, F. B. (2012). Production of hydrogen from ethanol: review of reaction mechanism and catalyst deactivation. *Chem. Rev.* 112, 4094–4123. doi:10.1021/cr2000114

Mattos, L. V., and Noronha, F. B. (2005). Hydrogen production for fuel cell applications by ethanol partial oxidation on Pt/CeO_2 catalysts: the effect of the reaction conditions and reaction mechanism. *J. Catal.* 233, 453–463. doi:10.1016/j.jcat.2005.04.022

Ni, M., Leung, D. Y. C., and Leung, M. K. H. (2007). A review on reforming bio-ethanol for hydrogen production. *Int. J. Hydrogen Energy.* 32, 3238–3247. doi:10.1016/j.ijhydene.2007.04.038

Ogo, S., and Sekine, Y. (2020). Recent progress in ethanol steam reforming using non-noble transition metal catalysts: a review. *Fuel Process. Technol.* 199, 106238. doi:10.1016/j.fuproc.2019.106238

Ogo, S., Shimizu, T., Nakazawa, Y., Mukawa, K., Mukai, D., and Sekine, Y. (2015). Steam reforming of ethanol over K promoted Co catalyst. *Appl. Catal. Gen.* 495, 30–38. doi:10.1016/j.apcata.2015.01.018

Passos, A. R., Martins, L., Pulcinelli, S. H., Santilli, C. V., and Briois, V. (2014). Effect of the balance between Co(II) and Co(0) oxidation states on the catalytic activity of cobalt catalysts for Ethanol Steam Reforming. *Catal. Today.* 229, 88–94. doi:10.1016/j.cattod.2013.10.080

Passos, A. R., Martins, L., Pulcinelli, S. H., Santilli, C. V., and Briois, V. (2017). Correlation of sol–gel alumina-supported cobalt catalyst processing to cobalt speciation, ethanol steam reforming activity, and stability. *ChemCatChem.* 9, 3918–3929. doi:10.1002/cctc.201700319

Riani, P., Garbarino, G., Cavattoni, T., and Busca, G. (Forthcoming 2020). CO2 hydrogenation and ethanol steam reforming over Co/SiO_2 catalysts: deactivation and selectivity switches. *Catal. Today.*. doi:10.1016/j.cattod.2020.05.002

Rouqerol, J., Llewellyn, P., and Rouqerol, F. (2007). Is the BET equation applicable to microporous adsorbents? *Stud. Surf. Sci. Catal.* 160, 49–56. doi:10.1016/S0167-2991(07)80008-5.

Słowik, G., Greluk, M., and MacHocki, A. (2016). Microscopic characterization of changes in the structure of KCo/CeO_2 catalyst used in the steam reforming of ethanol. *Mater. Chem. Phys.* 173, 219–237. doi:10.1016/j.matchemphys.2016.02.008

Sekine, Y., Nakazawa, Y., Oyama, K., Shimizu, T., and Ogo, S. (2014). Effect of small amount of Fe addition on ethanol steam reforming over Co/Al_2O_3 catalyst. *Appl. Catal. Gen.* 472, 113–122. doi:10.1016/j.apcata.2013.11.026

Sheng, P.-Y., Bowmaker, G. A., and Idriss, H. (2004). The reactions of ethanol over Au/CeO_2. *Appl. Catal. Gen.* 261, 171–181. doi:10.1016/J.APCATA.2003.10.046

Sohn, H., Celik, G., Gunduz, S., Dogu, D., Zhang, S., Shan, J., et al. (2017). Oxygen mobility in pre-reduced nano- and macro-ceria with Co loading: an AP-XPS, in-situ DRIFTS and TPR study. *Catal. Lett.* 147, 2863–2876. doi:10.1007/s10562-017-2176-4

Sohn, H., Soykal, I. I., Zhang, S., Shan, J., Tao, F., Miller, J. T., et al. (2016). Effect of cobalt on reduction characteristics of ceria under ethanol steam reforming conditions: AP-XPS and XANES studies. *J. Phys. Chem. C.* 120, 14631–14642. doi:10.1021/acs.jpcc.6b02490

Song, S., Akande, A. J., Idem, R. O., and Mahinpey, N. (2007). Inter-relationship between preparation methods, nickel loading, characteristics and performance in the reforming of crude ethanol over Ni/Al_2O_3 catalysts: a neural network approach. *Eng. Appl. Artif. Intell.* 20, 261–271. doi:10.1016/j.engappai.2006.06.014

Subramani, V., and Song, C. (2007). Advances in catalysis and processes for hydrogen production from ethanol reforming. *Catalysis.* 20, 65–106. doi:10.1039/b602364a

Tarach, K. A., Tekla, J., Makowski, W., Filek, U., Mlekodaj, K., Girman, V., et al. (2016). Catalytic dehydration of ethanol over hierarchical ZSM-5 zeolites: studies of their acidity and porosity properties. *Catal. Sci. Technol.* 6, 3568–3584. doi:10.1039/c5cy01866h

Torres, J. A., Llorca, J., Casanovas, A., Domínguez, M., Salvadó, J., and Montané, D. (2007). Steam reforming of ethanol at moderate temperature: multifactorial design analysis of Ni/La_2O_3-Al_2O_3, and Fe- and Mn-promoted Co/ZnO catalysts. *J. Power Sources.* 169, 158–166. doi:10.1016/j.jpowsour.2007.01.057

Trimm, D. L. (1999). Catalysts for the control of coking during steam reforming. *Catal. Today.* 49, 3–10. doi:10.1016/S0920-5861(98)00401-5

Vaidya, P. D., and Rodrigues, A. E. (2006). Insight into steam reforming of ethanol to produce hydrogen for fuel cells. *Chem. Eng. J.* 117, 39–49. doi:10.1016/J.CEJ.2005.12.008

Varga, E., Ferencz, Z., Oszkó, A., Erdohelyi, A., and Kiss, J. (2015). Oxidation states of active catalytic centers in ethanol steam reforming reaction on ceria based Rh promoted Co catalysts: an XPS study. *J. Mol. Catal. Chem.* 397, 127–133. doi:10.1016/j.molcata.2014.11.010

Vizcaíno, A. J., Carrero, A., and Calles, J. A. (2007). Hydrogen production by ethanol steam reforming over Cu–Ni supported catalysts. *Int. J. Hydrog. Energy.* 32, 1450–1461. doi:10.1016/J.IJHYDENE.2006.10.024

Wanat, E. C., Venkataraman, K., and Schmidt, L. D. (2004). Steam reforming and water-gas shift of ethanol on Rh and Rh-Ce catalysts in a catalytic wall reactor. *Appl. Catal. Gen.* 276, 155–162. doi:10.1016/j.apcata.2004.08.001

Wang, S., He, B., Tian, R., Wu, X., An, X., and Liu, Y. (2020). Novel core-shell-like Ni-supported hierarchical beta zeolite catalysts on bioethanol steam reforming. *Fuel.* 279, 118449. doi:10.1016/j.ijhydene.2020.04.109

Wang, X., Chen, H. Y., and Sachtler, W. M. H. (2000). Catalytic reduction of NO_x by hydrocarbons over Co/ZSM-5 catalysts prepared with different methods. *Appl. Catal. B Environ.* 26, L227–L239. doi:10.1016/S0926-3373(00)00125-9

Zanchet, D., Santos, J. B. O., Damyanova, S., Gallo, J. M. R., and Bueno, J. M. C. (2015). Toward understanding metal-catalyzed ethanol reforming. *ACS Catal.* 5, 3841–3863. doi:10.1021/cs5020755

Zhang, B., Tang, X., Li, Y., Xu, Y., and Shen, W. (2007). Hydrogen production from steam reforming of ethanol and glycerol over ceria-supported metal catalysts. *Int. J. Hydrog. Energy.* 32, 2367–2373. doi:10.1016/j.ijhydene.2006.11.003

Zhurka, M. D., Lemonidou, A. A., Anderson, J. A., and Kechagiopoulos, P. N. (2018). Kinetic analysis of the steam reforming of ethanol over Ni/SiO_2 for the elucidation of metal-dominated reaction pathways. *React. Chem. Eng.* 3, 883–897. doi:10.1039/c8re00145f

Conflict of Interest: The authors declare that the research was conducted in the absence of any commercial or financial relationships that could be construed as a potential conflict of interest.

Energy Materials

Juan Sieben

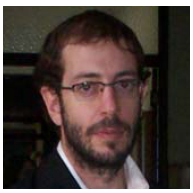

Dr. Juan Manuel Sieben is an Assistant Professor in Physical Chemistry at the National University of the South (UNS), Independent Researcher at CONICET, and a Team Leader at the Institute of Electrochemical Engineering and Corrosion, UNS, Argentina. In 2009, he received his Ph.D. in Chemistry from the National University of the South with a work focused on the synthesis of Pt-based supported electrocatalysts for the electrooxidation of methanol. Juan Manuel has co-authored over 40 papers and four book chapters. His current main research areas are related to the preparation and characterization of nanostructured materials for energy production and storage: direct alcohol fuel cells and hybrid supercapacitors.

Haihua Wang

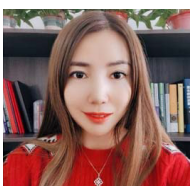

Prof. Haihua Wang is a Full Professor at Shaanxi University of Science and Technology (SUST). She received her Ph.D. from SUST before working as a postdoctoral researcher at the University of New Brunswick. Then, she worked with Prof. Mark C. Hersam at Northwestern University. She has published 33 patents and 147 papers, and she has won several esteemed prizes, including the Top Youth Talent Title, Youth Science and Technology Prize from Shaanxi Province, and the First Prize of Provincial Science and Technology Award. She has conducted more than 20 projects, and many technologies have been successfully commercialized for real industrial application.

Kewei Shu

Dr. Kewei Shu is an Associate Professor at Shaanxi University of Science and Technology, China, College of Chemistry and Chemical Engineering. He obtained his Ph. D. from the University of Wollongong, Australia, in 2016, and has worked at the University of Wollongong, Case Western Reserve University, and the University of Toronto as a post-doctoral researcher. His research interests include research on polymer solid electrolytes, 2D material preparation and energy storage application, and the design of novel battery systems.

frontiers in Materials

ORIGINAL RESEARCH
published: 10 November 2020
doi: 10.3389/fmats.2020.588399

Softwood Kraft Pulp-Derived Carbon-Supported PtNi Catalysts for the Electrooxidation of Ethanol

María Luz Nieva Lobos[1], *Juan Manuel Sieben*[2]* *and Elizabeth Laura Moyano*[1]

[1]INFIQC, Departamento de Química Organica, Facultad de Ciencias Químicas, Universidad Nacional de Córdoba, Córdoba, Argentina, [2]Instituto de Ingeniería Electroquímica y Corrosión (INIEC) and CONICET, Departamento de Ingeniería Química, Universidad Nacional del Sur, Bahía Blanca, Argentina

In this work, the biocarbons synthesized by fast pyrolysis at 350°C of raw (BK) and H_3PO_4 treated (TBK) fibrous fraction of non-bleached softwood kraft pulp has been proposed as novel supports for the deposition of PtNi nanocatalysts. The bimetallic nanoparticles were deposited by pulse microwave-assisted reduction using ethylene glycol both as solvent and reducing agent. The physicochemical properties of the resulting materials were evaluated by means of X-ray diffraction, transmission electron microscopy, energy dispersive X-ray microanalysis, and inductively coupled plasma atomic emission spectroscopy, whereas the electrochemical activity towards ethanol oxidation in acid medium was evaluated using cyclic voltammetry and chronoamperometry. Nanosized PtNi particles with average diameters in the range of 2.9–4.1 nm and a nickel content of ca. 30 at% were deposited over both softwood kraft pulp-derived carbon materials. The electrochemical measurements showed that the bimetallic nanoparticles deposited over the acid-treated biocarbon (PtNi/TBK) exhibit superior catalytic performance in terms of activity, onset potential, and poisoning tolerance. The mass activity of the PtNi nanocatalyst supported over TBK was about 1.3 and 6.3 times higher than that of the bimetallic nanoparticles deposited onto BK and Pt/C, respectively. The effect of the carbonaceous material on the electrocatalytic activity is discussed in detail.

Keywords: biocarbons, fast pyrolysis, PtNi nanoparticles, microwave-assisted synthesis, ethanol oxidation

OPEN ACCESS

Edited by:
Jong-Seok Oh,
Kongju National University,
South Korea

Reviewed by:
Biuck Habibi,
Azarbaijan Shahid Madani University,
Iran
Yawen Tang,
Nanjing Normal University, China

***Correspondence:**
Juan Manuel Sieben
jmsieben@uns.edu.ar

Specialty section:
This article was submitted to Energy Materials, a section of the journal Frontiers in Materials

Received: *28 July 2020*
Accepted: *15 October 2020*
Published: *10 November 2020*

Citation:
Nieva Lobos ML, Sieben JM and Moyano EL (2020) Softwood Kraft Pulp-Derived Carbon-Supported PtNi Catalysts for the Electrooxidation of Ethanol. Front. Mater. 7:588399. doi: 10.3389/fmats.2020.588399

INTRODUCTION

During the last years, the biocarbons have been proposed as the cheapest and eco-friendly alternative to replacing the commercial carbon black powders and other expensive materials such as carbon nanotubes and graphene in the electrodes of different electrochemical devices like fuel cells, supercapacitors, and batteries (Guo et al., 2014; da Silva et al., 2014; Nieva Lobos et al., 2016b; Liu et al., 2019; Pistone and Espro, 2020). Different biomass feedstock sources such as forestry and agro-industrial residues, as well as industrial and domiciliary wastes, can be employed for producing biocarbons by pyrolysis or hydrothermal methods. Accordingly, it is possible to effectively reduce energy consumption and fabrication costs and limit the emission of greenhouse gases. For instance, spruce and corncob hydrolysis by-products formed during bioethanol synthesis were employed to producing activated biocarbons via hydrothermal carbonization and subsequent chemical activation using KOH (Falco et al., 2013). A N-doped biocarbon material was fabricated by the pyrolysis of chitosan at 900°C under N_2 atmosphere and then utilized as support of Pt nanoparticles for methanol

electrooxidation (Zhao et al., 2014). On the other hand, a low-cost biosynthesis method using yeast cells as the precursor was used to fabricate a nitrogen- and phosphorus-doped biocarbon, which was employed as an electrode material for the oxygen reduction reaction (ORR) (Gong et al., 2015). More recently, coconut shells were used for the synthesis of biocarbons by hydrothermal carbonization and then subjected to physical, chemical, or thermal activation (Schonvogel et al., 2019). The coconut shell-derived carbon powders were used as supports of platinum nanoparticles for the ORR process.

Apart from those mentioned above, the pulp and paper mills produce huge amounts of residual biomass, which are usually disposed of in waste dumps or incinerated, thus causing serious damage to the environment (Reckamp et al., 2014). Moreover, the high concentration of lignocellulosic compounds in the wastewater produces eutrophication of water bodies, which endangers aquatic life (Haq and Raj, 2020). The treatment of these residues via fast pyrolysis can be a cost-effective and sustainable way to reduce contamination and to obtain valuable products such as biofuels and biocarbons. Reckamp et al. produced biochar and bio-oils via the fast pyrolysis of paper mill sludge subjected to acid hydrolysis and torrefaction pretreatments (Reckamp et al., 2014). Bengtsson and collaborators converted dry-jet wet spun fibers from a 70/30 w/w mixture of softwood kraft lignin and bleached softwood kraft pulp into carbon fibers by carbonization at various temperatures and different residence times (Bengstsson et al., 2020). Nieva Lobos et al. demonstrated that the fibrous fraction of unbleached softwood kraft pulp is an interesting material for the production of biocarbons via fast pyrolysis, since the content of lignin is very low (Nieva Lobos et al., 2016a). Herein, the kraft pulp residues can be transformed into valuable biocarbons through fast pyrolysis and the textural and surface properties can be tuned to provide a high accessible surface area and efficient anchoring sites to platinum-based catalysts for direct ethanol fuel cells (DEFCs).

Regarding platinum-based electrocatalysts, the bimetallic PtNi alloy system emerges as a promising alternative for the electrooxidation of ethanol in acidic electrolyte solutions because of the high resistance to dissolution of nickel atoms in the bimetallic alloy and the passivating role of Ni hydroxides at the direct ethanol fuel cell operating conditions (Antolini, 2017). Besides, nickel is a low-cost Earth-abundant transition metal. The beneficial effect of nickel on bimetallic PtNi catalysts for the electrooxidation of alcohols is associated either with its ability to form-OH labile species through the dissociation of water at a lower potential that on Pt, and the electronic and strain effects provoked by the cocatalyst in the platinum surface atoms (Antolini et al., 2005; Nørskov et al., 2009; Comignani et al., 2015; Altarawneh et al., 2018). Shen et al. studied the influence of Ni and Ru on the activity of PtNi and PtNiRu catalysts supported on graphene nanosheets for ethanol oxidation and discovered that Ni is responsible for reducing the bond strength and coverage of adsorbed poisoning species on Pt surface via strain and electronic effects (Shen et al., 2015). Beyhan and collaborators evaluated the performance of PtNi/C and PNiSn/C catalysts towards ethanol oxidation and revealed that nickel promotes the cleavage of the C-C bond (Beyhan, et al., 2013). Whereas Comignani et al. found that nickel oxide species facilitate the cleavage of the C-H and O-H bonds of ethanol both through the bifunctional mechanism and the ligand effect (Comignani et al., 2015). Habibi and coworkers studied the effect of Ni on PtNi nanoparticles supported on carbon-ceramic (Habibi and Dadashpour, 2013) and CuNiPt nanoparticles supported on graphitized pencil lead (Imanzadeh and Habibi, 2020) and suggested that the enhanced performance of the catalysts for the electrooxidation of ethanol is explained in terms of the bifunctional mechanism, the electronic effects and the augment in electroactive surface area due to the '"leaching out"' effect of the alloying element.

This work explores the possibility of using the biocarbons fabricated by fast pyrolysis of untreated and acid-treated fibrous fraction of kraft pulp waste as supports for the deposition of bimetallic PtNi nanoparticles. The as-synthesized biocarbons exhibited specific surface areas ranging from 306 to 454 $m^2\ g^{-1}$ and different oxygen and nitrogen contents. The bimetallic PtNi nanoparticles were deposited over the biocarbons derived from kraft pulp by pulse microwave-assisted reduction in ethylene glycol. Spherical PtNi particles of ca. 3.5 nm with a nickel content of about 30 at% were deposited over the surface of the biocarbons. The electrocatalytic performance of the as-prepared catalysts towards ethanol oxidation in acid medium was investigated by cyclic voltammetry and chronoamperometry. It was found that the bimetallic nanoparticles deposited on the surface of the biocarbon derived from acid-treated kraft pulp present a superior catalytic performance in terms of activity, onset potential and poisoning tolerance compared to the catalyst prepared with the untreated biocarbon, reaching peak current densities of 476 and 3,574 A g_{Pt}^{-1} at 25 and 60°C, respectively. The superior performance of the bimetallic nanoparticles supported over the acid-treated biocarbon was explained in terms of the carbon support effect on the properties of PtNi catalyst.

EXPERIMENTAL

Raw Material

Softwood kraft pulp (KP) was selected for the pyrolysis study. In the study, KP samples were chemical treated using a phosphoric acid solution (Anedra, 85% w/w). Typically, in the experiments 1.00 g of KP and 5 ml of 0.17 M H_3PO_4 aqueous solution were added in a round-bottom flask under magnetic stirring and kept at 80°C for 2 h. Afterward, the slurry was filtered under vacuum and the solid was dried for 8 h under reduced pressure at 40°C. The acid-treated material is named as A-KP from now on.

Characterization of Raw Materials

The samples KP and A-KP were characterized by elemental analysis with an Elemental Analyzer 2400 Serie II Perkin Elmer. The oxygen content was determined by difference, taking into account the ash content in the calculus. Ash content of kraft pulp materials was established by dry combustion at 575°C for 24 h. The raw and acid-treated kraft

pulp materials were also studied by X-ray diffraction (XRD). The X-ray patterns were acquired in a Philips PW1710 BASED instrument operating at 45 keV and 30 mA, using Cu-Kα radiation. Fourier Transform Infrared (FTIR) spectroscopy was carried out to analyze the surface chemistry of the samples. The spectra were obtained using a FTIR Bruker IFS 28v spectrometer, with a resolution of 2 cm^{-1} in the range of 4,000–400 cm^{-1} by using anhydrous KBr disks. Besides, pulp materials were studied by scanning electron microscopy (SEM) with a field emission scanning electron microscope FE-SEM, Sigma Zeiss apparatus. The content of cellulose, hemicellulose, and lignin in the starting biomass was determined using an ANKOM 200 fiber analyzer (ANKOM Technologies, USA), following a modified technique described by Goering and Van Soest with modifications (Van Soest et al., 1991).

Preparation of Biocarbons from Kraft Pulp

Biocarbons were prepared by pyrolysis of KP and A-KP. Pyrolysis experiments were performed under oxygen-free conditions using a quartz tubular reactor, which was placed in a tubular furnace with an internal thermocouple. Approximately 5.00 g of sample were put in a ceramic boat and then introduced in the middle of the pyrolysis reactor once the reaction temperature of 350°C and the vacuum conditions were reached. Ultra-dry nitrogen was used as the carrier gas to enhance the transportation of products to the condensation region at cryogenic temperatures. The flow rate of the carrier gas was kept at 0.1 ml s^{-1}, residence times were less than 5 s and the experiments lasted 20 min to attain the complete conversion of the biomass sample. Carbonaceous materials were removed from the ceramic boat and weighed. Biocarbon sample from KP is called BK while carbon from A-KP is called TBK, respectively. Additionally, BK and TBK were extensively washed with distilled water to remove remaining impurities in order to leave the porous structures free.

Physicochemical Characterization of Biocarbons

The physicochemical properties of BK and TBK samples were studied by elemental analysis, XRD, FTIR, and SEM using the instrumentation detailed in *Characterization of Raw Materials* for kraft pulp. Brunauer-Emmett-Teller (BET) surface area, total micropore volume and mesopore volume of the biochars were measured at least in duplicate by nitrogen gas sorption at −196°C using a NOVA 1000e porosimeter (Quantachrome, Boynton Beach, FL, USA). Samples were vacuum degassed overnight at 160°C before analysis.

The electrical conductivity of carbon powders was determined via the four-point procedure. The biocarbon sample (100.0 mg) was placed into a Teflon tube and then compressed at a pressure of 150 kPa between two brass electrodes of 8 mm in diameter. Electrical conductivity was calculated according to the following equation: $\sigma = h/(R \times A)$; where R is the resistance calculated by using Ohm's law, h is the powder thickness, and A is the surface area of the cylinder (Marinho et al., 2012). To ensure reproducibility the experiments were carried out in triplicate.

Synthesis of Catalysts

The bimetallic PtNi nanosized particles supported on the biocarbons were prepared by a pulse microwave-assisted method in ethylene glycol. A suitable amount of nickel (II) chloride hexahydrate (11.6 mg, $NiCl_2{\cdot}6H_2O$) and 100.0 mg of BK or TBK biocarbons were dissolved into 50 ml of ethylene glycol (EG) in a beaker by sonication for 60 min. Afterward, an appropriate volume of a diluted H_2PtCl_6 aqueous solution (0.0386 M) was added into the beaker. The suspension was sonicated for 15 min and then the pH value adjusted to 10.0 by adding 0.5 M KOH-EG solution. The deposition of the bimetallic PtNi nanoparticles on the biocarbons was carried out by microwave heating in an oven (2450 MHz, 700 W) under a pulse mode condition of 30 s on/45 s off for five pulses. The resulting slurries were cooled down to room temperature and the solid collected by vacuum filtration. The catalysts were rinsed repeatedly with bidistilled water and ethanol and finally dried for 24 h at 70°C in an oven. The nominal Pt:Ni atomic ratio was 2.35:1, and the total metal loading of the catalysts was 20 wt% on carbon. For comparison purposes, Pt/BK, Pt/TBK and Pt/C catalysts (20 wt% Pt on carbon) were synthesized using the same synthesis route. In the case of Pt/C catalyst, Vulcan XC-72 carbon black (BET area of 230 $m^2\ g^{-1}$, micropore volume of 0.36 $cm^3\ g^{-1}$, and conductivity of 0.195 S cm^{-1}) was used as the catalyst support (Comignani et al., 2017). Catalyst inks (1 mg ml^{-1}) were prepared by dispersing 10.0 mg of catalyst in a solution consisting of 7.96 ml of tridistilled water, 2 ml of isopropyl alcohol and 40 μL of Nafion ionomer solution (5 wt% in a mixture of lower aliphatic alcohols and water) by sonication for 45 min.

Electrochemical Characterization of Catalysts

The electrochemical experiments were run with a Princeton Applied Research VersaSTAT 3 potentiostat/galvanostat at 25 and 60°C. Three-electrode glass cells were employed to carry out the electrochemical tests. A saturated calomel electrode (*SCE*, +0.241 vs. *NHE*) located in a Luggin capillary served as the reference electrode while a platinum wire served as the counter electrode. The working electrodes were obtained by pipetting 20 μL of catalyst ink onto a polished glassy carbon rod (0.07 cm^2) to yield a catalyst loading of about 57 μg cm^{-2}. The electrodes were dried in air at room temperature for 3 h before use. The electrochemical behavior of the as-prepared electrocatalysts was performed by cyclic voltammetry (CV) in the range of −0.25–0.8 V for fifty cycles at a sweep rate of 0.05 V s^{-1} in 0.5 M H_2SO_4 at 25 °C. Before starting the experiments, all solutions were deaerated with pure N_2 for 30 min to remove dissolved electroactive oxygen. The performance of the electrodes for the alcohol electrooxidation was evaluated in 1 M EtOH/0.5 M H_2SO_4 in a potential range of −0.2 to 0.9 V at a scan rate of 0.05 V s^{-1}. The upper potential limit was restricted to 0.9 V in order to prevent or limit catalyst degradation and carbon corrosion. Furthermore, potentiostatic experiments (i.e., chronoamperometry) were carried out at an applied

potential of 0.5 V for 4,500 s. The catalytic activity is expressed in terms of current density per mass of Pt. The composition of the bimetallic catalysts before and after the long-term potentiostatic experiments were determined by EDX microanalysis.

The electroactive surface area (*ESA*) of the as-prepared electrocatalysts was determined by CO stripping voltammetry tests. CO stripping curves were obtained after bubbling CO through an electrochemical glass cell filled with N_2-purged 0.5 M H_2SO_4 solution for 20 min by holding the working electrode potential at -0.091 V, followed by N_2 bubbling to remove the excess of CO. Then, the CO stripping voltammogram curves were obtained by cycling the working electrode in the range of −0.091 to 0.8 V at a scan rate of 0.02 V s^{-1}. The stripping charges were determined between −0.091 and 0.8 V after current background correction. The *ESA* values were estimated by considering a monolayer charge of 420 μC cm^{-2} and an adsorption ratio of one CO molecule to each surface Pt site.

Physicochemical Characterization of Catalysts

The structure of the as-synthesized catalysts was evaluated by X-ray diffraction (XRD) using a Rigaku Dmax III C diffractometer with CuKα radiation source operated. The peak profiles in the X-ray patterns were fitted with the pseudo-Voigt function, employing the non-linear least-squares refinement procedure based on a finite-difference Marquardt algorithm. Lattice parameters and crystallite size were determined by Rietveld analysis. High-resolution transmission electronic microscopy (HR-TEM) images were obtained on a JEOL microscope (model JEM-2100 plus) operated at 200 keV. The average particle sizes were measured by counting approximately 200 particles in different sectors of each sample using free-software ImageJ. Furthermore, the composition distribution was investigated by elemental mapping using a microanalyzer INCA X-ray (Oxford Systems). The bulk composition of the catalysts was determined by energy dispersive X-ray (EDX) microanalysis with an EDAX probe coupled to a scanning electron microscope (SEM, JEOL 100). The analysis was performed in five different regions of each sample. The platinum and nickel loadings of the different catalysts were determined by inductively coupled plasma atomic emission spectrometry (ICP-AES) with a Shimadzu 1000 model III equipment.

RESULTS AND DISCUSSION

Characterization of Raw Material

The characteristics of the samples KP and A-KP are summarized in **Table 1**. The major organic elements in raw materials KP and A-KP are carbon and oxygen. For these materials, the oxygen and carbon content was similar, the concentration of hydrogen and nitrogen was very small, while sulfur was detected in traces. The main component of kraft pulp is cellulose, although hemicellulose and lignin are also present in few amounts. **Supplementary Figure S1** shows the X-ray diffraction patterns of KP and A-KP. It can be identified three-wide crystalline peaks at Bragg angles of around 16, 22 and 35°, which can be ascribed to the crystalline structure of cellulose (Klemm et al., 2005). The figures show that there are differences in the width of these peaks. It is observed that the width of the peaks of the KP is narrower than those of A-KP. Consequently, the chemical pretreatment of KP reduced the number of ordered microregions of the cellulose component, producing an increase in the presence of amorphous regions. This phenomenon has been observed in previous studies concerning the chemical treatment of cellulosic and lignocellulosic biomasses (Dobele et al., 2001; Zhang et al., 2009).

TABLE 1 | Properties of kraft pulp.

	KP[a]	A-KP[b]
C (wt%)[c]	46	43
N (wt%)[c]	0.8	0.7
H (wt%)[c]	5	4
O (wt%)[d]	41	40
S (wt%)[c]	0.03	0.04
Ash (wt%)[c]	7	11
Cellulose (g/Kg)[c]	81	-
Hemicellulose (g/Kg)[c]	9	-
Lignin (g/Kg)[c]	5	-

[a]*Raw kraft pulp.*
[b]*Acid-treated kraft pulp.*
[c]*Dry basis.*
[d]*Calculated by difference.*

To analyze the morphological change of kraft pulp after acid treatment, SEM measurements were performed. **Supplementary Figure S2A** and SI2B show the morphological characteristics of the kraft pulp sample before and after acid impregnation with phosphoric acid. For the non-treated sample (**Supplementary Figure S2A**), cellulose ribbons are clearly observed together with small amorphous regions. On the contrary, the A-KP sample is comprised of a great number of cellulose agglomerates with a very irregular surface. After acid treatment, the fibers are distinctly reduced in length compared with KP (**Supplementary Figure S2A**). According to these findings, the acid treatment caused more structural defects in the surface, probably by acid-catalyzed dehydration reactions of the cellulose component (Zhao et al., 2007).

The FT-IR spectra of KP and A-KP were very similar (**Supplementary Figure S3**). Samples were characterized by a dominant O-H stretch band (ca. 3,300 cm^{-1}) and a C-H band (ca. 2,900 cm^{-1}) attributed to the presence of aliphatic groups. The band at 1,638 cm^{-1} is ascribed to the bending mode of absorbed water. The bands at 1,428 and 1,363–1,362 cm^{-1} reveal the C-H symmetric and asymmetric deformations, respectively. The absorbance band at 1,314–1,313 cm^{-1} and 1,334 cm^{-1} are associated with the C-C and C-O skeletal vibrations. The region of 1,200–1,000 cm^{-1} is dominated by ring vibrations overlapped with stretching vibrations of (υ C-OH) side groups and the (υ C-O-C) glycosidic bond vibration. These bands are significant in both spectra, particularly the band at

TABLE 2 | Properties of biocarbons from kraft pulps.

Samples	Ultimate analysis (wt%)[a]				S_{BET}[c] (m^2 g^{-1})	Pore volume (cm^3 g^{-1})	σ[d] (S cm^{-1})
	C	H	N	O[b]			
BK[e]	71	2	1	21	306	1.2	0.029
TBK[f]	65	5	2	24	454	1.8	0.027

[a]*Dry basis.*
[b]*Calculated by difference.*
[c]*BET (Brunauer–Emmett–Teller) surface area.*
[d]*Electrical conductivity determined at a pressure of 150 kPa.*
[e]*Raw kraft pulp.*
[f]*Acid-treated kraft pulp.*

1,055–1,054 cm^{-1} is dominated by glycosidic bond (υ C-O-C) contribution. A small sharp band at 897–895 cm^{-1} is characteristic of β-glycosidic bonds between the sugar units in cellulose (Kacuráková et al., 2000).

Biocarbons Characterization

Table 2 shows the elemental analysis and superficial area for the biocarbons produced from fast pyrolysis of kraft pulp (BK) and acid-treated kraft pulp (TBK). These carbonaceous materials were obtained at 350°C. Comparing KP and A-KP with the carbons formed from these materials BK and TBK, respectively, it can be observed that the content of carbon increased after pyrolysis while the content of oxygen decreased (Tzong-Horng, 2010; González-García et al., 2013). This result would indicate that the raw material was richer in oxygen groups that could be eliminated after the thermal process due to the dehydration and carbonization reactions of the structural cellulose polymers. The specific surface area of the biocarbon obtained by the pyrolysis of KP is fairly good and this increased considerably with the acid treatment of the raw material. The increase in BET surface area can be ascribed to the liberation of certain volatile compounds as a result of the phosphoric acid activation treatment on the precursor material containing organic and inorganic materials. The surface area obtained mainly comes from the vaporization of organic matter during the pyrolysis process and chemical activation, leaving the porous surface. These results were consistent with previous studies concerning the production of biochar research (Kennedy et al., 2004; Tzong-Horng, 2010). In addition, the electrical conductivity values of both biocarbons were very close, indicating a similar degree of graphitization.

Figure 1 shows the morphology of BK and TBK carbons. The surface morphology was studied to know how affect the acid treatment to the raw material after pyrolysis. BK exhibited an irregular and roughness surface without any observable pore (**Figures 1A,B**). From the figure, it can be established that the shape of the cellulose macrofibrils was preserved after the pyrolysis process. **Figure 1C** shows the biocarbon obtained by the fast pyrolysis of acid-treated pulp. This material presented a rough surface showing irregular open and interconnected pores, which are of different sizes in the nanoscale range. This change in the morphology of the carbons can be associated with the chemical activation of starting material before the pyrolysis step which helped in the increase in porosity of the final material (El Qada et al., 2008; Sun et al., 2018). These pores are very useful for improving the specific surface area of biocarbons as was also seen in the obtained BET surface areas. **Supplementary Figure S4** shows the diffraction patterns of BK and TBK materials. In the case of BK, it can be seen the presence of

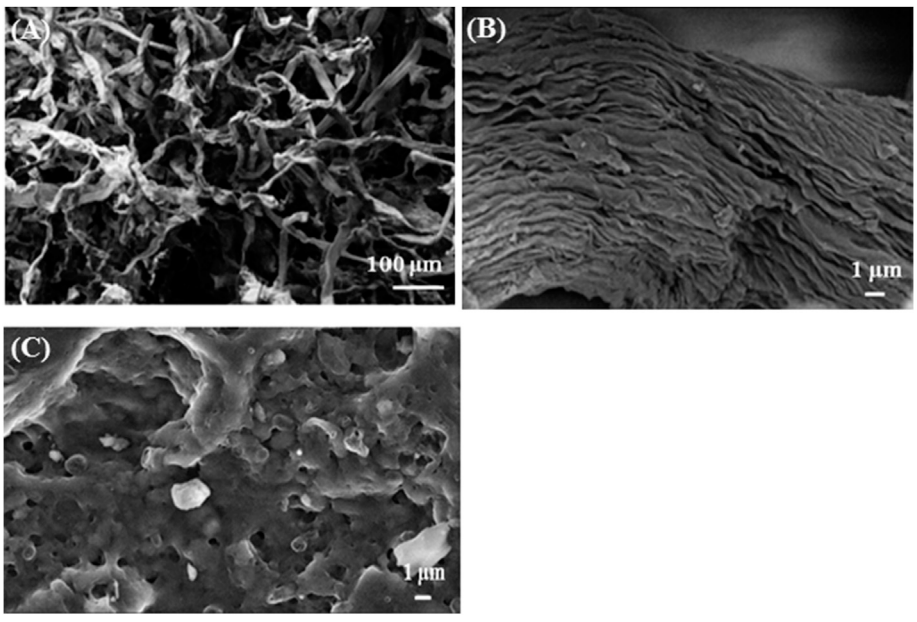

FIGURE 1 | Scanning electron microscope (SEM) images of: **(A)** BK at low magnification, **(B)** BK at higher magnification, and **(C)** TBK.

smaller signs that are due to calcite ($CaCO_3$) and quartz (SiO_2) between 25 and 35° that disappear when KP was treated with phosphoric acid.

FT-IR spectra corresponding to carbons from KP and A-KP are presented in **Figure 2**. The profile of both spectra is very similar in frequency absorption and intensity. The broad O-H band due to the stretching vibration mode of hydroxyl functional moieties is analogous to what is observed in the initial pulp samples. Contrary to what was obtained in the raw material, the bands associated with aliphatic/aromatic asymmetric C-H and symmetric C-H stretching can be seen as a broad and very weak peak at 2,990–2,820 cm^{-1}. In BK as well as TBK, carbonyl and olefinic groups can be easily detected. For instance, the absorption band at 1,706–1,700 cm^{-1} is assigned to C=O stretching vibrations that indicate the existence of ketones or aldehydes. The strong bands appearing in the 1,650–1,580 cm^{-1} region can be associated with C=C vibrations from aromatic rings. It is also evident for the appearance of these new peaks that the dehydration of the cellulose, the main constituent of pulps, has occurred. Also, for the same reason, the absorption patterns at 1,450–1,300 and 1,160–900 cm^{-1} were largely minimized for pulps during pyrolysis.

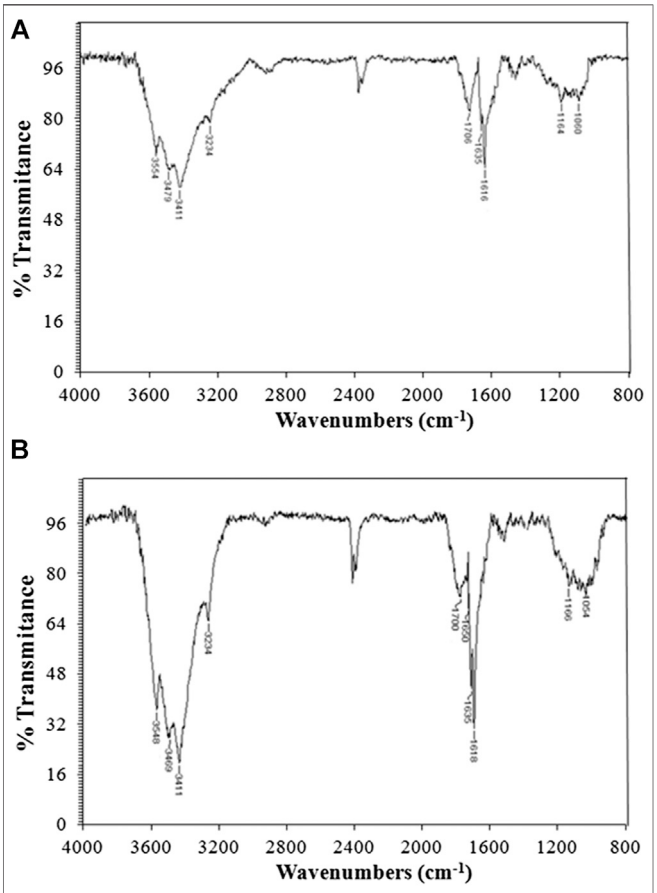

FIGURE 2 | FT-IR spectra of: **(A)** biocarbon from raw kraft pulp (BK) and **(B)** biocarbon from acid-treated kraft pulp (TBK).

Physicochemical Characterization of the As-Prepared Electrocatalysts

An EDX spectrum of the bimetallic PtNi nanoparticles supported on TBK biocarbon is displayed in **Figure 3A** and the results for the as-prepared electrocatalysts are summarized in **Table 3**. The spectrum exhibits the characteristic M and L X-ray lines of platinum and the K peaks of Ni. The average compositions of the bimetallic catalysts were in close agreement with the nominal values. In addition, the atomic composition of the electrocatalysts was also established by ICP-AES analysis. It can be observed that the Pt:Ni atomic ratios are very similar to the overall bulk compositions determined by EDX analysis.

Figure 3B shows the X-ray diffraction patterns of the as-synthesized PtNi nanoparticles supported on BK and TBK biocarbons. The diffractogram of Pt/C catalyst is also included for the sake of comparison. All diffraction patterns show four peaks at 2θ angles of ca. 40, 47, 68 and 82°, which are attributed to the (111), (200), (220) and (311) crystallographic planes of fcc platinum lattice structures (JCPDS Card No. 04–0783). It can be observed that the bimetallic PtNi nanoparticles supported on the biocarbons exhibit principally a single-phase disordered structure. On the other hand, the diffraction peaks of PtNi/BK and PtNi/TBK catalysts were slightly shifted towards higher 2θ angles compared to the reflections of Pt/C catalyst. This observation can be associated with the lattice contraction produced by partial substitution of Pt atoms with smaller Ni atoms, suggesting the formation of an alloy between Pt and Ni. Therefore, the lattice parameter (a_{fcc}) and lattice spacing (d_{hkl}) of PtNi/BK and PtNi/TBK catalysts are smaller than those of Pt/C (**Table 3**). The interplanar spacing between adjacent planes with the Miller indices (111) for PtNi/BK and PtNi/TBK are 2.22 and 2.21 Å respectively, while the d-spacing in Pt/C catalyst is 2.25 Å.

The atomic fraction of Ni in the solid solution can be estimated from Vegard's law using the following equation:

$$a_{PtNi} = (1 - x)a_{Pt} + x\,a_{Ni} \quad (1)$$

where x is the molar of Ni, a_{Pt} is the lattice constant of pure Pt (0.3923 nm, JCPDS Card No. 004–0783), a_{Ni} is the lattice constant of pure Ni (0.3524 nm, JCPDS Card No. 004–0850) and a_{PtNi} is the measured lattice constant of the alloy.

According to the calculations, the Ni content in the bimetallic alloy is 12 at% for the PtNi/BK catalyst and 19 at% for the PtNi/TBK catalyst. A comparison of the nickel contents determined from the EDX and ICP-AES analyses and the ratios calculated from the lattice parameters through the Vegard's law discloses that some fraction of the Ni atoms are forming a non-alloyed phase probably comprised of oxides and hydroxides. The absence of the diffraction peaks from NiOOH, $Ni(OH)_2$ and/or NiO species in the X-ray patterns of the bimetallic materials may be associated with the existence of an amorphous state. This is in accordance with previous results published in the literature (Zhou et al., 2011; Luo et al., 2013; Shen et al., 2015). It can be calculated that only about 37% of Ni atoms are forming an alloy with Pt in the PtNi/BK catalyst, while ca. 61% of Ni atoms are forming an

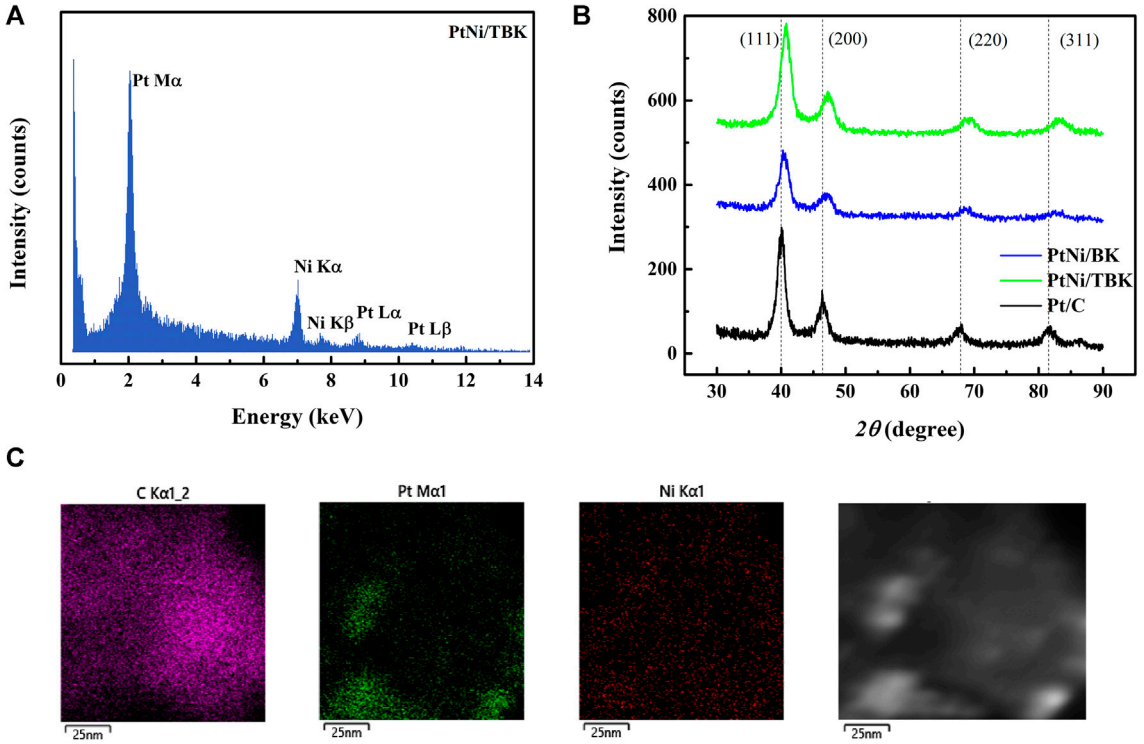

FIGURE 3 | (A) Representative EDX spectrum of PtNi/TBK catalyst. **(B)** X-ray diffraction patterns of the as-prepared electrocatalysts. **(C)** Representative EDX mapping image of PtNi/TBK catalyst and corresponding HAADF-STEM image.

alloy with the noble metal in the PtNi/TBK catalyst. **Figure 3C** displays a representative EDX mapping image of PtNi/TBK catalyst. The spherical nanoparticles exhibit a homogeneous distribution of Pt and Ni elements, revealing that both metals were reduced simultaneously onto the surface of the biocarbon support.

Furthermore, the average crystallite size (d_c) of the nanoparticles was calculated with direct use of the Rietveld procedure and the values are included in **Table 3**. The average crystallite size of the bimetallic PtNi nanoparticles supported on BK is larger than that of the particles deposited on TBK and also larger than that of the platinum nanoparticles dispersed over Vulcan XC-72R carbon black.

TABLE 3 | Characteristic parameters of the as-prepared catalysts.

Catalyst	Pt[a]	Ni[a]	Pt[b]	Ni[b]	a_{fcc}	d_c[c]	d_p[d]	*ECSA*[e] $m^2\ g_{Pt}^{-1}$
	at%				nm			
PtNi/BK	69.8	30.2	70.4	29.6	0.3872	4.1	3.6 ± 0.9	61.9
PtNi/TBK	70.3	29.7	71.5	28.5	0.3845	2.9	2.7 ± 0.6	68.8
Pt/C	100	0	100.0	0	0.3916	3.6	3.5 ± 0.7	60.2

[a]*Atomic composition determined by EDX (±3.1 at%).*
[b]*Atomic composition determined by ICP-AES (±1.5 at%).*
[c]*Crystallite size from XRD.*
[d]*Average particle size from HR-TEM.*
[e]*Electrochemical surface area per unit mass determined from CO stripping technique and ICP-AES analysis (±4.1 $m^2\ g^{-1}$).*

Some representative TEM and HR-TEM micrographs, along with the particle size distribution histograms of the bimetallic PtNi nanoparticles supported on BK and TBK biocarbons, are displayed in **Figure 4**. The average particle diameter of all electrocatalysts is compiled in **Table 3** and **Supplementary Table S1**. Overall it can be seen that the biocarbons were covered with well-distributed spherical nanosized particles with diameters ranging from 2.0 to 6 nm. The bimetallic nanoparticles formed over BK have an average diameter of 3.6 nm and the presence of few agglomerates can be observed, while the particles deposited on TBK have an average diameter of 2.7 nm with a narrow particle size distribution. On the other hand, Pt/C catalyst exhibits an average particle size of 3.5 nm, while Pt/BK and Pt/BTK materials have average diameters of 3.4 and 3.0 nm, respectively. The lower average particle diameter and the narrow particle distribution of PtNi/TBK compared to PtNi/BK can be likely explained in terms of the larger specific surface area, the higher roughness, and the higher amount of oxygen- and nitrogen-containing functional groups on the surface of the acid-treated biocarbon. Similar results were reported elsewhere (Antolini, 2009; Hsieh et al., 2013; Sebastián et al., 2013; Zhao et al., 2014; Comignani et al., 2017). On the one hand, the greater the specific BET surface area of the carbon support, the higher the number of surface defects that are present on its surface and the better the particle distribution over the carbonaceous support. And, on the other hand, the higher the number of oxygen and nitrogen functionalities the lower the particle size and the better

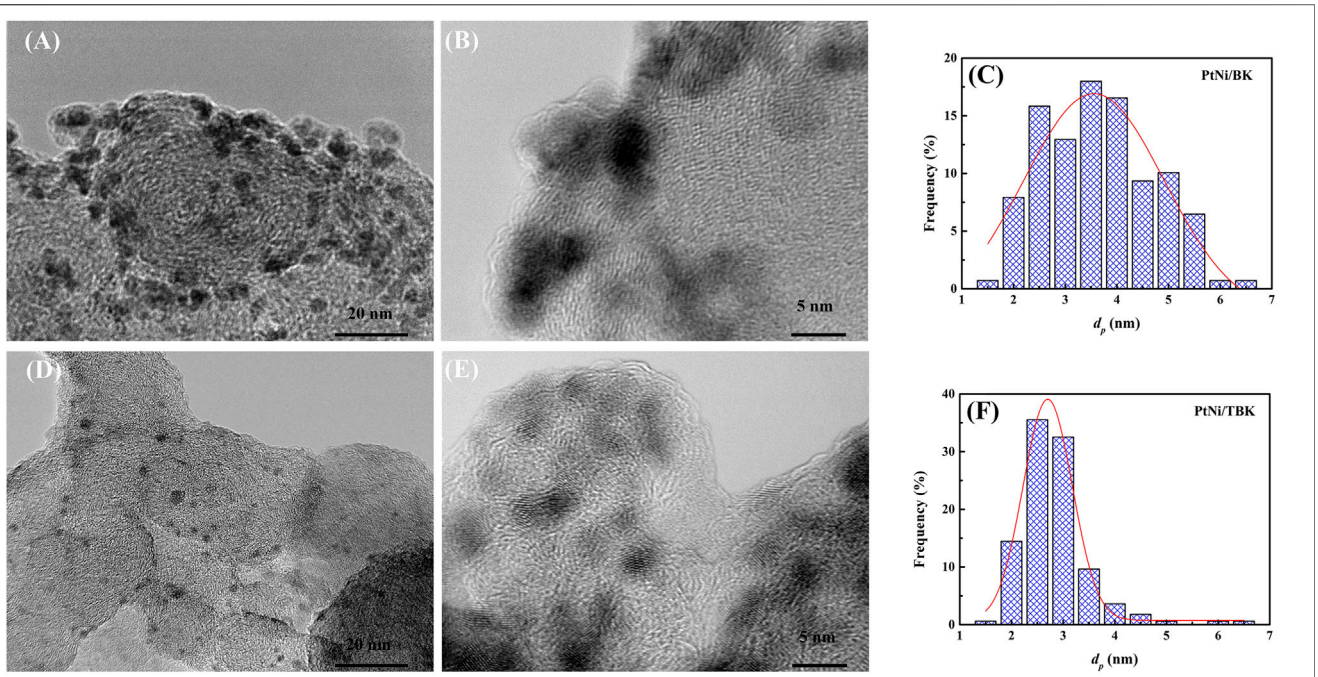

FIGURE 4 | Representative TEM and HR-TEM images and the corresponding particle size distribution histograms of the bimetallic PtNi nanoparticles supported on BK **(A–C)** and TBK **(D–F)** biocarbons.

the particle distribution due to the anchoring effect of surface groups.

Electrochemical Characterization

Figure 5A shows the CO stripping curves obtained at 25°C and a sweep rate of 0.02 V s^{-1}. The voltammetric response of Pt/C electrode was included for comparison. It is found that the onset potential for the electrooxidation of adsorbed CO on PtNi/BK and PtNi/TBK electrodes is shifted negatively by ca. 0.19 V relative to the Pt/C electrode. The oxidation of CO_{ad} on PtNi/BK and PtNi/TBK electrodes begins at 0.150 and 0.140 V respectively, while the onset potential for CO_2 formation on Pt/C is located at 0.34 V. And, the maximum of the CO_{ad} stripping peak on PtNi/BK and PtNi/TBK electrodes is centered at 0.43 and 0.45 V respectively, while it is shifted by ca. 80 mV to a more positive potential on Pt/C (0.53 V). From these results it can be deduced that the oxidative removal of CO on the PtNi nanoparticles supported onto the biocarbons is much easier than that on Pt/C electrode because of Ni atoms provides -OH labile groups through the dissociative adsorption of water at a lower potential that on Pt, and these -OH_{ad} groups facilitate the oxidation of adsorbed carbon monoxide to CO_2 via the so-called bifunctional mechanism (Watanabe and Motoo, 1975; Gasteiger et al., 1993) and because of some surface oxygen functionalities such as hydroxyl and carboxylic acid moieties also provides -OH_{ad} species to promote the oxidation of CO at Pt sites (Antonucci et al., 1994; Hsieh et al., 2013). In addition, the nickel atoms in the bimetallic alloy can modify the d-band properties of Pt atoms at the Fermi level due to the partial electron transfer from the oxophilic metal to Pt (Zhou et al., 2011; Luo et al., 2013; Wang et al. 2014; Zhang et al., 2017). This produces the downshift in the d-band center of Pt (i.e., ligand effect), thus weaken the Pt-CO bond (Goodenough et al., 1989; Nørskov et al., 2009).

The electrochemical surface areas per unit mass of platinum (*ECSA*) calculated from CO stripping of PtNi/KB, PtNi/TBK, Pt/BK, Pt/TBK and Pt/C are summarized in **Table 3** and **Supplementary Table S1**. The highest electrochemical surface area is achieved with the bimetallic nanoparticles supported on the acid-treated biochar, followed Pt/TBK, PtNi/BK, Pt/BK and Pt/C in order of decreasing average *ECSA* values. It can be deduced that the *ECSA* values are directly connected with the particle size, particle size distribution, and particle dispersion onto the different carbonaceous supports. As was commented earlier, this can be ascribed to the available number of anchoring sites for particle deposition, which depends on the BET surface area, the surface roughness and the amount of oxygen and nitrogen functionalities.

The electrooxidation of ethanol in acid environment was studied by cyclic voltammetry at 25 and 60°C and a sweep rate of 0.05 V s^{-1}. The voltammetric curves after fifty cycles are displayed in **Figures 5BC** and **Supplementary Figure S5**. The CV curves recorded at 25°C exhibit the typical features of the electrooxidation of the alcohol on Pt-based electrocatalysts, that is, one anodic peak during the forward scan direction and one anodic peak during the reverse scan direction. The anodic peak in the forward scan is attributed to the oxidation of different chemisorbed species formed through the dehydrogenation of adsorbed ethanol molecules, while the oxidation peak in the reverse scan is ascribed to both the oxidative removal of the

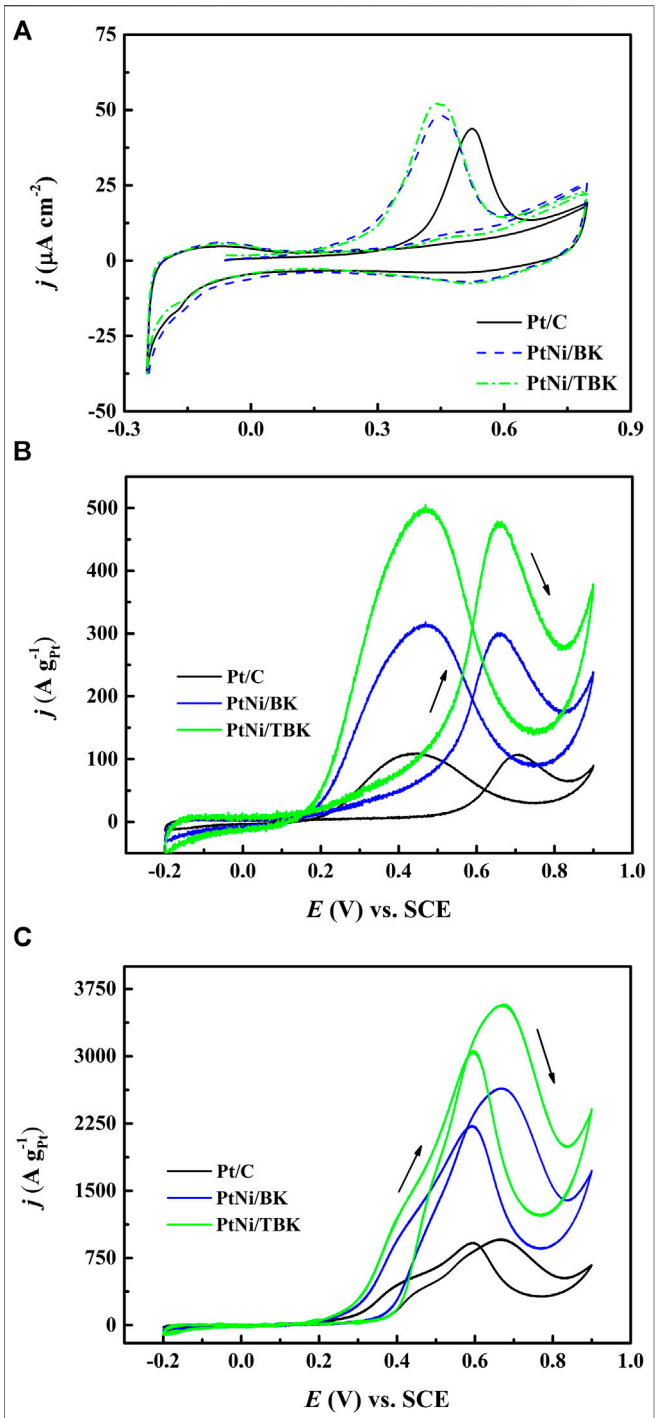

FIGURE 5 | (A) Voltammetric response for adsorbed CO stripping on the Pt/C, PtNi/BK and PtNi/TBK electrocatalysts in 0.1 M H_2SO_4 at 20 mV s^{-1}. Steady cyclic voltammograms (50th cycle) for the different electrodes in 1 M CH_3CH_2OH/0.5 M H_2SO_4 at 25°C **(B)** and 60°C **(C)**.

strongly adsorbed intermediates formed during the forward scan and the oxidation of freshly adsorbed ethanol molecules on free Pt sites. The onset potential for the EOR on PtNi/TBK electrode at 25°C was found to be located at 0.17 V, which is negatively shifted around 0.03 and 0.32 V with respect to the PtNi/BK electrode and Pt/C. The voltammetric curves also showed that the bimetallic PtNi nanoparticles supported on the biocarbon derived from the acid-treated KP displays the highest electroactivity over the whole potential range, followed by PtNi/BK and Pt/C in order of decreasing activity. As shown in **Figure 5B**, the PtNi/TBK electrode developed a maximum mass current density of 476 A g_{Pt}^{-1}, while forward peak current densities of 300 and 107 A g_{Pt}^{-1} were obtained for PtNi/BK and Pt/C electrodes, respectively. That is, the catalytic activity of PtNi/TBK for the EOR process was 1.6 and 7 times higher than that of PtNi/BK and Pt/C, respectively. Moreover, the maximum peak current density on PtNi/TBK catalyst occurred at 0.63 V, which was negatively shifted by ca. 30 and 50 mV with respect to the PtNi/BK and Pt/C electrodes. Therefore, the results point out that the EOR on the PtNi/TBK electrode was easier and faster, and needed less overpotential to occur when compared to the other electrocatalysts. On the other hand, the mass peak current density for Pt/BK was 142 A g_{Pt}^{-1} and for Pt/TBK was 160 A g_{Pt}^{-1}, which were 1.3 and 1.5 times higher than that of Pt/C (**Supplementary Figure S5**). Furthermore, the onset potential for the EOR on Pt/BK and Pt/TBK was negatively shifted as compared to Pt/C by 0.05 and 0.25 V, respectively. Accordingly, it can be demonstrated that the Pt nanoparticles deposited over the biocarbons are capable of catalyzing the ethanol oxidation reaction with greater efficiency than those supported on the commercial carbon black. This result can be explained in terms of the density of surface functional groups and the BET specific surface area of the carbonaceous materials.

Figure 5C shows the stabilized voltammetric response of the as-prepared electrocatalysts for ethanol electrooxidation at 60 °C. It can be observed that with increasing temperature, the onset potentials and the peak potentials shift slightly to less positive values. Besides, the mass specific activities rise up to 3,574, 2,645 and 959 A g_{Pt}^{-1} for PtNi/TBK, PtNi/BK and Pt/C, respectively, as the temperature of the solution increases from 25 to 60°C because of an overall enhancement of the reaction kinetics and a higher electrochemical conversion efficiency of ethanol to CO_2 and other reaction products (Lima et al., 2008; Sun et al., 2009; Altarawneh et al., 2018). Moreover, the shape of the voltammograms is somewhat different from that recorded at 25°C. In the positive scan, the potentiodynamic curves exhibited the main anodic oxidation peak centered at about 0.67, together with a shoulder peak at ca. 0.40 V. In the reverse scan, the oxidative peak occurred at 0.60 V with a shoulder on the left side at ca. 0.5 V. According to the literature, the anodic shoulders can likely be attributed to the formation of CO_2 via both oxidation of CO_{ad} preformed at lower overpotentials and cleavage of C-C bond and subsequent oxidation of the resulting adsorbed C1 species (Wang et al., 2006; Sun et al., 2009). The mass specific current densities of the shoulder peak were determined to be 1,300 A g_{Pt}^{-1} for PtNi/TBK, 1,092 A g_{Pt}^{-1} for PtNi/BK and 416 A g_{Pt}^{-1} for Pt/C. This result can be explained in terms of the thermal activation of the ethanol oxidation process, as was reported elsewhere (Sun et al., 2009). That is, the selectivity towards complete oxidation of ethanol to CO_2 is drastically enhanced with increasing reaction temperature while the

production of acetaldehyde and acetic acid is at the same time significantly reduced.

To obtain more information about the electrocatalytic performance of the bimetallic nanoparticles supported on the softwood kraft pulp-derived carbonaceous materials for the EOR in acid environment, we performed potentiostatic experiments at an applied potential of 0.5 V and temperatures of 25 and 60°C (**Figure 6**). It can be seen that in all *j-t* curves the current density abruptly decreases within the first minutes, due to the formation of different strongly adsorbed intermediates during the EOR. And then, the current densities decrease slowly with time elapsing and reach a pseudo stationary value after 3,000 s because of a relative balance between the oxidative removal of poisoning species at Pt sites via the bifunctional mechanism and the oxidation of freshly ethanol molecules on the regenerated Pt sites. The chronoamperometric curves display that the electrodes follow a similar trend in activity as observed in the potentiodynamic tests, that is, the catalytic activity for ethanol oxidation decreases in the order PtNi/TBK > PtNi/BK > Pt/C. The catalytic activities extracted from the CA curves after 75 min are compiled in **Table 4**. As noted, the bimetallic PtNi nanoparticles supported on TBK can oxidize the ethanol molecules in acid medium more efficiently than the other catalysts, and its catalytic activity at room temperature was improved by factors of 1.3 and 6.3 compared to PtNi/BK and Pt/C, respectively. Moreover, the stable current density at 60°C on PtNi/TBK catalyst was found to be about 1.6 and 7.2 times higher than on PtNi/BK and Pt/C, respectively. In addition, the EDX analysis of the samples before and after the long-term potentiostatic experiments was performed to evaluate the structural stability of the bimetallic nanoparticles (**Supplementary Figure S6; Supplementary Table S2**). By comparing the EDX results reported in **Table 3** with those included in **Supplementary Table S2**, it can be observed that the composition of catalysts remains almost unchanged after the EOR test, thus confirming the good structural stability of the bimetallic nanoparticles supported on the biocarbons.

Both potentiodynamic and potentiostatic experiments clearly show that the overall EOR process turns out to be more favorably on PtNi/TBK and PtNi/BK catalysts than on Pt/C. These results are in accordance with those extracted from the CO-stripping experiments. The better performance of the bimetallic catalysts can be partially explained by the ability of surface Ni and Ni related species to form labile -OH_{ad} at more negative potentials than Pt, and the partial electron transfer from Ni to Pt that generates the downshift in the d-band center of Pt, which markedly alters the metal electronic structures thus weakening the adsorption of CO and other poisoning reaction intermediates like acetaldehyde (Almeida et al., 2011; Antolini et al., 2005; Comignani et al., 2015). Besides, the compressive strain induced by incorporation of Ni result in lattice mismatch and d-band center downshifts of Pt, thereby also weakening the binding strength of CO and other intermediates on the surface of the catalysts (Nørskov, et al., 2009; Li et al., 2012). Apart from the favorable effect of Ni, the presence of labile hydroxyl species on the surface of the biocarbons could also contribute to the enhanced performance of the bimetallic nanoparticles (Antonucci et al., 1994).

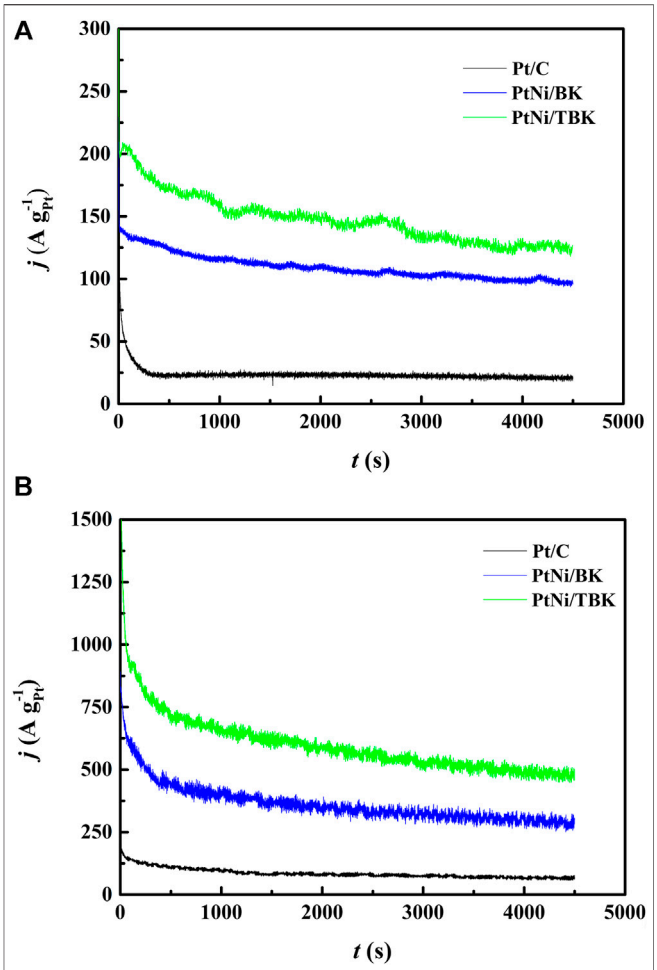

FIGURE 6 | Current-time curves at 0.5 V vs. *SCE* for Pt/C, PtNi/BK and PtNi/TBK electrodes in a 1 M CH_3CH_2OH + 0.5 M H_2SO_4 solution at 25°C **(A)** and 60°C **(B)**.

TABLE 4 | Specific mass activities of PtNi/TBK, PtNi/BK and Pt/C electrodes for ethanol oxidation in 1 M EtOH/0.5 M H_2SO_4 solution at an applied potential of 0.5 V vs. *SCE*.

	25°C	60°C
Catalyst	*j* A g_{Pt}^{-1}	
PtNi/BK	96	294
PtNi/TBK	125	480
Pt/C	20	67

In order to rationalize the better electrocatalytic performance of the PtNi/TKB catalyst compared to PtNi/BK electrode, it is important to consider the influence of the textural and surface properties of the biocarbons on the alloying degree of Ni with Pt, the chemical state of Ni, particle size and dispersion. But let us first turn our attention to discuss the direct influence of the biocarbons in the electrocatalytic oxidation of ethanol in the acid electrolyte. The surface oxygen and nitrogen functionalities, such

as carboxylic, hydroxyl and pyrrolic moieties, are capable of providing labile -OH species to facilitate the oxidation of adsorbed intermediates via the bifunctional mechanism (Zhou et al., 2010; Calderón et al., 2012; Hsieh et al., 2012; Zhang et al., 2014). Therefore, taking into account that the density of surface functional groups on TBK biocarbon is higher than that on the biocarbon synthesized with the raw kraft pulp material, more hydroxyl species can be supplied by TBK to oxidize the adsorbed poisoning intermediates and free the electroactive platinum sites for further ethanol oxidation, thus enhancing the overall EOR process. Similar results to those presented here were reported in the literature. For instance, Hsieh et al. found that the presence of surface oxygen functionalities on the surface of carbon nanotubes enhance the anti-poisoning ability of Pt nanoparticles for the electrooxidation of formic acid (Hsieh, et al. 2013). Calderon and coworkers established that the electrocatalytic response of bimetallic PtRu nanoparticles supported on carbon xerogels towards the electrooxidation of methanol is improved by the presence of oxygen functionalities, particularly the carboxylic groups (Calderón et al., 2012). Also, Asgardi et al. suggested that the presence of a larger number of surface oxygenated moieties on carbon support is a determining parameter for enhancing the activity of Pt-based nanoparticles for the EOR process (Asgardi et al., 2015). On the other hand, the electrical conductivity is expected to have a negligible influence on the EOR process because both biomass-derived carbonaceous materials presented similar conductivity values. Let us now shift the analysis from the direct correlation between the carbon support properties and the catalytic activity to the influence of the support properties on the bimetallic nanoparticles (i.e., an indirect relation between support properties and catalytic activity). The BET specific surface area and the density of surface functional groups have a positive effect on particle size and distribution, and thus in *ECSA*. Therefore, the resulting mass activity increased with increasing the electroactive surface area. So, the difference in the *ECSA* of catalysts can explain in part the better performance of PtNi/TBK catalyst with respect to PtNi/BK. In a previous report, we demonstrated that the functionalization of carbon supports via acid treatment caused a reduction in the particle size and induced better dispersion of nanoparticles, which in turn results in increased catalytic activity towards methanol and ethanol oxidation reactions (Comignani et al., 2017). Similar conclusions were reached for several investigations concerning the influence of textural properties and surface chemistry of carbon supports on the electrocatalytic properties of nanosized catalysts (Celorrio et al., 2012; Sebastián et al., 2012; Hsieh et al., 2013; Sebastián et al., 2014). For instance, Cellorrio et al. found that Pd nanoparticles supported on a highly oxidized Vulcan support exhibit better electrocatalytic activity for the oxidation of formic acid than the nanoparticles supported on the pristine carbon powder (Celorrio et al., 2012). Sebastián and collaborators found that the *ECSA* and ORR activity of carbon supported Pt nanoparticles depends on the density of surface oxygen functionalities and ghaphicity (Sebastián et al., 2012). With regards to alloying degree and the chemical state of Ni, it is noted that the different physicochemical surface properties of the biocarbons led to the formation of nanoparticles with different nickel content in the alloy. The causes for the different Ni content in the bimetallic alloy are not clear yet, and this will be the object of future studies. Although, it is hypothesized that the difference in the alloyed and non-alloyed Ni content could be associated with a more effective reduction of nickel ions on TBK than on BK due to its higher amount of surface functionalities and surface defects. Antolini indicated that the high activity of PtNi catalysts for the methanol oxidation is a consequence of the synergic effect between alloyed and non-alloyed nickel atoms, where alloyed Ni facilitates the dehydrogenation of the molecules and non-alloyed Ni makes easier the removal of adsorbed CO (Antolini, 2017). As indicated above, the observed difference in activity can to some extent be explained by a compromise between the number of alloyed and non-alloyed nickel atoms. The alloyed nickel atoms can accomplish a dual role. On the one hand, they can promote the dehydrogenation steps of the EOR and, on the other hand, they can modify the electronic structure of Pt atoms at the Fermi level, which weakens the bonding energy between Pt and CO-like intermediates. Whereas, the non-alloyed nickel atoms works as an $-OH_{ad}$ supplier that accelerates the oxidation of the poisoning intermediates via the bifunctional mechanism. Some authors studied the effect of Ni content on the electrocatalytic activity of PtNi catalysts, and found that the methanol oxidation reaction is favored by the presence of both alloyed and non-alloyed nickel

TABLE 5 | Performance of different electrocatalysts for the EOR process in acid medium.

Catalyst	Support	Electrolyte and fuel	E_{onset}[a], V	j_p[b], A g_{Pt}^{-1}	j[a,c], A g_{Pt}^{-1}	Reference
Pt nanowires	Porous carbon spheres from pectin	0.5 M H_2SO_4, 1 M EtOH	0.5 V	278 (RT[d])	30.0 (0.65 V)	Fan et al., 2015
PtSn/a-BC	Biocarbon from *Eucaliptus grandis* wood	0.5 M H_2SO_4, 1 M EtOH	0.19	71.1 (25 °C)	-	da Silva et al., 2014
$Pt_{2.3}Ni$/C octahedra	Carbon black	0.1 M $HClO_4$, 0.2 M EtOH	0.21	638 (RT)	65.9 (0.40 V)	Sulaiman et al., 2017
$PtSnO_2$/CNT	MWCNTs	1 M $HClO_4$, 1 M EtOH	0.46	554 (RT)	40.0 (0.4 V)	Song et al., 2016
PtSnRu nanorods	GC	0.5 M H_2SO_4, 1 M EtOH	0.45	437.9 (RT)	27.9 (0.4 V)	Huang et al., 2019
PtSnCe/C	Carbon black	0.5 M H_2SO_4, 0.5 M EtOH	0.25	380 (25 °C)	143.2 (0.36 V)	Jacob et al., 2015
Pt-Mo-Ni nanowires	GC	0.5 M H_2SO_4, 2 M EtOH	0.10	865.8 (RT)	109 (0.5 V)	Mao et al., 2017
$Pt_{0.7}Ni_{0.3}$	Biocarbon from acid-treated kraft pulp (TBK)	0.5 M H_2SO_4, 1 M EtOH	0.17	476 (25 °C)	125 (0.5 V)	This work

[a]*The electrode potentials were referred to the SCE scale.*
[b]*Sweep rate of 50 mV* s^{-1}.
[c]*Current density extracted from CA experiments.*
[d]*Room Temperature.*

atoms (Luo et al., 2013; Nassr et al., 2013; Wang et al., 2014). Probably, the higher efficiency of PtNi/TBK can be either explained in terms of the better tolerance to poisoning of alloyed than non-alloyed PtNi nanoparticles (Antolini, 2017) or a better compromise between the structural effects produced by alloyed nickel atoms (*i.e.*, electronic and compressive strain effects) and oxophilicity effect generated by non-alloyed nickel atoms (*i.e.*, bifunctional mechanism).

Finally, the as-prepared PtNi nanoparticles supported on the biocarbons synthesized from the treated fibrous fraction of unbleached softwood kraft-liner paper exhibited very competitive activities for the EOR when compared to recent results published in the literature (**Table 5**). For instance, da Silva et al. prepared activated biocarbon from *Eucalyptus grandis* wood (S_{BET} = 787 $m^2 g^{-1}$, V_T = 0.47 $cm^3 g^{-1}$ and O content = 9.86 at. %) as Pt and PtSn catalyst support for the EOR process and obtained peak current densities of 16.5 and 71.1 A g_{Pt}^{-1}, respectively (da Silva et al., 2014). Fang and coworkers synthesized pectin-derived porous carbon spheres (S_{BET} = 2,440 $m^2 g^{-1}$ and V_T = 1.28 $cm^3 g^{-1}$) as Pt catalyst support (Fan et al., 2015). The as-prepared electrocatalysts developed a peak current density of 278 A g_{Pt}^{-1} and an activity of ca. 30 A g_{Pt}^{-1} at 0.65 V vs. *SCE* for the EOR in acid environment.

Further research will be focused on evaluating the influence of the pretreatment and pyrolysis temperature on the textural and structural properties of the biocarbons obtained from softwood kraft pulp. The as-synthesized biocarbons will be employed as supports of Pt-based nanoparticles with low noble metal content and core-shell structure for ethanol and glycerol electrooxidations.

CONCLUSIONS

The pristine and phosphoric acid-treated fibers of unbleached softwood kraft pulp were used to fabricate biocarbons via fast pyrolysis. The biocarbon derived from the kraft pulp (BK) has a BET surface area of 306 $m^2 g^{-1}$ and a total pore volume 1.2 $cm^3 g^{-1}$, whereas the biocarbon derived from the acid-treated has a specific surface area of 454 $m^2 g^{-1}$ and a total pore volume of 1.8 $cm^3 g^{-1}$. Besides, the biocarbons also show different oxygen and nitrogen contents. The as-synthesized biocarbons were employed as supports of PtNi nanoparticles formed by pulse microwave-assisted reduction in ethylene glycol. PtNi particles with average diameters in the range of 2.9–4.1 nm and a nickel content of ca. 30 at% are obtained. It was determined that ca. 37% of Ni atoms are forming an alloy with Pt in the PtNi/BK catalyst, while ca. 61% of Ni atoms are forming an alloy in the PtNi/TBK catalyst.

The electrocatalytic properties of the as-synthesized electrocatalysts for the EOR in acid medium were tested by means of cyclic voltammetry and chronoamperometry at temperatures of 25 and 60°C. The experiments show that the PtNi/TBK material can catalyze the electrooxidation of ethanol more efficiently than the other catalysts, and its mass activity was improved by factors around 1.5 and 7 with respect to PtNi/BK and Pt/C, respectively. The better performance of the PtNi/TKB electrode was explained through the combination of several factors: 1) the higher density of surface functional groups on the surface of TBK, 2) the small average particle size and narrow particle distribution (i.e., higher ECSA value), and 3) the better compromise between the number of alloyed and non-alloyed nickel atoms.

DATA AVAILABILITY STATEMENT

The original contributions presented in the study are included in the article/**Supplementary Material**, further inquiries can be directed to the corresponding author/s.

AUTHOR CONTRIBUTIONS

MNL conducted the experiments, analyzed data and performed writing. JS conceived the idea, conducted the experiments, analyzed data and performed writing, review and editing. EM conceived the idea and performed writing.

FUNDING

This investigation was supported by ANPCyT, Universidad Nacional del Sur and Universidad Nacional de Córdoba through grants PICT2014 No. 3393, PGI 24/M167 and SECyT 313/16.

ACKNOWLEDGMENTS

MNL thanks CONICET for a postdoctoral fellowship.

SUPPLEMENTARY MATERIAL

The Supplementary Material for this article can be found online at: https://www.frontiersin.org/articles/10.3389/fmats.2020.588399/full#supplementary-material

REFERENCES

Almeida, T. S., Kokoh, K. B., Kokoh, K. B., and De Andrade, A. R. (2011). Effect of Ni on Pt/C and PtSn/C prepared by the Pechini method. *Int. J. Hydrogen Energy.* 36, 3803–3810. doi:10.1016/j.ijhydene.2010.12.066.

Altarawneh, R. M., Brueckner, T. M., Chen, B., and Pickup, P. G. (2018). Product distributions and efficiencies for ethanol oxidation at PtNi octahedra. *J. Power Sources.* 400, 369–376. doi:10.1016/j.jpowsour.2018.08.052.

Antolini, E. (2009). Carbon supports for low-temperature fuel cell catalysts. *Appl. Catal. B Environ.* 88, 1–24. doi:10.1016/j.apcatb.2008.09.030.

Antolini, E. (2017). Pt-Ni and Pt-M-Ni (M = Ru, Sn) anode catalysts for low-temperature acidic direct alcohol fuel cells: a review. *Energies.* 10, 42. doi:10.3390/en10010042.

Antolini, E., Salgado, J. R. C., and González, E. R. (2005). Carbon supported Pt75M25 (M=Co, Ni) alloys as anode and cathode electrocatalysts for direct

methanol fuel cells. *J. Electroanal. Chem.* 580, 145–154. doi:10.1016/j.jelechem.2005.03.023.

Antonucci, P. L., Alderucci, V., Giordano, N., Cocke, D. L., and Kim, H. (1994). On the role of surface functional groups in Pt carbon interaction. *J. Appl. Electrochem.* 24, 58–65. doi:10.1007/bf00243330.

Asgardi, J., Calderón, J. C., Alcaide, F., Querejeta, A., Calvillo, L., Lázaro, M. J., et al. (2015). Carbon monoxide and ethanol oxidation on PtSn supported catalysts: effect of the nature of the carbon support and Pt:Sn composition. *Appl. Catal. B Environ.* 168–169, 33–41. doi:10.1016/j.apcatb.2014.12.003.

Bengtsson, A., Hecht, P., Sommertune, J., Ek, M., Sedin, M., and Sjöholm, E. (2020). Carbon fibers from lignin-cellulose precursors: effect of carbonization conditions. *ACS Sustain. Chem. Eng.* 8, 6826–6833. doi:10.1021/acssuschemeng.0c01734.

Beyhan, S., Léger, J.-M., and Kadırgan, F. (2013). Pronounced synergetic effect of the nano-sized PtSnNi/C catalyst for ethanol oxidation in direct ethanol fuel cell. *Appl. Catal. B Environ.* 130–131, 305- 313. doi:10.1016/j.apcatb.2012.11.007.

Calderón, J. C., Mahata, N., Pereira, M. F. R., Figueiredo, J. L., Fernandes, V. R., Rangel, C. M., et al. (2012). Pt-Ru catalysts supported on carbon xerogels for PEM fuel cells. *Int. J. Hydrogen Energy.* 37, 7200–7211. doi:10.1016/j.ijhydene.2011.12.029.

Celorrio, V., Montes de Oca, M. G., Plana, D., Moliner, R., Fermín, D. J., and Lázaro, M. J. (2012). Electrochemical performance of Pd and Au-Pd core-shell nanoparticles on surface tailored carbon black as catalyst support. *Int. J. Hydrogen Energy.* 37, 7152–7160. doi:10.1016/j.ijhydene.2011.12.014.

Comignani, V., Sieben, J. M., Brigante, M. E., and Duarte, M. M. E. (2015). Carbon supported Pt-NiO nanoparticles for ethanol electro-oxidation in acid media. *J. Power Sources.* 278, 119–127. doi:10.1016/j.jpowsour.2014.12.063.

Comignani, V., Sieben, J. M., Sanchez, M. D., and Duarte, M. M. E. (2017). Influence of carbon support properties on the electrocatalytic activity of PtRuCu nanoparticles for methanol and ethanol oxidation. *Int. J. Hydrogen Energy.* 42, 24785–24796. doi:10.1016/j.ijhydene.2017.08.079.

da Silva, E. L., Ortega Vega, M. R., Correa, P. d. S., Cuña, A., Tancredi, N., and Malfatti, C. d. F. (2014). Influence of activated carbon porous texture on catalyst activity for ethanol electro-oxidation, *Int. J. Hydrogen Energy.* 39, 14760–14767. doi:10.1016/j.ijhydene.2014.07.103.

Dobele, G., Meier, D., Faix, O., Radtke, S., Rossinskaja, G., and Telysheva, G. (2001). Volatile products of catalytic flash pyrolysis of celluloses. *J. Anal. Appl. Pyrol.* 58–59, 453–463. doi:10.1016/S0165-2370(00)00128-5.

El Qada, E. N., Allen, S. J., and Walker, G. M. (2008). Influence of preparation conditions on the characteristics of activated carbons produced in laboratory and pilot scale systems. *Chem. Eng. J.* 142, 1–13. doi:10.1016/j.cej.2007.11.008.

Falco, C., Sieben, J. M., Brun, N., Sevilla, M., van der Mauelen, T., Morallón, E., et al. (2013). Hydrothermal carbons from hemicellulose-derived aqueous hydrolysis products as electrode materials for supercapacitors. *ChemSusChem.* 6, 374–382. doi:10.1002/cssc.201200817.

Fan, Y., Liu, P.-F., Yang, Z.-J., Jiang, T.-W., Yao, K.-L., Han, R., et al. (2015). Bi-functional porous carbon spheres derived from pectin as electrode material for supercapacitors and support material for Pt nanowires towards electrocatalytic methanol and ethanol oxidation. *Electrochim. Acta.* 163, 140–148. doi:10.1016/j.electacta.2015.02.157.

Gasteiger, H. A., Markovic, N., Ross, P. N., and Cairns, E. J. (1993). Methanol electrooxidation on well-characterized platinum-ruthenium bulk alloys. *J. Phys. Chem.* 97, 12020–12029. doi:10.1021/j100148a030.

Gong, X., Liu, S., Ouyang, C., Strasser, P., and Yang, R. (2015). Nitrogen- and phosphorus-doped biocarbon with enhanced electrocatalytic activity for oxygen reduction. *ACS Catal.* 5, 920–927. doi:10.1021/cs501632y.

González-García, P., Centeno, T. A., Urones-Garrote, E., Ávila-Brande, D., and Otero-Díaz, L. C. (2013). Microstructure and surface properties of lignocellulosic-based activated carbons. *Appl. Surf. Sci.* 265, 731–737. doi:10.1016/j.apsusc.2012.11.092.

Goodenough, J. B., Manoharan, R., Shukla, A. K., and Ramesh, K. V. (1989). Intraalloy electron transfer and catalyst performance: a spectroscopic and electrochemical study. *Chem. Mater.* 1, 391–398. doi:10.1021/cm00004a003.

Guo, C.-Z., Liao, W.-L., and Chen, C.-G. (2014). Design of a non-precious metal electrocatalyst for alkaline electrolyte oxygen reduction by using soybean biomass as the nitrogen source of electrocatalytically active center structures. *J. Power Sources.* 269, 841–847. doi:10.1016/j.jpowsour.2014.07.024.

Habibi, B., and Dadashpour, E. (2013). Carbon-ceramic supported bimetallic Pt-Ni nanoparticles as an electrocatalyst for electrooxidation of methanol and ethanol in acidic media. *Int. J. Hydrogen Energy.* 38, 5425–5434. doi:10.1016/j.ijhydene.2012.06.045.

Haq, I., and Raj, A. (2020). "Pulp and paper mill wastewater: ecotoxicological effects and bioremediation approaches for environmental safety," in *Bioremediation of industrial waste for environmental safety: volume II: biological agents and methods for industrial waste management.*. R. N. Bharagava and G. Saxena (Editors) (Singapore: Springer), 333–356.

Hsieh, C.-T., Chen, W.-Y., Tzou, D.-Y., Roy, A. K., and Hsiao, H.-T. (2012). Atomic layer deposition of Pt nanocatalysts on graphene oxide nanosheets for electro-oxidation of formic acid. *Int. J. Hydrogen Energy.* 37, 17837–17843. doi:10.1016/j.ijhydene.2012.08.139.

Hsieh, C.-T., Gu, J.-L., Tzou, D.-Y., Chu, Y.-C., and Chen, Y.-C. (2013). Microwave deposition of Pt catalysts on carbon nanotubes with different oxidation levels for formic acid oxidation. *Int. J. Hydrogen Energy.* 38, 10345–10353. doi:10.1016/j.ijhydene.2013.05.146.

Huang, T.-H., Zheng, H.-S., Cheng, Y.-M., Liu, C.-W., Lee, S.-W., Wang, J.-H., et al. (2019). The preparation and mechanistic study of highly effective PtSnRu ternary nanorod catalysts toward the ethanol oxidation reaction. *Sustain. Energy Fuels.* 3, 3352–3362. doi:10.1039/c9se00474b.

Imanzadeh, H., and Habibi, B. (2020). Electrodeposition of ternary CuNiPt alloy nanoparticles on graphenized pencil lead electrode as a new electrocatalyst for electro-oxidation of ethanol. *Solid State Sci.* 105, 106239. doi:10.1016/j.solidstatesciences.2020.106239.

Jacob, J. M., Corradini, P. G., Antolini, E., Abe Santos, N., Santos, N. A., and Perez, J. (2015). Electro-oxidation of ethanol on ternary Pt-Sn-Ce/C catalysts. *Appl. Catal. B Environ.* 165, 176–184. doi:10.1016/j.apcatb.2014.10.012.

Kacuráková, M., Capek, P., Sasinková, V., Wellner, N., and Ebringerová, A. (2000). FT-IR study of plant cell wall model compounds: pectic polysaccharides and hemicelluloses. *Carbohydr. Polym.* 43, 195–203. doi:10.1016/S0144-8617(00)00151-X.

Kennedy, L. J., Vijaya, J. J., and Sekaran, G. (2004). Effect of two-stage process on the preparation and characterization of porous carbon composite from rice husk by phosphoric acid activation. *Ind. Eng. Chem. Res.* 43, 1832–1838. doi:10.1021/ie034093f.

Klemm, D., Heublein, B., Fink, H., and Bohn, A. (2005). Cellulose: Fascinating biopolymer and sustainable raw material Angewandte. *Polym. Sci.* 44, 3358–3393. doi:10.1002/anie.200460587.

Li, M., Liu, P., and Adzic, R. R. (2012). Platinum monolayer electrocatalysts for anodic oxidation of alcohols. *J. Phys. Chem. Lett.* 3, 3480–3485. doi:10.1021/jz3016155.

Lima, F. H. B., Profeti, D., Lizcano-Valbuena, W. H., Ticianelli, E. A., and Gonzalez, E. R. (2008). Carbon-dispersed Pt-Rh nanoparticles for ethanol electro-oxidation. Effect of the crystallite size and of temperature. *J. Electroanal. Chem.* 617, 121–129. doi:10.1016/j.jelechem.2008.01.024.

Liu, W.-J., Jiang, H., and Yu, H.-Q. (2019). Emerging applications of biochar-based materials for energy storage and conversion. *Energy Environ. Sci.* 12, 1751–1779. doi:10.1039/C9EE00206E.

Luo, B., Xu, S., Yan, X., and Xue, Q. (2013). PtNi alloy nanoparticles supported on polyelectrolyte functionalized graphene as effective electrocatalysts for methanol oxidation. *J. Electrochem. Soc.* 160, F262–F268. doi:10.1149/2.056303jes.

Mao, J., Chen, W., He, D., Wan, J., Pei, J., Dong, J., et al. (2017). Design of ultrathin Pt-Mo-Ni nanowire catalysts for ethanol electrooxidation. *Sci. Adv.* 3, e1603068. doi:10.1126/sciadv.1603068.

Marinho, B., Ghislandi, M., Tkalya, E., Koning, C. E., and de With, G. (2012). Electrical conductivity of compacts of graphene, multi-wall carbon nanotubes, carbon black, and graphite powder. *Powder Technol.* 221, 351–358. doi:10.1016/j.powtec.2012.01.024.

Nørskov, J. K., Bligaard, T., Rossmeisl, J., and Christensen, C. H. (2009). Towards the computational design of solid catalysts. *Nat. Chem.* 1, 37–46. doi:10.1038/nchem.121.

Nassr, A. B. A. A., Sinev, I., Grünert, W., and Bron, M. (2013). PtNi supported on oxygen functionalized carbon nanotubes: in depth structural characterization and activity for methanol electrooxidation. *Appl. Catal. B Environ.* 142–143, 849–860. doi:10.1016/j.apcatb.2013.06.013.

Nieva Lobos, M. L., Campitelli, P., Volpe, M. A., and Moyano, E. L. (2016a). Catalytic and non-catalytic pyrolysis of Kraft pulp waste into anhydrosugars containing bio-oils and non-phytotoxic biochars. *J. Anal. Appl. Pyrol.* 122, 216–223. doi:10.1016/j.jaap.2016.09.021.

Nieva Lobos, M. L., Sieben, J. M., Comignani, V., Duarte, M., Volpe, M. A., and Moyano, E. L. (2016b). Biochar from pyrolysis of cellulose: an alternative catalyst support for the electro-oxidation of methanol. *Int. J. Hydrogen Energy.* 41, 10695–10706. doi:10.1016/j.ijhydene.2016.04.041.

Pistone, A., and Espro, C. (2020). Current trends on turning biomass wastes into carbon materials for electrochemical sensing and rechargeable battery applications. *Curr. Opin. Green Sustain. Chem.* 26, 100374. doi:10.1016/j.cogsc.2020.100374.

Reckamp, J. M., Garrido, R. A., and Satrio, J. A. (2014). Selective pyrolysis of paper mill sludge by using pretreatment processes to enhance the quality of bio-oil and biochar products. *Biomass Bioenergy.*. 71, 235–244. doi:10.1016/j.biombioe.2014.10.003.

Schonvogel, D., Nowotny, M., Woriescheck, T., Multhaupt, H., Wagner, P., Dyck, A., et al. (2019). Hydrothermal carbonization-derived carbon from waste biomass as renewable Pt support for fuel cell applications: role of carbon activation. *Energy Technol.* 7, 1900344. doi:10.1002/ente.201900344.

Sebastián, D., Lázaro, M. J., Moliner, R., Suelves, I., Aricò, A. S., and Baglio, V. (2014). Oxidized carbon nanofibers supporting PtRu nanoparticles for direct methanol fuel cells. *Int. J. Hydrogen Energy.* 39, 5414–5423. doi:10.1016/j.ijhydene.2013.12.005.

Sebastián, D., Ruíz, A. G., Suelves, I., Moliner, R., Lázaro, M. J., Baglio, V., et al. (2012). Enhanced oxygen reduction activity and durability of Pt catalysts supported on carbon nanofibers. *Appl. Catal. B Environ.* 115–116, 269–275. doi:10.1016/j.apcatb.2011.12.041.

Sebastián, D., Suelves, I., Pastor, E., Moliner, R., and Lázaro, M. J. (2013). The effect of carbon nanofiber properties as support for PtRu nanoparticles on the electrooxidation of alcohols. *Appl. Catal. B Environ.* 132–133, 13–21. doi:10.1016/j.apcatb.2012.11.018.

Shen, Y., Xiao, K., Xi, J., and Qiu, X. (2015). Comparison study of few-layered graphene supported platinum and platinum alloys for methanol and ethanol electro-oxidation. *J. Power Sources.* 278, 235–244. doi:10.1016/j.jpowsour.2014.12.062.

Song, H., Luo, M., Qiu, X., and Cao, G. (2016). Insights into the endurance promotion of PtSn/CNT catalysts by thermal annealing for ethanol electro-oxidation. *Electrochim. Acta.* 213, 578–586. doi:10.1016/j.electacta.2016.07.053.

Suleiman, J. E., Zhu, S., Xing, Z., Chang, Q., and Shao, M. (2017). Pt-Ni octahedra as electrocatalysts for ethanol electro-oxidation reaction. *ACS Catal.* 7, 5134–5141. doi:10.1021/acscatal.7b01435

Sun, F., Wang, L., Peng, Y., Gao, J., Pi, X., Qu, Z., et al. (2018). Converting biomass waste into microporous carbon with simultaneously high surface area and carbon purity as advanced electrochemical energy storage materials. *Appl. Surf. Sci.* 436, 486–494. doi:10.1016/j.apsusc.2017.12.067.

Sun, S., Halseid, M. C., Heinen, M., Jusys, Z., and Behm, R. J. (2009). Ethanol electrooxidation on a carbon-supported Pt catalyst at elevated temperature and pressure: a high-temperature/high-pressure DEMS study. *J. Power Sources.* 190, 2–13. doi:10.1016/j.jpowsour.2009.01.073.

Tzong-Horng, L. (2010). Development of mesoporous structure and high adsorption capacity of biomass-based activated carbon by phosphoric acid and zinc chloride activation. *Chem. Eng. J.* 158, 129–142. doi:10.1016/j.cej.2007.11.008

Van Soest, P. J., Robertson, J. B., and Lewis, B. A. (1991). Methods for dietary fiber, neutral detergent fiber, and nonstarch polysaccharides in relation to animal nutrition. *J. Dairy Sci.* 74, 3583–3597. doi:10.3168/jds.S0022-0302(91)78551-2.

Wang, H., Jusys, Z., and Behm, R. J. (2006). Ethanol electro-oxidation on carbon-supported Pt, PtRu and Pt3Sn catalysts: a quantitative DEMS study. *J. Power Sources.* 154, 351–359. doi:10.1016/j.jpowsour.2005.10.034.

Wang, L.-L., Zhang, D.-F., and Guo, L. (2014). Phase-segregated Pt-Ni chain-like nanohybrids with high electrocatalytic activity towards methanol oxidation reaction. *Nanoscale.* 6, 4635–4641. doi:10.1039/c4nr00139g.

Watanabe, M., and Motoo, S. (1975). Electrocatalysis by ad-atoms. *J. Electroanal. Chem. Interfacial Electrochem.* 60, 267–273. doi:10.1016/s0022-0728(75)80261-0.

Zhang, H., Zeng, Y., Cao, L., Yang, L., Fang, D., Yi, B., et al. (2017). Enhanced electrocatalytic performance of ultrathin PtNi alloy nanowires for oxygen reduction reaction. *Front. Energy.* 11, 260–267. doi:10.1007/s11708-017-0499-x.

Zhang, J., Zhang, J., Lin, L., Chen, T., Zhang, J., Liu, S., et al. (2009). Dissolution of microcrystalline cellulose in phosphoric acid-molecular changes and kinetics. *Molecules.* 14, 5027–5041. doi:10.3390/molecules14125027.

Zhang, Y., Zhu, R., Cui, Y., Zhong, J., Zhang, X., and Chen, J. (2014). PtRu nanoparticles supported on nitrogen-doped polyhedral mesoporous carbons as electrocatalyst for methanol oxidation. *Nanotechnology.* 25, 135607. doi:10.1088/0957-4484/25/13/135607.

Zhao, H., Kwak, J., Conradzhang, Z., Brown, H., Arey, B., and Holladay, J. 2007). Studying cellulose fiber structure by SEM, XRD, NMR and acid hydrolysis. *Carbohydr. Polym.* 68, 235–241. doi:10.1016/j.carbpol.2006.12.013.

Zhao, X., Zhu, J., Liang, L., Li, C., Liu, C., Liao, J., et al. (2014). Biomass-derived N-doped carbon and its application in electrocatalysis. *Appl. Catal. B Environ.* 154–155, 177–182. doi:10.1016/j.apcatb.2014.02.027.

Zhou, X.-W., Zhang, R.-H., Zhou, Z.-Y., and Sun, S.-G. (2011). Preparation of PtNi hollow nanospheres for the electrocatalytic oxidation of methanol. *J. Power Sources.* 196, 5844–5848. doi:10.1016/j.jpowsour.2011.02.088.

Zhou, Y., Neyerlin, K., Olson, T. S., Pylypenko, S., Bult, J., Dinh, H. N., et al. (2010). Enhancement of Pt and Pt-alloy fuel cell catalyst activity and durability via nitrogen-modified carbon supports. *Energy Environ. Sci.* 3, 1437–1446. doi:10.1039/C003710A.

Conflict of Interest: The authors declare that the research was conducted in the absence of any commercial or financial relationships that could be construed as a potential conflict of interest.

frontiers in Materials

MINI REVIEW
published: 14 January 2021
doi: 10.3389/fmats.2020.612134

Recent Advances in Non-nucleophilic Mg Electrolytes

Qijie Wu[1], *Kewei Shu*[2]*, *Lili Sun*[2] *and Haihua Wang*[2]*

[1]Intelligent Polymer Research Institute, University of Wollongong, North Wollongong, NSW, Australia, [2]Shaanxi Key Laboratory of Chemical Additives for Industry, Shaanxi University of Science and Technology, Xi'an, China

High-performance electrolyte is still a roadblock for the development of rechargeable magnesium (Mg) batteries. Grignard-type electrolytes were once the only choice in the early stage of rechargeable Mg batteries research. However, due to their nucleophilic nature and high reactivity, Grignard-type electrolytes have inherent safety issues and low oxidation stability, which restrict the development of rechargeable Mg batteries in terms of practical application. Recently, emerging novel Mg battery systems such as Mg-S, Mg-O_2/air batteries also require non-nucleophilic electrolytes with high oxidation stability. This short review summarizes recent advances in non-nucleophilic Mg electrolytes and aims to provide insights into electrochemical properties and active Mg ion structure of such electrolytes.

Keywords: Mg electrolyte, rechargeable Mg battery, non-nucleophilic, coordination Mg complex, energy storage

OPEN ACCESS

Edited by:
Anastasiia O. Krushynska, University of Groningen, Netherlands

Reviewed by:
Guosheng Li, Pacific Northwest National Laboratory (DOE), United States
Xing-Long Wu, Northeast Normal University, China

***Correspondence:**
Kewei Shu
shukw@sust.edu.cn
Haihua Wang
whh@sust.edu.cn

Specialty section:
This article was submitted to Energy Materials, a section of the journal Frontiers in Materials

Received: *30 September 2020*
Accepted: *17 November 2020*
Published: *14 January 2021*

Citation:
Wu Q, Shu K, Sun L and Wang H (2021) Recent Advances in Non-nucleophilic Mg Electrolytes. Front. Mater. 7:612134. doi: 10.3389/fmats.2020.612134

INTRODUCTION

After years of extensive research and evolution, rechargeable lithium-ion batteries (LIBs) have become the dominant secondary energy storage system. However, it is still a big challenge to meet the increasing demands for portable electronics and electric vehicles because of limited lithium resources. Rechargeable magnesium (Mg) batteries have been regarded as a promising candidate for novel LIBs technologies, owing to several considerable advantages (Liu et al., 2020) (Kim et al., 2020). Mg anode possesses a theoretical volumetric capacity of 3,833 mAh cm^{-2} that is five times higher than graphite anode–based LIB (Zhang et al., 2018). Mg has a much higher abundance than Li, ranking 8th among the most 40 abundant elements in the Earth's crust. The nondendritic feature of Mg enables easy manufacturing of Mg metal batteries compared to Li-based battery systems. Additional clear advantages over Li-based batteries include lower cost and better safety. However, the superiority of rechargeable Mg battery has not been fully illustrated due to several inherent problems. Specifically, the actual energy density is still much lower than expected because of low discharge voltage and capacity; also, the cycle performance of the battery is extremely poor. An important reason for unsatisfying working voltage and poor cyclability of Mg-based battery is the passivation effect on Mg anode in electrolytes. Surface passivation film consists of ionic Mg compounds is formed during stripping/plating, even in nonaqueous electrolytes (Lu et al., 1999; Gofer et al., 2003). Unlike the situation in Li or Na battery, such passivation film hinders Mg^{2+} migration, thus resulting in high overpotential and irreversible stripping/plating (Aurbach, 1999; Attias et al., 2019).

In the early stage of rechargeable Mg batteries research, the electrolytes that allow high efficient stripping/plating were only limited to Grignard reagents and their analogs (Muldoon et al., 2012). Gregory et al. first developed Mg electrolyte with reversible deposition properties, which is based on a Grignard reagent activated by $AlCl_3$ (Gregory et al., 1990). Since then, many researchers have focused on Mg organohaloaluminate salts generated by the complexation of Grignard reagents RMgX with $AlCl_3$ in the ether solutions (Aurbach et al., 2002, 2003). The development of a novel rechargeable

Mg-S, Mg-O_2/air battery system promotes the demand for non-nucleophilic Mg electrolytes. Sulfur and oxygen are prone to be attacked by nucleophiles, making conventional nucleophilic electrolyte incompatible for Mg-S, Mg-O_2/air batteries. Even for Mg-ion battery based on intercalation chemistry, nucleophilic electrolyte has its shortcomings. Due to the use of organomagnesium precursors, most of the nucleophilic Mg electrolytes have limited oxidative stability, which restricts the use of high-voltage cathode materials. The highly sensitive and corrosive feature of Grignard-based electrolytes creates difficulties in manufacturing.

The development of Grignard reagent free, non-nucleophilic Mg electrolyte can not only meet the requirements of rechargeable Mg-S and Mg-O_2/air battery but also stepwise fulfill the requirements of practical rechargeable Mg ion battery manufacturing. In this minireview, we briefly summarized the development and recent advances of non-nucleophilic electrolytes (**Table 1**). Their electrochemical performance and ionic coordination structure were discussed to provide new insights for the future development of high-performance Mg-based electrolytes.

ELECTROCHEMICAL PERFORMANCE OF NON-NUCLEOPHILIC MG ELECTROLYTES

Hexamethyldisilazide-Based Electrolytes

The first efficient non-nucleophilic Mg electrolyte was prepared by adding Lewis acid $AlCl_3$ to hexamethyldisilazide magnesium chloride (HMDSMgCl) in THF, demonstrating Coulombic efficiency (CE) of >95% with an increased Mg deposition current density by almost a factor of seven compared to HMDSMgCl-only electrolyte (Kim et al., 2011). Mg-S coin cell using HMDSMgCl-$AlCl_3$ electrolyte displayed discharge capacity of 1,200 mAh g^{-1} initially; however, it decreased to 394 mAh g^{-1} in the following cycle. Later on, stable, commercially available $(HMDS)_2Mg$ was used to replace HMDSMgCl, which exhibited very high oxidative stability (3.5 V vs. Mg) and reversible Mg deposition up to 40 cycles with an overpotential of <150 mV (Zhao-Karger et al., 2013). To overcome the drawback of byproduct $HMDSAlCl_2$ formation in $(HMDS)_2Mg$-$AlCl_3$ electrolyte, $MgCl_2$ was introduced to convert $HMDSAlCl_2$ into active species (Zhao-Karger et al., 2015). Such novel electrolyte displayed a discharge potential of ~1.65 V in Mg-S battery, which was close to the theoretical thermodynamic value. Liao et al. further developed the strategy by preparing [$(HMDS)MgCl_2$-Mg_2Cl_3] via reverse Schlenk equilibrium from the reaction between $(HMDS)_2Mg$ and $MgCl_2$. The substitution of $MgCl_2$ for Lewis acid $AlCl_3$ successfully avoided the possible Al deposition commonly observed in $AlCl_3$-containing electrolytes. It displayed comparable performance to HMDSMgCl-$AlCl_3$ in terms of ionic conductivity (0.5 mS cm^{-1}), oxidative stability (2.8 V vs. Mg), and Mg stripping/plating CE (99%) (Liao et al., 2015).

MACC Electrolytes

Using non-nucleophilic and cheap Mg^{2+} sources of $MgCl_2$, all-inorganic $MgCl_2$-$AlCl_3$ complex (MACC) electrolytes are of particular interest due to their simplicity and low cost. Early research on MACC electrolyte was prepared in 2005; however, it showed poor electrochemical properties with 0.9 V deposition overpotential and 37% cycling efficiency (Viestfrid et al., 2005). Several years later, R. Doe et al. demonstrated a series of MACC electrolytes in dimethoxyethane (DME) with reversible Mg deposition capability by simply increasing the $MgCl_2$ concentration (Doe et al., 2014). One of the best among them can reach CE of at least 99%, overpotential of <200 mV, and anodic stability up to 3.1 V during 50 cycles. The MACC complex is formed based on acid-based reaction, generating solvated $Mg_2Cl_3^+$ active cations, which is similar to that of the transmetalation process in Grignard-type complexes (Vestfried et al., 2007). Gewirth et al. (Barile et al., 2014) and Li et al. (Cheng et al., 2015) found that the overpotential of MACC electrolytes can be lowered by repeated CV scans or charge-discharge cycles, called the electrochemical conditioning process. Other inorganic chlorides, such as $InCl_3$, $SnCl_2$, $SbCl_3$, and $BiCl_3$, based binary chloride complex, were also investigated, which presented moderate Mg cycling performance (Barile et al., 2015). According to the retrosynthetic analysis of the Mg^{2+}/Cl^-/THF coordination cation formation process, Liu et al. developed a simple "mono-Cl abstraction" strategy to produce highly active MACC-derived electrolytes, which used $MgCl_2$ and Al-based Lewis acid ($AlCl_3$, $AlPh_3$, and $AlEtCl_2$) in THF solvent (Liu et al., 2014). The resulting electrolyte showed CE up to 100%, oxidation stability of 3.4 V, and improved electrophilic stability. A rechargeable Mg battery using Mo_6S_8 cathode and 0.3 M $MgCl_2$-$AlEtCl_2$ electrolyte delivered first discharge capacity of 104 mAh g^{-1} and can remain at 95.1% of the initial value after 100 cycles. By adding 0.03 M magnesium bis(trifluoromethane sulfonyl)imide [$Mg(TFSI)_2$] to the MACC electrolyte, the electrochemical performance and water-tolerant property can be significantly improved (He et al., 2019). The CE of $Mg(TFSI)_2$-MACC electrolyte was increased to 97%, with Mg deposition potential of ~350 mV even without the conditioning process. A fascinating feature of the electrolyte is its moisture and impurity durability. A Mo_6S_8-Mg battery with such electrolyte can deliver a capacity of 92 mAh g^{-1} at 0.2 C after 100 cycles.

$Mg(TFSI)_2$ and $Mg(CF_3SO_3)_2$ Based Electrolytes

$Mg(TFSI)_2$ possesses high solubility in various solvents, good ionic conductivity, and high oxidative stability. However, electrolytes using single $Mg(TFSI)_2$ displayed large overpotential (>2.0 V) and low CE (<50%) even at high temperatures (Ha et al., 2014). $Mg(TFSI)_2$ electrolytes were very sensitive to the impurity species, thus strongly affecting their Mg stripping/plating properties (Connell et al., 2016). Cl^- can protect Mg surface from passivation by a trace amount of moisture via complex and dynamic interaction between Cl^- and H_2O (Connell et al., 2016). Therefore, the introduction of $MgCl_2$ into $Mg(TFSI)_2$ electrolytes was an effective strategy to achieve reversible stripping/plating and reduced overpotential. Li et al. first reported $Mg(TFSI)_2$-$MgCl_2$ combination in DME and presented improved performance of 80% CE, 400 mV

overpotential, and 3.5 V anodic stability limit (Cheng et al., 2015). In addition to the consumption of water impurities, $MgCl_2$ can also help to form $[Mg_xCl_y]^{n+}$ electroactive species. Sa et al. confirmed that the active cation in $Mg(TFSI)_2$-$MgCl_2$/THF was dominated by the Cl^- component in electrolyte (Sa et al., 2016). When the $Cl^-/TFSI^-$ ratio increased from 1:5 to 1:2, CE was greatly improved from 12% to 93%; meanwhile, the average capacity in a Mo_6S_8-Mg rechargeable battery increased by 15%. Of note, the performance of $Mg(TFSI)_2$ based electrolytes is highly dependent on the purity of the Mg salt and can be improved by introducing scavenging reagent other than $MgCl_2$ (Shterenberg et al., 2015). By adding a trace amount of $Mg(BH_4)_2$ as moisture scavenger, reversible Mg stripping/plating cycling can be achieved in an $Mg(TFSI)_2$/tetraglyme (G4) electrolyte at onset potentials around -0.35 V (plating) and 0 V (stripping), with CE up to 84% over the initial cycles and ~75% for 500 cycles overall (Ma et al., 2017). Dimethylamine (DMA) was introduced as cosolvent to prepare a Cl-free, noncorrosive $Mg(TFSI)_2$ based electrolyte, exhibited promising Mg stripping/plating. It showed polarization of 210 mV over 1,500 min in symmetric Mg cell cycling, which was equivalent to the performance in APC electrolyte. When using DMA-THF-G4 as mixed solvent, the CE was increased to 75% compared to 38% from an $Mg(TFSI)_2$-G4 electrolyte (Fan et al., 2020).

Although $MgCl_2$ containing $Mg(TFSI)_2$ electrolytes have already been extensively studied and demonstrated good stripping/plating properties, $Mg(TFSI)_2$ for electrolyte still requires relatively high purity and low moisture level, which caused increased cost (Gao et al., 2017). As a relative "simple" Mg salt, low-cost trifluoromethanesulfonate [$Mg(CF_3SO_3)_2$, $Mg(OTf)_2$] is commercially available with high purity and ultralow moisture, thus providing an alternative choice other than $Mg(TFSI)_2$. A high-performance electrolyte was prepared by $Mg(OTf)_2$-$AlCl_3$-$MgCl_2$ dissolved in THF and G4 mixed solvents with anthracene as a stabilizing agent, which exhibited low overpotential of 200 mV and high CE up to 98.5% without any conditioning process (Yang et al., 2019). Mg-S battery based on such electrolyte presented the highest capacity of 1,193.8 mAh g^{-1} and maintained a capacity of 420 mAh g^{-1} without fluctuations for 50 cycles. Later on, an improved $Mg(OTf)_2$ based electrolyte was reported, by simply dissolving $Mg(OTf)_2$, $MgCl_2$, and $AlCl_3$ in DME (Huang et al., 2020). It showed high efficiency of 99.1% and good anodic stability up to 3.5 V, and also demonstrated excellent performance in Mg-S battery, with a high capacity of 866 mAh g^{-1} at 200 mA g^{-1} and power density of 550 W kg^{-1}.

Other $MgCl_2$-Containing Electrolytes

High-performance Mg electrolytes can be achieved using simple $MgCl_2$ salt only, with the help of proper sulfone as cosolvent. $MgCl_2$-sulfone-THF electrolyte enabled highly reversible Mg stripping/plating, without the introduction of $AlCl_3$, $Mg(TFSI)_2$, or $Mg(CF_3SO_3)_2$. Dipropyl sulfone (DPSO) with a melting point of 29–33°C was selected, combined with THF cosolvent and solute, successfully lowered the melting point of the resulting electrolyte below 10°C. $MgCl_2$/DPSO-THF electrolyte also presented a typical conditioning behavior during consecutive 200 CV cycles and then underwent significant performance improvement with CE value raising from 76.2% to 92.3% (Kang et al., 2017). In the galvanostatic charge-discharge test, the CE value rapidly increased from 68.5% initially to >90% in the following 150 cycles. A Mo_6S_8-Mg cell using the above-mentioned electrolyte displayed excellent cycle performance up to the 300th cycle with a constant specific capacity of 70–75 mAh g^{-1} and high CE value (98–99%).

Boron-Centered Mg Electrolytes

Chloride-based non-nucleophilic electrolytes are still corrosive to all cell parts to some extent. Boron- (B-) based anions are compatible with Mg anode and cell components; thus, they could be promising candidates for non-nucleophilic electrolytes (Zhang et al., 2017). The first B-based chloride-free electrolyte developed by Mohtadi et al. was $Mg(BH_4)_2$ in THF or DME (Mohtadi et al., 2012). The $Mg(BH_4)_2$/DME showed better electrochemical performance with stripping/plating onset potential at 0.03 V/0.34 V and CE of 67%. Rechargeable Mg battery using $Mg(BH_4)_2$/DME and Mo_6S_8 cathode delivered reversible cycling for 40 times at 128 mA g^{-1}. However, the reductivity of $Mg(BH_4)_2$ resulted in narrow electrochemical windows (1.7 V vs. Mg). A method for widening the electrochemical window of Mg electrolyte is to use weakly coordinating anions because the weakened coordination of anions to Mg^{2+} can mitigate the key step in the Mg^+-mediated reductive decomposition (Lau et al., 2019). Hydroborates with B clusters with weak coordination ability, such as $B_{12}H_{12}^{2-}$, were predicted to possess improved anodic stability of 3.2 V compared to BH_4^{2-}, thus suitable for potential B-based electrolyte anion (Carter et al., 2014). Unfortunately, the weakly coordinating property of $B_{12}H_{12}^{2-}$ renders $MgB_{12}H_{12}$ insoluble in low-polarity, commonly used ether solvents for Mg batteries. Modified clusters of hydroborates $CB_{11}H_{12}^{2-}$-based halogen-free, simple type electrolyte were prepared and exhibited high oxidative stability and improved solubility (Tutusaus et al., 2015). Due to charge reduction, $CB_{11}H_{12}^{2-}$ is more lipophilic than $B_{12}H_{12}^{2}$, thus more soluble in low-polarity ethers such as triglyme (G3) and G4 (Keyzer et al., 2016). Magnesium monocarborane (MMC) salt/G4 electrolytes have a high CE of >94.4% and anodic stability up to 3.8 V (Tutusaus et al., 2015). A series of Mg salts containing weakly coordinating fluorinated alkoxyborate anions was prepared, which exhibited good solubility in aprotic solvents due to the high electronegativity of fluorine atoms. Among them, the $Mg[B(hfip)_4]_2$/DME electrolyte presented a high CE of >98% of Mg stripping/plating for over 100 cycles (Zhao-Karger et al., 2017). The anodic current density was as high as 45 mA cm^{-2} and oxidative voltage stability was 4.3 V. J. Luo et al. reported that magnesium fluorinated pinacolatoborate, $Mg[B(O_2C_2(CF_3)_4)_2]_2$ (Mg-FPB) based electrolyte, is noncorrosive, highly electrochemically active, and more chemically stable (Luo et al., 2019). The electrolyte delivered excellent electrochemical performance, with CE >95%, overpotential of <197 mV, and anodic stability up to 4.0 V. Mg|Mg-FPB|Mg symmetric cell can cycle at 0.1 mA cm^{-2} for more than 500 h, with stable polarization.

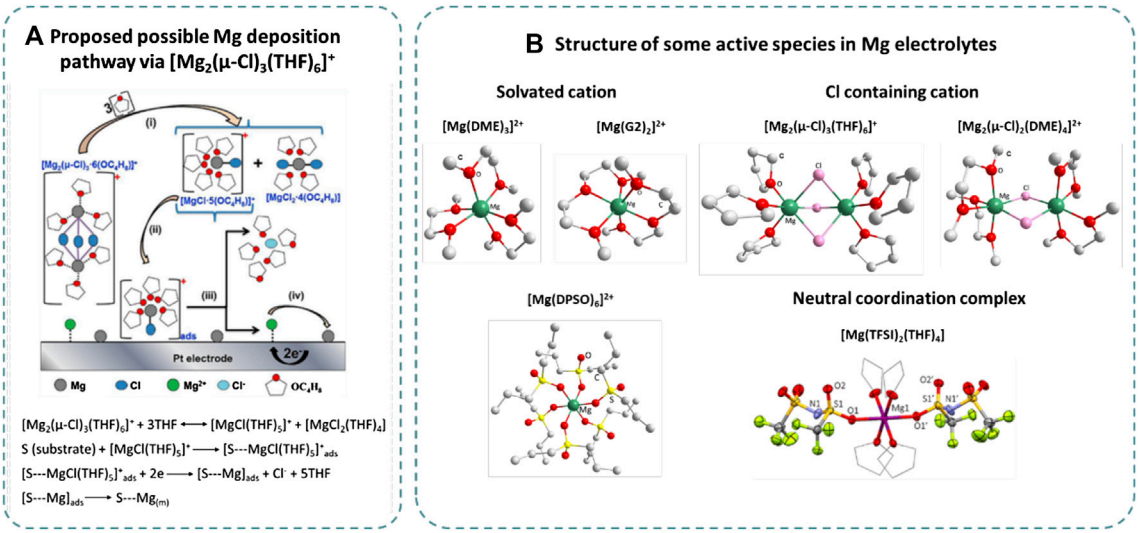

FIGURE 1 | (A) Proposed Mg deposition mechanism via $[Mg_2(\mu\text{-}Cl)_3(THF)_6]^+$ (Benmayza et al., 2013) and **(B)** structure of active species in non-nucleophilic Mg electrolyte (Cheng et al., 2015) (Liu et al., 2014) (Fan et al., 2020) (Kang et al., 2017) (Tutusaus et al., 2015), reproduced with permission.

ACTIVE MG CATIONS FOR REVERSIBLE DEPOSITION

It is still a big challenge to use simple Mg salts to obtain a high-performance Mg electrolyte. Ultrahigh purity is required because even residual moisture can cause the formation of a passivation layer that will inhibit reversible Mg stripping/plating. Of note, Cl-based electrolytes and most of the B-centered electrolytes exhibited good electrochemical performance without rigorous purification. It is believed that Mg-coordinated ions play a vital role in determining the performance of electrolytes (Shao et al., 2013).

An early study on the mechanism of Grignard-type electrolytes suggested that the active cation was $[MgCl(THF)_5]^+$ based on an electrochemical quartz crystal microbalance (EQCM) study (Aurbach et al., 2001). In the first reported HMDSCl-based non-nucleophilic electrolyte, $[Mg_2(\mu\text{-}Cl)_3(THF)_6][HMDSAlCl_3]$ crystal was isolated and determined by single-crystal X-ray diffraction. It is reasonable to presume that $[Mg_2(\mu\text{-}Cl)_3(THF)_6]^+$ was the active species because a similar cation has already been identified in previously reported Grignard-type electrolytes (Aurbach et al., 2003). The cation has two Mg octahedral coordination centers, three bridging Cl atoms (μ-Cl), and six coordination O atoms from THF. Since then, $[Mg_2(\mu\text{-}Cl)_3(THF)_6]^+$ became the most commonly accepted active cation in the Cl-THF electrolyte system (Liao et al., 2015)(Barile et al., 2014). See et al. (2016) compared the ion structure in as-prepared and conditioned MACC electrolyte to identify the active species (See et al., 2016). Surface-enhanced Raman spectroscopy (SERS), 27Al and 35Cl NMR, and X-ray pair distribution function (PDF) were applied, indicating that the active specie in MACC electrolyte both before and after conditioning was $[Mg_2(\mu\text{-}Cl)_3(THF)_6]^+$ (Esbenshade et al., 2015). $[Mg_2(\mu\text{-}Cl)_3(THF)_6]^+$ also existed in $Mg(TFSI)_2$-$MgCl_2$ electrolyte as confirmed by single-crystal XRD (Sa et al., 2016) and is predicted to be present in $Mg(CF_3SO_3)_2$-$MgCl_2$ electrolyte (Yang et al., 2019). One possible Mg deposition pathway via $[Mg_2(\mu\text{-}Cl)_3(THF)_6]^+$, as proposed based on electrochemical and *in situ* X-ray absorption spectroscopy measurement, was shown in **Figure 1A** (Benmayza et al., 2013). Solvent molecule plays a vital role in forming the active Mg coordination ions. A $[Mg_2(\mu\text{-}Cl)_2(DME)_4]^{2+}$ complex cation was present in MACC/DME and $Mg(TFSI)_2$-$MgCl_2$/DME, confirmed by single-crystal XRD (Cheng et al., 2015). The cation complex consists of two octahedrally coordinated Mg centers, each of which is bridged by two chlorine atoms and coordinated by four oxygen atoms from DME. The formation of solvated $Mg_2Cl_3^+$ is not thermodynamically favored in DME because of the difficulties in obtaining coordination number of six (Mizrahi et al., 2008). ESI-MS revealed that the coordination ion structure changed during the conditioning process in a $Mg(CF_3SO_3)_2$-$MgCl_2$-$AlCl_3$ electrolyte. Most of the $[Mg_2(\mu\text{-}Cl)_2(DME)_4]^{2+}$ cations were converted to $[Mg_3(\mu_3\text{-}Cl)(\mu_2\text{-}Cl)_2(DME)_7]^{3+}$ due to increase of Mg/Al ratio caused by Mg/Al codeposition (Huang et al., 2020).

Chloride-free B-centered electrolytes have very different electroactive cation structures, which are mainly solvated Mg cation paired with B-based anion. In the first reported $Mg(BH_4)_2$-DME electrolyte, it was proposed that $Mg(BH_4)_2$ was present in the form of $Mg[(\mu\text{-}H)_2BH_2]_2$, which could partially convert into $[Mg(\mu\text{-}H)_2BH_2]^+$ and BH_4^- (Mohtadi et al., 2012). Then, further dissociation occurs to generate Mg^{2+} and BH_4^-. The electrochemical performance of $Mg(BH_4)_2$ electrolyte can be further enhanced by the addition of $LiBH_4$, owing to weakened association within the ion pair as evidenced by IR spectrum. The CE was improved with increasing molar ratio of $LiBH_4/Mg(BH_4)_2$. The ion species in $Mg(CB_{11}H_{12})_2$ electrolytes were more complicated. $[Mg(THF)_6](CB_{11}H_{12})_2$, $[Mg(DME)_3](CB_{11}H_{12})_2$, and $[Mg(diglyme)_2]$ $(CB_{11}H_{12})_2$ can be

TABLE 1 | Performance of some non-nucleophilic Mg electrolytes.

Electrolytes	Concentration (M)/solvents	Conductivity (mS cm^{-1})	CE (%)	Mg plating potential (mV)/scan rate (mV S^{-1})	Anodic stability (V vs. Mg)	Battery type/capacity (mAh g^{-1})/ current density (mA g^{-1})	Ref.
HMDSMgCl-$AlCl_3$	0.4/THF	--	95	–250/20	2.5	--	Kim et al., (2011)
$(HMDS)_2Mg$-$AlCl_3$	0.25-0.75/THF	1.72	98	–400/25	3.3	Mo_6S_8-Mg/95/10	Zhao-Karger et al., (2013)
$(HMDS)_2Mg$-$AlCl_3$-$MgCl_2$	1.8-3.6-1.8/G2	--	--	–350/25	3.2	Mg-S/550/20	Zhao-Karger et al., (2015)
$(HMDS)_2Mg$-$MgCl_2$	1.25-5/THF	0.5	99	–240/20	2.8	Mo_6S_8-Mg/86/12.8	Liao et al., (2015)
$MgCl_2$-$AlCl_3$	0.25-0.125/DME	2	99	–200/25	3.1	Mo_6S_8-Mg/80/64	Doe et al., (2014)
$MgCl_2$-$AlCl_3$	0.04-0.02/THF	0.26	90	–290/25	3.4	Mo_6S_8-Mg/99/12.8	Barile et al., (2014)
$MgCl_2$-$AlEtCl_2$	0.4/DME	3.9	95	–220/20	3.5	Mo_6S_8-Mg/100/12.8	Liu et al., (2014)
$Mg(TFSI)_2$-$AlCl_3$-$MgCl_2$	0.03-0.03-0.06/THF	--	97	–350	2.6	Mo_6S_8-Mg/92/25.6	He et al., (2019)
$Mg(TFSI)_2$-$MgCl_2$	0.4/DME	--	80	–400/20	3.5	--	Cheng et al., (2015)
$Mg(TFSI)_2$-$MgCl_2$	0.5-0.25/THF	--	72	–500/20	3.2	Mo_6S_8-Mg/67/6.4	Sa et al., (2016)
$Mg(TFSI)_2$, 6 mM $Mg(BH_4)_2$	0.5/G4	--	75	–350/25	--	--	Ma et al., (2017)
$Mg(TFSI)_2$	0.5/DMA-THF-G4	--	75	–500/50	3.0	--	Fan et al., (2020)
$Mg(OTf)_2$-$AlCl_3$-$MgCl_2$	0.125-0.25-0.25/ THF-G4	1.88	95.5	–250/50	3.25	Mg-S/420/84	Yang et al., (2019)
$Mg(OTf)_2$-$AlCl_3$-$MgCl_2$	0.2-0.4-0.4/DME	--	99	–250/50	3.5	Mg-S/844/200	Huang et al., (2020)
$MgCl_2$	0.8/DPSO-THF	1.1	92.3	–430/20	3.0	Mo_6S_8-Mg/75/ 0.016 mA cm^{-2}	Kang et al., (2017)
$Mg(BH_4)_2$	0.5/THF	--	40	–200/20	2.2	Mo_6S_8-Mg/55/128	Mohtadi et al., (2012)
$Mg(CB_{11}H_{12})_2$	0.75/G4	1.8	94.4	–250/5	3.8	MnO_2-Mg/195/ 0.2 mA cm^{-2}	Tutusaus et al., (2015)
$Mg[B(hfip)_4]_2$	0.6/DME	6.8	98	–250/25	4.3	Mg-S/500/167	Zhao-Karger et al., (2017)
Mg-FPB	0.5/G2	3.95	95	300/50	4.0	MnO_2-Mg/150/ 0.01mA cm^{-2}	Luo et al., (2019)

collected as precipitates and were unfortunately unable to be redissolved (Tutusaus et al., 2015). The above solids could only be redissolved in larger glymes such as G3 and G4. The successful isolation of $[Mg(G4)_2(H_2O)](CB_{11}H_{12})_2$ characterized by single-crystal XRD indicates that $[Mg(Gx)_2]^{2+}$ (x = 3, 4) is highly possible to be the active Mg ion. Similarly, $[Mg(DME)_3]^{2+}$ paired by counterion $[B(hfip)_4]^{2-}$ was isolated and verified in $Mg[B(hfip)_4]$/DME electrolyte (Zhao-Karger et al., 2017). It can be redissolved in DME to allow highly efficient Mg stripping/plating. $[Mg(G2)_2]^{2+}$ was determined by single-crystal XRD in a noncorrosive magnesium fluorinated pinacolatoborate $Mg[B(O_2C_2(CF_3)_4)_2]_2$-G2 electrolyte (Luo et al., 2019).

Employing cosolvents can tune the Mg coordination ion formation, thus affecting the electrolyte properties. In a $MgCl_2$/DPSO-THF electrolyte, $[Mg(DPSO)_6]^{2+}$ cation complex was identified as active Mg ion, coupled by two $[MgCl_3(THF)]^-$ anions (Kang et al., 2017). The cosolvent THF can help form more stable anion $[MgCl_3(THF)]^-$ with weakened coordinating ability, thus allowing Mg^{2+} to be solvated solely by DPSO. The unique structures of such novel active ion enabled highly efficient reversible Mg deposition/dissolution. $Mg(HMDS)_2$-$MgCl_2$ based on certain sulfone/THF mixed solvent exhibited comparable Mg deposition reversibility and much higher thermal stability than that of pure THF-based counterparts (Merrill and Schaefer, 2018). The solvated $Mg_2Cl_3^+/MgCl^+$ ratio, which is affected by cosolvent type, was the key factor in anode reversibility. Butyl sulfone-/THF-based electrolyte with higher $Mg_2Cl_3^+/MgCl^+$ presented facilitated reversible Mg deposition than that of sulfolane/THF electrolyte. When dimethylamine (DMA) was introduced into a $Mg(TFSI)_2$/THF-G4 electrolyte, the CE can be significantly improved. A neutral coordination compound $Mg(TFSI)_2(THF)_4$ was identified, which successfully reduced the effective charge and accelerated the kinetics for reversible Mg deposition (Fan et al., 2020). It was suggested that the cosolvent DMA participated in the formation of the ion pair in the solvation shell by Mg···N interaction.

CONCLUSION REMARKS

Non-nucleophilic electrolytes have become new trends in Mg electrolyte research, especially considering the rapid development of Mg-S and Mg-O_2/air battery in recent years. Although many of the drawbacks in conventional Grignard-based electrolytes have been overcome by emerging non-nucleophilic electrolytes, it is still very challenging to prepare Mg electrolytes for practical application. Cl-based electrolytes including MACC, $Mg(TFSI)_2$-$MgCl_2$, and $(HMDS)_2Mg$-$MgCl_2$ have good processability and excellent performance but are still corrosive to many current collectors and cell components, especially when

strong Lewis acid $AlCl_3$ was involved. In Cl-free B-centered electrolytes, $Mg(BH_4)_2$ suffered from low anodic stability and limited solubility. Magnesium carbaborate and alkoxyborate originating from $Mg(BH_4)_2$ precursor have a wide electrochemical window, albeit with a complicated synthetic procedure. There are some common disadvantages of most Mg electrolytes, such as high raw materials price, moisture sensitivity, and long-term preconditioning behavior. Another key issue in the Mg electrolyte research is understanding the mechanism of Mg stripping/plating, including anode-electrolyte interfacial chemistry, Mg coordination chemistry, and Mg cation electrochemistry. Although there have already been rational hypotheses presented with support from theoretical simulation and experimental results, researchers still need to explore the chemical and electrochemical process during reversible Mg deposition in-depth.

In summary, developing non-nucleophilic, noncorrosive, less air-/moisture-sensitive electrolyte with wide electrochemical window and high Mg deposition reversibility is preferred to promote the development of practical rechargeable Mg batteries. It is highly recommended to prepare Mg electrolyte from low-cost, commercially available materials via a facile procedure. Further investigation is also needed to better understand the ion structure of electrolyte, electrode-electrolyte interface, and their effect on the electrochemical performance.

AUTHOR CONTRIBUTIONS

All authors have made a substantial, direct, and intellectual contribution to the work and approved it for publication.

ACKNOWLEDGMENTS

The authors sincerely acknowledge the National Natural Science Foundation of China (Nos. 52003147, 21978164, 21808249, and 21806097); Key Research and Development Program of Shaanxi Province (No. 2020GY-243); Innovation Supporting Plan of Shaanxi Province-Innovation Research Team (No. 2018TD-015); National High-End Foreign Expert Project (No. GDW20186100428); Industrialization Project of Shaanxi Education Department (No. 19JC010).

REFERENCES

Attias, R., Salama, M., Hirsch, B., Goffer, Y., and Aurbach, D. (2019). Anode-electrolyte interfaces in secondary magnesium batteries. *Joule* 3, 27–52. 10.1016/j.joule.2018.10.028

Aurbach, D. (1999). "Chapter 6: the electrochemical behavior of active metal electrodes in nonaqueous solutions," in *Nonaqueous Electrochemistry*. Hoboken, NJ: Wiley. 296–301. doi:10.1002/3527600655

Aurbach, D., Gizbar, H., Schechter, A., Chusid, O., Gottlieb, H. E., Gofer, Y., et al. (2002). Electrolyte solutions for rechargeable magnesium batteries based on organomagnesium chloroaluminate complexes. *J. Electrochem. Soc.* 149, A115. doi:10.1149/1.1429925

Aurbach, D., Schechter, A., Moshkovich, M., and Cohen, Y. (2001). On the mechanisms of reversible magnesium deposition processes. *J. Electrochem. Soc.* 148, A1004. doi:10.1149/1.1387980

Aurbach, D., Weissman, I., Gofer, Y., and Levi, E. (2003). Nonaqueous magnesium electrochemistry and its application in secondary batteries. *Chem. Rec.* 3, 61–73. doi:10.1002/tcr.10051

Barile, C. J., Barile, E. C., Zavadil, K. R., Nuzzo, R. G., and Gewirth, A. A. (2014). Electrolytic conditioning of a magnesium aluminum chloride complex for reversible magnesium deposition. *J. Phys. Chem. C.* 118, 27623–27630. doi:10.1021/jp506951b

Barile, C. J., Nuzzo, R. G., and Gewirth, A. A. (2015). Exploring salt and solvent effects in chloride-based electrolytes for magnesium electrodeposition and dissolution. *J. Phys. Chem. C.* 119, 13524–13534. doi:10.1021/acs.jpcc.5b03508

Benmayza, A., Ramanathan, M., Arthur, T. S., Matsui, M., Mizuno, F., Guo, J., et al. (2013). Effect of electrolytic properties of a magnesium organohaloaluminate electrolyte on magnesium deposition. *J. Phys. Chem. C.* 117, 26881–26888. doi:10.1021/jp4077068

Carter, T. J., Mohtadi, R., Arthur, T. S., Mizuno, F., Zhang, R., Shirai, S., et al. (2014). Boron clusters as highly stable magnesium-battery electrolytes. *Angew. Chemie Int. Ed.* 53, 3173–3177. doi:10.1002/anie.201310317

Cheng, Y., Stolley, R. M., Han, K. S., Shao, Y., Arey, B. W., Washton, N. M., et al. (2015). Highly active electrolytes for rechargeable Mg batteries based on a [Mg2(μ-Cl)2]2+ cation complex in dimethoxyethane. *Phys. Chem. Chem. Phys.* 17, 13307–13314. doi:10.1039/C5CP00859J

Connell, J. G., Genorio, B., Lopes, P. P., Strmcnik, D., Stamenkovic, V. R., and Markovic, N. M. (2016). Tuning the reversibility of Mg anodes via controlled surface passivation by H2O/Cl– in organic electrolytes. *Chem. Mater.* 28, 8268–8277. doi:10.1021/acs.chemmater.6b03227

Doe, R. E., Han, R., Hwang, J., Gmitter, A. J., Shterenberg, I., Yoo, H. D., et al. (2014). Novel, electrolyte solutions comprising fully inorganic salts with high anodic stability for rechargeable magnesium batteries. *Chem. Commun.* 50, 243–245. doi:10.1039/C3CC47896C

Esbenshade, J. L., Barile, C. J., Fister, T. T., Bassett, K. L., Fenter, P., Nuzzo, R. G., et al. (2015). Improving electrodeposition of Mg through an open circuit potential hold. *J. Phys. Chem. C.* 119, 23366–23372. doi:10.1021/acs.jpcc.5b07825

Fan, S., Asselin, G. M., Pan, B., Wang, H., Ren, Y., Vaughey, J. T., et al. (2020). A simple halogen-free magnesium electrolyte for reversible magnesium deposition through cosolvent assistance. *ACS Appl. Mater. Interfaces* 12, 10252–10260. doi:10.1021/acsami.9b18833

Gao, T., Hou, S., Wang, F., Ma, Z., Li, X., Xu, K., et al. (2017). Reversible S0/MgSx redox chemistry in a MgTFSI2/MgCl2/DME electrolyte for rechargeable Mg/S batteries. *Angew. Chemie Int. Ed.* 56, 13526–13530. doi:10.1002/anie.201708241

Gofer, Y., Turgeman, R., Cohen, H., and Aurbach, D. (2003). XPS investigation of surface chemistry of magnesium electrodes in contact with organic solutions of organochloroaluminate complex salts. *Langmuir* 19, 2344–2348. doi:10.1021/la026642c

Gregory, T. D., Hoffman, R. J., and Winterton, R. C. (1990). Nonaqueous electrochemistry of magnesium: applications to energy storage. *J. Electrochem. Soc.* 137, 775–780. doi:10.1149/1.2086553

Ha, S.-Y., Lee, Y.-W., Woo, S. W., Koo, B., Kim, J.-S., Cho, J., et al. (2014). Magnesium(II) bis(trifluoromethane sulfonyl) imide-based electrolytes with wide electrochemical windows for rechargeable magnesium batteries. *ACS Appl. Mater. Interfaces* 6, 4063–4073. doi:10.1021/am405619v

He, Y., Li, Q., Yang, L., Yang, C., and Xu, D. (2019). Electrochemical-conditioning-free and water-resistant hybrid AlCl3/MgCl2/Mg(TFSI)2 electrolytes for rechargeable magnesium batteries. *Angew. Chemie Int. Ed.* 58, 7615–7619. doi:10.1002/anie.201812824

Huang, D., Tan, S., Li, M., Wang, D., Han, C., An, Q., et al. (2020). Highly efficient non-nucleophilic Mg(CF3SO3)2-based electrolyte for high-power Mg/S battery. *ACS Appl. Mater. Interfaces* 12, 17474–17480. doi:10.1021/acsami.0c00196

Kang, S.-J., Lim, S.-C., Kim, H., Heo, J. W., Hwang, S., Jang, M., et al. (2017). Non-grignard and Lewis acid-free sulfone electrolytes for rechargeable magnesium batteries. *Chem. Mater.* 29, 3174–3180. doi:10.1021/acs.chemmater.7b00248

Keyzer, E. N., Glass, H. F. J., Liu, Z., Bayley, P. M., Dutton, S. E., Grey, C. P., et al. (2016). Mg(PF6)2-Based electrolyte systems: understanding electrolyte–electrode interactions for the development of Mg-ion batteries. *J. Am. Chem. Soc.* 138, 8682–8685. doi:10.1021/jacs.6b04319

Kim, H. S., Arthur, T. S., Allred, G. D., Zajicek, J., Newman, J. G., Rodnyansky, A. E., et al. (2011). Structure and compatibility of a magnesium electrolyte with a sulphur cathode. *Nat. Commun.* 2, 427. doi:10.1038/ncomms1435

Kim, K., Guo, Q., Tang, L., Zhu, L., Pan, C., Chang, C., et al. (2020). Reversible insertion of Mg-Cl superhalides in graphite as a cathode for aqueous dual-ion batteries. *Angew. Chemie Int. Ed.* 59, 19924–19928. doi:10.1002/anie.202009172

Lau, K.-C., Seguin, T. J., Carino, E. V, Hahn, N. T., Connell, J. G., Ingram, B. J., et al. (2019). Widening electrochemical window of Mg salt by weakly coordinating perfluoroalkoxyaluminate anion for Mg battery electrolyte. *J. Electrochem. Soc.* 166, A1510–A1519. doi:10.1149/2.0751908jes

Liao, C., Sa, N., Key, B., Burrell, A. K., Cheng, L., Curtiss, L. A., et al. (2015). The unexpected discovery of the Mg(HMDS)2/MgCl2 complex as a magnesium electrolyte for rechargeable magnesium batteries. *J. Mater. Chem.* 3, 6082–6087. doi:10.1039/C5TA00118H

Liu, F., Wang, T., Liu, X., and Fan, L.-Z. (2020). Challenges and recent progress on key materials for rechargeable magnesium batteries. *Adv. Energy Mater.* 2000787. doi:10.1002/aenm.202000787

Liu, T., Shao, Y., Li, G., Gu, M., Hu, J., Xu, S., et al. (2014). A facile approach using MgCl2 to formulate high performance Mg2+ electrolytes for rechargeable Mg batteries. *J. Mater. Chem.* 2, 3430–3438. doi:10.1039/C3TA14825D

Lu, Z., Schechter, A., Moshkovich, M., and Aurbach, D. (1999). On the electrochemical behavior of magnesium electrodes in polar aprotic electrolyte solutions. *J. Electroanal. Chem.* 466, 203–217. 10.1016/S0022-0728(99)00146-1

Luo, J., Bi, Y., Zhang, L., Zhang, X., and Liu, T. L. (2019). A stable, non-corrosive perfluorinated pinacolatoborate Mg electrolyte for rechargeable Mg batteries. *Angew. Chemie Int. Ed.* 58, 6967–6971. doi:10.1002/anie.201902009

Ma, Z., Kar, M., Xiao, C., Forsyth, M., and MacFarlane, D. R. (2017). Electrochemical cycling of Mg in Mg[TFSI]2/tetraglyme electrolytes. *Electrochem. commun.* 78, 29–32. 10.1016/j.elecom.2017.03.018

Merrill, L. C., and Schaefer, J. L. (2018). Conditioning-free electrolytes for magnesium batteries using sufone–ether mixtures with increased thermal stability. *Chem. Mater.* 30, 3971–3974. doi:10.1021/acs.chemmater.8b00483

Mizrahi, O., Amir, N., Pollak, E., Chusid, O., Marks, V., Gottlieb, H., et al. (2008). Electrolyte solutions with a wide electrochemical window for rechargeable magnesium batteries. *J. Electrochem. Soc.* 155, A103. doi:10.1149/1.2806175

Mohtadi, R., Matsui, M., Arthur, T. S., and Hwang, S.-J. (2012). Magnesium borohydride: from hydrogen storage to magnesium battery. *Angew. Chemie Int. Ed.* 51, 9780–9783. doi:10.1002/anie.201204913

Muldoon, J., Bucur, C. B., Oliver, A. G., Sugimoto, T., Matsui, M., Kim, H. S., et al. (2012). Electrolyte roadblocks to a magnesium rechargeable battery. *Energy Environ. Sci.* 5, 5941–5950. doi:10.1039/C2EE03029B

Sa, N., Pan, B., Saha-Shah, A., Hubaud, A. A., Vaughey, J. T., Baker, L. A., et al. (2016). Role of chloride for a simple, non-grignard Mg electrolyte in ether-based solvents. *ACS Appl. Mater. Interfaces* 8, 16002–16008. doi:10.1021/acsami.6b03193

See, K. A., Chapman, K. W., Zhu, L., Wiaderek, K. M., Borkiewicz, O. J., Barile, C. J., et al. (2016). The interplay of Al and Mg speciation in advanced Mg battery electrolyte solutions. *J. Am. Chem. Soc.* 138, 328–337. doi:10.1021/jacs.5b10987

Shao, Y., Liu, T., Li, G., Gu, M., Nie, Z., Engelhard, M., et al. (2013). Coordination Chemistry in magnesium battery electrolytes: how ligands affect their performance. *Sci. Rep.* 3, 3130. doi:10.1038/srep03130

Shterenberg, I., Salama, M., Yoo, H. D., Gofer, Y., Park, J.-B., Sun, Y.-K., et al. (2015). Evaluation of (CF3SO2)2N−(TFSI) based electrolyte solutions for Mg batteries. *J. Electrochem. Soc.* 162, A7118–A7128. doi:10.1149/2.0161513jes

Tutusaus, O., Mohtadi, R., Arthur, T. S., Mizuno, F., Nelson, E. G., and Sevryugina, Y. V. (2015). An efficient halogen-free electrolyte for use in rechargeable magnesium batteries. *Angew. Chemie Int. Ed.* 54, 7900–7904. doi:10.1002/anie.201412202

Vestfried, Y., Chusid, O., Goffer, Y., Aped, P., and Aurbach, D. (2007). Structural analysis of electrolyte solutions comprising Magnesium−Aluminate Chloro−Organic complexes by Raman spectroscopy. *Organometallics* 26, 3130–3137. doi:10.1021/om061076s

Viestfrid, Y., Levi, M. D., Gofer, Y., and Aurbach, D. (2005). Microelectrode studies of reversible Mg deposition in THF solutions containing complexes of alkylaluminum chlorides and dialkylmagnesium. *J. Electroanal. Chem.* 576, 183–195. 10.1016/j.jelechem.2004.09.034

Yang, Y., Wang, W., Nuli, Y., Yang, J., and Wang, J. (2019). High active magnesium trifluoromethanesulfonate-based electrolytes for magnesium–sulfur batteries. *ACS Appl. Mater. Interfaces* 11, 9062–9072. doi:10.1021/acsami.8b20180

Zhang, Z., Cui, Z., Qiao, L., Guan, J., Xu, H., Wang, X., et al. (2017). Novel design concepts of efficient Mg-ion electrolytes toward high-performance magnesium–selenium and magnesium–sulfur batteries. *Adv. Energy Mater.* 7, 1602055. doi:10.1002/aenm.201602055

Zhang, Z., Dong, S., Cui, Z., Du, A., Li, G., and Cui, G. (2018). Rechargeable magnesium batteries using conversion-type cathodes: a perspective and minireview. *Small Methods* 2, 1800020. doi:10.1002/smtd.201800020

Zhao-Karger, Z., Gil Bardaji, M. E., Fuhr, O., and Fichtner, M. (2017). A new class of non-corrosive, highly efficient electrolytes for rechargeable magnesium batteries. *J. Mater. Chem.* 5, 10815–10820. doi:10.1039/C7TA02237A

Zhao-Karger, Z., Zhao, X., Fuhr, O., and Fichtner, M. (2013). Bisamide based non-nucleophilic electrolytes for rechargeable magnesium batteries. *RSC Adv.* 3, 16330–16335. doi:10.1039/C3RA43206H

Zhao-Karger, Z., Zhao, X., Wang, D., Diemant, T., Behm, R. J., and Fichtner, M. (2015). Performance improvement of magnesium sulfur batteries with modified non-nucleophilic electrolytes. *Adv. Energy Mater.* 5, 1401155. doi:10.1002/aenm.201401155

Conflict of Interest: The authors declare that the research was conducted in the absence of any commercial or financial relationships that could be construed as a potential conflict of interest.

Environmental Materials

Meicheng Wen

Dr. Meicheng Wen received his Ph.D. degree in Division of Materials and Manufacturing Science, Osaka University, in 2016. He was a specially appointed assistant professor in the Division of Materials and Manufacturing Science at Osaka University from 2016 to 2017. He is currently an Associate Professor at the Institute of Environmental Health and Pollution Control, Guangdong University of Technology, China. His research mainly focuses on the preparation of porous materials and their applications in energy conversion and environmental remediation. He has published 46 research articles in international journals and 13 patents, and he is involved in several industrial projects.

frontiers in Materials

REVIEW
published: 09 October 2020
doi: 10.3389/fmats.2020.595667

Advances in Catalytic Oxidation of Volatile Organic Compounds over Pd-Supported Catalysts: Recent Trends and Challenges

Shengnan Song[1], *Siyuan Zhang*[1], *Xiaolong Zhang*[1], *Priyanka Verma*[2] *and Meicheng Wen*[1]*

[1]Guangdong Key Laboratory of Environmental Catalysis and Health Risk Control, Guangzhou Key Laboratory Environmental Catalysis and Pollution Control, School of Environmental Science and Engineering, Institute of Environmental Health and Pollution Control, Guangdong University of Technology, Guangzhou, China, [2]School of Chemistry, University of Southampton, Southampton, United Kingdom

Volatile organic compounds (VOCs) are poisonous and regarded as the paramount source for the formation of secondary organic aerosols, ozone, and photochemical smog, greatly affecting human health and environment quality. In order to abate VOC emission, catalytic oxidation is widely applied in industries and is believed to be an efficient and economically feasible way for the elimination of VOCs. This review is primarily concentrated on summarizing the recent progress and developments in the catalytic oxidation of various VOCs over Pd-supported catalysts. Despite their high catalytic performances at much lower temperatures, the wide use of Pd-supported catalysts in the industry has been limited by their high cost, low thermal stability, and incomplete oxidation of VOCs. Hence, the intrinsic properties of the active sites and supports, the reaction conditions, the deactivation mechanism, and the strategy to reveal the catalytic oxidation pathway are also systematically summarized. This review aims to give a deep comprehension and guidance for the development of efficient and cost-effective Pd-supported catalysts in the near future.

Keywords: catalytic oxidation, Pd-supported catalysts, volatile organic compounds, deactivation mechanism, reaction pathway

OPEN ACCESS

Edited by:
David Salinas Torres, University of Alicante, Spain

Reviewed by:
Zaizhu Lou, Jinan University, China
Xufang Qian, Shanghai Jiao Tong University, China

***Correspondence:**
Meicheng Wen
meicheng.wen@gdut.edu.cn

Specialty section:
This article was submitted to Environmental Materials, a section of the journal Frontiers in Materials

Received: *17 August 2020*
Accepted: *08 September 2020*
Published: *09 October 2020*

Citation:
Song S, Zhang S, Zhang X, Verma P and Wen M (2020) Advances in Catalytic Oxidation of Volatile Organic Compounds over Pd-Supported Catalysts: Recent Trends and Challenges. Front. Mater. 7:595667. doi: 10.3389/fmats.2020.595667

INTRODUCTION

It is well known that organic compounds with the boiling point below 250°C and saturated vapor pressure equivalent to the atmospheric pressure (101.325 kPa) are identified as volatile organic compounds (VOCs). The types of released VOCs include aromatics, aliphatic hydrocarbons, oxygenated VOCs, halogenated VOCs, sulfur- or nitrogen-containing VOCs, and so on. Although the release of VOCs originates from the nature and human activities, the anthropogenic source accounts for a large proportion for VOC emission. Urbanization and industrialization have further led to the continuous increase in the emission of VOCs (Boeglin et al., 2006; Qiu et al., 2014). The anthropogenic sources were usually linked with chemical industries, gas station, food processing, petrochemical processing, production of plastics, solvent use, and many other industrial activities (Liotta, 2010; Scire and Liotta, 2012; Liao et al., 2015). Due to the high volatility at ambient conditions, the majority of VOCs can be easily emitted into the atmosphere and be absorbed through the human respiratory tract, skin, and digestive tract, and are harmful to the

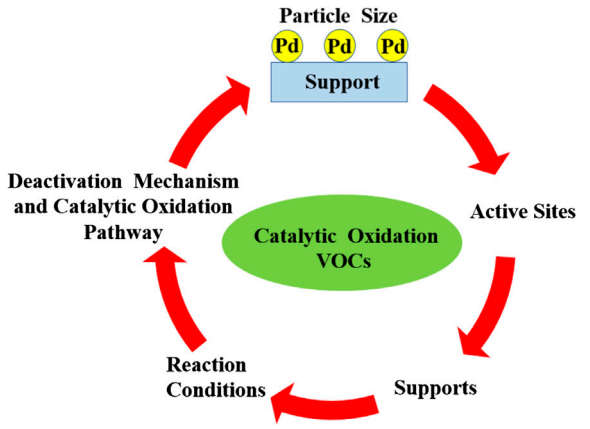

SCHEME 1 | Factors influencing the catalytic oxidation of volatile organic compounds over Pd-supported catalysts.

respiratory system and central nervous system even at low concentrations (Srivastava et al., 2005; Boeglin et al., 2006; Ahn et al., 2017; Odoom-Wubah et al., 2019c). Furthermore, some of the VOCs are used in the formation of secondary organic aerosols (Boltic et al., 2013; Zang et al., 2019), reducing air quality, and may trigger stratospheric ozone depletion (Dumanoglu et al., 2014; Liang et al., 2017). Therefore, efficient VOC destruction is of paramount significance from the perspectives of environment and human health.

The techniques used for the elimination of VOCs include recovery and destruction. Recovery techniques such as absorption, adsorption, and membrane separation are more adaptable to efficient disposal of high concentration VOCs. However, execution of these techniques is restricted by a complicated process and high cost (Iranpour et al., 2005; Vu et al., 2009; Tomatis et al., 2016). Catalytic oxidation appears to be an effective way for the removal of VOCs due to its higher destructive efficiency and lower operating temperatures (Zhang et al., 2016). It can completely mineralize VOCs to carbon dioxide (CO_2) and H_2O instead of transforming them to by-products with high toxicity. Furthermore, catalytic oxidation can also be applied to eliminate extremely dilute VOC streams.

Preparation of catalysts with high activity and stability is critically important in VOC catalytic oxidation. Catalysts for VOC combustion can be divided into the following categories: 1) non-noble metal oxides (Kim and Shim, 2010), 2) supported noble metals (Liotta, 2010), and 3) alloy metal nanoparticle catalysts (Aguero et al., 2009; Zeng et al., 2015). Among these, noble metal catalysts (Au, Pt, Rh, Pd, etc.) possess superior catalytic activity and durability for VOC catalytic oxidation under low temperature (Gulsnet and Magnoux, 1997). Currently, Pd is preferred in the industrial application of VOC abatement over the other noble metals (Au, Pt, and Ru) (Bendahou et al., 2008; Aznárez et al., 2015; Xiong et al., 2018; Odoom-Wubah et al., 2019a) on account of its unique electron configuration and high chemical stability during VOC catalytic oxidation (Kamal et al., 2016). Significant achievements have been obtained by using Pd as a catalyst for the elimination of VOCs. It has been proved that the catalytic performance of Pd-based catalysts is highly dependent on the particle size, chemical state, loading amount of Pd, and physical and chemical properties of the supporting materials. However, deactivation phenomena frequently appear in the forms of coking, poisoning, and thermal sintering during catalytic VOC oxidation over Pd-based catalysts, which cause a decrease in catalytic activity. Complete understanding of the reaction mechanism is vital for the development of highly efficient catalysts for VOC oxidation. The present work mainly focuses on previous reviews of catalytic oxidation of VOCs over Pd-supported catalysts (**Scheme 1**). Moreover, the intrinsic properties of catalysts and the reaction conditions for the catalytic performance over Pd catalysts are described. The deactivation mechanism and the tactics to disclose the catalytic oxidation pathway are summarized in detail too. We believe that this review is meaningful in offering a deep understanding and guidance to the preparation of highly efficient and cost-effective Pd catalysts.

Pd-SUPPORTED CATALYSTS

Generally, supported catalysts consist of two parts: the active site and the supporting material. Therefore, it is reasonable to take these two parts into consideration as factors influencing the catalytic activity of Pd-supported catalysts. As for the active sites, more attention has been paid to the Pd particle size and the chemical state of Pd. In consideration of the supporting materials, the support type, acidity, and metal–support interaction, which are intrinsic properties of the support, play a vital role in the catalytic performance of Pd-supported catalysts. Hence, we mainly introduce the influence of particle size and chemical state of Pd, as well as the intrinsic properties of the supports for the reason that most of the investigations about Pd catalysts are focused on that.

Active Sites

Influence of Pd Particle Size

The size of Pd nanoparticles (Pd NPs) is an interesting and promising factor that influences catalytic performances. It is well known that Pd NPs with high surface-to-volume ratio can greatly enhance the catalytic activity by providing additional active sites per unit area; because of this, the catalytic activity is closely correlated to Pd particle size (Kim and Shim, 2009; Bedia et al., 2010; Wang et al., 2013; Liu J. et al., 2014; Li et al., 2017). On the other hand, high-temperature reduction could decrease the surface Pd particle size by encapsulating and trapping it with the support and subsequently promoting the activation of O_2, which is beneficial to the degradation of VOCs (Li et al., 2017). Lupescu et al. stated that Pd below 8.8 nm was essential for the rapid formation of PdO and efficient re-dispersion of Pd (Lupescu et al., 2016). Lowering the size of Pd NPs can increase the interface between the Pd and support, offering more available mobile oxygen (Giraudon et al., 2008a). To

TABLE 1 | Catalytic oxidation of volatile organic compounds (VOCs) with different Pd states.

Catalyst	VOCs	Pd state	References
Pd/CeO_2	Propene	Pd^0	Gil et al. (2015)
Pd/Co_3AlO	Toluene	Pd^0	Li et al. (2011)
Al_2O_3@Pd–CoAlO	Toluene	Pd^0	Zhao et al. (2016)
Pd/Al_2O_3	Toluene	Pd^0	Weng et al. (2019)
Pd/TiO_2	Formaldehyde	Pd^0	Huang and Leung (2011)
Pd/ZSM-5/MCM-48	Benzene	Pd^0, Pd^{2+}	He et al. (2010a)
Pd/SBA-15	Benzene	Pd^0, Pd^{2+}	He et al. (2012c)
Pd/ZSM-5/KIT-6	Trichloroethylene	Pd^0, Pd^{2+}	He et al. (2012a)

obtain superior catalytic activity and higher atom-utilization efficiency, many investigations are concerned with the preparation of catalysts with smaller size of Pd NPs. Single-atom catalysts exhibit great potential in generating metal centers as atomically dispersed sites for achieving high activity and selectivity (Yang et al., 2012). Besides, due to the ultra-small size (less than 2 nm), these metal nanoclusters exhibit unique and even unexpected properties that are not observed in bulk metal and conventional metal nanoparticles (Yang et al., 2012; Flytzani-Stephanopoulos, 2017; Yuan et al., 2020). Dai et al. revealed that single-atom platinum supported on ordered mesoporous iron oxide showed higher catalytic activity and better water resistance than its nanoparticulated counterpart, achieving a benzene conversion of 90% at 198°C (Yang K. et al., 2019). Wang and coworkers also indicated that nanoceria-supported atomic Pt catalysts exhibited superior catalytic performance for the oxidation of methane (Xie et al., 2018). However, there are no reports based on the utilization of single-atom Pd catalysts in the catalytic oxidation of VOCs, which should be paid more attention to in future studies.

Influence of the Pd Chemical State

The chemical state of Pd is one of the important factors affecting Pd catalytic activity, but the effects of Pd state on the catalytic activity remain controversial (**Table 1**). Numerous studies have demonstrated that the catalytic activity of Pd-supported catalysts is closely related to the oxidation state of Pd (Li et al., 2011; Gil et al., 2015; Zhao et al., 2016; Weng et al., 2019; Zhao X. et al., 2019). Some authors proposed that metallic Pd was more active in VOC oxidation than its oxidized state (Tidahy et al., 2008; Huang and Leung, 2011; Wang et al., 2018a; Zhao X. et al., 2019), as it can provide more active sites for the oxidation of hydrocarbons (Jinjun et al., 2005). The superior catalytic performance of Pd/TiO_2 for HCHO oxidation relied on the metallic Pd NP with a strong capacity for oxygen activation (Huang and Leung, 2011). The Pd^0 species were also found to be more active than PdO for o-xylene oxidation reaction (Wang et al., 2018a). Jeong et al. reported that hydrogen-treated catalysts showed higher oxidation activities than air-treated catalysts for possessing more metallic Pd (Ihm et al., 2004). However, a series of studies indicate that both Pd^0 and PdO act as active sites for oxidation reaction (He et al., 2009; He et al., 2010a; He et al., 2012a; He et al., 2012c). In the presence of O_2, a portion of metallic Pd was oxidized to Pd^{2+} and subsequently reduced by HCs. Therefore, the mixture of metallic Pd and Pd^{2+} was responsible for the oxidation reaction of benzene, toluene, and ethyl acetate over Pd/SBA-15 catalyst (He et al., 2012c). Navarrete et al. stated that the existence of cerium oxide in $Pd/\gamma\text{-}Al_2O_3$–Ce permitted the coexistence of Pd^0 and PdO species, which favored the catalytic combustion of benzene and inhibited the deposition of carbonaceous species on the Pd surface (Padilla et al., 2008).

Supporting Materials

The catalytic oxidation of VOCs over Pd-supported catalysts strongly depends on the physical and chemical properties of the support, such as the support type, the acid–base properties, and the metal–support interaction. The supporting materials can profoundly affect the catalytic performance of Pd catalysts by tuning the nanoparticle size, dispersion, and chemical state. It is generally accepted that active phase dispersion is a decisive factor in the determination of catalytic performances for noble-metal–loaded catalysts. In general, support materials with larger specific surface areas permit higher dispersion of the active phase and assist in the easy adsorption of substrate to display enhanced activity, particularly in oxidation reactions. The acid properties of supports were also found to play an important role in affecting the dispersion and oxidation state of Pd NPs, thus influencing the catalytic performance for VOC catalytic oxidation. The existence of a strong interaction between the support and active phase also exerts a constructive effect on increasing the catalytic activity, selectivity, and stability. The development of an active and stable catalyst is one of the most crucial factors in the VOC oxidation process. The traditional supports can no longer satisfy the aforementioned aspects for VOC oxidation because of their weak thermostability and lower specific surface area. As a consequence, several researchers take great interest in the modification of the supporting materials to improve the catalytic performance.

Influence of the Support Type

For Pd-based catalysts, the support effect is profound, and their activity has also been found to be closely related to the type of support materials. Different types of supports have been comprehensively investigated for hydrocarbon catalytic oxidation (**Table 2**). Giraudon et al. reported that superior catalytic performance of Pd/TiX was observed than of Pd/ZrX for chlorobenzene oxidation. This was attributed to the better reducibility of the TiO_2 support (Ti^{4+} into Ti^{3+}), allowing for enhanced oxygen mobility (Giraudon et al., 2008b). Moulijn stated that the catalytic activity of Pd supported on carbon-based monoliths for combustion of m-xylene was correlated with the surface area of the support, and the mesoporous

TABLE 2 | Reported Pd-supported catalysts for the oxidation of volatile organic compounds (VOCs).

Catalyst	Support	VOCs	Temp/°C	Conversion/%	References
Pd–Mn	TiO_2	Acetone	259	100	Zhao Q. et al. (2019)
Pd	Carbon	m-Xylene	170	100	Pérez-Cadenas et al. (2008)
Pd	Co_3O_4	o-Xylene	249	90	Wang et al. (2015)
Pd	UiO-66	Toluene	200	100	Bi et al. (2020)
Au–Pd	Cr_2O_3	Toluene	165	90	Wu et al. (2016)
Pd–Pt	Ce/γ-Al_2O_3	Benzene	190	95	Chen et al. (2019a)
Pd–Ce	γ-Al_2O_3	Toluene	200	90	Ren et al. (2020)
Pd–W	TiO_2	Propane	375	100	Taylor et al. (2012)

sample possessed the best catalytic performance compared with the monolithic support and microporous sample (Pérez-Cadenas et al., 2008). The same conclusion was evidenced by He and coworkers, in which they revealed that the excellent catalytic performance of Pd/Co_3O_4 might be due to the mesoporous structure of the support by exposing more active species (Wang et al., 2015). The supports with mesopores (such as SBA-15 and MCM-48) possessing narrow pore size distribution, high surface area, are considered as one of the best supports for the preparation of Pd catalysts (Shi et al., 2013). On the other hand, metal–organic frameworks are also frequently used in adsorption (Zhang et al., 2019b) and photocatalysis (Zhang et al., 2018). Pd NPs supported on UiO-66 displayed narrow size dispersion and achieved superior catalytic performances for toluene oxidation (Bi et al., 2020). Qi et al. proposed that the size of support also had an impact on the Pd dispersion and influenced the catalytic performance of benzene oxidation due to the number of adsorbed sites and interface effect (Zhao et al., 2011). They studied and compared the synthesis of Pd NPs on nano-sized and micro-sized molecular sieves and concluded on the superior catalytic performance of nano-sized molecular sieves because of their higher external surface area and shorter channel length.

Influence of Acidity of the Supports

It was reported that the acidity of supports significantly affects the catalytic performance of Pd-supported catalysts in VOC oxidation (He et al., 2010a; He et al., 2010d; Venezia et al., 2011; Wang et al., 2018b). Yazawa et al. investigated the catalytic combustion of propane over palladium supported on various carriers (MgO, ZrO_2, Al_2O_3, SiO_2, SiO_2-ZrO_2, SiO_2-Al_2O_3, and SO_4^{2-}-ZrO_2), finding that the supports with moderate acidity showed the highest catalytic conversion of VOCs (Yazawa et al., 1999). Wang et al. indicated that a catalyst with a low concentration of strong acid sites and higher redox ability was beneficial for butyl acetate oxidation (Yue et al., 2014). The supported Pd NPs with Brønsted acid sites had been reported to invoke catalytic enhancement by promoting adsorption and activation of reactant molecules during the catalytic process (Zang et al., 2019). The ease of oxidation of Pd NPs on acidic supports in contrast to the neutral or basic supports was justified because of their electrophilic nature forming electron-deficient Pd atoms (Okumura et al., 2003b; Hong et al., 2007; He et al., 2012a). Furthermore, the oxidation state of Pd NPs was dependent on the acid–base characteristics of the support, and the acidic supports are favorable for oxidation of Pd particles (He et al., 2012d). The Al in the support could offer acid sites, which were favorable for the oxidation of Pd NPs, thus improving the catalytic oxidation of toluene (He et al., 2012b). Based on the strength of acidity of support materials, the accelerated transformation of Pd^0 to Pd^{2+} can promote the catalytic oxidation of VOCs (He et al., 2010a). Furthermore, the acidity of the supports is considered to be crucial for the catalysts with high Pd dispersion and found to be beneficial in promoting the catalytic reaction (Tidahy et al., 2006; He et al., 2010c; Jin et al., 2011; Yang et al., 2016; Dai et al., 2018). Okumura et al. reported the support acid property had a significant influence on the dispersion of Pd and the Brønsted acid sites were responsible for the generation of highly dispersed Pd species (Okumura et al., 2003a).

Influence of Metal–Support Interaction

Metal–support interactions have been observed on various supported Pd catalysts for catalytic oxidation of VOCs (Tauster et al., 1978; Ryndin et al., 1981). Rooke et al. investigated the catalytic performance over Pd NP catalysts on various supports. The Pd impregnated on hierarchically porous Nb_2O_5 or Ta_2O supports displayed enhanced catalytic oxidation activity of toluene compared with hierarchically porous TiO_2 and ZrO_2, which was dependent on the metal–support interaction (Rooke et al., 2012). Hao et al. also found that the strong synergistic effect between Co_3O_4 and PdO was the main factor determining the catalytic activity but not the amount of the surface palladium species for the catalytic oxidation of toluene (Li et al., 2011). Due to the strong metal–support interaction, enhanced dispersion, and hydrothermal stability, Pd has been employed in various oxidation catalytic reactions (Kim et al., 2016). The interaction between the metal and support strongly affected the state of Pd NPs for VOC catalytic oxidation. The oxidation of Pd into PdO was promoted by the reducible oxides, whereas the non-reducible oxides boosted the reduction of Pd (Bernal et al., 2005; Ramírez-López et al., 2010). Pd NPs supported on ZrO_2 were more prone to generate a strong metal–support interaction with Brønsted acid sites rather than the interfacial structure, accelerating toluene oxidation and improving the catalytic efficiency (Yang et al., 2020). The high activity for benzene destruction on calcified shrimp waste–supported Pd NPs was dependent on high Pd metal dispersion, and the synergistic effect between the small Pd NPs and the shrimp waste support (Odoom-Wubah et al., 2019b).

TABLE 3 | Reported alloyed nanoparticles catalysts for volatile organic compounds (VOCs) catalytic oxidation.

Catalyst	Support	VOCs	Temp/°C	Conversion/%	References
Pt	γ-Al_2O_3	Benzene	220	90	Chen et al. (2019a)
Pd	γ-Al_2O_3	Benzene	295	90	Chen et al. (2019a)
Pd–Pt	γ-Al_2O_3	Benzene	190	90	Chen et al. (2019a)
Au	TiO_2	Toluene	400	100	Hosseini et al. (2012)
Pd	TiO_2	Toluene	260	100	Hosseini et al. (2012)
Au-Pd	TiO_2	Toluene	230	100	Hosseini et al. (2012)
Pd	KL-NY	Benzene	320	100	Zuo et al. (2014)
Pt	KL-NY	Benzene	280	100	Zuo et al. (2014)
Pd–Pt	KL-NY	Benzene	240	100	Zuo et al. (2014)
Pd	γ-Al_2O_3	Toluene	226	90	Ren et al. (2020)
Pd–Ce	γ-Al_2O_3	Toluene	200	90	Ren et al. (2020)

Influence of the Modification of the Support

Garcia et al. stated that the activity of titania-supported Pd catalysts was greatly enhanced by the modification with vanadium for the oxidation of short-chain alkanes, which was attributed to the improved redox properties of the catalysts (Garcia et al., 2005). Barakat et al. verified that doping with foreign ions into the skeleton of the support and noble metal loading offered a stable activity of the catalysts toward the catalytic destruction of toluene at low temperatures (Barakat et al., 2014a). A synergistic effect was observed for the catalytic oxidation of benzene when vanadium was added to Pd/TiO_2 catalysts (Garcia et al., 2006). Another study by Li and coworkers reported that doping of Al ions into the skeleton of TiO_2 inhibited the electron transfer from TiO_2 to Pd by enhancing anatase stabilization and increasing defects in TiO_2. The optimal catalytic performance for ethanol conversion and CO_2 production over the Pd-supported Al-doped TiO_2 was attributed to the enhanced structural properties of Al-doped TiO_2 (Zhu et al., 2017). With the addition of Ce to Al_2O_3, the catalytic activity for VOC oxidation was higher than that of pure Al_2O_3 for Pd-based catalysts (Pitkäaho et al., 2013; Gil et al., 2015; Liao et al., 2016; Hosseini et al., 2017). Zuo et al. emphasized the role of ceria added to Pd/SP (shell powder) for increasing the surface area and total pore volume and decreasing the sintering ability of SP (Zuo et al., 2013). Chen et al. concluded that the physical/chemical adsorption of Pd/MCM-22 was greatly improved with the addition of Y_2O_3, which was beneficial to the oxidation reaction (Chen et al., 2019b). He et al. demonstrated that the catalytic oxidation of benzene over Pd-supported ZSM-5/MCM-48 was much higher than that on individual ZSM-5 and MCM-48 support materials (He et al., 2010a).

ALLOYED NANOPARTICLE CATALYSTS

Although catalysts with a single noble metal possess excellent catalytic activities based on the results reported in the documentation, alloyed NP (bimetallic NPs and trimetallic NPs) catalysts create exceptional physicochemical properties that are distinctly different from those of their monometallic counterparts (Yu et al., 2015; Wei et al., 2020). Moreover, the combination of properties correlated to distinct metals may have a synergetic effect on the catalytic competence of the catalysts (**Table 3**). Alloyed catalysts exhibit unique and more flexible surface structures than monometallic catalysts, in which these flexible surface structures are beneficial to tailoring the affinity of surface adsorbates to substrates, giving rise to high catalytic activity (Chen and Rodionov, 2016).

Bimetallic NP catalysts are extensively applied for the catalytic oxidation of VOCs due to their superior catalytic performance attributed to the extraordinary structure and the synergistic effect between the bimetallic NPs. It has been reported that Au-Pd/meso-Cr_2O_3 catalysts showed an extraordinary catalytic performance for toluene oxidation because of the strong interaction between Au–Pd NPs and Cr_2O_3 as compared to the single-metal catalysts (Wu et al., 2016). Chen et al. pointed out that the superior catalytic performance of Pd–Pt NP catalysts in benzene oxidation was primarily due to the nano-effects of Pd–Pt and the interactions among the active substances (Chen et al., 2019a). The catalytic combustion of toluene and propene on Pd (shell)–Au (core)/TiO_2 displayed the highest catalytic activity, correlating to the Pd-shell and Au-core morphology (Hosseini et al., 2012). Hutchings et al. investigated the oxidation of toluene over the Au–Pd catalysts and demonstrated that the Au acted as an electronic promoter for Pd (Enache et al., 2006; bin Saiman et al., 2012). The complete conversion of benzene could be achieved at approximately 230°C owing to the enhancement of the oxidation properties over Pd catalysts with the addition of Ce and Pt (Zuo et al., 2014). Researchers have attempted to improve low-temperature activity and stability of Pd-supported catalysts through introducing non-noble metals to the catalysts, concerning the high cost and the rare supply of the noble metals. Ultrafine dispersed Pd–Cu nanoalloys anchored on porous carbon showed high catalytic activity, durability, and tolerance toward ethanol oxidation due to their advanced structure and composition (Yang W. et al., 2019). $Pd_{0.01}Mn_{0.2}/Ti$ catalyst exhibited superior catalytic performance for acetone oxidation than its counterpart catalyst in the absence of Mn due to the presence of high valence states of Mn in the catalyst (Zhao Q. et al., 2019). The bimetallic Pd–Ce/γ-Al_2O_3 catalyst displayed better catalytic performance than Pd/γ-Al_2O_3, further indicating that Ce loading improved the catalytic activity by reducing the amount of precious metals incorporated within the catalyst (Ren et al., 2020). The high water-resistant ability of the supported Pd–W bimetallic catalysts was ascribed to the presence of the facile redox

cycle of the active Pd^{2+}/Pd^0 couple (Liang et al., 2019). The addition of Mo in Pd/Al_2O_3 catalyst efficiently improved the activity and stability by increasing the Pd dispersion and changing the partial PdO (He et al., 2014). With the introduction of NiO, the activity of Pd/SBA-15 was greatly improved on account of the strong synergistic effect of PdO–NiO (Tang et al., 2017). The synergistic relationship between Pd and W accounted for the high activity in the oxidation of propane. Besides, the presence of W led to the epitaxial orientation of Pd NPs (Taylor et al., 2012).

INFLUENCE OF REACTION CONDITIONS

As for the Pd-supported catalysts, not only the intrinsic properties of the catalysts but also the reaction conditions as well as the composition of the reactant VOCs greatly influenced the oxidation behaviors of VOCs.

Influence of Humidity

The effect of humidity on the catalytic performance for VOC oxidation over Pd catalysts has been extensively studied as H_2O plays a vital role in the catalytic oxidation process. Water often exists in the flue gases released from the industries or as the products of VOC catalytic oxidation.

It is difficult to determine the role of water in VOC catalytic destruction, for the reason that the catalyst component, VOC type, and reaction conditions may exert a measure of influence over it (He et al., 2019). In general, water vapor has been observed to play an inhibiting role in VOC oxidation (Liotta, 2010); the inhibitory role of H_2O adsorption under low temperature was reversible, which resulted in the decrease in the catalytic activity. A previous work reported by Madcot et al. proposed that the addition of relatively large quantities of water inhibited the catalytic activity for the oxidation of propane and propene over Pd/Al_2O_3 catalysts due to the decrease in the active surface (Marécot et al., 1994). Similar results were also reported by Arias and coworkers, suggesting that the high concentration water in the feed favored the catalyst deactivation on account of the competitive adsorption and oxidation of VOCs and water molecules on the active site (de la Peña O'Shea et al., 2005). The adsorption behavior of VOCs on the catalyst surface was correlated to the polarity of the VOC molecules (Xia et al., 2018). In consideration of the hydrophobicity of the n-propane thiol and n-chloropropane, the inhibition effect was observed in the adsorption of VOCs for the blocking effect of the water layer on the catalyst surface (He et al., 2020). Meanwhile, the presence of water was conducive to the adsorption of polar VOCs but caused an inhibition to the desorption of VOCs, hence restraining their degradation. Upon increasing the temperature, the existence of water molecules can lead to the formation of hydroperoxyl intermediate species and hence favor the activation of oxygen in VOC oxidation (Chang et al., 2016). Wang et al. indicated that the introduction of water vapor facilitated the toluene adsorption over Pd-UiO-66-EG and hindered the desorption of toluene (Bi et al., 2020). The inhibitory effect of the existence of water vapor for toluene oxidation disappeared at higher temperature conditions. Although water presumably exists as an inhibitor, in some cases, it may play a positive role in VOC destruction. Gonzalez-Marcos and coworkers found that the presence of water could promote deep oxidation of trichloroethylene to CO_2 and thus reduce selectivity of CO over Pd/Al_2O_3 catalysts. Upon increasing the concentration of water, the promotion of CO complete oxidation by the water–gas shift reaction was observed along with the reduced selectivity for the formation of C_2Cl_4 and Cl_2 (Gonzalez-Velasco et al., 2000). In-depth research focusing on the role of water for VOC oxidation should be investigated for detailed understanding.

Influence of Reactant Composition

Industrial flue gas steams contain various compositions and concentrations of VOCs with different physicochemical properties. Thus, the catalytic removal process of mixtures of VOCs is more complex than that of single-component VOCs. An inhibitory (Santos et al., 2010a; Santos et al., 2010b) or promoting effect (Barakat et al., 2014b) might be observed on the catalytic oxidation of mixed VOCs. However, some research groups have reported the concurrent removal of mixed VOCs. The presence of other VOCs always occupies some active sites over the support through chemisorption, leading to the decrease in the concentration of rate-determinant species. For the catalytic oxidation of VOC mixtures (benzene, toluene, and ethyl acetate) over Pd/SBA-15, Hao et al. reported that the presence of benzene or toluene inhibited the oxidation process of ethyl acetate, and the catalytic oxidation of benzene and toluene restricted each other, while the promotion effect was observed for ethyl acetate on toluene (He et al., 2012c). Dai et al. pointed out that because of the existence of the competitive adsorption of the mixture of the VOCs over the Au–Pd/α-MnO_2, a higher temperature was needed for the complete oxidation of these VOCs. The exothermic character of the complete oxidation reaction exerted a promoting effect on VOC oxidation (Xia et al., 2018). However, Barakat et al. stated that Pd/5%V-TiO_2 possessed the superior activity for the oxidation of a butanone–toluene mixture than that of single-component butanone (Barakat et al., 2014b). It was because in the presence of toluene, butanone showed a higher affinity to the surface of the catalyst, thus ensuring a faster oxidation process than when alone in the gaseous stream. The actual reasons for the inhibitory and promoting effects in the oxidation of VOC mixtures over the Pd catalysts need further study in the future work.

DEACTIVATION OF Pd-SUPPORTED CATALYSTS

Catalyst deactivation is a great concern for the catalysts in the industrial catalytic processes because it is relevant to practical application in light of the cost for regeneration or restoration of their activity. It can take place in the following forms: coke (carbonaceous deposits), chlorine, nitrogen, sulfur poisoning, and thermal sintering.

Formation of Coke

The catalyst deactivation caused by coke is a major problem in the petrochemical industry as it causes a gradual decline in catalytic activity. Generally, the formation of coke occurs in the pores and on the external surface of catalysts (Gulsnet and Magnoux, 1997; Guisnet et al., 2009) *via* undesired side reactions (Becker and Förster, 1997) during the catalytic oxidation process. It is generally accepted that coke formation includes hydrogen transfer (acid catalysts), dehydrogenation of adsorbed hydrocarbons (bifunctional catalysts), condensation, and rearrangement steps. Besides, retention of the "coke" molecules on the catalysts is mainly ascribed to their strong adsorption and low volatility (gas-phase reactions) or low solubility (liquid-phase reactions) (Guisnet and Magnoux, 2001). The produced carbonaceous intermediates will prevent the reaction VOC oxidation and retard the deep catalytic oxidation process. In principle, coke may affect catalyst activity in two ways: through active site coverage (poisoning) and pore blockages (active sites rendered inaccessible to reactants) (Guisnet and Magnoux, 1994). Yang et al. revealed that carbon was easily deposited on the catalyst surface and significantly restricted the interaction between toluene and the surface active sites, resulting in the catalyst deactivation (Yang, 2020). Similar results were also suggested by Jeong et al. for n-hexane destruction over the Pd/γ-Al_2O_3 catalysts. The initial activity of reduced catalysts was higher at lower temperatures than the oxidized catalysts which displayed a gradual deactivation under the existence of carbonaceous intermediate species (Ihm et al., 2004). Coke is prone to form on the catalysts with large amounts of acid sites that participate in coke production as a side reaction, thus resulting in catalyst deactivation (He et al., 2009; He et al., 2012d). Dégé et al. claimed that the lower the number of the acid sites, the slower the coke formation and the faster the o-xylene oxidation on the Pd/HFAU catalysts (Dege et al., 2000). Although higher acidity can accelerate the catalytic reaction and bring about higher activity, Pd/beta displayed the highest activity for VOC removal compared with Pd/ZSM-5, Pd/SBA-15, Pd/MCM-48, and Pd/MCM-41, but showed poor stability for its higher acidity, causing the formation of coke (He et al., 2009). The mesoporous SiO_2-supported Pt–Pd catalyst exhibited high catalytic activity, and no coke was formed during the catalytic combustion of toluene (Wang H. et al., 2017). In most instances, the catalyst can be regenerated from the coke deactivation by oxidizing under air or treating the catalyst at much high temperature conditions. Hence, more endeavors should be devoted to prepare catalysts with anti-coking ability and finding the equilibrium point between high activity and coke formation over Pd-supported catalysts based on the acidity of the supports.

Chlorine, Nitrogen, and Sulfur Poisoning

A promising and superior candidate for industrial applications should have high catalytic performance and outstanding stability. However, sometimes the catalysts may suffer from deactivation, especially with heteroatom-containing VOCs. Catalyst poisoning occurs in a way by disabling the active sites of the catalysts. The mineralization rate of the VOCs with heteroatoms was lower than that of VOCs without heteroatoms, as the heteroatom-containing functional groups decelerated the mineralization process (He et al., 2020). For example, the presence of chlorine in the catalysts caused deactivation in catalytic oxidation of chlorinated VOCs. The inhibitory effects of chorine were caused by the partial blockage of metal active sites, thus decreasing their ability for the chemisorption of reactants (Kondarides and Verykios, 1998). On the other hand, the formation of less active oxychlorinated species (MO_xCl_y) takes place (Paulis et al., 2001). Aranzabal et al. reported that the increasing amounts of environmentally undesirable chlorine at temperatures below 400°C were produced over Pd/alumina catalyst for dichloroethane gas-phase oxidation due to its activity in Deacon reaction (Aranzabal et al., 2006). Pd catalysts usually display superior activity for the catalytic oxidation of hydrocarbons (Xiong et al., 2018); however, it also suffers from severe deactivation, which can be attributed to the formation of polychlorinated [$PhCl_x$ (x = 2–6)] by-products through the chlorination of the organic skeleton (van den Brink et al., 2000). Leclercq et al. claimed that the pre-reduced Pd/$LaBO_3$ was more active than the perovskite alone for chlorobenzene (PhCl) transformation but substantially increased the chlorination rate of PhCl (Giraudon et al., 2008a). Cao and his coworkers found that the decrease in the selectivity of the Pd/TiO_2 catalyst was observed in the long-term stability test for catalytic combustion of dichloromethane, which was related to the deposition of carbon species and chlorine poisoning, thereby blocking the active sites for dichloromethane decomposition. Furthermore, their results indicated that the adsorption of chlorine species could change the chemical states of Pd and produced inactive species (Cao et al., 2018). However, alloying of gold with Pd supported on the three-dimensionally ordered macroporous CeO_2 improved the catalytic stability and chlorine tolerance in trichloroethylene combustion (Zhang et al., 2019a). Nitrogen-containing VOCs caused the deactivation of catalysts and decreased the catalytic performance by the formation of toxic intermediates (HCN, NO, N_2O, NH_3, CO, etc.) and sulfur-containing VOCs deactivated the catalyst by covering the active sites on the surface. Pd catalysts were unsuitable for nitrile oxidation on account of undesirable generation of NO_x (Krocher and Elsener, 2009). Pd/SBA-15 displayed a higher conversion of acetonitrile along with the production of harmful by-products (Zhang et al., 2014). The low porosity of Pd/S-2GA (grafting) resulted in higher NO_x yield for n-butylamine combustion, as high porosity can promote the diffusion of NH_x and decrease the contact between NH_x and Pd active sites, thereby decreasing the yield of NO_x (Ma et al., 2020). The presence of OH radicals promotes the conversion of NH_3/NH^{4+} to NO_3^- through the strong oxidizing ability of the OH radicals (Kim and Choi, 2002). Yu et al. stated that the poisoning effect of sulfur was attributed to the formation of aluminum sulfate on Pd/Al_2O_3 over 473 K (Yu and Shaw, 1998).

Influence of Thermal Sintering

Although noble metals including Pd are highly active in the catalytic oxidation of VOCs, they can also be deactivated by thermal sintering, which leads to the loss of catalytic surface area

TABLE 4 | Catalytic oxidation of representative VOCs with different kinetic models.

Catalyst	VOCs	Kinetic model	References
Pd/C	Toluene	Langmuir–Hinshelwood	Bedia et al. (2010)
$Pd/LaBO_3$ (B = Co, Fe, Ni, Mn)	Chlorobenzene	MVK	Yang et al. (2012)
Pd/ZSM-5/MCM-48	Benzene	MVK	He et al. (2010b)
Pd–Ce/γ-Al_2O_3	Toluene	MVK	Ren et al. (2020)
TiO_2/PdW	Benzene	MVK	Liang et al. (2019)
Pd/ZSM-5	Benzene	MVK	He et al. (2010a)
Pd/HY	Methanol	MVK	Jablonska et al. (2015)
Pd/Al_2O_3	Trichloroethylene	Eley–Rideal	Aranzabal 2003)

MVK, Mars–van Krevelen; VOCs, volatile organic compounds.

and alters the physicochemical properties of catalysts influencing the thermal stability under oxidative conditions (Krocher and Elsener, 2009; Wang N. F. et al., 2017). The catalyst can also be deactivated by a decrease in the number of active sites or change in the active site distribution ascribed to catalyst structural variations induced by thermal sintering (Bartholomew, 2001). Furthermore, the thermal sintering of the active phase is generally irreversible. Thermal sintering of the Pd atoms, clusters, and NPs caused catalyst deactivation during prolonged operation *via* Ostwald ripening (Xu et al., 2011; Spezzati et al., 2017). Monolayer films of $Pd@CeO_2$ core–shell nanocomposites exhibited excellent thermal stability and strong resistance to sintering in comparison with the bare Pd NPs (Adijanto et al., 2013). Confining noble metal nanoparticles or metal oxide in zeolite crystals prevents the agglomeration of active phases due to the size confinement of zeolite (Wu et al., 2019). The introduction of mesopores into zeolites can avoid the formation of coke and active phase sintering, and promote the mass transfer. Transition metal oxide functionalized mesoporous ZSM-5 single crystals with b-axis-aligned mesopores (M-ZSM-5-Oms) act as efficient and stable support for dispersing PdO. The Pd/M-ZSM-5-Oms displayed extraordinary catalytic performance and thermal stability for the degradation of benzene under low-temperature reaction conditions (Liu F. J. et al., 2014).

REACTION MECHANISMS

Catalytic oxidation is a dynamic and complex *in situ* surface reaction process. The research studies about the surface oxidation mechanisms of VOCs over Pd-supported catalysts play an important role to elucidate the total catalytic process and the relationship between the catalytic performance and the catalyst structure.

Kinetic Models

Many research groups have explored the reaction mechanism of Pd-based catalysts to oxidize VOCs. In general, three degradation mechanisms were proposed to describe the catalytic combustion of VOCs over Pd-supported catalysts: Mars–van Krevelen (MVK) model (two-stage redox model), Langmuir–Hinshelwood (L-H) model, and the Eley–Rideal (E-R) model (**Table 4**). The MVK model is based on the assumption of a constant oxygen surface concentration on the catalyst, with reaction occurring through the interaction between reactant molecules and an oxidized portion of the catalyst (Tidahy et al., 2006). The L-H mechanism emphasizes the surface reaction between the adsorbed molecules on analogous active sites, and the surface reaction between the adsorbed reactant and molecules from the gas phase was included in the E-R mechanism (Kamal et al., 2016). Among them, the MVK kinetic model is usually adapted to elucidate the VOC oxidation process over Pd-supported catalysts (He et al., 2010a; He et al., 2010b; Jablonska et al., 2015; Liang et al., 2019). However, unlike the conventional Pd-based catalysts in which the MVK mechanism governs the oxidation of VOCs, the catalytic oxidation of toluene over Pd supported on mesoporous activated carbons followed the L-H mechanism (Bedia et al., 2010). The catalytic oxidation of gaseous trichloroethylene on Pd/alumina catalysts was explained by the E-R–type mechanism (Aranzabal, 2003). Therefore, it can be concluded that the validity of each mechanism is determined by the catalyst composition and the VOC composition.

Mechanism Studies of Volatile Organic Compound Oxidation

The reaction mechanism differs under the variations of the reaction circumstances, such as the catalyst elemental composition, physicochemical properties, the pollutant composition, and reaction conditions. Generally, the degradation process of VOCs may contain several steps of surface reactions, following the transformation of long carbon chain to short carbon chain species (CO_2 as the final product). The investigation of the reaction mechanism or the oxidation pathway over the catalyst was studied by analyzing the gaseous intermediates and the product accumulated on the catalyst surface on the basis of a series of characterization techniques. Gas chromatography–mass spectrometer is the most widely used analytical instrument for the identification of intermediates based on the discrepancy of the charge–mass ratio (Bi et al., 2020). Proton transfer reaction–mass spectrometry based on the proton affinity of the VOCs can be also applied to investigate the reaction process of VOC oxidation (Zhong et al., 2020). Furthermore, IR spectroscopy, as a common characterization technology, is frequently utilized in detecting the intermediates formed in the oxidation process, such as *in situ* diffuse reflectance Fourier transform infrared spectroscopy (*in situ* DRIFT) and Fourier transform infrared spectroscopy (FT-IR) (Ryczkowski, 2001;

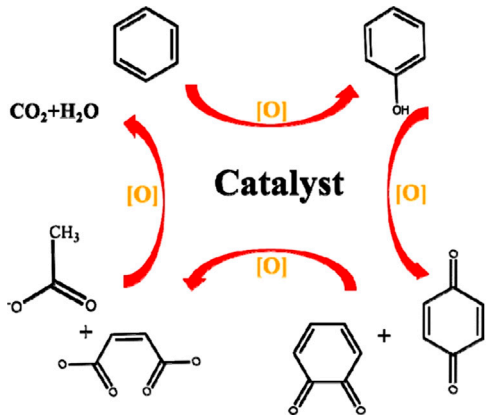

FIGURE 1 | Proposed mechanism of benzene oxidation over the TiO_2/PdW-S catalyst. Reprinted with permission from ref 151. Copyright (2019) American Chemical Society.

Yang K. et al., 2019). Based on the changes in vibrational frequency and intensity of the probe, the properties of the active centers can be deduced. Other characterization techniques (H_2-TPR, VOC-TPD, XPS, etc.) have also been utilized to elucidate the reaction mechanism.

A series of investigations have been carried out for a deep understanding of the oxidation pathway or reaction mechanism of some typical VOC oxidation. Dong et al. reported the catalytic oxidation mechanism of propane over hierarchical silicalite-1 zeolite enveloping Pd–CeO_2 nanowires by analyzing intermediate species through *in situ* DRIFTS during the catalytic reaction process (Dong et al., 2020). It was proposed that the overall catalytic oxidation reaction included three steps: 1) adsorption of propane over the S-1 shell and reaction with lattice oxygen from cerium oxide to form enolate or acetone species; 2) decomposition of enolate or acetone species and subsequent formation of bicarbonate and formate species by lattice oxygen; and 3) further oxidation of bicarbonate and formate species into H_2O and CO_2, which underwent refilling of the lattice of cerium oxide by the gaseous oxygen. The benzene oxidation pathway over TiO_2/PdW-S was proposed by Liang et al. (Liang et al., 2019) (**Figure 1**). It was proposed that benzene was initially oxidized by the surface oxygen to form phenolate species, followed by the transformation of phenolate species into the benzoquinone (e.g., o-benzoquinone and p-benzoquinone) species. At the same time, the carboxylate (e.g., acetate and maleate) species were also formed by the dissociation of bezene ring. Finally, the carboxylate species went through further oxidation into H_2O and CO_2 followed by the recovering of the catalyst. He et al. reported that the MVK kinetic model was valid for toluene oxidation and the oxidation step was decisive for the oxidation activity of Pd-supported catalysts (He et al., 2012b). The transformation of toluene to CO_2 and H_2O occurred over the oxidized Pd catalyst, and the reduced Pd catalyst was recovered by the adsorption and dissociation of O_2. Ning and coworkers investigated the catalytic performance of noble metal (Pd, Pt, Ru, and Rh) catalysts for chlorobenzene catalytic destruction. The reaction mechanism was proposed based on the result of the *in situ* FTIR analysis (Liu et al., 2019). The oxidation reaction started with the adsorption of chlorobenzene on the catalyst surface. Due to the lower bond energy of C–Cl than C–H, the breakage of C–Cl and the formation of surface phenolate species occurred. The *o*-benzoquinone or *p*-benzoquinone species were produced with the further oxidation of phenolate species. Following this, benzene ring was destructed to small-molecule intermediates (maleate, maleic, or anhydride) under nucleophilic oxygen (e.g., O_2^{2-}, O^-, or O^{2-}) attack. Subsequently, the produced intermediates were further oxidized to COx, H_2O, HCl, and Cl_2. It is well known that the characterization techniques used until now are conducive to get a better comprehension of the reaction mechanism; however, more studies need to be carried out to reflect the whole catalytic process more intuitively.

CONCLUSIONS

Facing the increasingly urgent demand for the abatement of VOCs, catalytic oxidation has become a promising technique for its high efficiency and economic feasibility, compared with other technologies for VOC removal. Generally, supported noble metal catalysts possess superior activity than non-noble metal oxides and mixed metal catalysts for VOC catalytic oxidation. Pd-supported catalysts are most extensively investigated for the catalytic oxidation of VOCs owing to their excellent catalytic performance. Although Pd-based catalysts usually displayed high activity, they still suffer from several disadvantages, such as lower activity due to the presence of water and multicomponent VOCs, the formation of coke, and low resistance to heteroatom poisoning (such as Cl, S, and N).

Therefore, more attention should be paid to extend the application of Pd-supported catalysts with high activity and stability. Future efforts should be devoted to the following aspects:

(1) With the aim to find the equilibrium point between activity and the formation of coke on the Pd-supported catalysts, the promoting effect of the support's acidity on the catalytic oxidation of VOCs should be investigated in depth.
(2) It is well known that VOC mixtures are always produced along with industrial emissions. Therefore, the mutual effect on the catalytic oxidation of mixed VOCs should be seriously taken into consideration, which can give insights for developing low-cost and efficient catalysts for industrial applications.
(3) It was demonstrated that the heteroatom-containing (such as S, F, N, Cl, and Br) VOCs are highly toxic to the Pd catalyst due to the formation of strong Pd–heteroatom chemical bond. Therefore, catalysts with high stability and strong resistance to heteroatom poisoning are highly desirable.
(4) New characterization techniques and the combination of existing characterization techniques to study catalyst poisoning and to reveal migration and transformation of intermediate species during the VOC degradation process should be explored.

(5) Efficient degradation of VOCs with low-cost and high efficiency is still a great challenge. Attention should also be paid to the preparation of single-atom catalysts, as single-atom catalysts can obtain 100% atomic utilization, greatly reducing the cost of catalysts.

AUTHOR CONTRIBUTIONS

SN wrote and formatted this review. SZ and XZ communicated and revised this manuscript. PV revised the manuscript. MW supervised and revised the manuscript.

FUNDING

This study was financially supported by the National Natural Science Foundation of China (21707020) and the Natural Science Foundation of Guangdong Province, China (2019A1515011469).

ACKNOWLEDGMENTS

PV would like to acknowledge The Royal Society-Newton International Fellowship for her postdoctoral research funding (NIF\R1\180185) at the University of Southampton.

REFERENCES

Adijanto, L., Bennett, D. A., Chen, C., Yu, A. S., Cargnello, M., Fornasiero, P., et al. (2013). Exceptional thermal stability of Pd@CeO_2 core-shell catalyst nanostructures grafted onto an oxide surface. *Nano Lett.* 13, 2252–2257. doi:10.1021/nl4008216

Aguero, F. N., Barbero, B. P., Gambaro, L., and Cadús, L. E. (2009). Catalytic combustion of volatile organic compounds in binary mixtures over MnOx/Al_2O_3 catalyst. *Appl. Catal. B Environ.* 91 (1–2), 108–112. doi:10.1016/j.apcatb.2009.05.012

Ahn, C. W., You, Y.-W., Heo, I., Hong, J. S., Jeon, J.-K., Ko, Y.-D., et al. (2017). Catalytic combustion of volatile organic compound over spherical-shaped copper–manganese oxide. *J. Ind. Eng. Chem.* 47, 439–445. doi:10.1016/j.jiec.2016.12.018

Aranzabal, A. (2003). The reaction pathway and kinetic mechanism of the catalytic oxidation of gaseous lean TCE on Pd/alumina catalysts. *J. Catal.* 214 (1), 130–135. doi:10.1016/S0021-9517(02)00091-X

Aranzabal, A., González-Marcos, J. A., Ayastuy, J. L., and González-Velasco, J. R. (2006). Kinetics of Pd/alumina catalysed 1,2-dichloroethane gas-phase oxidation. *Chem. Eng. Sci.* 61 (11), 3564–3576. doi:10.1016/j.ces.2005.12.031

Aznárez, A., Gil, A., and Korili, S. A. (2015). Performance of palladium and platinum supported on alumina pillared clays in the catalytic combustion of propene. *RSC Adv.* 5 (100), 82296–82309. doi:10.1039/C5RA15675K

Barakat, T., Idakiev, V., Cousin, R., Shao, G.-S., Yuan, Z.-Y., Tabakova, T., et al. (2014a). Total oxidation of toluene over noble metal based Ce, Fe and Ni doped titanium oxides. *Appl. Catal. B Environ.* 146, 138–146. doi:10.1016/j.apcatb.2013.05.064

Barakat, T., Rooke, J. C., Cousin, R., Lamonier, J.-F., Giraudon, J.-M., Su, B.-L., et al. (2014b). Investigation of the elimination of VOC mixtures over a Pd-loaded V-doped TiO_2 support. *New J. Chem.* 38, 2066–2074. doi:10.1039/C3NJ01190A

Bartholomew, C. H. (2001). Mechanisms of catalyst deactivation. *Appl. Catal. Gen.* 212, 17–60. doi:10.1016/S0926-860X(00)00843-7

Becker, L., and Förster, H. (1997). Investigations of coke deposits formed during deep oxidation of benzene over Pd and Cu exchanged Y-type zeolites. *Appl. Catal. Gen.* 153, 31–41. doi:10.1016/S0926-860X(96)00344-4

Bedia, J., Rosas, J. M., Rodríguez-Mirasol, J., and Cordero, T. (2010). Pd supported on mesoporous activated carbons with high oxidation resistance as catalysts for toluene oxidation. *Appl. Catal. B Environ.* 94 (1–2), 8–18. doi:10.1016/j.apcatb.2009.10.015

Bendahou, K., Cherif, L., Siffert, S., Tidahy, H. L., Benaïssa, H., and Aboukaïs, A. (2008). The effect of the use of lanthanum-doped mesoporous SBA-15 on the performance of Pt/SBA-15 and Pd/SBA-15 catalysts for total oxidation of toluene. *Appl. Catal. Gen.* 351 (1), 82–87. doi:10.1016/j.apcata.2008.09.001

Bernal, S., Blanco, G., Pintado, J. M., Rodríguez-Izquierdo, J. M., and Yeste, M. P. (2005). An alternative way of reporting on the redox behaviour of ceria-based catalytic materials: temperature-chemical environment-oxidation state diagrams. *Catal. Commun.* 6 (9), 582–585. doi:10.1002/sia.1266

Bi, F., Zhang, X., Chen, J., Yang, Y., and Wang, Y. (2020). Excellent catalytic activity and water resistance of UiO-66-supported highly dispersed Pd nanoparticles for toluene catalytic oxidation. *Appl. Catal. B Environ.* 269, 118767. doi:10.1016/j.apcatb.2020.118767

bin Saiman, M. I., Brett, G. L., Tiruvalam, R., Forde, M. M., Sharples, K., Thetford, A., et al. (2012). Involvement of surface-bound radicals in the oxidation of toluene using supported Au-Pd nanoparticles. *Angew. Chem. Int. Ed. Engl.* 51 (24), 5981–5985. doi:10.1002/anie.201201059

Boeglin, M. L., Wessels, D., and Henshel, D. (2006). An investigation of the relationship between air emissions of volatile organic compounds and the incidence of cancer in Indiana counties. *Environ. Res.* 100 (2), 242–254. doi:10.1016/j.envres.2005.04.004

Boltic, Z., Ruzic, N., Jovanovic, M., Savic, M., Jovanovic, J., and Petrovic, S. (2013). Cleaner production aspects of tablet coating process in pharmaceutical industry: problem of VOCs emission. *J. Clean. Prod.* 44, 123–132. doi:10.1016/j.jclepro.2013.01.004

Cao, S., Fei, X., Wen, Y., Sun, Z., Wang, H., and Wu, Z. (2018). Bimodal mesoporous TiO_2 supported Pt, Pd and Ru catalysts and their catalytic performance and deactivation mechanism for catalytic combustion of dichloromethane (CH_2Cl_2). *Appl. Catal. Gen.* 550, 20–27. doi:10.1016/j.apcata.2017.10.006

Chang, C. R., Huang, Z.-Q., and Li, J. (2016). The promotional role of water in heterogeneous catalysis: mechanism insights from computational modeling. *Wiley Interdiscip. Rev. Comput. Mol. Sci.* 6 (6), 679–693. doi:10.1002/wcms.1272

Chen, T., and Rodionov, V. O. (2016). Controllable catalysis with nanoparticles: bimetallic alloy systems and surface adsorbates. *ACS Catal.* 6 (6), 4025–4033. doi:10.1021/acscatal.6b00714

Chen, Z., Li, J., Yang, P., Cheng, Z., Li, J., and Zuo, S. (2019a). Ce-modified mesoporous γ-Al_2O_3 supported Pd-Pt nanoparticle catalysts and their structure-function relationship in complete benzene oxidation. *Chem. Eng. J.* 356, 255–261. doi:10.1016/j.cej.2018.09.040

Chen, Z., Situ, D., Zheng, J., and Cheng, Z. (2019b). Y-modified MCM-22 supported PdOx nanocrystal catalysts for catalytic oxidation of toluene. *Catalysts* 9 (11), 902. doi:10.3390/catal9110902

Dai, Q. G., Zhu, Q., Lou, Y., and Wang, X. (2018). Role of Brønsted acid site during catalytic combustion of methane over PdO/ZSM-5: dominant or negligible? *J. Catal.* 357, 29–40. doi:10.1016/j.jcat.2017.09.022

Dege, P., Pinard, L., Magnoux, P., and Guisnet, M. (2000). Catalytic oxidation of volatile organic compounds II. Influence of the physicochemical characteristics of Pd/HFAU catalysts on the oxidation of o-xylene. *Appl. Catal. B Environ.* 27, 17–26. doi:10.1016/S0926-3373(00)00135-1

de la Peña O'Shea, V. A., Álvarez-Galván, M. C., Fierro, J. L. G., and Arias, P. L. (2005). Influence of feed composition on the activity of Mn and PdMn/Al_2O_3 catalysts for combustion of formaldehyde/methanol. *Appl. Catal. B Environ.* 57 (3), 191–199. doi:10.1016/j.apcatb.2004.11.001

Dong, T., Liu, W., Ma, M., Peng, H., Yang, S., Tao, J., et al. (2020). Hierarchical zeolite enveloping Pd-CeO_2 nanowires: an efficient adsorption/catalysis bifunctional catalyst for low temperature propane total degradation. *Chem. Eng. J.* 393, 124717. doi:10.1016/j.cej.2020.124717

Dumanoglu, Y., Kara, M., Altiok, H., Odabasi, M., Elbir, T., and Bayram, A. (2014). Spatial and seasonal variation and source apportionment of volatile organic compounds (VOCs) in a heavily industrialized region. *Atmos. Environ.* 98, 168–178. doi:10.1016/j.atmosenv.2014.08.048

Enache, D. I., Edwards, J. K., Landon, P., and Solsona, B. (2006). Solvent-free oxidation of primary alcohols to aldehydes using Au-Pd/TiO_2 catalysts. *Science* 311 (5759), 362–365. doi:10.1126/science.1120560

Flytzani-Stephanopoulos, M. (2017). Supported metal catalysts at the single-atom limit - a viewpoint. *Chin. J. Catal.* 38 (9), 1432–1442. doi:10.1016/S1872-2067(17)62886-9

Garcia, T., Solsona, B., Cazorlaamoros, D., Linaressolano, A., and Taylor, S. (2006). Total oxidation of volatile organic compounds by vanadium promoted palladium-titania catalysts: comparison of aromatic and polyaromatic compounds. *Appl. Catal. B Environ.* 62 (1–2), 66–76. doi:10.1016/j.apcatb.2005.06.016

Garcia, T., Solsona, B., Murphy, D., Antcliff, K., and Taylor, S. (2005). Deep oxidation of light alkanes over titania-supported palladium/vanadium catalysts. *J. Catal.* 229 (1), 1–11. doi:10.1016/j.jcat.2004.09.018

Gil, S., Garcia-Vargas, J., Liotta, L., Pantaleo, G., Ousmane, M., Retailleau, L., et al. (2015). Catalytic oxidation of propene over Pd catalysts supported on CeO_2, TiO_2, Al_2O_3 and M/Al_2O_3 oxides (M = Ce, Ti, Fe, Mn). *Catalysts* 5 (2), 671–689. doi:10.3390/catal5020671

Giraudon, J. M., Elhachimi, A., and Leclercq, G. (2008a). Catalytic oxidation of chlorobenzene over Pd/perovskites. *Appl. Catal. B Environ.* 84 (1–2), 251–261. doi:10.1016/j.apcatb.2008.04.023

Giraudon, J. M., Nguyen, T. B., Leclercq, G., Siffert, S., Lamonier, J.-F., Aboukaïs, A., et al. (2008b). Chlorobenzene total oxidation over palladium supported on ZrO_2, TiO_2 nanostructured supports. *Catal. Today.* 137 (2–4), 379–384. doi:10.1016/j.cattod.2008.02.019

Gonzalez-Velasco, J. R., Aranzabal, A., López-Fonseca, R., Ferret, R., and González-Marcos, J. A. (2000). Enhancement of the catalytic oxidation of hydrogen-lean chlorinated VOCs in the presence of hydrogen-supplying compounds. *Appl. Catal. B Environ.* 24, 33–43. doi:10.1016/S0926-3373(99)00087-9

Guisnet, M., Costa, L., and Ribeiro, F. R. (2009). Prevention of zeolite deactivation by coking. *J. Mol. Catal. Chem.* 305 (1–2), 69–83. doi:10.1016/j.molcata.2008.11.012

Guisnet, M., and Magnoux, P. (1994). Fundamental description of deactivation and regeneration of acid zeolites. *Stud. Surf. Sci. Catal.* 88, 53–68. doi:10.1016/S0167-2991(08)62729-9

Gulsnet, M., and Magnoux, P. (1997). Deactivation by coking of zeolite catalysts. Prevention of deactivation. Optimal conditions for regeneration. *Catal. Today.* 36, 477–483. doi:10.1016/S0920-5861(96)00238-6

Guisnet, M., and Magnoux, P. (2001). Organic chemistry of coke formation. *Appl. Catal. Gen.* 212, 83–96. doi:10.1016/S0926-860X(00)00845-0

He, C., Cheng, J., Zhang, X., Douthwaite, M., Pattisson, S., and Hao, Z. (2019). Recent advances in the catalytic oxidation of volatile organic compounds: a review based on pollutant sorts and sources. *Chem. Rev.* 119 (7), 4471–4568. doi:10.1021/acs.chemrev.8b00408

He, C., Li, J., Cheng, J., Li, L., Li, P., Hao, Z., et al. (2009). Comparative studies on porous material-supported Pd catalysts for catalytic oxidation of benzene, toluene, and ethyl acetate. *Ind. Eng. Chem. Res.* 48, 6930–6936. doi:10.1021/ie900412c

He, C., Li, J., Li, P., Cheng, J., Hao, Z., and Xu, Z.-P. (2010a). Comprehensive investigation of Pd/ZSM-5/MCM-48 composite catalysts with enhanced activity and stability for benzene oxidation. *Appl. Catal. B Environ.* 96 (3–4), 466–475. doi:10.1016/j.apcatb.2010.03.005

He, C., Li, J., Zhang, X., Yin, L., Chen, J., and Gao, S. (2012a). Highly active Pd-based catalysts with hierarchical pore structure for toluene oxidation: catalyst property and reaction determining factor. *Chem. Eng. J.* 180, 46–56. doi:10.1016/j.cej.2011.10.099

He, C., Li, P., Cheng, J., Hao, Z.-P., and Xu, Z.-P. (2010b). A comprehensive study of deep catalytic oxidation of benzene, toluene, ethyl acetate, and their mixtures over Pd/ZSM-5 catalyst: mutual effects and kinetics. *Water Air Soil Pollut.* 209, 365–376. doi:10.1007/s11270-009-0205-7

He, C., Li, P., Cheng, J., Li, J., and Hao, Z. (2010c). Preparation and investigation of Pd/Ti-SBA-15 catalysts for catalytic oxidation of benzene. *Environ. Prog. Sustain. Energy.* 29 (4), 435–442. doi:10.1002/ep.10427

He, C., Li, Q., Li, P., Wang, Y., Zhang, X., Cheng, J., et al. (2010d). Templated silica with increased surface area and expanded microporosity: synthesis, characterization, and catalytic application. *Chem. Eng. J.* 162 (3), 901–909. doi:10.1016/j.cej.2010.06.037

He, C., Xu, L., Yue, L., Chen, Y., Chen, J., and Hao, Z. (2012b). Supported nanometric Pd hierarchical catalysts for efficient toluene removal: catalyst characterization and activity elucidation. *Ind. Eng. Chem. Res.* 51 (21), 7211–7222. doi:10.1021/ie201243c

He, C., Yue, L., Zhang, X., Li, P., Dou, B., Ma, C., et al. (2012c). Deep catalytic oxidation of benzene, toluene, ethyl acetate over Pd/SBA-15 catalyst: reaction behaviors and kinetics. *Asia Pac. J. Chem. Eng.* 7 (5), 705–715. doi:10.1002/apj.621

He, C., Zhang, F., Yue, L., Shang, X., Chen, J., and Hao, Z. (2012d). Nanometric palladium confined in mesoporous silica as efficient catalysts for toluene oxidation at low temperature. *Appl. Catal. B Environ.* 111, 46–57. doi:10.1016/j.apcatb.2011.09.017

He, F., Muliane, U., Weon, S., and Choi, W. (2020). Substrate-specific mineralization and deactivation behaviors of TiO_2 as an air-cleaning photocatalyst. *Appl. Catal. B Environ.* 275, 119145. doi:10.1016/j.apcatb.2020.119145

He, Z., He, Z., Wang, D., Bo, Q., Fan, T., and Jiang, Y. (2014). Mo-modified Pd/Al_2O_3 catalysts for benzene catalytic combustion. *J. Environ. Sci.* 26 (7), 1481–1487. doi:10.1016/j.jes.2014.05.014

Hong, J., Chu, W., Chen, M., Wang, X., and Zhang, T. (2007). Preparation of novel titania supported palladium catalysts for selective hydrogenation of acetylene to ethylene. *Catal. Commun.* 8 (3), 593–597. doi:10.1016/j.catcom.2006.08.010

Hosseini, M., Barakat, T., Cousin, R., Aboukaïs, A., Su, B.-L., De Weireld, G., et al. (2012). Catalytic performance of core–shell and alloy Pd–Au nanoparticles for total oxidation of VOC: the effect of metal deposition. *Appl. Catal. B Environ.* 111–112, 218–224. doi:10.1016/j.apcatb.2011.10.002

Hosseini, M., Haghighi, M., Kahforoushan, D., and Zarrabi, M. (2017). Sono-dispersion of ceria and palladium in preparation and characterization of Pd/Al_2O_3-clinoptilolite-CeO_2 nanocatalyst for treatment of polluted air via low temperature VOC oxidation. *Process Saf. Environ. Protect.* 106, 284–293. doi:10.1016/j.psep.2016.06.028

Huang, H. B., and Leung, D. Y. C., (2011). Complete oxidation of formaldehyde at room temperature using TiO_2 supported metallic Pd nanoparticles. *ACS Catal.* 1 (4), 348–354. doi:10.1021/cs200023p

Ihm, S.-K., Jun, Y.-D., Kim, D.-C., and Jeong, K.-E. (2004). Low-temperature deactivation and oxidation state of Pd/γ-Al_2O_3 catalysts for total oxidation of n-hexane. *Catal. Today.* 93–95, 149–154. doi:10.1016/j.cattod.2004.06.096

Iranpour, R., Cox, H. H. J., Deshusses, M. A., and Schroeder, E. D. (2005). Literature review of air pollution control biofilters and biotrickling filters for odor and volatile organic compound removal. *Environ. Prog.* 24 (3), 254–267. doi:10.1002/ep.10077

Jablonska, M., Król, A., Kukulska-Zając, E., Tarach, K., Girman, V., Chmielarz, L., et al. (2015). Zeolites Y modified with palladium as effective catalysts for low-temperature methanol incineration. *Appl. Catal. B Environ.* 166–167, 353–365. doi:10.1016/j.apcatb.2014.11.047

Jin, L. Y., Ma, R.-H., Lin, J.-J., Meng, L., Wang, Y.-J., and Luo, M.-F. (2011). Bifunctional Pd/Cr_2O_3–ZrO_2Catalyst for the oxidation of volatile organic compounds. *Ind. Eng. Chem. Res.* 50 (18), 10878–10882. doi:10.1021/ie200599v

Jinjun, L., Zheng, J., Zhengping, H., Xiuyan, X., and Yahui, Z. (2005). Pillared laponite clays-supported palladium catalysts for the complete oxidation of benzene. *J. Mol. Catal. Chem.* 225 (2), 173–179. doi:10.1016/j.molcata.2004.08.040

Kamal, M. S., Razzak, S. A., and Hossain, M. M. (2016). Catalytic oxidation of volatile organic compounds (VOCs)-a review. *Atmos. Environ.* 140, 117–134. doi:10.1016/j.atmosenv.2016.05.031

Kim, M. Y., Kyriakidou, E. A., Choi, J.-S., Toops, T. J., Binder, A. J., Thomas, C., et al. (2016). Enhancing low-temperature activity and durability of Pd-based diesel oxidation catalysts using ZrO_2 supports. *Appl. Catal. B Environ.* 187, 181–194. doi:10.1016/j.apcatb.2016.01.023

Kim, S., and Choi, W. (2002). Kinetics and mechanisms of photocatalytic degradation of $(CH_3)_nNH_{4-n}^+$ ($0 \le n \le 4$) in TiO_2 suspension: the role of OH radicals. *Environ. Sci. Technol.* 36, 2019–2025. doi:10.1021/es015560s

Kim, S. C., and Shim, W. G. (2009). Properties and performance of Pd based catalysts for catalytic oxidation of volatile organic compounds. *Appl. Catal. B Environ.* 92 (3–4), 429–436. doi:10.1016/j.apcatb.2009.09.001

Kim, S. C., and Shim, W. G. (2010). Catalytic combustion of VOCs over a series of manganese oxide catalysts. *Appl. Catal. B Environ.* 98 (3–4), 180–185. doi:10.1016/j.apcatb.2010.05.027

Kondarides, D. I., and Verykios, X. E. (1998). Effect of chlorine on the chemisorptive properties of Rh/CeO_2 catalysts studied by XPS and temperature programmed desorption techniques. *J. Catal.* 174, 52–64. doi:10.1006/jcat.1997.1938

Krocher, O., and Elsener, M. (2009). Hydrolysis and oxidation of gaseous HCN over heterogeneous catalysts. *Appl. Catal. B Environ.* 92, 75–89. doi:10.1016/j.apcatb.2009.07.021

Li, P., He, C., Cheng, J., Ma, C. Y., Dou, B. J., and Hao, Z. P. (2011). Catalytic oxidation of toluene over Pd/Co_3AlO catalysts derived from hydrotalcite-like compounds: effects of preparation methods. *Appl. Catal. B Environ.* 101 (3–4), 570–579. doi:10.1016/j.apcatb.2010.10.030

Li, Y., Zhang, C., Ma, J., Chen, M., Deng, H., and He, H. (2017). High temperature reduction dramatically promotes Pd/TiO_2 catalyst for ambient formaldehyde oxidation. *Appl. Catal. B Environ.* 217, 560–569. doi:10.1016/j.apcatb.2017.06.023

Liang, X., Chen, X., Zhang, J., Shi, T., Sun, X., Fan, L., et al. (2017). Reactivity-based industrial volatile organic compounds emission inventory and its implications for ozone control strategies in China. *Atmos. Environ.* 162, 115–126. doi:10.1016/j.atmosenv.2017.04.036

Liang, Y., Liu, Y., Deng, J., Zhang, K., Hou, Z., Zhao, X., et al. (2019). Coupled palladium-tungsten bimetallic nanosheets/TiO_2 hybrids with enhanced catalytic activity and stability for the oxidative removal of benzene. *Environ. Sci. Technol.* 53 (10), 5926–5935. doi:10.1021/acs.est.9b00370

Liao, H. C., Zuo, P., and Liu, M. (2016). Study on the correlation between the surface active species of Pd/cordierite monolithic catalyst and its catalytic activity. *Mater. Sci. Eng. B* 211, 45–52. doi:10.1016/j.mseb.2016.04.015

Liao, H. T., Chou, C. C.-K., Chow, J. C., Watson, J. G., Hopke, P. K., and Wu, C.-F. (2015). Source and risk apportionment of selected VOCs and PM2.5 species using partially constrained receptor models with multiple time resolution data. *Environ. Pollut.* 205, 121–130. doi:10.1016/j.envpol.2015.05.035

Liotta, L. F. (2010). Catalytic oxidation of volatile organic compounds on supported noble metals. *Appl. Catal. B Environ.* 100 (3–4), 403–412. doi:10.1016/j.apcatb.2010.08.023

Liu, F. J., Zuo, S., Wang, C., Li, J., Xiao, F.-S., and Qi, C. (2014). Pd/transition metal oxides functionalized ZSM-5 single crystals with b-axis aligned mesopores: efficient and long-lived catalysts for benzene combustion. *Appl. Catal. B Environ.* 148–149, 106–113. doi:10.1016/j.apcatb.2013.10.054

Liu, J., Wang, H., Chen, Y., Yang, M., and Wu, Y. (2014). Effects of pretreatment atmospheres on the catalytic performance of $Pd/\gamma\text{-}Al_2O_3$ catalyst in benzene degradation. *Catal. Commun.* 46, 11–16. doi:10.1016/j.catcom.2013.10.031

Liu, X., Chen, L., Zhu, T., and Ning, R. (2019). Catalytic oxidation of chlorobenzene over noble metals (Pd, Pt, Ru, Rh) and the distributions of polychlorinated by-products. *J. Hazard Mater.* 363, 90–98. doi:10.1016/j.jhazmat.2018.09.074

Lupescu, J. A., Schwank, J. W., Fisher, G. B., Chen, X., Peczonczyk, S. L., and Drews, A. R. (2016). Pd model catalysts: effect of aging duration on lean redispersion. *Appl. Catal. B Environ.* 185, 189–202. doi:10.1016/j.apcatb.2015.12.012

Ma, M., Jian, Y., Chen, C., and He, C. (2020). Spherical-like Pd/SiO_2 catalysts for n-butylamine efficient combustion: effect of support property and preparation method. *Catal. Today.* 339, 181–191. doi:10.1016/j.cattod.2018.11.024

Marécot, P., Fakche, A., Kellali, B., Mabilon, G., Prigent, P., and Barbier, J. (1994). Propane and propene oxidation over platinum and palladium on alumina: effects of chloride and water. *Appl. Catal. B Environ.* 3, 283–294. doi:10.1016/0926-3373(94)00003-4

Odoom-Wubah, T., Li, Q., Adilov, I., Huang, J., and Li, Q. (2019a). Towards efficient Pd/Mn_3O_4 catalyst with enhanced acidic sites and low temperature reducibility for benzene abatement. *Mol. Catal.* 477, 110558. doi:10.1016/j.mcat.2019.110558

Odoom-Wubah, T., Li, Q., Mulka, R., Chen, M., Huang, J., Li, Q., et al. (2019b). Calcified shrimp waste supported Pd NPs as an efficient catalyst toward benzene destruction. *ACS Sustain. Chem. Eng.* 8 (1), 486–497. doi:10.1021/acssuschemeng.9b05671

Odoom-Wubah, T., Li, Q., Wang, Q., Usha, M. Z. R., Huang, J., and Li, Q. (2019c). Template-free synthesis of carbon self-doped ZnO superstructures as efficient support for ultra fine Pd nanoparticles and their catalytic activity towards benzene oxidation. *Mol. Catal.* 469, 118–130. doi:10.1016/j.mcat.2019.03.013

Okumura, K., Kobayashi, T., Tanaka, H., and Niwa, M. (2003a). Toluene combustion over palladium supported on various metal oxide supports. *Appl. Catal. B Environ.* 44 (4), 325–331. doi:10.1016/S0926-3373(03)00101-2

Okumura, K., Matsumoto, S., Nishiaki, N., and Niwa, M. (2003b). Support effect of zeolite on the methane combustionactivity of palladium. *Appl. Catal. B Environ.* 40, 151–159. doi:10.1016/S0926-3373(02)00149-2

Padilla, J. M., Del Angel, G., and Navarrete, J. (2008). Improved $Pd/\gamma\text{-}Al_2O_3$-Ce catalysts for benzene combustion. *Catal. Today.* 133–135, 541–547. doi:10.1016/j.cattod.2007.12.053

Paulis, M., Peyrard, H., and Montes, M. (2001). Influence of chlorine on the activity and stability of Pt/Al_2O_3 catalysts in the complete oxidation of toluene. *J. Catal.* 199 (1), 30–40. doi:10.1006/jcat.2000.3146

Pérez-Cadenas, A. F., Morales-Torres, S., Kapteijn, F., Maldonado-Hódar, F. J., Carrasco-Marín, F., Moreno-Castilla, C., et al. (2008). Carbon-based monolithic supports for palladium catalysts: the role of the porosity in the gas-phase total combustion of m-xylene. *Appl. Catal. B Environ.* 77 (3–4), 272–277. doi:10.1016/j.apcatb.2007.07.030

Pitkäaho, S., Nevanperä, T., Matejova, L., Ojala, S., and Keiski, R. L. (2013). Oxidation of dichloromethane over Pt, Pd, Rh, and V_2O_5 catalysts supported on Al_2O_3, Al_2O_3-TiO_2 and Al_2O_3-CeO_2. *Appl. Catal. B Environ.* 138–139, 33–42. doi:10.1016/j.apcatb.2013.01.058

Qiu, K., Yang, L., Lin, J., Wang, P., Yang, Y., Ye, D., et al. (2014). Historical industrial emissions of non-methane volatile organic compounds in China for the period of 1980–2010. *Atmos. Environ.* 86, 102–112. doi:10.1016/j.atmosenv.2013.12.026

Ramírez-López, R., Elizalde-Martinez, I., and Balderas-Tapia, L. (2010). Complete catalytic oxidation of methane over Pd/CeO_2-Al_2O_3: the influence of different ceria loading. *Catal. Today.* 150 (3–4), 358–362. doi:10.1016/j.cattod.2009.10.007

Ren, S., Liang, W., Li, Q., and Zhu, Y. (2020). Effect of Pd/Ce loading on the performance of Pd-Ce/gamma-Al_2O_3 catalysts for toluene abatement. *Chemosphere* 251, 126382. doi:10.1016/j.chemosphere.2020.126382

Rooke, J. C., Barakat, T., Siffert, S., and Su, B.-L. (2012). Total catalytic oxidation of toluene using Pd impregnated on hierarchically porous Nb_2O_5 and Ta_2O_5 supports. *Catal. Today.* 192 (1), 183–188. doi:10.1016/j.cattod.2011.10.011

Ryczkowski, J. (2001). IR spectroscopy in catalysis. *Catal. Today.* 68, 263–381. doi:10.1016/S0920-5861(01)00334-0

Ryndin, Y. A., Hicks, R. F., Bell, A. T., and Yermakov, Y. I. (1981). Effects of metal-support interactions on the synthesis of methanol over palladium. *J. Catal.* 70, 287–297. doi:10.1016/0021-9517(81)90341-9

Santos, V. P., Carabineiro, S. A. C., Tavares, P. B., Pereira, M. F. R., Órfão, J. J. M., and Figueiredo, J. L. (2010a). Oxidation of CO, ethanol and toluene over TiO_2 supported noble metal catalysts. *Appl. Catal. B Environ.* 99 (1–2), 198–205. doi:10.1016/j.apcatb.2010.06.020

Santos, V. P., Pereira, M. F. R., Órfão, J. J. M., and Figueiredo, J. L. (2010b). The role of lattice oxygen on the activity of manganese oxides towards the oxidation of volatile organic compounds. *Appl. Catal. B Environ.* 99 (1–2), 353–363. doi:10.1016/j.apcatb.2010.07.007

Scire, S., and Liotta, L. F. (2012). Supported gold catalysts for the total oxidation of volatile organic compounds. *Appl. Catal. B Environ.* 125, 222–246. doi:10.1016/j.apcatb.2012.05.047

Shi, H. X., Chen, J., Li, G., Nie, X., Zhao, H., Wong, P.-K., et al. (2013). Synthesis and characterization of novel plasmonic Ag/AgX-CNTs (X = Cl, Br, I) nanocomposite photocatalysts and synergetic degradation of organic pollutant under visible light. *ACS Appl. Mater. Interfaces.* 5 (15), 6959–6967. doi:10.1021/am401459c

Spezzati, G., Su, Y., Hofmann, J. P., Benavidez, A. D., DeLaRiva, A. T., McCabe, J., et al. (2017). Atomically dispersed Pd-O species on CeO_2(111) as highly active sites for low-temperature CO oxidation. *ACS Catal.* 7 (10), 6887–6891. doi:10.1021/acscatal.7b02001

Srivastava, A., Joseph, A. E., Patil, S., More, A., Dixit, R. C., and Prakash, M. (2005). Air toxics in ambient air of Delhi. *Atmos. Environ.* 39 (1), 59–71. doi:10.1016/j.atmosenv.2004.09.053

Tang, W., Deng, Y., and Chen, Y. (2017). Promoting effect of acid treatment on Pd-Ni/SBA-15 catalyst for complete oxidation of gaseous benzene. *Catal. Commun.* 89, 86–90. doi:10.1016/j.catcom.2016.10.032

Tauster, S. J., Fung, S. C., and Garten, R. L. (1978). Strong metal-support interactions. Group 8 noble metals supported on titanium dioxide. *J. Am. Chem. Soc.* 100 (1), 170–175. doi:10.1021/ja00469a029

Taylor, M. N., Zhou, W., Garcia, T., Solsona, B., Carley, A. F., Kiely, C. J., et al. (2012). Synergy between tungsten and palladium supported on titania for the

catalytic total oxidation of propane. *J. Catal.* 285, 103–114. doi:10.1016/j.jcat.2011.09.019

Tidahy, H. L., Hosseni, M., Siffert, S., Cousin, R., Lamonier, J.-F., Aboukaïs, A., et al. (2008). Nanostructured macro-mesoporous zirconia impregnated by noble metal for catalytic total oxidation of toluene. *Catal. Today.* 137, 335–339. doi:10.1016/j.cattod.2007.09.008

Tidahy, H. L., Siffert, S., Lamonier, J.-F., Zhilinskaya, E. A., Aboukaïs, A., Yuan, Z.-Y., et al. (2006). New Pd/hierarchical macro-mesoporous ZrO_2, TiO_2 and ZrO_2-TiO_2 catalysts for VOCs total oxidation. *Appl. Catal. Gen.* 310, 61–69. doi:10.1016/j.apcata.2006.05.020

Tomatis, M., Xu, H.-H., He, J., and Zhang, X.-D. (2016). Recent development of catalysts for removal of volatile organic compounds in flue gas by combustion: a review. *J. Chem.* 2016, 1–15. doi:10.1155/2016/8324826

van den Brink, R. W., Krzan, M., Feijen-Jeurissen, M. M. R., Louw, R., and Mulder, P. (2000). The role of the support and dispersion in the catalytic combustion of chlorobenzene on noble metal based catalysts. *Appl. Catal. B Environ.* 24, 255–264. doi:10.1016/S0926-3373(99)00113-7

Venezia, A. M., Di Carlob, G., Liottaa, L. F., Pantaleoa, G., and Kantchevac, M. (2011). Effect of Ti(IV) loading on CH_4 oxidation activity and SO_2 tolerance of Pd catalysts supported on silica SBA-15 and HMS. *Appl. Catal. B Environ.* 106 (3–4), 529–539. doi:10.1016/j.apcatb.2011.06.013

Vu, V. H., Belkouch, J., Ould-Dris, A., and Taouk, B. (2009). Removal of hazardous chlorinated VOCs over Mn-Cu mixed oxide based catalyst. *J. Hazard Mater.* 169 (1–3), 758–765. doi:10.1016/j.jhazmat.2009.04.010

Wang, H., Yang, W., Tian, P., Zhou, J., Tang, R., and Wu, S. (2017). A highly active and anti-coking Pd-Pt/SiO_2 catalyst for catalytic combustion of toluene at low temperature. *Appl. Catal. Gen.* 529, 60–67. doi:10.1016/j.apcata.2016.10.016

Wang, N. F., Li, S., Zong, Y., and Yao, Q. (2017). Sintering inhibition of flame-made Pd/CeO_2 nanocatalyst for low-temperature methane combustion. *J. Aerosol Sci.* 105, 64–72. doi:10.1016/j.jaerosci.2016.11.017

Wang, Y., Xiao, L., Zhao, C., Liu, F., and Li, S. (2018a). Catalytic combustion of toluene with Pd/$La_{0.8}Ce_{0.2}MnO_3$ supported on different zeolites. *Environ. Prog. Sustain. Energy.* 37 (1), 215–220. doi:10.1002/ep.12656

Wang, Y., Zhang, C., and He, H. (2018b). Insight into the role of Pd state on Pd-based catalysts in o-xylene oxidation at low temperature. *ChemCatChem* 10 (5), 998–1004. doi:10.1002/cctc.201701547

Wang, Y., Zhang, C., Liu, F., and He, H. (2013). Well-dispersed palladium supported on ordered mesoporous Co_3O_4 for catalytic oxidation of o-xylene. *Appl. Catal. B Environ.* 142–143, 72–79. doi:10.1016/j.apcatb.2013.05.003

Wang, Y., Zhang, C., Yu, Y., Yue, R., and He, H. (2015). Ordered mesoporous and bulk Co_3O_4 supported Pd catalysts for catalytic oxidation of o-xylene. *Catal. Today.* 242, 294–299. doi:10.1016/j.cattod.2014.06.032

Wei, Y., Zhang, X., Liu, Y., Jia, C., and Yang, P. (2020). Ternary PtNiCu self-assembled nanocubes for plasmon-enhanced electrocatalytic hydrogen evolution and methanol oxidation reaction in visible light. *Electrochim. Acta.* 349, 136366. doi:10.1016/j.electacta.2020.136366

Weng, X., Shi, B., Liu, A., Sun, J., Xiong, Y., Wan, H., et al. (2019). Highly dispersed Pd/modified-Al_2O_3 catalyst on complete oxidation of toluene: role of basic sites and mechanism insight. *Appl. Surf. Sci.* 497, 143747. doi:10.1016/j.apsusc.2019.143747

Wu, S. M., Yang, X.-Y., and Janiak, C. (2019). Confinement effects in zeolite-confined noble metals. *Angew. Chem. Int. Ed. Engl.* 58 (36), 12340–12354. doi:10.1002/anie.201900013

Wu, Z., Deng, J., Xie, S., Yang, H., Zhao, X., Zhang, K., et al. (2016). Mesoporous Cr_2O_3-supported Au-Pd nanoparticles: high-performance catalysts for the oxidation of toluene. *Microporous Mesoporous Mater.* 224, 311–322. doi:10.1016/j.micromeso.2015.11.061

Xia, Y., Xia, L., Liu, Y., Yang, T., Deng, J., and Dai, H. (2018). Concurrent catalytic removal of typical volatile organic compound mixtures over Au-Pd/alpha-MnO_2 nanotubes. *J. Environ. Sci.* 64, 276–288. doi:10.1016/j.jes.2017.06.025

Xie, P., Pu, T., Nie, A., Hwang, S., Purdy, S. C., Yu, W., et al. (2018). Nanoceria-supported single-atom platinum catalysts for direct methane conversion. *ACS Catal.* 8 (5), 4044–4048. doi:10.1021/acscatal.8b00004

Xiong, H. F., Wiebenga, M. H., Carrillo, C., Gaudet, J. R., Pham, H. N., Kunwar, D., et al. (2018). Design considerations for low-temperature hydrocarbon oxidation reactions on Pd based catalysts. *Appl. Catal. B Environ.* 236, 436–444. doi:10.1016/j.apcatb.2018.05.049

Xu, Q., Kharas, K. C., Croley, B. J., and Datye, A. K. (2011). The sintering of supported Pd automotive catalysts. *ChemCatChem* 3 (6), 1004–1014. doi:10.1002/cctc.201000392

Yang, K., Liu, Y., Deng, J., Zhao, X., Yang, J., Han, Z., et al. (2019). Three-dimensionally ordered mesoporous iron oxide-supported single-atom platinum: highly active catalysts for benzene combustion. *Appl. Catal. B Environ.* 244, 650–659. doi:10.1016/j.apcatb.2018.11.077

Yang, L., Ma, J., Hu, W., Dai, Q., Wang, L., Zhan, W., et al. (2016). Low-temperature methane combustion over Pd/H-ZSM-5: active Pd sites with specific electronic properties modulated by acidic sites of H-ZSM-5. *ACS Catal.* 6 (12), 8127–8139. doi:10.1021/acscatal.6b01801

Yang, W., Wang, H., and Fu, F. (2019). PdCu nanoalloys deposited on porous carbon as a highly efficient catalyst for ethanol oxidation. *Mater. Chem. Phys.* 228, 175–179. doi:10.1016/j.matchemphys.2019.02.075

Yang, X., Ma, X., Yu, X., and Ge, M. (2020). Exploration of strong metal-support interaction in zirconia supported catalysts for toluene oxidation. *Appl. Catal. B Environ.* 263, 118355. doi:10.1016/j.apcatb.2019.118355

Yang, X., Wang, A., Qiao, B., Li, J., Liu, J., and Zhang, T. (2012). Single-atom catalysts: a new frontier in heterogeneous catalysis. *Acc. Chem. Res.* 46, 1740–1748. doi:10.1021/ar300361m

Yang, Y. (2020). Carbon deposits during catalytic combustion of toluene on Pd-Pt-based catalysts. *Catal. Sci. Technol.* 10, 2452–2461. doi:10.1039/D0CY00101E

Yazawa, Y., Yoshida, H., Takagi, N., Komai, S.-i., Satsuma, A., and Hattori, T. (1999). Acid strength of support materials as a factor controlling oxidation state of palladium catalyst for propane combustion. *J. Catal.* 187 (1), 15–23. doi:10.1006/jcat.1999.2583

Yu, T. C., and Shaw, H. (1998). The effect of sulfur poisoning on methane oxidation over palladium supported on g-alumina catalysts. *Appl. Catal. B Environ.* 18, 105–114. doi:10.1016/S0926-3373(98)00031-9

Yu, W. Y., Zhang, L., Mullen, G. M., Henkelman, G., and Buddie Mullins, C. (2015). Oxygen activation and reaction on Pd-Au bimetallic surfaces. *J. Phys. Chem. C* 119 (21), 11754–11762. doi:10.1021/acs.jpcc.5b02970

Yuan, C. Z., Zhan, L.-Y., Liu, S.-J., Chen, F., Lin, H., Wu, X.-L., et al. (2020). Semi-sacrificial template synthesis of single-atom Ni sites supported on hollow carbon nanospheres for efficient and stable electrochemical CO_2 reduction. *Inorg. Chem. Front.* 7 (8), 1719–1725. doi:10.1039/C9QI01688K

Yue, L., He, C., Hao, Z., Wang, S., and Wang, H. (2014). Effects of metal and acidic sites on the reaction by-products of butyl acetate oxidation over palladium-based catalysts. *J. Environ. Sci.* 26 (3), 702–707. doi:10.1016/S1001-0742(13)60439-8

Zang, M., Zhao, C., Wang, Y., Liu, X., Cheng, Y., and Chen, S. (2019). Low temperature catalytic combustion of toluene over three-dimensionally ordered $La_{0.8}Ce_{0.2}MnO_3$/cordierite catalysts. *Appl. Surf. Sci.* 483, 355–362. doi:10.1016/j.apsusc.2019.03.320

Zeng, J., Liu, X., Wang, J., Lv, H., and Zhu, T. (2015). Catalytic oxidation of benzene over MnOx/TiO_2 catalysts and the mechanism study. *J. Mol. Catal. Chem.* 408, 221–227. doi:10.1016/j.molcata.2015.07.024

Zhang, R., Shi, D., Liu, N., Cao, Y., and Chen, B. (2014). Mesoporous SBA-15 promoted by 3d-transition and noble metals for catalytic combustion of acetonitrile. *Appl. Catal. B Environ.* 146, 79–93. doi:10.1016/j.apcatb.2013.03.028

Zhang, X., Liu, Y., Deng, J., Yu, X., Han, Z., Zhang, K., et al. (2019a). Alloying of gold with palladium: an effective strategy to improve catalytic stability and chlorine-tolerance of the 3DOM CeO_2 supported catalysts in trichloroethylene combustion. *Appl. Catal. B Environ.* 257, 117879, doi:10.1016/j.apcatb.2019.117879

Zhang, X., Lv, X., Shi, X., and Yang, Y. (2019b). Enhanced hydrophobic UiO-66 (University of Oslo 66) metal-organic framework with high capacity and selectivity for toluene capture from high humid air. *J. Colloid Interface Sci.* 539, 152–160. doi:10.1016/j.jcis.2018.12.056

Zhang, X., Yang, Y., Huang, W., Yang, Y., Wang, Y., He, C., et al. (2018). g-C_3N_4/UiO-66 nanohybrids with enhanced photocatalytic activities for the oxidation of dye under visible light irradiation. *Mater. Res. Bull.* 99, 349–358. doi:10.1016/j.materresbull.2017.11.028

Zhang, Z., Jiang, Z., and Shangguan, W. (2016). Low-temperature catalysis for VOCs removal in technology and application: a state-of-the-art review. *Catal. Today.* 264, 270–278. doi:10.1016/j.cattod.2015.10.040

Zhao, Q., Ge, Y., Fu, K., Zheng, Y., Liu, Q., Song, C., et al. (2019). Catalytic performance of the Pd/TiO_2 modified with MnOx catalyst for acetone total oxidation. *Appl. Surf. Sci.* 496, 143579. doi:10.1016/j.apsusc.2019.143579

Zhao, S., Hu, F., and Li, J. (2016). Hierarchical core–shell Al_2O_3@Pd-CoAlO microspheres for low-temperature toluene combustion. *ACS Catal.* 6 (6), 3433–3441. doi:10.1021/acscatal.6b00144

Zhao, W., Liu, Y., Wang, L., Chu, J., Qu, J., Hao, Z., et al. (2011). Catalytic combustion of benzene on the Pd/nanosize Al-HMS. *Microporous Mesoporous Mater.* 138 (1–3), 215–220. doi:10.1016/j.micromeso.2010.08.013

Zhao, X., Zhang, R., Liu, Y., Deng, J., Xu, P., Lv, S., et al. (2019). Pd/meso-CoO derived from in situ reduction of the one-step synthesized Pd/meso-Co_3O_4: high performance catalysts for benzene combustion. *New J. Chem.* 43, 12358–12368. doi:10.1039/C9NJ03039E

Zhong, J., Zeng, Y., Zhang, M., and Feng, W. (2020). Toluene oxidation process and proper mechanism over Co_3O_4 nanotubes: investigation through in-situ DRIFTS combined with PTR-TOF-MS and quasi in-situ XPS. *Chem. Eng. J.* 397, 125375. doi:10.1016/j.cej.2020.125375

Zhu, J., Mu, W., Su, L., Li, X., Guo, Y., Zhang, S., et al. (2017). Al-doped TiO_2 mesoporous material supported Pd with enhanced catalytic activity for complete oxidation of ethanol. *J. Solid State Chem.* 248, 142–149. doi:10.1016/j.jssc.2017.01.028

Zuo, S., Du, Y., Liu, F., Han, D., and Qi, C. (2013). Influence of ceria promoter on shell-powder-supported Pd catalyst for the complete oxidation of benzene. *Appl. Catal. Gen.* 451, 65–70. doi:10.1016/j.apcata.2012.10.041

Zuo, S., Sun, X., Lv, N., and Qi, C. (2014). Rare earth-modified kaolin/NaY-supported Pd-Pt bimetallic catalyst for the catalytic combustion of benzene. *ACS Appl. Mater. Interfaces.* 6 (15), 11988–11996. doi:10.1021/am500138q

Conflict of Interest: The authors declare that the research was conducted in the absence of any commercial or financial relationships that could be construed as a potential conflict of interest.

Mechanics of Materials

Osama R. Bilal

Dr. Osama R. Bilal is an Assistant Professor in the Department of Mechanical Engineering at the University of Connecticut. He received his Ph.D. in Aerospace Engineering from the University of Colorado Boulder. Before joining UCONN, he held a postdoctoral fellowship in the Department of Mechanical Engineering at the California Institute of Technology and the Institute of Theoretical Physics at ETH Zurich. His research interest spans the realization of programmable metamaterials, soft robotics, topology optimization, and fluid-structure interaction. Osama is the recipient of several awards, including the ETH postdoctoral fellowship and the Graduate Student Service Award (CU-Boulder). More info can be found at http://www.orbilal.com/

Yuanyuan Li

Dr. Yuanyuan Li is currently an Assistant Professor at the Department of Fiber and Polymer Technology, KTH Royal Institute of Technology, and a PI in the Wallenberg Wood Science Center, Sweden. She received her Ph.D. degree from Nanjing Forestry University in China and visited the University of Maryland, USA, during her doctoral studies. Afterward, she moved to KTH as a post-doctoral fellow and was promoted to Assistant Professor in 2020. Her current research focus is on wood nanotechnology development and applications, including wood nanostructure understanding, nano-structural control, and applications like transparent wood and wood aerogel.

frontiers in Materials

ORIGINAL RESEARCH
published: 17 December 2020
doi: 10.3389/fmats.2020.606877

Demultiplexing Infrasound Phonons With Tunable Magnetic Lattices

*Audrey A. Watkins and Osama R. Bilal**

Department of Mechanical Engineering, University of Connecticut, Storrs, CT, United States

Controlling infrasound signals is crucial to many processes ranging from predicting atmospheric events and seismic activities to sensing nuclear detonations. These waves can be manipulated through phononic crystals and acoustic metamaterials. However, at such ultra-low frequencies, the size (usually on the order of meters) and the mass (usually on the order of many kilograms) of these materials can hinder its potential applications in the infrasonic domain. Here, we utilize tunable lattices of repelling magnets to guide and sort infrasound waves into different channels based on their frequencies. We construct our lattices by confining meta-atoms (free-floating macroscopic disks with embedded magnets) within a magnetic boundary. By changing the confining boundary, we control the meta-atoms' spacing and therefore the intensity of their coupling potentials and wave propagation characteristics. As a demonstration of principle, we present the first experimental realization of an infrasound phonon demultiplexer (i.e., guiding ultra-low frequency waves into different channels based on their frequencies). The realized platform can be utilized to manipulate ultra-low frequency waves, within a relatively small volume, while utilizing negligible mass. In addition, the self-assembly nature of the meta-atoms can be key in creating re-programmable materials with exceptional nonlinear properties.

Keywords: phononic crystals, acoustic metamaterials, programmable matter, infrasound waves, magnetic lattices

OPEN ACCESS

Edited by:
Anastasiia O. Krushynska, University of Groningen, Netherlands

Reviewed by:
Vincent Laude, Institut Franche Comté Électronique Mécanique Thermique et Optique Sciences et Technologies (FEMTO-ST), France
Guoliang Huang, University of Missouri, United States
Yue-Sheng Wang, Tianjin University, China

****Correspondence:***
Osama R. Bilal
osama.bilal@uconn.edu

Specialty section:
This article was submitted to Mechanics of Materials, a section of the journal Frontiers in Materials

Received: *15 September 2020*
Accepted: *28 October 2020*
Published: *17 December 2020*

Citation:
Watkins AA and Bilal OR (2020) Demultiplexing Infrasound Phonons With Tunable Magnetic Lattices. Front. Mater. 7:606877. doi: 10.3389/fmats.2020.606877

INTRODUCTION

Infrasound waves are ubiquitous in nature, appearing in animal communications (von Muggenthaler et al., 2003; Barklow, 2004; Von Muggenthaler, 2013), natural phenomena such as earthquakes and volcanic eruptions (Garcés et al., 2003; Fee and Matoza, 2013; Nakano et al., 2018; Ripepe et al., 2018), and man made systems such as machinery and explosions. These waves can cause high volumes of damage to their surroundings, particularly when originating from natural phenomena (Le Pichon et al., 2010). Deciphering infrasound waves can lead to potential detection of various natural phenomena prior to their occurrences, offering a type of early warning system through their detection. Phononic crystals and acoustic metamaterials, defined as artificial arrangements of spatial patterns, can manipulate waves at different frequency ranges from a few Hertz to a few Terahertz (Deymier, 2013; Maldovan, 2013; Hussein et al., 2014; Khelif and Adibi, 2015). These phononic metamaterials usually consist of unit cells that repeat periodically. Phononic crystals have the ability to affect waves through Bragg scattering (Kushwaha et al., 1993), while metamaterials utilize resonances to affect waves (Liu et al., 2000). The wave controlling characteristics of phononic crystals and acoustic metamaterials have a variety of potential applications, including vibration and sound insulation (Yang et al., 2010; Mei et al., 2012; Ma et al., 2015), seismic wave protection (Kim and Das, 2012; Brûlé et al., 2014), wave guiding (Torres et al., 1999; Rupp et al., 2007), frequency

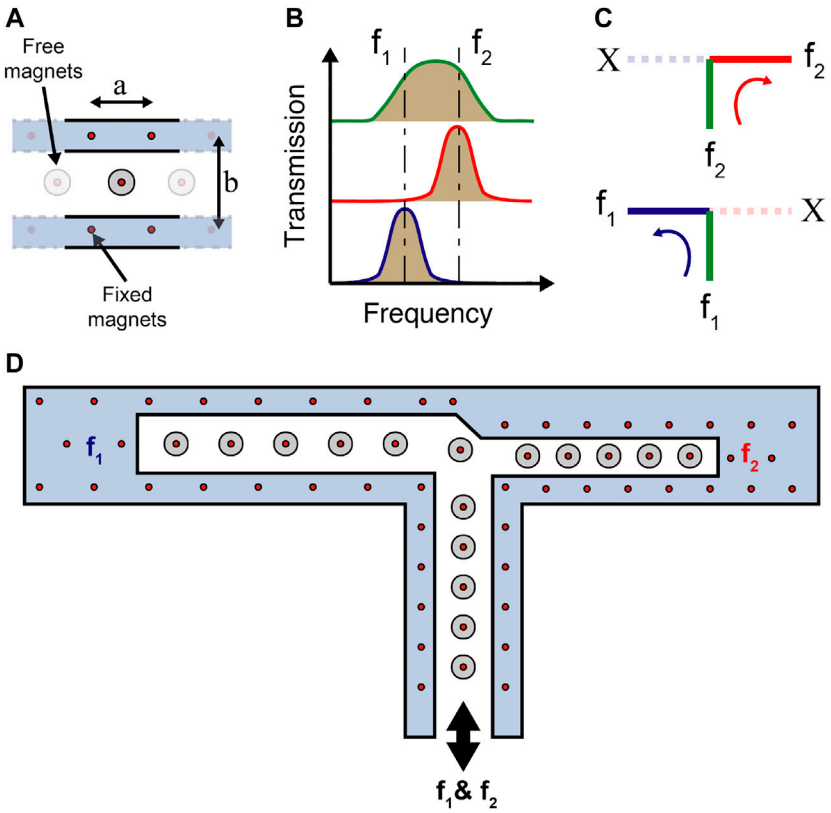

FIGURE 1 | Design concept. **(A)** Schematic of a unit cell depicting the locations of *a* and *b* as well as the fixed and free magnets. **(B)** Transmission spectrum of channel 1 (blue), 2 (green), and 3 (red). **(C)** A visual representation of two different frequencies (f_1 and f_2) passing through the channels. **(D)** A full schematic of the t-shaped demultiplexer with f_1 and f_2 excited at the vertical channel (CH. 2) and sorted into their respective channels.

filtering (Rupp et al., 2010), acoustic lenses, (Molerón et al., 2014), and sensors (Ke et al., 2011; Amoudache et al., 2014).

The presence of scattering in phononic crystals and resonances in metamaterials gives rise to specific frequency ranges where waves cannot propagate (i.e., band gaps). In a scattering-based band gap, the unit cell size has to be on the same order of the targeted frequency wavelength. This usually translates into a meter sized structure that affects waves at ultra-low frequencies (Brûlé et al., 2014). Resonance based metamaterials can open band gaps where the targeted frequency wavelength does not correlate with the unit cell size (i.e, subwavelength band gaps). However, opening band gaps at ultra-low frequencies could translate to a resonator with mass on the order of many kilograms (Palermo et al., 2016; Colombi et al., 2020) or coupling stiffness that is prone to fatigue. In addition, most phononic metamaterial realizations have fixed operational frequency. Once a sample is fabricated, its band gap frequency, for example, cannot change (Matar et al., 2013; Bergamini et al., 2014; Bilal et al., 2017a).

In this paper we utilize tunable lattices of repelling magnets to guide and sort infrasound waves into different channels based on their frequencies. We realize these lattices by confining meta-atoms (free-floating macroscopic disks with embedded magnets) within a magnetic boundary. We control the spacing between the meta-atoms by changing the magnetic potential of the confining boundary. The same meta-atoms with different lattice constants and coupling intensity can have different wave propagation characteristics by design. As a demonstration of principle, we experimentally realize an infrasound phonon demultiplexer (i.e., guiding ultra-low frequency waves into different channels based on their frequencies). By constructing channels with identical building blocks, yet different boundary potentials, we can demultiplex infrasound waves based on their frequencies. There exist multiple theoretical proposals for realizing phonon demultiplexers (Pennec et al., 2004; Hussein et al., 2005; Pennec et al., 2005; Vasseur et al., 2011; Rostami-Dogolsara et al., 2016; Zou et al., 2017; Moradi and Bahrami, 2019; Babaki and Nazari, 2020; Ben-Ali et al., 2020; Gharibi and Bahrami, 2020; Motaei and Bahrami, 2020) with few experimental demonstrations (Mohammadi and Adibi, 2011; Faiz et al., 2020; Bilal et al., 2020). However, demultiplexing infrasound phonons has not been observed.

DESIGN METHODOLOGY

To design our infrasound phonon demultiplexer, we start by considering a unit cell composed of a disk with a concentrically

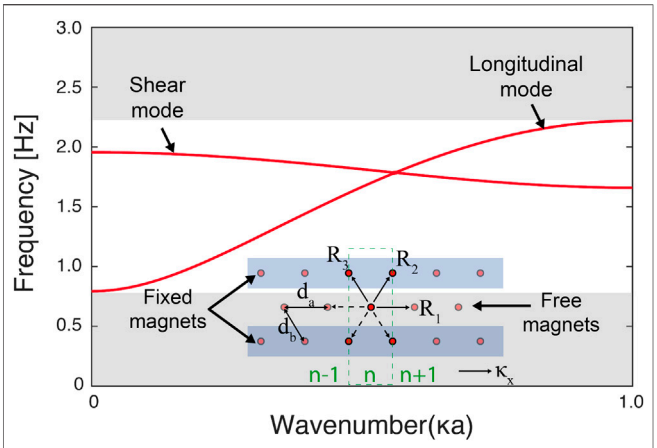

FIGURE 2 | Dispersion curves. Numerical dispersion curves for both the shear and longitudinal modes for a lattice with $a = 15.4\ mm$, $b = 24.5\ mm$ and $m = 0{:}118\ g$. The band gaps are shaded in gray. The inset shows a unit cell n along with its lattice vectors.

embedded magnet, referred to as meta-atoms hereinafter. The meta-atoms are confined between two arrays of fixed, identical, permanent magnets (**Figure 1A**). The fixed magnets create a boundary potential to hold the meta-atoms in place. The fixed magnets are equally spaced by a length a. The two arrays of fixed magnets are separated by a distance b. Both a and b define the equilibrium position of the meta-atoms. The assembly of these meta-atoms for a given a and b gives rise to various band gaps within the frequency spectrum. By changing the values of a and b, we can change the relative position of pass bands and band gaps. Each one of these designs (with a given a and b) can work as a designated channel for specific frequency phonons, while rejecting the phonons within the band gap frequency ranges. We connect multiple channels composed of different configurations of a and b, allowing only certain frequencies to pass in each channel. As a demonstration of principle, we connect three channels in a T-shaped configuration to function as a demultiplexer for infrasound phonons (**Figure 1D**). The left and right junctions of the T-shaped waveguide have out-of-sync pass and stop bands, while the vertical junction has a pass band encompassing both pass band frequencies (**Figure 1B**). For example, when exciting the vertical junction at a frequency f_1 within the band gap of the right junction, the wave propagates only through the left channel (CH.1). Similarly, when exciting the vertical junction at a frequency f_2 within the band gap of the left junction, the wave propagates only through the right channel (CH.3) (**Figure 1C**).

RESULTS

To analyze our magnetic lattices, we first consider the basic building block of our structure, a single meta-atom and its coupling to the boundary. We use Bloch's theorem to generate the dispersion curves of our magnetic lattice (Bloch, 1929). The dispersion analysis of our unit cell takes into account the nearest neighbor interaction between the meta-atoms (**Figure 2** inset). Each meta-atom (i.e., the disk with the embedded concentric magnet) is coupled to four fixed boundary magnets and one other freely moving meta-atom on each side. Each meta-atom has two degrees of freedom (i.e., movement in x and y direction). The dispersion equation for our system can be written as:

$$\left[-\omega^2\mathbf{M} + \mathbf{K}(\boldsymbol{\kappa})\right]\boldsymbol{\phi} = 0, \tag{1}$$

where ω is the frequency, $\boldsymbol{\kappa}$ is the wavenumber, $\boldsymbol{\phi} = [u\ \ v]^T$ is the Bloch displacement vector in x and y direction, $\boldsymbol{M} = \begin{bmatrix} m & 0 \\ 0 & m \end{bmatrix}$ is the mass matrix and $\boldsymbol{K}$ is the stiffness matrix (Jiao and Gonella, 2019):

$$\mathbf{K}(\boldsymbol{\kappa}) = 2\sum_{i=1}^{3}\left\{f_{,d}(d_i)\boldsymbol{e_i}\otimes\boldsymbol{e_i}[\delta_{i1}cos(\boldsymbol{\kappa}\cdot\boldsymbol{R_i}) - 1]\right\} + 2 \times \sum_{i=1}^{3}\left\{\frac{f(d_i)}{d_i}(\boldsymbol{I} - \boldsymbol{e_i}\otimes\boldsymbol{e_i})[\delta_{i1}cos(\boldsymbol{\kappa}\cdot\boldsymbol{R_i}) - 1]\right\}, \tag{2}$$

where $d_1 = d_a$ is the distance between the meta-atoms, $d_{2,3} = d_b$ is the distance between the meta-atoms and the boundary, δ is the Kronecker delta function and ⊗ is the dyadic product. The stiffness matrix in **Eq. 2** takes into account the repulsive forces between the magnetic particles following an inverse power law in the form $f(d) = Ad^{\gamma}$ and $f_{,d}(d)$ as its first derivative. For a dipole-dipole interaction (Mehrem et al., 2017) $A = 3\mu B^2/4\pi$, where μ is the permeability of air and B is the magnetic moment. $\boldsymbol{R}_1 = d_a\boldsymbol{e}_1$, $\boldsymbol{R}_2 = d_b\boldsymbol{e}_2$ and $\boldsymbol{R}_3 = d_b\boldsymbol{e}_3$ are the lattice vectors and $\boldsymbol{e}_1 = [1\quad 0]^T$, $\boldsymbol{e}_2 = [d_a/2d_b\quad b/2d_b]^T$, and $\boldsymbol{e}_3 = [-d_a/2d_b\quad b/2d_b]^T$ are the unit vectors.

The dispersion curves for an example magnetic lattice with $a = 15.4\ mm$, $b = 24.5\ mm$, $\gamma = -4$, $m = 0.118\ g$ and $A = 1.0935 \times 10^{-12}$ shows a pass band sandwiched between two band gaps (**Figure 2**). The dispersion analysis considers both longitudinal and shear modes. The two branches within the dispersion curves correlate with the two degrees of freedom of the meta-atoms. Both branches correlate with pure modes, due to the diagonal nature of the eigenvalue problem. The pass band in **Figure 2** shows both modes overlapping. The lower band gap is a result of the boundary coupling, while the top band gap is the cut off frequency for the lattice. The width of the lower band gap can be reduced to zero in the limit of a vanishing boundary coupling (e.g., large b). The width of the pass band and its position within the frequency spectrum is more sensitive to the inter-coupling between the meta-atoms than their coupling with the boundary (i.e., the lattice constant a). A larger influence of the lattice constant a stems from the fact that a change in a changes both d_a and d_b in **Figure 2** inset), while a change in the value of b only changes d_b. In addition to the geometric parameters of the lattice, the position of the pass band can be dynamically tuned by nondestructive external factors such as an external magnetic field (Matar et al., 2013; Bilal et al., 2017a; Bilal et al., 2017b; Wang et al., 2018; Palermo et al., 2019; Wang et al., 2020).

The purpose of the demultiplexer is to allow for the propagation of waves through the input channel, while selectively attenuating waves based on their frequencies through the output channels. To

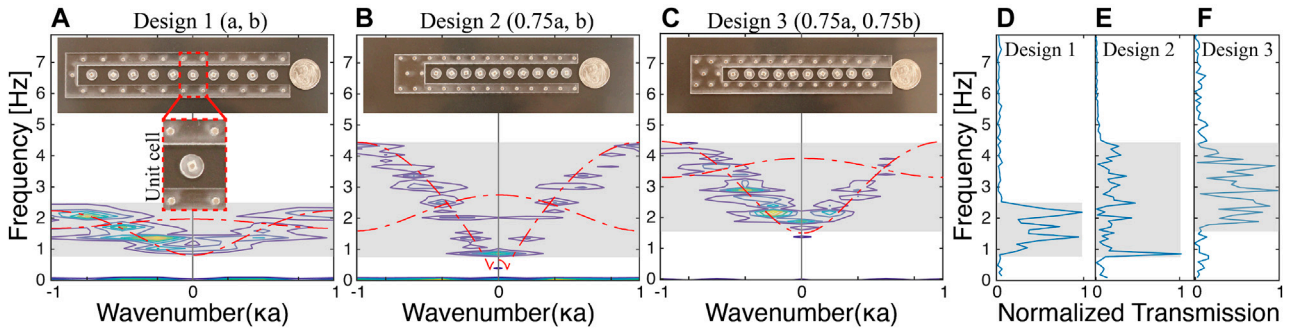

FIGURE 3 | Characterization of individual channels. The experimentally measured dispersion curves plotted as contours with the numerical dispersion curves superimposed as dashed red lines for **(A)** design 1 with a = 15.4 *mm*, b = 24.5 *mm* **(B)** design 2, with a = 11.5 *mm*, b = 24.5 *mm*, and **C)** design 3, with a = 11.5 *mm*, b = 18.4 *mm*. The insets show the experimental samples used. The measured normalized transmission at the center of lattice for **D)** design 1, **E)** design 2, and **F)** design

achieve such functionality, we design an input channel with a pass band that encompasses all operational frequencies, while each output channel has a pass band in only one of the operational frequency ranges. Our demultiplexer channels are designed by utilizing identical meta-atoms with varying boundary coupling b and lattice spacing a. The modification of a and b allows for the control of the band gap position within the frequency spectrum. Three designs are created; design 1 with dimensions a and b, design 2 with 0.75a and b and design 3 with 0.75a and 0.75b. The dispersion curves for each design are plotted with dashed red lines in (**Figures 3A–C**) based on **Eq. 1**.

To experimentally verify the analytically computed dispersion curves, we fabricate three separate U-shaped boundaries with the parameters of designs one to three out of acrylic glass using a laser cutter (Full-spectrum 24 pro-series). The meta-atoms (i.e., disks) are identical across all three designs with a radius r_{disk} = 4 mm. The meta-atoms are placed within the boundary and the magnets oriented with the north pole facing upwards. The fixed magnets inside the boundary are oriented in the same way. To minimize friction, we attach a glass slide at the bottom of each disk and float them on an air bearing (New way S1030002). Each design is excited separately with a chirp signal between 0.1 and 10 Hz at its open end with a mechanical shaker (Brüel and Kjær 4,180) and a function generator (Keysight Technologies 33512B). The motion of the disks is captured using a computer vision camera (Blackfly S USB3) and the resulting images are analyzed using the digital image correlation software (DICe).

The displacement profiles of all the meta-atoms in each design (characterized separately) are post-processed using 2D fast Fourier transform (2D-FFT). The resulting FFT corresponds to the longitudinal dispersion curve of each design, as we only consider the x-displacement in our analysis (**Figure 3**). For all three cases, the measured displacement signals through DICe show displacements in the y-direction on the same order as noise. The experimental dispersion curves for the three designs match well with the numerically calculated ones. In addition, we plot the measured transmission at a central meta-atom in each design. The pass band region within the transmission spectrum matches well with the dispersion curves for all three designs. Design 1 has a pass band between 0.8 and 2.5 Hz, while design 3 has a pass band between 1.6 and 4.5 Hz. Both designs have operational frequency ranges that do not overlap (e.g., below 1.6 Hz and above 2.5 Hz). Design 2 has a pass band between 0.8 and 4.5 Hz, which encompasses the pass bands of both design 1 and 3. This pass band range gives channel 2 the characteristic to act as an input channel for our demultiplexer.

To test our design principle we connect the three distinct channels made out of designs 1, 2 and 3. We note that the meta-atoms behave as a self-assembled fluidic material. Therefore, once the three designs are merged within a T-junction, the meta-atoms' equilibrium positions are altered. To ensure that the position of the meta-atom within each unit cell is as close as possible to the equilibrium position as in the separate experiments, we add an extra meta-atom and a boundary magnet at the junction point. To verify the operational frequencies of the T-shaped assembly, we excite the input channel (design 2) with a chirp signal from 0.1 to 10 Hz. A fast Fourier transform is performed on the displacements of the central meta-atoms in each channel and repeated for a total of three trials (**Figures 4A–C**). The FFT of the three trials along with its average, for each channel, is plotted in log-scale (**Figures 4D–F**). The transmission of channel 1 is between 0.9 and 2.3 Hz, for channel 2 is between 0.8 and 3.4 Hz, and for channel 3 is between 1.7 and 2.7 Hz. The operational frequency of each channel is altered slightly. This may be due to the imbalance in the force potentials between the different channels which causes a shift in the equilibrium position of each meta-atom.

To characterize the performance of the demultiplexer at a single operational frequency, we excite the input channel with two sine waves, separately, and measure the transmission at each output terminal (**Figure 5A**). The device is first excited at a frequency f_1 = 1.1 Hz, corresponding to an operational frequency for channel 1 (left). The FFT of the displacement of the central meta-atoms in each channel shows a clear transmission of the wave from CH.2 to CH.1, while the wave is attenuated at CH.3 (**Figure 5B**). When excited at a frequency f_2 = 2.4 Hz, the wave is transmitted through CH.3, while attenuated in CH.1 (**Figure 5C**). The ratio of transmission (T) at f_1 is 0.88, calculated as T_{CH1}/T_{CH2}, and the ratio of transmission at f_2 is 0.59, calculated as T_{CH3}/T_{CH2}. The ratio

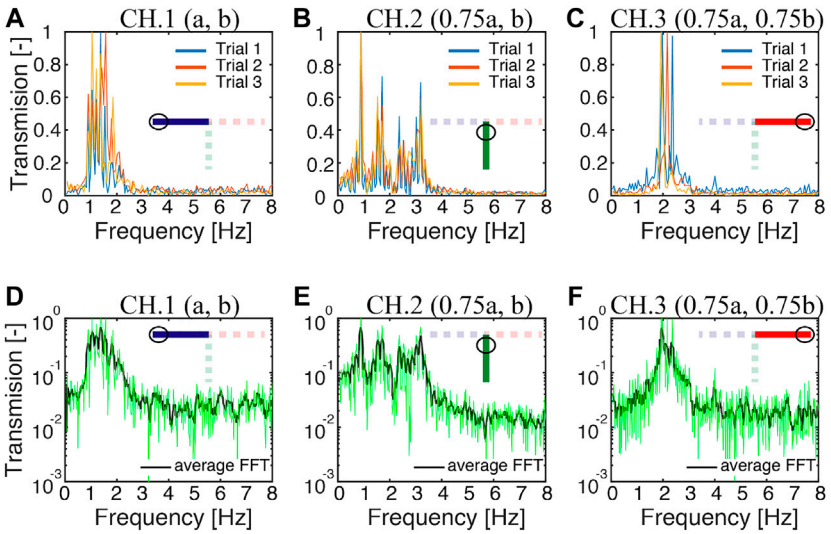

FIGURE 4 | Chirp signal transmission through the demultiplexer. Fast Fourier transform of the displacement of the central meta-atom and their average over three trials for **(A, D)** channel 1, **(B, E)** channel 2, and **(C, F)** channel 3. The input channel is excited with a chirp signal between 0.1–10 Hz. The inset shows the corresponding channel in the T-shaped demultiplexer.

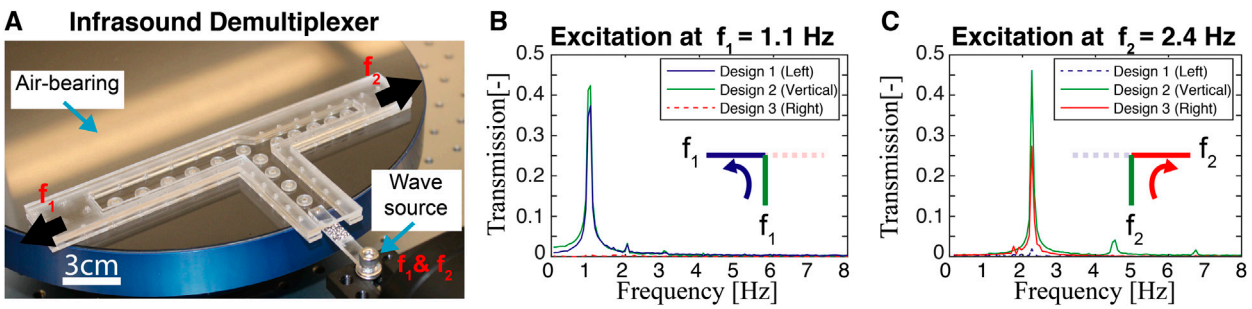

FIGURE 5 | Infrasound demultiplexer. **(A)** The experimental setup for the T-shaped demultiplexer positioned on an air bearing. The demultiplexer is filled with identical meta-atoms confined between different magnetic boundaries. A mechanical shaker drives the input channel through an arm with an embedded magnet. The signal transmission at **(B)** f_1 = 1.1 Hz and **C)** f_2 = 2.4 Hz.

of transmission for the attenuated signals at CH.1 and CH.3 are 7 and 1%, respectively. We attribute the relatively lower transmission ratio through channel 3 (in comparison to channel 2) to the coupling asymmetry at the junction point between the three channels. We note the existence of the second and the third harmonic of the excitation frequency in **Figure 5B,C**, due to the inherent nonlinearity in magnetic lattices. Such nonlinear response can be harnessed by increasing the amplitude of the excitation and introducing defects within the lattice (Boechler et al., 2011; Mehrem et al., 2017; Deng et al., 2018; Molerón et al., 2019; Chong et al., 2020; Jiao and Gonella, 2020).

CONCLUSION

In conclusion, we utilize tunable magnetic lattices to control the propagation of infrasound waves. We tune the wave propagation characteristics of these lattices by changing their boundary couplings while using the same meta-atoms. Different designs are combined to create a T-shaped demultiplexer consisting of one input channel and two output channels. The device is characterized experimentally, validating both dispersion curves and transmission frequency spectrum. This platform can be utilized to manipulate ultra-low frequency waves, within a relatively small space. The inherent nonlinear potentials between the meta-atoms can be harnessed to demonstrate phenomena with no linear parallel such as amplitude dependent response, bifurcation, chaos and solitons (Porter et al., 2015; Mehrem et al., 2017; Amendola et al., 2018; Gendelman and Vakakis, 2018; Kim and Yang, 2019; Grinberg and Matlack, 2020; Ramakrishnan and Frazier, 2020). In addition, the self-assembly of the meta-atoms can be key in creating re-programmable materials with exceptional properties (Culha et al., 2020).

DATA AVAILABILITY STATEMENT

All the data supporting the findings in this study are available in the article. Further data and methods are available from the corresponding author upon request.

AUTHOR CONTRIBUTIONS

AW performed the research and wrote the manuscript. OB designed the research, performed the research and wrote the manuscript.

REFERENCES

Amendola, A., Krushynska, A., Daraio, C., Pugno, N. M., and Fraternali, F. (2018). Tuning frequency band gaps of tensegrity mass-spring chains with local and global prestress. *Int. J. Solid Struct.* 155, 47. doi:10.1016/j.ijsolstr.2018.07.002

Amoudache, S., Pennec, Y., Djafari Rouhani, B., Khater, A., Lucklum, R., and Tigrine, R. (2014). Simultaneous sensing of light and sound velocities of fluids in a two-dimensional phoXonic crystal with defects. *J. Appl. Phys.* 115, 134503. doi:10.1063/1.4870861

Babaki, J., and Nazari, F. (2020). Heterostructure based demultiplexer using solid-solid phononic crystal ring resonators. *J. Phys. D Appl. Phys.* 53, 375301. doi:10.1088/1361-6463/ab904b

Barklow, W. E. (2004). Low-frequency sounds and amphibious communication in Hippopotamus amphibious. *J. Acoust. Soc. Am.* 115, 2555. doi:10.1121/1.4783854

Ben-Ali, Y., Ouariach, A., Khaled, A., and Bria, D. (2020). Double Frequency Filtering in One Dimensional Comb-Like Phononic Structure Containing a Segment Defect. *Mater. Today* 13–21. doi:10.1007/978-3-030-62199-5_2

Bergamini, A., Delpero, T., Simoni, L. D., Lillo, L. D., Ruzzene, M., and Ermanni, P. (2014). Phononic crystal with adaptive connectivity. *Adv. Mater.* 26, 1343. doi:10.1002/adma.201305280

Bilal, O. R., Foehr, A., and Daraio, C. (2017b). Bistable metamaterial for switching and cascading elastic vibrations. *Proc. Natl. Acad. Sci. U.S.A.* 114, 4603. doi:10.1073/pnas.1618314114

Bilal, O. R., Foehr, A., and Daraio, C. (2017a). Reprogrammable phononic metasurfaces. *Adv. Mater.* 29, 1700628. doi:10.1002/adma.201700628

Bilal, O. R., Hwee Yee, C., Rys, J., Schumacher, C., and Daraio, C. (2020). Experimental realization of phonon demultiplexing in three-dimensions. arXiv e-prints, [Preprint]. Avaialable at: https://arxiv.org/abs/2009.12025 (Accessed Sepetember 25, 2020).

Bloch, F. (1929). Über die Quantenmechanik der Elektronen in Kristallgittern. *Z. Phys.* 52, 555–600. doi:10.1007/bf01339455

Boechler, N., Theocharis, G., and Daraio, C. (2011). Bifurcation-based acoustic switching and rectification. *Nat. Mater.* 10, 665–668. doi:10.1038/nmat3072

Brûlé, S., Javelaud, E., Enoch, S., and Guenneau, S. (2014). Experiments on seismic metamaterials: molding surface waves. *Phys. Rev. Lett.* 112, 133901. doi:10.1103/physrevlett.112.133901

Chong, C., Wang, Y., Marechal, D., Charalampidis, E., Moleron, M., Martinez, A. J., et al. (2020). Nonlinear localized modes in two-dimensional hexagonally-packed magnetic lattices. arXiv [Preprint]. Available at: https://arxiv.org/abs/2009.10300 (Accessed September 22, 2020).

Colombi, A., Zaccherini, R., Aguzzi, G., Palermo, A., and Chatzi, E. (2020). Mitigation of seismic waves: metabarriers and metafoundations bench tested. *J. Sound Vib.* 485, 115537. doi:10.1016/j.jsv.2020.115537

Culha, U., Davidson, Z. S., Mastrangeli, M., and Sitti, M. (2020). Statistical reprogramming of macroscopic self-assembly with dynamic boundaries. *Proc. Natl. Acad. Sci. U.S.A.* 117, 11306. doi:10.1073/pnas.2001272117

Deng, B., Wang, P., He, Q., Tournat, V., and Bertoldi, K. (2018). *Nat. Commun.* 9, 1. doi:10.1038/s41467-018-05908-9

Deymier, P. A. (2013). *Acoustic metamaterials and phononic crystals*. Amsterdam, Netherlands: Springer Science & Business Media, Vol. 173.

Faiz, M. S., Addouche, M., Zain, A. R. M., Siow, K. S., Chaalane, A., and Khelif, A. (2020). Experimental demonstration of a multichannel elastic wave filter in a phononic crystal slab. *Appl. Sci.* 10, 4594. doi:10.3390/app10134594

Fee, D., and Matoza, R. S. (2013). An overview of volcano infrasound: from Hawaiian to plinian, local to global. *J. Volcanol. Geotherm. Res.* 249, 123–139. doi:10.1016/j.jvolgeores.2012.09.002

Garcés, M., Hetzer, C., Merrifield, M., Willis, M., and Aucan, J. (2003). Observations of surf infrasound in Hawai'i. *Geophys. Res. Lett.* 30, 2264. doi:10.1029/2003gl018614

Gendelman, O. V., and Vakakis, A. F. (2018). Introduction to a topical issue "nonlinear energy transfer in dynamical and acoustical Systems". *Phil. Trans. R. Soc. A.* 376, 20170129. doi:10.1098/rsta.2017.0129

Gharibi, H., and Bahrami, A. (2020). Phononic crystals for sensing FAMEs with demultiplexed frequencies. *J. Mol. Liq.* 305, 112841. doi:10.1016/j.molliq.2020.112841

Grinberg, I., and Matlack, K. H. (2020). Nonlinear elastic wave propagation in a phononic material with periodic solid-solid contact interface. *Wave Motion* 93, 102466. doi:10.1016/j.wavemoti.2019.102466

Hussein, M. I., Hulbert, G. M., and Scott, R. A. (2005). Hierarchical Design of Phononic Materials and Structures. *ASME Int. Mech. Eng. Cong. Exp.* 42258, 163–172. doi:10.1115/IMECE2005-81325

Hussein, M. I., Leamy, M. J., and Ruzzene, M. (2014). Closure to "Discussion of 'Dynamics of Phononic Materials and Structures: Historical Origins, Recent Progress, and Future Outlook'". *Appl. Mech. Rev.* 66, 046002. doi:10.1115/1.4027795

Jiao, W., and Gonella, S. (2019). Nonlinear harmonic generation in two-dimensional lattices of repulsive magnets. arXiv [Preprint]. Available at: https://arxiv.org/pdf/1911.10410 (Accessed August 25, 2020).

Jiao, W., and Gonella, S. (2020). Nonlinear harmonic generation in two-dimensional lattices of repulsive magnets. arXiv [Preprint]. Available at: https://arxiv.org/abs/2007.03855 (Accessed July 8, 2020).

Ke, M., Zubtsov, M., and Lucklum, R. (2011). Sub-wavelength phononic crystal liquid sensor. *J. Appl. Phys.* 110, 026101. doi:10.1063/1.3610391

Khelif, A., and Adibi, A. (2015). *Phononic crystals*. Springer.

Kim, E., and Yang, J. (2019). Review: Wave propagation in granular metamaterials. *Funct. Compos. Struct.* 1, 012002. doi:10.1088/2631-6331/ab0c7e

Kim, S.-H., and Das, M. P. (2012). Seismic waveguide of metamaterials. *Mod. Phys. Lett. B* 26, 1250105. doi:10.1142/s0217984912501059

Kushwaha, M. S., Halevi, P., Dobrzynski, L., and Djafari-Rouhani, B. (1993). Acoustic band structure of periodic elastic composites. *Phys. Rev. Lett.* 71, 2022. doi:10.1103/physrevlett.71.2022

Le Pichon, A., Blanc, E., and Hauchecorne, A. (2010). *Infrasound monitoring for atmospheric studies*. Springer.

Liu, Z., Zhang, X., Mao, Y., Zhu, Y., Yang, Z., Chan, C., et al. (2000). Locally resonant sonic materials. *Science* 289, 1734. doi:10.1126/science.289.5485.1734

Ma, F., Wu, J. H., Huang, M., Zhang, W., and Zhang, S. (2015). A purely flexible lightweight membrane-type acoustic metamaterial. *J. Phys. D Appl. Phys.* 48, 175105. doi:10.1088/0022-3727/48/17/175105

Maldovan, M. (2013). Sound and heat revolutions in phononics. *Nature* 503, 209. doi:10.1038/nature12608

Matar, O. B., Vasseur, J., and Deymier, P. A. (2013). *Acoustic metamaterials and phononic crystals*. Amsterdam, Netherlands: Springer, 253–280.

Mehrem, A., Jimenez, N., Salmerón-Contreras, L., García-Andrés, X., García-Raffi, L., Picó, R., et al. (2017). Nonlinear dispersive waves in repulsive lattices. *Phys. Rev.* 96, 012208. doi:10.1103/physreve.96.012208

Mei, J., Ma, G., Yang, M., Yang, Z., Wen, W., and Sheng, P. (2012). Dark acoustic metamaterials as super absorbers for low-frequency sound. *Nat. Commun.* 3, 756. doi:10.1038/ncomms1758

Mohammadi, S., and Adibi, A. (2011). On chip complex signal processing devices using coupled phononic crystal slab resonators and waveguides. *AIP Adv.* 1, 041903. doi:10.1063/1.3676168

Molerón, M., Chong, C., Martínez, A. J., Porter, M. A., Kevrekidis, P. G., and Daraio, C. (2019). Nonlinear excitations in magnetic lattices with long-range interactions. *New J. Phys.* 21, 063032. doi:10.1088/1367-2630/ab0118

Molerón, M., Serra-Garcia, M., and Daraio, C. (2014). Acoustic Fresnel lenses with extraordinary transmission. *Appl. Phys. Lett.* 105, 114109. doi:10.1063/1.4896276

Moradi, P., and Bahrami, A. (2019). Three channel GHz-ranged demultiplexer in solid-solid phononic crystals. *Chin. J. Phys.* 59, 291. doi:10.1016/j.cjph.2019.03.005

Motaei, F., and Bahrami, A. (2020). Eight-channel acoustic demultiplexer based on solid-fluid phononic crystals with hollow cylinders. *Photonics Nanostruct. Fundam. Appl.* 39, 100765. doi:10.1016/j.photonics.2020.100765

Nakano, M., Hori, T., Araki, E., Kodaira, S., and Ide, S. (2018). Shallow very-low-frequency earthquakes accompany slow slip events in the Nankai subduction zone. *Nat. Commun.* 9, 1. doi:10.1038/s41467-018-03431-5

Palermo, A., Krödel, S., Marzani, A., and Daraio, C. (2016). Engineered metabarrier as shield from seismic surface waves. *Sci. Rep.* 6, 39356. doi:10.1038/srep39356

Palermo, A., Wang, Y., Celli, P., and Daraio, C. (2019). Tuning of surface-acoustic-wave dispersion via magnetically modulated contact resonances. *Physical Review Applied* 11, 044057. doi:10.1103/physrevapplied.11.044057

Pennec, Y., Djafari-Rouhani, B., Vasseur, J., Khelif, A., and Deymier, P. A. (2004). Tunable filtering and demultiplexing in phononic crystals with hollow cylinders. *Phys. Rev.* 69, 046608. doi:10.1103/physreve.69.046608

Pennec, Y., Djafari-Rouhani, B., Vasseur, J., Larabi, H., Khelif, A., Choujaa, A., et al. (2005). "Channel drop pro-cess of elastic wave in a two dimensional phononic crystal," in IEEE Ultrasonics Symposium 2005, Rotterdam, Netherlands, September 18–21, 2005 (IEEE), Vol. 1, 69–72.

Porter, M. A., Kevrekidis, P. G., and Daraio, C. (2015). Granular crystals: Nonlinear dynamics meets materials engineering. *Phys. Today* 68, 44. doi:10.1063/pt.3.2981

Ramakrishnan, V., and Frazier, M. J. (2020). Transition waves in multi-stable metamaterials with space-time modulated potentials. *Appl. Phys. Lett.* 117, 151901. doi:10.1063/5.0023472

Ripepe, M., Marchetti, E., Delle Donne, D., Genco, R., Innocenti, L., Lacanna, G., et al. (2018). Infrasonic early warning system for explosive eruptions. *J. Geophys. Res. Solid Earth* 123, 9570. doi:10.1029/2018jb015561

Rostami-Dogolsara, B., Moravvej-Farshi, M. K., and Nazari, F. (2016). Designing switchable phononic crystal-based acoustic demultiplexer. *IEEE Trans. Ultrason. Ferroelectrics Freq. Contr.* 63, 1468. doi:10.1109/tuffc.2016.2586489

Rupp, C. J., Dunn, M. L., and Maute, K. (2010). Switchable phononic wave filtering, guiding, harvesting, and actuating in polarization-patterned piezoelectric solids. *Appl. Phys. Lett.* 96, 111902. doi:10.1063/1.3341197

Rupp, C. J., Evgrafov, A., Maute, K., and Dunn, M. L. (2007). Design of phononic materials/structures for surface wave devices using topology optimization. *Struct. Multidiscip. Optim.* 34, 111. doi:10.1007/s00158-006-0076-0

Torres, M., Montero de Espinosa, F. R., García-Pablos, D., and García, N. (1999). Sonic band gaps in finite elastic media: surface states and localization phenomena in linear and point defects. *Phys. Rev. Lett.* 82, 3054. doi:10.1103/physrevlett.82.3054

Vasseur, J., Matar, O. B., Robillard, J., Hladky-Hennion, A.-C., and Deymier, P. A. (2011). Band structures tunability of bulk 2D phononic crystals made of magneto-elastic materials. *AIP Adv.* 1, 041904. doi:10.1063/1.3676172

Von Muggenthaler, E. (2013). *Proceedings of meetings on acoustics ICA2013*. Acoustical Society of America, Vol. 19, 010012.

von Muggenthaler, E., Reinhart, P., Lympany, B., and Craft, R. B. (2003). Songlike vocalizations from the sumatran rhinoceros (dicerorhinus sumatrensis). *Acoust Res. Lett. Online* 4, 83. doi:10.1121/1.1588271

Wang, Y.-F., Wang, Y.-Z., Wu, B., Chen, W., and Wang, Y.-S. (2020). Tunable and Active Phononic Crystals and Metamaterials. *Appl. Mech. Rev.* 72, 35. doi:10.1115/1.4046222

Wang, Y., Yousefzadeh, B., Chen, H., Nassar, H., Huang, G., and Daraio, C. (2018). Observation of Nonreciprocal Wave Propagation in a Dynamic Phononic Lattice. *Phys. Rev. Lett.* 121, 194301. doi:10.1103/physrevlett.121.194301

Yang, Z., Dai, H., Chan, N., Ma, G., and Sheng, P. (2010). Acoustic metamaterial panels for sound attenuation in the 50–1000 Hz regime. *Appl. Phys. Lett.* 96, 041906. doi:10.1063/1.3299007

Zou, Q., Liu, W., Yu, T., Liu, N., Wang, T., and Liao, Q. (2017). Decoupling of multiple coupled phononic crystal waveguides: application to acoustic demultiplexing. *J. Phys. D Appl. Phys.* 50, 125102. doi:10.1088/1361-6463/aa5873

Conflict of Interest: The authors declare that the research was conducted in the absence of any commercial or financial relationships that could be construed as a potential conflict of interest.

frontiers in Materials

ORIGINAL RESEARCH
published: 12 February 2021
doi: 10.3389/fmats.2021.605931

Olive Stone Delignification Toward Efficient Adsorption of Metal Ions

*Ying Gao[1,2], Maria del Carmen Aliques Tomas[2], Jonas Garemark[2], Xia Sheng[2], Lars Berglund[2] and Yuanyuan Li[2]**

[1]Co-Innovation Center of Efficient Processing and Utilization of Forest Resources, Nanjing Forestry University, Nanjing, China, [2]Wallenberg Wood Science Center, Department of Fiber and Polymer Technology, KTH Royal Institute of Technology, Stockholm, Sweden

Olive stone is an important biomaterial waste product generated in large amount. As a lignocellulose material, olive stone could be a sustainable resource for biosorbents. In this work, olive stone powder delignification using sodium chlorite ($NaClO_2$) was performed to enhance metal ion adsorption capacity. The influence of the treatment on olive stone powder physical-chemical properties was studied, including specific surface area, surface chemistry, morphology, etc. The white, delignified olive stone powder was applied for metal ions (Fe^{3+}, Cu^{2+}, and Zn^{2+}) adsorption. Olive stone delignification not only increases the accessibility of the olive stone powder but also broadens the applications to materials design with optical functions by the generation of a white powder.

Keywords: biosorbent, delignification, metal ion, olive stone, white powder

OPEN ACCESS

Edited by:
David Salinas Torres, University of Alicante, Spain

Reviewed by:
Mohammed Ouzzine, Université Sultan Moulay Slimane, Morocco
Shahla Rezaei, Tehran University of Medical Sciences, Iran

****Correspondence:***
Yuanyuan Li
yua@kth.se

Specialty section:
This article was submitted to Mechanics of Materials, a section of the journal Frontiers in Materials

Received: *13 September 2020*
Accepted: *08 January 2021*
Published: *12 February 2021*

Citation:
Gao Y, Aliques Tomas MdelC, Garemark J, Sheng X, Berglund L and Li Y (2021) Olive Stone Delignification Toward Efficient Adsorption of Metal Ions. Front. Mater. 8:605931. doi: 10.3389/fmats.2021.605931

INTRODUCTION

Improving clean water is a vital part of the sustainable development goals agreed by 195 nations in 2015 (Lozano, 2018). Heavy metal ion contamination of aqueous media from industrial activities is an increasing threat to both the environment and human health. Therefore, removal of heavy metal ions (such as cadmium, copper, iron, lead, nickel, zinc, arsenic etc.) is vital and urgent. Reported techniques to remove heavy metal ions include adsorption, ion exchange, chemical precipitation, electrochemical treatment etc. (Saleem et al., 2019) Among them, bio-adsorption shows a pronounced advantage as a bioremediation of heavy metal ions due to its low cost, high capacity, wide pH range and the possibility of metal recovery (Gautam et al., 2014).

Olive stone is a lignocellulosic material composed of hemicellulose, cellulose, lignin, as well as appreciable amounts of phenolic compounds and protein (Rodríguez-Gutiérrez et al., 2014). It is one of the most important solid waste products generated from olive oil production. In Spain, approximately 400 thousand tons/year of stone waste was produced from olive oil industries (Rodríguez et al., 2008). Olive stone is usually in the form of small particles due to the crushing operations in the olive oil production process. Normally, olive stones are considered as pollutants, since their disposal creates environmental problems. Meanwhile, the use of waste products from plants for industrial products contributes strongly to the reduction of greenhouse gases (Vera et al., 2020). Compared with forest products, agricultural waste products have lower water consumption footprint (Wong et al., 2016). Therefore, increasing attention is paid to olive stone valorization.

Using olive stone as an adsorbent resource for metal ions in aqueous solutions has been successfully demonstrated (Budinova et al., 2006). The design principles to achieve a good metal ion adsorption capacity include: a high specific surface area and an appropriate surface functionalization for better interaction with metal ions. Carbonization is one approach that generates a high specific surface area, leading to a good adsorption capacity. In a typical process, olive stone is subjected to a high temperature

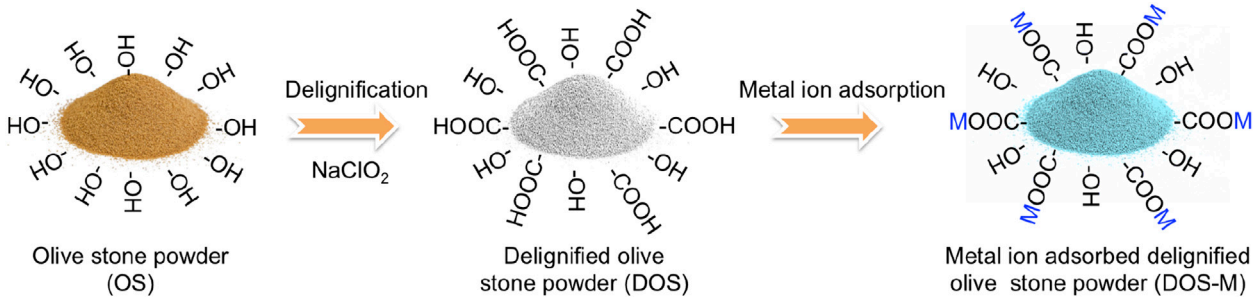

FIGURE 1 | Schematic showing olive stone delignification and the metal ion adsorption process. M represents metal ions.

(normally 300–800°C) in an inert gas atmosphere (includes N_2, CO_2, H_2O, etc.). (Aziz et al., 2009b; Blázquez et al., 2014; Jiang et al., 2020). Chemical or physical activations are often included with the aim of improving specific surface area. With this approach, high production cost and low yield (normally less than 50 wt%) are restrictions for large-scale production. More information regarding carbonized olive stone based adsorbent can be found in a recent review (Saleem et al., 2019). Another strategy to enhance metal ion adsorption capacity is the introduction of surface functional groups (carboxylic groups, carbonyl groups, sulfonic acid groups, etc.). High concentration acid treatment (De Hoces et al., 2010) and succinic acid grafting (Aziz et al., 2009a) have been reported. However, the safety and corrosive problems associated with concentrated acid and the complex chemical modification process with succinylated olive stone are barriers for further applications.

Delignification is an approach to tune the nanostructure of lignocellulosic materials (such as wood) and to increase their specific surface area (Keplinger et al., 2020). Reported methods include sulfite pulping (Li et al., 2019), acid chlorite bleaching (Li et al., 2018), ionic liquids or deep eutectic solvents treatments (Chen et al., 2019). Among the methods, sodium chlorite ($NaClO_2$) delignification is commonly used due to the combination of delignification and bleaching effects (Li et al., 2020). During $NaClO_2$ treatment, lignin aromatic structure undergoes oxidative ring-opening reactions to form acidic groups, the C-2, C-3, or C-6 of the monomeric sugar units in polysaccharide chains are oxidized to carbonyl or carboxylic groups, which is beneficial for metal ion adsorption (Li et al., 2017a). The bleaching effect of $NaClO_2$ treatment could endow the materials design with optical functionalities, such as the fabrication of transparent composites (Li et al., 2016).

In this work, $NaClO_2$ delignification was applied on olive stone powder to increase specific surface area and introduce carboxylic groups. The delignified olive stone powder was further demonstrated for metal ion adsorption with increased adsorption capacity. **Figure 1** shows the delignification of olive stone powder and the proposed metal ion adsorption mechanism. In addition, white olive stone powder was obtained. The white olive stone powder makes it possible to reflect color changes due to metal ion adsorption. Furthermore, white olive stone powder fabrication paves the way for applications where light absorption needs to be avoided, such as transparent biocomposites.

EXPERIMENTAL SECTION

Delignification

Olive stone powder was provided by BioPowder (Malta) with a particle size of 100–315 μm and a moisture content of 9.5%. Delignification was performed according to the literature but with minor changes (Li et al., 2017a). The samples were treated using $NaClO_2$ (Sigma Aldrich) as the reaction agent in an acetate buffer solution (pH = 4.6) at 80°C with stirring (500 rpm) until the powder become totally white. $NaClO_2$ concentrations were 3 wt% and 5 wt% and the powder concentration varies from 5 to 15 wt%. Detailed parameters variations are shown in **Supplementary Table S1** in the supporting materials. In case that the samples do not turn white in 6 h, a filtration process was carried out and new fresh chemicals were added. After the reaction, the samples were carefully filtrated on a filter (0.65 μm, Durapore ®Membrane Filter) and thoroughly washed with deionized water. This was repeated at least three times for each powder samples. Oven drying process at 105°C was carried out to obtain samples for yield calculation, Fourier Transform Infrared Spectroscopy (FTIR), surface charge density, and metal ions adsorption measurements. Liquid N_2 freeze-drying process was carried out to obtain samples for Field-Emission Scanning Electron Microscope (FE-SEM), X-Ray Diffraction Analysis (XRD), BET specific surface area and porosity characterizations.

Characterization Methods

Yield

The yield of the materials after the reaction was determined according to **Eq. 1**. W_b is the weight of samples before the reaction. W_a is the weight of samples after the reaction. The weight of the materials was obtained by weighting the oven-dried samples.

$$Yield = \frac{W_a}{W_b} \times 100\% \quad (1)$$

Lignin Content

The lignin content (Klason lignin) was determined using the TAPPI method TAPPI T222 om-02 (Tappi, 2011). The carbohydrates in original olive powder and delignified olive stone powder were hydrolyzed and solubilized by sulfuric acid (72%). Then the samples were diluted using distilled water until the concentration of sulfuric acid was 3%. After that the samples

were placed in an autoclave for 60 min at 125°C. Then all the samples were filtered under vacuum through fiber glass filter. The acid-insoluble lignin was filtered off, dried, and weighed. Three parallel measurements were done to get the data.

BET Specific Surface Area and Porosity

The BET specific surface area was evaluated by N_2 physisorption. The experiment was carried out on a Micrometrics, ASAP 2020. Prior to the N_2 adsorption, the samples were degassed at 90°C for 2 days. The analysis of the materials was obtained after carrying out measurements of N_2 adsorption-desorption isotherms at liquefaction temperature (196°C) under relative vapor pressure of 0.05–0.25. The BET specific surface area was then calculated from the attained isotherms.

Field-Emission Scanning Electron Microscope

FE-SEM (Hitachi S-4800 Japan) was applied to obtain the morphological information of the materials. The dried samples were coated with platinum-palladium using a sputter coater (Cressington 208HR, United Kingdom) before performing the FE-SEM analysis. During the characterization, the accelerating voltage was set at 1 kV.

Fourier Transform Infrared Spectroscopy

FTIR analysis was performed using a FTIR spectrometer (Spectrum 100/Spotlight 400, PekinElmer, Norwalk, CT). FTIR spectra were recorded between a wavelength of 600 and 4,000 cm^{-1}. The spectrum was processed through PerkinElmer Spectrum software.

X-Ray Diffraction Analysis (XRD)

XRD was performed in a powder diffractometer (Thermo Fisher Scientific ARL X'TRA powder diffractometer). CuKα radiation (λ = 1.540 60 Å) at 40 mA and 45 kV was applied. The program has a scan interval of 5° <2θ < 50°, with a step size of 0.04° (2θ). The crystallinity index (CrI) was calculated with peak height method according to **Eq. 2**. I_{200} is the intensity of the [200] crystalline peak and $I_{Amorphous}$ is the intensity of amorphous peak.

$$CrI = \frac{I_{200} - I_{Amorphous}}{I_{200}} \times 100\% \quad (2)$$

Charge Density

The change of surface charge density of olive stone powder was measured by conductive titration (856 Conductimeter Module, Metrohm). The olive stone powder was first protonated using HCl (0.1 M, 5 ml). Then titration was performed using NaOH (0.05 M). When the conductance decreased till the equivalence point, the charge density was calculated according to the NaOH consumption.

Metal Ions Adsorption Test

Fe^{3+}, Cu^{2+} and Zn^{2+} are often found in the effluents from industries (electroplating company, pulp and paper company, etc.). High concentration of Fe^{3+}, Cu^{2+} or Zn^{2+} in water is a threat to both the environment and human health. Therefore, Fe^{3+}, Cu^{2+} and Zn^{2+} are used for metal ion adsorption test. Dissolving appropriate amounts of $FeCl_3.6H_2O$ (s, Sigma Aldrich), $CuCl_2.2H_2O$ (s, Sigma Aldrich) and $ZnCl_2$ (s, Sigma Aldrich) in deionized water to prepare approximately 100 mg/L stock solution of salts separately. Then diluted the stock solution to 80 mg/L (salt concentration) to prepare experimental solution of Fe^{3+}, Cu^{2+}, and Zn^{2+}. The metal ion adsorption test was performed according to the literature with minor changes (Alslaibi et al., 2014a). In brief, metal ions adsorption was studied by agitating 250 ml of 80 mg/L experimental solution of Fe^{3+}, Cu^{2+}, and Zn^{2+} with 0.5 g olive stone under vigorous stirring at pH 4.5 for 2.5 h until it reached equilibrium. All the pH measurements were conducted using a pH meter (Mettler-Toledo AG 8603). The initial pH levels of the experimental solutions were adjusted using 0.1 M solution of HCl and NaOH. After stirring, the solid was removed by filtration through a 0.2 μm pore size filter paper. The final metal concentration in the filtrate as well as in the initial solution was determined using Inductively Coupled Plasma Optical Emission Spectrometer (ICP-OES, iCAP 6,000, Thermo Fisher Scientific). The sobbed metal concentrations were obtained from the difference between the initial and final metal concentrations in solution. The amount of adsorption of metal ions was calculated using **Eq. 3**:

$$Adsorption\ capacity = \frac{(C_0 - C_1)V}{W} \quad (3)$$

C_0 and C_1 (mg/L) are the ion concentrations of Fe^{3+}, Cu^{2+}, and Zn^{2+} at the initial and after absorbed by olive stone powder, respectively; V (L) is the volume of solution; and W(g) is the weight of dry olive stone powder.

RESULTS AND DISCUSSION

Characterization of the Delignified Olive Stone Powder

Lignin accounts for around 23.1 to 40.4 wt% of olive stone (De Hoces et al., 2010; Rodríguez et al., 2008) Removing lignin could improve the specific surface area and accessibility of olive stone powder. In addition, lignin is a main contributor to the brown color of lignocellulose materials (Li et al., 2017b). Delignification using $NaClO_2$ is an industrially established approach to remove lignin and bleach woody materials (Li et al., 2016). In this work, $NaClO_2$ based delignification was applied to treat olive stone powder. Parameter optimization was done first to obtain white olive stone powder with the aim of a high yield and high surface charge. **Supplementary Table S2** in supporting information shows the yield and reaction time for delignification process with various $NaClO_2$ and powder concentrations. With 5 wt% $NaClO_2$ and powder concentration of 15 wt%, a relative high yield of 66.9 wt% was obtained. The weight loss is mainly due to the removal of lignin as well as partial degradation of hemicellulose and cellulose. A significant increase in surface charge was detected after delignification (**Table 1** and **Supplementary Table S3**). The surface charge of OS is 47 μeq/g, while the value is 364 μeq/g for DOS with 3 wt% $NaClO_2$ treatment

TABLE 1 | Lignin content, surface charge, BET specific surface area (BET SSA) and crystallinity index (CrI) of original olive stone powder (OS) and delignified olive stone powder (DOS).

	Lignin content (wt%)	Surface charge* (μeq/g)	BET SSA* (m^2/g)	CrI (%)
OS	29.4	47	0.44	66
DOS	3.1	665	1.52	74

** Represents the properties that show significant difference between OS and DOS. The data reported are average data based on three parallel measurements.*

and 665 μeq/g for DOS with 5 wt% $NaClO_2$ treatment. The increased surface charge is beneficial for metal ion adsorption. Considering the high yield and surface charge, the delignified samples used in the following are obtained with $NaClO_2$ concentration of 5 wt%, powder concentration of 15 wt% at a delignification temperature of 80°C.

The olive stone powder is light brown initially with a powder size of 100–315 μm (**Figure 2A**). The particles are bundles of elongated cells as shown in **Figure 2B**. A rough and dense surface is detectable. There are plasmodesma structures for interconnection between adjacent cells (**Figure 2C**). After delignification, the olive stone powder becomes white as shown in **Figure 2D**. Lignin content was changed from 29.4 wt% for original olive stone to 3.1 wt% for delignified olive stone (**Table 1**). Around 90% of the lignin was thus eliminated after the treatment. In **Figures 2D, E**, most of the cells are separated from cell aggregates, leading to a decreased particle size (normally less than 100 μm). There are layers of cell materials peeling off from the particles, which can be seen form **Figure 2E** and **Supplementary Figure S1** in supporting information. Fibril structures are apparent on the edge of the particles (**Figure 2F**). The decreased particle size, peeling off of the cell wall as well as the fibril structures generated all contribute to an increased specific surface area. At the same time, EDX mapping showed that DOS sample has C, O, Na, Cl and Pt elements after delignification while OS only has C, O and Pt elements (**Supplementary Figure S3**). The Pt in both samples was derived from coating, and the trace amount of Na and Cl inside DOS came from the salts used in the delignification process.

FTIR was applied to monitor the chemical structure change after delignification (**Figure 2G**). The peak at 1732 cm^{-1} and 2906 cm^{-1} are assigned to the stretching vibration of the carbonyl group. The broadening and intensity increase of

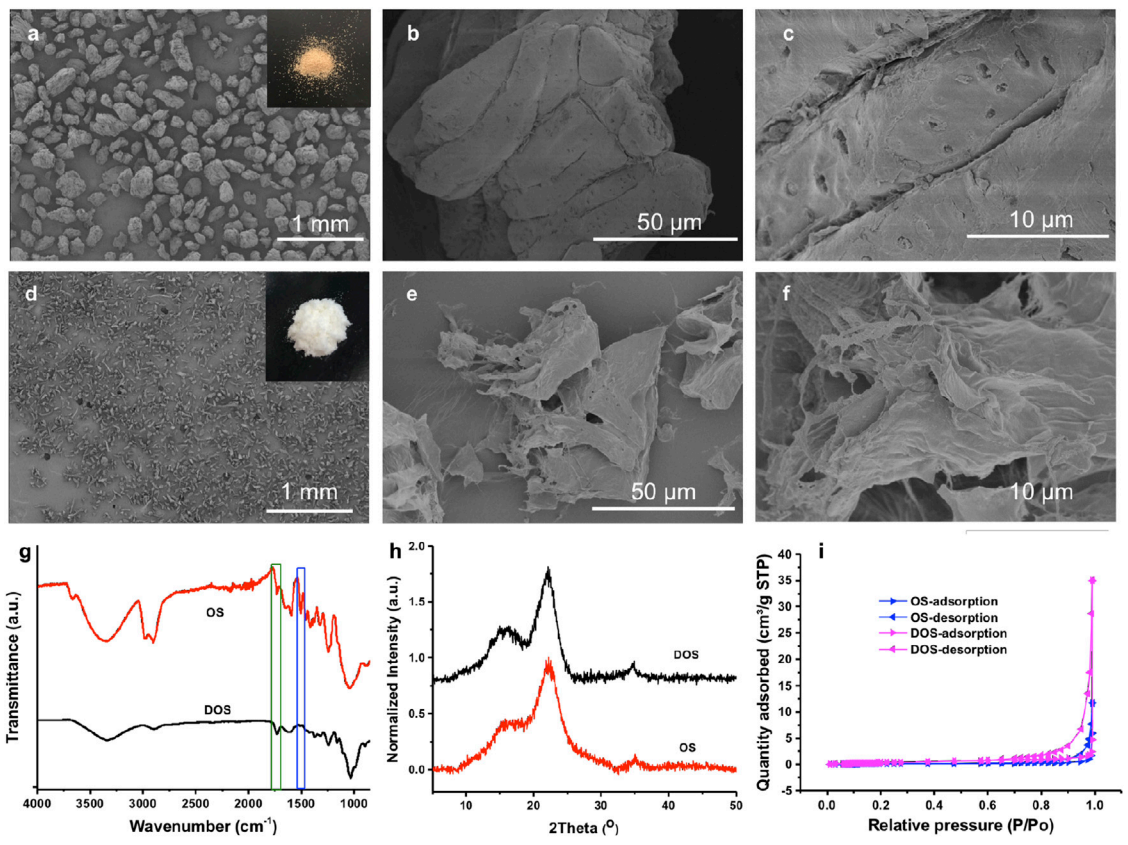

FIGURE 2 | SEM images of original olive stone powder **(A–C)**, and delignified olive stone powder **(D–F)**. Inset images in **(A)** and **(D)** are photos of original stone powder and delignified olive stone powder respectively. **(G–I)** are the FTIR spectra, XRD spectra, and nitrogen adsorption-desorption isotherms of original olive stone powder (OS) and delignified olive stone powder (DOS) respectively.

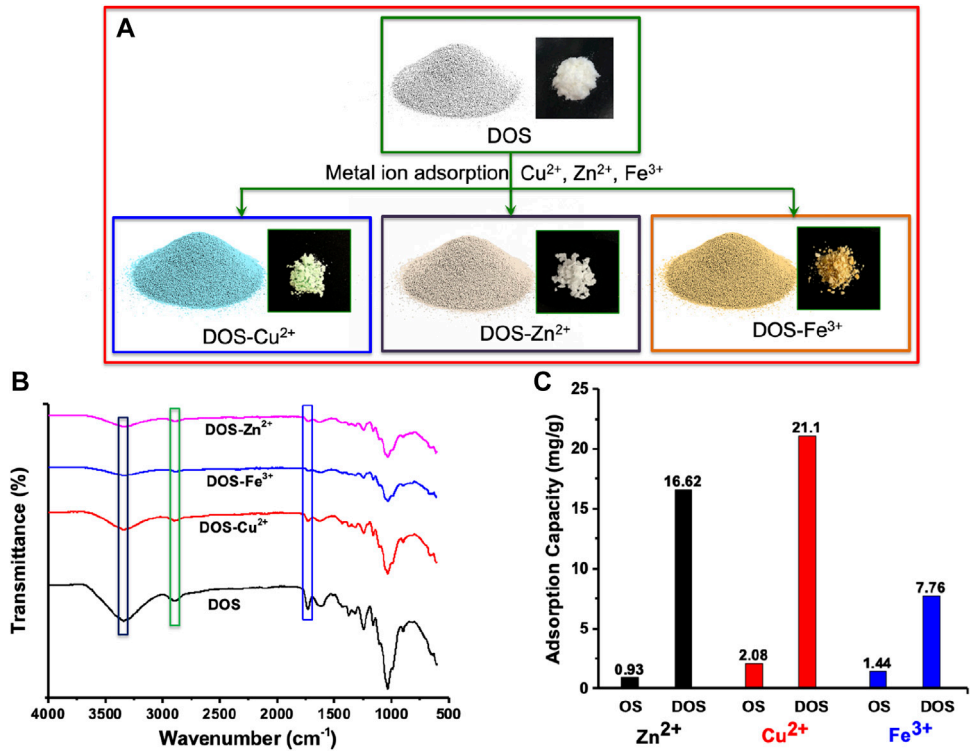

FIGURE 3 | (A) illustrates color change of delignified olive stone powder after differences in metal ion adsorption. **(B)** FTIR spectra of delignified olive stone powder after adsorption of Fe^{3+}, Cu^{2+}, and Zn^{2+}. **(C)** metal ion absorption of original olive stone powder (OS) and delignified olive stone powder (DOS) for different metal ions.

the peak at 1732 cm^{-1} indicates the introduction of carbonyl groups in the delignified olive stone powder. This was mainly due to the generation of carboxylic groups during the treatment. This was further supported by the increased surface charge from 47 μeq/g for original olive stone powder to 665 μeq/g for delignified olive stone powder. The peak at around 1500 cm^{-1} is assigned to aromatic rings, a characteristic peak for lignin. The peak disappears after delignification, in support of lignin removal.

Both original olive stone powder and delignified olive stone powder show the same cellulose crystal structure. **Figure 2H** shows the relative XRD spectra. The peaks at 22.6°, between 14.5° and 16.5°, and around 34°, correspond to the presence of cellulose I in the materials. With peak intensity method, the crystallnity index (CrI) is 66% for original olive stone powder and 74% for delignified olive stone powder (**Table 1**). This increase in CrI is mainly due to the removal of lignin and hemicellulose, which are considered as amorphous components.

A high specific surface area is preferred for a high metal ion adsorption capacity. BET SSA was obtained through physisorption measurements of N_2 on powders. **Figure 2I** shows the N_2 adsorption-desorption isotherms. In both graphs, a hysteresis cycle is observed, a characteristic aspect of type V isotherms. The BET SSA of delignified olive stone powder is 1.52 m^2/g, lager than that of original olive stone powder (0.44 m^2/g). The pore volume is 0.000530 cm^3/g for DOS, higher than that of OS (0.000187 cm^3/g). One reason for the difference is that, lignin, some hemicellulose and cellulose are eliminated (around 33.1% weight loss), leading to the formation of pores and increased surface area. In addition, decreased particle size and fibril structures contribute to increased specific surface area.

Metal Ion Adsorption Test

The adsorption of Fe^{3+}, Cu^{2+}, and Zn^{2+} were demonstrated by batch technique under pH of 4.5. The powder color changed after metal ion adsorption. Photos of the olive stone powders are shown in **Figure 3A**. The white powder became light blue after Cu^{2+} adsorption and became light yellow after Fe^{3+} adsorption. It remains colorless after Zn^{2+} adsorption. This is an advantage of delignified olive stone powder that adsorption of specific metal ions could be reflected through color change. For carbonized black powders or brown original olive stone powder with lignin, the metal ion color change is not apparent after adsorption. In addition, the difference between a low concentration metal ions adsorption and a high concentration adsorption is visually apparent by color differences. The sample with a high Cu^{2+} concentration is dark blue, while the sample with a low Cu^{2+} concentration is light blue (**Supplementary Figure S2** in the supporting information).

The hypothesis for metal ion adsorption mechanisms on DOS powder is the ion exchange of the metal ion with the H^+ in the carboxylic groups. FTIR spectra reflect the exchange between

metal ion and carboxylic groups (**Figure 3B**). The decreased peak intensities at 1732 cm^{-1} and 2,906 cm^{-1} are due to the decrease of carboxylic group stretch dimer H-bonded. These peaks and bands prove the presence of the hydroxyl group and the carboxylic groups of cellulose and hemicellulose in the biosorbent, which are responsible for the metal adsorption. The broad band that appeared at 3338 cm^{-1} is characteristic stretching vibration of the hydroxyl group due to hydrogen bonding O–H to a carboxyl, phenol or alcohol group. The results of the adsorbent before and after adsorption were compared. There are significant changes in peaks at 3338 cm^{-1}, 2906 cm^{-1} and 1732 cm^{-1}. These red shifts indicate that the hydroxyl and carboxyl groups are involved in the adsorption of the metals (Parthasarathy and Narayanan, 2014).

A high metal ion adsorption capacity is required for real applications. In this work, the adsorption capacity of delignified olive stone powder is 7.76 mg/g for Fe^{3+}, 21.1 mg/g for Cu^{2+}, and 16.62 mg/g for Zn^{2+} respectively (**Figure 3C**). These values are much higher than that of original olive stone powder with a capacity of 1.44 mg/g for Fe^{3+}, 2.08 mg/g for Cu^{2+}, and 0.93 mg/g for Zn^{2+}. The values are among the highest adsorption data reported in the literature(Alslaibi et al., 2013; Hodaifa et al., 2014; Bohli et al., 2015; Amar et al., 2020). **Supplementary Table S4** in the supporting information is the summary of the olive stone based adsorbents for Fe^{3+}, Cu^{2+}, and Zn^{2+} adsorption(Alslaibi et al., 2014a), (Bohli et al., 2015), (Amar et al., 2020), (Galiatsatou et al., 2002; Alslaibi et al., 2014b; Bohli and Ouederni, 2016; Bohli et al., 2017; Fernández-González et al., 2018, Fernández-González et al., 2020). A high adsorption capacity is usually realized through carbonization combined with proper activation (**Supplementary Table S4**). With carbonization, the yield is low (less than 50%), embodied energy of the powder increased and the process cost is strongly increased. With delignification, the yield is high (normally higher than 50%) and the treatment process is easy to be scaled up at a low cost. Meanwhile, the delignified olive stone powder can desorb metal ions easily by the use of strong acid. After addition of 2M HCl into Cu^{2+} adsorbed samples followed by stirring for 1 h, the sample released Cu^{2+} into the water again and returned to white appearance. This demonstrates the possibility to recycle the olive stone powder as a metal ion adsorbent.

CONCLUSION

Delignification was applied to olive stone powder resulting in a high surface charge due to introduction of carboxylic groups and an increased specific surface area mainly ascribing to the lignin removal, decreased particle size as well as fibril structure generation. Delignified olive stone powder was further applied for metal ion adsorption showing an improved adsorption capacity. The adsorption capacities are 7.76 mg/g for Fe^{3+}, 21.1 mg/g for Cu^{2+}, and 16.62 mg/g for Zn^{2+} respectively, which are among the highest values in the literature. The method is scalable with a relatively low cost. In addition, delignification results in white olive stone powder. This broadens the applications of olive stone powders with optical functionalities such as transparent composites. There is a green perspective to use agricultural waste products, such as olive stone powder.

DATA AVAILABILITY STATEMENT

The original contributions presented in the study are included in the article/**Supplementary Material**, further inquiries can be directed to the corresponding author.

AUTHOR CONTRIBUTIONS

YG did the experiments, analyzed data, and wrote the manuscript. MT did part of the experiments and wrote part of the manuscript. JG did the XRD and BET measurements. XS did the surface charge and FTIR characterization. YL conceived the idea, designed the experiments, and supervised the work. LB conceived the idea and supervised the work. All authors provided critical feedback and edited the manuscript.

FUNDING

This project has received funding from the European Research Council (ERC) under the European Union's Horizon 2020 research and innovation program (Grant Agreement No. 742733) at KTH Royal Institute of Technology and the funding from Vetenskapsrådet (VR, No. 2017-05349). YG acknowledges financial support from project funded by the National First-class Disciplines (PNFD) and the Priority Academic Program Development of Jiangsu Higher Education Institutions (PAPD).

ACKNOWLEDGMENTS

The company, BioPowder, was acknowledged for supplying the olive stone powder. Hui Chen and Xuan Yang are acknowledged for the help in the lignin content measurements. Yi Yang is acknowledged for the help of metal ions concentration test.

SUPPLEMENTARY MATERIAL

The Supplementary Material for this article can be found online at: https://www.frontiersin.org/articles/10.3389/fmats.2021.605931/full#supplementary-material.

REFERENCES

Alslaibi, T. M., Abustan, I., Ahmad, M. A., and Abu Foul, A. (2014a). Comparison of activated carbon prepared from olive stones by microwave and conventional heating for iron (II), lead (II), and copper (II) removal from synthetic wastewater. *Environ. Prog. Sustain. Energy.* 33 (4), 1074–1085. doi:10.1002/ep.11877

Alslaibi, T. M., Abustan, I., Ahmad, M. A., and Abu Foul, A. (2014b). Preparation of activated carbon from olive stone waste: optimization study on the removal of Cu2+, Cd2+, Ni2+, Pb2+, Fe2+, and Zn2+ from aqueous solution using response surface methodology. *J. Dispersion Sci. Technol.* 35 (7), 913–925. doi:10.1080/01932691.2013.809506

Alslaibi, T. M., Abustan, I., Ahmad, M. A., and Foul, A. A. (2013). Application of response surface methodology (RSM) for optimization of Cu2+, Cd2+, Ni2+, Pb2+, Fe2+, and Zn2+ removal from aqueous solution using microwaved olive stone activated carbon. *J. Chem. Technol. Biotechnol.* 88 (12), 2141–2151. doi:10.1002/jctb.4073

Amar, M. B., Walha, K., and Salvadó, V. (2020). Evaluation of olive stones for Cd(II), Cu(II), Pb(II) and Cr(VI) biosorption from aqueous solution: equilibrium and kinetics. *Int. J. Environ. Res.* 14 (2), 193–204. doi:10.1007/s41742-020-00246-5

Aziz, A., Elandaloussi, el. H., Belhalfaoui, B., Ouali, M. S., and De Ménorval, L. C. (2009a). Efficiency of succinylated-olive stone biosorbent on the removal of cadmium ions from aqueous solutions. *Colloids Surf. B Biointerfaces* 73 (2), 192–198. doi:10.1016/j.colsurfb.2009.05.017

Aziz, A., Ouali, M. S., Elandaloussi, el. H., De Menorval, L. C., and Lindheimer, M. (2009b). Chemically modified olive stone: a low-cost sorbent for heavy metals and basic dyes removal from aqueous solutions. *J. Hazard Mater.* 163 (1), 441–447. doi:10.1016/j.jhazmat.2008.06.117

Blázquez, G., Calero, M., Ronda, A., Tenorio, G., and Martín-Lara, M. A. (2014). Study of kinetics in the biosorption of lead onto native and chemically treated olive stone. *J. Ind. Eng. Chem.* 20 (5), 2754–2760. doi:10.1016/j.jiec.2013.11.003

Bohli, T., and Ouederni, A. (2016). Improvement of oxygen-containing functional groups on olive stones activated carbon by ozone and nitric acid for heavy metals removal from aqueous phase. *Environ. Sci. Pollut. Res. Int.* 23 (16), 15852–15861. doi:10.1007/s11356-015-4330-0

Bohli, T., Ouederni, A., Fiol, N., and Villaescusa, I. (2015). Evaluation of an activated carbon from olive stones used as an adsorbent for heavy metal removal from aqueous phases. *Compt. Rendus Chem.* 18 (1), 88–99. doi:10.1016/j.crci.2014.05.009

Bohli, T., Ouederni, A., and Villaescusa, I. (2017). Simultaneous adsorption behavior of heavy metals onto microporous olive stones activated carbon: analysis of metal interactions. *Euro-Mediterranean J. Environ. Integr.* 2 (1), 1–15. doi:10.1007/s41207-017-0030-0

Budinova, T., Petrov, N., Razvigorova, M., Parra, J., and Galiatsatou, P. (2006). Removal of arsenic(III) from aqueous solution by activated carbons prepared from solvent extracted olive pulp and olive stones. *Ind. Eng. Chem. Res.* 45 (6), 1896–1901. doi:10.1021/ie051217a

Chen, Z., Dang, B., Luo, X., Li, W., Li, J., Yu, H., et al. (2019). Deep eutectic solvent-assisted *in Situ* wood delignification: a promising strategy to enhance the efficiency of wood-based solar steam generation devices. *ACS Appl. Mater. Interfaces.* 11 (29), 26032–26037. doi:10.1021/acsami.9b08244

De Hoces, M. C., Blázquez García, G., Gálvez, A. R., and Martín-Lara, M. Á. (2010). Effect of the acid treatment of olive stone on the biosorption of lead in a packed-bed column. *Ind. Eng. Chem. Res.* 49 (24), 12587–12595. doi:10.1021/ie1013597

Fernández-González, R., Martín-Lara, M. A., Blázquez, G., Tenorio, G., and Calero, M. (2020). Hydrolyzed olive cake as novel adsorbent for copper removal from fertilizer industry wastewater. *J. Clean. Prod.* 268, 121935. doi:10.1016/j.jclepro.2020.121935

Fernández-González, R., Martín-Lara, M. A., Iáñez-Rodríguez, I., and Calero, M. (2018). Removal of heavy metals from acid mining effluents by hydrolyzed olive cake. *Bioresour. Technol.* 268, 169–175. doi:10.1016/j.biortech.2018.07.124

Galiatsatou, P., Metaxas, M., and Kasselouri-Rigopoulou, V. (2002). Adsorption of zinc by activated carbons prepared from solvent extracted olive pulp. *J. Hazard Mater.* 91 (1–3), 187–203. doi:10.1016/s0304-3894(02)00008-0

Gautam, R. K., Mudhoo, A., Lofrano, G., and Chattopadhyaya, M. C. (2014). Biomass-derived biosorbents for metal ions sequestration: adsorbent modification and activation methods and adsorbent regeneration. *J. Environ. Chem. Eng.* 2 (1), 239–259. doi:10.1016/j.jece.2013.12.019

Hodaifa, G., Alami, S. B. D., Ochando-Pulido, J. M., and Víctor-Ortega, M. D. (2014). Iron removal from liquid effluents by olive stones on adsorption column: breakthrough curves. *Ecol. Eng.* 73, 270–275. doi:10.1016/j.ecoleng.2014.09.049

Jiang, J., Carrillo-Enríquez, N., Oguzlu, H., Han, X., Bi, R., Saddler, J., et al. (2020). Acidic deep eutectic solvent assisted isolation of lignin containing nanocellulose from thermomechanical pulp. *Carbohydr. Polym.* 247, 116727. doi:10.1016/j.carbpol.2020.116727

Keplinger, T., Wittel, F. K., Rüggeberg, M., and Burgert, I. (2020). Wood derived cellulose scaffolds—processing and Mechanics. *Adv. Mater.*, e2001375. doi:10.1002/adma.202001375

Li, K., Wang, S., Chen, H., Yang, X., Berglund, L. A., and Zhou, Q. (2020). Self-densification of highly mesoporous wood structure into a strong and transparent film. *Adv. Mater.* 32 (42), e2003653. doi:10.1002/adma.202003653

Li, T., Zhai, Y., He, S., Gan, W., Wei, Z., Heidarinejad, M., et al. 2019). A radiative cooling structural material. *Science* 364 (6442), 760–763. doi:10.1126/science.aau9101

Li, Y., Fu, Q., Rojas, R., Yan, M., Lawoko, M., and Berglund, L. (2017a). Lignin-retaining transparent wood. *ChemSusChem*. 10 (17), 3445–3451. doi:10.1002/cssc.201701089

Li, Y., Yang, X., Fu, Q., Rojas, R., Yan, M., and Berglund, L. A. (2017b). Towards centimeter thick transparent wood through interface manipulation. *J. Mater. Chem.* 6 (3), 1094–1101. doi:10.1039/C7TA09973H

Li, Y., Fu, Q., Yu, S., Yan, M., and Berglund, L. (2016). Optically transparent wood from a nanoporous cellulosic template: combining functional and structural performance. *Biomacromolecules* 17 (4), 1358–1364. doi:10.1021/acs.biomac.6b00145

Li, Y., Yang, X., Fu, Q., Rojas, R., Yan, M., and Berglund, L. (2018). Towards centimeter thick transparent wood through interface manipulation. *J. Mater. Chem.* 6 (3), 1094–1101. doi:10.1039/c7ta09973h

Lozano, R. (2018). Measuring progress from 1990 to 2017 and projecting attainment to 2030 of the health-related Sustainable Development Goals for 195 countries and territories: a systematic analysis for the Global Burden of Disease Study 2017. *Lancet* 392 (10159), 2091–2138. doi:10.1016/S0140-6736(18)32281-5

Parthasarathy, P., and Narayanan, S. K. (2014). Effect of hydrothermal carbonization reaction parameters on. *Environ. Prog. Sustain. Energy* 33, 676–680.

Rodríguez, G., Lama, A., Rodríguez, R., Jiménez, A., Guillén, R., and Fernández-Bolaños, J. (2008). Olive stone an attractive source of bioactive and valuable compounds. *Bioresour. Technol.* 99 (13), 5261–5269. doi:10.1016/j.biortech.2007.11.027

Rodríguez-Gutiérrez, G., Rubio-Senent, F., Lama-Muñoz, A., García, A., and Fernández-Bolaños, J. (2014). Properties of lignin, cellulose, and hemicelluloses isolated from olive cake and olive stones: binding of water, oil, bile acids, and glucose. *J. Agric. Food Chem.* 62 (36), 8973–8981. doi:10.1021/jf502062b

Saleem, J., Shahid, U. B., Hijab, M., Mackey, H., and McKay, G. (2019). Production and applications of activated carbons as adsorbents from olive stones. *Biomass Conv. Bioref.* 9 (4), 775–802. doi:10.1007/s13399-019-00473-7

Tappi (2011). Lignin in wood and pulp, T222 om-02, 1–7.

Vera, I., Hoefnagels, R., Kooij, A., Moretti, C., and Junginger, M. (2020). A carbon footprint assessment of multi-output biorefineries with international biomass supply: a case study for The Netherlands. *Biofuels. Bioprod. Bioref.* 14 (2), 198–224. doi:10.1002/bbb.2052

Wong, A., Zhang, H., and Kumar, A. (2016). Life cycle water footprint of hydrogenation-derived renewable diesel production from lignocellulosic biomass. *Water Res.* 102, 330–345. doi:10.1016/j.watres.2016.06.045

Conflict of Interest: The authors declare that the research was conducted in the absence of any commercial or financial relationships that could be construed as a potential conflict of interest.

Polymeric and Composite Materials

Monica Boffito

Dr. Monica Boffito achieved a degree in Biomedical Engineering in 2010 and obtained her Ph.D. in Biomedical Engineering in 2014 at Politecnico di Torino, Italy. She has documented experience in biomaterial design [mainly poly(urethane)s], characterization, and processing into 3D scaffolds or injectable hydrogels (e.g., thermo-, pH-, and light-sensitive hydrogels and supramolecular hydrogels). After receiving her Ph.D., she worked at Politecnico di Torino, first as post-doctoral fellow and then as a researcher with a fixed-term contract, becoming a tenure-track researcher in 2019. She is the author of 29 publications in peer-reviewed journals, five book chapters, and two patents. She has an h-index of 14 with around 600 citations (SCOPUS).

frontiers in Materials

ORIGINAL RESEARCH
published: 23 November 2020
doi: 10.3389/fmats.2020.594515

Using Poloxamer® 407 as Building Block of Amphiphilic Poly(ether urethane)s: Effect of its Molecular Weight Distribution on Thermo-Sensitive Hydrogel Performances in the Perspective of Their Biomedical Application

Rossella Laurano[1], Michela Abrami[2], Mario Grassi[2], Gianluca Ciardelli[1], Monica Boffito[1†] and Valeria Chiono[1†]*

[1] *Department of Mechanical and Aerospace Engineering, Politecnico di Torino, Torino, Italy,* [2] *Department of Engineering and Architecture, Università degli Studi di Trieste, Trieste, Italy*

OPEN ACCESS

Edited by:
Miriam Navlani-García, University of Alicante, Spain

Reviewed by:
Mehdi Derradji, Polytechnic School of Algiers, Algeria
Dagmar Merinska, Tomas Bata University in Zlín, Czechia

***Correspondence:**
Monica Boffito
monica.boffito@polito.it

†These authors have contributed equally to the supervision of the first author.

Specialty section:
This article was submitted to Polymeric and Composite Materials, a section of the journal Frontiers in Materials

Received: *14 August 2020*
Accepted: *19 October 2020*
Published: *23 November 2020*

Citation:
Laurano R, Abrami M, Grassi M, Ciardelli G, Boffito M and Chiono V (2020) Using Poloxamer® 407 as Building Block of Amphiphilic Poly(ether urethane)s: Effect of its Molecular Weight Distribution on Thermo-Sensitive Hydrogel Performances in the Perspective of Their Biomedical Application. Front. Mater. 7:594515. doi: 10.3389/fmats.2020.594515

Due to its hydroxyl terminal groups, Poloxamer® 407 (P407), a commercially available poly(ethylene oxide)-poly(propylene oxide)-poly(ethylene oxide) (PEO-PPO-PEO) triblock copolymer can be used as macrodiol for the synthesis of high molecular weight amphiphilic poly(ether urethane)s (PEUs). This work was aimed at studying the effect of P407 purification by removing PEO-PPO diblock copolymer by-products on the chemical properties of PEU polymer and the physical properties of PEU hydrogels. Removal of PEO-PPO diblock copolymers (P407_P) was found to preserve the thermo-responsiveness of resulting hydrogels, although slightly lower gelation onset temperature (T_{onset}) was found for P407_P (15.3°C) *vs*. P407 (16.7°C) hydrogels (25% w/V) as assessed through temperature ramp test. P407 and P407_P were then reacted with 1,6-diisocyanatohexane and 1,4-cyclohexanedimethanol to synthesize two different PEUs, coded as CHP407 and CHP407_P, respectively. Lower Number Average Molecular Weight ($\overline{M_n}$) and higher polydispersity Index (D) was measured for CHP407 ($\overline{M_n}$: 34 kDa, D: 1.6) respect to CHP407_P ($\overline{M_n}$: 40 kDa, D: 1.4) as a consequence of macrodiol purification. CHP407_P hydrogels formed bigger micelles (43.9 ± 4.1 nm *vs*. 28.7 ± 4 nm) while showed similar critical micellar temperatures (22.1°C *vs*. 21.6°C) respect to CHP407 formulations. Sol-to-gel transition of CHP407 and CHP407_P hydrogels was similar while CHP407_P gelation time at 37°C was longer as assessed by tube inverting test. The rheological analysis showed slightly lower T_{onset} for CHP407_P hydrogels (15% w/V), probably due to larger micelle size, promoting micellar assembly. However, CHP407_P hydrogels showed a significantly lower critical strain than CHP407 hydrogels, as assessed by strain sweep test, suggesting their higher brittleness due to a lower density of intermicellar bridge chains. Nano-scale hydrogel characterization by Low-Field Nuclear Magnetic Resonance spectroscopy supported previous findings, showing lower spin-spin relaxation time (i.e., 1,259 ms) for CHP407_P than for CHP407 hydrogels (i.e., 1,560 ms)

at 37°C, which suggested the formation of a more tightly packed network for CHP407_P than CHP407 hydrogel. Finally, lower swelling capability and resistance against dissolution were measured for CHP407_P hydrogels. Overall, the here-reported results suggested that the heterogeneous structure in the CHP407 hydrogel network caused by the presence of diblock copolymer-based macrodiols improved PEU hydrogel properties in light of their applicability in the biomedical field.

Keywords: poly(ether urethane)s, reagent purity, hydrogel performances, nanoscale characterization, micellar hydrogels, thermo-sensitive hydrogels

INTRODUCTION

Linear poly(urethane)s are known to be a versatile family of synthetic block-copolymers resulting from the reaction between three main building blocks, namely a macrodiol, a diisocyanate and a chain extender. The versatility of this class of polymers basically derives from their LEGO-like structure, which allows the synthesis of materials with different properties by simply changing their building blocks. Due to this unique feature, poly (urethane)s are widely used in extremely different fields, e.g., transportation, packaging, electronics and chemical and textile industries. Based on the selected reagents, the poly(urethane) family can be further subdivided into many sub-classes, such as thermoplastic, elastomeric, water-soluble and stimuli-responsive poly(urethane)s. For instance, thermoplastic poly (urethane)s have been usually synthesized using poly (ε-caprolactone), poly(lactic acid) or poly(hydroxyalcanoate)s as building blocks (Chen et al., 2013; Wang et al., 2019; Ping et al., 2005, Chen et al., 2003). On the other hand, water-soluble poly(urethane)s have been commonly designed by embedding poly(ethylene glycol) (PEG) moieties into their backbone (Caddeo et al., 2019; Doseva et al., 2004). Furthermore, through a proper selection of poly(ethylene glycol)-based building blocks, molecular weight and molar ratio, it is possible to synthesize amphiphilic water-soluble poly(urethane)s which aqueous solutions show a thermo-responsive behavior (Polo Fonseca et al., 2016; Ronco et al., 2017; Boffito et al., 2019). Among stimuli-responsive poly (urethane)s, different strategies have been explored to provide polymers with sensitivity to external stimuli. For instance, Boffito and colleagues (Boffito et al., 2020) synthesized a multi-functional poly(ether urethane) (PEU) by selecting an amphiphilic macrodiol (i.e., Poloxamer® 407) and a chain extender exposing primary amines (i.e., N-Boc Serinol) to ensure hydrogel thermo-sensitivity and acid pH-responsiveness, respectively. In another work, to provide poly (urethane)s with responsiveness to light irradiation, Pereira et al. (2010) reacted poly(ε-caprolactone) diol or poly (propylene glycol) with isophorone diisocyanate and 2-hydroxyethyl methacrylate, thus exposing photo-sensitive moieties. Differently, to the same final purpose, Laurano et al. (2020) selected an amino-group bearing chain extender (i.e., N-Boc diethanolamine) to first synthesize a high molecular weight poly(urethane), which was later functionalized with thioglycolic acid through carbodiimide-mediated reactions to expose thiol groups. Within each sub-class of poly(urethane)s, many works have been published on the investigation of the influence of reagent properties on the final polymer mechanical, biological and stability behaviors (Zhang et al., 2010; Ng et al., 1973; Tanaka and Kunimura, 2002; Gradinaru et al., 2012; Sartori et al., 2013; Silvestri et al., 2014; Mystkowska et al., 2017; Doseva et al., 2004, Lee et al., 2018). However, to the best of our knowledge, no works have been reported focusing on the relationship occurring between reagent purity and the resultant poly(urethane) properties and deriving performances. Poloxamers® are a family of commercial amphiphilic triblock copolymers extensively applied for the synthesis of PEUs forming hydrogels with improved thermo-sensitivity and stability in watery medium compared to Poloxamer®-based systems (Boffito et al., 2016; Cohn et al., 2006; Bonilla-Hernández et al., 2020; Whang et al., 2018; Lan et al., 1996). Within the Poloxamer® family, Poloxamer® 407 (P407) is a poly(ethylene oxide)-poly(propylene oxide)-poly(ethylene oxide) (PEO-PPO-PEO) triblock copolymer with 70% wt PEO content. However, P407 also contains PEO-PPO diblock copolymers resulting from the synthesis procedure and not completely removed during the purification steps. Therefore, P407 is characterized by a bimodal molecular weight distribution profile, with the low molecular weight component potentially affecting the physico-chemical properties of synthesized PEUs. In a recently published work, Fakhari et al. (2017) proposed a purification method able to reduce the PEO-PPO content, preserving hydrogel thermo-sensitivity and improving their mechanical behavior. Based on results on purified P407 and on a recently published method for the synthesis of a high molecular weight PEU containing P407 blocks (Laurano and Boffito 2020), this work was aimed at studying the properties of the PEU synthesized from P407, before and after its purification. Specifically, P407 was first subjected to the purification procedure (P407_P) proposed by Fakhari et al. (2017) and characterized to assess the repeatability of the published protocol. Subsequently, both P407 as such and P407_P were reacted with 1,6-hexamethylene diisocyanate and 1,4-cyclohexanedimethanol to obtain a high molecular weight PEU. The success of the synthesis was verified through infrared spectroscopy and chromatographic analyses. Subsequently, PEU chain capability to arrange into organized micelles upon dissolution in aqueous media was studied by estimating the micelle average hydrodynamic diameters and the critical micellar temperature (CMT). Then, hydrogel thermo-responsiveness and structural changes were studied both at the

macro-scale through rheological characterization, and at the nano-scale exploiting an innovative, non-destructive technique named Low-Field Nuclear Magnetic Resonance spectroscopy (LF-NMR) (Li et al., 2017). Lastly, hydrogel dissolution and swelling behavior in contact with simulated body fluids (i.e., Trizma® buffer, pH 7.4) was investigated, defining the most promising PEU formulation for biomedical applications.

MATERIALS AND METHODS

Poloxamer® 407 Purification

To remove impurities and by-product low molecular weight chains, i.e., diblock copolymers composed of poly(ethylene oxide)-poly(propylene oxide) (PEO-PPO), Poloxamer® 407 (P407, PEO-PPO-PEO triblock copolymer, $\overline{M_n}$ 12,600 Da, 70% wt PEO, Sigma-Aldrich, Italy) was subjected to a purification step according to the method reported by Fakhari et al. (2017) with slight modifications. More in detail, at each time point, the time required for a complete phase separation was reduced to 7 h (see **Supplementary Material** for a detailed description of the adopted protocol).

Hereafter, the purified macrodiol will be referred to with the acronym P407_P.

Purified Poloxamer® 407 Characterization

To assess the successful removal of low molecular weight chains and to verify the repeatability of the procedure, Size Exclusion Chromatography (SEC) and Attenuated Total Reflectance Fourier Transform Infrared (ATR-FTIR) spectroscopy were performed on P407_P samples belonging to three different purified batches. The same analyses were also performed on the commercial P407 for comparison. Furthermore, rheological characterization was conducted on P407_P hydrogels to investigate changes in hydrogel thermo-responsiveness with respect to P407 formulations.

Size Exclusion Chromatography

SEC analyses were performed through an Agilent Technologies 1,200 Series (CA, United States) equipped with a Refractive Index (RI) detector and two Waters Styragel columns (HR1 and HR4) conditioned at 55°C. N,N-dimethylformammide (DMF, CHROMASOLV Plus, inhibitor free, for HPLC, 99.9%, Carlo Erba Reagents, Italy), added with 0.1% w/V LiBr (Sigma-Aldrich, Italy), was used as mobile phase. A calibration curve based on poly(ethylene glycol) standards was defined in the range of peak molecular weight M_P 4,000–200,000 Da. Before analyses, 2 mg of polymer were dissolved in 1 ml of mobile phase and filtered through a 0.45 μm syringe filter (poly(tetrafluoroethylene) membrane, Whatman). Number Average Molecular Weight ($\overline{M_n}$), Weight Average Molecular Weight ($\overline{M_w}$) and polydispersity index (D) were estimated using the Agilent ChemStation software. The molecular weight distribution profiles were reported as average data of the three analyzed batches, while $\overline{M_n}$, $\overline{M_w}$ and D were reported as mean ± standard deviation.

Attenuated Total Reflectance Fourier Transform Infrared Spectroscopy

ATR-FTIR spectroscopy was conducted to verify the integrity of the characteristic P407 bonds and the absence of residual $(NH_4)_2SO_4$ salt content. Analyses were performed at room temperature (RT) using a Perkin Elmer spectrum 100 equipped with an ATR accessory (UATR KRSS) with diamond crystal. Spectra resulted from 32 scans in the range 4,000–600 cm^{-1} with a resolution of 4 cm^{-1}. Results were elaborated using the Perkin Elmer software and reported as average spectra.

Rheological Characterization

The rheological characterization was conducted using a stress-controlled rheometer (MCR302, Anton Paar Gmbh, Graz, Austria) equipped with a 50 mm parallel plate geometry and a Peltier system for temperature control. Samples were prepared by dissolving the polymer at 25% w/V concentration in double distilled water at 4°C overnight. Sol-to-gel transition was studied through temperature ramp tests carried out in the range 0–40°C, at 2°C/min rate and 0.1 s^{-1} frequency to avoid micelle disentanglement phenomena during the initial phase of the gelation process. On the other hand, strain sweep tests were conducted at 37°C (10 Hz, strain range 0.01–500% (Boffito et al., 2016)) to investigate gel resistance to applied deformation. Lastly, frequency sweep tests were performed within the linear viscoelastic region (frequency range 0.1–100 rad/s, strain 0.1%) at 25°C, 30°C and 37°C to characterize gel viscoelastic properties. For each analysis the sample was poured on the lower plate of the rheometer in the sol state at 0°C, heated at the test temperature and equilibrated for 10 min to reach thermal stability before testing.

Poly(ether urethane) Synthesis

Materials

PEUs were synthesized using either commercial P407 or P407_P as macrodiol, 1,4-cyclohexanedimethanol (CDM) as chain extender and 1,6-hexamethylene diisocyanate (HDI) as diisocyanate. CDM, HDI and dibutyltin dilaurate (DBTDL) were purchased from Sigma-Aldrich, Italy. Before use, reagents were properly treated to remove residual water and stabilizers (Pontremoli et al., 2018). Briefly, the macrodiol was dried under reduced pressure (approx. 200 mbar) at 100°C for 8 h and then cooled down to RT under vacuum; HDI was distilled under reduced pressure; CDM was stored at RT and under vacuum in a desiccator; 1,2-dichloroethane (DCE) was poured over activated molecular sieves (3 Å, activation at 120°C overnight, Sigma-Aldrich, Italy) and maintained overnight under nitrogen atmosphere. All solvents were purchased from Carlo Erba Reagents (Italy) in analytical grade.

Synthesis Protocol

PEU synthesis was carried out following the pre-polymerization method recently described by Boffito et al. (2019). Briefly, the

macrodiol (P407 or P407_P) was initially dissolved in anhydrous DCE (20% w/V concentration) at 80°C under stirring and continuous nitrogen flow. Subsequently, HDI was added at 2:1 molar ratio with respect to the macrodiol and the pre-polymerization reaction proceeded for 150 min after the addition of a catalytic amount of DBTDL (0.1% w/w with respect to the macrodiol). At the end of the first step, the mixture was cooled down to 60°C and CDM (3% w/V in anhydrous DCE) was added to the isocyanate-terminated pre-polymer solution at unitary molar ratio respect to the macrodiol. This second step of the reaction was carried on for 90 min and finally terminated through the addition of anhydrous methanol. The polymer was finally collected by precipitation in petroleum ether (4:1 volume ratio with respect to DCE total volume). To remove the catalyst and residual by-products, the polymer was then dissolved in DCE (20% w/V) and purified through precipitation in a mixture of diethyl ether/methanol (98/2 V/V, 5:1 volume ratio with respect to DCE). Finally, the PEU was collected through centrifugation (Hettik, MIKRO 220R) at 0°C and 6,000 rpm for 20 min, dried overnight under the fume hood and stored at 4°C under nitrogen atmosphere until use.

Hereafter, the synthesized PEUs will be referred to with the acronyms CHP407 and CHP407_P, where C and H identify the chain extender and the diisocyanate, respectively, while P407 and P407_P refer to the macrodiol used for the synthesis.

Poly(ether urethane) Characterization

Size Exclusion Chromatography

To verify the successful synthesis of a high molecular weight polymer and to investigate the influence of macrodiol purity on the resultant PEU molecular weight distribution profile, SEC analysis was performed on both CHP407 and CHP407_P according to the method previously described for macrodiol characterization. The molecular weight distribution profiles were reported as average data of samples belonging to three different syntheses, while $\overline{M}_n$, $\overline{M}_w$ and D were reported as mean ± standard deviation.

Attenuated Total Reflectance Fourier Transform Infrared Spectroscopy

To assess the appearance of the characteristic vibrational bands of urethane bonds, ATR-FTIR spectroscopy was performed on both CHP407 and CHP407_P according to the protocol previously reported for macrodiol characterization. Analyses were performed in triplicate and results were reported as average spectra.

Dynamic Light Scattering

To investigate the relationship existing between PEU molecular weight distribution profile and micelle average hydrodynamic diameter, Dynamic Light Scattering (DLS) measurements were performed on both CHP407 and CHP407_P samples. To this aim, PEUs were dissolved at 0.5% w/V concentration in physiological saline solution (0.9% w/V NaCl). Analyses were performed at 25°C, 30°C, and 37°C, according to the protocol reported by Laurano et al. (2020), using a Zetasizer Nano S90 (Malvern Instruments, Worcestershire, United Kingdom) instrument. Before analysis, samples were equilibrated at the testing temperature for 15 min and then analyzed according to Pradal et al. (2013). The reported hydrodynamic diameters resulted from the average of three different analyzed samples. Data were reported as mean ± standard deviation.

Critical Micellar Temperature Evaluation

To investigate the effect of PEU molecular weight distribution profile on the temperature at which micelle nucleation begins, the CMT of PEU-based aqueous solutions was estimated using a fluorescent dye (1,6-diphenyl-1,3,5-hexatriene, DPH, Sigma-Aldrich, Italy) as micellization marker. Samples (1 ml) were prepared by dissolving the polymer at 0.5% w/V concentration in physiological saline solution (0.9% w/V NaCl). Then, DPH (0.4 mM in methanol) was added to each sample at 10 μl/ml. Analyses were conducted according to the method described by Alexandridis et al. (1994). Briefly, CHP407 and CHP407_P solutions were heated between 5°C and 40°C at 1°C/step, each step consisting of 5 min equilibration followed by UV/Vis spectra recording in the 500–300 nm spectral range (Perkin Elmer, Lambda 25). Finally, CMT was defined as the first inflection of the sigmoidal curve obtained by plotting the absorbance intensity at 356 nm *vs.* temperature as described by Boffito et al. (2016).

Poly(ether urethane)-Based Hydrogel Preparation

CHP407- and CHP407_P-based hydrogels were prepared in Bijou sample containers with an inner diameter of 17 mm (Carlo Erba Reagents, Italy) by dissolving the polymer at predefined concentrations (ranging between 5% w/V and 25% w/V) in physiological saline solution (0.9% w/V NaCl). To avoid micellization and/or gelation phenomena, which would prevent complete polymer dissolution, samples were kept at 4°C overnight.

Poly(ether urethane)-Based Hydrogel Characterization

Tube Inverting Test

Tube Inverting Test was performed to qualitatively determine the Critical Gelation Concentration (CGC) of CHP407- and CHP407_P-based solutions and to evaluate their sol-to-gel transition temperature. Specifically, samples (1 ml) were prepared as previously described and subjected to a controlled heating from 5°C to 70°C. Each step consisted of a 1 ± 0.1°C temperature increase within 30 s followed by temperature maintenance for 5 min and tube inversion that allowed the visual inspection of the sol-to-gel transition. Sol and gel conditions were defined as reported by Laurano and Boffito (2020). Briefly, "flow liquid sol" and "no flow solid gel" within 30 s of vial inversion identified the sol and gel states, respectively.

Gelation Time Test at Physiological Temperature

Gelation time test was performed at 37°C to estimate the time required by CHP407- and CHP407_P-based solutions to undergo sol-to-gel transition at physiological temperature. Specifically,

samples (1 ml) were prepared according to the above reported protocol and put in an incubator (Memmert IF75) equilibrated at 37°C. Then, at predefined time points (1–10 min, 1 min/step) samples were taken from the incubator and inverted for 30 s for the visual inspection of their sol/gel state. Conditions of sol and gel were defined as in the Tube Inverting Test. At each time point, the samples were equilibrated at 4°C for 8 min before incubation at 37°C to ensure that all systems were in the sol state at the beginning of the test.

Rheological Characterization

The influence of macrodiol purification on the capability of PEU aqueous solutions to undergo a sol-to-gel transition upon temperature increase was thoroughly investigated by means of rheological temperature ramp, frequency sweep and strain sweep tests. Specifically, CHP407 and CHP407_P samples were prepared by dissolving the polymer in physiological saline solution at the optimized concentration as defined in the Tube Inverting and Gelation Time tests. Then, both sol-gel systems were analyzed according to the protocol previously described for macrodiol rheological characterization.

Low Field Nuclear Magnetic Resonance Spectroscopy

To investigate whether the macrodiol molecular weight polydispersity could affect the PEU chain self-assembly capability into micelles in aqueous media, LF-NMR spectroscopy was exploited for an in depth nano-scale characterization. Specifically, analyses were performed on both CHP407 and CHP407_P systems using a Bruker Minispec mq20 (0.47T, Germany). The spin-spin relaxation times T_2 of PEU-based systems were measured according to the Carr-Purcell-Meiboom-Gill sequence with a 90°–180° pulse separation of 0.25 ms (number of scans = 4, delay = 5 s). To this aim, samples (500 μl at the optimized concentration) were prepared in NMR glass tubes (diameter 8 mm) and stored at 4°C until use. Then, they were incubated at 37 °C and the T_2 value was recorded at 0, 4, 8, and 10 min. Subsequently, the T_2 discrete distribution was obtained following the protocol published by Marizza et al. (2016).

Hydrogel Behavior in Aqueous Environment

Swelling and stability tests were carried out on CHP407_P hydrogels to evaluate if the absence of low molecular weight components into the macrodiol used for its synthesis could affect the stability of the systems in a watery environment. CHP407 hydrogels were also characterized for comparison. Samples (1 ml) were first prepared as previously described. Then, they were weighed to record their initial weight (W_i) and incubated at 37°C for 15 min to allow a complete sol-to-gel transition. Subsequently, 1 ml of Trizma® (0.1 M, pH 7.4, Sigma-Aldrich, Italy), previously equilibrated at 37°C to avoid gel destabilization, was added to each vial and samples were incubated for 6 h, 1, 2, 3, 7, and 14 days. Complete medium refresh was performed every other day. At each time step, three samples were taken, the residual medium was removed and the hydrogels were weighed (W_f) to assess their absorption ability (Apparent swelling %). Then, the samples were freeze-dried and weighed again ($W_{freeze\text{-}dried\_f}$) to quantify their weight loss (Weight loss %). Control samples (not incubated in Trizma® solutions) were also freeze-dried and weighed ($W_{freeze\text{-}dried\_i}$). Buffer absorption and system stability in aqueous environment were estimated according to the following equations:

$$Apparent\ swelling\ (\%) = \frac{W_f - W_i}{W_f} x\ 100 \quad (1)$$

$$Weight\ loss\ (\%) = \frac{W_{freeze-dried\_i} - W_{freeze-dried\_f}}{W_{freeze-dried\_i}} x\ 100 \quad (2)$$

Statistical Analysis

Statistical analysis was performed using GraphPad Prism 8.0 for MacOsX (GraphPad Software, La Jolla, CA, United States; www.graphpad.com). Two-way ANOVA analysis followed by Bonferroni's multiple comparison test was used to compare results. The statistical significance of each comparison was assessed as reported in (Boffito et al., 2016).

RESULTS AND DISCUSSION

Poloxamer® 407 is a commercial PEO-PPO-PEO triblock copolymer. However, it also contains PEO-PPO diblocks as by-products of the reaction synthesis. Therefore, P407 shows a bimodal molecular weight distribution profile (Fakhari et al., 2017). If it is exploited as starting reagent for the synthesis of a higher molecular weight polymer (e.g., PEUs), the presence of these by-products in the mixture may affect the resultant polymer properties. Therefore, in this work P407 was first subjected to a purification step (Fakhari et al., 2017) to remove the residual impurities and low molecular weight polymeric component (i.e., diblock copolymers). Then, the effects of P407 purification on the synthesis of a high molecular weight PEU as well as on the gelation mechanism and properties of PEU-based hydrogels were thoroughly investigated.

Poloxamer® 407 Physico-Chemical Characterization

Commercially available P407 was purified according to the protocol recently reported by Fakhari et al. (2017). The success and the repeatability of the treatment were verified through SEC and ATR-FTIR analyses, while changes in hydrogel thermo-sensitivity were assessed by means of rheological tests. Results on P407_P characterization were reported as **Supplementary Material**.

Poly(ether urethane) Chemical Characterization

To investigate whether the macrodiol purification could affect the success of poly(ether urethane) synthesis, ATR-FTIR spectroscopy was conducted on CHP407_P samples synthesized from three different batches of P407_P. The

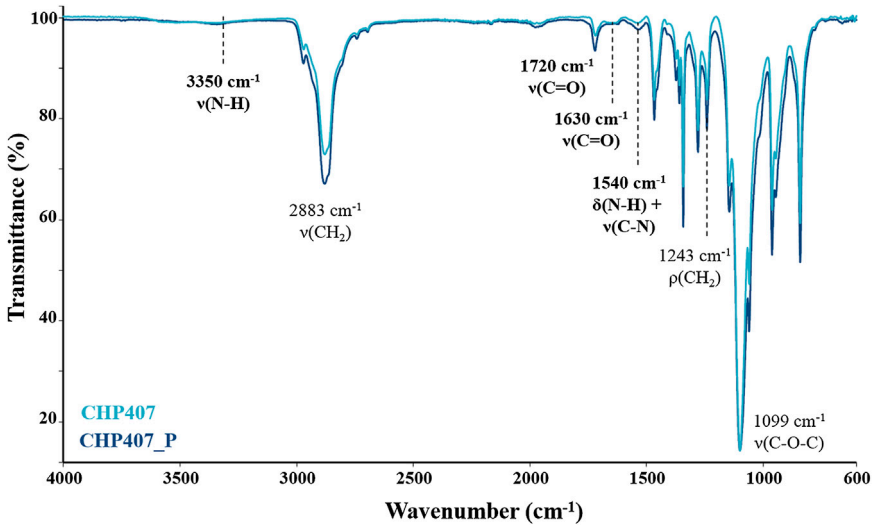

FIGURE 1 | Average ATR-FTIR spectra of CHP407 (light blue) and CHP407_P (dark blue) polymers. The bands proving the success of the synthesis are highlighted in bold.

average CHP407_P spectrum was then compared to that of CHP407 (**Figure 1**).

Irrespective of the macrodiol used, both spectra showed the characteristic bands ascribed to newly formed urethane bonds, thus proving the success of the synthesis. Specifically, the bands at 1,720 cm^{-1} and 1,630 cm^{-1} can be ascribed to the stretching vibration of carbonyl groups; the band at 3,350 cm^{-1} can be attributed to the stretching vibration of N-H bonds, while at 1,540 cm^{-1} the spectrum showed the bending vibration band of N-H bonds together with the stretching vibration band of C-N bonds (Laurano et al., 2019; Laurano et al., 2020).

Additionally, the Weight Average Molecular Weight ($\overline{M}_w$) and the Number Average Molecular Weight ($\overline{M}_n$) of the synthesized PEUs, measured through SEC analysis, were higher respect to that of the macrodiol, further confirming the synthesis of a high molecular weight polymer. Moreover, average CHP407_P molecular weights were slightly higher than for CHP407 (**Table 1**): the removal of PEO-PPO diblocks in the macrodiol avoids the formation of low molecular weight PEU chains (i.e., polymeric chains containing diblock instead of triblock macrodiol copolymers). Furthermore, the achievement of a more uniform molecular weight distribution was further proved by a reduction in the polydispersity index measured for CHP407_P PEU.

To deeply investigate changes in the molecular weight fractions in both polymers, contributing to the definition of such average values, the molecular weight distribution profiles of both CHP407 and CHP407_P were compared (**Figure 2**).

As reported in **Figure 2**, the maximum of the CHP407_P profile (M_i = 53,349 Da) was centered at values approx. equal to its $\overline{M}_w$ (i.e., 58,896 ± 1,160 Da), thus suggesting that the majority of CHP407_P chains were characterized by the same molecular weight. Conversely, the maximum of CHP407 profile was identified at 72,821 Da, hence significantly higher with respect to its $\overline{M}_w$ (i.e., 53,769 ± 1,365 Da). This result suggested the presence in CHP407 samples of a huge amount of low molecular weight chains, which lowered the Weight Average Molecular Weight. Indeed, while the lowest measured molecular weight for CHP407_P (M_i) was 10,550 Da, lower M_i values were registered for CHP407.

TABLE 1 | Number Average Molecular Weight ($\overline{M}_n$), Weight Average Molecular Weight ($\overline{M}_w$) and polydispersity index (D) estimated for CHP407 and CHP407_P polymers.

	Poly(ether urethane) parameters		
	$\overline{M}_n$ (Da)	$\overline{M}_w$ (Da)	D
CHP407	34,040 ± 1,290	53,769 ± 1,365	1.6 ± 0.03
CHP407_P	40,097 ± 980	58,896 ± 1,160	1.4 ± 0.02

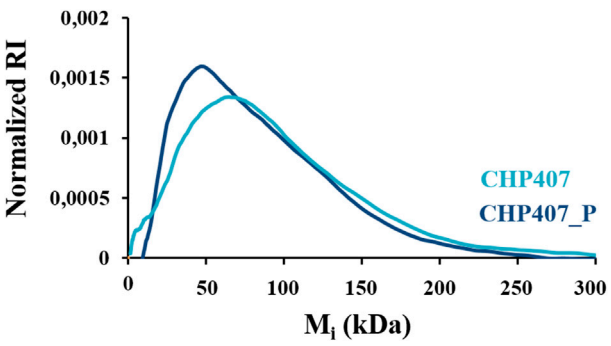

FIGURE 2 | Normalized Refractive Index (RI) signal as a function of molecular weight M_i measured for CHP407 (light blue spectrum) and CHP407_P (dark blue spectrum).

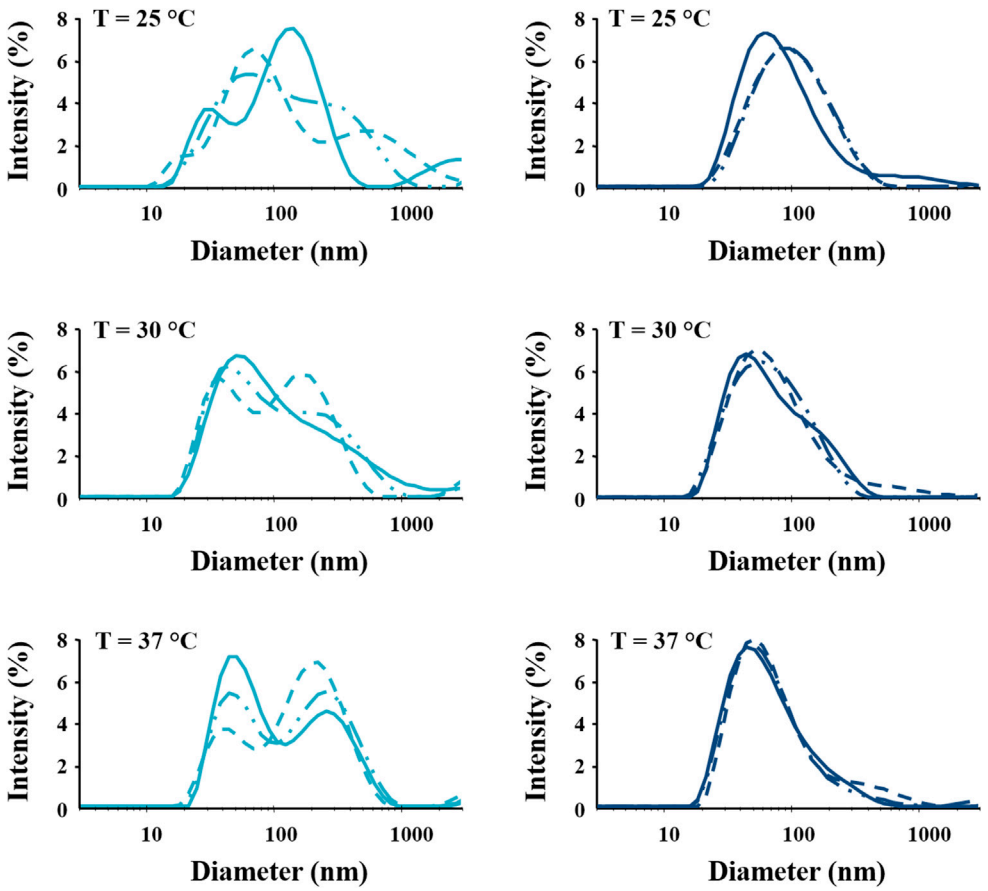

FIGURE 3 | Distribution patterns (by intensity) of micelle hydrodynamic diameter measured in CHP407 (light blue) and CHP407_P (dark blue) solutions at 0.5% w/V concentration. Analyses were performed in triplicate (continuous, dashed and dashed-dot lines represent the three registered patterns) at 25°C, 30°C and 37°C.

Thermo-sensitivity Evaluation of Poly(ether urethane)-Based Systems

CHP407 and CHP407_P chain capability to arrange into micelles upon temperature increase, derived from the presence of P407 or P407_P in their chains, was first investigated in not-gelling solutions through DLS measurements and by estimating their CMTs. Then, hydrogel thermo-sensitivity was definitely proved through Tube Inverting and Gelation Time tests, rheological characterization and Low Field Nuclear Magnetic Resonance spectroscopy. Lastly, hydrogel behavior in watery environment was investigated through swelling/stability tests.

Dynamic Light Scattering Measurements

DLS is a conventional technique usually applied to estimate the average hydrodynamic diameters of spherical structures, such as nanoparticles (Lim et al., 2013; Hoo et al., 2008). In this work, DLS measurements were adapted to investigate the effects of diblock removal from the macrodiol on the self-assembly capability of CHP407_P chains through the estimation of micelle hydrodynamic diameters. The same analyses were also performed on CHP407 for comparison. **Figures 3**, **4** report DLS intensity and volume patterns, respectively, measured at 25°C, 30°C, and 37°C for three different CHP407 and CHP407_P solutions.

As reported in **Figure 3** and **Table 2**, irrespective of the tested temperature, it was not possible to estimate a micelle average hydrodynamic diameter for CHP407 samples from the DLS intensity patterns, thus suggesting the simultaneous presence of both unimers and micelles, which continuously aggregate and disaggregate. Hence, the presence of a wide molecular weight polydispersity did not allow the formation of stable structures. Conversely, CHP407_P profiles turned out to be highly repeatable already at 25°C, with an average hydrodynamic diameter which can be attributed to micelles. These observations suggested the formation of more stable micelles as a consequence of the more uniform chain molecular weights.

For what concerns the distribution patterns by volume (**Figure 4**), both systems were able to give highly repeatable DLS measurements. Furthermore, despite the differences registered in the intensity patterns, both CHP407 and CHP407_P systems showed a unique hydrodynamic diameter distribution, which average value is characteristic of micelles (Boffito et al., 2016). However, at 25°C the average

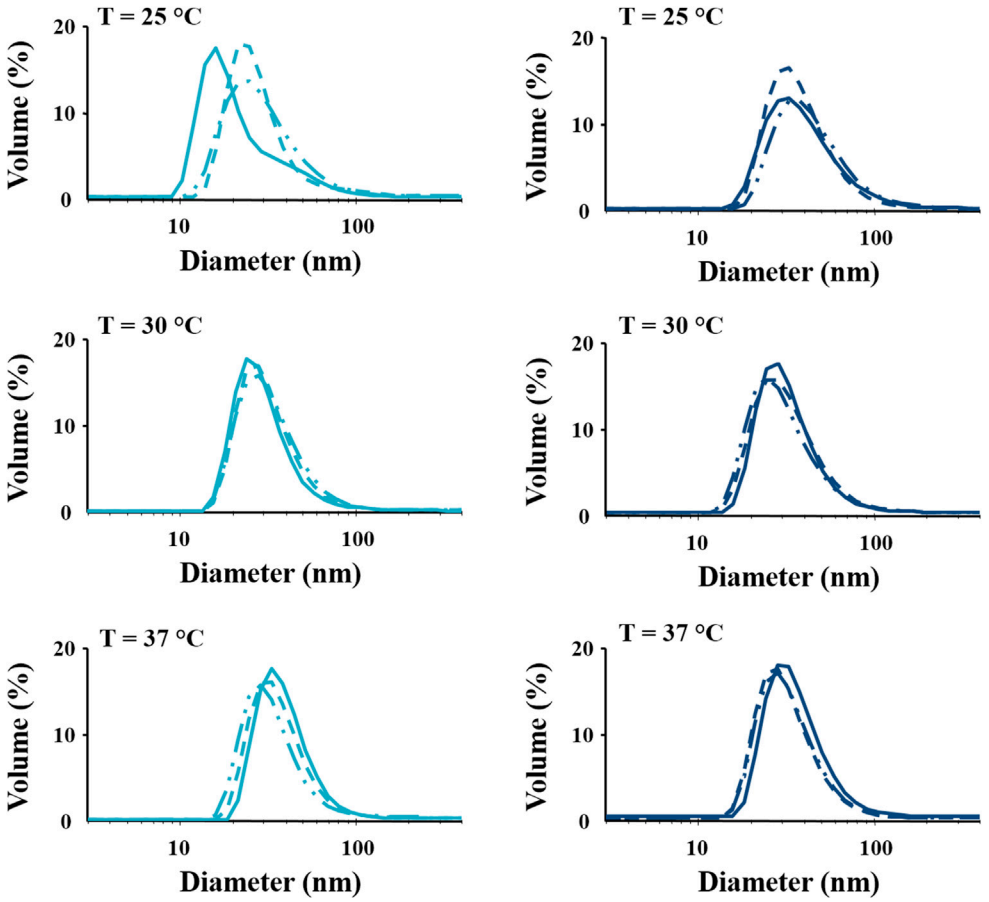

FIGURE 4 | Distribution patterns (by volume) of micelle hydrodynamic diameter measured in CHP407 (light blue) and CHP407_P (dark blue) solutions at 0.5% w/V concentration. Analyses were performed in triplicate (continuous, dashed and dashed-dotted lines represent the three registered patterns) at 25°C, 30°C and 37°C.

TABLE 2 | Micelle average hydrodynamic diameters by intensity and by volume measured for CHP407 and CHP407_P solutions (0.5% w/V concentration) at 25°C, 30°C, and 37°C.

	Micelle Hydrodynamic Diameter by Intensity (nm)		
	25°C	**30°C**	**37°C**
CHP407	-	-	-
CHP407_P	120.7 ± 15.4	82.2 ± 2.8	91.9 ± 1.8
	Micelle Hydrodynamic Diameter by Volume (nm)		
	25°C	**30°C**	**37°C**
CHP407	28.73 ± 4.02	34.60 ± 1.02	40.10 ± 1.42
CHP407_P	43.94 ± 4.13	35.25 ± 0.72	39.49 ± 1.78

hydrodynamic diameter of CHP407_P micelles turned out to be significantly higher with respect to CHP407 ones (**Table 2**). This evidence suggested that the absence of low molecular weight chains in CHP407_P led to the formation of bigger micelles at lower temperatures if compared to CHP407. On the other hand, further temperature increase leveled off this difference as comparable average hydrodynamic diameters were measured at 30°C and 37°C.

Estimation of the Critical Micellar Temperature

The CMT was estimated for both CHP407 and CHP407_P formulations to investigate whether the presence of a more uniform polymer molecular weight distribution could affect the temperature at which micelles begin to nucleate. To this aim, the fluorescent DPH dye was selected as micellization marker because it is almost non-fluorescent in water and gives a signal at 356 nm only when solubilized into the micelle hydrophobic core (**Figure 5**).

For both formulations, no DPH encapsulation was observed up to 20°C, suggesting the presence of polymeric chains in the form of unimers. At higher temperature, measured absorbance increased, with slightly higher values for CHP407 with respect to CHP407_P. These observations suggested the formation of a slightly higher amount of DPH-loaded CHP407 micelles, probably ascribed to an easier micelle nucleation process as a consequence of low molecular weight chains present within the system. This hypothesis was further supported by the estimated CMT value, which was measured to be slightly lower for CHP407 solution respect to

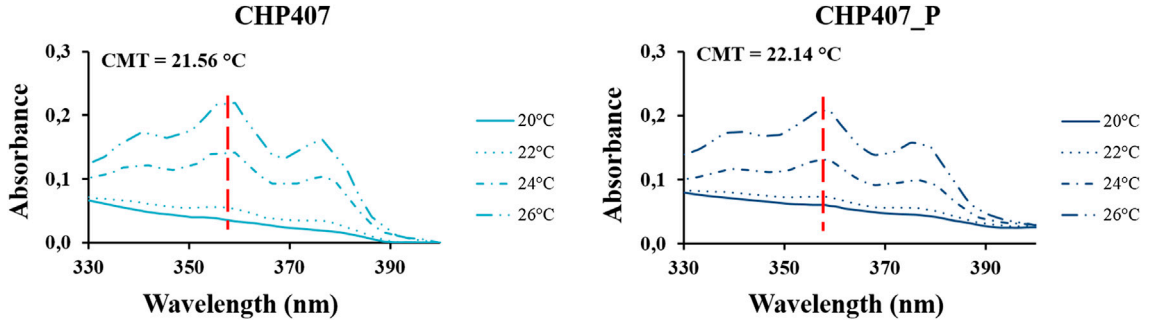

FIGURE 5 | UV/Vis spectra recorded in the 330–400 nm wavelength range for CHP407 and CHP407_P formulations (0.5% w/V concentration) upon temperature increase in the range 20°C–26°C. The red dashed lines mark the absorbance measured at 356 nm.

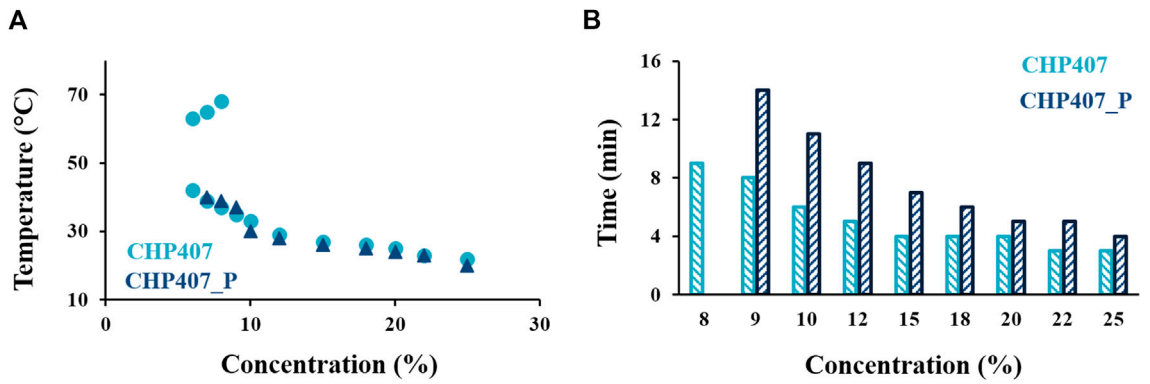

FIGURE 6 | Tube Inverting Test **(A)** conducted on CHP407 (light blue) and CHP407_P (dark blue) hydrogels (5%–25% w/V concentration range in physiological saline solution) within 5°C–70°C range (1°C/step, systematic error ±0.5°C). Gelation time test **(B)** at physiological temperature (1 min/step, systematic error ±30 s) performed on CHP407 (light blue) and CHP407_P (dark blue) hydrogels prepared by dissolving the polymer in physiological saline solution at different concentrations (5%–25% w/V).

CHP407_P one (i.e., 21.56°C *vs.* 22.14°C, respectively). Upon temperature increase up to 28°C, CHP407_P sample became turbid and thus, further absorbance measurements were not allowed. This evidence was probably attributed to the more uniform chain molecular weight distribution. Indeed, being the majority of the polymeric chains characterized by almost the same molecular weight, CHP407_P micelles most likely gave a more organized network, leading to higher crystallinity, which macroscopically resulted in a turbid solution.

Tube Inverting and Gelation Time Tests

Hydrogel capability to undergo a sol-to-gel transition in response to temperature increase was first qualitatively studied through the Tube Inverting test. Moreover, this test allowed also the definition of the CGC, i.e., the lowest polymer concentration able to form a solid gel. On the other hand, Gelation Time test conducted at 37°C gave information about hydrogel gelation timing in physiological-like conditions. As illustrated in **Figure 6A**, the gelation temperature of both CHP407 and CHP407_P hydrogels was strongly dependent on their polymeric concentration according to data reported in previous works on similar PEU-based systems (Boffito et al., 2016). Specifically, upon a decrease in polymer concentration a significant increase in the gelation temperature was observed, irrespective of the tested polymer. However, the CGC turned out to be slightly different for the two analyzed systems: 6% w/V and 7% w/V (error: ± 0.5% w/V) for CHP407 and CHP407_P gels, respectively. CHP407_P showed lightly lower gelation temperatures up to 10% w/V concentration and then slightly higher gelation temperature values from 10% w/V up to 7% w/V concentration compared to CHP407 systems. Furthermore, differently from CHP407 hydrogels, CHP407_P gels were not able to undergo a gel-to-sol transition upon further temperature increase (i.e., at temperatures higher than 60°C), further supporting the hypothesis on the formation of networks characterized by a higher crystallinity and thermal stability within a wider temperature range.

Concerning hydrogel gelation timing (**Figure 6B**), both systems showed a decrease in the time required to ensure a complete sol-to-gel transition at 37°C upon an increase in hydrogel concentration (Boffito et al., 2016). However, at each tested polymer concentration, CHP407_P hydrogels required more time to complete their gelation compared to CHP407

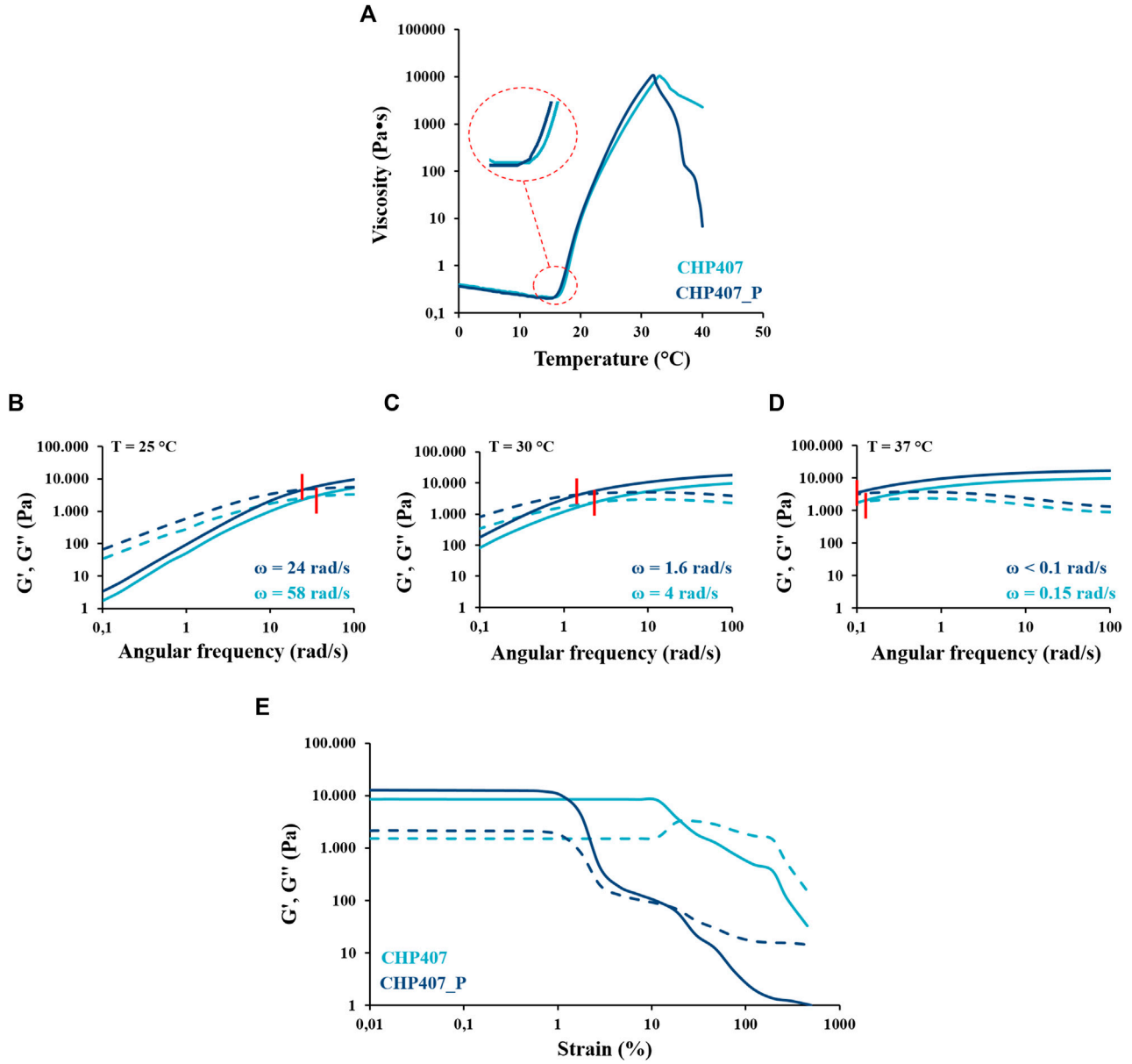

FIGURE 7 | (A) Viscosity profiles vs. temperature during sol-to-gel transition through temperature ramp test performed on CHP407 (light blue) and CHP407_P (dark blue) solutions (15% w/V concentration). **(B–D)** Frequency sweep test: storage (G'–continuous line) and loss (G"–dashed line) moduli registered for CHP407 (G', G"–light blue) and CHP407_P (G', G"–dark blue) gels at 25°C, 30°C, and 37°C. Red bars mark G'/G″ crossover point (ω). **(E)** Strain sweep test: storage (G'–continuous line) and loss (G"–dashed line) moduli registered as a function of applied deformation in the range 0.01%–500% for CHP407 (light blue) and CHP407_P (dark blue) sol-gel systems at 37°C.

formulations, as high molecular weight chains were not able to quickly arrange into a well-organized gel network, in agreement with findings on P407_P *vs.* P407 (see **Supplementary Material**). Nevertheless, despite these observations, the most promising hydrogel formulation able to undergo gelation at approx. physiological temperature within few minutes turned out to be the 15% w/V concentrated one for both CHP407 and CHP407_P gels. Indeed, these formulations showed a gelation temperature of 27°C and 26°C and a gelation time of 4 and 7 min for CHP407 and CHP407_P samples, respectively and thus, suitable for biomedical applications. Therefore, this composition was selected as the optimal one for the design of smart hydrogels and their further characterization.

Rheological Characterization

Rheological characterization was conducted on both CHP407_P and CHP407 sol-gel systems at the optimized concentration to thoroughly investigate changes in the temperature-driven gelation mechanism ascribable to their different molecular weight distribution and building block composition.

As proper of fluid behavior, the viscosity of both analyzed samples initially decreased as a function of temperature (**Figure 7A**), reaching a minimum value that was measured to be 0.3 Pa·s and 0.2 Pa·s for CHP407 and CHP407_P solutions, respectively. Although these values were very similar for both systems, in accordance with the slight differences in their average molecular weight values (**Table 1**), the gelation onset temperature (T_{onset}, defined at the minimum of viscosity) registered for CHP407_P hydrogel (i.e., 12.7°C) was slightly lower with respect to the CHP407 sample (i.e., 14.6°C). These data further supported DLS measurements (**Table 2**), which evidenced that CHP407_P formed bigger micelles at lower temperatures compared to CHP407 systems, favoring gelation start. Indeed, CHP407_P system was able to achieve the critical micellar volume required to begin the gelation process (Boffito et al., 2016) at slightly lower temperatures compared to CHP407 system. Differently, no differences were observed in micelle nucleation kinetics toward the achievement of the gel state upon further heating.

The process of gel formation and development upon temperature increase was studied through frequency sweep tests performed on both CHP407 and CHP407_P sol-gel systems (**Figures 7B–D**). Based on the conventionally defined relationship occurring between the storage (G') and the loss (G") moduli (Laurano and Boffito, 2020), both systems turned out to be mainly in the sol state at 25°C, in a biphasic phase at 30°C and not-completely developed gels at 37°C. The frequency at which G' becomes higher than G" ($\omega_{G'/G"\ crossover}$) is a peculiar parameter which marks the transition from viscous to elastic states. At each analyzed temperature, the crossover frequency of CHP407_P gels was measured to be lower respect to CHP407 (**Figures 7B–D**), suggesting the prevalent elastic behavior of CHP407_P formulation at each tested temperature.

Furthermore, at 37°C CHP407_P hydrogel was stronger compared to CHP407 hydrogel, as evidenced by the higher G'-G" delta (i.e., $\Delta_{G'-G"}$ = 10,468 and 6,894 Pa for CHP407_P and CHP407 hydrogels, respectively) measured at 0.01% deformation in strain sweep test (**Figure 7E**).

However, CHP407_P gels showed a significantly lower critical deformation (1.4%) compared to CHP407 sample (15.1%). This result suggested that the formation of a more organized network lowered hydrogel capability to resist against mechanical deformation. On the contrary, the presence in CHP407 formulations of chains characterized by different molecular weights favored the formation of "bridges" among micelles and thus, the establishment of an interconnected and more deformable network. The higher degree of organization and rigidity of CHP407_P network compared to CHP407 resulted in its drastic failure at low deformation. Differently, in CHP407 micro-cracks initially appeared within the gel network with G" increasing up to a maximum value, as typical of a strain hardening behavior. Upon G" reached a maximum value, macro-cracks appeared within the gel network leading to the complete failure of CHP407 gels with G" becoming higher than G', as typical of fluids.

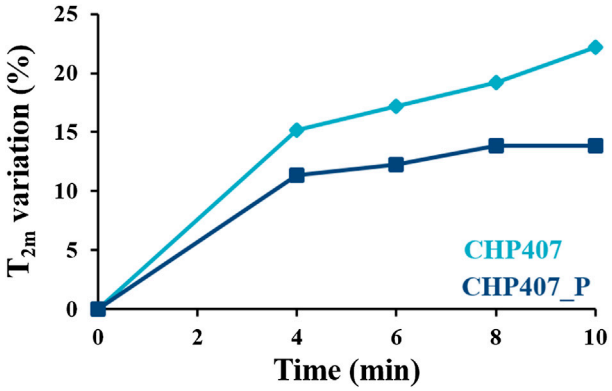

FIGURE 8 | Spin-spin relaxation time variation (%) respect to data measured at time zero as a function of time during temperature increase in the range 4°C–37°C for CHP407- and CHP407_P-based systems (light and dark blue, respectively).

Low Field Nuclear Magnetic Resonance Spectroscopy

To thoroughly investigate hydrogel structural changes occurring at the nano-scale in response to temperature increase, both CHP407 and CHP407_P samples were characterized exploiting the versatility of LF-NMR spectroscopy. This non-destructive technique provides information about water organization with respect to the surrounding polymeric chains by measuring the variation of water hydrogen spin-spin relaxation times (T_2) upon a very quick change in the orientation of an applied homogeneous magnetic field. Specifically, being permanent dipoles, water hydrogens are able to follow the direction of an applied magnetic field. Upon changes in magnetic field direction, changes in water hydrogen spin can be detected. The time water molecules require to recover their initial orientation, which is directly connected to T_2, depends on multiple parameters, such as temperature and polymeric chain spatial organization; thus, T_2 variations entail modifications in hydrogel structure. In the case of gels characterized by uniformity in the mesh size distribution, a unique relaxation time would exist. However, in a realistic polymeric system a poly-dispersed mesh size distribution occurs and thus, more than one relaxation time appear. In particular, each T_{2i} corresponds to a mesh class characterized by a specific size (ξ_i) (Abrami et al., 2018). The fraction of meshes characterized by the same T_{2i}/ξ_i is represented by the parameter A_i, so that the sum of all A_i is equal to 1. The weighed average of all the identified contributions defines the mean spin-spin relaxation time T_{2m}.

During sol-to-gel transition, T_{2m} generally decreases as a consequence of the reduced water mobility induced by the formation of the polymeric network upon temperature increase (Li et al., 2017; Malmierca et al., 2014). However, if the formation of the polymeric structure does not imply a clear increase in the fraction of the polymeric surface exposed to water molecules, the effect of temperature (which contributes to T_{2m} increase) cannot be negligible; consequently, T_{2m} can increase.

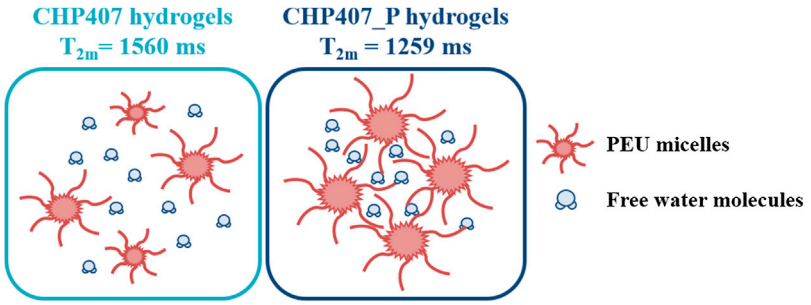

FIGURE 9 | Schematic representation of CHP407 and CHP407_P hydrogel internal structure at 37°C inspired by LF-NMR data.

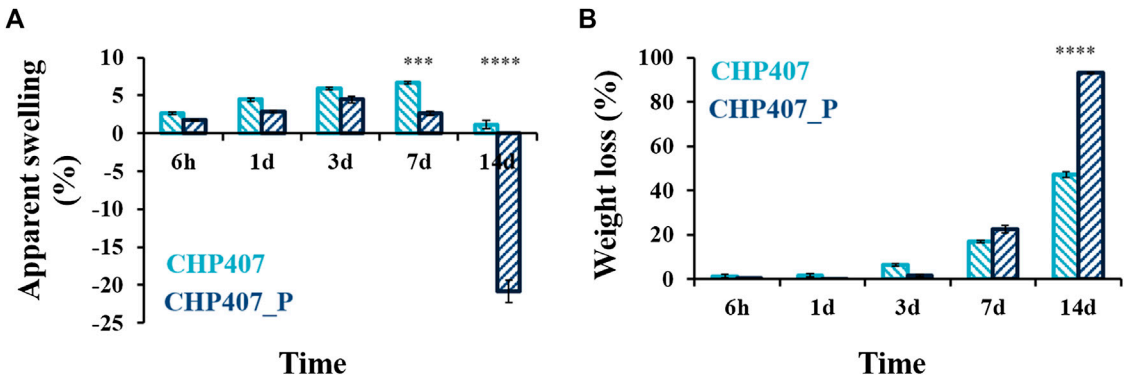

FIGURE 10 | Apparent swelling **(A)** and weight loss **(B)** percentages measured for CHP407 (light blue) and CHP407_P (dark blue) samples upon incubation in Trizma® buffer at 37°C for 6 h, 1, 3, 7, and 14 days. Data were reported as average values ± standard deviation.

In the presence of micellar gels, T_{2m} values are affected by both the formation of a network (decreasing water mobility and T_{2m}) and the effect of temperature increase (increasing T_{2m}) because micelle-based networks are not strong enough to make the temperature contribution negligible. Furthermore, during gel formation upon chain arrangement in the form of micelles, the polymeric superficial area interacting with water molecules reduces, resulting in a decrease of bound water and an increase of free water contribution.

Figure 8 reports the percentage variation (respect to data at time zero–see **Supplementary Table S1**) of T_{2m} as a function of time, for CHP407 and CHP407_P samples during temperature increase from 4 to 37°C. Hence, different time-points correspond to different temperatures. Data showed an increase of T_{2m} value for both CHP407 and CHP407_P systems over time, indicating a temperature dependence of this parameter.

At each time point, CHP407_P hydrogels showed lower T_{2m} values respect to CHP407. As both samples were subjected to the same heating ramp, differences in T_{2m} as a function of time were ascribed to differences in the hydrogel network structure. In CHP407 system, the presence of both high and low molecular weight chains allowed an initially faster micelle packing upon temperature increase (evidenced in **Figure 8** by higher T_{2m}–time curve slope of CHP407 compared to CHP407_P system). However, at 37°C CHP407 did not form a fully developed gel (in agreement with frequency sweep tests **Figures 7B–D**), as suggested by the increasing trend of T_{2m} values (no plateau value was achieved, suggesting that the process of gel formation was still in progress). On the contrary, gelation kinetics for CHP407_P formulation was initially slower but, once the micelle formed, their aggregation proceeded more rapid as a consequence of their uniform size, leading to a more stable and organized network at 37°C (suggested by the plateau value of T_{2m}) in agreement with rheological data.

Considering T_{2m} values at 10 min of analysis (i.e., systems in the gel state), CHP407-based gels showed a higher relaxation time compared to CHP407_P-based ones (i.e., 1,560 and 1,259 ms, respectively), reflecting a different internal structure pertaining to the two systems (**Figure 9**). This result can be attributed to the presence of polymeric chains characterized by different molecular weights. Indeed, the low molecular weight chains in CHP407 could act as blemishes during gel formation, thus leading, in the end, to a looser network. On the contrary, the narrower CHP407_P molecular weight distribution, as a consequence of P407 purification, resulted in tighter micelle packing, limiting

water molecules movements in the interstitial spaces among micelles.

Hydrogel Behavior in Aqueous Environment

In the perspective of hydrogel application in a physiological environment, swelling/stability tests were performed on CHP407 and CHP407_P systems in contact with simulated body fluids (i.e., Trizma® buffer, pH 7.4 at 37°C) at 37°C to evaluate the effects of macrodiol purification on the resultant poly (ether urethane) behavior in an aqueous environment (**Figure 10**).

Both systems showed similar fluid absorption capability and weight loss percentages up to 3 days of incubation. Conversely, a statistically significant difference was observed after 7 days of incubation, as CHP407 gels were able to absorb significantly higher amounts of external fluids (i.e., 6.7% *vs.* 2.7% for CHP407 and CHP407_P, respectively). At 14 days, negative apparent swelling percentages were registered for CHP407_P gels, thus suggesting that dissolution/erosion phenomena had completely overcome fluid absorption capability (i.e., CHP407_P gel dissolution achieved *ca.* 93% on day 14). Therefore, such results further supported the hypothesis formulated from LF-NMR data on a different nano-scale chain organization. Specifically, the removal of low molecular weight chains led to the formation of a highly organized network and, consequently, to detrimental effects on hydrogel stability over time. Indeed, in CHP407_P gels the presence of strongly packed micelles hindered the absorption of a considerable amount of fluids within the first days of incubation, but then, once water molecules started to infiltrate within the network, it underwent collapse due to its inability to resist deformation during swelling.

CONCLUSION

Poly(urethane)s are a class of synthetic polymers with *ad hoc* engineered structures, resulting from the accurate selection of the building blocks. Thus, poly(urethane)s show peculiar physico-chemical and mechanical features deriving from reagent properties and from their successful interactions. This work aimed at investigating the influence of macrodiol (i.e., Poloxamer® 407) molecular weight distribution on the resultant PEU polymer and hydrogel properties. To this aim, P407 was first subjected to a purification procedure to remove PEO-PPO diblock copolymers and impurities, while preserving its chemical structure (as assessed through ATR-FTIR spectroscopy). Then, SEC was exploited to verify the successful removal of by-products and the repeatability of the process. Moreover, purified P407 (i.e., P407_P) was also characterized in terms of thermo-responsiveness, showing slightly lower gelation onset temperatures (i.e., T_{onset} = 15.3°C *vs.* 16.7°C), faster gelation kinetics and slightly higher critical deformation (i.e., 3.5% *vs.* 2.3%) respect to not-purified P407 control sample. Subsequently, both P407 and P407_P macrodiols were exploited to synthesize CHP407 and CHP407_P, respectively, which turned out to show the same characteristic urethane vibrational bands, but different molecular weights and polydispersity indexes (i.e., $\overline{M}_n$ = 34 kDa *vs.* 40 kDa and D = 1.6 *vs.* 1.4 for CHP407 and CHP407_P, respectively). Moreover, the presence of a purified macrodiol in PEU chains also affected their capability to arrange into organized structures, giving more stable and bigger micelles for CHP407_P than for CHP407 systems (e.g., 43.94 ± 4.13 nm *vs.* 28.73 ± 4.02 nm).

Rheological temperature ramp tests showed that CHP407_P sol-gel systems were able to reach the critical micellar volume and thus, start their gelation process at lower temperatures compared to CHP407 ones (i.e., T_{onset} = 12.7°C *vs.* 14.6°C). Moreover, frequency sweep test data evidenced the prevalence of elastic behavior at increasingly lower frequencies for CHP407_P hydrogels respect to CHP407 at each analyzed temperature.

Additionally, rheological analysis also showed a considerably lower critical deformation (i.e. 1.4% *vs.* 15.1%) for CHP407_P, suggesting decreased deformability, attributed to the lack of micelle inter-bridges and the formation of a highly organized and rigid gel network.

These observations were further supported by an innovative analysis technique, i.e., the Low-Field Nuclear Magnetic Resonance spectroscopy, which allowed the nano-scale investigation of hydrogel network arrangement. Results confirmed the formation of a more organized structure, with a more packed network in the case of CHP407_P, resulting in limitations in water molecule mobility in the interstitial spaces among micelles.

However, the improved micelle packing by CHP407_P together with the lack of micelle inter-bridges caused a remarkable reduction of hydrogel stability in watery environment with almost complete dissolution/erosion of CHP407_P after 14 days of incubation.

Overall the results evidenced the influence of the purity of the starting P407 macrodiol on final PEU properties. In detail, a PEU with a narrower molecular weight distribution was synthesized from the purified macrodiol, after the removal of PEO-PPO diblock copolymers. In CHP407_P hydrogel, thermo-responsiveness was demonstrated involving the initial aggregation of significantly larger micelles than for CHP407 hydrogel. For this reason, the sol-to-gel transition of CHP407_P hydrogel began at slightly lower temperature (i.e., the critical volume required for the onset of gelation was achieved at lower temperature) and then proceeded with slightly faster kinetics, as suggested by frequency sweep tests. Due to their more regular structure with tightly packed homogeneous micelles, CHP407_P hydrogels showed reduced apparent swelling degree compared to CHP407 hydrogels. However, CHP407_P hydrogels were supposed to have a decreased density of inter-bridges among micelles, as they are generally formed by lower molecular weight chains. Hence, the decreased number of inter-bridges among micelles in CHP407_P hydrogels was probably the cause of their lower resistance to deformation and faster dissolution/erosion in aqueous medium. On the contrary, CHP407 hydrogels showed improved swelling capability and the ability to sustain higher deformations, attributed to the higher density of inter-bridges among micelles. In conclusion, the removal of

low molecular weight chains was detrimental for the performance of thermo-sensitive PEU hydrogels in the perspective of their future application in the field of drug delivery, or as bio-inks for bioprinting. Overall results could pave the way to the preparation of PEU thermo-sensitive hydrogels with superior mechanical properties and stability in physiological conditions, making use of amphiphilic macrodiols with different block structure (e.g., mixture of di-block and triblock copolymers).

DATA AVAILABILITY STATEMENT

All datasets presented in this study are included in the article/ **Supplementary Material**.

AUTHOR CONTRIBUTIONS

RL designed the experiments, performed the analyses, analyzed the data and wrote the paper; MA and MG performed the LF-NMR analyses; GC, MB and VC designed the experiments and provided scientific and financial support to the work. All authors reviewed the draft.

FUNDING

This project has received funding from the European Union's Horizon 2020 research and innovation program under grant agreement No. 685872-MOZART (www.mozartproject.eu) and from the European Research Council (ERC) under the European Union's Horizon 2020 research and innovation programme grant agreement No. 772168 (www.biorecar.polito.it).

SUPPLEMENTARY MATERIAL

The Supplementary Material for this article can be found online at: https://www.frontiersin.org/articles/10.3389/fmats.2020.594515/full#supplementary-material

REFERENCES

Abrami, M., Chiarappa, G., Farra, R., Grassi, G., Marizza, P., and Grassi, M. (2018). Use of low-field NMR for the characterization of gels and biological tissues. *Admet Dmpk.* 6, 34–46. doi:10.5599/admet.6.1.430

Alexandridis, P., Holzwarth, J. F., and Hatton, T. A. (1994). Micellization of poly(ethylene oxide)-poly(propylene oxide)-poly(ethylene oxide) triblock copolymers in aqueous solutions: thermodynamics of copolymer association. *Macromolecules* 27, 2414–2425. doi:10.1021/ma00087a009

Boffito, M., Gioffredi, E., Chiono, V., Calzone, S., Ranzato, E., Martinotti, S., et al. (2016). Novel polyurethane-based thermosensitive hydrogels as drug release and tissue engineering platforms: design and *in vitro* characterization. *Polym. Int.* 65, 756–769. doi:10.1002/pi.5080

Boffito, M., Pontremoli, C., Fiorilli, S., Laurano, R., Ciardelli, G., and Vitale-Brovarone, C. (2019). Injectable thermosensitive formulation based on polyurethane hydrogel/mesoporous glasses for sustained co-delivery of functional ions and drugs. *Pharmaceutics* 11, 501–521. doi:10.3390/pharmaceutics11100501

Boffito, M., Torchio, A., Tonda-Turo, C., Laurano, R., Gisbert Garzaran, M., Berkmann, J. C., et al. (2020). Hybrid injectable sol-gel systems based on thermo-sensitive polyurethane hydrogels carrying pH-sensitive mesoporous silica nanoparticles for the controlled and triggered release of therapeutic agents. *Front. Bioeng. Biotechnol.* 8, 384–408. doi:10.3389/fbioe.2020.00384

Bonilla-Hernández, M., Zapata-Catzin, G. A., de Jesús Castillo-Cruz, O., Vargas-Coronado, R. F., Cervantes-Uc, J. M., Xool-Tamayo, J. F., et al. (2020). Synthesis and characterization of metformin-pluronic based polyurethanes for controlled drug delivery. *Int. J. Polym. Mater.* 1. doi:10.1080/00914037.2020.1740996

Caddeo, S., Mattioli-Belmonte, M., Cassino, C., Barbani, N., Dicarlo, M., Gentile, P., et al. (2019). Newly-designed collagen/polyurethane bioartificial blend as coating on bioactive glass-ceramics for bone tissue engineering applications. *Mater. Sci. Eng. C* 96, 218–233. doi:10.1016/j.msec.2018.11.012

Chen, F.-T., Duo, Y.-Q., Luo, S.-G., Luo, Y.-J., and Tan, H.-M. (2003). Novel segmented thermoplastic polyurethanes elastomers based on tetrahydrofuran ethylene oxide copolyethers as high energetic propellant binders. *Propellants, Explos. Pyrotech.* 28, 7–11. doi:10.1002/prep.200390007

Chen, S.-H., Tsao, C.-T., Chou, H.-C., Chang, C.-H., Hsu, C.-T., Chuang, C.-N., et al. (2013). Synthesis of poly(lactic acid)-based polyurethanes. *Polym. Int.* 62, 1159–1168. doi:10.1002/pi.4400

Cohn, D., Lando, G., Sosnik, A., Garty, S., and Levi, A. (2006). PEO-PPO-PEO-based poly(ether ester urethane)s as degradable reverse thermo-responsive multiblock copolymers. *Biomaterials* 27, 1718–1727. doi:10.1016/j.biomaterials.2005.10.035

Doseva, V., Shenkov, S., Valisey, S., and Baranovsky, V. Y. (2004). Synthesis and properties of water soluble polyurethanes based on poly(ethylene glycol). *J. Appl. Polym. Sci.* 91, 3651–3658. doi:10.1002/app.13604

Fakhari, A., Corcoran, M., and Schwarz, A. (2017). Thermogelling properties of purified poloxamer 407. *Heliyon* 3, 1–26. doi:10.1016/j.heliyon.2017.e00390

Gradinaru, L. M., Ciobanu, C., Vlad, S., Bercea, M., and Popa, M. (2012). Thermoreversible poly(isopropyl lactate diol)-based polyurethane hydrogels: effect of isocyanate on some physical properties. *Ind. Eng. Chem. Res.* 51, 12344–12354. doi:10.1021/ie301690e

Hoo, C. M., Starostin, N., West, P., and Mecrtney, M. L. (2008). A comparison of atomic force microscopy (AFM) and dynamic light scattering (DLS) methods to characterize nanoparticle size distributions. *J. Nanopart. Res.* 10, 89–96. doi:10.1007/s11051-008-9435-7

Lan, P., Corneillie, S., Schacht, E., Davies, M., and Shard, A. (1996). Synthesis and characterization of segmented polyurethanes based on amphiphilic polyether diols. *Biomaterials* 17, 2273–2280. doi:10.1016/0142-9612(96)00056-7

Laurano, R., and Boffito, M. (2020). Thermosensitive micellar hydrogels as vehicles to deliver drugs with different wettability. *Front. Bioeng. Biotechnol.* 8, 708. doi:10.3389/fbioe.2020.00708

Laurano, R., Boffito, M., Torchio, A., Cassino, C., Chiono, V., and Ciardelli, G. (2019). Plasma treatment of polymer powder as an effective tool to functionalize polymers: case study application on an amphiphilic polyurethane. *Polymers* 11, 2109. doi:10.3390/polym11122109

Laurano, R., Cassino, C., Ciardelli, G., Chiono, V., and Boffito, M. (2020). Polyurethane-based thiomers: a new multifunctional copolymer platform for biomedical applications. *React. Funct. Polym.* 146, 104413. doi:10.1016/j.reactfunctpolym.2019.104413

Lee, S. Y., Wu, S. C., Chen, H., Tsai, L. L., Tzeng, J. J., Lin, C. H., et al. (2018). Synthesis and characterization of polycaprolactone-based polyurethanes for the fabrication of elastic guided bone regeneration membrane. *BioMed Res. Int.* 2018, 3240571. doi:10.1155/2018/3240571

Li, Y., Li, X., Chen, C., Zhao, D., Su, Z., Ma, G., et al. (2017). Sol-gel transition characterization of thermosensitive hydrogels based on water mobility variation provided by low field NMR. *J. Polym. Res.* 25, 1–10. doi:10.1007/s10965-017-1185-8

Lim, J., Yeap, S. P., Che, H. X., and Low, S. C. (2013). Characterization of magnetic nanoparticle by dynamic light scattering. *Nanoscale Res. Letters.* 8, 381–395. doi:10.1186/1556-276x-8-381

Malmierca, M. A., González-Jiménez, A., Mora-Barrantes, I., Posadas, P., Rodríguez, A., Ibarra, L., et al. (2014). Characterization of network structure and chain dynamics of elastomeric ionomers by means of ^{1}H Low-Field NMR. *Macromolecules* 47, 5665–5667. doi:10.1021/ma501208g

Marizza, P., Abrami, M., Keller, S. S., Posocco, P., Laurini, E., Goswami, K., et al. (2016). Synthesis and characterization of UV photocrosslinkable hydrogels with poly(N-vinyl-2-pyrrolidone): determination of the network mesh size distribution. *Int. J. Polym. Mater.* 65, 516–525. doi:10.1080/00914037.2015.1129964

Mystkowska, J., Mazurek-Budzyńska, M., Piktel, E., Niemirowicz, K., Karalus, W., Deptuła, P., et al. (2017). Assessment of aliphatic poly(ester-carbonate-urea-urethane)s potential as materials for biomedical application. *J. Polym. Res.* 24, 144. doi:10.1007/s10965-017-1296-2

Ng, H. N., Allegrezza, A. E., Seymour, R. W., and Cooper, S. L. (1973). Effect of segment size and polydispersity on the properties of polyurethane block polymers. *Polymer* 14, 255–261. doi:10.1016/0032-3861(73)90085-2

Pereira, I.H.L., Ayres, E., Patrício, P.S., Góes, A.M., Gomide, V.S., Junior, E.P., et al. (2010). Photopolymerizable and injectable polyurethanes for biomedical applications: synthesis and biocompatibility. *Act. Biomater.* 6, 3056–3066. doi:10.1016/j.actbio.2010.02.036

Ping, P., Wang, W., Chen, X., and Jing, X. (2005). Poly(ε-caprolactone) polyurethane and its shape-memory property†. *Biomacromolecules* 6, 587–592. doi:10.1021/bm049477j

Polo Fonseca, L., Bergamo Trinca, R., and Felisberti, M. I. (2016). Thermo-responsive polyurethane hydrogels based on poly(ethylene glycol) and poly(caprolactone): physico-chemical and mechanical properties. *J. Appl. Polym. Sci.* 133 (25), 43573–43583. doi:10.1002/app.43573

Pontremoli, C., Boffito, M., Fiorilli, S., Laurano, R., Torchio, A., Bari, A., et al. (2018). Hybrid injectable platforms for the *in situ* delivery of therapeutic ions from mesoporous glasses. *Chem. Eng. J.* 340, 103–113. doi:10.1016/j.cej.2018.01.073

Pradal, C., Jack, K. S., Grøndahl, L., and Cooper-White., J. J. (2013). Gelation kinetics and viscoelastic properties of pluronic and α-cyclodextrin-based pseudopolyrotaxane hydrogels. *Biomacromolecules* 14, 3780–3792. doi:10.1021/bm401168h

Ronco, L. I., Basterretxea, A., Mantione, D., Aguirresarobe, R. H., Minari, R. J., Gugliotta, L. M., et al. (2017). Temperature responsive PEG-based polyurethanes "à la carte". *Polymer* 122, 117–124. doi:10.1016/j.polymer.2017.06.043

Sartori, S., Boffito, M., Serafini, P., Caporale, A., Silvestri, A., Bernardi, E., et al. (2013). Synthesis and structure-property relationship of polyester-urethanes and their evaluation for the regeneration of contractile tissues. *React. Funct. Polym.* 73, 1366–1376. doi:10.1016/j.reactfunctpolym.2013.01.006

Silvestri, A., Sartori, S., Boffito, M., Mattu, C., Di Rienzo, A. M., Boccafoschi, F., et al. (2014). Biomimetic myocardial patches fabricated with poly(ε-caprolactone) and polyethylene glycol-based polyurethanes. *J. Biomed. Mater. Res.* 102, 1002–1013. doi:10.1002/jbm.b.33081

Tanaka, H., and Kunimura, M. (2002). Mechanical properties of thermoplastic polyurethanes containing aliphatic polycarbonate soft segments with different chemical structures. *Polym. Eng. Sci.* 42, 1333–1349. doi:10.1002/pen.11035

Wang, C., Wang, H., Zou, F., Chen, S., and Wang, Y. (2019). Development of polyhydroxyalkanoate-based polyurethane with water-thermal response shape-memory behavior as new 3d elastomers scaffolds. *Polymers* 11, 1030. doi:10.3390/polym11061030

Whang, C.-H., Lee, H. K., Kundu, S., Murthy, S. N., and Jo, S. (2018). Pluronic-based dual-stimuli sensitive polymers capable of thermal gelation and pH-dependent degradation for *in situ* biomedical application. *J. Appl. Polym. Sci.* 135, 46552. doi:10.1002/app.46552

Zhang, T., Wu, W., Wang, X., and Mu, Y. (2010). Effect of average functionality on properties of UV-curable waterborne polyurethane-acrylate. *Prog. Org. Coating.* 68, 201–207. doi:10.1016/j.porgcoat.2010.02.004

Conflict of Interest: The authors declare that the research was conducted in the absence of any commercial or financial relationships that could be construed as a potential conflict of interest.

Quantum Materials

Marcos H. D. Guimaraes

Dr. Marcos Guimarães is an Assistant Professor at the Zernike Institute for Advanced Materials at the University of Groningen, the Netherlands. He received his BSc and MSc degrees from the Federal University of Minas Gerails, Brazil, and his Ph.D. degree from the University of Groningen in 2015. He conducted his postdoctoral research at Cornell University, USA, and Eindhoven University of Technology, Netherlands. Dr. Guimarães started his group in 2019 at the University of Groningen, focusing on the interplay between charge, spin, and photons in two-dimensional materials. His distinctions include the NWO Rubicon and Veni grants and a Kavli Institute Fellowship.

Jan Hidding

Jan Hidding, born in Groningen, the Netherlands, finished his Master's in Nanoscience at the University of Groningen in 2018, where he performed multiple research projects on a broad range of topics, ranging from antibodies and aptamers to mechanical properties of cancerous cells using atomic force microscopy and to ultrafast 2-dimensional spectroscopy on organic light-harvesting self-assembled molecules. Currently, he is pursuing his Ph.D. with the group of Prof. Marcos Guimaraes and Prof. Bart van Wees, where he focuses on spin-orbit torques using two-dimensional materials and spin-photocurrents in van der Waals heterostructures.

Lichuan Jin

Prof. Lichuan Jin is an associate professor in the State Key Laboratory of Electronic Thin Films and Integrated Devices, University of Electronic Science and Technology. His research is mainly focused on quantum magnetic materials and spintronics. In his research career so far, he has prepared a series of new materials which exhibit unusual magnetic, optical, and semiconductor properties. His current research interests include new strategies to obtain functional magnonic devices and spintronics heterojunctions with emphasis on the interactions of magnon, electron spin, and charge. Lichuan Jin has published over 90 peer-reviewed papers in the fields of magnetic materials and spintronics.

frontiers in Materials

MINI REVIEW
published: 16 November 2020
doi: 10.3389/fmats.2020.594771

Spin-Orbit Torques in Transition Metal Dichalcogenide/Ferromagnet Heterostructures

Jan Hidding and Marcos H. D. Guimarães**

Zernike Institute for Advanced Materials, University of Groningen, Groningen, Netherlands

In recent years, there has been a growing interest in spin-orbit torques (SOTs) for manipulating the magnetization in nonvolatile magnetic memory devices. SOTs rely on the spin-orbit coupling of a nonmagnetic material coupled to a ferromagnetic layer to convert an applied charge current into a torque on the magnetization of the ferromagnet (FM). Transition metal dichalcogenides (TMDs) are promising candidates for generating these torques with both high charge-to-spin conversion ratios, and symmetries and directions which are efficient for magnetization manipulation. Moreover, TMDs offer a wide range of attractive properties, such as large spin-orbit coupling, high crystalline quality and diverse crystalline symmetries. Although numerous studies were published on SOTs using TMD/FM heterostructures, we lack clear understanding of the observed SOT symmetries, directions, and strengths. In order to shine some light on the differences and similarities among the works in literature, in this mini-review we compare the results for various TMD/FM devices, highlighting the experimental techniques used to fabricate the devices and to quantify the SOTs, discussing their potential effect on the interface quality and resulting SOTs. This enables us to both identify the impact of particular fabrication steps on the observed SOT symmetries and directions, and give suggestions for their underlying microscopic mechanisms. Furthermore, we highlight recent progress of the theoretical work on SOTs using TMD heterostructures and propose future research directions.

Keywords: spin-orbit torques (SOT), transition metal dichalcogenides (TMD), van der Waals materials, spin-orbitronics, Two-dimensional materials (2D materials)

OPEN ACCESS

Edited by:
Myung Gwan Hahm,
Inha University, South Korea

Reviewed by:
Bipin Kumar Gupta,
National Physical Laboratory (CSIR), India
Narayanan Tharangattu Narayanan,
Tata Institute of Fundamental Research, India

****Correspondence:***
Marcos H. D. Guimarães
m.h.guimaraes@rug.nl
Jan Hidding
jan.hidding@rug.nl

Specialty section:
This article was submitted to Quantum Materials, a section of the journal Frontiers in Materials

Received: *14 August 2020*
Accepted: *12 October 2020*
Published: *16 November 2020*

Citation:
Hidding J and Guimarães MHD (2020) Spin-Orbit Torques in Transition Metal Dichalcogenide/Ferromagnet Heterostructures. Front. Mater. 7:594771. doi: 10.3389/fmats.2020.594771

INTRODUCTION

Spin-orbit torques (SOTs) are promising candidates for effective manipulation of magnetization through electric currents with applications in nonvolatile magnetic memory and logic devices. SOTs convert an electric current into a magnetic torque in non-magnetic/ferromagnetic heterostructure, i.e., an electric current through the stack can modulate the direction of the ferromagnet's magnetization (Gambardella and Miron, 2011; Manchon et al., 2019). Devices showing large SOT efficiencies usually rely on a nonmagnetic material with large spin-orbit coupling in contact with a ferromagnet (FM). Transition metal dichalcogenides (TMDs), with chemical formula MX_2, where M is a transition metal (e.g., Mo, and W) and X a chalcogen element (e.g., S and Se), can provide large spin-orbit coupling and pristine surfaces which can result in a more intimate contact between the TMD and the FM layer. Furthermore, this family of materials offers a wide range of electronic and crystalline properties and symmetries. Although numerous articles were

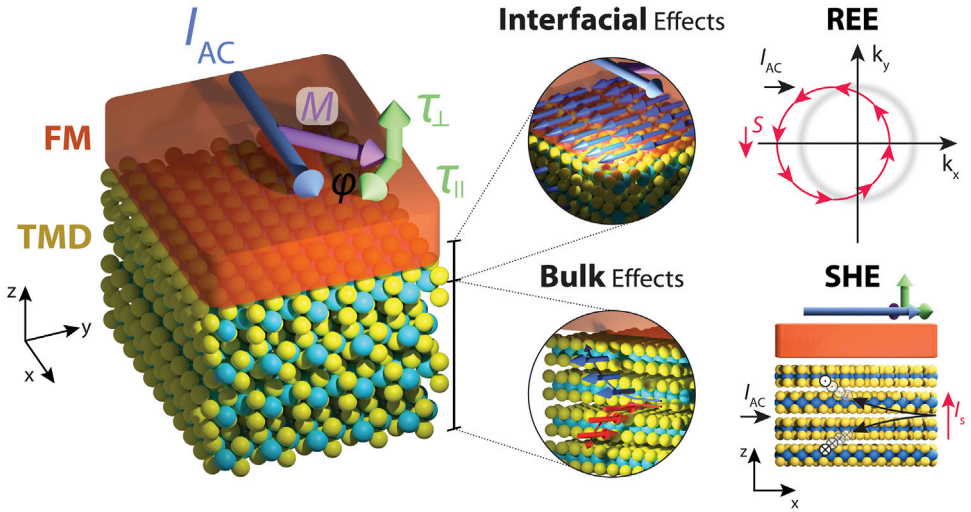

FIGURE 1 | Schematics of SOTs in TMD/FM heterostructures. A charge current, usually oscillating at low (RF) frequencies for SHH (ST-FMR) measurements is applied along a device consisting of a TMD layer and a FM. The magnetization of the FM layer, oriented along an external magnetic field, observes a current-induced SOT in-plane ($\boldsymbol{\tau}_{\parallel}$) and out-of-plane ($\boldsymbol{\tau}_{\perp}$), indicated by the green arrows. These torques may arise from multiple microscopic effects arising in the bilayer, which may originate either from the TMD/FM interface (top), e.g., through the Rashba-Edelstein Effect (REE), or the bulk of the material (bottom), as for example through a spin Hall effect (SHE) in the TMD layer.

published on SOTs in TMD/ferromagnetic heterostructures, a clear understanding of the different mechanisms underlying observed SOTs remain yet to be understood.

In this mini-review, we give an overview of the recent progress on SOTs in TMD/FM heterostructures. Materials with high charge-to-spin conversion efficiencies, such as WTe_2 and $TaTe_2$ (Safeer et al., 2019; Zhao et al., 2020; Hoque et al., 2020), are often considered as good candidates for large SOT efficiencies. However, large charge-to-spin conversion efficiencies are no guarantee for large SOT efficiencies, as SOTs are often an emergent phenomenon, depending on proximity effects (spin-orbit coupling and magnetic exchange), wavefunction overlap, and interface spin transparency (spin mixing conductance) as well. Indeed, the observed torques in TMD/FM heterostructures cannot always be explained by well-known effects such as the bulk spin Hall effect (SHE) (Dyakonov and Perel, 1971; Hirsch, 1999; Sinova et al., 2015) or the interfacial Rashba-Edelstein Effect (REE) (Edelstein, 1990; Ganichev et al., 2002; Kato et al., 2004; Mihai Miron et al., 2010; Ganichev et al., 2016) (**Figure 1**), indicating that other mechanisms involving material specific properties or interfacial effects are into play. This is supported by recent works suggesting that both the type of ferromagnetic layer (Dolui and Nikolic, 2020; Go and Lee, 2020) and the interface properties between the TMD and the ferromagnetic layer (Amin et al., 2020; Sousa et al., 2020; Go et al., 2020) (Sahoo et al., 2020; Kumar et al., 2020; Xue et al. 2020) are of paramount importance for the observed SOTs, allowing for enhanced and unconventional SOTs.

To describe to different torques, we use the notation in terms of odd ($\tau_o^{\zeta} \propto \hat{m} \times \hat{\zeta}$) or even ($\tau_e^{\zeta} \propto \hat{m} \times (\hat{\zeta} \times \hat{m})$) with respect to the magnetization direction ($\hat{m}$), with $\zeta = x, y, z$. These torques are also named, respectively, field-like (FL) and damping-like (DL) torques in many papers in literature (Manchon et al., 2019), with directions out-of-plane or in-plane with respect to the TMD/FM plane (**Figure 1**). For a fair comparison between the results in literature we use the torque conductivities ($\sigma_{o(e)}^{\zeta}$) to quantify the SOT strength, which expresses the torques per unit area per unit electric field. This figure of merit is adopted rather than the torque efficiency ($\xi_{FL(AD)}^{j_c}$), because the electric field across the device can be more accurately determined when compared to the current density (Nguyen et al., 2016).

DISCUSSION ON RECENT PROGRESS

The field of SOTs using TMD-based devices has been rapidly developed in the past 5 years. Experimental studies have used different TMD sources (e.g., mechanical exfoliation or chemical vapor deposition, CVD), FM materials, deposition methods (e.g., sputtering or electron-beam evaporation), and measurement techniques, namely second-harmonic Hall (SHH) (Garello et al., 2013; Hayashi et al., 2014; Avci et al., 2014; Ghosh et al., 2017) or spin-torque ferromagnetic resonance (ST-FMR) (Liu et al., 2011; Fang et al., 2011; Berger et al., 2018). So far, it is unclear how these different techniques and procedures affect the measured SOTs.

In this section, we discuss the results for semiconducting, semi-metallic and metallic TMDs, giving an overview of their fabrication and measurement techniques (**Table 1**). Comparing the TMDs in this way allows us to pinpoint important differences and similarities in the observed torques.

Semi-Conducting TMDs

Shao *et al.* were one of the first to examine SOTs in TMD/FM heterostructures (Shao et al., 2016). There, SOTs were quantified

TABLE 1 | Recent studies on TMD/FM heterostructures with their fabrication techniques and spin torque conductivities.

Reference	SOT material (thickness)	Fabrication technique	Ferro-magnet	Deposition technique	Measurement technique	Spin torque conductivity [$\times 10^3 (\hbar/2e)(\Omega m)^{-1}$]	Proposed mechanism/ Source
	Semiconducting						
(Shao et al., 2016)	MoS_2 (1 L)	CVD	CoFeB (3 nm)	Magnetron sputtering	SHH	$\sigma_o^y = 2.88$	REE
(Shao et al., 2016)	WeS_2 (1 L)	CVD	CoFeB (3 nm)	Magnetron sputtering	SHH	$\sigma_o^y = 5.52$	REE
(Zhang et al., 2016)	MoS_2 (1 L)	CVD	Py (5 nm)	Magnetron sputtering	ST-FMR	σ_e^y =Observed	Interfacial
(Lv et al., 2018)	WS_2 (1 L)	CVD	Py (10 nm)	E-beam evaporation	ST-FMR	σ_o^y =Observed	REE
						σ_e^y =Observed	REE
	Semi-metallic						
(MacNeill et al., 2017a)	WTe_2 (1.8–15 nm)	Exfoliation	Py (6 nm)	Sputtering	ST-FMR/SHH	$\sigma_o^y = 9 \pm 3$	Interfacial
						$\sigma_e^y = 8 \pm 2$	Interfacial
						$\sigma_e^z = 3.6 \pm 0.8$	Interfacial
						$\sigma_o^z = 0$	-
(MacNeill et al., 2017b)	WTe_2 (1 L–16 nm)	Exfoliation	Py (6 nm)	Sputtering	ST-FMR/SHH	σ_o^y =Observed	Oersted
						σ_e^y =Observed	-
						σ_e^z =Observed	-
						$\sigma_o^z = 0$	-
(Li et al., 2018)	WTe_2 (5.6–31 nm)	Exfoliation	Py (6 nm)	Sputtering	SHH	$\sigma_o^y = 1.3 \times 10^2$	Fermi arcs
						σ_e^y =Observed	-
(Shi et al., 2019)	WTe_2 (5.8–122 nm)	Exfoliation	Py (6 nm)	Sputtering	ST-FMR/SHH	$\sigma_e^y = 6 \times 10^1$(l//b)	
						$\sigma_e^y = 5.95$ (l//a)	Bulk
						σ_e^z =Observed (l//a)	
(Stiehl et al., 2019b)	$TaTe_2$ (4.5–19.7 nm)	Exfoliation	Py (6 nm)	Sputtering	ST-FMR/SHH	σ_e^y =Weak	-
						σ_o^z =Sometimes observed	-
						$\sigma_e^z = 0$	-
						σ_o^x =Observed (Dresselhaus)	Oersted (resist. anisotropy)
(Stiehl et al., 2019a)	$MoTe_2$ (1 L–14.2 nm)	Exfoliation	Py (6 nm)	Sputtering	ST-FMR	$\sigma_o^y = 15$	Oersted
						$\sigma_e^y = 5.8 \pm 0.16$	Interfacial
						$\sigma_e^z = 1.02 \pm 0.03$	Interfacial
						$\sigma_o^z = 0.81 \pm 0.05$(t > 3 nm)	Interfacial
(Xu et al., 2020)	$PtTe_2$ (3–20 nm)	CVD	Py (2.5, 5.0, 7.5, 10 nm)	Sputtering	ST-FMR	σ_o^y =Observed	-
						$\sigma_e^y = 1.6 \times 10^2$	SHE + TSS
	Metallic						
(Guimarães et al., 2018)	$NbSe_2$ (1–10 L)	Exfoliation	Py (6 nm)	Sputtering	ST-FMR	$\sigma_o^y = 40$	Oersted
						$\sigma_e^y = 3$	REE
						$\sigma_e^z = 0$	-
						$\sigma_o^z = 1$	Strain
(Husain et al., 2020)	1T-TaS_2 (1 L)	Ion-beam sputtering	Py	-	ST-FMR/SHH	σ_o^y =Negligible	-
						$\sigma_e^y = 2.63 \times 10^2$	Interfacial

by the non-resonant SHH measurements on monolayer (1L) MoS_2 and WSe_2 coupled with CoFeB (3 nm). They observed a temperature independent out-of-plane FL torque τ_o^y $(\hat{m} \times \hat{y})$ for both devices with a corresponding torque conductivity of $\sigma_o^y = 2.88 \times 10^3\,(\hbar/2e)\,(\Omega m)^{-1}$ and $5.52 \times 10^3\,(\hbar/2e)\,(\Omega m)^{-1}$ for MoS_2 and WSe_2, respectively. No in-plane DL torque of the form τ_e^y $(\hat{m} \times (\hat{y} \times \hat{m}))$ was observed in either of their devices. This DL torque is observed in SOT measurements on Pt/Py bilayers and is often ascribed to the SHE (Ramaswamy et al., 2018). Since the monolayer TMDs are much less conductive than the FM layer, the SOTs here are interfacial in nature, and the results point to the REE mechanism (Miron et al., 2011; Haney et al., 2013; Amin and Stiles, 2016a; Amin and Stiles, 2016b).

Interestingly, in a concurrent work, Zhang *et al.* obtained different results using a high-frequency technique, ST-FMR, on 1L-MoS_2/Permalloy ($Ni_{80}Fe_{20}$ – Py) 5 nm (Zhang et al., 2016). There, they identified an in-plane DL τ_e^y $(\hat{m} \times (\hat{y} \times \hat{m}))$ and an out-of-plane FL torque τ_o^y $(\hat{m} \times \hat{y})$. A torque ratio, $\tau_o^y/\tau_e^y = 0.19 \pm 0.01$ was obtained, indicating that τ_e^ydominates over τ_o^y, in contrast to the results by Shao and co-workers. This result was repeated using different deposition techniques of the FM layer (sputtering or electron-beam deposition), indicating that the observed torque is independent on the Py deposition technique. The different measurement techniques used by the two groups could explain the discrepancy in the observed torques. However, it has been shown that the SOTs quantified by ST-FMR and SHH techniques agree within the experimental accuracy for several systems (MacNeill et al., 2017a; MacNeill et al., 2017b; Stiehl et al., 2019b; Shi et al., 2019).

The discrepancy between results for MoS_2/FM bilayers suggests that not only the spin-orbit material but also the type of ferromagnetic material (CoFeB vs Py) can play a significant role in the observed torques. This is theoretically substantiated in a recent work (Dolui and Nikolic, 2020), where calculations on $MoSe_2$/Co, WSe_2/Co and $TaSe_2$/Co heterostructures were performed. They find that the hybridization of the Co wavefunctions with those of the TMDs leads to dramatic transmutation of the electronic and spin structure of the Co layers, even within eight layers away from the interface. This suggests that injecting unpolarized spin currents in these spin-orbit-proximitized layers of Co generates nonequilibrium spin densities, which in turn leads to a nonzero local torque on the magnetization. Both the spin polarization direction and magnitude were shown to differ between the different TMDs and complex spin textures were obtained for the spin-orbit-proximitized layers. These results indicate that the FM material can play an active role in the type of SOTs observed. Moreover, recent theoretical works (Sousa et al., 2020) pointed out that different scattering mechanisms lead to different torque symmetries, indicating that the sample quality, symmetry and nature of scatterers also plays a role here. Different FM materials in FM/TMD heterostructures might therefore exhibit different SOTs as was the case for Shao *et al.* and Zhang *et al.*

More recently, WS_2 was studied by Lv *et al.* in a 1L-WS_2/Py (10 nm) heterostructure (Lv et al., 2018) using CVD-grown WS_2 and electron-beam evaporated Py layer. The authors observe both a DL torque τ_e^y and a FL torque τ_o^y in their ST-FMR measurements, which are ascribed to the interfacial REE. Furthermore, they observed a gate-dependent SOT ratio ranging from $\tau_o^y/\tau_e^y = 0.05$ to 0.22 within a range of $V_g = -60$ V to 60 V, absent in their reference sample of Pt/Py. Gate-dependent SOTs were observed in SHH measurements on a topological insulator (Fan et al., 2016), but not yet reported in TMD/FM heterostructures. The increasing SOT ratio with gate-voltage could be explained by an increased carrier density leading to an enhanced current at the WS_2/Py interface. The modulation of SOT strength using a gate voltage is a step toward applications for data storage and processing and more research should be done to improve the gate tunability of SOTs in TMD/FM heterostructures (Li et al., 2020; Filianina et al., 2020; Dieny et al., 2019).

Semi-Metallic TMDs

In addition to semiconducting TMDs, a variety of semi-metallic TMDs have been studied, with special focus given to low-symmetry crystals. A particularly interesting candidate is WTe_2, belonging to space group $Pmn2_1$. In a WTe_2/FM heterostructure, however, the symmetries are reduced to a single mirror plane perpendicular to the a-axis and the identity, space group *Pm*. The low device symmetry allows for unconventional SOTs, such as an out-of-plane DL torque τ_e^z $(\hat{m} \times (\hat{z} \times \hat{m}))$, which is especially interesting for applications in high-density memory devices since these torques are very effective for magnetization switching of perpendicular magnetic anisotropy materials (Ramaswamy et al., 2018).

MacNeill *et al.* were the first to examine SOTs using WTe_2 (MacNeill et al., 2017a). Using ST-FMR, the authors observed τ_e^z, along the conventional SOTs τ_o^y and τ_e^y, and extracted a torque conductivity of $\sigma_e^z = 3.6 \pm 0.8 \times 10^3\ (\hbar/2e)\,(\Omega m)^{-1}$ with the current driven along the low-symmetry a-axis. The other FL and DL torque conductivities were measured at $\sigma_o^y = 9 \pm 3 \times 10^3\ (\hbar/2e)\,(\Omega m)^{-1}$ and $\sigma_e^y = 8 \pm 2 \times 10^3\ (\hbar/2e)\,(\Omega m)^{-1}$, respectively. The magnitude of τ_e^z was found to depend on the angle between the electric current and the WTe_2 a-axis, showing a gradual decrease of the torque ratio τ_e^z/τ_o^y when the projection of the current on the b-axis increases, giving support to its origin being correlated with the crystal symmetry. Even though an initial thickness dependence on the torques revealed little variation, a more thorough study with a wider thickness range ($t = 0.7 - 16$ nm) revealed additional bulk contributions to the SOTs in addition to the interfacial ones (MacNeill et al., 2017b). The thickness dependence of $|\tau_o^y|$, shows a strong increase with increasing WTe_2 thickness, suggesting it originates from an Oersted field produced by the current in the WTe_2 layer. The unusual out-of-plane DL torque τ_e^z shows a slowly decreasing magnitude with increasing thickness ($t \geq 4$ nm), while thinner layers show significant device-to-device variations. In the same work, the authors indicated that the in-plane DL torque τ_e^y possesses a similar thickness dependence as τ_e^z. These torques remain large down a WTe_2 monolayer, suggesting that their microscopic origin is interfacial with some possible (smaller) additional bulk contribution.

Subsequent studies indicated a strong temperature dependence (2 – 300 K) on τ_o^y with the current flowing along the b-axis of WTe_2 using ST-FMR measurements (Li et al., 2018). While this temperature dependence was observed for thicker samples (20 and 31 nm), thinner samples (5.6 and 7.0 nm) only showed a weak temperature dependence. Furthermore, for a current applied along the a-axis (I//a), no temperature dependence is observed. A torque conductivity as high as $\sigma_o^y = 1.3 \times 10^5\ (\hbar/2e)\,(\Omega m)^{-1}$was reported. Calculations of the Oersted field contribution to τ_o^y could not explain the large enhancement. The enhanced SOT at low temperatures with I//b-axis was therefore ascribed to a spin accumulation created by spin-momentum locking in Fermi arcs which exist only along the b-axis, experimentally observed for WTe_2 nanoribbons with thicknesses in the range of 10–40 nm (Li et al., 2017). The origin of the relatively high τ_o^y which remains for thinner devices, is ascribed to the REE.

More recently, WTe_2/Py heterostructures have been shown to be very efficient for current-induced in-plane magnetization switching, with switching current densities in the order of 10^5 A/cm^2 (Shi et al., 2019). In the same work, the authors also reported a thickness dependence on the spin Hall efficiency in WTe_2, with larger values at higher thicknesses. However, the ST-FMR results show a significant frequency dependence and the role of artifacts such as skin-depth effects could not be ruled out. Nevertheless, the low threshold for current-induced magnetization switching indicates a promising direction for TMDs in future applications. Interestingly, these structures have also shown the presence of a Dzyaloshinskii-Moriya interaction, an essential ingredient for chiral magnetism.

The anisotropic in-plane conductivity in low-symmetry crystals can also impact SOTs. Results on $TaTe_2$/Py heterostructures have shown SOTs with Dresselhaus-like symmetries ($\hat{m} \times \hat{x}$) (Stiehl et al., 2019b). These torques have been shown to arise from Oersted-fields, generated by in-plane transverse current components due to conductivity anisotropy of $TaTe_2$. A similar, albeit smaller effect has been shown to be present in WTe_2/Py bilayers. Apart from the regular Oersted torque and Dresselhaus-like torque in the $TaTe_2$/Py heterostructures, the other torques are small or zero. Cross-sectional high-angle annular dark-field scanning transmission electron microscopy (HAADF-STEM) has indicated intermixing at the $TaTe_2$/Py interface which is likely to affect the effective SOTs due to a change in the local electronic environment and the spin mixing conductance of the interface. Interestingly, a change in the SOTs in topological-insulator/ferromagnet devices due to intermixing at the interface has been recently reported (Bonell et al., 2020). Here we point out that in addition to the changes in the SOTs arising from the different electronic structures for devices using different FM layers (e.g., Py, Co, CoFeB), the materials intermixing should also be carefully considered and potentially quantified in order to obtain a more in-depth understanding of the microscopic mechanisms involved.

Interestingly, both $TaTe_2$ and WTe_2 have shown to induce an in-plane magnetic anisotropy on Py, indicating a strong interaction between the semi-metallic TMDs and the FM layer. The anisotropy induced by WTe_2 was shown to be about 10 s of mT and one order of magnitude larger than the one induced by $TaTe_2$. Additionally, the two TMDs induced anisotropy in different directions with respect to their crystal orientations, hinting toward the dependence of the induced magnetic anisotropy and the electronic structure of the TMD.

Another interesting semi-metallic TMD is β-$MoTe_2$ which, different than WTe_2 and similar to $TaTe_2$, possess inversion symmetry in its bulk form. Using β-$MoTe_2$/Py bilayers Stiehl *et al.* observe the presence of an out-of-plane DL torque τ_e^z using ST-FMR measurements (Stiehl et al., 2019a). This is allowed by the inversion symmetry breaking at the β-$MoTe_2$/Py interface and indicates that inversion asymmetry in the bulk is not a strict requirement for τ_e^z to be observed. The authors report a thickness independent torque conductivity of $\sigma_e^z = 1.02 \pm 0.03 \times 10^3\ (\hbar/2e)\,(\Omega m)^{-1}$, 1/3 of the value reported for WTe_2. The standard in-plane DL torque τ_e^y was also observed with $\sigma_e^y = 5.8 \pm 0.16 \times 10^3\ (\hbar/2e)\,(\Omega m)^{-1}$, and showed no apparent thickness dependence. The lack of a thickness dependent on τ_e^z and τ_e^y for both WTe_2 and β-$MoTe_2$, strongly suggests an interfacial origin for these SOTs.

In addition to the out-of-plane DL torque τ_e^z, the low crystal symmetries of WTe_2 and β-$MoTe_2$ also allow for the presence of an in-plane FL torque τ_o^z ($\hat{m} \times \hat{z}$). While this torque was not observed in WTe_2, it was present in β-$MoTe_2$ devices. There, both τ_e^z and τ_o^z have shown similar temperature dependences, but different thickness dependences, hinting toward two microscopic mechanisms for τ_o^z: one related and another unrelated to τ_e^z. However, the physical mechanisms that generate these torques are still unknown.

More recently, $PtTe_2$/Py devices (Xu et al., 2020) have shown a high spin-torque conductivity for the in-plane DL torque $\sigma_e^y = 1.6 \times 10^5\ (\hbar/2e)\,(\Omega m)^{-1}$. This value is one order of magnitude (or larger) than the values encountered in other TMD-based devices and comparable to devices based on heavy-metal or topological-insulators. This large spin-torque conductivity has been ascribed to a combination of the SHE and spin-momentum locking in topological surface states of $PtTe_2$, as previously observed in topological insulators (Mellnik et al., 2014; Wang et al., 2015; Wang et al., 2017; Clark et al., 2018).

Metallic TMDs

Despite offering stronger spin-orbit interaction and higher conductivity, metallic TMDs have received less attention than their semi-metallic and semiconducting counterparts. To date, only two experimental studies have been reported (Guimarães et al., 2018; Husain et al., 2020).

Thickness dependent ST-FMR measurements on $NbSe_2$ (1–10 layers)/Py heterostructures revealed an in-plane DL torque τ_e^y with a torque conductivity ($\sigma_e^y = 3 \times 10^3\ (\hbar/2e)\,(\Omega m)^{-1}$) comparable to other TMD/Py heterostructures and observable down to a monolayer of $NbSe_2$ (Guimarães et al., 2018). Similar to β-$MoTe_2$/Py (Stiehl et al., 2019a), τ_e^y shows only a weak thickness dependence. An out-of-plane FL torque ($\sigma_o^y = 40 \times 10^3\ (\hbar/2e)\,(\Omega m)^{-1}$) was also observed, and attributed to Oersted fields due to their linear scaling with $NbSe_2$ thickness. However, for thin $NbSe_2$ layers, the estimated

Oersted-field contribution overestimates the observed torque magnitude, and, for monolayer $NbSe_2$ a sign change is observed. These observations for τ_e^y and τ_o^y indicate a contribution from interfacial torques.

In addition to the SOTs with conventional symmetries, an in-plane FL torque τ_o^z $(\hat{m} \times \hat{z})$ was observed in some devices. Since the trigonal symmetry of $NbSe_2$ does not allow for their presence, and given the seemly random thickness dependence of τ_o^z, the authors argue that these torques could arise from uncontrollable strain from the fabrication procedure, which reduces the $NbSe_2$ symmetries. Although τ_e^z is subject to the same symmetry constraints, $\tau_e^z = 0$ for all measured devices, which is in contrast to the torques obtained for WTe_2, where $\tau_o^z = 0$, and $\tau_e^z \neq 0$ (MacNeill et al., 2017a; MacNeill et al., 2017b). This indicates that symmetry analysis alone is not sufficient to predict the observed torques in these systems and that other microscopic factors related to, for example, interface quality (Hayashi et al., 2014; Sousa et al., 2020), Berry curvature (Kurebayashi et al., 2014), or local atomic point-group symmetries (Zhang et al., 2014) could play an important role.

A large spin-torque conductivity of $\sigma_e^y = 2.63 \times 10^5 (\hbar/2e)(\Omega m)^{-1}$ has been recently reported for the metallic monolayer TaS_2/Py heterostructures (Husain et al., 2020) using ST-FMR measurements. This result is attributed to a clean interface which is supported by cross-sectional TEM imaging. Using DFT calculations, the authors observe a considerable redistribution of the band structure which they hold accountable for the prominent DL torque.

CONCLUSION

In this review, we have given an overview of the current status of the field of SOTs in TMD/FM heterostructures. A multitude of SOT symmetries, magnitudes and directions were observed, which could not always be explained by well-known effects such as the SHE and REE. Different mechanisms that do not rely on a large spin-orbit coupling, such as anisotropic in-plane conductivity and uniaxial strain, can also play an important role. Additionally, interfacial effects such as spin-orbit filtering, spin-orbit precession and spin-momentum locking in topological surface states may affect the observed torques. In combination with the large torque conductivities obtained at clean interfaces, this suggests that the TMD/FM interface quality is of paramount importance for both the torque magnitude and direction. Lastly, the ferromagnetic layer, often considered to play a passive role, can have a significant effect on the observed SOTs due to changes of the electronic structure and intermixing at the interface. Dzyaloshinskii–Moriya interaction (DMI) has been shown to arise at TMD/FM interfaces demonstrating a strong interaction between these materials (Kumar et al., 2020; Shi et al., 2019; Wu et al., 2020). The large interfacial DMI in these heterostructures could be explored in future devices combining chiral magnetic structures and SOTs.

Although the crystal symmetry allows for a reasonable prediction of the allowed SOTs, a better understanding of the underlying microscopic mechanisms is key in qualitatively explaining the observed SOTs. In this regard, thickness dependent measurements provide a tool to better differentiate bulk effects from interfacial effects. However, as the contributions of different effects are measured all at once, it remains difficult to distinguish the numerous mechanisms underlying the torques with the current experimental techniques. To clarify the role of the ferromagnetic layer, a variety of devices with different FM materials should be fabricated.

Van der Waals heterostructures composed of TMDs, two-dimensional magnetic materials and graphene should allow for the study of SOTs at the ultimate thickness. Due to their small thickness, in addition to possibly reducing the device footprint, atomically-thin materials are more susceptible to external stimuli, such as gate-voltages, strain and illumination. Along these lines, interesting predictions point to the modulation of SOT and magnetization by gate-voltages in these structures (Dolui et al., 2019; Zollner et al., 2020). The exploration of gate-tunable SOTs in TMD/FM heterostructures could serve as a first step toward non-volatile data processing and storage as well as processing-in-memory applications. By giving an overview of the current status of the field, we hope to facilitate progress on elucidating the different underlying physical mechanisms for the SOTs.

AUTHOR CONTRIBUTIONS

Both authors compiled the studies and wrote the manuscript.

ACKNOWLEDGMENTS

We acknowledge funding from the Dutch Research Council (NWO) Start-Up Grant (STU.019.014), the European Union Horizon 2020 research and innovation program under grant agreements No 696656 and 785219 (Graphene Flagship Core 2 and Core 3), and the Zernike Institute for Advanced Materials.

REFERENCES

Amin, V. P., Haney, P. M., and Stiles, M. D. (2020). Interfacial spin-orbit torques. arXiv: 2008.01182.

Amin, V. P., and Stiles, M. D. (2016a). Spin transport at interfaces with spin-orbit coupling: Formalism. *Phys. Rev. B* 94, 104419. doi:10.1103/PhysRevB.94.104419

Amin, V. P., and Stiles, M. D. (2016b). Spin transport at interfaces with spin-orbit coupling: Phenomenology. *Phys. Rev. B* 94, 104420. doi:10.1103/PhysRevB.94.104420

Avci, C. O., Garello, K., Gabureac, M., Ghosh, A., Fuhrer, A., Alvarado, S. F., et al. (2014). Interplay of spin-orbit torque and thermoelectric effects in ferromagnet/normal-metal bilayers. *Phys. Rev. B* 90, 224427. doi:10.1103/PhysRevB.90.224427

Berger, A. J., Edwards, E. R. J., Nembach, H. T., Karenowska, A. D., Weiler, M., and Silva, T. J. (2018). Inductive detection of fieldlike and dampinglike ac inverse spin-orbit torques in ferromagnet/normal-metal bilayers. *Phys. Rev. B* 97, 094407. doi:10.1103/PhysRevB.97.094407

Bonell, F., Goto, M., Sauthier, G., Sierra, J. F., Figueroa, A. I., Costache, M. V., et al. (2020). Control of spin-orbit torques by interface engineering in topological insulator heterostructures. *Nano Lett.* 20, 5893–5899. doi:10.1021/acs.nanolett.0c01850

Clark, O. J., Neat, M. J., Okawa, K., Bawden, L., Marković, I., Mazzola, F., et al. (2018). Fermiology and superconductivity of topological surface states in PdTe2. *Phys. Rev. Lett.* 120, 1–7. doi:10.1103/PhysRevLett.120.156401

Dieny, B., Prejbeanu, I. L., Garello, K., Gambardella, P., Freitas, P., Lehndorff, R., et al. (2019). Opportunities and challenges for spintronics in the microelectronic industry. arXiv:1908.10584.

Dolui, K., and Nikolic, B. K. (2020). Spin-orbit-proximitized ferromagnetic metal by monolayer transition metal dichalcogenide: atlas of spectral functions, spin textures and spin-orbit torques in Co/MoSe2, Co/WSe2 and Co/TaSe2 heterostructures. *Phys. Rev. Mater.* 4, 104007.

Dolui, K., Petrovic, M. D., Zollner, K., Plechac, P., Fabian, J., and Nikolic, B. K. (2019). First-principles theory of proximity spin-orbit torque on a two-dimensional magnet: current-driven antiferromagnet-to-ferromagnet reversible transition in bilayer CrI3. *Nano Lett.* 20, 2288.

Dyakonov, M. I., and Perel, V. I. (1971). Current-induced spin orientation of electrons in semiconductors. *Phys. Lett.* 35, 459–460. doi:10.1016/0375-9601(71)90196-4

Edelstein, V. M. (1990). Spin polarization of conduction electrons induced by electric current in two-dimensional asymmetric electron systems. *Solid State Commun.* 73, 233–235. doi:10.1016/0038-1098(90)90963-C

Fan, Y., Kou, X., Upadhyaya, P., Shao, Q., Pan, L., Lang, M., et al. (2016). Electric-field control of spin-orbit torque in a magnetically doped topological insulator. *Nat. Nanotechnol.* 11, 352–359. doi:10.1038/nnano.2015.294

Fang, D., Kurebayashi, H., Wunderlich, J., Výborný, K., Zârbo, L. P., Campion, R. P., et al. (2011). Spin-orbit-driven ferromagnetic resonance. *Nat. Nanotechnol.* 6, 413–417. doi:10.1038/nnano.2011.68

Filianina, M., Hanke, J.-P., Lee, K., Han, D.-S., Jaiswal, S., Rajan, A., et al. (2020). Electric-field control of spin-orbit torques in perpendicularly magnetized W/CoFeB/MgO films. *Phys. Rev. Lett.* 124, 217701. doi:10.1103/PhysRevLett.124.217701

Gambardella, P., and Miron, I. M. (2011). Current-induced spin-orbit torques. *Phil. Trans. R. Soc. A.* 369, 3175–3197. doi:10.1098/rsta.2010.0336

Ganichev, S. D., Ivchenko, E. L., Bel'kov, V. V., Tarasenko, S. A., Sollinger, M., Weiss, D., et al. (2002). Spin-galvanic effect. *Nature* 417, 153–156. doi:10.1038/417153a

Ganichev, S. D., Trushin, M., and Schliemann, J. (2016). Spin polarisation by current. *arXiv*.

Garello, K., Miron, I. M., Avci, C. O., Freimuth, F., Mokrousov, Y., Blügel, S., et al. (2013). Symmetry and magnitude of spin-orbit torques in ferromagnetic heterostructures. *Nat. Nanotechnol.* 8, 587–593. doi:10.1038/nnano.2013.145

Ghosh, A., Garello, K., Avci, C. O., Gabureac, M., and Gambardella, P. (2017). Interface-enhanced spin-orbit torques and current-induced magnetization switching of Pd/Co/AlOx layers. *Phys. Rev. Applied.* 7, 014004. doi:10.1103/PhysRevApplied.7.014004

Go, D., Freimuth, F., Hanke, J.-P., Xue, F., Gomonay, O., Lee, K.-J., et al. (2020). Theory of current-induced angular momentum transfer dynamics in spin-orbit coupled systems. *Phys. Rev. Res.* 2, 033401.

Go, D., and Lee, H.-W. (2020). Orbital torque: torque generation by orbital current injection. *Phys. Rev. Research.* 2, 013177. doi:10.1103/PhysRevResearch.2.013177

Guimarães, M. H. D., Stiehl, G. M., Macneill, D., Reynolds, N. D., Ralph, D. C., Guimaraes, M. H. D., et al. (2018). Spin-orbit torques in NbSe2/permalloy bilayers. *Nano Lett.* 18, 1311–1316. doi:10.1021/acs.nanolett.7b04993

Haney, P. M., Lee, H.-W., Lee, K.-J., Manchon, A., and Stiles, M. D. (2013). Current induced torques and interfacial spin-orbit coupling: semiclassical modeling. *Phys. Rev. B* 87, 174411. doi:10.1103/PhysRevB.87.174411

Hayashi, M., Kim, J., Yamanouchi, M., and Ohno, H. (2014). Quantitative characterization of the spin-orbit torque using harmonic Hall voltage measurements. *Phys. Rev. B* 89, 144425. doi:10.1103/PhysRevB.89.144425

Hirsch, J. E. (1999). Spin Hall effect. *Phys. Rev. Lett.* 83, 1834–1837. doi:10.1103/PhysRevLett.83.1834

Hoque, A. M., Khokhriakov, D., Karpiak, B., and Dash, S. P. (2020). Charge-spin conversion in layered semimetal TaTe2 and spin injection in van der Waals heterostructures. *Phys. Rev. Research.* 2, 033204. doi:10.1103/PhysRevResearch.2.033204

Husain, S., Chen, X., Gupta, R., Behera, N., Kumar, P., Edvinsson, T., et al. (2020). Damping-like torque in monolayer 1T-TaS2. aarXiv:2004.02649.

Kato, Y. K., Myers, R. C., Gossard, A. C., and Awschalom, D. D. (2004). Current-induced spin polarization in strained semiconductors. *Phys. Rev. Lett.* 93, 176601. doi:10.1103/PhysRevLett.93.176601

Kumar, A., Chaurasiya, A. K., Chowdhury, N., Mondal, A. K., Bansal, R., Barvat, A., et al. (2020). Direct measurement of interfacial Dzyaloshinskii-Moriya interaction at the MoS2/Ni80Fe20 interface. *Appl. Phys. Lett.* 116, 232405. doi:10.1063/5.0009828

Kurebayashi, H., Sinova, J., Fang, D., Irvine, A. C., Skinner, T. D., Wunderlich, J., et al. (2014). An antidamping spin-orbit torque originating from the Berry curvature. *Nat. Nanotechnol.* 9, 211–217. doi:10.1038/nnano.2014.15

Li, P., Wen, Y., He, X., Zhang, Q., Xia, C., Yu, Z.-M., et al. (2017). Evidence for topological type-II Weyl semimetal WTe2. *Nat. Commun.* 8, 2150. doi:10.1038/s41467-017-02237-1

Li, P., Wu, W., Wen, Y., Zhang, C., Zhang, J., Zhang, S., et al. (2018). Spin-momentum locking and spin-orbit torques in magnetic nano-heterojunctions composed of Weyl semimetal WTe2. *Nat. Commun.* 9, 1–10. doi:10.1038/s41467-018-06518-1

Li, X., Casamento, J., Dang, P., Zhang, Z., Afuye, O., Mei, A. B., et al. (2020). Spin-orbit torque field-effect transistor (SOTFET): proposal for a magnetoelectric memory. *Appl. Phys. Lett.* 116, 242405. doi:10.1063/5.0002909

Liu, L., Moriyama, T., Ralph, D. C., and Buhrman, R. A. (2011). Spin-torque ferromagnetic resonance induced by the spin Hall effect. *Phys. Rev. Lett.* 106, 036601. doi:10.1103/PhysRevLett.106.036601

Lv, W., Jia, Z., Wang, B., Lu, Y., Luo, X., Zhang, B., et al. (2018). Electric-field control of spin-orbit torques in WS2/permalloy bilayers. *ACS Appl. Mater. Interfaces.* 10, 2843–2849. doi:10.1021/acsami.7b16919

MacNeill, D., Stiehl, G. M., Guimaraes, M. H. D., Buhrman, R. A., Park, J., and Ralph, D. C. (2017a). Control of spin-orbit torques through crystal symmetry in WTe2/ferromagnet bilayers. *Nat. Phys.* 13, 300–305. doi:10.1038/nphys3933

MacNeill, D., Stiehl, G. M., Guimarães, M. H. D., Reynolds, N. D., Buhrman, R. A., and Ralph, D. C. (2017b). Thickness dependence of spin-orbit torques generated by WTe2. *Phys. Rev. B* 96, 1–8. doi:10.1103/PhysRevB.96.054450

Manchon, A., Železný, J., Miron, I. M., Jungwirth, T., Sinova, J., Thiaville, A., et al. (2019). Current-induced spin-orbit torques in ferromagnetic and antiferromagnetic systems. *Rev. Mod. Phys.* 91, 035004. doi:10.1103/RevModPhys.91.035004

Mellnik, A. R., Lee, J. S., Richardella, A., Grab, J. L., Mintun, P. J., Fischer, M. H., et al. (2014). Spin-transfer torque generated by a topological insulator. *Nature* 511, 449–451. doi:10.1038/nature13534

Mihai Miron, I., Gaudin, G., Auffret, S., Rodmacq, B., Schuhl, A., Pizzini, S., et al. (2010). Current-driven spin torque induced by the Rashba effect in a ferromagnetic metal layer. *Nat. Mater.* 9, 230–234. doi:10.1038/nmat2613

Miron, I. M., Garello, K., Gaudin, G., Zermatten, P.-J., Costache, M. V., Auffret, S., et al. (2011). Perpendicular switching of a single ferromagnetic layer induced by in-plane current injection. *Nature* 476, 189–193. doi:10.1038/nature10309

Nguyen, M.-H., Ralph, D. C., and Buhrman, R. A. (2016). Spin torque study of the spin Hall conductivity and spin diffusion length in platinum thin films with varying resistivity. *Phys. Rev. Lett.* 116, 126601. doi:10.1103/PhysRevLett.116.126601

Ramaswamy, R., Lee, J. M., Cai, K., and Yang, H. (2018). Recent advances in spin-orbit torques: moving towards device applications. *Appl. Phys. Rev.* 5, 031107. doi:10.1063/1.5041793

Safeer, C. K., Ontoso, N., Ingla-Aynés, J., Herling, F., Pham, V. T., Kurzmann, A., et al. (2019). Large multidirectional spin-to-charge conversion in low-symmetry semimetal MoTe2 at room temperature. *Nano Lett.* 19, 8758–8766. doi:10.1021/acs.nanolett.9b03485

Sahoo, K. R., Chakravarthy, T. P., Sharma, R., Bawari, S., Mundlia, S., Sasmal, S., et al. (2020). Probing proximity-tailored high spin-orbit coupling in 2D materials. *Adv Quantum Tech.* 3, 2000042. doi:10.1002/qute.202000042

Shao, Q., Yu, G., Lan, Y.-W., Shi, Y., Li, M.-Y., Zheng, C., et al. (2016). Strong rashba-edelstein effect-induced spin-orbit torques in monolayer transition metal dichalcogenide/ferromagnet bilayers. *Nano Lett.* 16, 7514–7520. doi:10.1021/acs.nanolett.6b03300

Shi, S., Liang, S., Zhu, Z., Cai, K., Pollard, S. D., Wang, Y., et al. (2019). All-electric magnetization switching and Dzyaloshinskii-Moriya interaction in WTe2/ferromagnet heterostructures. *Nat. Nanotechnol.* 14, 945–949. doi:10.1038/s41565-019-0525-8

Sinova, J., Valenzuela, S. O., Wunderlich, J., Back, C. H., and Jungwirth, T. (2015). Spin Hall effects. *Rev. Mod. Phys.* 87, 1213–1260. doi:10.1103/RevModPhys.87.1213

Sousa, F. J., Tatara, G., and Ferreira, A. (2020). Emergent spin-orbit torques in two-dimensional material/ferromagnet interfaces. arXiv:2005.09670.

Stiehl, G. M., Li, R., Gupta, V., Baggari, I. E., Jiang, S., Xie, H., et al. (2019a). Layer-dependent spin-orbit torques generated by the centrosymmetric transition metal dichalcogenide β–MoTe2. *Phys. Rev. B* 100, 184402. doi:10.1103/PhysRevB.100.184402

Stiehl, G. M., MacNeill, D., Sivadas, N., El Baggari, I., Guimarães, M. H. D., Reynolds, N. D., et al. (2019b). Current-induced torques with dresselhaus symmetry due to resistance anisotropy in 2D materials. *ACS Nano.* 13, 2599–2605. doi:10.1021/acsnano.8b09663

Wang, Y., Deorani, P., Banerjee, K., Koirala, N., Brahlek, M., Oh, S., et al. (2015). Topological surface states originated spin-orbit torques inBi2Se3. *Phys. Rev. Lett.* 114, 257202. doi:10.1103/PhysRevLett.114.257202

Wang, Y., Zhu, D., Wu, Y., Yang, Y., Yu, J., Ramaswamy, R., et al. (2017). Room temperature magnetization switching in topological insulator-ferromagnet heterostructures by spin-orbit torques. *Nat. Commun.* 8, 1364. doi:10.1038/s41467-017-01583-4

Wu, Y., Zhang, S., Zhang, J., Wang, W., Zhu, Y. L., Hu, J., et al. (2020). Néel-type skyrmion in WTe2/Fe3GeTe2 van der Waals heterostructure. *Nat. Commun.* 11, 3–8. doi:10.1038/s41467-020-17566-x

Xu, H., Wei, J., Zhou, H., Feng, J., Xu, T., Du, H., et al. (2020). High spin Hall conductivity in large-area type-II Dirac semimetal PtTe 2. *Adv. Mater.* 32, 2000513. doi:10.1002/adma.202000513

Xue, F., Rohmann, C., Li, J., Amin, V., and Haney, P. (2020). Unconventional spin-orbit torque in transition metal dichalcogenide -ferromagnet bilayers from first-principles calculations. *Phys. Rev. B* 102, 014401.

Zhang, W., Sklenar, J., Hsu, B., Jiang, W., Jungfleisch, M. B., Xiao, J., et al. (2016). Research Update: spin transfer torques in permalloy on monolayer MoS2. *Apl. Mater.* 4, 032302. doi:10.1063/1.4943076

Zhang, X., Liu, Q., Luo, J.-W., Freeman, A. J., and Zunger, A. (2014). Hidden spin polarization in inversion-symmetric bulk crystals. *Nat. Phys.* 10, 387–393. doi:10.1038/nphys2933

Zhao, B., Khokhriakov, D., Zhang, Y., Fu, H., Karpiak, B., Hoque, A. M., et al. (2020). Observation of charge to spin conversion in Weyl semimetal WTe2 at room temperature. *Phys. Rev. Research.* 2, 1–8. doi:10.1103/physrevresearch.2.013286

Zollner, K., Petrovic, M. D., Dolui, K., Plechac, P., Nikolic, B. K., and Fabian, J. (2020). Scattering-induced and highly tunable by gate damping-like spin-orbit torque in graphene doubly proximitized by two-dimensional magnet Cr2Ge2Te6 and monolayer WS2. *Phys. Rev. Res*. 2, 043057.

Conflict of Interest: The authors declare that the research was conducted in the absence of any commercial or financial relationships that could be construed as a potential conflict of interest.

frontiers in Materials

REVIEW
published: 09 December 2020
doi: 10.3389/fmats.2020.594386

Quantum Spin-Wave Materials, Interface Effects and Functional Devices for Information Applications

Jiapeng Xu[1], Lichuan Jin[1], Zhimin Liao[2,3], Qi Wang[4], Xiaoli Tang[1], Zhiyong Zhong[1] and Huaiwu Zhang[1]*

[1]State Key Laboratory of Electronic Thin Films and Integrated Devices, University of Electronic Science and Technology of China, Chengdu, China, [2]Beijing Key Laboratory of Quantum Devices, Peking University, Beijing, China, [3]Collaborative Innovation Center of Quantum Matter, Peking University, Beijing, China, [4]Faculty of Physics, University of Vienna, Vienna, Austria

With the continuous miniaturization of electronic devices and the increasing speed of their operation, solving a series of technical issues caused by high power consumption has reached an unprecedented level of difficulty. Fortunately, magnons (the quanta of spin waves), which are the collective precession of spins in quantum magnetic materials, making it possible to replace the role of electrons in modern information applications. In the process of information transmission, nano-sized spin-wave devices do not transport any physical particles; therefore, the corresponding power consumption is extremely low. This review focuses on the emerging developments of the spin-wave materials, tunable effects, and functional devices applications. In the materials front, we summarize the magnetic properties and preparation characteristics of typical insulating single-crystalline garnet films or metallic alloy films, the development of new spin-wave material system is also introduced. Afterward, we introduce the emerging electric control of spin-wave effects originating from the interface transitions, physical or chemical, among these films including, voltage-controlled magnetic anisotropy, magneto-ionic transport, electric spin-torque, and magnon-torque. In the functional devices front, we summarize and elaborate on the low dispassion information processing devices and sensors that are realized based on spin waves.

Keywords: spin waves, magnetic materials and devices, functional devices, magnetoelectric coupling, Interface effects

OPEN ACCESS

Edited by:
Ashok Kumar,
National Physical Laboratory (CSIR), India

Reviewed by:
Xiaotian Wang,
Southwest University, China
Atul Thakre,
Yeungnam University, South Korea
Jiji Thomas Joseph Pulikkotil,
National Physical Laboratory (CSIR), India

****Correspondence:***
Lichuan Jin
lichuanj@uestc.edu.cn

Specialty section:
This article was submitted to Quantum Materials, a section of the journal Frontiers in Materials

Received: *13 August 2020*
Accepted: *26 October 2020*
Published: *09 December 2020*

Citation:
Xu J, Jin L, Liao Z, Wang Q, Tang X, Zhong Z and Zhang H (2020) Quantum Spin-Wave Materials, Interface Effects and Functional Devices for Information Applications. Front. Mater. 7:594386. doi: 10.3389/fmats.2020.594386

INTRODUCTION

With the rapid development of science and technology, the revolution of electronic information technology has greatly changed our lives just within the course of few decades. The technological achievements of this decade have subverted people's imagination a century ago. First invented in 1959, the integrated circuits have developed rapidly over the past 60 years. One of the key factors is Moore's Law (Moore, 1965). In the past few decades, people have always regarded Moore's Law as the core driving force for the development of the electronic information industry. Nevertheless, since 2005, one of the key elements of maintaining Moore's Law, the miniaturization of semiconductor devices, has been significantly slowed down due to intrinsic physical constraints (Theis and Wong, 2017). This brings the imminent question, how long does Moore's Law sustain? If Moore's Law comes to an end, what would be the future of the integrated circuit industry? Three approaches are proposed in the related literature as the key plans to perpetuate the development of the integrated

circuit industry, namely "more Moore" (Li, 2012), "more than Moore" (Graef, 2011; Salah, 2017) and "beyond CMOS" (Hutchby et al., 2002; Bernstein et al., 2010; Nikonov and Young, 2013; Nikonov and Young, 2015; Pan and Naeemi, 2017).

Spin-wave devices based on magnetic materials are a new type of devices proposed under "beyond COMS" concept to replace the traditional charge transport devices (Rana and Otani, 2019). Spin is an intrinsic particles' property described in quantum mechanics, and spin waves are collective precession generated by the interaction of electron spins in metals, semiconductors, and insulators (Kruglyak et al., 2010). Spin-wave devices use wave amplitude, phase, and frequency as the carrier of information transmission and processing. The process of spin-wave propagation is only based on electron spin interactions, thus no physical particle transportation is involved. This results in extremely low power consumption by the spin-wave devices compared to the conventional CMOS devices (Kajiwara et al., 2010; Khitun et al., 2010). In addition, spin-wave sensors have a higher level of thermal stability and the innovative principle of magnetism provides them with unique advantages. Comparing with the conventional sensors, these provide the spin-wave sensors with a higher sensitivity, thermal stability, and lower cost (Goto et al., 2015; Matatagui et al., 2017).

Spin waves usually propagate in the waveguides made of magnetic thin films or strips. The spin-wave dispersion (the relationship between the spin-wave frequency f and the wave number k) depends on various parameters, such as the waveguide geometry (Chumak et al., 2014), Oersted field induced by the electric current (Rousseau et al., 2015) and spin-wave material properties (Qin et al., 2018), etc. Among these parameters, the magnetic material determines the basic performance of the device. Therefore, the choice of material is a key factor in the application of the spin-wave devices.

Single-crystal yttrium iron garnet (YIG) has a small Gilbert damping constant, a narrow ferromagnetic resonance linewidth, and other highlights (Dubs et al., 2017). Nevertheless, its saturation magnetization is rather small which limits its spin-wave frequency. Other spin-wave alloy materials, such as permalloy, CoFeB, and Heusler alloy have a higher saturation magnetization and Curie temperature (Chumak et al., 2017), but their Gilbert damping constants are one to two orders of magnitude larger than YIG. Materials with such a high Gilbert damping constant are not conducive to the propagation and practical application of spin waves. The preparation of spin-wave thin films needs to consider both the film quality and film thickness, but these two indicators are usually opposed to each other. To pursue better spin-wave characteristics and new magnetic physical phenomena, the exploring of new materials aims at emerging fields such as antiferromagnetic materials (Nishitani et al., 2010), YIG modification (Sharma and Kuanr, 2018) and topological magnon insulators (Wang et al., 2018c). The structure design of spin-wave materials is mainly focused on magnonic crystals (Nikitov et al., 2001; Chumak et al., 2008; Krawczyk and Grundler, 2014). At the same time, the new interface effects found in magnetic heterostructures provide innovative means for spin-wave manipulation.

Various magnetoelectric effects, including voltage-controlled magnetic anisotropy (VCMA) (Dieny and Chshiev, 2017), magneto-ionic transport (Tan et al., 2019), electric spin-torque (Madami et al., 2011; Divinskiy et al., 2018) and magnon-torque (Wang et al., 2019), are capable of improving the spin-wave manipulation efficiency while effectively reduce the power consumption during the process. Therefore, magnetoelectric effects enable the development of all-voltage-controlled spin-wave devices with extremely low power consumption.

Spin-wave functional devices have also been developed steadily based on spin-wave materials and the related effects and are becoming a mature technology. The basic manipulation processes required by spin-wave logic devices such as spin-wave phase shift (Wang et al., 2018b), signal division (Heussner et al., 2017), and channeling (Wagner et al., 2016) are also achieved. Spin-wave sensors have also attracted increasing attention due to their high level of thermal stability (Goto et al., 2015), accuracy (Matatagui et al., 2017).

The above-mentioned recent developments enable spin waves to find their roles in modern information applications. In this paper, an application chain of the spin-wave information technology is constructed. The application chain is built upon the spin-wave materials, their novel interface effects, and spin-wave functional devices. We start from the magnetic properties and preparation characteristics of typical spin-wave materials. Then we introduce the latest developments including recent exploration of new (e.g., antiferromagnetic spin-wave materials, modified YIG and topological magnon insulators), and structurally designed materials (e.g., magnonic crystals). We then summarize the origins, mechanisms, and applications of novel magnetoelectric effects in magnetic heterostructures, including VCMA, magneto-ionic transport, electric spin-torque, and magnon-torque. After reviewing the spin-wave materials and interface effects, we further introduce the internal principles and outstanding advantages of the latest spin-wave functional devices from the perspective of information processing and sensing. Finally, we conclude the current status of spin-wave technology, and further provide some insights on the future development trends in this research area.

QUANTUM SPIN-WAVE THEORY AND MATERIALS

Basic Theory of Spin-Wave

The existence of several major energy terms in micromagnetic theory provides an explanation for the concept of effective field in the process of spin-wave propagation. These energy terms can be considered as Zeeman energy, exchange energy, magnetocrystalline anisotropy energy and demagnetizing energy.

Under the static magnetic field $\overrightarrow{B}$, the energy of a magnetic moment $\overrightarrow{\mu_i}$ at site i is

$$U_i = -\overrightarrow{\mu_i} \cdot \overrightarrow{B} \tag{2.1}$$

We consider only the Heisenberg interaction, so that the exchange energy is given by

$$U_{exc} = -2J\sum_i \overrightarrow{S_i}\cdot\overrightarrow{S_{i+1}} \tag{2.2}$$

J is the nearest neighbor exchange parameter, $\overrightarrow{S_i}$ is spin angular momentum operators at site i. Consider now a simple ferromagnet with Zeeman and exchange energies only, we can write the spin Hamiltonian as

$$\widehat{H} = -g\mu_B\sum_i H_z S_i^z - J\sum_{i,\delta}\overrightarrow{S_i}\cdot\overrightarrow{S_{i+\delta}} \tag{2.3}$$

Where μ_B is the Bohr magneton and g is the spectroscopic splitting factor. $H_z = H_0 - N_z 4\pi M + H_A$, which including the influence of external field H_0, demagnetization energy and magnetocrystalline anisotropy field H_A. The second term of **Eq. 2.3** represents the exchange energy, where $\overrightarrow{\delta}$ is the vector connecting point i and the nearest neighbors. The detailed reasoning process refers to the literature (Rezende, 2020).

The effective field can be obtained

$$H_{eff} = -\frac{1}{\mu_0}\frac{\delta\varepsilon}{\delta\mathbf{M}} \tag{2.4}$$

where $\varepsilon = \varepsilon_{ex} + \varepsilon_{ze} + \varepsilon_k + \varepsilon_d$, which is the sum of the total energy of magnetic materials per unit volume. M is the magnetization intensity. When the local magnetic moment reaches the equilibrium state under the action of the effective field H_{eff}, the magnetic moment μ will be arranged in parallel along the direction of the effective field to achieve the lowest energy of the system. But when it deviates from the equilibrium state, it feels a torque

$$\tau = \mu\times\mu_0 H_{eff} \tag{2.5}$$

Under the semi-classical approximation, the relationship between magnetic moment μ and angular momentum L is as follows:

$$\mu = -|\gamma|L \tag{2.6}$$

γ is the gyromagnetic ratio. According to the law of conservation of angular momentum, the time rate of change of angular momentum is equal to the torque τ

$$\frac{dL}{dt} = \tau \tag{2.7}$$

From **Eqs 2.5–2.7**, we obtained

$$\frac{d\mu}{dt} = -|\gamma|\mu_0\left(\mu\times H_{eff}\right) \tag{2.8}$$

In a ferromagnet, the magnetization M is the magnetic moment per unit volume, and Landau-Lifeshitz (LL) equation can be obtained by replacing μ

$$\frac{dM}{dt} = -|\gamma|\mu_0\left(M\times H_{eff}\right) \tag{2.9}$$

In the above equation, if the magnetization vector M is not parallel to the effective field H_{eff}, the magnetic moment μ will keep precessing around the direction of H_{eff}, which obviously does not meet the physical law. To solve this problem, T. Gilbert introduced the damping term, and the magnetic moment will be parallel to the effective field direction gradually under the damping action. Landau-Lifshitz and Gilbert (LLG) equation is obtained, where α is the dimensionless damping factor

$$\frac{dM}{dt} = -|\gamma|\mu_0\left(M\times H_{eff}\right) + \frac{\alpha}{M_s}\left(M\times\frac{dM}{dt}\right) \tag{2.10}$$

The spin-wave is the non-uniform precession of the magnetic moments, and the adjacent magnetic moments are not parallel. For a standard ellipsoid, the effective field can be expressed by

$$H_{eff} = (H - N_z M_s)e_z + H_{ex} + H_{demag} \tag{2.11}$$

where $H_{ex} = -2Ak^2/\mu_0 M_s m$ represents the exchange field, $H_{\mathrm{demag}} = -k(\mathrm{km})/k^2$ represents the demagnetizing field, H is the external magnetic field parallel to the Z axis. Substituting **Eq. 2.11** into the LLG equation, we can get the frequency expression of the spin-wave

$$\omega = \sqrt{(\omega_H - N_z\omega_M + \omega_{ex}k^2)\left(\omega_H - N_z\omega_M + \omega_{ex}^2 + \omega_M\sin^2\theta\right)} \tag{2.12}$$

where $\omega_H = \gamma H$, $\omega_M = \gamma M_s$, $\omega_{\mathrm{ex}} = 2\gamma A/\mu_0 M_s$, θ satisfy the following relations

$$k = k\left(\sin\theta e_x + \cos\theta e_y\right) \tag{2.13}$$

Equation 2.12 represents the relationship between the spin-wave frequency ω and the wave vector k, which is also called the spin-wave dispersion relationship.

It is worth mentioning that, in addition to solving the governing equation of spin-wave propagation using the classical LLG equation, another method using first-principles is also very successful (see reference (Tancogne-Dejean et al., 2020)). Tancogne-Dejean et al. obtained systematic dynamical properties through the time-dependent Kohn–Sham equations in real time, which reveals the transverse magnetic excitation spectrum of the magnet, and provides an important reference to analyze magnonic excitation within the first-principles framework.

Magnetic Properties of Typical Spin-Wave Materials

We have witnessed an unprecedented progress in the discovery of new materials, structures and effects during the last 100 years. The exquisite blueprints drawn by the scientists and researchers and materialized by the industry fundamentally affected and changed our day-to-day life. Similarly, spin-wave materials have been rapidly developed by the introduction of spin-wave functional devices. During the last few decades, in-depth investigations have shown that magnetic materials, such as YIG (Dubs et al., 2017), permalloy (Michelini et al., 2002), CoFeB (Conca et al., 2013) and Heusler alloy (Kubota et al., 2009) provide clear advantages as spin-wave carriers.

Chumak et al. (2017) summarized the magnetization parameters and spin-wave characteristics of the above-mentioned four typical spin-wave materials, and concluded that the spin-wave materials should have four basic requirements: a) a small-value Gilbert damping constant that ensures that propagation of spin waves without excessive dissipation; b) a high saturation magnetization that ensures sufficient spin-wave frequency and group velocity; c) a high-value Curie temperature that provides thermal stability; and d) ease of processing. Gilbert damping constant, the intrinsic parameter of spin-wave materials, determines the group velocity of spin waves, and the product of spin-wave group velocity and lifetime is the mean free path of spin waves. Since the mean free path represents the transmission capacity of spin waves in the waveguide, Gilbert damping constant is one of the most important parameters of spin-wave materials. The saturation magnetization of spin-wave materials also determines the propagating frequency and group velocity. Furthermore, Curie temperature represents the critical point for ferromagnetic/ferrimagnetic materials to transform into paramagnetic materials, which is the key factor to evaluate the thermal stability of spin-wave electronic devices.

As it is seen in **Table 1**, Gilbert damping constant of single-crystal YIG thin film (μm-thick) is in order of 10^{-5}. The lifetime of spin waves in μm-thick YIG thin films is in order of hundreds of nanoseconds, and the mean free path is in order of thousands of microns. This set of characteristics is unmatched by any other materials. This is because YIG has a weak spin-orbit interaction, which results in a weaker magnon-phonon coupling than other magnetic materials. Therefore, YIG demonstrates an extremely low magnetic loss and Gilbert damping constant (Dubs et al., 2017). Note that permalloy and CoFeB are amorphous, and Heusler alloy is single crystal. Compared to YIG, spin-wave alloy materials still have a big gap in spin-wave propagation characteristics, but they generally have a higher saturation magnetization and Curie temperature. Therefore, the spin waves have a higher frequency in alloy materials, and metal-based spin-wave devices are more stable at high temperature. It should be also noted that permalloy is known for its high permeability, low coercivity, and low magnetic anisotropy (Chin, 1971; Michelini et al., 2002), and is an important part of spin valve devices (Tanoue and Tabuchi, 2001). Heusler alloy with semi-metallic properties have a very large spin polarization effect (Hillebrands and Felser, 2006) due to the energy gap in the up and down spin channel at its Fermi level, which results in generating fully spin-polarized conduction electrons (Kubota et al., 2009).

Preparation Characteristics of Typical Spin-Wave Materials

Table 2 summarizes the preparation characteristics of the thin films made of the above four spin-wave materials, including the main preparation technologies, substrate materials, and main preparation parameters. Magnetron sputtering is relatively common among various preparation technologies. This is because magnetron sputtering is easy to adjust and capable of sputtering the high-melting-point target materials made of different metals, alloys, and oxides (Kelly and Arnell, 2000). In addition, permalloy thin films prepared by electrochemical deposition have the most prominent feature of rapid growth (Zubar et al., 2018). Among the thin film parameters, thickness and surface roughness are considered as the key factors for preparing micro-nano spin-wave electronic devices.

In general, thinning thickness is one of the main development trends in spin-wave materials. However, the magnetization dynamic characteristics of YIG ultra-thin films with nanometer-level thickness are not constant and their spin-wave attenuation length, group velocity, Gilbert damping, and other spin-wave characteristics may decline. The lowest Gilbert damping constant for such films is around 2×10^{-4} (Onbasli et al., 2014). Although YIG ultra-thin provides great advantages over other type of materials, it is far from YIG bulk materials. This is mainly due to the internal structure, composition phase and surface morphology of the films. Therefore, the preparation technology of nanometer-thick spin-wave films remains to be further explored.

YIG thin films are generally grown on gadolinium gallium garnet (GGG) substrates with (111) orientation. The main preparation techniques include liquid phase epitaxy (LPE), pulsed laser deposition (PLD), and magnetron sputtering (MS). The details of LPE has been developed in 1970s and fuses solute and flux with a proper composition at a high temperature to form saturated melt for film preparation. The supercooling effect is then achieved by cooling within a large temperature range. Due to the supercooled precipitation of solute, YIG thin films with the same lattice constant as the substrate then grow on the substrate at a constant temperature. Although the preparation process is complex and the preparation cost is high, it is still one of the best choices for the preparation of μm-thick YIG films (Levinstein et al., 1971; Dubs et al., 2017). YIG films prepared by LPE method are relatively thick, and the typical root mean square (RMS) surface roughness value is maintained at a high level, between 0.3–0.8 nm. Another preparation technology, PLD, is recently considered as the mainstream choice of YIG ultrathin films. The basic preparation process of PLD is using a high-energy pulsed laser to ionizes the specific target. The plasma plume generated is then deposited and then nucleated on the surface of the GGG substrate. The PLD requires oxygen atmosphere, and its main advantage is the ability to obtain a more accurate stoichiometric ratio than that of other preparation technologies. This enables preparation of YIG ultra-thin films with thickness as low as 5 nm, and up to the standard surface roughness and magnetic properties (Sun et al., 2012; d'Allivy Kelly et al., 2013). MS can also be used to prepare YIG thin films, but the obtained Gilbert damping constant is generally about three times larger than that of PLD. This is because the sputtering parameters have an important influence on the microstructure of the films (Liu et al., 2014). For instance, a higher annealing temperature and a longer annealing time tend to aggravate the diffusion effect of atoms at the interface.

The preparation techniques of permalloy materials are mainly based on electrochemical deposition (ED), magnetron sputtering

TABLE 1 | Magnetic parameters and spin-wave characteristics of four typical spin-wave materials (Chumak et al., 2017) (licensed under CC BY 3.0).

	μm-thick YIG	nm-thick YIG	Permalloy	CoFeB	Heusler alloy
Chemical composition	$Y_3Fe_5O_{12}$	$Y_3Fe_5O_{12}$	$Ni_{81}Fe_{19}$	$Co_{40}Fe_{40}B_{20}$	$Co_2Mn_{0.6}Fe_{0.4}Si$
Structure	Single crystal	Single crystal	Amorphous	Amorphous	Single crystal
Gilbert damping	5×10^{-5}	2×10^{-4}	7×10^{-3}	4×10^{-3}	3×10^{-3}
Saturation magnetization ($kA{\cdot}m^{-1}$)	140	140	800	1,250	1,000
Exchange constant ($pJ{\cdot}m^{-1}$)	3.6	3.6	16	15	13
Curie temperature (K)	560	560	550–870	1,000	>980
Lifetime (ns)	604.9	150.2	1.3	1.6	2.6
Velocity (km/s)	33.7	0.23	2.0	3.5	2.6
Mean free path (μm)	20,400	35.1	2.7	5.7	6.9
Ratio of mean free path to wavelength	64.9	27.9	2.1	4.5	5.5

(MS), and molecular beam epitaxy (MBE). The most prominent characteristics of ED is the capability of achieving an extremely fast film deposition rate at the room temperature. However, its higher surface roughness has a negative impact on the film quality (Lamrani et al., 2015; Zubar et al., 2018), and using the electrolyte solution raises concerns on potential environmental pollution. The thin film prepared by MS under vacuum has a more uniform composition. Furthermore, permalloy is easier to deposit comparing to other materials. Therefore, the thickness of permalloy prepared by MS can be as low as 1 nm (Michelini et al., 2002). For the MBE, the substrate temperature required is relatively low and the film deposition rate is also small. As the entire deposition process is precisely controlled, the pressure of preparation is as low as 5×10^{-6} mTorr (Tanaka et al., 2010; Ohtake et al., 2011). A crucial disadvantage of the MBE is its high production cost which is due to its long preparation cycle, and high environmental pollution management costs.

The most common preparation technology for CoFeB and Heusler alloy is MS. MS was used in the preparation of pure aluminum films and alloy films as early as 1970s (McLeod and Hartsough, 1977), and was widely used in the preparation of various high-quality films in the past decades (Kelly and Arnell, 2000). The gas pressure during magnetron sputtering deposition of amorphous CoFeB thin films has a great influence on the magnetization dynamics (Xu et al., 2012). The sputtered Heusler alloy has the best spin-wave properties among the three alloys. The gilbert damping constant in Heusler alloy thin film can reach to 3×10^{-3} (Trudel et al., 2010), and the maximum spin-wave attenuation length is around 16.7 μm (Sebastian et al., 2012), which is closely related to the unique semi-metallic property of Heusler alloy (Kubota et al., 2009).

Development of New Spin-Wave Material Systems

Antiferromagnetic Spin-Wave Materials

Antiferromagnets are highly magnetically ordered materials with periodic and symmetrical magnetic moments. In contrast with ferromagnetic materials, the magnetic moments of adjacent atoms in antiferromagnetic materials are antiparallel and two sets of opposite magnetic sublattices are closely coupled (Kittel, 1951). Therefore, below Neel temperature, antiferromagnetic materials macroscopically appear to be nonmagnetic. This special antiferromagnetic structure results in no net magnetism in the ground state. Such a characteristic result in increased robustness to the external stray magnetic fields. This further causes easily magnetic excitation at terahertz frequencies under the interaction of its internal strong exchange coupling and other external disturbances, e.g., laser irradiation (Nishitani et al., 2010). In addition, the maximum driven velocity of antiferromagnetic domain wall is several orders of magnitude larger than that of ferromagnetic domain wall (Shiino et al., 2016). Although some studies have explained the antiferromagnetic ordering of $CaFe_2As_2$ based on the interaction between spin waves and magnetic exchange (see, e.g., Zhao et al., 2009), the antiferromagnetic properties need further investigations.

Recently, researchers paid a lot of attention to antiferromagnetic spin waves and magnons. By applying other technologies, antiferromagnetic materials (especially NiO) have shown unique advantages in magnon excitation and spin-wave manipulation at high frequency and high speed. Nishitani et al. (2010) realized THz spin-wave excitation of antiferromagnetic single-crystal NiO under femtosecond laser irradiation and showed that Raman scattering is the likely mechanism behind this phenomenon. The relativistic kinematics of antiferromagnets explain that by increasing the domain wall velocity to the spin-wave group velocity, the domain wall is capable to emit THz spin waves (Shiino et al., 2016). Furthermore, it is shown that the energy can be transferred to the magnon mode by optical excitation. This has been proved through experiments by inverse Faraday effect and inverse Cotton-Mouton effect, where the excitation efficiency of the latter is about three orders of magnitude higher than that of the former (Tzschaschel et al., 2017).

High frequency magnon excitation in antiferromagnetic materials shows remarkable characteristics. Further, using antiferromagnetic ordering for quick controlling of the spin and polarization degrees of freedom in spin waves provides great technical advantages. For instance, by controlling the spin degree of freedom in a terahertz pulsed electric field at the femtosecond timescale, Kampfrath et al. (2011) demonstrated switching of coherent spin waves in antiferromagnetic materials at the frequency of 1 THz. Further, Lan et al. (2017) used domain walls as spin-wave polarizers and retarders by using the polarization degree of freedom of the spin waves. This was

TABLE 2 | The preparation characteristics of the thin films made of four typical spin-wave materials. Main preparation technologies include liquid phase epitaxy (LPE), pulsed laser deposition (PLD), magnetron sputtering (MS), electrochemical deposition (ED), and molecular beam epitaxy (MBE). Room temperature is abbreviated as RT.

	YIG				Permalloy		CoFeB	Heusler alloy
Main preparation technologies	LPE	PLD	MS	ED	MS	MBE	MS	MS
Substrate materials	GGG (111)	GGG (111)	GGG (111)	Si (100)	Si (100)/MgO (001)	MgO (100)/(110)/(111)	SiO_2/Si (100)	GaAs (001)/MgO (001)
Main preparation parameters Typical thickness (nm)	≥100	5–30	10–100	5–100	≥3.5	≥5	5–100	5–100
Typical growth rate (nm/min)	100–500	≈3	0.3–16	810	≈5	≈0.6	≈4	≈4.8
Deposition temperature (°C)	800–1000	650–850	RT	RT	30–350	100–500	RT	RT
Growth atmosphere	Air	Oxygen	Argon	Air	Argon	Air	Argon	Argon
Gas pressure (mTorr)	–	20–200	10–40	–	1–4	$\leq 5 \times 10^{-6}$	1–3.5	1.5–3
Root mean square roughness (nm)	0.3–0.8	0.1–0.3	0.1–0.4	0.4–2.2	0.25–1.5	≈0.3	≈0.4	≈0.2
Annealing temperature (°C)	–	700–800	740–840	–	800	–	200–400	300–500

mainly due to capability of antiferromagnets to accommodate both left-circular and right-circular polarized spin-wave modes.

Antiferromagnetic materials also create the smallest spin-wave waveguide on record. For the first time, Patil et al. (2016) reported propagation of 43 THz spin waves in NiO nanorods with a length of 700 nm. Such a small size is explained based on the unique antiferromagnetism and geometric characteristics of NiO nanorods, and based on the fact that magneto-optical Faraday effect is the key factor in the process of spin-wave detection. Traditional Brillouin scattering spectroscopy can only be used to detect and observe spin waves with a few microns of wavelength.

Modification of Yttrium Iron Garnet

Modification of YIG is usually referred to the preparation of new materials by doping YIG (Rare-Earth-Doped Yttrium Iron Garnets, R: YIG) or replacing Y (Rare-Earth Iron Garnets, RIG) with other rare Earth elements. Modified YIG materials provide outstanding advantages in terms of spin-wave performance and magneto-optical properties.

Table 3 summarizes the characteristics of the modified YIG made by doping or substituting YIG with Eu, Lu, Tm, and other rare Earth elements. Comparing the modified YIG in **Table 3**, with those of pure YIG materials in **Table 1**, it is seen that the spin-wave damping property in modified YIG is not improved, and the Gilbert damping constant in pure YIG is the smallest (5×10^{-5}). In Ce: YIG, the Gilbert damping constant of $Y_{2.85}C_{0.15}Fe_5O_{12}$ is 2.8×10^{-3} (Sharma and Kuanr, 2018). With the increase of Ce content, the Gilbert damping constant of $Y_2C_1Fe_5O_{12}$ increases to the order of 10^{-2} (Kehlberger et al., 2015), and the similar situation occurs in La: YIG (Sharma and Kuanr, 2018; Jin et al., 2019). If Y is completely replaced by other rare Earth elements (e.g., Eu, Lu and Tm), the Gilbert damping constant in RIG is around 10^{-2} in order of magnitude, showing its highest level (Rosenberg et al., 2018; Crossley et al., 2019). These data indicate that YIG has unique advantages in spin-wave propagating characteristics, which is difficult to be replaced.

Although modification of YIG with the rare Earth elements material does not improve Gilbert damping constant, it provides special advantages in magneto-optical and other magnetic properties. For instance, Bi: YIG and BIG provide the largest magneto-optical constant in the iron garnet family and its Faraday rotation angle reached 60°/μm in the visible light range (λ = 430 nm). Furthermore, Ce: YIG demonstrates both enhanced Faraday effect (Gomi et al., 1991) and enhanced magneto-optical Kerr effect (Kehlberger et al., 2015). These excellent magneto-optical properties are of great significance to the design of integrated magneto-optical devices such as isolators and circulators. In addition, YIG films modified by rare Earth elements Ce (Lage et al., 2017), Bi (Sellappan et al., 2017; Soumah et al., 2018), Eu (Rosenberg et al., 2018) and Tm (Quindeau et al., 2017) can be used to control the magnetic anisotropy of the films. By reducing the thickness of these modified YIG films to a certain extent, the films show perpendicular magnetic anisotropy. Some believe that this is due to the magnetoelastic anisotropy caused by the epitaxial mismatch strain of the film on the substrate (Sellappan et al., 2017; Rosenberg et al., 2018). Another explanation for this is that

TABLE 3 | Gilbert damping constant and other magnetic properties of YIG films modified by rare Earth elements.

Materials	Gilbert damping constant	Features
Rare-Earth-doped yttrium iron garnets		
Ce: YIG ($Y_{2.85}C_{0.15}Fe_5O_{12}$)	2.8×10^{-3}	Excellent magneto-optical performance; VCMA
Ce: YIG ($Y_2C_1Fe_5O_{12}$)	2×10^{-2}–4.8×10^{2}	
La: YIG ($Y_{2.97}L_{0.03}Fe_5O_{12}$)	2×10^{-3}	The damping factor changes significantly with temperature
La: YIG ($Y_{2.85}L_{0.15}Fe_5O_{12}$)	3.15×10^{-3}	
Bi: YIG ($Y_2B_1Fe_5O_{12}$)	3×10^{-4}	Excellent magneto-optical performance; VCMA
Nd: YIG ($Y_{2.85}N_{0.15}Fe_5O_{12}$)	3.8×10^{-3}	—
Rare-Earth iron garnets		
EIG ($Eu_3Fe_5O_{12}$)	2.5×10^{-2}	VCMA
LIG ($Lu_3Fe_5O_{12}$)	1×10^{-3}	In-plane magnetic anisotropy
TIG ($Tm_3Fe_5O_{12}$)	1.4×10^{-2}	VCMA

the transformation of the easy magnetic axis orientation is the result of competition between decreasing saturation magnetization and the constant uniaxial perpendicular anisotropy (Popova et al., 2013).

Topological Magnonics

The topological phase of matter and non-traditional chiral edge mode are believed to exist in various classical systems. The edge mode is robust to disturbances and is not sensitive to material parameters. Recently, the topological origin of the unidirectional magnetostatic surface spin waves has been deduced (Shindou et al., 2013; Yamamoto et al., 2019), implying that the topological phase of matter exists in a broader field including spintronics. For the first time, Chisnell et al. (2015) developed a two-dimensional topological magnon insulator, in which the degree of freedom of spin is similar to that of electrons in electronic topological insulators. This corroborates the existence of protecting chiral edge modes of spin waves. Collective spin excitations of chiral surface states were found in a three-dimensional topological insulator Bi_2Se_3 (Kung et al., 2017). Compared with the calculations, it is determined that this is a new type of transverse chiral spin waves, and the strong spin-orbit coupling ensures the robustness of the spin waves.

The polarized Raman spectrum of Bi_2Sn_3 was measured experimentally, showing a resonance peak at 150 meV. It was found that the experimental result is in coincidence with the theoretical result of transverse chiral spin waves (calculated Raman spectrum), determined that the mode of spin waves propagate in three-dimensional topological insulator Bi_2Sn_3 is transverse chirality. The main computational process of Raman response is as follows (for a more detailed calculation process, see reference Kung et al. (2017)):

The chiral surface state of three-dimensional topological insulators can be expressed by the Hamiltonian operator

$$\widehat{H}(\mathbf{k}) = \frac{k^2}{2_m^*}\widehat{\sigma}_0 + \nu_1 \boldsymbol{\sigma}\cdot\mathbf{k} \tag{2.14}$$

where m^* is the effective mass, $\widehat{\sigma}$ is the Pauli matrix, and $\widehat{\sigma}_0$ is a 2×2 unit matrix, $\mathbf{k}$ describes hexagonal warping of the surface states away from the Dirac point. The low and high-energy Dirac cones of the surface state can be obtained, which are $l_{1,2}$ and $u_{1,2}$, respectively. Therefore, the resonance part of the Raman vertex can be written as

$$\gamma(\mathbf{k}) = \frac{\left(\mathbf{e}_s\cdot\mathbf{p}_{u_1u_2}\right)\left(\mathbf{e}_I\cdot\mathbf{p}_{u_2l_1}\right)}{E_{u_2}(\mathbf{k}) - E_{l_1}(\mathbf{k}) - \Omega_L} + \frac{\left(\mathbf{e}_s\cdot\mathbf{p}_{u_1l_2}\right)\left(\mathbf{e}_I\cdot\mathbf{p}_{l_2l_1}\right)}{E_{l_2}(\mathbf{k}) - E_{l_1}(\mathbf{k}) - \Omega_L} \tag{2.15}$$

The two terms in the right-hand side of **Eq. 215**, respectively, represent the interaction mechanism between holes to electrons, and holes to holes. Due to the characteristics of Bi_2Se_3, the second term is basically dispersion-free and the first term is small, which is consistent with the experiment (only one resonance is observed). The initial and final states of the Raman vertex form a 2×2 space, then the Raman response function is written as

$$R(\omega, T) \infty \chi_{ZZ}''(\omega, T)/\left(\mathrm{E_g} - \Omega_\mathrm{L}\right)^2 \tag{2.16}$$

Where $\widehat{\chi}(\omega, T)$ represents the multi-body interaction, which can be approximated by Hubbard-like interaction

$$\widehat{\chi}(\omega, T) = -\widehat{\Pi}(\omega, T)\left(1 + \frac{U}{2}\widehat{\Pi}(\omega, T)\right)^{-1} \tag{2.17}$$

$\widehat{\Pi}(\omega, T)$ is obtained by analytic continuation of

$$\Pi_{\alpha\beta}(i\omega_n) = T\sum_{\varepsilon_m}\int_{\mathrm{k}} \mathrm{Tr}\left[\widehat{\sigma}_\alpha \widehat{G}_\mathrm{k}(i\varepsilon_m + i\omega_n)\widehat{\sigma}_\beta \widehat{G}_\mathrm{k}(i\varepsilon_m)\right] \tag{2.18}$$

where $\int_{\mathbf{k}} \equiv \int [d^2k/(2\pi)^2]$, $\widehat{G}_\mathrm{k}^{-1}(i\varepsilon_m) = i\varepsilon_m - \widehat{H}(\mathbf{k}) + E_F + i\mathrm{sgn}(\varepsilon_m)\Gamma/2$, $\widehat{H}(\mathbf{k})$ is given by **Eq. 2.14**, Γ is the impurity broadening. The results show that the peak state, amplitude, and signal change with temperature of calculated Raman spectrum are almost consistent with the actual measured Raman spectrum.

With the continuous in-depth research, spin waves with robust topological properties brought to the attention of the research community, see, e.g., Roldán-Molina et al. (2016) and Chen et al. (2018). Topological chiral edge spin waves (TESWs) generally exist in perpendicularly magnetized ferromagnets with a honeycomb lattice as shown in **Figure 1A** (Wang et al., 2018c). For example, $Lu_2V_2O_7$ (Onose et al., 2010) with pyrochlore structure and Cu[1,3-bdc] (Chisnell et al.,

2015) with kagome structure are topological magnetic materials. TESWs are a result of competition among Heisenberg exchange, Dzyaloshinskii–Moriya interaction and other physical mechanisms (Roldán-Molina et al., 2016; Chen et al., 2018), which are caused by spin-orbit coupling.

This topological chiral edge mode is different from the traditional magnetostatic spin-wave mode but is similar to the topological protected edge state in electronic topological insulators. As shown in **Figure 1B**, the excited spin waves propagate in a single direction along the surface or edge of the sample and are insensitive to sample's geometry, defects, and external disturbances. This enables utilization of such materials as an appropriate information carrier in spin-wave information applications (Wang et al., 2017). Due to the unique advantages of TESWs, Wang et al. (2017) and Wang et al. (2018c) proposed the concept of "topological magnonics" using sample edges and domain walls to control the propagation of TESW. This enables designing topological spin-wave diodes, beam splitters, and interferometers (**Figure 1C**), thus opens up a new research direction namely robust, reconfigurable and scalable topological spin-wave circuits.

Magnonic Crystals

Magnonic crystals are formed by periodically adjusting material parameters, see, e.g., Ciubotaru et al., (2013), Obry et al. (2013), Banerjee et al. (2017), and Richardson et al. (2018) or external fields, see, e.g., Chumak et al. (2009) and Ustinov et al. (2019). As an artificial magnetic crystal, magnonic crystals are an important component of spin-wave devices. By using the periodic characteristics of magnonic crystals, the dispersion relationship and propagation characteristics of spin waves can be adjusted statically or dynamically. This also enables spin-wave filtering and other functions. **Figure 2A** shows a magnonic crystal with a groove array, where the width and height of the groove determine the propagating characteristics of the passing spin waves (Richardson et al., 2018).

Figure 2B shows the spin-wave propagation characteristics (left side) and dispersion relationship (right side) of magnonic crystal in **Figure 2A**. It can be clearly seen that the spin waves are forbidden to a certain extent at specific frequencies (4.18, 4.23 and 4.3 GHz) known as "band gaps," while other frequencies can freely propagate. This is because of period change in the width, thickness, internal and external field parameters of magnonic crystals. In this periodic structure, Bragg scattering has a certain impact on the spectrum of the spin waves and generate "band gaps" that exclude the transmission of spin waves (Chumak et al., 2017).

Table 4 presents the status of development in different magnonic crystals at home and abroad in detail, including classification, designing mechanisms, respective characteristics, and the corresponding realized applications. As shown in **Table 4**, magnonic crystals can be divided into three categories: static, reconfigurable, and dynamic. Among them, the geometry and inherent magnetism of the static magnonic crystals vary periodically, hence it is unchangeable once the magnonic crystal is manufactured (Choudhury et al., 2017; Sadovnikov et al., 2018). The magnetic properties of reconfigurable magnonic crystals can be changed as needed which means that the propagation characteristics of spin waves can be flexibly changed (Vogel et al., 2015; Albisetti et al., 2016). The magnetic properties of dynamic magnonic crystals can also be changed, and the adjustment speed is even faster than the spin-wave propagation speed. **Figure 2C** is a schematic diagram of dynamic magnonic crystal based on current regulation. By changing the current, the transverse magnetic field of the magnetic crystal is also changed, thus the propagation characteristics of the passing spin waves can be adjusted accordingly, see, e.g., Chumak et al. (2009) and Rana and Otani (2019).

As a typical representative of the structure design of spin-wave materials, magnonic crystals are widely used in spin-wave devices. Filtering characteristics of magnonic crystals also facilitate building spin-wave filters. In addition to the filtering function, magnonic crystals are used in spin-wave logic devices (Nikitin et al., 2015), spin-wave transistors (Chumak et al., 2014), and spin-wave thermo electron applications (Albisetti et al., 2016), etc., and play a significant role in versatile development of multifunctional spin-wave devices.

INTERFACIAL MAGNETOELECTRIC EFFECTS

Voltage-Controlled Magnetic Anisotropy

Magnetic properties of materials controlled by electric field (voltage) are seen in many material systems. For example, in ferromagnetic materials, the magnetism can be manipulated by changing the number and density of charge carriers, while in multiferroic materials, coupling between electric field and magnetization occurs through electrical polarization (Matsukura et al., 2015). Voltage-controlled magnetic anisotropy (VCMA) generally occurs in metal (ferromagnet)/metal oxide (insulator) structures and can be also referred to as electrical manipulation of interfacial perpendicular magnetic anisotropy (iPMA). The most common VCMA structure is Fe (Co)/MgO heterojunction. Applying an electric field in the interface between the metal film and insulator, due to the spin-orbit coupling interaction (Fe 3d-orbitals of strongly bond with the O 2p-orbitals) leading to charge transfer from 3d-orbitals to 2p-orbitals. Because the occupancy of 3d-orbitals electrons determines the direction and magnitude of magnetic anisotropy of ferromagnet films, the applied electric field can be used to control iPMA (Rana and Otani, 2019). The Fermi energy position at the interface is also changed due to hybridization between the orbits. This can be considered as an adjustment of Fermi energy position on magnetic anisotropy (Matsukura et al., 2015). Furthermore, in VCMA the change of iPMA is linearly proportional to the applied electric field (Duan et al., 2008), i.e., $\Delta K_S = \beta E$, where ΔK_S is the change of iPMA and β is VCMA coefficient.

VCMA provides a breakthrough for the development of spin-wave devices and spin-wave manipulations. The conventional methods of controlling spin waves by current-induced Oersted field or spin-transfer torque increase the thermal management

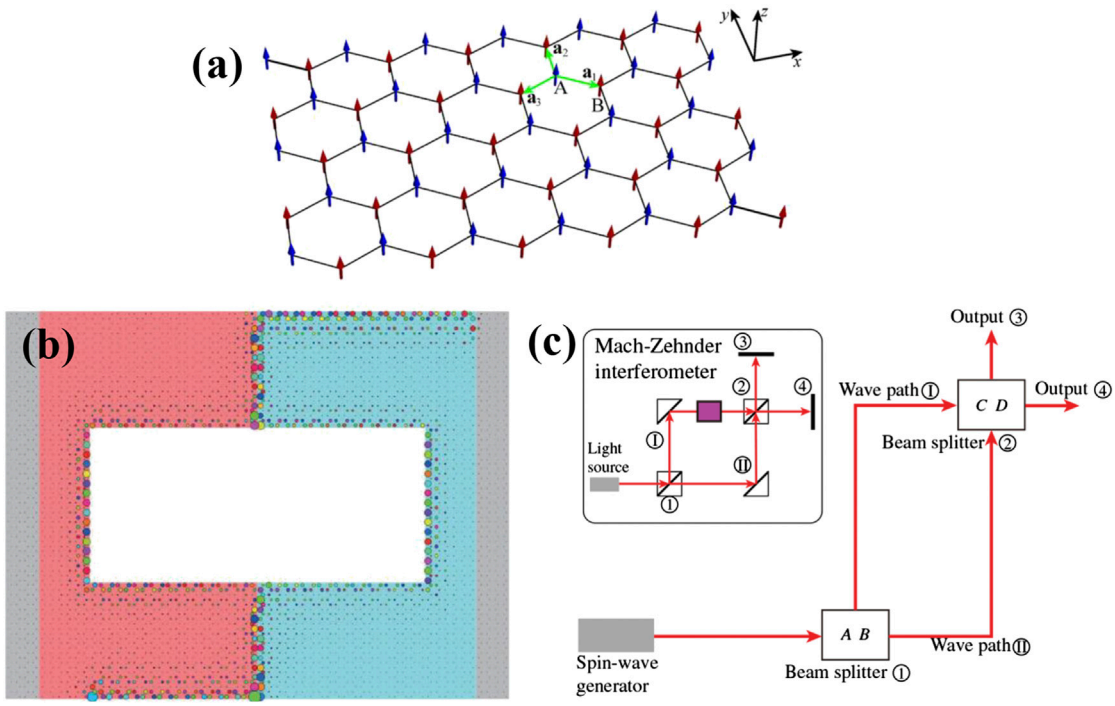

FIGURE 1 | (A) Schematic diagram of perpendicularly magnetized ferromagnet with a honeycomb lattice for propagating TESWs. The blue and red arrows indicate the magnetic moment vectors on sublattices A and B. Green arrows are three adjacent site vectors a_1, a_2 and a_3 (Wang et al., 2017). Reproduced with the permission from https://journals.aps.org/prb/abstract/10.1103/PhysRevB.95.014435. **(B)** TESWs interferometer, in which spin waves propagate or split along the domain walls, where the length of propagation path determines the phase and amplitude of spin waves (the size of different color symbols). In this setting interference occurs, where two spin waves with different phases are merged (Wang et al., 2018c). Reproduced with the permission from https://journals.aps.org/prapplied/abstract/10.1103/PhysRevApplied.9.024029. **(C)** Schematic diagram of TESWs interferometer in **(B)**, the illustration is optical Mach-Zehnder interferometer and a beam enters beam splitter ① and gets divided into two beams, and the two beams are recombined at the second beam splitter ②, and the outputs ③ and ④ depend on the interference result of the two beams at beam splitter ② (Wang et al., 2018c). Reproduced with the permission from https://journals.aps.org/prapplied/abstract/10.1103/PhysRevApplied.9.024029.

cost and further damages the life cycle of the devices. The spin-wave manipulation methods based on VCMA however only need enough electrons to charge and discharge the capacitor. This significantly reduces the power dissipation and adds non-volatile function compared to the charge-current methods (Matsukura et al., 2015). In the following we introduce the basic operations of VCMA including spin-wave excitation, conduction, phase shift and amplification.

Spin-wave excitations by VCMA can be divided into linear and nonlinear parametric excitations. Conventional parametric excitation system requires a high threshold value of the magnetic field which leads to a high energy consumption and Joule heating (Urazhdin et al., 2010). In this context, VCMA achieves nonlinear parametric excitation with a lower energy consumption in an elliptical nano magnetic tunnel junction (see **Figure 3A**; Chen et al., 2017). The magnetization direction of $Co_{20}Fe_{60}B_{20}$/MgO interface is also controlled by the voltage instead of the magnetic field pumping used in the original system. Spin waves are excited by nonlinear parameters where VCMA is combined with magnetization parameter resonance. The driving voltage is as low as 0.136 V which reduces the threshold value and energy consumption of the process. However, the nonlinear relationship and the amplitude of excited spin waves results in complexities in the application of spin-wave logic devices, and a certain value of threshold is still needed. To solve this issue, a linear parametric excitation method based on VCMA is proposed in Rana et al. (2017). As shown in **Figure 3B**, the top strip Au electrode is deposited on the waveguide made of multi-layer thin film. Further, the perpendicular magnetic anisotropy at the interface between CoFeB and MgO is regulated by applying a radio frequency (RF) voltage on the electrode. Spin waves with short wavelength are locally excited in linear form without requiring a voltage threshold as shown in Rana et al. (2017).

One of the difficulties in using spin waves to replace charge-currents as information transport carrier is to find solution to control spin waves propagation as effectively as using voltage to control the current flow. There are several techniques to design the spin-wave propagation channel among them making the spin-wave waveguide into strips has been investigated in Urazhdin et al. (2014) and Vogt et al. (2014). The issue however is that once the waveguide is completed, the function is fixed. Another technique is to control the propagation of spin waves by using Oersted field inside the waveguide (Sadovnikov et al., 2016; Heussner et al., 2017). In this technique, Oersted magnetic field is driven by direct current. As mentioned before, this inevitably brings about a high energy consumption as well as

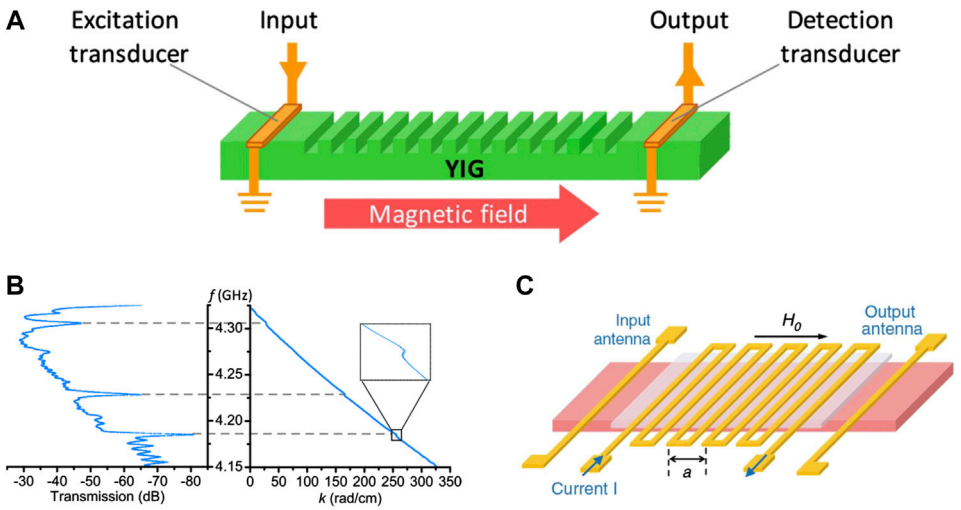

FIGURE 2 | (A) A static magnonic crystal with a groove array, where the width and height of the groove determine the propagation characteristics of the passing spin waves (Richardson et al., 2018). Reproduced with the permission from https://journals.aps.org/prl/abstract/10.1103/PhysRevLett.121.107204. **(B)** The spin-wave propagation characteristics (left side) and the dispersion relationship (right side) of magnonic crystal in **(A)**. It is clearly seen that spin waves are forbidden to a certain extent at specific frequencies (4.18, 4.23 and 4.3 GHz) known as "band gaps" while they can propagate freely in other frequencies (Richardson et al., 2018). Reproduced with the permission from https://journals.aps.org/prl/abstract/10.1103/PhysRevLett.121.107204. **(C)** A schematic diagram of dynamic magnonic crystal based on current regulation; by changing the current, the transverse magnetic field of the magnetic crystal is also changed, thus the propagation characteristics of the passing spin waves can be adjusted (Rana and Otani, 2019) (licensed under CC BY 4.0).

nonlocal Oersted field problems. VCMA also provides a new approach for designing spin-wave nano propagation channels. Using micromagnetic simulation, Rana and Otani (2018) showed that the spin-wave propagation channels designed based on VCMA are very simple. They further showed that these channels provide a unique advantage by controlling a few closely spaced spin-wave nanochannels at the same time. As shown in **Figure 4A**, by applying a positive voltage to the electrode above the waveguide, a perpendicular magnetic anisotropy is created in the direction out of the plane. This induces the magnetostatic forward volume-like spin waves that are propagated along *X* direction in the electrode covering area of the waveguide. The propagation of spin waves is terminated by setting the electrode voltage to 0 (see **Figures 4B–D**). Based on this principle, a variety of spin-wave nanochannels are designed including single channel, multi-channels, curved channel and Y-shaped channel. It is also shown in Rana and Otani (2018) that by using VCMA, the spin waves can be effectively switched in multiple channels.

Spin-wave phase shifter is one of the key components in spin-wave logic devices (Kostylev et al., 2005; Lee and Kim, 2008). The phase shift operation of spin waves is usually completed using Oersted magnetic field induced by current (Schneider et al., 2008; Hansen et al., 2009). In addition to producing a lot of Joule heat, this also affects the normal operation of other components because of the nonlocality of Oersted field. Rana and Otani (2018) realized XNOR and NAND gates by the phase shifters based on VCMA. The underlying mechanism is that VCMA affects the spin-wave dispersion, therefore, applying a positive voltage to the electrode, increases the vector of the spin waves passing through the waveguide. As shown in **Figure 4F**, different voltage values are corresponded to different wave vectors. Note that the spin-wave phase is equal to the product of wave vector and the propagation distance. Therefore, different phase accumulation occurs, where spin waves with different wave vectors pass through the waveguide under the action of VCMA.

In addition to the above basic operations, VCMA may be used for spin-wave amplifications. There is no study on directly inducing the amplitude enhancement of spin waves by VCMA, but some researches have shown that indirect amplification of spin waves can be achieved by reducing the magnetic damping of materials (Divinskiy et al., 2018). Okada et al. (2014) found that where the film thickness is determined, Gilbert damping constant and interface magnetic anisotropy energy density are linearly decreased with increasing the applied electric field while the modulation ratio is fixed. In a case where the film thickness is 1.4 nm, by increasing the voltage from 0 to 0.15 V the damping constant decreases from 0.0126 to 0.0122. Although the attenuation degree is only 3%, it is expected to effectively reduce the spin-wave damping by increasing the electric field intensity and modulation ratio. Although both the damping constant and the VCMA are explained by the second-order perturbation of the spin-orbit interaction (Bruno, 1989; Kamberský, 2007), the research on the relationship between them is still nonexistence.

Magneto-Inonic Transport

Previous studies have shown that ion migration in materials changes the thermal conductivity (Padture et al., 2002), optical properties (Lu et al., 2017), electrical conductivity (Waser et al.,

TABLE 4 | Classifications, designing mechanisms, respective characteristics and realized applications of magnonic crystals.

Classifications	Designing mechanisms	Characteristics	Applications
Static magnonic crystals	Thickness variation	Simplicity and high efficiency	Spin-wave filter; generator; memorizer; transistor
	Two-component magnonic crystal	Band gaps have a large adjustable range	
	Width variation	Small size	
	Saturation magnetization variation	Small range of variation	
	Magnetic dot array or antidot array	Many variates	
Reconfigurable magnonic crystals	Periodic local heating by laser, electronic element, or other means	Temperature gradient is the key variate	Spin-wave filter; thermo electron applications
	Remanence variation	Waveguide has domains of two magnetization orientations	
Dynamic magnonic crystals	Voltage controlled perpendicular magnetic anisotropy or dielectric constant	Low power consumption	Spin-wave filter; logic devices; spectrum transformation
	Current-induced change of transverse magnetic field in waveguide	Only one single and strong band gap appears	
	Current-induced change of effective waveguide geometry	Relatively small size	
	Surface acoustic wave above waveguide variation	Combination of Bragg scattering and Doppler frequency shift	

2009), magnetic properties (Bi et al., 2014), etc. Various functions in new devices can be achieved by using the electric field-controlled ion migration effect. The modulation of magnetic moments and anisotropy through ion migration is called magneto-ionic transport. This can influence the hybridization of 3d-orbitals in ferromagnets and 2p-orbitals in oxygen on oxides, thereby modulating the VCMA effect between interfaces (Li et al., 2017). Magneto-ionic transport can also effectively improve the magnetism controlling efficiency, reduce the processing power consumption, and increase the operation speed which are beneficial in development of spintronic devices.

Magneto-ionic transport can be divided into two categories according to the different transporting ions. The first category is anion transportation represented by oxygen ion (Bi et al., 2014; Bauer et al., 2015; Gilbert et al., 2016a; Gilbert et al., 2016b; Grutter et al., 2016; Li et al., 2017), and the second is cation transportation including lithium and hydrogen ions (Dasgupta et al., 2016; Zhu et al., 2016; Tan et al., 2019). Oxygen ion transportation usually occurs in metal/metal oxide heterostructures. The principle of material selection should not only consider the VCMA effect between interfaces, but also ensure a sufficiently low activation energy for ion transportation. **Figure 5A** shows a typical magnetic heterostructure: Co/GdOx, in which GdOx material has high oxygen ion mobility which provides guarantee for effective transportation of ions in heterostructure controlled by the electric field (Bi et al., 2014; Bauer et al., 2015). Transportation of lithium ions also requires involvement of metal oxides with a lower activation energy, such as $LiFe_5O_8$ (Zhu et al., 2016), and $Li_{0.72}CuFe_2O_4$ (Dasgupta et al., 2016). Controlling the magnetic properties of materials by lithium ion transportation usually requires participation of other metal ions. For example, the redox reaction of Fe ions (Zhu et al., 2016) or Cu ions (Dasgupta et al., 2016) occurs in the process of lithium ion delamination or intercalation. The magnetic properties of materials are changed by the chemical properties of Fe or Cu ions.

Due to the oxidation or reduction reactions that occur during ion migration, the magneto-ionic transport can also be considered as electrochemical control of magnetism. Taking Co/GdOx heterostructure in **Figures 5A,B** as an example, by applying a negative voltage bias (**Figure 5A**), an oxidation reaction occurs at the anode. Co is then transformed into non-magnetic CoO material and the magnetism is completely eliminated. By applying a positive voltage bias (**Figure 5B**), a reduction reaction is occurred at the cathode and CoO is converted into metal Co, recovering perpendicular magnetic anisotropy across the Co/GdOx interface. Nevertheless, by continuous application of a positive bias, the out-of-plane perpendicular magnetic anisotropy at the interface cannot be preserved forever and turns into in-plane magnetism. There are two explanations for this observation. Bi et al. (2014) believed that when the reaction proceeded to an appropriate level and Co was embedded in CoO to form superparamagnetic Co islands, the perpendicular magnetic anisotropy could be formed at the interface, otherwise, when CoO layer is completely reduced to continuous Co layer in the metal state, only in-plane magnetic

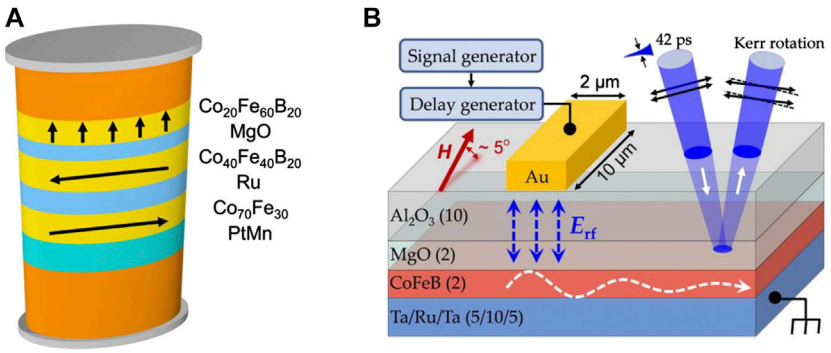

FIGURE 3 | Spin-wave excitation devices based on VCMA. **(A)** Schematic diagram of nonlinear parameter excitation device. Due to iPMA, $Co_{20}Fe_{60}B_{20}$ magnetization equilibrium direction is perpendicular to the plane. In cases where the microwave voltage frequency applied by the top electrode is twice of the spin-wave frequency, short wavelength spin waves are excited (Chen et al., 2017). Reprinted with the permission from Chen, Y.-J., Lee, H.K., Verba, R., Katine, J.A., Barsukov, I., Tiberkevich, V., et al. (2017). Parametric resonance of magnetization excited by electric field. Nano letters 17 (1), 572-577. Copyright 2017 American Chemical Society. **(B)** Schematic diagram of linear parameter excitation device: applying an RF voltage on Au electrode to locally excite spin waves (Rana et al., 2017) (licensed under CC BY 4.0).

anisotropy is presented. Tan et al. (2019) believed that this phenomenon was caused by the accumulation of hydrogen atoms at the interface. They further experimentally observed bubbles formed by hydrogen accumulation (**Figure 5C**). When the circuit is disconnected, the redox reaction is interrupted due to the inability of electrons to move. Therefore, hydrogen atoms remain at the interface and cannot be removed, thus in-plane magnetism remains in the Co layer. By closing the circuit, the hydrogen atoms are then expelled from the device in the redox reaction, therefore the in-plane magnetism is disappeared and replaced by the perpendicular magnetic anisotropy.

With the assistance of magneto-ionic transport, the process of controlling magnetism by electric field becomes quicker and more convenient, enabling further development of voltage-controlled spintronic devices. Electronically controlled ion migration however still needs further improvements in the following aspects. Firstly, the switching speed at room temperature needs to be increased. The switching time of modern hard disk drives is as small as 10 ms while it usually takes several minutes for oxygen ions to migrate at high temperature (>100°C) and produce a large enough magnetic transition (Bi et al., 2014; Bauer et al., 2015). Although the existing $Co/SrCoO_{2.5}$ heterostructures are capable of achieving a switching time of 0.2 ms at room temperature, its coercive force is only a few Oersted which limits its practical applications (Li et al., 2017). Secondly, reliability and non-volatility of these devices need to be enhanced. Although hydrogen ion migration has achieved more than 2,000 cycles at a relatively high speed (Tan et al., 2019), the device retention time can only last for a few days, which is not conducive to permanent data storage. PdH, a hydrogen storage material used in hydrogen ion transportation, has a high hydrogen mobility, but it is easy to eject hydrogen under vacuum or high temperature conditions (Gilbert et al., 2017). Therefore, finding a hydrogen storage material with higher quality is one of the next important challenges to be addressed.

Electrical Spin-Torque and Magnon-Torque

Electrical spin-torque can be divided into spin-transfer, and spin-orbit torque depending on its generation mechanisms. It is usually used to flip the magnetic moments of magnetic domains and is considered as the process of transferring spin angular momentum. Magnon-torque which is derived from magnon currents (spin waves), and electric spin-torque have similar functions but they are different in other aspects. These two kinds of torques existing in different heterostructures are widely used in switching magnetization of material and other fields. In the following we introduce them separately.

Existence of the spin-transfer torque (STT) effect was predicted by Berger (1996), and Slonczewski (1996), in 1996. Many experimental studies also confirmed its existence in the multilayer structures (such as Co/Cu/Co) composed of ferromagnetic and non-ferromagnetic films alternately (Tsoi et al., 1998; Myers et al., 1999; Katine et al., 2000). STT is usually observed with giant magnetoresistance effect as probe (Katine et al., 2000). By passing current through a magnetic tunnel junction vertically, the spin angular momentums carried by conducted electrons are transferred to the localized electrons in the free layer. This changes the relative magnetization direction between free layer and fixed layer as well as the resistance of magnetic tunnel junction (Myers et al., 1999). There are usually two mechanisms for the STT to change the magnetic properties of the thin films both based on polarized electrons to reverse the magnetization direction of the free layer. The electrons in the first mechanism are polarized under the positive influence of the reference layer. The polarization direction is parallel to the reference layer, therefore, passing the polarized electrons through a thin free layer forces the magnetization direction of the free layer to become parallel with the direction of the reference layer. In the second mechanism the polarized electrons are formed due to the negative influence of the reference layer. The polarization direction is the opposite to that of the reference layer, therefore, flowing the electrons through the

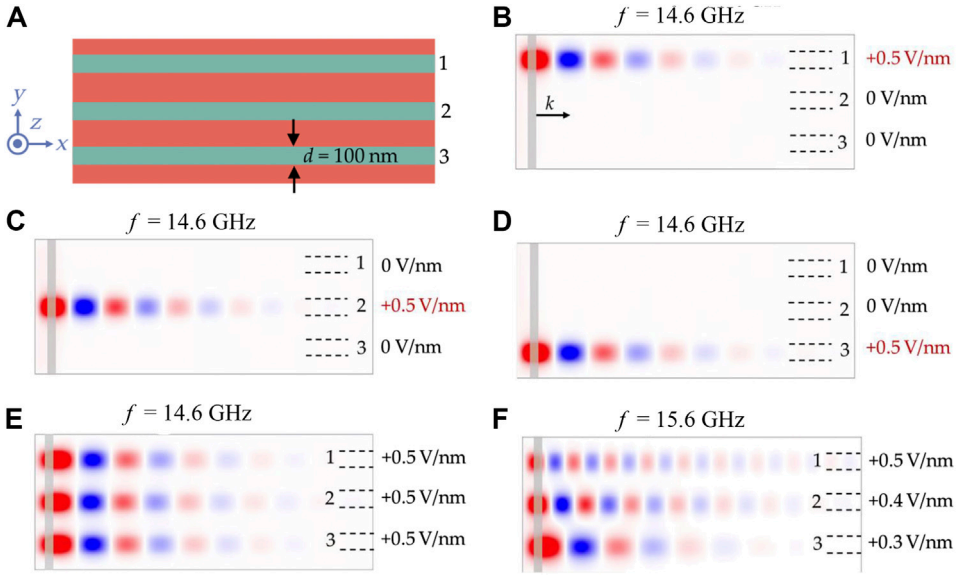

FIGURE 4 | (A) Top view of the waveguide (Rana and Otani, 2018). Due to VCMA, three spin-wave channels with a width of 100 nm are formed by three separate metal electrodes. **(B–F)** Spatial distribution diagram of dynamic magnetization. **(B)** A voltage is applied to the upper electrode to form a spin wave-channel; **(C)** A voltage is applied to the middle electrode to form a spin-wave channel; **(D)** A voltage is applied to the lower electrode to form a spin-wave channel; **(E)** Three spin-wave channels can be opened simultaneously; **(F)** Different phase accumulation occurs, where spin waves with different wave vectors pass through the waveguide. **(A–F)** Reproduced with the permission from https://journals.aps.org/prapplied/abstract/10.1103/PhysRevApplied.9.014033.

free layer forces the magnetization direction of the free layer becomes antiparallel to that of the reference layer.

Spin-orbit torque (SOT) usually exists in a two-layer structure composed of ferromagnet and nonmagnetic heavy metal (platinum, tantalum, tungsten, etc.) films (Fukami et al., 2016). In SOT, similar to the STT, the spin-torque of the polarized current is used to flip the magnetic moments of the magnetic domains (Katine et al., 2000). Once direct current flows through the plane of nonmagnetic heavy metal film at a certain angle, spin current is induced in a direction perpendicular to the thin films thus spin-torque is exerted on the magnetic moment of ferromagnet and changes its magnetization direction. In SOT, the spin-torque may be caused by Rashba effect (Emori et al., 2016), or Spin Hall effect (Fukami et al., 2016), or both (Fan et al., 2014), but it can be eventually interpreted as a strong spin-orbit coupling between heavy metal materials, therefore, the spin-torque is called the spin-orbit torque.

Magnetoresistive random access memory (MRAM) can be directly constructed under electric control based on STT and SOT, instead of using magnetic field generated by current to reverse magnetization in traditional magnetoresistive effect. This provides a significant practical value (Fong et al., 2016; Nozaki et al., 2019). STT-MRAM can achieve the level of integration density similar to the DRAM (Dynamic RAM), while obtain an excellent performance level similar to the SRAM (Static RAM). Although STT-MRAM is compatible with the CMOS manufacturing process, there exist some performance issues related to the energy efficiency of writing (Fong et al., 2016). As an improved version of STT-MRAM, SOT-MRAM provides more advantages. Since spin-orbital torque in SOT-MRAM is originated from heavy metals, the writing path does not pass through the magnetic tunnel junction and is separated from the reading path. Therefore, barrier breakdown can be almost avoided. The spin-orbit torque also achieves a higher writing speed due to the perpendicular magnetic anisotropic magnetic tunnel junction (Nozaki et al., 2019). Currently, almost all types of memories are faced with the dilemma of stable non-volatility and high working energy. It is believed that STT/SOT-MRAM will be able to make an important impact on the development of new memories with a low working and standby energy consumption.

In addition to their applications in memory, STT and SOT play an important role in spin-wave manipulation and the development of spin-wave devices (Madami et al., 2011; Divinskiy et al., 2018; Houshang et al., 2018; Fulara et al., 2019). Madami et al. (2011) used STT effect to excite spin waves in a multilayer heterostructure as shown in **Figure 6A** (CoFe layer as reference/fixed layer and NiFe layer as free layer). They managed to show the existence of propagating spin waves as opposed to localized spin waves. It is also found that a negative excitation current results in detecting a higher intensity of spin-wave intensity much larger than that of thermal spin-wave intensity. Interestingly, by applying a positive current the spin-wave signal cannot not be detected. It is concluded that the spin-wave frequency is linearly proportional to the injected direct current. Divinskiy et al. (2018) found that SOT is capable of achieving the excitation of coherent propagating spin waves. They also show that SOT is also capable of spin waves amplification by compensating Gilbert damping in the spin-wave propagation. The experimental diagram is shown in **Figure 6B**. By combining theory with experiment, it was also proved that the anti-damping torque brought by spin current can, to a certain extent,

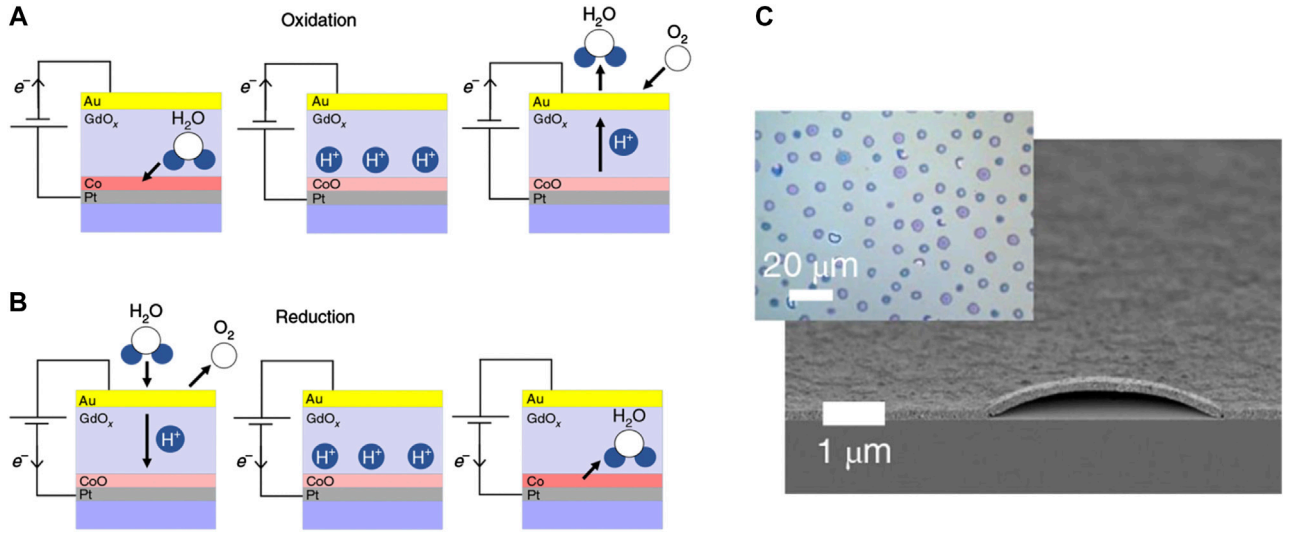

FIGURE 5 | (A,B) Schematic diagram of Co/GdOx heterostructure and ongoing electrochemical reactions (Tan et al., 2019). **(A)** Applying a negative bias voltage causes an oxidation reaction at the anode: Co will be transformed into non-magnetic CoO material, and the magnetism will be eliminated; **(B)** Applying a positive bias voltage causes a reduction reaction at the cathode: CoO is converted into metal Co, recovering perpendicular magnetic anisotropy across the Co/GdOx interface; **(C)** Cross-sectional scanning electron microscope image of hydrogen accumulation after the positive bias voltage is continuously applied. **(A–C)** Reprinted with permission from Tan, A.J., Huang, M., Avci, C.O., Büttner, F., Mann, M., Hu, W., et al. (2019). Magneto-ionic control of magnetism using a solid-state proton pump. Nature materials 18 (1), 35–41. Copyright 2019 Springer.

compensate the propagation damping of spin waves. According to damping compensation formula: $a = a_0\left(I - \frac{I}{I_0}\right)$ (Slavin and Tiberkevich, 2009), setting $I = I_0$, in theory the Gilbert damping, ⍰, can be completely compensated or eliminated. With the continuous progress in STT and SOT, nanoscale electrically controlled spin-wave devices and computing systems are expected to embrace further development.

Magnon-torque is different from electric spin-torque in that the former comes from spin waves and the latter from spin currents. In contrast to the spin currents, no electron flow is required in spin-wave propagation. Therefore, the effects of joule heat are avoided as well as the corresponding power consumption. Furthermore, as it is seen in **Table 1** the mean free path of spin-wave propagation is usually a few microns that even exceeds the propagation distance of 1,000 microns in high-quality bulk YIG. Nevertheless, the dissipation distance of spin currents is only on the nanometer scale (Bass and Pratt Jr, 2007). Because of the above advantages, it is of great scientific value to use magnon-torque to reverse the magnetization direction of materials. Wang et al. (2019) reported promising experimental results for magnetization switching based on magnon-torque.

Figure 7A shows the schematic diagram of a spin-torque ferromagnetic resonance (ST-FMR) measurement system. It is seen that the magnon current (spin waves), J_M, induced by RF current, J_C, is propagated perpendicular to the film plane, passes through NiO layer, and reversing the magnetization direction of NiFe layer. NiO is the only carrier of magnon current because it can isolate the spin polarized current. **Figure 7B** shows the variation of spin-torque ratio, θ_i, for three NiO layers with different thicknesses versus temperature, T, in which $\theta_i = J_i/J_C$ represents the generation ratio of input current to magnon current. At thickness of t_{NiO} = 25 nm, the spin-torque ratio is generally high, with the maximum value exceeding 0.4, and 0.3 at the room temperature, which is close to the electric spin-torque ratio (about 0.67). Experiments further confirmed that this magnon-torque is mainly affected by the magnon current rather than other factors (temperature, Oersted magnetic field, etc.). Experiments also corroborate successful realization of magnetization switching of permalloy (Py) in Bi_2Se_3/NiO/Py and Bi_2Se_3/NiO/Cu/Py heterostructures.

Application of magnon-torque in magnetization switching caused a paradigm change in the related fields of studies especially in magnon transport, and further broadened the scope of research on spintronics. In the current state-of-the-art, however, the generation of magnon-torque still needs external current injection and the efficiency of magnetization switching is lower than that of mature electric spin-torque (STT and SOT). With the continuous innovation of research on excitation and transportation of magnons (spin waves), we expect to see the application of magnon-torque in magnetic applications such as MRAM.

FUNCTIONAL SPIN-WAVE DEVICES

Information Processing Devices

Spin-wave devices take spin-wave as the carrier of information transmission and processing. Compared with the traditional CMOS devices which take charge-current as the carrier, low power consumption is one of the biggest advantages of spin-wave devices. However, many operations (such as excitation,

phase shifting and amplification) of spin waves require external energy or other forms of assistance. To meet the requirements in ultra-low power consumption of spin-wave devices, it is not sufficient to only focus on the energy dissipation in the process of spin-wave propagation. It is further essential to reduce the power dissipation during the manipulation of spin waves. This is one of the main motivations behind continuous development of the spin-wave information processing devices. With the involvement of electrical current or voltage (Sekiguchi et al., 2012), and various novel interface effects (Rana and Otani, 2018; Wang et al., 2018b), researchers have designed a variety of spin-wave electronic devices, such as spin-wave phase shifter, signal splitter, and logic gate. Phase shifter is one of the most critical components in the spin-wave logic circuits. By adjusting the phases of two or more beams of spin waves from the same source, interference occurs upon their convergence resulting in the signal of spin-wave to be weakened, or strengthened corresponding logical value of 0 or 1, respectively.

Charge-current based electrical method is one of the main techniques used in the earlier spin-wave electronic devices (Lee and Kim, 2008). In 2008, Schneider et al. (2008) used Oersted field generated by current to regulate and design a phase shifter, as shown in **Figure 8A**. Oersted field affects the transmission dispersion of spin-wave and causes phase shift in spin-wave. By cutting of the current, Oersted field disappears and the spin-wave original propagation characteristics are recovered. However, in this method, using electric current causes a high-power consumption and the corresponding Joule heat may become unacceptable. Furthermore, the application area of Oersted field is difficult to be accurately controlled. This may affect other components in the system. In order to reduce the influence of Joule heating, in 2015, Zhong et al. (Wang et al., 2014; Chen et al., 2015; Chen et al., 2016) proposed using the polarized spin current generated by the STT effect to directly act on the waveguide. This changed the magnetization state of the original spin-wave, resulting in phase shifting as shown in **Figure 8B**. The experimental results show that a 180° phase shifting effect can be achieved using three phase shifters.

The signal splitter is of great significance for selective switching of spin-wave signals where there are multiple spin-wave channels. In 2017, Heussner et al. (2017) designed a spin-wave signal splitter based on charge-current. As shown in **Figure 8A**, a direct current is applied along the *y*-axis in the brown region to generate an Oersted field, while an external *y*-axis bias magnetic field is applied across the whole device. The spin wave is excited from the left end and then propagates to the right end. Compared with the original case, in which the spin waves can only propagate at a specific angle (**Figure 8B**), it is found that the spin-wave transmission trajectory can be adjusted under the action of Oersted field after applying a 100 mA current (**Figure 8C**). This is because Oersted field generated by current causes deviation in the direction of total magnetic field from the original external magnetic field in a certain angle, thus changing the dispersion of spin-wave and further changing the trajectory of transmission. Based on this principle, a signal splitter for connecting different waveguides is designed, as shown in **Figures 8D–F**. Since it can realize switching and on-off control between different waveguides, it is very beneficial to the circuit design of multistage cascade. Furthermore, the spin-wave multiplexer was realized by charge-current (Vogt et al., 2014) and the spin-wave directional coupler was realized by spin-wave dipole exchange effect (Yu et al., 2013; Wang et al., 2018a).

There still exist many issues in charge-current based spin-wave electronic devices. Oersted field and other related effects induced by current input are difficult to be control accurately in the whole system. Furthermore, a large amount of Joule heat generated during operation have negative effects on micro/nano-scale spin-wave electronic devices. To address this issues research attention was directed to voltage-controlled spin-wave electronic devices. In 2011, Liu and Vignale (2011), the electric field is used to directly manipulate the spin-wave dispersion and realized the effective control of the spin-wave phase under the spin-orbit coupling. As it is seen in **Figure 9A**, the electric field radiates from the center to the annular waveguide. A series of micro coupling effects occur during the spin-wave passing through the waveguide which result in a phase shift of 180°. This can be used for the designing spin-wave interferometer which then lays a foundation for the development of ultra-low power consumption spin-wave logic devices. This is because the phase-shifting process of spin-wave does not require current input. Different from the spin-orbit coupling effect, other researchers proposed a designing method for the spin-wave phase shifter accomplished by electric field through electromagnetic coupling and Dzyaloshinskii-Moriya interaction (DMI) (Wang et al., 2018b). **Figure 9B** is a schematic diagram of this phase shifter. Under the action of the left electric field application area, the dispersion of spin-wave appearing asymmetric structure during propagation to the right. Therefore, different phase offsets appear under different electric field intensities. In *Voltage-Controlled Magnetic Anisotropy*, we also discuss spin-wave phase shifting operation based on VCMA.

In addition to the electrical methods, using domain walls to control the phase and amplitude of spin waves is another important modulation method (Han et al., 2019). **Figure 10A** is the experimental setup, **Figures 10B,C** are the magneto-optical Kerr effect (MOKE) images of the devices, in which the bright and dark colors represent the domains with up and down magnetization. An obvious domain wall can be observed in the device of **Figure 10C**, while the device in **Figure 10B** is uniform. **Figure 10D** is the simulated propagation of spin waves, the upper and lower waveguides for spin-wave propagation corresponding to (b) uniform state and (c) domain wall state, respectively. The single dotted line indicates an inserted domain wall and the dotted rectangular indicates a phase shifting of nearly 180° after spin-wave passing through the domain wall. Han et al. proved that the phase shift induced by magnetic domain wall will not be influenced by magnetic domain configuration (i.e., up-down or down-up), and the deviation of five experimental phase shifting results is less than 10%. In addition, the amplitude of spin-wave is decreased by a factor of 4.3 times after passing through the domain wall. It is due to the reflection of spin-wave at the domain wall edge caused by the quasi-rigid boundary condition of the magnetic moments.

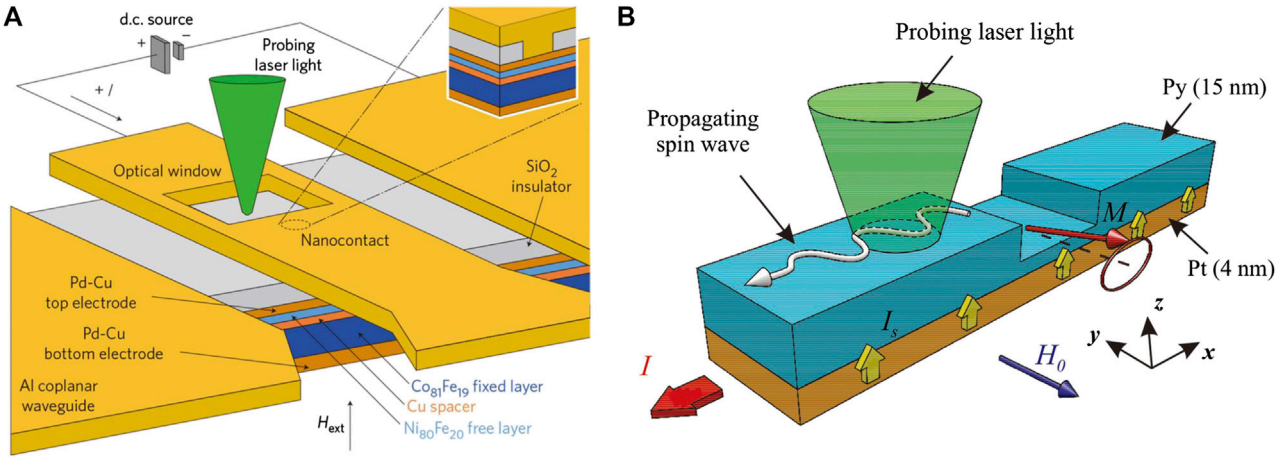

FIGURE 6 | (A) Cross-section of spin-wave excitation device based on STT. An aluminum coplanar waveguide is deposited on the STT multilayer structure, and an optical window is etched on the waveguide conductor center near the nanocontact point. Polarized current is injected into the STT structure through the nanocontact point to realize spin-wave excitation (Madami et al., 2011). Reprinted with permission from Madami, M., Bonetti, S., Consolo, G., Tacchi, S., Carlotti, G., Gubbiotti, G., et al. (2011). Direct observation of a propagating spin wave induced by spin-transfer torque. Nature nanotechnology 6 (10), 635. Copyright 2011 Springer. **(B)** Schematic diagram of spin-wave excitation and amplification device based on SOT. A current in the direction of -x is applied to the permalloy (Py) layer, and a spin polarized current in the direction of z is generated. The Py layer is the spin-wave waveguide with a rectangular notch with a width of 200 nm and a depth of 10 nm in the center. By complete compensation of the damping at the waveguide notch, the spin wave is generated at the notch and propagated along the -x direction. The spin wave is then amplified during propagation (Divinskiy et al., 2018). Reproduced with the permission from https://doi.org/10.1002/adma.201802837.

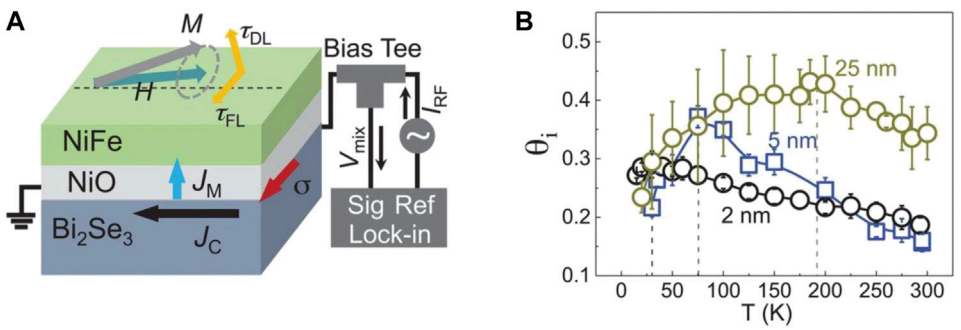

FIGURE 7 | (A) Schematic diagram of spin-torque ferromagnetic resonance (ST-FMR) measurement system (Wang et al., 2019). J_C is the RF current, σ is spin polarization direction, and J_M is magnon current. **(B)** Variation of spin-torque ratio θ_i of three NiO layers with different thicknesses versus temperature T, where $\theta_i = J_i/J_C$ represents the generation ratio of input current to magnon current. **(A–B)** Reprinted with permission from Wang, Y., Zhu, D., Yang, Y., Lee, K., Mishra, R., Go, G., et al. (2019). Magnetization switching by magnon-mediated spin torque through an antiferromagnetic insulator. Science 366 (6469), 1125–1128. Copyright 2019 American Association for the Advancement of Science.

The author further studied the interaction between spin waves and magnetic domain wall, and finds that the position of magnetic domain wall is changed after spin-wave passing through it, and the magnetic domain wall always moves against the flow direction of spin-wave. This is attributed to the effect of spin-torque in magnon current. The mutual control between the spin waves and the domain wall means that all the operations in the spin-wave devices can be completed by only one spin-wave. This provided the possibility of the realization of all-magnon spin-wave devices.

As it is seen in the above, phase shifting operation based on charge-current is associated with high level of power consumption and the generated Oersted field reduces the operational accuracy of spin-wave devices. New spin-wave information processing devices are being developed with low power consumption, compatibility with micro/nano-scale devices and non-volatility. The ultimate goal is to realize all-voltage-controlled or all-magnon spin-wave logic devices in which voltage-controlled spin-wave device only needs enough electrons to charge and discharge a capacitor, and all-magnon spin-wave device can be achieved without any intervention of external field.

Spin-Wave Sensors

Sensors are often used to transform measured information into information that can be directly read, e.g., electrical signals. In recent years, with the continuous development of magnetism researches, the concept of spin-wave sensors is formed. In spin-

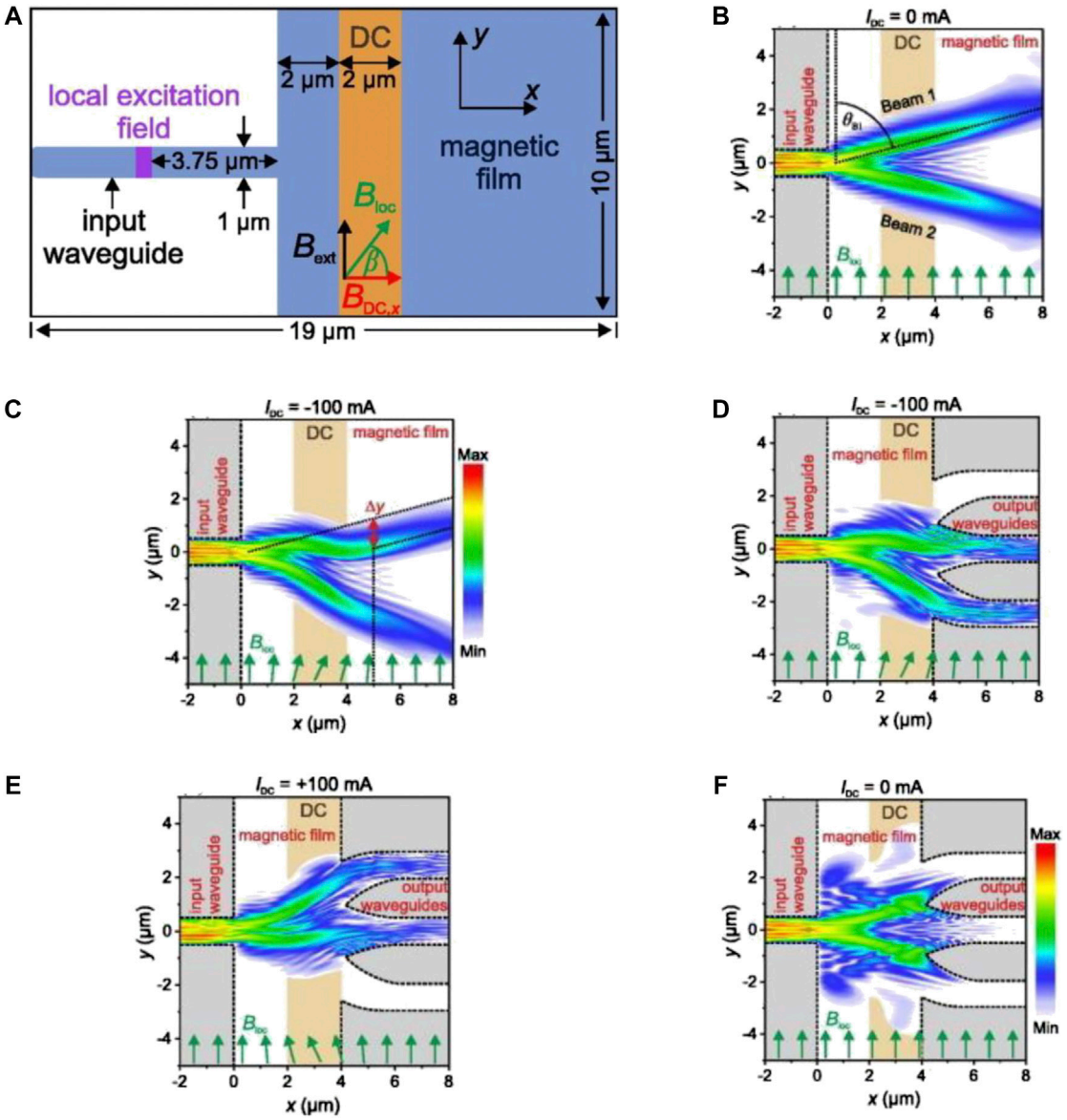

FIGURE 8 | Spin-wave signal divider based on charge current. **(A)** Schematic diagram of simulation structure (Heussner et al., 2017). **(B–F)** Dynamic magnetization results. **(B)** Without applied current; **(C)** Applying a negative direct current of −100 mA; **(D)** Switching between waveguides after applying a negative direct current of −100 mA; **(E)** Switching between waveguides after applying a positive direct current of 100 mA; **(F)** Switching between waveguides without applied current. **(A–F)** Reprinted from Heussner, F., Serga, A., Brächer, T., Hillebrands, B., and Pirro, P. (2017). A switchable spin-wave signal splitter for magnonic networks. Applied Physics Letters 111 (12), 122401. With the permission of AIP Publishing.

wave sensors the output is not in form of electrical signal but spin-wave signals. In addition to energy conservation efficiency and avoiding the influence of Joule heating there are other reasons to pursue such sensors. In the following, we introduce several spin-wave sensors with different sensing functions including gas sensors (Matatagui et al., 2015b; Matatagui et al., 2017), magnetic sensors (Inoue et al., 2011; Goto et al., 2015), and humidity sensors (Matatagui et al., 2015a) and further discuss their basic operational principles and characteristics.

Aiming at gas identification and detection, researchers from The National Autonomous University of Mexico (Matatagui et al., 2015b; Matatagui et al., 2017), successively developed a toxic gas sensor in 2015 and improved its performance in 2017. This initiated a new field of research on "magnonic e-noses." In this sensor, magnetic nanoparticles react with gas to induce a frequency shift to the spin-wave oscillator. This ensures high sensitivity, short response time, good reproducibility and recyclability. **Figures 11A,B** illustrate the basic structure, and working principle of the gas sensor, respectively. Once the magnetic nanoparticles layer reacts with the gas in the environment, the total magnetic field of the sensor system will be affected. This changes the oscillation frequency of the

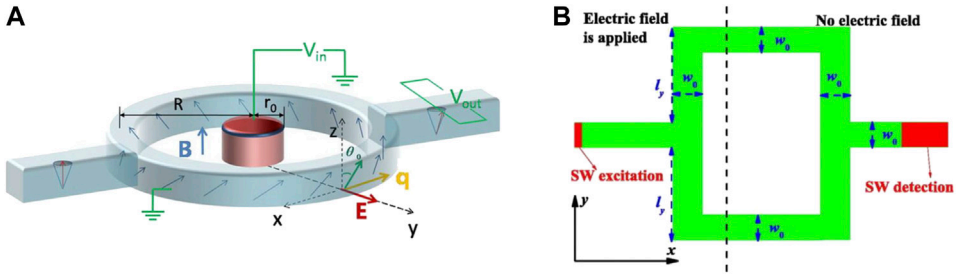

FIGURE 9 | (A) Schematic diagram of voltage-controlled spin-wave phase shifter based on spin-orbit coupling interaction (Liu and Vignale, 2011). Reproduced with the permission from https://journals.aps.org/prl/abstract/10.1103/PhysRevLett.106.247203. **(B)** Schematic diagram of voltage-controlled spin-wave phase shifter based on DMI (Wang et al., 2018b). Reprinted from Wang, X.-g., Chotorlishvili, L., Guo, G.-h., and Berakdar, J. (2018). Electric field-controlled spin waveguide phase shifter in YIG. Journal of Applied Physics 124 (7), 073903. With the permission of AIP Publishing.

magnetostatic surface spin-wave oscillator. Since the frequency shifts caused by different gases are different, the sensor can identify all kinds of gases (Matatagui et al., 2015b). On this basis, Matatagui et al. (2017) added the types of nanoparticles and formed a gas sensor array composed of $CuFe_2O_4$, $ZnFe_2O_4$, $MnFe_2O_4$ and $CoFe_2O_4$ particles. Due to the different sensitivity of various nanoparticles to a given type of gas by combining four sensing results through certain calculations classification accuracy of 100% was achieved. This gas sensor is not only excellent in performance, but also simple and inexpensive. However, it needs further researches in practical applications such as identifying or detecting the components of a mixed gas and distinguishing between different gases with different levels of concentrations.

Magnetic field sensor is another achievement in the field of spin-wave applications. High-precision magnetic field measurement is usually completed by a superconducting quantum interference device (Drung et al., 2007), and a giant magnetoimpedance element (Yoshinaga et al., 2000). The former requires ultra-low temperature and the quality of soft magnetic material required by the latter needs to be further improved. An ultra-high precision magnetic field sensor at room temperature is yet to be realized. Inoue et al. (2011) provided a potential solution to this problem by using one-dimensional static magnonic crystal. As described in *Magnonic Crystals*, the spin-wave band gaps are used to prevent the propagation of the spin-wave of particular frequencies in the magnonic crystal. These gaps are realized by periodic adjustments in the media on the surface of the magnonic crystal. It should be noted that the frequencies of the band gaps are very sensitive to the magnetic field applied to the crystal. As shown in **Figure 11C**, the black arrows represent the great change of band gap frequency with the increase of applied magnetic field. The change of band gap frequency then influences the propagation characteristics of spin-wave. Based on this principle, researchers demonstrated a high-performance magnetic field sensor.

To solve the thermal stability problem of this sensor at a high temperature, Goto et al. (2015) suppressed the temperature sensitivity of the sensor by using a spin-wave differential channel composed of two YIG films. The results showed that the thermal stability of the spin-wave phases was improved by three orders of magnitude, and the magnetic field measurement accuracy was further improved. The authors showed that their proposed magnetic field sensor provides four significant advantages: 1) It can work at room temperature; 2) The field sensitivity is one order of magnitude higher than that of giant magneto-impedance element; 3) It can measure a wide range of magnetic fields; and, 4) It has a simple structure and small size. In the future, the sensor can also be developed into three-dimensional magnetic field measurement (by improving the dimension of magnon crystal). With the continuous improvement of measurement accuracy, such sensors are expected to play an important role in brain-computer interface (detecting the local three-dimensional magnetic field from the brain) and other applications.

Humidity measurement is another important sensing function which has widespread applications in various industries, e.g., food storage, high-tech instruments, pharmacy, and biomedicine. Similar to the gas sensors, the measurement of vapor compounds can be realized using magnetostatic a spin-wave oscillator as a key component (Matatagui et al., 2015a). **Figure 11D** shows a three-dimensional schematic diagram of ultra-high frequency humidity sensor. The sensor is mainly composed of a spin-wave oscillator and a coplanar waveguide probe in which the waveguide humidity probe is coupled with adjustable magnetostatic surface spin-wave oscillator and placed in the test chamber. The water absorbing material polyvinylpyrrolidone (PVP) polymer is coated on the right coplanar waveguide. For different humidity levels, the relative expansion of PVP caused by the absorption of water molecules leads to thickness change in the PVP layer. This then affects the dielectric constant of the coplanar waveguide gap and adjusts the oscillation frequency. The experiment tested the relative humidity in an environment with a range of 12.5%–95%. It was found that except for 95% relative humidity, all the other experimental groups reached more than 90% of the maximum frequency shift within one minute and could quickly recover to the initial state after being exposed to dry air. Researchers use this sensor to monitor human respiration in real time. Although humidity is rapidly changed due to respiration, the sensor is capable of quick response and recovery. This enables the sensor to diagnose respiratory diseases quickly. By coupling the spin-wave

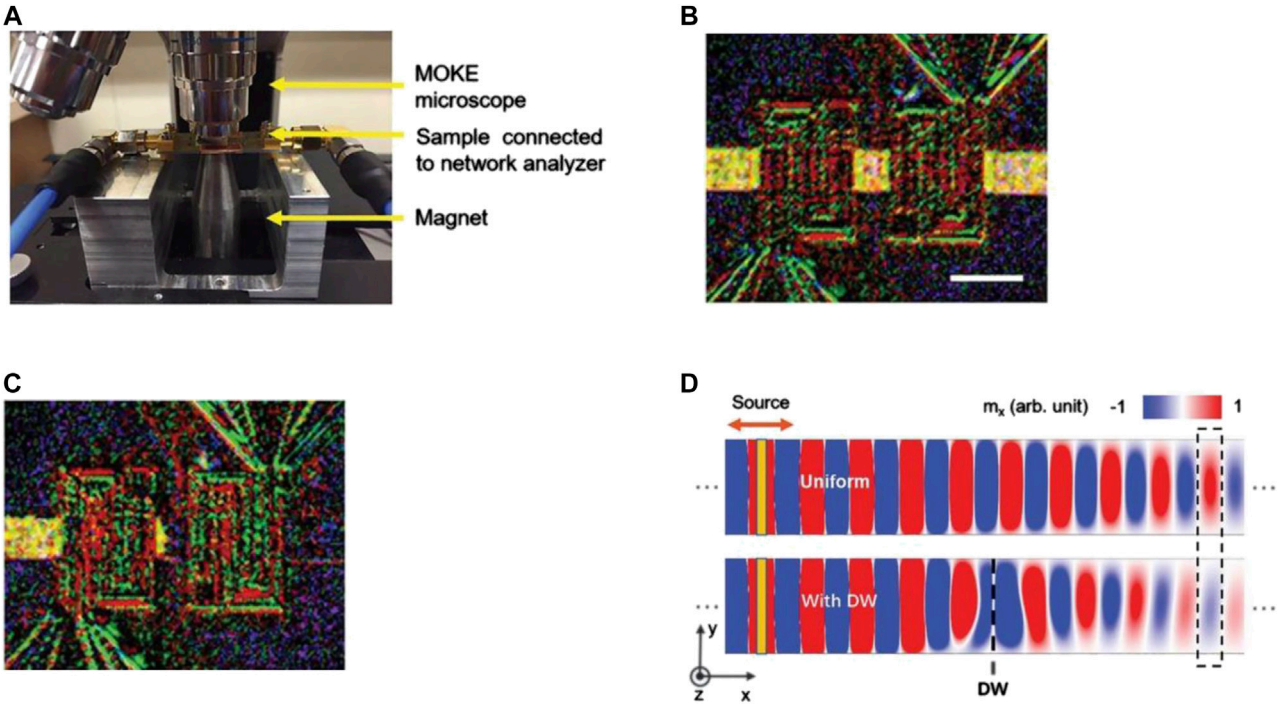

FIGURE 10 | (A) Experimental setup for controlling the phase and amplitude of spin waves by a domain wall (Han et al., 2019). **(B), (C)** Magneto-optic Kerr effect (MOKE) images. The light and dark colors represent domains with opposite magnetization directions. In **(B)** the waveguide is uniform, and in **(C)** there is a domain wall in the middle of the waveguide. **(D)** Simulation diagram of spin-wave propagation. The upper and lower waveguides correspond to **(B)** uniform state and **(C)** domain wall state, respectively. The single dotted line indicates an inserted domain wall and the dotted rectangular indicates a phase shifting of nearly 180° after spin-wave passes through the domain wall. **(A–D)** Reprinted with permission from Han, J., Zhang, P., Hou, J.T., Siddiqui, S.A., and Liu, L. (2019). Mutual control of coherent spin waves and magnetic domain walls in a magnonic device. Science 366 (6469), 1121–1125. Copyright 2019 American Association for the Advancement of Science.

oscillator with a coplanar waveguide, a new type of humidity detector operating at a frequency up to 8 GHZ is realized with significant advantages in high sensitivity and repeatability.

To sum up, the principle of spin-wave sensors is to use the spin-wave oscillator or magnonic crystal to convert the information to spin-wave signals (such as spin-wave frequency) for characterization and test. Whether gas sensor (Matatagui et al., 2015b; Matatagui et al., 2017) and humidity sensor based on spin-wave oscillators (Matatagui et al., 2015a), or a magnetic field sensor based on magnonic crystal (Inoue et al., 2011; Goto et al., 2015), they all using magnetostatic surface spin wave as the output signal carrier. This is because the spin-wave can achieve a high frequency and also has a high load Q value, low transmission loss, small wavelength, and high tunability (Matatagui et al., 2015b). These spin-wave characteristics and the innovative principle of magnetism provide a set of unique advantages to spin-wave sensors compared with the traditional sensors, e.g., higher sensitivity, lower cost, and improved thermal stability.

Current Status and Challenges of Spin-Wave Devices

After discussing the classification and functions of spin-wave devices, we will introduce the characteristics and challenges of spin-wave devices, especially their performance compared with other typical devices, including two mature silicon-based COMS (high-performance and low-power), graphene PN junction, spin-transfer torque/domain wall (STT/DW) devices, and spin-wave devices. COMS and graphene PN junction belong to electronic devices, while STT/DW devices and spin-wave devices are classified as spintronics applications. All data are from reference Nikonov and Young (2013).

Toward the device size, adder (adder-32b in this case) is fabricated using COMS or graphene PN junction, with the area of 63 or 46.7 μm^2 respectively, while the area of the adder achieved by spin wave is only 2.1 μm^2. In fact, the size of a single spin-wave logic gate is about twice that of a MOSFET, but the spintronic majority gate has more functions, making the spin-wave logic circuit require fewer components. Spin-wave devices only have a disadvantage in switching delay, essentially because the magnonic speed is about two orders of magnitude smaller than that of the electron.

As emphasized before, spin-wave devices take spin-wave as the information carrier, which consumes very little energy, and most of the energy is used in aspects such as spin-wave excitation or detection. The switching energy consumption per logical unit of the spin-wave device is only 0.26 fJ, and the power density is 1.1 W/cm^2. Although the power density of

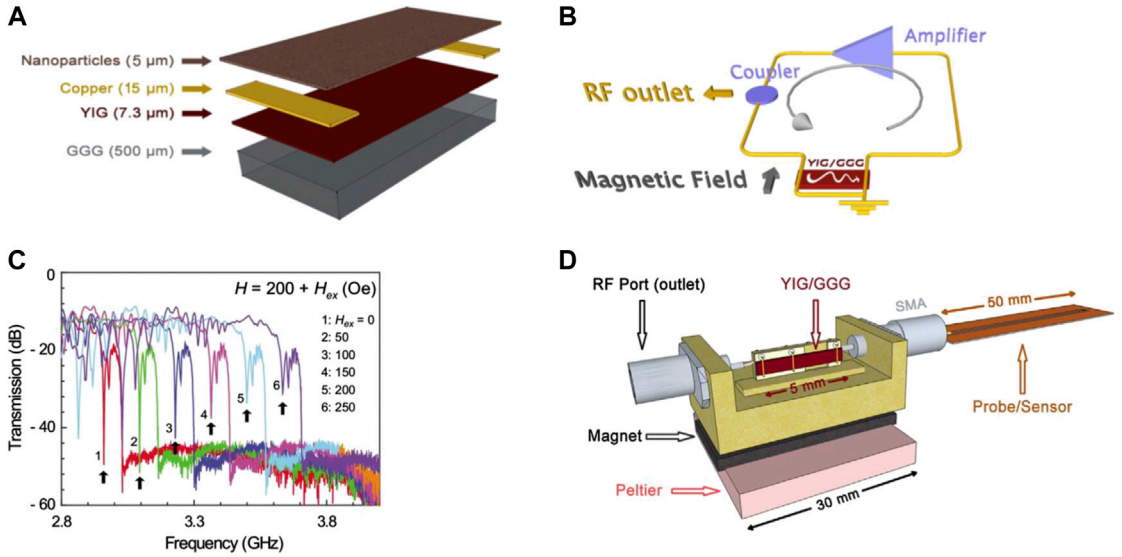

FIGURE 11 | (A) Schematic diagram of the spin-wave gas sensor composed of multilayer films (Matatagui et al., 2015b). **(B)** Working principle diagram of the spin-wave gas sensor (Matatagui et al., 2015b). **(A,B)** Reprinted from Matatagui, D., Kolokoltsev, O., Qureshi, N., Mejía-Uriarte, E., and Saniger, J. (2015). A magnonic gas sensor based on magnetic nanoparticles. Nanoscale 7 (21), 9607–9613. With the permission of RSC Publishing. **(C)** Variation of band gap frequency of magnonic crystal in the spin-wave magnetic field sensor with increasing external bias magnetic field. The black arrows represent the change in the band gap frequency caused by increasing theapplied magnetic field. The change in band gap frequency affects the propagation characteristics of spin-wave (Inoue et al., 2011). Reprinted from Inoue, M., Baryshev, A., Takagi, H., Lim, P.B., Hatafuku, K., Noda, J., et al. (2011). Investigating the use of magnonic crystals as extremely sensitive magnetic field sensors at room temperature. Applied Physics Letters 98 (13), 132511. With the permission of AIP Publishing. **(D)** Three-dimensional schematic diagram of ultra-high frequency humidity sensor. The sensor is mainly composed of a spin-wave oscillator and a coplanar waveguide probe, in which the waveguide humidity probe is coupled with adjustable magnetostatic surface spin-wave oscillator and placed in the test chamber (Matatagui et al., 2015a). Reprinted with permission from Matatagui, D., Kolokoltsev, O., Qureshi, N., Mejía-Uriarte, E., and Saniger, J. (2015). A novel ultra-high frequency humidity sensor based on a magnetostatic spin wave oscillator. Sensors and Actuators B: Chemical 210, 297–301. Copyright 2015 Elsevier.

low-power COMS is negligible at present, its computing throughput (integer operations per second per unit area) is the lowest among the five types of devices, only 0.05 Pops/s/cm^2, while the computing throughput of spin-wave device is 3.99 Pops/s/cm^2, which is the same order of magnitude as that of high-performance COMS.

Although spin-wave devices perform better than existing CMOS technology and other emerging devices (such as graphene PN junction) in many aspects, but there are other problems. First of all, the cascade and fan-out technology of the spin-wave signal is not mature enough, and the matching of cascade, multi-band transmission and further reduction of loss have a lot of room for optimization. Secondly, the development of spin-wave logic circuit has not formed mature market rules, the spin-wave transmission mode and basic materials of all kinds of spin-wave devices (such as phase shifters, amplifiers and filters) are very chaotic. Finally, the fabrication technology of the spin-wave device is not integrated with the traditional silicon-based processing technology. Therefore, facing the mature CMOS technology and market, the commercialization process of the spin-wave integrated circuit is still under great pressure. However, with the development of the basic research related to spin-wave materials, spin-wave effects and device design is accelerating, we have many reasons to believe that spin-wave integrated circuit technology will advance to a new level in the next decade.

CONCLUSION AND OUTLOOK

We described a complete application chain of spin-wave information technology. The top and bottom ends of the chain are the base materials of spin-wave, and the functional spin-wave devices, respectively. Connecting the top and bottom ends is also accomplished by the emerging new interface effects. Magnetic materials represented by YIG, permalloy, CoFeB and Heusler alloy demonstrate excellent spin-wave properties, laying a material foundation for the development of spin-wave technology in the past few decades, while the construction of new spin-wave material system focuses on the preparation, exploitation and structural design of materials. In new preparation technologies the thickness of the spin-wave films is reduced while their original magnetization dynamic characteristics are maintained. New spin-wave materials are utilized in new fields such as antiferromagnets, YIG modification and topological magnonics. The structural design of spin-wave material is mainly reflected in the researches of magnonic crystals whose magnetic parameters change periodically.

The tunable interface effects explain the microphysical phenomena after the continuous miniaturization of the spin-wave device. VCMA is a key component of the potential solution for realizing all-voltage-controlled spin-wave devices. Facilitated by magneto-ionic transport, the process of controlling magnetism of materials by electric field becomes faster and more convenient.

This further enables further development of voltage-controlled spin-wave devices. The physical mechanism of both STT effect and SOT effect is to quickly flip the magnetic domain moment by using the electric spin-torque. This mechanism become the design core of the new memory MRAM and further improve the efficiency of the spin-wave excitation and amplification. Magnon-torque corresponding to the electric spin-torque has its own characteristics in terms of low energy consumption and long dissipation distance.

In view of the development of spin-wave functional devices the challenges are improving the working efficiency of devices, and reducing their power consumption. Compared with the traditional sensors, spin-wave sensors provide great advantages in the measurement or identification of physical and chemical indexes such as gas, magnetic field, and humidity. We anticipate that by continuous development new magnetoelectric effects, ultra-low power consumption spin-wave information processing devices will achieve new frontiers in aspects such as phase shifting, signal dividing and channeling, etc.

In the face of Moore's law slowing down or even failing, there are still many challenges for the entry of spin-wave functional devices into the market, but we can find some rules for the future direction. From the perspective of spin waves and spin-wave materials, there are three aspects that need more development and advancement, that is, to achieve lower loss, higher frequency and robustness of spin wave propagation. The existing spin-wave material with the lowest Gilbert damping is YIG, which has reached the order of 10^{-5} (μm-thick) by liquid phase epitaxy, but the α of spin-wave alloys materials are generally in the order of 10^{-3} and need to be further optimized (spin-wave alloys have other unique advantages). Spin wave has covered the GHz band. If the intrinsic characteristics of antiferromagnetic materials can be used, the realization and application of THz spin-wave devices could be possible under the interaction of internal strong exchange coupling in antiferromagnets and external disturbance like laser irradiation. The robustness of the spin wave is the basis of the transmission of the spin wave in the long-distance complex environment. In addition to reducing magnetic damping of material itself and improve the spin-wave group velocity, perhaps we can learn from the topological protection edge state in electronic topological insulators, and realize almost lossless propagation of spin waves on waveguide surfaces, corners or even defects.

From the perspective of spin-wave functional devices, more time and efforts are needed before realizing the integration, easy regulation and unified standards of devices. There is no doubt that the integration and miniaturization of devices is the mainstream of the current development of spin-wave devices, therefore higher requirements are put forward for the preparation process (such as film thickness, quality and ease of processing) and reliability (such as temperature stability) of devices. At present, the manipulation technologies of spin-wave devices are far from mature enough. A fast, simple and reversible solution must be found to ensure the diversity and high efficiency of the function, maybe we can achieve the goal by adopting all-voltage-controlled regulation method on the basis of dynamic magnonic crystals. Although the current chaotic transmission patterns of the spin wave and the standards for basic materials must be harmonized before the spin-wave integrated device can be successfully marketed, we still have high expectations for the success of this process.

AUTHOR CONTRIBUTIONS

JX has made substantial contributions to the data collection and writing of this work. LJ has made significant contributions to the framework design and other works. ZL, QW, XT and ZZ have made critical and important revisions to the draft. LJ and HZ have approved the final version to be published. All authors listed have made a substantial, direct, and intellectual contributions to the work, and approved it for publication.

FUNDING

This work was supported by the National Natural Science Foundation of China under Grant Nos. 51702042 and 61734002, National Key Research and Development Plan under Grant No. 2016YFA0300801 and 2016YFA0300802, National Key Scientific Instrument and Equipment Development Project No. 51827802.

REFERENCES

Albisetti, E., Petti, D., Pancaldi, M., Madami, M., Tacchi, S., Curtis, J., et al. (2016). Nanopatterning reconfigurable magnetic landscapes via thermally assisted scanning probe lithography. *Nat. Nanotechnol.* 11 (6), 545. doi:10.1038/nnano.2016.25

Banerjee, C., Choudhury, S., Sinha, J., and Barman, A. (2017). Pseudo-one-dimensional magnonic crystals for high-frequency nanoscale devices. *Phys. Rev. Appl.* 8 (1), 014036. doi:10.1103/physrevapplied.8.014036

Bass, J., and Pratt, W. P., Jr. (2007). Spin-diffusion lengths in metals and alloys, and spin-flipping at metal/metal interfaces: an experimentalist's critical review. *J. Phys.: Condens. Matter.* 19 (18), 183201. doi:10.1088/0953-8984/19/18/183201

Bauer, U., Yao, L., Tan, A. J., Agrawal, P., Emori, S., Tuller, H. L., et al. (2015). Magneto-ionic control of interfacial magnetism. *Nat. Mater.* 14 (2), 174–181. doi:10.1038/nmat4134

Berger, L. (1996). Emission of spin waves by a magnetic multilayer traversed by a current. *Phys. Rev. B.* 54 (13), 9353. doi:10.1103/physrevb.54.9353

Bernstein, K., Cavin, R. K., Porod, W., Seabaugh, A., and Welser, J. (2010). Device and architecture outlook for beyond CMOS switches. *Proc. IEEE.* 98 (12), 2169–2184. doi:10.1109/jproc.2010.2066530

Bi, C., Liu, Y., Newhouse-Illige, T., Xu, M., Rosales, M., Freeland, J., et al. (2014). Reversible control of Co magnetism by voltage-induced oxidation. *Phys. Rev. Lett.* 113 (26), 267202. doi:10.1103/physrevlett.113.267202

Bruno, P. (1989). Tight-binding approach to the orbital magnetic moment and magnetocrystalline anisotropy of transition-metal monolayers. *Phys. Rev. B.* 39 (1), 865. doi:10.1103/physrevb.39.865

Chen, L., Chung, J.-H., Gao, B., Chen, T., Stone, M. B., Kolesnikov, A. I., et al. (2018). Topological spin excitations in honeycomb ferromagnet CrI 3. *Phys. Rev. X.* 8 (4), 041028. doi:10.1103/physrevx.8.041028

Chen, X., Wang, Q., Bai, F., Tang, X., Zhang, H., and Zhong, Z. (2016). A methodology to design spin-wave-based logic gates in a single ferromagnetic nanostripe using spin-transfer torque effects. *IEEE Trans. Magn.* 52 (7), 1–4. doi:10.1109/tmag.2016.2524637

Chen, X., Wang, Q., Liao, Y., Tang, X., Zhang, H., and Zhong, Z. (2015). Control phase shift of spin-wave by spin-polarized current and its application in logic gates. *J. Magn. Magn Mater.* 394, 67–69. doi:10.1016/j.jmmm.2015.06.043

Chen, Y.-J., Lee, H. K., Verba, R., Katine, J. A., Barsukov, I., Tiberkevich, V., et al. (2017). Parametric resonance of magnetization excited by electric field. *Nano Lett.* 17 (1), 572–577. doi:10.1021/acs.nanolett.6b04725

Chin, G. (1971). Review of magnetic properties of Fe-Ni alloys. *IEEE Trans. Magn.* 7 (1), 102–113. doi:10.1109/tmag.1971.1067014

Chisnell, R., Helton, J., Freedman, D., Singh, D., Bewley, R., Nocera, D., et al. (2015). Topological magnon bands in a kagome lattice ferromagnet. *Phys. Rev. Lett.* 115 (14), 147201. doi:10.1103/physrevlett.115.147201

Choudhury, S., Barman, S., Otani, Y., and Barman, A. (2017). Efficient modulation of spin waves in two-dimensional octagonal magnonic crystal. *ACS Nano.* 11 (9), 8814–8821. doi:10.1021/acsnano.7b02872

Chumak, A., Neumann, T., Serga, A., Hillebrands, B., and Kostylev, M. (2009). A current-controlled, dynamic magnonic crystal. *J. Phys. D: Appl. Phys.* 42 (20), 205005. doi:10.1088/0022-3727/42/20/205005

Chumak, A., Serga, A., Hillebrands, B., and Kostylev, M. (2008). Scattering of backward spin waves in a one-dimensional magnonic crystal. *Appl. Phys. Lett.* 93 (2), 022508. doi:10.1063/1.2963027

Chumak, A., Serga, A., and Hillebrands, B. (2017). Magnonic crystals for data processing. *J. Phys. D: Appl. Phys.* 50 (24), 244001. doi:10.1088/1361-6463/aa6a65

Chumak, A. V., Serga, A. A., and Hillebrands, B. (2014). Magnon transistor for all-magnon data processing. *Nat. Commun.* 5 (1), 4700. doi:10.1038/ncomms5700

Ciubotaru, F., Chumak, A. V., Obry, B., Serga, A. A., and Hillebrands, B. (2013). Magnonic band gaps in waveguides with a periodic variation of the saturation magnetization. *Phys. Rev. B.* 88 (13), 134406. doi:10.1103/physrevb.88.134406

Conca, A., Greser, J., Sebastian, T., Klingler, S., Obry, B., Leven, B., et al. (2013). Low spin-wave damping in amorphous Co40Fe40B20 thin films. *J. Appl. Phys.* 113 (21), 213909. doi:10.1063/1.4808462

Crossley, S., Quindeau, A., Swartz, A., Rosenberg, E., Beran, L., Avci, C., et al. (2019). Ferromagnetic resonance of perpendicularly magnetized Tm3Fe5O12/Pt heterostructures. *Appl. Phys. Lett.* 115 (17), 172402. doi:10.1063/1.5124120

d'Allivy Kelly, O., Anane, A., Bernard, R., Ben Youssef, J., Hahn, C., Molpeceres, A. H., et al. (2013). Inverse spin Hall effect in nanometer-thick yttrium iron garnet/Pt system. *Appl. Phys. Lett.* 103 (8), 082408. doi:10.1063/1.4819157

Dasgupta, S., Das, B., Li, Q., Wang, D., Baby, T. T., Indris, S., et al. (2016). Toward on-and-off magnetism: reversible electrochemistry to control magnetic phase transitions in spinel ferrites. *Adv. Funct. Mater.* 26 (41), 7507–7515. doi:10.1002/adfm.201603411

Dieny, B., and Chshiev, M. (2017). Perpendicular magnetic anisotropy at transition metal/oxide interfaces and applications. *Rev. Mod. Phys.* 89 (2), 025008. doi:10.1103/revmodphys.89.025008

Divinskiy, B., Demidov, V. E., Urazhdin, S., Freeman, R., Rinkevich, A. B., and Demokritov, S. O. (2018). Excitation and amplification of spin waves by spin-orbit torque. *Adv. Mater.* 30 (33), 1802837. doi:10.1002/adma.201802837

Drung, D., Abmann, C., Beyer, J., Kirste, A., Peters, M., Ruede, F., et al. (2007). Highly sensitive and easy-to-use SQUID sensors. *IEEE Trans. Appl. Supercond.* 17 (2), 699–704. doi:10.1109/tasc.2007.897403

Duan, C.-G., Velev, J. P., Sabirianov, R. F., Zhu, Z., Chu, J., Jaswal, S. S., et al. (2008). Surface magnetoelectric effect in ferromagnetic metal films. *Phys. Rev. Lett.* 101 (13), 137201. doi:10.1103/physrevlett.101.137201

Dubs, C., Surzhenko, O., Linke, R., Danilewsky, A., Brückner, U., and Dellith, J. (2017). Sub-micrometer yttrium iron garnet LPE films with low ferromagnetic resonance losses. *J. Phys. D: Appl. Phys.* 50 (20), 204005. doi:10.1088/1361-6463/aa6b1c

Emori, S., Nan, T., Belkessam, A. M., Wang, X., Matyushov, A. D., Babroski, C. J., et al. (2016). Interfacial spin-orbit torque without bulk spin-orbit coupling. *Phys. Rev. B.* 93 (18), 180402. doi:10.1103/physrevb.93.180402

Fan, X., Celik, H., Wu, J., Ni, C., Lee, K.-J., Lorenz, V. O., et al. (2014). Quantifying interface and bulk contributions to spin–orbit torque in magnetic bilayers. *Nat. Commun.* 5 (1), 1–8. doi:10.1038/ncomms4042

Fong, X., Kim, Y., Venkatesan, R., Choday, S. H., Raghunathan, A., and Roy, K. (2016). Spin-transfer torque memories: devices, circuits, and systems. *Proc. IEEE.* 104 (7), 1449–1488. doi:10.1109/jproc.2016.2521712

Fukami, S., Zhang, C., DuttaGupta, S., Kurenkov, A., and Ohno, H. (2016). Magnetization switching by spin-orbit torque in an antiferromagnet-ferromagnet bilayer system. *Nat. Mater.* 15 (5), 535–541. doi:10.1038/nmat4566

Fulara, H., Zahedinejad, M., Khymyn, R., Awad, A., Muralidhar, S., Dvornik, M., et al. (2019). Spin-orbit torque–driven propagating spin waves. *Sci. Adv.* 5 (9), eaax8467. doi:10.1126/sciadv.aax8467

Gilbert, D. A., Burks, E. C., Ushakov, S. V., Abellan, P., Arslan, I., Felter, T. E., et al. (2017). Tunable low density palladium nanowire foams. *Chem. Mater.* 29 (22), 9814–9818. doi:10.1021/acs.chemmater.7b03978

Gilbert, D. A., Grutter, A. J., Arenholz, E., Liu, K., Kirby, B. J., Borchers, J. A., et al. (2016a). Structural and magnetic depth profiles of magneto-ionic heterostructures beyond the interface limit. *Nat. Commun.* 7, 12264. doi:10.1038/ncomms12264

Gilbert, D. A., Olamit, J., Dumas, R. K., Kirby, B. J., Grutter, A. J., Maranville, B. B., et al. (2016b). Controllable positive exchange bias via redox-driven oxygen migration. *Nat. Commun.* 7 (1), 1–8. doi:10.1038/ncomms11050

Gomi, M., Furuyama, H., and Abe, M. (1991). Strong magneto-optical enhancement in highly Ce-substituted iron garnet films prepared by sputtering. *J. Appl. Phys.* 70 (11), 7065–7067. doi:10.1063/1.349786

Goto, T., Kanazawa, N., Buyandalai, A., Takagi, H., Nakamura, Y., Okajima, S., et al. (2015). Spin wave differential circuit for realization of thermally stable magnonic sensors. *Appl. Phys. Lett.* 106 (13), 132412. doi:10.1063/1.4916989

Graef, M. (2011). Positioning more than Moore characterization needs and methods within the 2011 ITRS. *AIP Conf. Proc.* 1395 (1), 345–350.

Grutter, A. J., Gilbert, D. A., Alaan, U., Arenholz, E., Maranville, B. B., Borchers, J. A., et al. (2016). Reversible control of magnetism in La0. 67Sr0. 33MnO3 through chemically-induced oxygen migration. *Appl. Phys. Lett.* 108 (8), 082405. doi:10.1063/1.4942645

Han, J., Zhang, P., Hou, J. T., Siddiqui, S. A., and Liu, L. (2019). Mutual control of coherent spin waves and magnetic domain walls in a magnonic device. *Science.* 366 (6469), 1121–1125. doi:10.1126/science.aau2610

Hansen, U.-H., Demidov, V. E., and Demokritov, S. O. (2009). Dual-function phase shifter for spin-wave logic applications. *Appl. Phys. Lett.* 94 (25), 252502. doi:10.1063/1.3159628

Heussner, F., Serga, A., Brächer, T., Hillebrands, B., and Pirro, P. (2017). A switchable spin-wave signal splitter for magnonic networks. *Appl. Phys. Lett.* 111 (12), 122401. doi:10.1063/1.4987007

Hillebrands, B., and Felser, C. (2006). High-spin polarization of Heusler alloys. *J. Phys. Appl. Phys.* 39 (5). doi:10.1088/0022-3727/39/5/e01

Houshang, A., Khymyn, R., Fulara, H., Gangwar, A., Haidar, M., Etesami, S., et al. (2018). Spin transfer torque driven higher-order propagating spin waves in nano-contact magnetic tunnel junctions. *Nat. Commun.* 9 (1), 1–6. doi:10.1038/s41467-018-06589-0

Hutchby, J. A., Bourianoff, G. I., Zhirnov, V. V., and Brewer, J. E. (2002). Extending the road beyond CMOS. *IEEE Circ. Dev. Mag.* 18 (2), 28–41. doi:10.1109/101.994856

Inoue, M., Baryshev, A., Takagi, H., Lim, P. B., Hatafuku, K., Noda, J., et al. (2011). Investigating the use of magnonic crystals as extremely sensitive magnetic field sensors at room temperature. *Appl. Phys. Lett.* 98 (13), 132511. doi:10.1063/1.3567940

Jin, L., Wang, Y., Lu, G., Li, J., He, Y., Zhong, Z., et al. (2019). Temperature dependence of spin-wave modes and Gilbert damping in lanthanum-doped yttrium-iron-garnet films. *AIP Adv.* 9 (2), 025301. doi:10.1063/1.5085922

Kajiwara, Y., Harii, K., Takahashi, S., Ohe, J., Uchida, K., Mizuguchi, M., et al. (2010). Transmission of electrical signals by spin-wave interconversion in a magnetic insulator. *Nature.* 464 (7286), 262–266. doi:10.1038/nature08876

Kamberský, V. (2007). Spin-orbital Gilbert damping in common magnetic metals. *Phys. Rev. B.* 76 (13), 134416. doi:10.1103/physrevb.76.134416

Kampfrath, T., Sell, A., Klatt, G., Pashkin, A., Mährlein, S., Dekorsy, T., et al. (2011). Coherent terahertz control of antiferromagnetic spin waves. *Nat. Photon.* 5 (1), 31–34. doi:10.1038/nphoton.2010.259

Katine, J., Albert, F., Buhrman, R., Myers, E., and Ralph, D. (2000). Current-driven magnetization reversal and spin-wave excitations in Co/Cu/Co pillars. *Phys. Rev. Lett.* 84 (14), 3149. doi:10.1103/physrevlett.84.3149

Kehlberger, A., Richter, K., Onbasli, M. C., Jakob, G., Kim, D. H., Goto, T., et al. (2015). Enhanced magneto-optic Kerr effect and magnetic properties of $CeY_2Fe_5O_{12}$ epitaxial thin films. *Phys. Rev. Appl.* 4 (1), 014008. doi:10.1103/physrevapplied.4.014008

Kelly, P. J., and Arnell, R. D. (2000). Magnetron sputtering: a review of recent developments and applications. *Vacuum.* 56 (3), 159–172. doi:10.1016/s0042-207x(99)00189-x

Khitun, A., Bao, M., and Wang, K. L. (2010). Magnonic logic circuits. *J. Phys. D: Appl. Phys.* 43 (26), 264005. doi:10.1088/0022-3727/43/26/264005

Kittel, C. (1951). Theory of antiferromagnetic resonance. *Phys. Rev.* 82 (4), 565. doi:10.1103/physrev.82.565

Kostylev, M., Serga, A., Schneider, T., Leven, B., and Hillebrands, B. (2005). Spin-wave logical gates. *Appl. Phys. Lett.* 87 (15), 153501. doi:10.1063/1.2089147

Krawczyk, M., and Grundler, D. (2014). Review and prospects of magnonic crystals and devices with reprogrammable band structure. *J. Phys.: Condens. Matter.* 26 (12), 123202. doi:10.1088/0953-8984/26/12/123202

Kruglyak, V. V., Demokritov, S. O., and Grundler, D. (2010). Magnonics. *J. Phys. D: Appl. Phys.* 43 (26), 264001. doi:10.1088/0022-3727/43/26/264001

Kubota, T., Tsunegi, S., Oogane, M., Mizukami, S., Miyazaki, T., Naganuma, H., et al. (2009). Half-metallicity and Gilbert damping constant in Co_2FexMn_1−xSi Heusler alloys depending on the film composition. *Appl. Phys. Lett.* 94 (12), 122504. doi:10.1063/1.3105982

Kung, H.-H., Maiti, S., Wang, X., Cheong, S.-W., Maslov, D., and Blumberg, G. (2017). Chiral spin mode on the surface of a topological insulator. *Phys. Rev. Lett.* 119 (13), 136802. doi:10.1103/physrevlett.119.136802

Lage, E., Beran, L., Quindeau, A. U., Ohnoutek, L., Kucera, M., Antos, R., et al. (2017). Temperature-dependent Faraday rotation and magnetization reorientation in cerium-substituted yttrium iron garnet thin films. *Appl. Mater.* 5 (3), 036104. doi:10.1063/1.4976817

Lamrani, S., Guittoum, A., Schaefer, R., Hemmous, M., Neu, V., Pofahl, S., et al. (2015). Morphology, structure and magnetic study of permalloy films electroplated on silicon nanowires. *J. Magn. Magn Mater.* 396, 263–267. doi:10.1016/j.jmmm.2015.07.111

Lan, J., Yu, W., and Xiao, J. (2017). Antiferromagnetic domain wall as spin wave polarizer and retarder. *Nat. Commun.* 8 (1), 1–7. doi:10.1038/s41467-017-00265-5

Lee, K.-S., and Kim, S.-K. (2008). Conceptual design of spin wave logic gates based on a Mach–Zehnder-type spin wave interferometer for universal logic functions. *J. Appl. Phys.* 104 (5), 053909. doi:10.1063/1.2975235

Levinstein, H. J., Licht, S., Landorf, R., and Blank, S. L. (1971). Growth of high-quality garnet thin films from supercooled melts. *Appl. Phys. Lett.* 19 (11), 486–488. doi:10.1063/1.1653784

Li, H.-B., Lu, N., Zhang, Q., Wang, Y., Feng, D., Chen, T., et al. (2017). Electric-field control of ferromagnetism through oxygen ion gating. *Nat. Commun.* 8 (1), 1–7. doi:10.1038/s41467-017-02359-6

Li, M. (2012). Review of advanced CMOS technology for post-Moore era. *Sci. China Phys. Mech. Astron.* 55 (12), 2316–2325. doi:10.1007/s11433-012-4930-3

Liu, T., Chang, H., Vlaminck, V., Sun, Y., Kabatek, M., Hoffmann, A., et al. (2014). Ferromagnetic resonance of sputtered yttrium iron garnet nanometer films. *J. Appl. Phys.* 115 (17), 17A501. doi:10.1063/1.4852135

Liu, T., and Vignale, G. (2011). Electric control of spin currents and spin-wave logic. *Phys. Rev. Lett.* 106 (24), 247203. doi:10.1103/physrevlett.106.247203

Lu, N., Zhang, P., Zhang, Q., Qiao, R., He, Q., Li, H.-B., et al. (2017). Electric-field control of tri-state phase transformation with a selective dual-ion switch. *Nature.* 546 (7656), 124–128. doi:10.1038/nature22389

Madami, M., Bonetti, S., Consolo, G., Tacchi, S., Carlotti, G., Gubbiotti, G., et al. (2011). Direct observation of a propagating spin wave induced by spin-transfer torque. *Nat. Nanotechnol.* 6 (10), 635. doi:10.1038/nnano.2011.140

Matatagui, D., Kolokoltsev, O., Qureshi, N., Mejía-Uriarte, E., Ordoñez-Romero, C., Vázquez-Olmos, A., et al. (2017). Magnonic sensor array based on magnetic nanoparticles to detect, discriminate and classify toxic gases. *Sensor. Actuator. B Chem.* 240, 497–502. doi:10.1016/j.snb.2016.08.174

Matatagui, D., Kolokoltsev, O., Qureshi, N., Mejía-Uriarte, E., and Saniger, J. (2015a). A novel ultra-high frequency humidity sensor based on a magnetostatic spin wave oscillator. *Sensor. Actuator. B Chem.* 210, 297–301. doi:10.1016/j.snb.2014.12.118

Matatagui, D., Kolokoltsev, O. V., Qureshi, N., Mejía-Uriarte, E. V., and Saniger, J. M. (2015b). A magnonic gas sensor based on magnetic nanoparticles. *Nanoscale.* 7 (21), 9607–9613. doi:10.1039/C5NR01499A

Matsukura, F., Tokura, Y., and Ohno, H. (2015). Control of magnetism by electric fields. *Nat. Nanotechnol.* 10 (3), 209–220. doi:10.1038/nnano.2015.22

McLeod, P., and Hartsough, L. (1977). High-rate sputtering of aluminum for metallization of integrated circuits. *J. Vac. Sci. Technol.* 14 (1), 263–265. doi:10.1116/1.569136

Michelini, F., Ressier, L., Degauque, J., Baules, P., Fert, A., Peyrade, J., et al. (2002). Permalloy thin films on MgO (001): epitaxial growth and physical properties. *J. Appl. Phys.* 92 (12), 7337–7340. doi:10.1063/1.1520723

Moore, G. E. (1965). Cramming more components onto integrated circuits. *Proc. IEEE.* 38 (8), 114–117. doi:10.1109/jproc.1998.658762

Myers, E. B., Ralph, D., Katine, J., Louie, R., and Buhrman, R. (1999). Current-induced switching of domains in magnetic multilayer devices. *Science.* 285 (5429), 867–870. doi:10.1126/science.285.5429.867

Nikitin, A. A., Ustinov, A. B., Semenov, A. A., Chumak, A. V., Serga, A. A., Vasyuchka, V. I., et al. (2015). A spin-wave logic gate based on a width-modulated dynamic magnonic crystal. *Appl. Phys. Lett.* 106 (10), 102405. doi:10.1063/1.4914506

Nikitov, S., Tailhades, P., and Tsai, C. (2001). Spin waves in periodic magnetic structures-magnonic crystals. *J. Magn. Magn Mater.* 236 (3), 320–330. doi:10.1016/s0304-8853(01)00470-x

Nikonov, D. E. and Young, I. A. (2015). Benchmarking of beyond-CMOS exploratory devices for logic integrated circuits. *IEEE J. Explor. Solid-State Comput. Devices Circuits.* 1, 3–11. doi:10.1109/jxcdc.2015.2418033

Nikonov, D. E., and Young, I. A. (2013). Overview of beyond-CMOS devices and a uniform methodology for their benchmarking. *Proc. IEEE.* 101 (12), 2498–2533. doi:10.1109/JPROC.2013.2252317

Nishitani, J., Kozuki, K., Nagashima, T., and Hangyo, M. (2010). Terahertz radiation from coherent antiferromagnetic magnons excited by femtosecond laser pulses. *Appl. Phys. Lett.* 96 (22), 221906. doi:10.1063/1.3436635

Nozaki, T., Yamamoto, T., Miwa, S., Tsujikawa, M., Shirai, M., Yuasa, S., et al. (2019). Recent progress in the voltage-controlled magnetic anisotropy effect and the challenges faced in developing voltage-torque MRAM. *Micromachines.* 10 (5), 327.doi:10.3390/mi10050327

Obry, B., Pirro, P., Brächer, T., Chumak, A. V., Osten, J., Ciubotaru, F., et al. (2013). A micro-structured ion-implanted magnonic crystal. *Appl. Phys. Lett.* 102 (20), 202403. doi:10.1063/1.4807721

Ohtake, M., Tanaka, T., Matsubara, K., Kirino, F., and Futamoto, M. (2011). Epitaxial growth of permalloy thin films on MgO single-crystal substrates. *J. Phys. Conf. Ser.* 303, 01201510. doi:1088/1742-6596/303/1/012015

Okada, A., Kanai, S., Yamanouchi, M., Ikeda, S., Matsukura, F., and Ohno, H. (2014). Electric-field effects on magnetic anisotropy and damping constant in Ta/CoFeB/MgO investigated by ferromagnetic resonance. *Appl. Phys. Lett.* 105 (5), 052415. doi:10.1063/1.4892824

Onbasli, M., Kehlberger, A., Kim, D. H., Jakob, G., Kläui, M., Chumak, A. V., et al. (2014). Pulsed laser deposition of epitaxial yttrium iron garnet films with low Gilbert damping and bulk-like magnetization. *Appl. Mater.* 2 (10), 106102. doi:10.1063/1.4896936

Onose, Y., Ideue, T., Katsura, H., Shiomi, Y., Nagaosa, N., and Tokura, Y. (2010). Observation of the magnon Hall effect. *Science.* 329 (5989), 297–299. doi:10.1126/science.1188260

Padture, N. P., Gell, M., and Jordan, E. H. (2002). Thermal barrier coatings for gas-turbine engine applications. *Science.* 296 (5566), 280–284. doi:10.1126/science.1068609

Pan, C., and Naeemi, A. (2017). "Beyond-cmos non-boolean logic benchmarking: insights and future directions," in The design, automation & test in europe conference & exhibition (DATE), Lausanne, Switzerland, 31 March 2017 [abstract].

Patil, R. A., Su, C.-W., Chuang, C.-J., Lai, C.-C., Liou, Y., and Ma, Y.-R. (2016). Terahertz spin-wave waveguides and optical magnonics in one-dimensional NiO nanorods. *Nanoscale.* 8 (26), 12970–12976. doi:10.1039/c6nr02531e

Popova, E., Galeano, A. F. F., Deb, M., Warot-Fonrose, B., Kachkachi, H., Gendron, F., et al. (2013). Magnetic anisotropies in ultrathin bismuth iron garnet films. *J. Magn. Magn Mater.* 335, 139–143. doi:10.1016/j.jmmm.2013.02.003

Qin, H., Both, G.-J., Hämäläinen, S. J., Yao, L., and van Dijken, S. (2018). Low-loss YIG-based magnonic crystals with large tunable bandgaps. *Nat. Commun.* 9 (1), 1–10. doi:10.1038/s41467-018-07893-5

Quindeau, A., Avci, C. O., Liu, W., Sun, C., Mann, M., Tang, A. S., et al. (2017). Tm3 Fe5 O12/Pt heterostructures with perpendicular magnetic anisotropy for

spintronic applications. *Adv. Electron. Mater.* 3 (1), 1600376. doi:10.1002/aelm.201600376

Rana, B., Fukuma, Y., Miura, K., Takahashi, H., and Otani, Y. (2017). Excitation of coherent propagating spin waves in ultrathin CoFeB film by voltage-controlled magnetic anisotropy. *Appl. Phys. Lett.* 111 (5), 052404. doi:10.1063/1.4990724

Rana, B., and Otani, Y. (2019). Towards magnonic devices based on voltage-controlled magnetic anisotropy. *Commun. Phys.* 2 (1), 1–12. doi:10.1038/s42005-019-0189-6

Rana, B., and Otani, Y. (2018). Voltage-controlled reconfigurable spin-wave nanochannels and logic devices. *Phys. Rev. Appl.* 9 (1), 014033. doi:10.1103/physrevapplied.9.014033

Rezende, S. M. (2020). *Fundamentals of magnonics*. Manhattan, NY, United States: Springer International Publishing.

Richardson, D., Kalinikos, B. A., Carr, L. D., and Wu, M. (2018). Spontaneous exact spin-wave fractals in magnonic crystals. *Phys. Rev. Lett.* 121 (10), 107204. doi:10.1103/physrevlett.121.107204

Roldán-Molina, A., Nunez, A., and Fernández-Rossier, J. (2016). Topological spin waves in the atomic-scale magnetic skyrmion crystal. *New J. Phys.* 18 (4), 045015. doi:10.1088/1367-2630/18/4/045015

Rosenberg, E. R., Beran, L., Avci, C. O., Zeledon, C., Song, B., Gonzalez-Fuentes, C., et al. (2018). Magnetism and spin transport in rare-earth-rich epitaxial terbium and europium iron garnet films. *Phys. Rev. Mater.* 2 (9), 094405. doi:10.1103/physrevmaterials.2.094405

Rousseau, O., Rana, B., Anami, R., Yamada, M., Miura, K., Ogawa, S., et al. (2015). Realization of a micrometre-scale spin-wave interferometer. *Sci. Rep.* 5, 9873. doi:10.1038/srep09873

Sadovnikov, A., Beginin, E., Odincov, S., Sheshukova, S., Sharaevskii, Y. P., Stognij, A., et al. (2016). Frequency selective tunable spin wave channeling in the magnonic network. *Appl. Phys. Lett.* 108 (17), 172411. doi:10.1063/1.4948381

Sadovnikov, A., Gubanov, V., Sheshukova, S., Sharaevskii, Y. P., and Nikitov, S. (2018). Spin-wave drop filter based on asymmetric side-coupled magnonic crystals. *Phys. Rev. Appl.* 9 (5), 051002. doi:10.1103/physrevapplied.9.051002

Salah, K. (2017). "More than moore and beyond CMOS: new interconnects schemes and new circuits architectures," in The 2017 IEEE 19th electronics Packaging technology conference (EPTC), Singapore, December 6–9, 2017. [abstract]

Schneider, T., Serga, A. A., Leven, B., Hillebrands, B., Stamps, R. L., and Kostylev, M. P. (2008). Realization of spin-wave logic gates. *Appl. Phys. Lett.* 92 (2), 022505. doi:10.1063/1.2834714

Sebastian, T., Ohdaira, Y., Kubota, T., Pirro, P., Brächer, T., Vogt, K., et al. (2012). Low-damping spin-wave propagation in a micro-structured Co2Mn0.6Fe0.4Si Heusler waveguide. *Appl. Phys. Lett.* 100 (11), 112402. doi:10.1063/1.3693391

Sekiguchi, K., Yamada, K., Seo, S.-M., Lee, K.-J., Chiba, D., Kobayashi, K., et al. (2012). Time-domain measurement of current-induced spin wave dynamics. *Phys. Rev. Lett.* 108 (1), 017203. doi:10.1103/physrevlett.108.017203

Sellappan, P., Tang, C., Shi, J., and Garay, J. E. (2017). An integrated approach to doped thin films with strain-tunable magnetic anisotropy: powder synthesis, target preparation and pulsed laser deposition of Bi:YIG. *Mater. Res. Lett.* 5 (1), 41–47. doi:10.1080/21663831.2016.1195779

Sharma, V., and Kuanr, B. K. (2018). Magnetic and crystallographic properties of rare-earth substituted yttrium-iron garnet. *J. Alloys Compd.* 748, 591–600. doi:10.1016/j.jallcom.2018.03.086

Shiino, T., Oh, S.-H., Haney, P. M., Lee, S.-W., Go, G., Park, B.-G., et al. (2016). Antiferromagnetic domain wall motion driven by spin-orbit torques. *Phys. Rev. Lett.* 117 (8), 087203. doi:10.1103/physrevlett.117.087203

Shindou, R., Matsumoto, R., Murakami, S., and Ohe, J.-i. (2013). Topological chiral magnonic edge mode in a magnonic crystal. *Phys. Rev. B.* 87 (17), 174427. doi:10.1103/physrevb.87.174427

Slavin, A., and Tiberkevich, V. (2009). Nonlinear auto-oscillator theory of microwave generation by spin-polarized current. *IEEE Trans. Magn.* 45 (4), 1875–1918. doi:10.1109/tmag.2008.2009935

Slonczewski, J. C. (1996). Current-driven excitation of magnetic multilayers. *J. Magn. Magn Mater.* 159 (1), L1. doi:10.1016/0304-8853(96)00062-5

Soumah, L., Beaulieu, N., Qassym, L., Carrétéro, C., Jacquet, E., Lebourgeois, R., et al. (2018). Ultra-low damping insulating magnetic thin films get perpendicular. *Nat. Commun.* 9 (1), 1–6. doi:10.1038/s41467-018-05732-1

Sun, Y., Song, Y.-Y., Chang, H., Kabatek, M., Jantz, M., Schneider, W., et al. (2012). Growth and ferromagnetic resonance properties of nanometer-thick yttrium iron garnet films. *Appl. Phys. Lett.* 101 (15), 152405. doi:10.1063/1.4759039

Tan, A. J., Huang, M., Avci, C. O., Büttner, F., Mann, M., Hu, W., et al. (2019). Magneto-ionic control of magnetism using a solid-state proton pump. *Nat. Mater.* 18 (1), 35–41. doi:10.1038/s41563-018-0211-5

Tanaka, T., Ohtake, M., Kirino, F., and Futamoto, M. (2010). Microstructure of NiFe epitaxial thin films grown on MgO single-crystal substrates. *IEEE Trans. Magn.* 46 (2), 345–348. doi:10.1109/tmag.2009.2031620

Tancogne-Dejean, N., Eich, F. G., and Rubio, A. (2020). Time-dependent magnons from first principles. *J. Chem. Theor. Comput.* 16 (2), 1007–1017. doi:10.1021/acs.jctc.9b01064

Tanoue, S., and Tabuchi, K. (2001). Magnetoresistance characteristics of NiFe/Cu/CoFe/IrMn spin valves at elevated temperature. *J. Vac. Sci. Technol. B.* 19 (2), 563–566. doi:10.1116/1.1349211

Theis, T. N., and Wong, H.-S. P. (2017). The end of moore's law: a new beginning for information technology. *Comput. Sci. Eng.* 19 (2), 41–50. doi:10.1109/mcse.2017.29

Trudel, S., Gaier, O., Hamrle, J., and Hillebrands, B. (2010). Magnetic anisotropy, exchange and damping in cobalt-based full-Heusler compounds: an experimental review. *J. Phys. D: Appl. Phys.* 43 (19), 193001. doi:10.1088/0022-3727/43/19/193001

Tsoi, M., Jansen, A., Bass, J., Chiang, W.-C., Seck, M., Tsoi, V., et al. (1998). Excitation of a magnetic multilayer by an electric current. *Phys. Rev. Lett.* 80 (19), 4281. doi:10.1103/physrevlett.80.4281

Tzschaschel, C., Otani, K., Iida, R., Shimura, T., Ueda, H., Günther, S., et al. (2017). Ultrafast optical excitation of coherent magnons in antiferromagnetic NiO. *Phys. Rev. B.* 95 (17), 174407. doi:10.1103/physrevb.95.174407

Urazhdin, S., Demidov, V., Ulrichs, H., Kendziorczyk, T., Kuhn, T., Leuthold, J., et al. (2014). Nanomagnonic devices based on the spin-transfer torque. *Nat. Nanotechnol.* 9 (7), 509–513. doi:10.1038/nnano.2014.88

Urazhdin, S., Tiberkevich, V., and Slavin, A. (2010). Parametric excitation of a magnetic nanocontact by a microwave field. *Phys. Rev. Lett.* 105 (23), 237204. doi:10.1103/physrevlett.105.237204

Ustinov, A. B., Drozdovskii, A. V., Nikitin, A. A., Semenov, A. A., Bozhko, D. A., Serga, A. A., et al. (2019). Dynamic electromagnonic crystal based on artificial multiferroic heterostructure. *Commun. Phys.* 2 (1), 1–7. doi:10.1038/s42005-019-0240-7

Vogel, M., Chumak, A. V., Waller, E. H., Langner, T., Vasyuchka, V. I., Hillebrands, B., et al. (2015). Optically reconfigurable magnetic materials. *Nat. Phys.* 11 (6), 487–491. doi:10.1038/nphys3325

Vogt, K., Fradin, F. Y., Pearson, J. E., Sebastian, T., Bader, S. D., Hillebrands, B., et al. (2014). Realization of a spin-wave multiplexer. *Nat. Commun.* 5 (1), 1–5. doi:10.1038/ncomms4727

Wagner, K., Kákay, A., Schultheiss, K., Henschke, A., Sebastian, T., and Schultheiss, H. (2016). Magnetic domain walls as reconfigurable spin-wave nanochannels. *Nat. Nanotechnol.* 11 (5), 432–436. doi:10.1038/nnano.2015.339

Wang, Q., Pirro, P., Verba, R., Slavin, A., Hillebrands, B., and Chumak, A. V. (2018a). Reconfigurable nanoscale spin-wave directional coupler. *Sci, Adv.* 4 (1), e1701517. doi:10.1126/sciadv.1701517

Wang, Q., Zhang, H., Tang, X., Fangohr, H., Bai, F., and Zhong, Z. (2014). Dynamic control of spin wave spectra using spin-polarized currents. *Appl. Phys. Lett.* 105 (11), 112405. doi:10.1063/1.4896027

Wang, X.-g., Chotorlishvili, L., Guo, G.-h., and Berakdar, J. (2018b). Electric field controlled spin waveguide phase shifter in YIG. *J. Appl. Phys.* 124 (7), 073903. doi:10.1063/1.5037958

Wang, X., Su, Y., and Wang, X. (2017). Topologically protected unidirectional edge spin waves and beam splitter. *Phys. Rev. B.* 95 (1), 014435. doi:10.1103/physrevb.95.014435

Wang, X., Zhang, H., and Wang, X. (2018c). Topological magnonics: a paradigm for spin-wave manipulation and device design. *Physical Review Applied.* 9 (2), 024029. doi:10.1103/physrevapplied.9.024029

Wang, Y., Zhu, D., Yang, Y., Lee, K., Mishra, R., Go, G., et al. (2019). Magnetization switching by magnon-mediated spin torque through an antiferromagnetic insulator. *Science.* 366 (6469), 1125–1128. doi:10.1126/science.aav8076

Waser, R., Dittmann, R., Staikov, G., and Szot, K. (2009). Redox-based resistive switching memories–nanoionic mechanisms, prospects, and challenges. *Adv. Mater.* 21 (25–26), 2632–2663. doi:10.1002/adma.200900375

Xu, F., Huang, Q., Liao, Z., Li, S., and Ong, C. (2012). Tuning of magnetization dynamics in sputtered CoFeB thin film by gas pressure. *J. Appl. Phys.* 111 (7), 07A304. doi:10.1063/1.3670605

Yamamoto, K., Thiang, G. C., Pirro, P., Kim, K.-W., Everschor-Sitte, K., and Saitoh, E. (2019). Topological characterization of classical waves: the topological origin of magnetostatic surface spin waves. *Phys. Rev. Lett.* 122 (21), 217201. doi:10.1103/physrevlett.122.217201

Yoshinaga, T., Mohri, K., Ueno, S., Uchiyama, T., and Cai, C. (2000). "Complementary magneto-impedance effect in quenched amorphous wire," in The 2000 IEEE international magnetics conference (INTERMAG), Toronto, ON, Canada, April 9, 2000. [abstract].

Yu, H., Duerr, G., Huber, R., Bahr, M., Schwarze, T., Brandl, F., et al. (2013). Omnidirectional spin-wave nanograting coupler. *Nat. Commun.* 4 (1), 1–9. doi:10.1038/ncomms3702

Zhao, J., Adroja, D., Yao, D.-X., Bewley, R., Li, S., Wang, X., et al. (2009). Spin waves and magnetic exchange interactions in CaFe2As2. *Nat. Phys.* 5 (8), 555–560. doi:10.1038/nphys1336

Zhu, X., Zhou, J., Chen, L., Guo, S., Liu, G., Li, R. W., et al. (2016). *In situ* nanoscale electric field control of magnetism by nanoionics. *Adv. Mater.* 28 (35), 7658–7665. doi:10.1002/adma.201601425

Zubar, T., Sharko, S., Tishkevich, D., Kovaleva, N., Vinnik, D., Gudkova, S., et al. (2018). Anomalies in Ni-Fe nanogranular films growth. *J. Alloys Compd.* 748, 970–978. doi:10.1016/j.jallcom.2018.03.245

Conflict of Interest: The authors declare that the research was conducted in the absence of any commercial or financial relationships that could be construed as a potential conflict of interest.

Smart Materials

Xinglong Gong

Dr. Xinglong Gong is a Professor of Engineering Science at the University of Science and Technology of China (USTC), Hefei, Anhui, P.R. China. He received his Ph.D. degree in Mechanics from both the USTC and Saitama University (Japan), in 1996. Then, he worked at the Nihon Dempa Kogyo Co., Ltd., Japan, for 7 years, as an Engineer and then a Chief Engineer. In 2003, he joined the Department of Modern Mechanics, USTC, as a Full Professor. His research interests cover soft matter materials, including magnetorheological fluid, electrorheological fluid, magnetorheological elastomer, shear thickening materials, and polymer nanocomposites as well as their application in the vibration isolator, vibration absorber, anti-shock equipment, and body armor.

He was supported by the 100-Talent Programme of the Chinese Academy of Sciences in 2003 and by the National Science Foundation for Distinguished Young Scholars of China in 2011. Since 2003, Prof. Gong has authored more than 280 research papers which were indexed by SCI and EI, including over 50 published in top journals (Advanced Functional Materials, Nano Energy, Journal of Rheology, Composites Science and Technology, Journal of Materials Chemistry, Applied Physics Letters, etc.). Moreover, Prof. Gong has been authored 23 patents.

Xuan Shouhu

Dr. Shouhu Xuan is a Full Professor at the University of Science and Technology of China (USTC). He got a B.S. degree from Anhui Normal University in 2003 and received his Ph.D. degree from USTC in 2008. After working as a post-doc for 2 years at the Chinese University of Hong Kong, he joined the Department of Modern Mechanics, USTC, in 2010. He received the Young Scholarship of Chinese Rheology Society award in 2016 and the National Science Foundation for Excellent Young Scholars of China in 2018. His research interests cover Smart Composites, Rheology, and Magnetic nanomaterials.

Shuaishuai Sun

Dr. Shuaishuai Sun, an Associate Research Fellow of the Faculty of Engineering and Information Sciences, is an expert in magnetorheology and mechatronics. His interest in engineering came from a visit to a factory during his undergraduate studies where he decided that he wanted to build the next generation of vehicles. Dr. Sun has also collaborated on a national level with the Australian firm M&S Engineering Pty Ltd. Since 2015, Dr. Sun has worked with Professor Shiwu Zhang from the University of Science and Technology of China to extend his expertise in the field of robotics. This collaboration has led to the creation of the adaptive robotic leg. The design is based on MR technology in which significantly improved locomotive energy efficiency allows the robot to move better.

frontiers in Materials

ORIGINAL RESEARCH
published: 30 October 2020
doi: 10.3389/fmats.2020.598973

Deformation Dependent Sound Absorption Property of a Novel Magnetorheological Membrane Sound Absorber

Chuanlin Sun[1], *Xufeng Cao*[1], *Xiaoling Zhou*[2], *Xinglong Gong*[1]* *and Shouhu Xuan*[1]*

[1]CAS Key Laboratory of Mechanical Behavior and Design of Materials, CAS Center for Excellence in Complex System Mechanics, Department of Modern Mechanics, University of Science and Technology of China (USTC), Hefei, China, [2]Shanghai Key Laboratory of Spacecraft Mechanism, Shanghai Institute of Aerospace System Engineering, Shanghai, China

A novel membrane sound absorber based on the magnetorheological membrane (MRM) is developed for active sound absorption. Due to its good flexibility and stretch-ability, the MRM consisting of carbonyl iron particles (CIPs) and polydimethylsiloxane elastomer matrix can be easily deformed. The deformation of MRM is investigated by the digital image correlation method. The off-plane displacement is positively related to both of the CIPs mass fractions and magnetic field strength. The sound absorption performance of MRM sound absorber is investigated and it is found that the thickness of the membrane, CIPs mass fractions, and air cavity length behind the membrane significantly influence the sound absorption performance. The magnetic field can adjust the sound absorption frequency without affecting the high acoustical absorption coefficients. The double-layer membrane structure has two sound absorption peaks within the testing frequency range and further improves the frequency adjustability of the sound absorber. Therefore, it is expected to be a particularly promising alternative for active sound absorption. Finally, the numerical solutions calculated by the equivalent circuit method also support the experimental results.

Keywords: magnetorheological elastomer, magnetostriction, membrane, deformation, sound absorber

OPEN ACCESS

Edited by:
Jong-Seok Oh,
Kongju National University,
South Korea

Reviewed by:
Xufeng Dong,
Dalian University of Technology, China
Anastasiia O. Krushynska,
University of Groningen, Netherlands

***Correspondence:**
Xinglong Gong
gongxl@ustc.edu.cn,
Shouhu Xuan
xuansh@ustc.edu.cn

Speciality section:
This article was submitted to Smart Materials, a section of the journal Frontiers in Materials

Received: *26 August 2020*
Accepted: *06 October 2020*
Published: *30 October 2020*

Citation:
Sun C, Cao X, Zhou X, Gong X and Xuan S (2020) Deformation Dependent Sound Absorption Property of a Novel Magnetorheological Membrane Sound Absorber. Front. Mater. 7:598973. doi: 10.3389/fmats.2020.598973

INTRODUCTION

The membrane sound absorber is a widely used sound absorption structure, which is of thin thickness, high sound absorption coefficients and wide tunable frequency range (Zhao et al., 2017; Gai et al., 2018; Liu et al., 2019a), and has attracted great interest to researchers who want to reduce sound emissions in the last decades. A typical membrane absorber is composed of a single membrane and an air cavity behind it. The sound absorption properties of membrane absorbers are mainly influenced by the surface density, membrane tension and air cavity length (Jimenez et al., 2016; Ahmed et al., 2019). In recent years, most of the researches were focused on the traditional membrane sound absorbers. Maa firstly proposed the basic theory and design principles of the micro-perforated panel absorbers (Maa, 1975). His theoretical work laid the foundation for other similar sound absorption structures (Reto and Kurt, 2015; Takeshi and Kimihiro, 2015; Arenas and Ugarte, 2016). Kang and Fuchs concluded the equivalent circuit method for different kinds of membrane sound absorbers (Kang and Fuchs, 1999). Kimihiro et al. investigated the resonance effect of micro-perforated membrane absorbers and discussed the absorption mechanisms of membrane-type absorbers (Kimihiro et al., 2009). Very recently, Zhu et al. installed a

lightweight membrane-type resonator in the back cavity of perforated membrane absorbers to combine into a compound sound absorber and further improved the adjusting ability for sound absorption (Zhu et al., 2018b).

The membrane sound absorber with tunable acoustic properties is very important for their practical application. However, the acoustic properties of the existing membranes are usually un-tunable once the materials are prepared. Magnetorheological (MR) materials are a kind of smart materials (Ju et al., 2016; Xu et al., 2018) whose mechanical properties can be controlled by applying an external magnetic field. The mechanical properties and magnetic controlled deformation of MR materials have been systematically investigated. Due to the tunable mechanical characteristics, MR materials have been widely used in vibration control (Fu et al., 2016; Liu et al., 2019b; Zhang et al., 2019), magnetic sensing (Ding et al., 2018; Ren et al., 2018; Hu et al., 2020), magnetic controlled movement (Lum et al., 2016; Chen et al., 2018; Ubaidillah et al., 2019) and robot manufacturing (Eric et al., 2014; Feng et al., 2017; Vien et al., 2019). In consideration of their easy deformation, tunable mechanical properties and contactless magnetic actuation, the MR materials are expected to have wonderful performance in sound absorption. However, few works have been reported on employing MR materials in sound absorption and investigating their acoustic mechanism.

In this work, the MR membrane (MRM) is used to replace the normal membrane in traditional membrane absorbers to develop a novel magnetorheological sound absorber. The magnetic field dependent mechanical properties, deformation and sound absorption capacity were investigated. A finite element simulation was carried out to confirm the experimental results of the deformation. The sound absorption performance of the MRM sound absorber was measured and the MRM sound absorber had excellent sound absorption properties and frequency adjustable performance. The equivalent circuit method was employed to calculate the sound absorption coefficient and the numerical results agreed with the experimental discussion. Therefore, the magnetorheological membrane sound absorbers are expected to be a particularly promising alternative for active sound absorption.

EXPERIMENT

Materials

Carbonyl iron particles (CIPs) were brought from BASF in Germany and the average size of CIPs is 7μm. Fe_3O_4 particles were produced by Chengxin Metal Materials Co., Ltd. The polydimethylsiloxane (PDMS) precursor and curing agent (Sylgard 184) were obtained from Dow Corning.

Preparation of the Magnetorheological Membranes

The fabrication processes of the magnetorheological membranes were schematically illustrated in **Figure 1**. The PDMS matrix, curing agent and iron particles were mixed up in different proportions and the mixture was vacuumed to remove trapped bubbles for 30 min. The ratio of the matrix to the curing agent was 10:1 and the CIPs mass fractions were set as 10, 20, 30, and 50 wt% respectively. After that, the mixture was poured on the rotor of a spin coater. The rotor rotated at 1,000–1,500 rpm for 1 min and the mixture was homogenized to be a membrane. Then, the membrane was cured at 100°C for 10 min to be vulcanized. Finally, the prepared magnetorheological membranes were fixed by the rigid ring with a radius of 15 mm and thickness of 2 mm for sound absorption test.

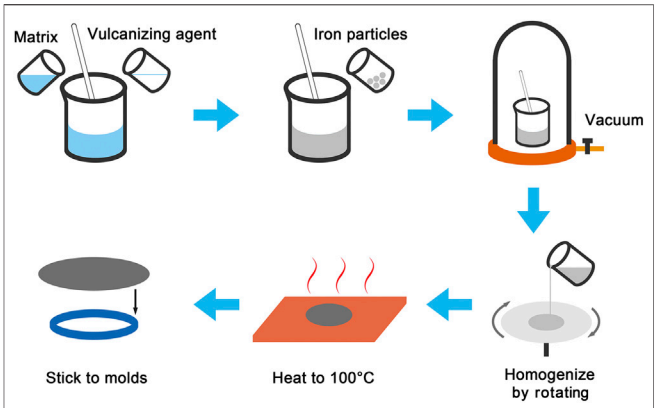

FIGURE 1 | Schematic diagram of the material preparation process.

Magnetic Induced Deformation of Magnetorheological Membranes

The digital image correlation (DIC) method was employed to investigate the magnetic induced deformation of MRMs and the scheme of the commercial DIC analyzer (PMLAB DIC-3D, Nanjing PMLAB Sensor Tech. Co., Ltd.) was shown in **Figure 4A**. DIC is a far-field and full field measurement with strong anti-interference ability and high measurement accuracy (Gao et al., 2015; Enrico et al., 2017). It has been widely applied in measuring the deformation of materials or structures (Zhang et al., 2005; Jiang et al., 2007). The MRM was fixed by a rigid ring and sprayed with white paint spots evenly as marks. Two pictures of the painted membrane were taken from different directions and the location information of the marked points were recorded. Then, the membrane deformed under the magnetic field and another two pictures were taken to record the deformation. Finally, the deformation of the MRM was calculated. In this experiment, the deformation of MRMs with different components was measured to investigate the influence factors of displacement. The prepared MRMs were placed 2 mm above the central axis of an electromagnet coil. The outer and inner diameters of the electromagnet coil were 95 and 50 mm respectively. The size of the electromagnet coil was large enough to ensure that the magnetic field around the sample was relatively uniform. The magnetic fields at the center of the MRM surface were adjusted from 60 and 180 mT by controlling the current in the electromagnet coil.

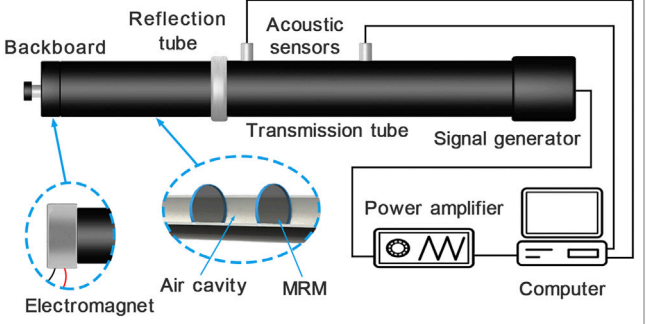

FIGURE 2 | Schematic diagram of the acoustic tube.

Sound Absorption of the Magnetorheological Membrane Sound Absorber

The sound absorption tests were carried out by an acoustic test system. The system consists a signal generator, a power amplifier, a sound transmission tube, a sound reflection tube, two acoustic sensors and a computer used for calculation (**Figure 2**). The MRM was fixed by a rigid ring with a radius of 15 mm and thickness of 2 mm and placed on the front end of the sound reflection tube. The sound waves used in experimental tests were pink noise, which was one of the most commonly used acoustic waves in acoustic tests.

When the samples were tested, the acoustical signal was generated from the signal generator controlled by the computer, amplified by the power amplifier, and spread into the sound transmission tube. Then, the acoustical signal was reflected at the sample and returned to the sound transmission tube. In the whole process, two acoustic sensors located at the sound transmission tube recorded the amplitude and phase information of the acoustic signal. In order to guarantee the accuracy of test results, the power amplifier was supposed to make sure that the incident acoustic signals were controlled between 90 and 110 dB. Finally, the acoustic signals were processed with the transfer function method in the computer to calculate the sound absorption curve. When the magnetic field was applied, the backboard was replaced by an electromagnet coil (**Figure 2**), which could play the same role as the backboard.

RESULT AND DISCUSSION

Characterization of Magnetorheological Membranes

The physical pictures and SEM images of the MRMs were shown in **Figures 3A–D**. The surface of MRMs was smooth and the colors of the surface darkened gradually as the increasing of CIPs mass fractions (**Figure 3A**). Subtle ripples on the membrane surface observed in the SEM were due to the rotation during the preparation process (**Figure 3B**). CIPs were evenly distributed in the PDMS matrix (**Figure 3C**). MRMs were 40–180 μm in thickness and they tended to be stuck together because of their extra thin thickness, thus they were usually fixed on the framework during the experiment. When the rheological properties were investigated, MR elastomers with different mass fractions were prepared as disks with 0.5 mm in thickness and 10 mm in radius. Magnetic field scanning tests were carried out by the commercial rheometer (Physica MCR 301, Anton Paar) and **Figure 3F** shows their rheological properties. The initial storage moduli of MR elastomers were only 0.29 MPa, which meant that they were relatively easy to deform. The storage modulus increased with increasing of the magnetic field and tended to be stable when the magnetic field exceeded 400 mT. At the same time, the samples with higher mass fraction were strengthened more obviously by the magnetic field. Therefore, the mechanical properties of MR materials can be controlled by the external magnetic field. The hysteresis loops were also measured to characterize the magnetization of MRMs (**Figure 3E**). The magnetization had an important influence on the mechanical behavior in a magnetic field. With increasing of CIPs from 10 to 50 wt%, the saturation magnetizations were proportional to CIPs mass fractions and could reach to 96.26 emu/g. These high magnetizations must be responded for large magnetic deformation.

Magnetic induced deformation of Magnetorheological Membranes

When MRMs were exposed to a magnetic field, the ferromagnetic particles in MRMs were magnetized under the magnetic field and magnetic dipoles were induced within adjacent ferromagnetic particles. The magnetic dipoles were subject to magnetic forces in the magnetic field and drove the matrix to deform. The magnetic dipole moment $\vec{m}$ and the force on the magnetic dipoles $\vec{F}$ were controlled by the following expressions (Boyer and Timothy, 1998):

$$\vec{B} = \left(3\hat{n}\hat{n}\cdot\vec{m} - \vec{m}\right)\mu_0 \Big/ 4\pi r^3 \quad (1)$$

$$\vec{F} = \nabla\left(\vec{m}\cdot\vec{B}\right) \quad (2)$$

where $\vec{B}$ is the magnetic flux density, $\vec{m}$ is the magnetic dipole moment, μ_0 is the permeability of vacuum, r is the radius of the magnetic particles and $\hat{n}$ is the unit vector of r. The hysteresis loops displayed in **Figure 3E** demonstrated the magnetization of the MR materials under a certain magnetic field. Obviously, the samples with higher CIPs mass fractions performed stronger magnetization.

The deformations of MRMs were measured by the DIC method. The MRM was fixed flat on a frame and set on the central axis of an electromagnet coil. At the initial state, its off-plane displacement was zero. Then the MRM sagged inward slowly with increasing of the magnetic field. **Figure 4B** showed the image of the membrane deformation and the membrane was significantly deformed by applying the magnetic field. The results of the deformation test were displayed in **Figure 4E**, where the

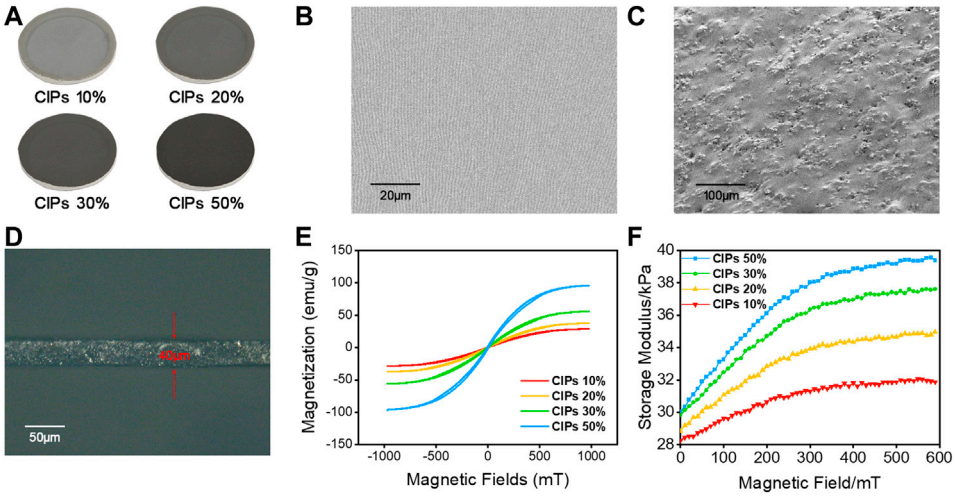

FIGURE 3 | Diagram of the samples with different mass fractions **(A)**, SEM images of the surface **(B)** and the longitudinal section **(C)**, thickness of the sample under the optical microscope **(D)**, storage modulus **(E)** and hysteresis loops **(F)** of the samples with different mass fractions.

solid data points represented the experimental off-plane displacement of the membrane. The max off-plane displacement obtained by applying a 180 mT magnetic field to the 50 wt% CIP-MRM could reach as large as 1.69 mm. The deformation was significantly related to the magnetic field strength. A larger deformation was obtained under a larger magnetic field, because the stronger magnetic dipoles were induced in the CIPs were magnetized into stronger magnetic dipoles under large magnetic fields. At the same time, the mass fraction of CIPs also had a distinct influence on the deformation. The schematic diagram of the deformation of membranes with different mass fractions were showed in **Figure 4D**. The mass fractions of CIPs directly determined the number of magnetic dipoles. The MRMs with higher mass fractions can be magnetized to form more magnetic dipoles which further led to stronger magnetic force.

The finite element simulation of the deformation was carried out to calculate the numerical value of the deformation under different magnetic field. The simulation was carried out by the COMSOL Multiphysics. The solids included the MRM, electromagnet coil, iron core, and air region. The current in the electromagnet coil was adjusted to turn the magnetic field to be similar to the magnetic field intensity in the forenamed experiment. Each solid was endowed with the corresponding material properties including the mechanical and magnetic parameters. The inside selection was chosen as the mesh operation and then the deformation could be obtained. The deformed shape of the membrane was displayed in **Figure 4C**. The dotted curves represented the numerical off-plane displacement of the membrane (**Figure 4E**). The max numerical off-plane displacement was 1.78 mm, which was closely similar to the experimental result. The numerical and experimental curves had the same tend and the experimental results were consistent with the numerical consequences.

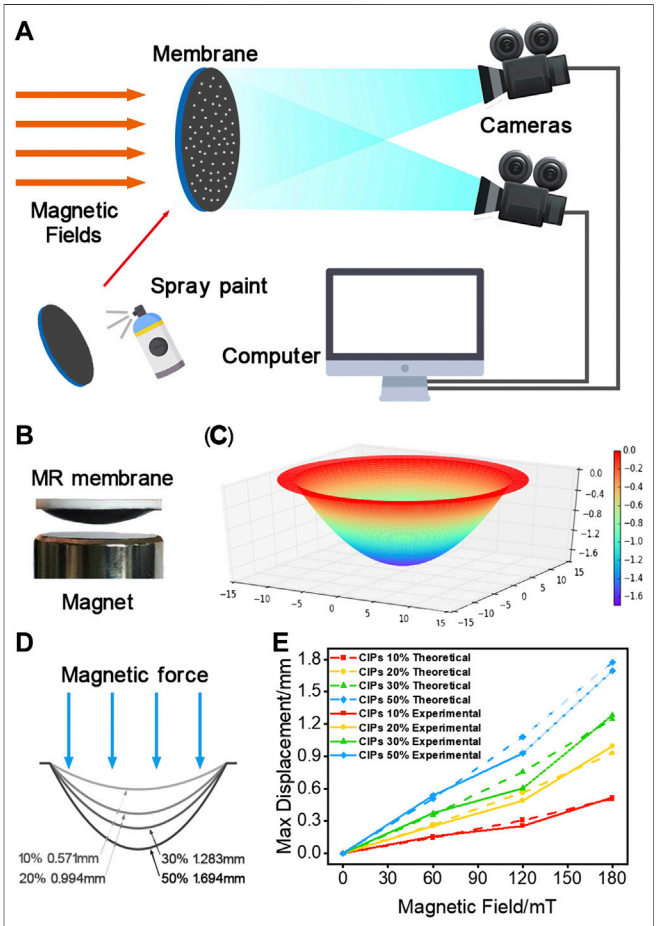

FIGURE 4 | Schematic diagram of the DIC **(A)**. Deformation of the MRMs under a magnetic field **(B)**. Simulation result **(C)** and deformation diagram **(D)** of MRMs. Comparison of experimental and theoretical results for the max off-plane displacements **(E)**.

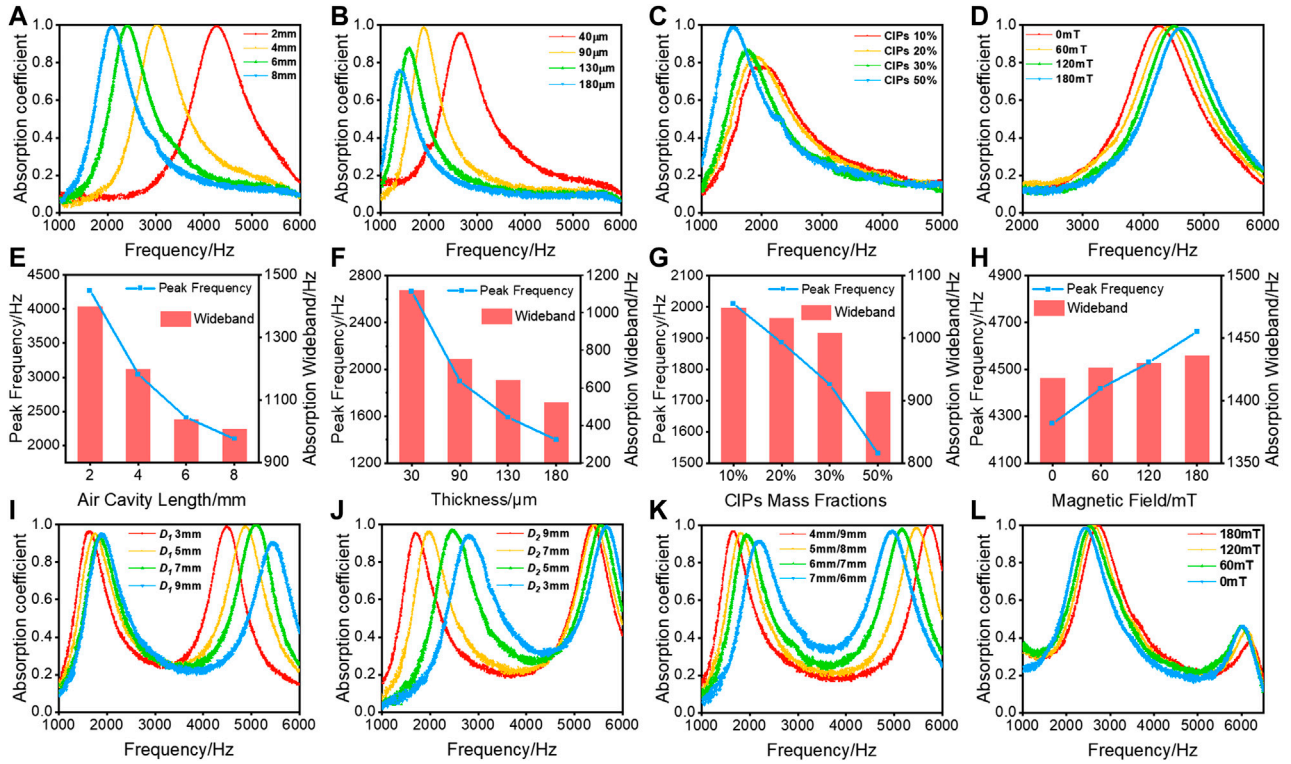

FIGURE 5 | The influences of the air cavity length behind the membrane **(A)**, the thickness of the membrane **(B)**, mass fractions of CIPs **(C)**, the magnetic field **(D)** on the sound absorption curves. The peak frequency and the sound absorption wideband corresponding to the above image **(E–H)**. The sound absorption curves of the double-layer membrane structure with the varied length of the air cavity **(I–K)**. Influences of the magnetic field on the double-layer membrane structure **(L)**.

Sound Absorption of the Magnetorheological Membrane Sound Absorber

When a sound wave encountered a wall or other obstacle, part of the sound energy was reflected, and part of the sound energy was absorbed by the wall or obstacle and converted into heat energy. The other part of the sound energy was transmitted to the other side. The sound absorption capacity of a certain material or structure was called the sound absorption coefficient. The definition of the sound absorption coefficient can be expressed as follows (Soltani and Zerrebini, 2012):

$$\alpha = \frac{E_a + E_t}{E} = \frac{E - E_r}{E} = 1 - r \tag{3}$$

where α is the sound absorption coefficient, r is the sound reflection coefficient, E is the total sound energy incident on the material, E_a is the sound energy absorbed by the material, E_t is the sound energy transmitted through the material, E_r is the sound energy reflected by the material. The sound absorption coefficient is normally between 0 and 1. The materials with lager sound absorption coefficient have better sound absorption performance. Generally, the materials with a sound absorption coefficient smaller than 0.2 have little sound absorption capacity and they are not suitable for sound absorption. The materials with a sound absorption coefficient greater than 0.4 can be used for sound absorption in practical application. Furthermore, if the sound absorption coefficient is larger than 0.5, this kind of material is considered to have excellent sound absorption capacity.

The sound absorption tests were carried out by the acoustic tube under different conditions. The thickness of MRMs, mass fractions of CIPs, air cavity length behind the membrane, and magnetic field strength were main factors that affected the sound absorption performance. The thickness and CIPs mass fraction of the control group were 40 μm and 50 wt% respectively. As shown in **Figures 5A-D**, the sound adsorption curves were unimodal in the measured frequency range. The MRM and air cavity behind the membrane formed a sound-absorbing structure together and this structure had its own natural frequency. When the sound wave was incident on the sound absorption structure, the acoustic energy would be transformed into the thermal energy and kinetic energy due to the damping and vibration. If the frequency of the incident sound wave was close to the natural frequency of the sound absorption structure, the resonance phenomenon occurred. The vibration of the sound absorption structure and the sound energy dissipation increased significantly, thus the sound absorption coefficient reached the maximum value. Although the natural frequency of a composite structure is difficult to estimate in a simple way, it is usually positively related to modulus and inversely related to mass or surface density. Obviously, most MRM sound absorbers have excellent

sound absorption properties at their natural frequencies where the sound absorption coefficient is close to 1. This is because the MRM is thin and easy to deform, and it can vibrate intensely at the resonant frequency.

Here, the sound absorption wideband is defined as the frequency range where the sound absorption coefficient is larger than half of the max sound absorption coefficient. The sound absorption wideband is usually positively related to the max sound absorption coefficient and the peak frequency (Lee and Lee, 2007; Zhu et al., 2018b). The peak value of the sound adsorption and sound absorption wideband were displayed in **Figures 5E-H**. The air cavity length behind the membrane has the most significant influence on the sound absorption frequency. The peak sound absorption frequency changed from 4,260 to 2,088 Hz when the air cavity length behind the membrane increased from 2 to 8 mm (**Figures 5A,E**). The peak sound absorption coefficients were all close to 1 in **Figure 5A**. Therefore, the air cavity length behind the membrane can adjust the natural frequency in a wide frequency range without changing the good deformability of MRMs. Specially, the sound absorption frequency can be adjusted drastically while ensuring a high sound absorption coefficient.

On the contrary, with increasing of MRMs thickness, the peak sound absorption shifted to the lower frequency and the sound absorption coefficient decreased (**Figure 5B**). Though the natural frequency was adjusted by increasing the membrane thickness, the MRMs became harder and more difficult to be vibrated. In this case, less sound energy was consumed by vibration, thus the sound absorption coefficient decreased. Moreover, the membrane with lower CIPs mass fraction exhibited lower sound absorption coefficient, because it was too soft for effective vibration (**Figure 5C**). The magnetic field can attract MRMs to deform in the direction of the magnetic field and its influence on the sound absorption properties was similar to the air cavity length behind the membrane (**Figure 5D**). They both adjusted the sound absorption properties by changing the air cavity length. Here, the magnetic field can tune the whole structure without touching or modifying structure, and this characteristic is of great significance in practical application.

Furthermore, a double-layer membrane structure was investigated to improve the control of the sound absorption frequency. The double-layer membrane structure was developed by putting another membrane in the air cavity of the initial structure and formed two air cavities (**Figure 2** sectional view). The sound absorption tests of the double-layer membrane structure were investigated. Different from the single-layer membrane, there were two sound absorption peaks on the sound absorption curve of the double-layer membrane structure (**Figures 5I–L**), thus it has two closer natural frequencies. The air cavities length behind two membranes was the most effective parameter to control the sound absorption properties. It can adjust the sound absorption frequency easily and maintain a high sound absorption coefficient simultaneously. The distance between two membranes was recorded as D_1 and the distance between the back membrane and the container wall was recorded as D_2 (**Figure 6C**). The two sound absorption frequencies were

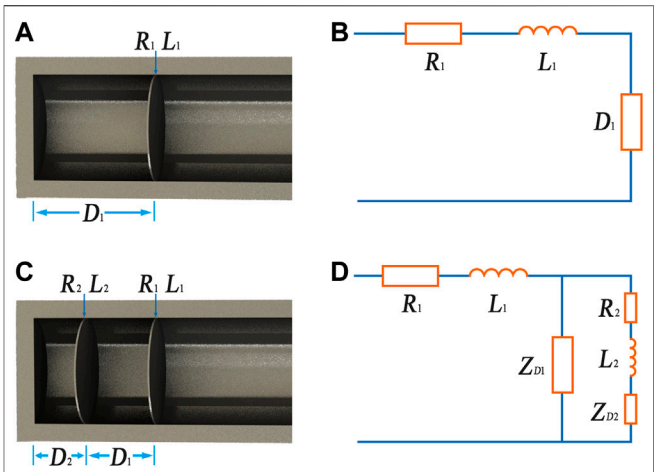

FIGURE 6 | Schematic diagram **(A)** and equivalent circuit **(B)** of the single-layer membrane structure, schematic diagram **(C)** and equivalent circuit **(D)** of the double-layer membrane structure.

significantly related to D_1 and D_2 as shown in **Figures 5I-K**. The increased D_1 or D_2 would decrease the sound absorption frequency. However, the effects of them were not exactly the same. When D_1 remained constant and D_2 increased, the low frequency peak moved to low frequency and the high frequency peak stayed still. Correspondingly, when D_2 remained constant and D_1 increased, the high frequency peak moved to low frequency and the low frequency peak was kept. If D_1 and D_2 were changed at the same time (their sum kept constant), the two sound absorption peaks would move closer or away to each other. By combining these two adjustment methods, it is convenient to design a sound absorber with tuning sound absorption frequency within the tested frequency range. The influence of the magnetic field on the double-layer membrane structure was also investigated. Similar to the single-layer membrane structure, the magnetic field can decrease the air cavities length and lead the sound absorption peak shift to the high frequency. Here, due to the limitation of the small magnetic field, the adjustment range is not particularly wide.

Numerical Solutions of Sound Absorption Coefficients

In order to further understand the sound absorption performance of the sound absorption structure, an equivalent circuit method was employed to predict the sound absorption curves (Kang and Fuchs, 1999). The equivalent circuit was displayed in **Figure 6**, in which R and L were the acoustic resistance and reactance of the membrane, D was the air cavity length and Z_c was the impedance of the air cavity. The impedance of the entire equivalent circuit Z_0 can be calculated by this equivalent circuit. The normalized specific acoustic impedance of the entire equivalent circuit z was defined as follows:

$$z = \frac{Z_0}{\rho c} \tag{4}$$

Then, the sound absorption coefficient can be calculated by a classic formula:

$$\alpha = \frac{4Re(z)}{[1 + Re(z)]^2 + [Im(z)]^2} \quad (5)$$

where z is the normalized specific acoustic impedance of the entire equivalent circuit and it consists of two parts, the acoustic impedance of the membrane z_m **6** and the acoustic impedance air cavity z_c **7**:

$$z_m = \frac{R + jL}{\rho c} = r + j\omega m \quad (6)$$

$$z_c = -jcot\frac{\omega D}{c} \quad (7)$$

where ρ is the density of air, c is the sound velocity in air, m is the surface density of the membrane, ω is the angular frequency and $\omega = 2\pi f$, f is the frequency, D is the air cavity length, r is the normalized specific sound resistance and $r = 80.42df^{1/2}$, d is the membrane thickness. According to the equivalent circuit diagram in **Figure 6B**, the normalized specific acoustic impedance z can be calculated as follows:

$$z = z_m + z_c = r + j\left(\omega m - cot\frac{\omega D}{c}\right) \quad (8)$$

Then, the final expression of the sound absorption coefficient can be expressed as:

$$\alpha = \frac{4r}{[1 + r]^2 + \left[\omega m - cot\frac{\omega D}{c}\right]^2} \quad (9)$$

The sound absorption coefficient reaches the maximum value when $\omega m = \cot\left(\frac{\omega D}{c}\right)$ and the maximum absorption coefficient is:

$$\alpha_{max} = \frac{4r}{[1 + r]^2} \quad (10)$$

For the case of double membranes, there are two air cavities between the membranes and the container wall. The expression of equivalent impedance can be derived with the equivalent circuit diagram in **Figure 6D** as follows:

$$\begin{aligned} z &= r_1 + j\omega m_1 + \left[\frac{1}{z_{D1}} + \frac{1}{r_2 + j\omega m_2 + z_{D2}}\right]^{-1} \\ &= r_1 + j\left[\omega m_1 - \cot\left(\frac{\omega D_1}{c}\right)\right] \\ &\quad + \frac{cot^2(\omega D_1/c)}{r_2 + j[\omega m_2 - cot(\omega D_1/c) - cot(\omega D_2/c)]} \end{aligned} \quad (11)$$

Then the sound absorption coefficient of double membranes can be calculated by bringing the **Eq. 11** into the **Eq. 5**, as shown in **Figure 7**. The solid curves and the dash dot curves represented the experiment results and the numerical results respectively. **Figures 7A,B** showed the influences of the air cavity length and magnetic field strength on the sound absorption curves. The curves of numerical solutions basically coincided with the experimental results. The simulation of the double-layer membrane structure was displayed in **Figures 7C,D**. The sound absorption frequencies of the numerical curves and the experimental curves were slightly different, but the sound absorption curves of them were similar overall.

The parameters studied in this work all indirectly adjusted the sound absorption coefficient by changing the acoustic impedance of the structure. The membrane thickness and CIPs mass fractions changed the acoustic impedance of the membrane. The air cavity length behind the membrane and the magnetic field strength determined the acoustic impedance of the air cavity. More importantly, the increased thickness and mass fractions of CIPs also affected the deformability of the membrane. Therefore, with increasing of the MRM thickness and CIPs mass fractions, the max sound absorption coefficient decreased. Contrastively, the air cavity length behind the membrane and the strength of magnetic fields only changed the acoustic impedance of the air cavity to adjust the sound absorption coefficient but not the properties of MRMs, so they had little negative influence on the max sound absorption coefficient. As a result, the tunable range of the frequency for this kind of sound absorption structure is wide and the adjustment can be achieved by the remote magnetic field without touching the structure.

Finally, the MR membranes with Fe_3O_4 particles (Fe_3O_4-MRMs) were also investigated as a comparison (**Figure 8**). The saturation magnetization of Fe_3O_4 particles was smaller than CIPs. The mass fraction and thickness of the Fe_3O_4-MRMs were kept as the same to CIP-MRMs. Then, the deformation behavior of the Fe_3O_4-MRMs was tested and the results showed the max off-plane displacement of Fe_3O_4-MRMs was 1.27 mm. In comparison to the CIP-MRMs, the simulated deformation result for Fe_3O_4-MRMs was significantly lower under the same conditions, which must be responded for the weak magnetically induced dipoles (**Figure 8A**). **Figures 8B,C** displayed the comparison of the sound absorption curves and sound absorption frequency of the two kinds of MR membranes. Obviously, the frequency adjustment ability of Fe_3O_4-MRMs was relatively poorer, which should be due to the smaller deformation. Therefore, the deformation is the key to control sound absorption performance. The larger deformation gives chances to adjusted the sound absorption frequency in a wider frequency range.

CONCLUSION

This work reported a novel sound absorber based on MRMs and the sound absorber exhibited a magnetic field tunable absorption frequency with a wide range absorption efficiency. The thin MRMs were easy to be deformed under an external magnetic field. The max off-plane displacement reaches as large as 1.69 mm when a 180 mT magnetic field

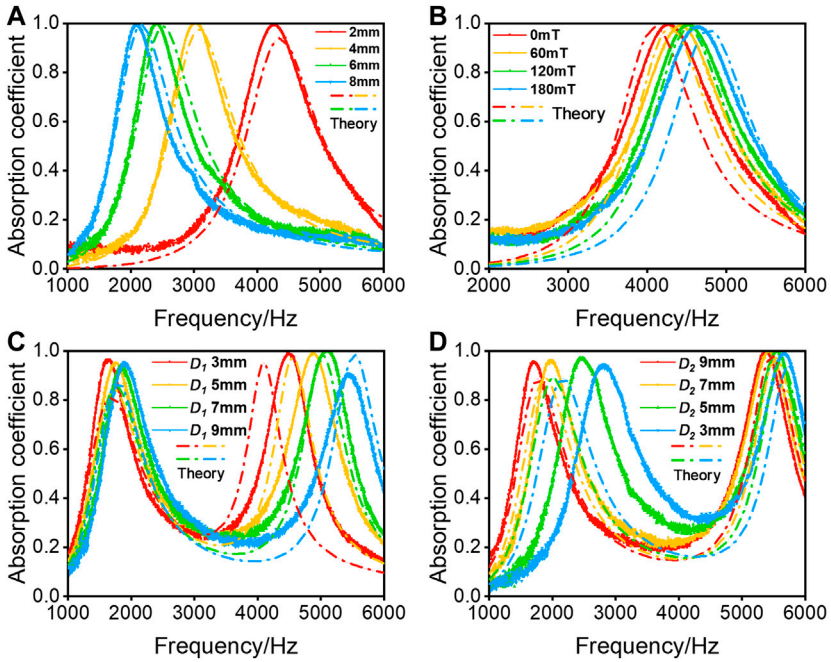

FIGURE 7 | Comparison of experimental and numerical results: the air cavities length **(A)**, the magnetic field **(B)**, the length of the front cavity of double-layer membrane structure **(C)**, the length of the back cavity of double-layer membrane structure **(D)**.

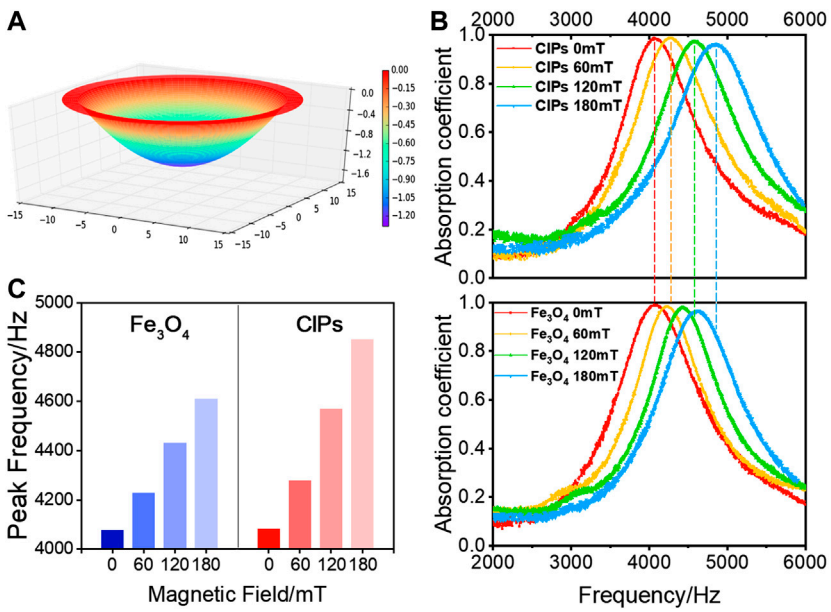

FIGURE 8 | Deformation and sound absorption properties of the Fe_3O_4-MRMs: deformation simulation diagram **(A)**, comparison of the sound absorption curves between Fe_3O_4-MRMs and CIP-MRMs **(B)**, comparison of the peak frequency between the Fe_3O_4-MRMs and CIP-MRMs **(C)**.

is applied on the 50 wt% CIP-MRM. The numerical analysis carried out by the finite element method confirmed that the off-plane displacement was positively related to the CIPs mass fractions and the magnetic field strength. Then, the influence of the membrane thickness, CIPs mass fractions, air cavity length behind the membrane, and the strength of the magnetic field on the sound absorption properties were investigated. The air cavity length and the strength of the magnetic field

not only adjusted the sound absorption frequency but also maintained the high sound absorption coefficient. As a result, the strength of the magnetic field can tune the sound absorption structure without touching or modifying the structure, thus it is of high potential for active sound absorption and remote control.

DATA AVAILABILITY STATEMENT

The original contributions presented in the study are included in the article, further inquiries can be directed to the corresponding author/s.

AUTHOR CONTRIBUTIONS

CS performed all the experiments and wrote the draft of the manuscript. XC, XZ, SX and XG revised and discussed the manuscript.

FUNDING

The financial supports from the National Natural Science Foundation of China (Grant No. 11822209, 12072338, 11702174), Joint Fund of USTC-National Synchrotron Radiation Laboratory (KY2090000055) and the Strategic Priority Research Program of the Chinese Academy of Sciences (Grant No. XDB22040502) are gratefully acknowledged.

REFERENCES

Ahmed, A., Noureddine, A., Morvan, O., and Olivier, D. (2019). Numerical and experimental investigations on the acoustic performances of membraned Helmholtz resonators embedded in a porous matrix. *J. Sound Vib.* 459, 114873. doi:10.1016/j.jsv.2019.114873

Arenas, J. P., and Ugarte, F. (2016). A note on a circular panel sound absorber with an elastic boundary condition. *Appl. Acoust.* 114, 10–17. doi:10.1016/j.apacoust.2016.07.002

Boyer, T. H., and Timothy, H. (1998). The force on a magnetic dipole. *Am. J. Phys.* 56, 688–692. doi:10.1119/1.15501

Chen, S. W., Li, R., Li, X., and Wang, X. J. (2018). Magnetic field induced surface micro-deformation of magnetorheological elastomers for roughness control. *Front. Mater.* 5, 76. doi:10.3389/fmats.2018.00076

Ding, L., Xuan, S., Pei, L., Wang, S., Hu, T., Zhang, S., and Gong, X. (2018). Stress and magnetic field bimode detection sensors based on flexible Cl/CNTs-PDMS sponges. *ACS Appl. Mater. Interfaces* 10, 30774–30784. doi:10.1021/acsami.8b11333

Enrico, D., Marta, P., Marco, P., Mario, G., Luca, C., and Gianluca, T. (2017). Precision of digital volume correlation approaches for strain analysis in bone imaged with micro-computed tomography at different dimensional levels. *Front. Mater.* 4, 31. doi:10.3389/fmats.2017.00031

Eric, D., Jiang, Z., Guo, Z. L., Edwards, M. R., and Metin, S. (2014). Continuously distributed magnetization profile for millimeter-scale elastomeric undulatory swimming. *Appl. Phys. Lett.* 104, 1121–1122. doi:10.1063/1.4874306

Feng, J. B., Xuan, S. H., Ding, L., and Gong, X. L. (2017). Magnetoactive elastomer/PVDF composite film based magnetically controllable actuator with real-time deformation feedback property. *Compos. Part A: Appl. Sci. Manuf.* 103, 25–34. doi:10.1016/j.compositesa.2017.09.004

Fu, J., Li, P. D., Wang, Y., Liao, G. Y., and Yu, M. (2016). Model-free fuzzy control of a magnetorheological elastomer vibration isolation system: analysis and experimental evaluation. *Smart Mater. Struct.* 25, 035030. doi:10.1088/0964-1726/25/3/035030

Gai, X. L., Xing, T., Li, X. H., Zhang, B., Cai, Z. N., and Wang, F. (2018). Sound absorption properties of microperforated panel with membrane cell and mass blocks composite structure. *Appl. Acoust.* 137, 98–107. doi:10.1016/j.apacoust.2018.03.013

Gao, Y., Cheng, T., Su, Y., Xu, X. H., Zhang, Y., and Zhang, Q. C. (2015). High-efficiency and high-accuracy digital image correlation for three-dimensional measurement. *Opt. Lasers Eng.* 65, 73–80. doi:10.1016/j.optlaseng.2014.05.013

Hu, T., Xuan, S. H., Ding, L., and Gong, X. L. (2020). Liquid metal circuit based magnetoresistive strain sensor with discriminating magnetic and mechanical sensitivity. *Sens. Actuators B Chem.* 314, 128095. doi:10.1016/j.snb.2020.128095

Jiang, H. F., Zhang, Q. C., Chen, X. D., Chen, Z. J., Jiang, Z. Y., Wu, X. P., et al. (2007). Three types of Portevin–Le Chatelier effects: experiment and modelling. *Acta Mater.* 55, 2219–2228. doi:10.1016/j.actamat.2006.10.029

Jiménez, N., Huang, W., Romero-Garcia, V., Pagneux, V., and Groby, J.-R. (2016). Ultra-thin metamaterial for perfect and quasi-omnidirectional sound absorption. *Appl. Phys. Lett.* 109, 121902.1–121902.4. doi:10.1063/1.4962328

Ju, B. X., Tang, R., Zhang, D. Y., Yang, B. L., Yu, M., Liao, C. R., et al. (2016). Dynamic mechanical properties of magnetorheological elastomers based on polyurethane matrix. *Polym. Compos.* 37, 1587–1595. doi:10.1002/pc.23330

Kang, J., and Fuchs, H. V. (1999). Predicting the absorption of open weave textiles and micro-perforated membranes backed by an air space. *J. Sound Vib.* 220, 905–920. doi:10.1006/jsvi.1998.1977

Kimihiro, S., Masayuki, M., and Motoki, Y. (2009). A note on the relationship between the sound absorption by microperforated panels and panel/membrane-type absorbers. *Appl. Acoust.* 70, 1131–1136. doi:10.1016/j.apacoust.2009.03.003

Lee, Y. Y., and Lee, E. W. M. (2007). Widening the sound absorption bandwidths of flexible micro-perforated curved absorbers using structural and acoustic resonances. *Int. J. Mech. Sci.* 49, 925–934. doi:10.1016/j.ijmecsci.2007.01.008

Liu, C. R., Wu, J. H., Lu, K., Zhao, Z. T., and Huang, Z. (2019a). Acoustical siphon effect for reducing the thickness in membrane-type metamaterials with low-frequency broadband absorption. *Appl. Acoust.* 148, 1–8. doi:10.1016/j.apacoust.2018.12.008

Liu, X. H., Wang, N. N., Wang, K., Huang, H., Li, W. H., Sarkodie-Gyan, T., and Li, W. (2019b). Optimizing vibration attenuation performance of a magnetorheological damper-based semi-active seat suspension using artificial intelligence. *Front. Mater.* 6, 269. doi:10.3389/fmats.2019.00269

Lum, G. Z., Ye, Z., Dong, X. G., Marvi, H., Erin, O., Hu, W. Q., et al. (2016). Shape-programmable magnetic soft matter. *Proc. Natl. Acad. Sci. U.S.A.* 113, E6007–E6015. doi:10.1073/pnas.1608193113

Maa, D. Y. (1975). Theory and design of microperforated panel sound-absorbing constructions. *Sci. China Ser. A* xviii, 55–71. doi:10.1126/science.187.4182.1213

Ren, L., Sun, S. S., Casillasgarcia, G., Nancarrow, M. J. B., Peleckis, G., Turdy, M., et al. (2018). A liquid-metal-based magnetoactive slurry for stimuli-responsive mechanically adaptive electrodes. *Adv. Mater.* 30, 1802595. doi:10.1002/adma.201802595

Reto, P., and Kurt, H. (2015). Predicting sound absorption coefficients of lightweight multilayer curtains using the equivalent circuit method. *Appl. Acoust.* 92, 27–41. doi:10.1016/j.apacoust.2015.01.003

Soltani, P., and Zerrebini, M. (2012). The analysis of acoustical characteristics and sound absorption coefficient of woven fabrics. *Text. Res. J.* 82, 875–882. doi:10.1177/0040517511402121

Takeshi, O., and Kimihiro, S. (2015). A finite-element formulation for room acoustics simulation with microperforated panel sound absorbing structures: verification with electro-acoustical equivalent circuit theory and wave theory. *Appl. Acoust.* 95, 20–26. doi:10.1016/j.apacoust.2015.02.012

Ubaidillah, S., Purnomo, E. D., Ismail, H., Choi, S.-B., Aziz, A. A., and Mazlan, S. A. (2019). Swelling, thermal, and shear properties of a waste tire rubber based magnetorheological elastomer. *Front. Mater.* 6, 47. doi:10.3389/fmats.2019.00047

Vien, Q. N., Duy, T. L., Dai, H. L., Nguyen, Q. H., and Choi, S. B. (2019). Material characterization of MR fluid on performance of MRF based braker. *Front. Mater.* 6, 125. doi:10.3389/fmats.2019.00125

Xu, J. Q., Wang, P. F., Pang, H. M., Wang, Y. P., Wu, J., Xuan, S. H., et al. (2018). The dynamic mechanical properties of magnetorheological plastomers under high strain rate. *Compos. Sci. Technol.* 159, 50–58. doi:10.1016/j.compscitech.2018.02.030

Zhang, Q. C., Jiang, Z. Y., Jiang, H. F., Chen, Z. J., and Wu, X. P. (2005). On the propagation and pulsation of Portevin-Le Chatelier deformation bands: an experimental study with digital speckle pattern metrology. *Int. J. Plast.* 21, 2150–2173. doi:10.1016/j.ijplas.2005.03.017

Zhang, Y. F., Fang, F. Z., Huang, W., Chen, Y. C., and Yu, M. (2019). Dynamic mechanical hysteresis of magnetorheological elastomers subjected to the cyclic loading and periodic magnetic field. *Front. Mater.* 6, 292. doi:10.3389/fmats.2019.00292

Zhao, J. J., Li, X. H., Wang, Y. Y., Wang, W. J., Zhang, B., and Gai, X. L. (2017). Membrane acoustic metamaterial absorbers with magnetic negative stiffness. *J. Acous. Soc. Am.* 141, 840–846. doi:10.1121/1.4976042

Zhu, X. Z., Chen, Z. B., Jiao, Y. H., and Wang, Y. P. (2018b). Broadening of the sound absorption bandwidth of the perforated panel using a membrane-type resonator. *J. Vib. Acoust.* 140, 031014. doi:10.1016/j.ijmecsci.2007.01.00810.1115/1.4038942

Conflict of Interest: The authors declare that the research was conducted in the absence of any commercial or financial relationships that could be construed as a potential conflict of interest.

frontiers in Materials

ORIGINAL RESEARCH
published: 19 February 2021
doi: 10.3389/fmats.2021.594843

Experimental Study of a Variable Stiffness Seat Suspension Installed With a Compact Rotary MR Damper

Shuaishuai Sun[1,2,3], Jian Yang[4], Penghui Wang[1,3], Masami Nakano[2], Longjiang Shen[5], Shiwu Zhang[3] and Weihua Li[1]**

[1]School of Mechanical, Materials, Mechatronic and Biomedical Engineering, University of Wollongong, Wollongong, NSW, Australia, [2]New Industry Creation Hatchery Center (NICHe), Tohoku University, Sendai, Japan, [3]CAS Key Laboratory of Mechanical Behavior and Design of Materials, Department of Precision Machinery and Instrumentation, University of Science and Technology of China, Hefei China, [4]School of Electrical Engineering and Automation, Anhui University, Hefei, China, [5]Hunan Bogie Engineering Research Center, Zhuzhou, China

Traditional MR seat suspension without stiffness control is not able to avoid the resonance between the excitation and the seat, though it can dampen the vibration energy. To solve this problem, this paper proposed a variable stiffness (VS) magnetorheological (MR) damper to implement an advanced seat suspension. Its natural frequency can be shifted away from the excitation frequency through the variations of stiffness, thereby realizing the non-resonance control. The new seat suspension is designed and prototyped first, and then its dynamic property under different energizing current, excitation amplitude, and excitation frequency was tested using an MTS machine. The testing results verified its stiffness controllability. The vibration attenuation performance of the seat suspension was also evaluated on a vibration shaking table. The vibration reduction performance of the seat suspension was evaluated under two kinds of excitations, i.e., harmonic excitation and random excitation; the experimental results indicate that the new seat suspension outperforms passive seat suspensions regarding their ride comfort.

Keywords: seat suspension, variable stiffness, compact rotary MR damper, vibration control, non-resonance

OPEN ACCESS

Edited by:
Miao Yu,
Chongqing University, China

Reviewed by:
Xian-Xu Bai,
Hefei University of Technology, China
Luwei Zhou,
Fudan University, China

****Correspondence:***
Shuaishuai Sun
sssun@ustc.edu.cn
Weihua Li
weihuali@uow.edu.au

Specialty section:
This article was submitted to Smart Materials, a section of the journal Frontiers in Materials

Received: *14 August 2020*
Accepted: *25 January 2021*
Published: *19 February 2021*

Citation:
Sun S, Yang J, Wang P, Nakano M, Shen L, Zhang S and Li W (2021) Experimental Study of a Variable Stiffness Seat Suspension Installed With a Compact Rotary MR Damper. Front. Mater. 8:594843. doi: 10.3389/fmats.2021.594843

INTRODUCTION

Vibration transferred from uneven road surfaces, vibrating tools, and vibrating machinery to a vehicle driver's body significantly reduces the driver's comfort. This problem is much more serious in the mining industry, construction sites, and agriculture fields. Long-time exposure to the vibration will cause significant health disorders to seat occupants (National Hazard Exposure Worker Surveillance, 2009, Motmans, 2012). For example, vibration has significant negative impacts on the driver's health, it is also easy to induce drivers' fatigue, which has been a primary contributing factor in a significant percentage of crashes, including fatal crashes (DETR, 2000, Haworth, 1998; Legislative Assembly of Queensland: Parliamentary Travelsafe Committee, 2005). Physical pain is very common in jobs that involve driving, especially those over long hours and distances, and over rough environments with off-road vehicles or machinery operation (such as construction machines or trucks, mining vehicles, and excavators). To actively reduce the driver's fatigue and improve the driver's health, an advanced seat suspension which is able to provide better ride comfort is urgently needed.

To date, passive (Zhao et al., 2018), semi-active (Gad et al., 2017; Sun et al., 2017; Ning et al., 2018; Phu et al., 2018), and active (Ning et al., 2017; Alfadhli et al., 2018; Maciejewski et al., 2018) seat

suspensions have been proposed. A passive seat suspension is simple, reliable, and cost-effective. However, it cannot provide a controllable force and consequently, its performance is inevitably limited. While maintaining the geometric and dynamical properties of a passive suspension structure, an active or semi-active device has been considered for incorporation in modern seat suspension structures to meet the increasingly demanding requirements. In particular, semi-active seat suspensions offer desirable performance comparable to that brought by active seats without requiring high power consumption and expensive hardware (Li et al., 2014; Sun et al., 2019; Yang et al., 2020b). In the past decades, a kind of smart material, magnetorheological fluid (MRF), has been a preferred choice to make semi-active devices realistic (Yu et al., 2009; Guo et al., 2015; Yu et al., 2016; Yu et al., 2018; Deng et al., 2019; Nguyen et al., 2019; Tu et al., 2019). MRF has magnetically sensitive rheological properties and has gained in popularity since entering the commercial automotive market. MRF is very responsive to magnetic field, with an estimated response time of less than 10 ms (Carlson and Jolly, 2000; Eshaghi et al., 2015; Nakano, 2015; Abe et al., 2019), and requires relatively low power to operate (Li et al., 2003; Hu et al., 2014; Liu et al., 2019; Yu et al., 2019). Semi-active seat suspensions using MR dampers have oriented a new research direction and achieved improved performance on vibration mitigations. For example, Choi and Han (Choi and Han, 2007; Phu et al., 2018) applied MR dampers to attenuate the vertical vibration of a seat. Wereley's group (Choi and Wereley, 2005; Wereley et al., 2011) investigated the application of an MR damper in a helicopter crew seat to enhance its crashworthiness. Bai applied MR seat suspension for mitigating ground vehicle crashes and vibrations (Bai et al., 2013; Bai and Wereley, 2014).

Despite the success on the development of the MR seat suspension, there are still several critical drawbacks making it hard to satisfy various complex working scenarios. For a traditional MR seat suspension without stiffness control, its primary feature is to provide controllable damping to dissipate the vibration energy so as to reduce the adverse impact, however, it lacks the capability to vary its stiffness, which makes it fail to avoid the vibration resonance. The vibration excitations cover a wide range of frequencies so that it is highly possible to match the resonance frequency of the seat suspension; once this happens, the seat suspension will undergo fierce vibration even under variable damping control. In addition, for a more versatile seat suspension, it is required to provide not only high stiffness to effectively maintain the ride stability but also the low stiffness to keep the ride comfort. However, the traditional MR seat suspension without stiffness control cannot meet this conflicting stiffness requirement because it can only set the spring to be stiff to guarantee the ride stability and stroke sufficiency, sacrificing the ride comfort. Furthermore, different suspension stiffness is also required to satisfy a different spectrum of roads and weight of occupants. To summarize, the traditional MR seat suspension without stiffness control is not able to realize non-resonance control or to adapt to different road spectra and drivers' weights.

In order to satisfy the above requirements, a new MR seat suspension with controllable stiffness needs to be developed. The main challenge to implement such a seat suspension is to find an appropriate mechanism to realize variable stiffness. Additionally, the components of the seat suspension have to be compact so that they can be installed into the seat without complicated structure change. Following the requirements and objectives, this paper proposed a new seat suspension which can perform variable stiffness. Its primary attractions are that it includes a rotary MR damper which uses controllable damping to realize variable stiffness, and that the compact structure enables the VS MR rotary damper to be installed on the seat suspension without any configuration changes. The property of stiffness controllability is able to shift the suspension's natural frequency away from the excitation frequency to avoid vibration resonance. In particular, the initial suspension stiffness can be designed to be low to achieve good ride comfort and then it can be adjusted in real time to guarantee its ride stability. Additionally, the stiffness of the seat suspension can be adjusted according to the road spectrum and the weight of the occupants. The structure of this paper is detailed as follows. *Structure and Working Mechanism of the New Seat Suspension Section* illustrates the structure and working mechanism of the new seat suspension. In *Experimental Characterization section*, the experimental characterisations of MR fluids (MRF) and the MR seat suspension are presented and accordingly, the effective stiffness and equivalent damping were analyzed. The vibration attenuation performance of the new MR seat suspension is evaluated in *Evaluation of the Vibration Isolation Performance section* and *Conclusion Section* draws the conclusion.

STRUCTURE AND WORKING MECHANISM OF THE NEW SEAT SUSPENSION

Structure of the New Seat Suspension

The new seat suspension was developed by installing a VS rotary MR damper underneath a commercialized vehicle seat, as shown in **Figure 1C**. **Figure 1A** provides the detailed schematic structure of the VS MR rotary damper which is composed of a gear box, a torsion spring, and an MR damping unit. One end of the torsion spring is fixed with the cylinder of the gear box, and the other end is fixed with the cylinder of the MR damper *via* a spring seat. The damping unit is responsible for generating controllable torque based on the rheological property of MRF, i.e., it provides high torque when its electromagnetic coil is powered with a large current, and otherwise, it provides small torque. The gear box with the gear ratio of 5:1 then works to amplify the output torque of the damping unit to satisfy the required maximum force of the seat suspension. As the torsional spring connects the damping unit and the gear box, the variability of the stiffness can be realized by adjusting the amount of the current applied to the MR damper.

Assembling of the New Seat Suspension

Figure 1B shows the assembling of the VS MS rotary damper to the seat suspension. The seat suspension has two scissor

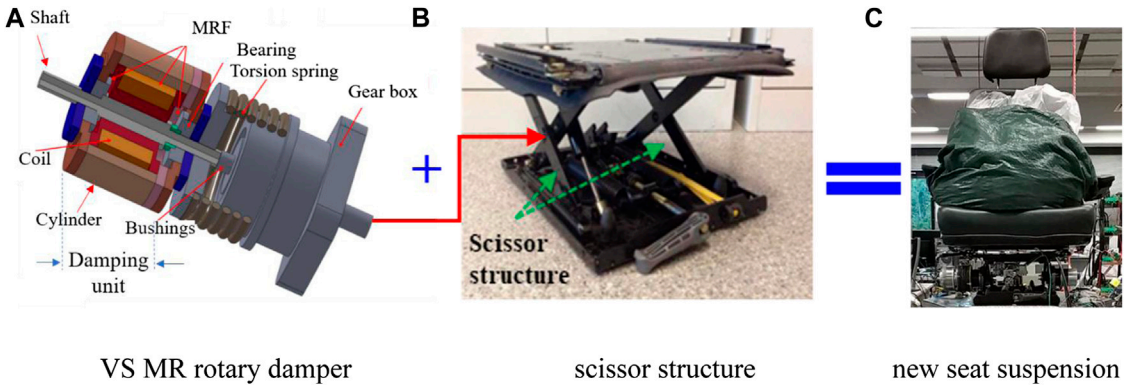

FIGURE 1 | *The* structure *and prototype* of *the VS MR suspension*.

structures at its two flanks, one of which will be installed with the VS MR damper. **Figure 1B** shows that the damper was installed to the left side of the seat suspension, specifically, the shaft of the VS MR damper is fixed to one beam of the scissor structure while the cylinder of the damper is fixed with the other one in the same scissor structure. When this seat is subjected to vertical vibration, the two beams of the scissor structure rotate relatively in opposite directions, which drives the rotary MR damper to rotate. In this way, the vertical linear vibration is transformed into rotational motions in the rotary damper.

Working Principle of the New Seat Suspension

The VS rotary MR damper is responsible for providing controllable stiffness to the seat suspension. The realization of the controllable stiffness relies on the cooperation between the spring and the damping variability provided by the damping unit. The damping of the MR damping unit increases gradually as the current applied to power the electromagnetic coil increases, accordingly, the relative rotation between the shaft and the cylinder of the damping unit will become increasingly difficult. In this case, the deformation of the torsional spring will increase under the same external excitation and the VS MR rotary damper will perform higher stiffness. The applied current controls the deformation of the torsional spring and thus the overall suspension stiffness. Specifically, the shaft can rotate easily with respect to its cylinder when the damping of the damping unit is small. In this case, the torsional spring will not perform any deformation, thereby the VS MR rotary damper demonstrates low stiffness. Alternatively, when the damping is large enough and the torque produced by the torsional spring cannot overcome the damping force, the damper cylinder has no relative motion with respect to the shaft and the torsional spring will be deformed during operation. In this scenario, the VS rotary damper performs the maximum stiffness. The medium stiffness which falls between the minimum and the maximum can be realized by adjusting the amount of the applied current.

EXPERIMENTAL CHARACTERIZATION

Characterization of MR Fluids

MRF used in this work is bought from Beijing Guohao Sensing Technology Research Institute, China (model: GH-MRF-250, density: 2.55 g cm^{-3}). Its shear properties were measured using a rheometer (Physica MCR 301, the Anton Paar Company, Germany). **Figure 2A** shows the yield stress characteristics of the MRF with respect to different magnetic flux density. From this figure it can be seen that the increase of the magnetic flux density results in the increase of the yield stress of MRF. **Figure 2B** presents the viscosity information of MRF vs. shear rate. The viscosity in **Figure 2B** was measured without the presence of magnetic field and the shear rate was increased from 0.1 s^{-1} to 1,000 s^{-1}. It is seen that the viscosity decreases sharply then tends to level off when the shear rate keeps increasing. Using the MRF, the MR damping unit shown in **Figure 1A** is able to perform controllable torque and accordingly, the output force generated by the whole VS MR damper can be controlled by the applied DC current.

Dynamic Testing of the MR Seat Suspension Using an MTS Machine

The factors affecting the performance of the seat suspension mainly include the applied DC current to the magnetic coil of the rotary MR damper, the displacement amplitude and the loading frequency of the external vertical excitation. To investigate how these factors influence the suspension performance, dynamic tests were designed and conducted to explore the hysteretic behavior of the seat suspension under various currents, loading frequencies and amplitudes. With these tests, the equivalent damping and the effective stiffness of the seat suspension under different loading conditions can be calculated. The experimental setup using an MTS machine (*Materials Test Systems, Landmark Servohydraulic Test Systems, MODEL 370.02, United States*) is shown in **Figure 3**.

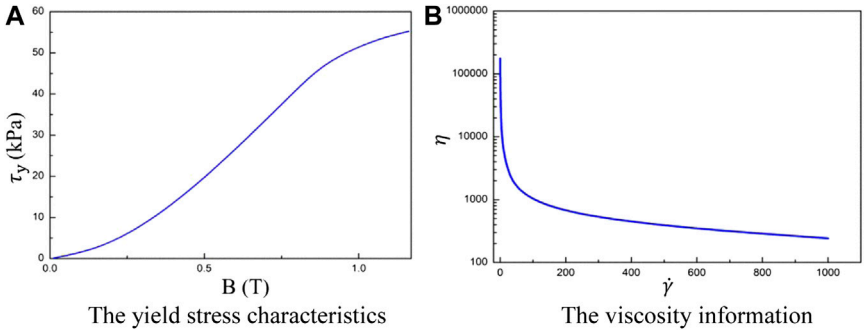

FIGURE 2 | Property of the MRFs. **(A)** The yield stress characteristics **(B)** The viscosity information.

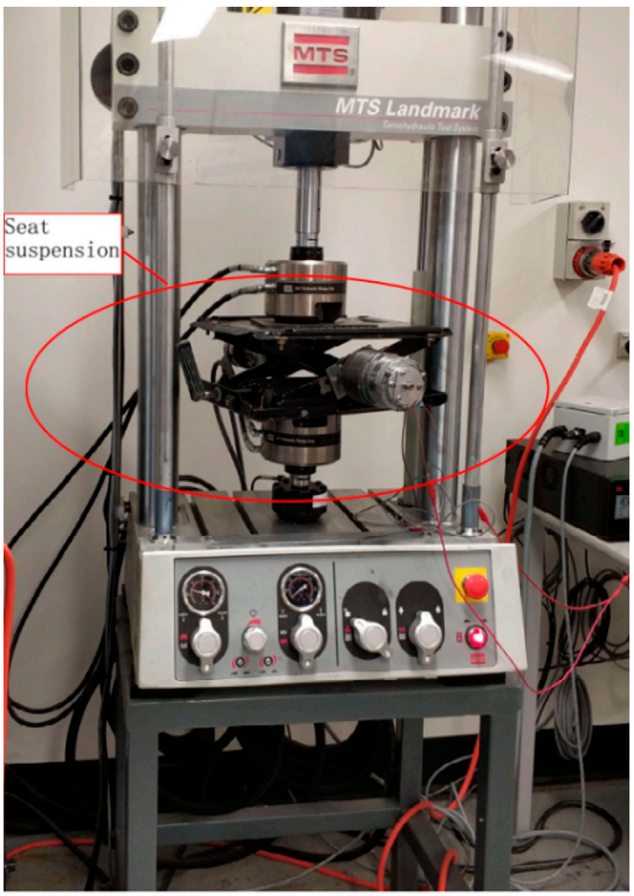

FIGURE 3 | Experimental setup of the MTS testing.

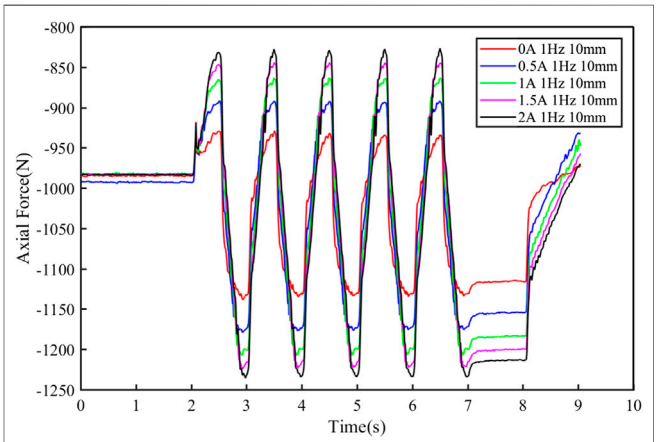

FIGURE 4 | The generated force under different currents in time domain.

Performance under different currents

The field-dependent properties are the most important features for a smart system as it determines its real time controllability. Therefore, a series of coil currents were used to energize the suspension to obtain its field-dependent behaviors. The sinusoidal signal with a frequency of 1 Hz and the displacement amplitude set as constant (5, 10, and 15 mm) was chosen as the excitation. For each testing case, the current was changed from 0 to 2 A with a step of 0.5 A. Therefore, a total of 15 cases were conducted. And for each testing, sufficient loops have been run before collecting the satisfactory data to guarantee the consistency. **Figure 4** shows the axial force generated under various currents by the seat suspension in the time domain. It is in a vertical direction and it provides damping force to the seat suspension. It can be seen that the maximum force increases when the current is increased, which corresponds to the mechanism that the MR rotary damper shows increasing stiffness when the applied current increases.

In order to provide a closer observation of the field-dependent property, **Figure 5A–C** plot the hysteresis loops of the force and displacement relationship under varied currents. Each contour was obtained under a constant amplitude of external excitation, i.e., 5, 10, and 15 mm, respectively. It is found that under certain excitation amplitudes, the stiffness increases obviously when the current is changed from 0 to 0.5 A, however, its increasing rates decrease when the current further increases. For different amplitudes, the same phenomenon in terms of the field-dependent property can be observed. For each hysteresis loop, the effective stiffness to be analyzed in the following section is

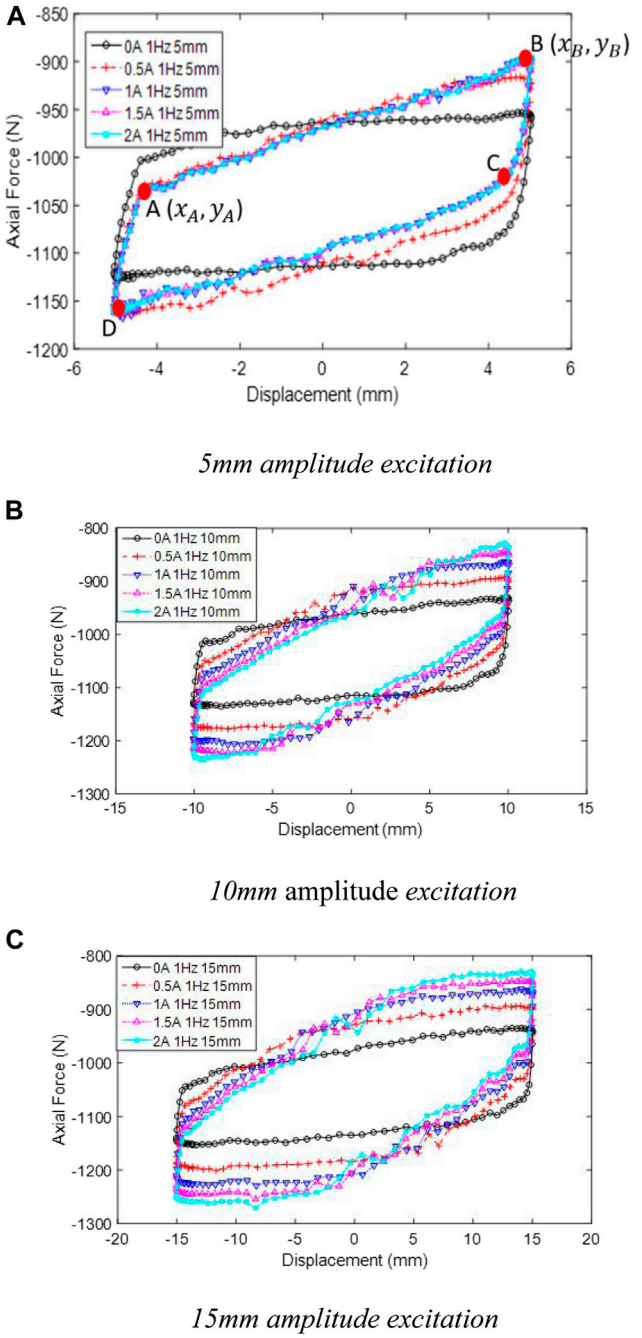

FIGURE 5 | Force-displacement loops under different currents and amplitudes. **(A)** 5 mm amplitude excitation. **(B)** 10 mm amplitude excitation. **(C)** 15 mm amplitude excitation

obtained by calculating the slope of segment AB, as indicated in **Figure 5A**, using the following expression:

$$k_{eff} = \frac{1}{n-1}\sum_{n=2}^{\infty}\frac{y_n - y_{n-1}}{x_n - x_{n-1}} \quad (1)$$

where n indicates the number of the dots on segment AB, (x_n, y_n) represents the coordinate of the nth dot. As segments AD and BC

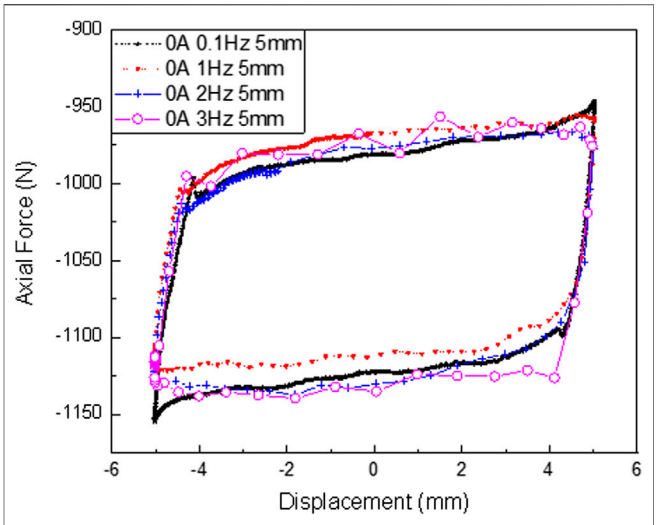

FIGURE 6 | Force-displacement loops with no current applied under different frequencies.

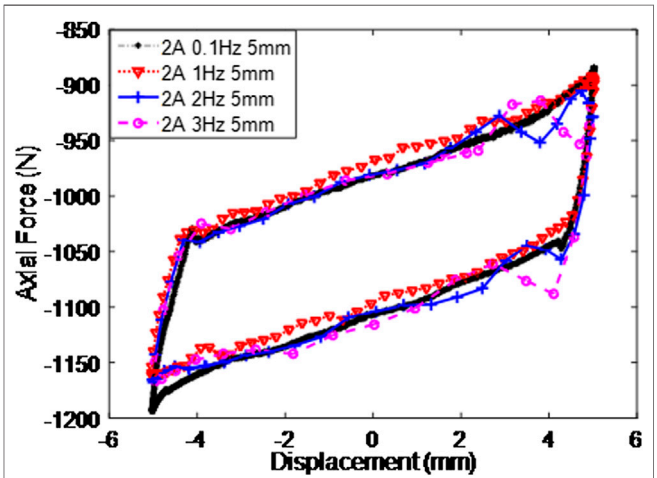

FIGURE 7 | Force-displacement loops with 2 A current applied under different frequencies.

were generated by friction damping of the seat suspension, they are not included into the calculation of the effective stiffness.

Performance under different frequencies

To investigate the influence of the loading frequency on the suspension performance, a series of tests under various frequencies were conducted. The chosen frequencies for the test were 0.1, 1, 2, and 3 Hz. The displacement amplitude was set as 5 mm. And two current values (0A and 2 A) were chosen for this test.

Figure 6 shows the testing results under various frequencies with the current to be 0 A and **Figure 7** provides its performance under 2 A. It can be seen that the loading frequency induces very slight influence on the hysteresis loops whether a current was applied or not, indicating that changing the loading frequency

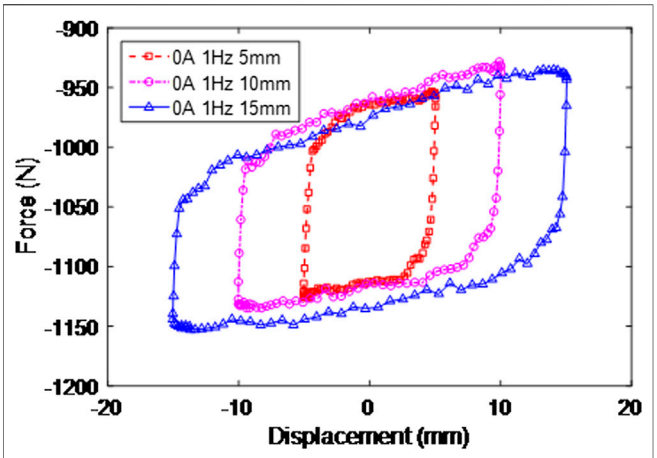

FIGURE 8 | Force-displacement loops with no current applied under different excitation amplitudes.

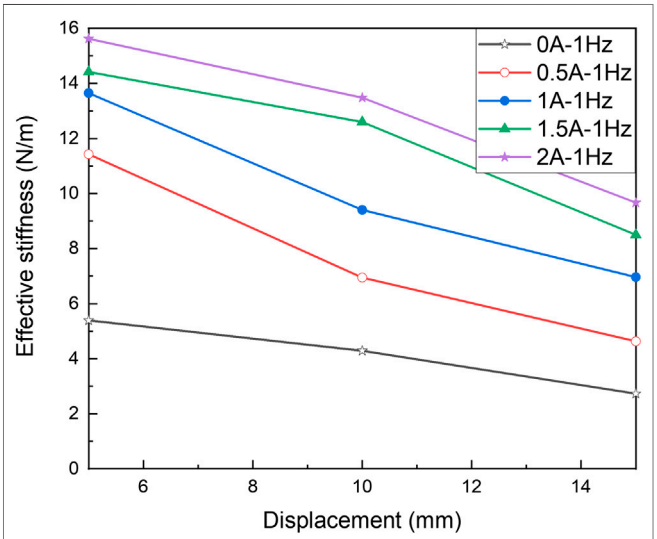

FIGURE 9 | The effective stiffness of the MR seat suspension under different excitation amplitudes.

will not generate obvious influence on the peak force, the stiffness, or the damping. Therefore, it is concluded that the variations of loading frequency will not induce obvious change to the suspension performance. By comparing **Figure 6** and **Figure 7**, it can be seen that a larger axial force was produced under 2 A. This can be explained by the field-dependent property as shown in **Figure 5**.

Dynamic property under different displacements

This sub-section tests the seat suspension performance under different displacements, the values of which were set as 5, 10, and 15 mm. The loading frequency was set as 1 Hz and the current was set as 0 A. The experimental results indicating the force-displacement relationship are shown in **Figure 8**.

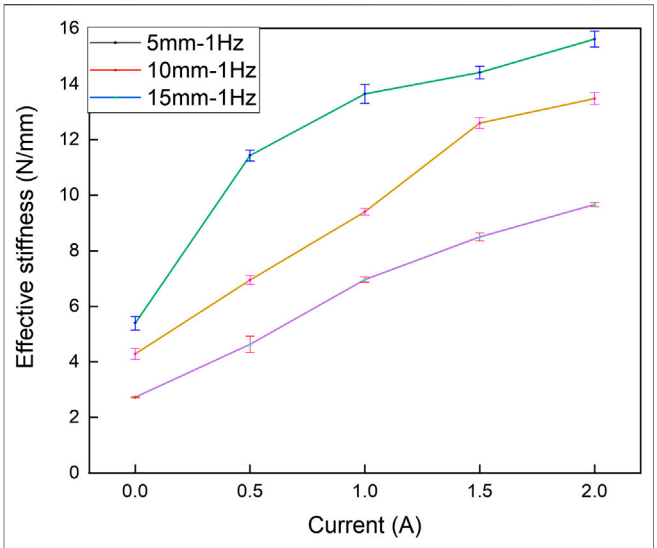

FIGURE 10 | The effective stiffness of the MR seat suspension applied with different currents.

The Analysis of the Effective Stiffness and Equivalent Damping

Effective stiffness analysis

For a seat suspension, the ride comfort experienced by the driver or passenger is an important indication to evaluate its performance. And the ride comfort is closely influenced by the stiffness achievable by the seat suspension. **Figure 9** and **Figure 10** present the calculated effective stiffness corresponding to different amplitudes and currents. The effective stiffness was calculated using the experimentally obtained data sets which have been plotted in **Figure 5**.

Figure 9 and **Figure 10** plot the relationship between the effective stiffness and the displacement as well as the current. Both of these two figures show that for a fixed current, the stiffness reduces when the amplitude increases. However, when the amplitude is a constant, the stiffness increases as the current increases. But the increasing rate of the stiffness decreases when the current further increases, which verifies that the overall stiffness increases with the increasing current until a damping force is large enough to overcome the force generated by the torsional spring. The calculation results are consistent with the observations in **Figure 5**. The error bars with standard deviation for the calculated effective stiffness are also provided in **Figure 10**. They show that the effective stiffness for each group of experimental data is distributed centered on average with acceptable standard deviations.

Equivalent damping calculation

To study the energy-dissipation performance of this VS MR suspension, the equivalent viscous damping coefficient was calculated. The equivalent viscous damping coefficient can be obtained from (Li et al., 2000):

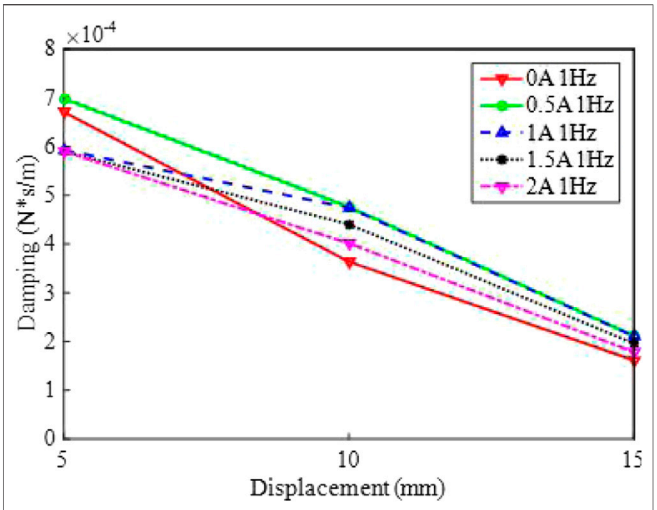

FIGURE 11 | The equivalent damping of the MR seat suspension under different excitation amplitudes.

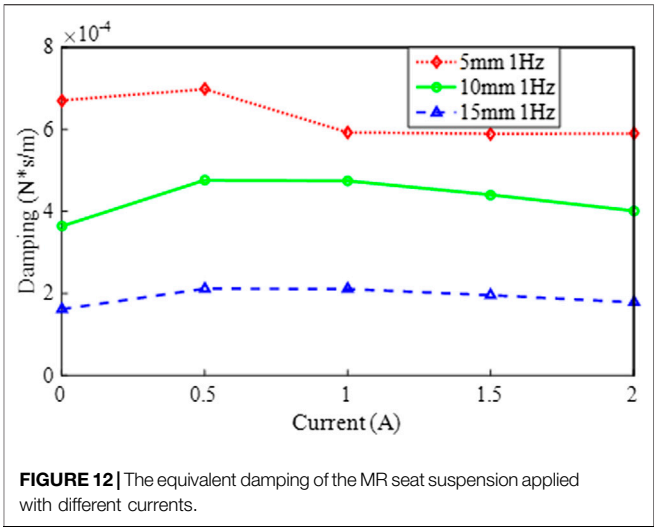

FIGURE 12 | The equivalent damping of the MR seat suspension applied with different currents.

$$C_{eq} = \frac{EDC}{2\pi^2 f \Delta^2} \tag{2}$$

where *EDC* is the energy dissipated per cycle, or the area enclosed by the hysteresis loop, f is the loading frequency and Δ is the maximum displacement of the external excitation. The enclosed area can be calculated using MATLAB, then the equivalent viscous damping coefficient can be calculated according to **Eq. 1**. The calculated equivalent damping is presented in **Figure 11** and **Figure 12**.

Figure 11 and **Figure 12** plot the relationship between the equivalent damping coefficient and the current as well as the displacement amplitude. It is seen from **Figure 11** that the damping coefficient shows a reducing trend with the increasing amplitude at a fixed current, however, for a constant amplitude, the viscous damping coefficient shows slight fluctuation which first increases and then drops down when the current further increases. **Figure 12** also reflects the phenomenon that the viscous damping is sensitive to the current variation but less sensitive to the variations of displacement amplitude.

EVALUATION OF THE VIBRATION ISOLATION PERFORMANCE

Figure 13 shows the experimental setup to evaluate the vibration isolation performance of the proposed suspension system. Different excitations including random excitation and harmonic excitation were generated by a shaking table to excite the seat suspension. Two accelerometers were used to measure the accelerations of the excitation and the seat suspension, respectively. Considering that an appropriate controller is critically important for the suspension system to achieve good performance, a controller based on the short-time Fourier Transform (STFT) (Yang et al., 2020a) was developed and implemented, aiming to control the stiffness and realize the non-resonant control. The STFT algorithm is responsible for detecting the vibration frequency; then this excitation frequency will be compared with the natural frequency of the seat suspension. When the excitation frequency is close to the natural frequency of the seat suspension, the stiffness of the seat suspension will be adjusted to shift its natural frequency away from the excitation frequency to avoid resonance. Upon the establishment of the controller, experimental evaluation of the seat suspension was conducted. The acceleration of the seat suspension as well as the transmissibility are the main evaluation criteria. The acceleration signal measured from the shaking table was sent to the controller for processing to determine the dominant vibration frequency. The frequency controller then calculates the desired control output through STFT algorithms and sends it to a power amplifier. The amplified current was then sent to the damper to control its stiffness. During the experiment, three different suspensions were evaluated, i.e., passive-off, passive-on, and semi-active suspensions. Passive-off suspension means there is no current applied to the damper; passive-on suspension means a constant current (2 A) was applied to the damper; and semi-active suspension means the suspension is controlled by the STFT controller in real time. The passive-on and passive-off suspensions are given as reference to compare with the semi-active suspensions. The evaluation results are presented in **Figure 14** and **Figure 15B**.

Figure 14 illustrates the acceleration transmissibility of the three suspensions. As it is the ratio of the seat acceleration to the excitation acceleration, the lower its value means the better its performance. It can be seen that the natural frequency of the passive-off case is smaller than that of the passive-on case. That is because the stiffness of the VS rotary MR damper increases when the applied current increases and accordingly, the natural frequency increases. The two transmissibility from the passive-on and passive-off cases have an intersected frequency, as indicated by letter P in **Figure 14**. It can be seen that the transmissibility under the

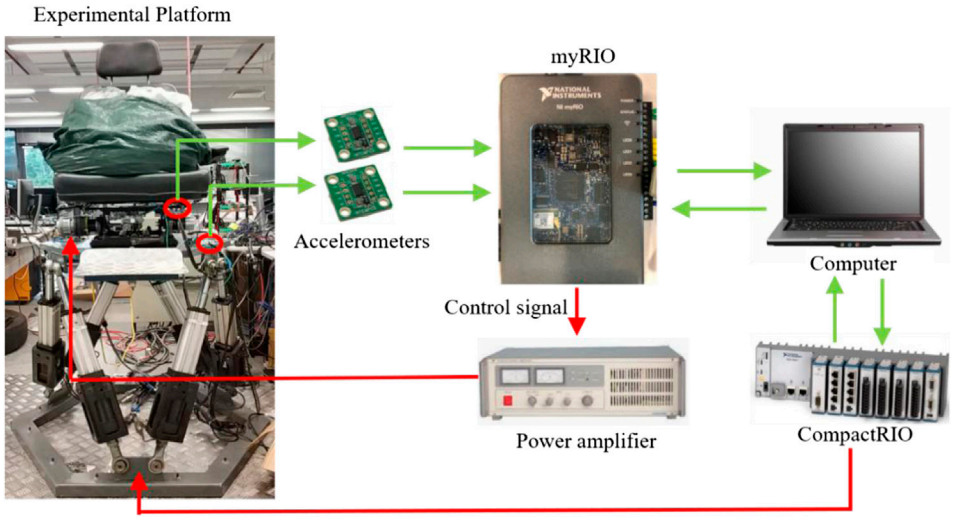

FIGURE 13 | Experimental setup for evaluating the vibration isolation performance (CompactRIO: Crio-9074, mit 400 MHz CPU, 128 MB DRAM, 256 MB Speicher, FPGA mit 2 Millionen Gattern, eight Slots).

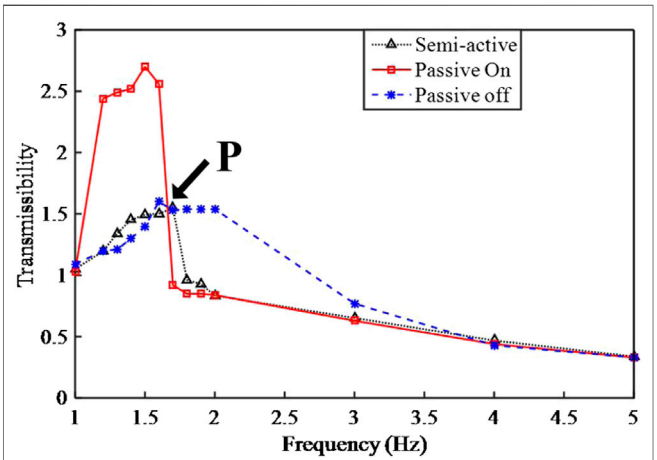

FIGURE 14 | Vibration transmissibility of the three different suspensions.

passive-on case is the lowest when the excitation frequency is less than this intersected frequency, otherwise, the transmissibility under the passive-off case is the lowest. Therefore, a minimum transmissibility can be generated by connecting these two segments. Then it is observed that the transmissibility of the semi-active control mode can just track the minimum transmissibility: it almost keeps consistent with the transmissibility under the passive-on case before the intersected frequency and then drops down to the transmissibility of the passive-off case once the excitation frequency is higher than the intersected frequency. Therefore, it can be concluded that the VS MR seat suspension under the semi-active control performs best at reducing the acceleration response. A video indicating the performance comparing the passive suspension and semi-active suspension under three representative frequencies, i.e., 1.3, 1.5, and 1.6 Hz is provided as a supporting material. **Figure 15B** presents the acceleration responses of the seat suspensions under random excitation. The random excitation is generated by the method presented in Ref (Yang et al., 2000c), which has been widely adopted to evaluate the suspension performance and shown in **Figure 15A**. This evaluation result further proves that the suspension acceleration of the semi-active suspension remains the smallest for the whole-time history compared with the other two passive cases.

In order to better understand the improvement of the semi-active seat suspension over the passive ones, ISO 2631is introduced as shown in **Table 1** (International Organization for Standardization, 1997) which has categorized the comfort levels according to a human's likely reactions to various magnitudes of vibration. Accordingly, the Z-axial weighted RMS values which have considered the passengers' ride comfort were calculated and tabulated in **Table 2**. It can be seen from **Table 2** that the comfort level achieved by the passive off suspension and the passive on suspension is level C which represents "fairly uncomfortable," however, the comfort level achieved by the semi-active suspension is level B which indicates "a little uncomfortable." The comparison has demonstrated that semi-active suspension has brought a higher level of comfort to the passengers.

CONCLUSION

A rotary MR damper which is able to perform variable stiffness characteristics was successfully developed and then used to implement a semi-active seat suspension, aiming to overcome the drawback of a traditional MR damper that it cannot realize the non-resonance control. The seat suspension was then characterized using MTS machine in terms of the field-dependent response, the amplitude-dependent response, and the

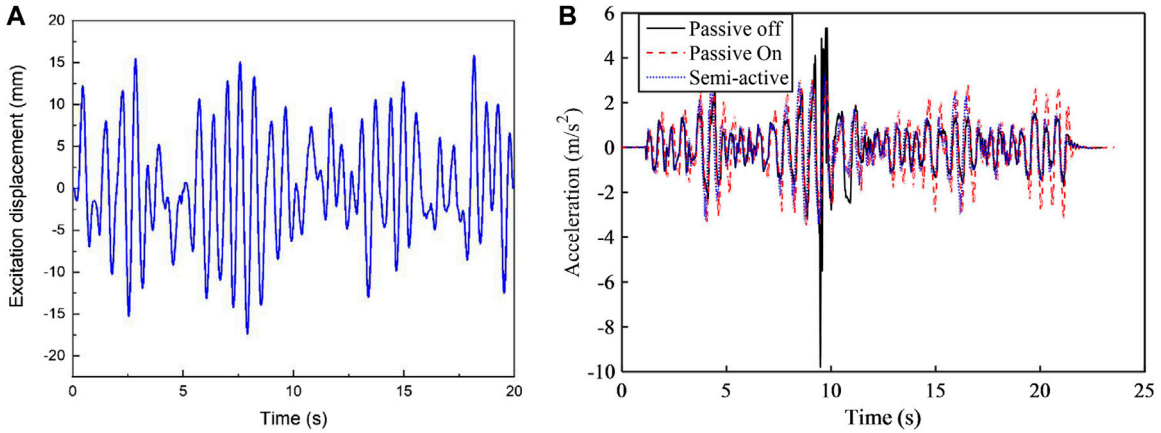

FIGURE 15 | Acceleration performance of the random excitation. **(A)** excitation, **(B)** response.

TABLE 1 | Approximate indications of likely reactions to various magnitudes of vibration.

<0.315 m/s^2	**Not uncomfortable (A)**
0.315~0.63 m/s^2	A little uncomfortable (B)
0.5~1 m/s^2	Fairly uncomfortable (C)
0.8~1.6 m/s^2	Uncomfortable (D)
1.25~2.5 m/s^2	Very uncomfortable (E)
>2 m/s^2	Extremely uncomfortable (F)

TABLE 2 | The weighted RMS values of accelerations for the three suspensions.

Suspension types	Passive off	Passive on	Semi-active
Weighted RMS	0.7087	0.7017	0.6195
Comfort level	C	C	B

frequency-dependent responses. The testing results demonstrated that the stiffness and the generated force increase in response to the increasing current but decrease slightly when the displacement amplitude increases. This variability of the stiffness indicate that the new seat suspension is able to satisfy the conflicting requirement of the stiffness, i.e., it can provide not only high stiffness to guarantee the riding stability but also low stiffness to achieve better ride comfort. In addition, the suspension stiffness is not sensitive to the variations of the loading frequency. As for the damping property, the experimental results show that the equivalent damping coefficient decreases when the displacement amplitude increases and that the applied increasing current induces a slight influence on the equivalent damping. The vibration isolation experiments have compared the responses of different suspensions. The results have demonstrated that the seat suspension with the semi-active control performs the best in reducing the suspension acceleration.

DATA AVAILABILITY STATEMENT

The raw data supporting the conclusions of this article will be made available by the authors, without undue reservation.

AUTHOR CONTRIBUTIONS

SS and JY contributed equally to this work. SS, JY, and PW: methodology, software and formal analysis. SS, and WL: conceptualization. SS, JY, PW, MN, and LS: validation and investigation. SS, SZ, and WL: resource and data curation. SS and JY: writing–original draft preparation and visualization. All authors: writing–review and editing. SS, and WL: supervision and project administration.

FUNDING

This research is supported by ARC Linkage Project (Grand No. LP150100040), JSPS Grant-in-Aid for Research Activity Start-up (Grand No. 19K23476), for Young researcher B (Grand No. 20K14688) and for JSPS fellowship (Grand No. 19F19712), and the National Key R&D Program of China (Grant Nos. 2018YFB1201703).

REFERENCES

Abe, H., Naka, T., Sato, K., Suzuki, Y., and Nakano, M. (2019). Shape-controlled syntheses of magnetite microparticles and their magnetorheology. *Int. J. Mol. Sci.* 20, 3617. doi:10.3390/ijms20153617

Alfadhli, A., Darling, J., and Hillis, A. J. (2018). An active seat controller with vehicle suspension feedforward and feedback states: an experimental study. *Appl. Sci.* 8, 603. doi:10.3390/app8040603

Bai, X.-X., Hu, W., and Wereley, N. M. (2013). Magnetorheological damper utilizing an inner bypass for ground vehicle suspensions. *IEEE Trans. Magn.* 49, 3422–3425. doi:10.1109/tmag.2013.2241402

Bai, X.-X., and Wereley, N. M. (2014). "Magnetorheological impact seat suspensions for ground vehicle crash mitigation," in SPIE smart structures and Materials + nondestructive evaluation and health monitoring, San Deigo, CA, April 2014 (International Society for Optics and Photonics).

Carlson, J. D., and Jolly, M. R. (2000. MR fluid, foam and elastomer devices. *Mechatronics* 10, 555–569. doi:10.1016/s0957-4158(99)00064-1

Choi, S.-B., and Han, Y.-M. (2007). Vibration control of electrorheological seat suspension with human-body model using sliding mode control. *J. Sound Vib.* 303, 391–404. doi:10.1016/j.jsv.2007.01.027

Choi, Y.-T., and Wereley, N. M. (2005). Biodynamic response mitigation to shock loads using magnetorheological helicopter crew seat suspensions. *J. Aircraft,* 42, 1288–1295. doi:10.2514/1.6839

Deng, H., Deng, J., Yue, R., Han, G., Zhang, J., Ma, M., et al. (2019). Design and verification of a seat suspension with variable stiffness and damping. *Smart Mater. Struct.* 28. doi:10.1088/1361-665x/ab18d4

DETR, (2000), *Tomorrow's Roads-Safer for Everyone*. London, United Kingdom: Department of the Environment, Transport and the Regions.

Eshaghi, M., Rakheja, S., and Sedaghati, R. (2015). An accurate technique for pre-yield characterization of MR fluids. *Smart Mater. Struct.* 24. doi:10.1088/0964-1726/24/6/065018

Gad, S., Metered, H., Bassuiny, A., and Abdel Ghany, A. (2017). Multi-objective genetic algorithm fractional-order PID controller for semi-active magnetorheologically damped seat suspension. *J. Vib. Contr.* 23, 1248–1266. doi:10.1177/1077546315591620

Guo, C., Gong, X., Zong, L., Peng, C., and Xuan, S. (2015). Twin-tube-and bypass-containing magneto-rheological damper for use in railway vehicles. *Proc. Inst. Mech. Eng. - Part F J. Rail Rapid Transit* 229, 48–57. doi:10.1177/0954409713497199

Haworth, N. L., Triggs, T. J., and Grey, E. M. (1998). Report No. CR72. *Driver fatigue: concepts, measurement and crash countermeasures*. Canberra, CBR: Federal office of road safety Monash University.

Hu, G., Ru, Y., and Li, W. (2014). Design and development of a novel displacement differential self-induced magnetorheological damper. *J. Intell. Mater. Syst. Struct.* 26, doi:10.1177/1045389X14533429

Legislative Assembly of Queensland: Parliamentary Travelsafe Committee, (2005). Report No. 43. *Driving on empty: fatigue driving in queensland*. Brisbane, BNE: Queensland Government.

International Organization for Standardization, (1997). *Mechanical vibration and shock—evaluation of human exposure to whole-body vibration—Part 1: general requirements*. Geneva, CH: ISO International Standard.

Li, W. H., Du, H., Chen, G., Yeo, S. H., and Guo, N. (2003). Nonlinear viscoelastic properties of MR fluids under large-amplitude-oscillatory-shear. *Rheol. Acta* 42, 280–286. doi:10.1007/s00397-002-0285-4

Li, W., Yao, G., Chen, G., Yeo, S., and Yap, F. (2000). Testing and steady state modeling of a linear MR damper under sinusoidal loading. *Smart Mater. Struct.* 9, 95. doi:10.1088/0964-1726/9/1/310

Li, Y., Li, J., Li, W., and Du, H. (2014). A state-of-the-art review on magnetorheological elastomer devices. *Smart Mater. Struct.,* 23, 123001. doi:10.1088/0964-1726/23/12/123001

Liu, X., Wang, N., Wang, K., Huang, H., Li, Z., Sarkodie-Gyan, T., et al. (2019). Optimizing vibration attenuation performance of a magnetorheological damper-based semi-active seat suspension using artificial intelligence. *Front. Mater.* 6, 269, doi:10.3389/fmats.2019.00269

Maciejewski, I., Krzyzynski, T., and Meyer, H. (2018). Modeling and vibration control of an active horizontal seat suspension with pneumatic muscles. *J. Vib. Contr.* doi:10.1177/1077546318763435

Motmans, R. (2012). Reducing whole body vibration in forklift drivers. *Work,* 41 Suppl 1, 2476–2481. doi:10.3233/WOR-2012-0484-2476

Nakano, M. (2015). MR effect enhancement of bidisperse MR fluids containing micron-and nano-sized iron particles. *Bull. Am. Phys. Soc.,* 60.

National Hazard Exposure Worker Surveillance, (2009). *Vibration exposure and the provision of vibration control measures in Australian workplaces.* Safe Work Australia, Available at: https://www.safeworkaustralia.gov.au/doc/national-hazard-exposure-worker-surveillance-vibration-exposure-and-provision-vibration-control.

Nguyen, H. Q., Choi, S.-B., Hiep, L. D., and Tuan, L. D. (2019). Material characterization of MR fluid on performance of MRF based brake. *Front. Mater.,* 6, 125. doi:10.3389/fmats.2019.00125

Ning, D., Du, H., Sun, S., Li, W., and Li, W. (2018). An energy saving variable damping seat suspension system with regeneration capability. *IEEE Trans. Ind. Electron.* 65, 8080–8091. doi:10.1109/tie.2018.2803756

Ning, D., Sun, S., Zhang, F., Du, H., Li, W., and Zhang, B. (2017). Disturbance observer based Takagi-Sugeno fuzzy control for an active seat suspension. *Mech. Syst. Signal Process.* 93, 515–530. doi:10.1016/j.ymssp.2017.02.029

Phu, D. X., Quoc Hung, N., and Choi, S.-B. (2018). A novel adaptive controller featuring inversely fuzzified values with application to vibration control of magneto-rheological seat suspension system. *J. Vib. Contr.* 24, 5000–5018. doi:10.1177/1077546317740479

Sun, S., Ning, D., Yang, J., Du, H., Zhang, S., Li, W., et al. (2017). Development of an MR seat suspension with self-powered generation capability. *Smart Mater. Struct.* 26, 085025. doi:10.1088/1361-665x/aa76b6

Sun, S., Tang, X., Yang, J., Ning, D., Du, H., Zhang, S., et al. (2019). A new generation of magnetorheological vehicle suspension system with tunable stiffness and damping characteristics. *IEEE Trans. Ind. Inf.* 15, 4696–4708. doi:10.1109/tii.2018.2890290

Tu, J., Li, Z., Zhang, J., Gao, K., Liao, J., and Gao, J. (2019). Development, test, and mechanical model of the leak-proof magnetorheological damper. *Front. Mater.,* 6, 118. doi:10.3389/fmats.2019.00118

Wereley, N. M., Choi, Y.-T., and Singh, H. J. (2011). Adaptive energy absorbers for drop-induced shock mitigation. *J. Intell. Mater. Syst. Struct.* 22, 515–519. doi:10.1177/1045389x10393767

Yang, B., Chen, S., Sun, S., Deng, L., Li, Z., Li, W., et al. (2020a). Vibration suppression of tunnel boring machines using non-resonance approach. *Mech. Syst. Signal Process.* 145, 106969. doi:10.1016/j.ymssp.2020.106969

Yang, J., Christie, M., Sun, S., Ning, D., Nakano, M., Li, Z., et al. (2020b). Integration of an omnidirectional self-powering component to an MRE isolator towards a smart passive isolation system. *Mech. Syst. Signal Process.,* 144, 106853. doi:10.1016/j.ymssp.2020.106853

Yang, J., Ning, D., Sun, S., Zheng, J., Lu, H., Nakano, M., et al. (2020c). A semi-active suspension using a magnetorheological damper with nonlinear negative-stiffness component. *Mech. Syst. Signal Process.,* 147, 107071. doi:10.1016/j.ymssp.2020.107071

Yu, J., Dong, X., Wang, X., Pan, C., and Zhou, Y. (2019). Asymmetric dynamic model of temperature-dependent magnetorheological damper and application for semi-active system. *Front. Mater.* 6, 227. doi:10.3389/fmats.2019.00227

Yu, J., Dong, X., Zhang, Z., and Chen, P. (2018). A novel scissor-type magnetorheological seat suspension system with self-sustainability. *J. Intell. Mater. Syst. Struct.* 30, 1045389X1775425. doi:10.1177/1045389X17754256

Yu, M., Dong, X., Choi, S., and Liao, C. (2009). Human simulated intelligent control of vehicle suspension system with MR dampers. *J. Sound Vib.* 319, 753–767. doi:10.1016/j.jsv.2008.06.047

Yu, M., Yang, P., Fu, J., Liu, S., and Choi, S.-B. (2016). A theoretical model for the field-dependent conductivity of magneto-rheological gels and experimental verification. *Sensor Actuator Phys.* 245, 127–134. doi:10.1016/j.sna.2016.05.008

Zhao, L., Yu, Y., Zhou, C., and Yang, F. (2018). Modelling and validation of a seat suspension with rubber spring for off-road vehicles. *J. Vib. Contr.* 24, 4110–4121. doi:10.1177/1077546317719348

Conflict of Interest: The authors declare that the research was conducted in the absence of any commercial or financial relationships that could be construed as a potential conflict of interest.

Structural Materials

Wil Srubar

Dr. Wil Srubar is an Associate Professor of Civil and Architectural Engineering and Materials Science at the University of Colorado Boulder, where he leads the Living Materials Laboratory. Dr. Srubar holds a Ph.D. from Stanford University and BS and MS degrees from Texas A&M University and the University of Texas at Austin, respectively. He has received >$8M in funding for his research, which integrates biology, polymer science, and cement chemistry to create low-carbon, biomimetic, and living material technologies for the built environment. His work has been highlighted in The New York Times, The Conversation, and The Huffington Post.

frontiers in Materials

REVIEW
published: 29 January 2021
doi: 10.3389/fmats.2020.594989

Nanoscale Construction Biotechnology for Cementitious Materials: A Prospectus

Xu Chen[1], *Marimikel Charrier*[1] *and Wil V. Srubar III*[1,2]*

[1]Department of Civil, Environmental, and Architectural Engineering, University of Colorado Boulder, Boulder, CO, United States, [2]Materials Science and Engineering Program, University of Colorado Boulder, Boulder, CO, United States

Climate change, infrastructure resilience, and resource recovery from waste have emerged as grand challenges for civil engineers in the 21st century. Wicked problems associated with these global grand challenges are necessitating innovative, multidisciplinary thinking and multiscale, integrated solutions that are spurring the development of a new field—*construction biotechnology*. While the field of construction biotechnology spans multiple scales, this review highlights the promise and potential of nanoscale (<100 nm) biotechnological applications to civil engineering. While the field of nanotechnology has revolutionized other industries, applications of nanotechnology in civil engineering have remained limited due to techno-economic and environmental barriers. Biological production of functional nanoparticles (NPs), however, offers new economical routes to develop resilient, high-performance cementitious materials while simultaneously addressing critical needs related to wastewater treatment and resource recovery. Recent research has elucidated that biological production of NPs exhibit preferred—and genetically controllable—morphological characteristics that could tailor the structure-property relationships of civil engineering materials. The natural ability of microorganisms to immobilize heavy metals (*eg*, Hg, Cr, Zn, Cd, Cu, Ag)—and the *programmability* of microorganisms to do so *via* synthetic biology—as well as their ability to sequester greenhouse gases and neutralize volatile organic compounds affords civil engineers a grand opportunity to treat wastewater, recover rare earth elements, and minimize air pollution. In addition to featuring state-of-the-art research in the field, this review summarizes the opportunities and challenges of nanoscale biotechnology and proposes a roadmap of research for civil engineers of the 21st century.

Keywords: nanotechnology, heavy metal remediation, Sustainability, cementitious materials, construction biotechnology

OPEN ACCESS

Edited by:
Chang-Mou Wu,
National Taiwan University of Science and Technology, Taiwan

Reviewed by:
Masoud Mozafari,
University of Toronto, Canada
Umapathi Reddicherla,
Inha University, South Korea

***Correspondence:**
Wil V. Srubar III
wsrubar@colorado.edu

Specialty section:
This article was submitted to Structural Materials, a section of the journal Frontiers in Materials.

Received: *14 August 2020*
Accepted: *04 November 2020*
Published: *29 January 2021*

Citation:
Chen X, Charrier M and Srubar WV (2021) Nanoscale Construction Biotechnology for Cementitious Materials: A Prospectus. Front. Mater. 7:594989. doi: 10.3389/fmats.2020.594989

1 INTRODUCTION

Among the grand societal challenges of our time, climate change, infrastructure resilience, and resource recovery from waste are of critical importance (DeJong et al., 2011). Given the ubiquity of concrete and its projected increase in utilization over the next few decades, the development of resilient *and* sustainable cementitious materials will be a key solution to these challenges. *Resilience* of cementitious materials refers to high performance (e.g., strength) and other capabilities (e.g., self-

healing) that offer great resistance to—and recovery from—disasters. While *sustainability* has commonly been investigated in terms of reduced emissions associated with the manufacturing process, it could also refer to imparting additional functionalities with *in situ* environmental benefits (e.g., heavy metal immobilization).

To develop high-performance cementitious materials, nanotechnology has proven to be a highly effective tool. With addition of a variety of nanoparticles (e.g., SiO_2, ZrO_2, TiO_2, CuO), the setting time and diffusivity of concrete are reduced, while the strength and high-temperature stability are increased (Sobolev et al., 2006; Rashad, 2013a, Rashad, 2013b; Reches, 2018). While compressive strength is the most critical performance criteria for cementitious materials, decreased diffusivity prevents/reduces the ingress of water and aggressive ions (e.g., sulfate and chloride) and, thus, greatly enhances concrete durability (Mindess, 2019).

Enhanced performance of concrete *via* nanotechnology minimizes needs for repair or replacement, thus reducing economic and environmental cost. However, the manufacturing of nanoparticles is quite energy-intensive (Colvin, 2003; Jayapalan et al., 2013). For example, the manufacture one ton of TiO_2 NPs consumes ~32–40 GJ during a conventional procedure (Osterwalder et al., 2006). In addition to high energy consumption, the use of toxic chemicals, such as non-polar solvents used during synthesis or chemicals used to functionalize NP surfaces, are safety concerns for environmental and human health (Li et al., 2011; Tiquia-Arashiro and Rodrigues, 2016). Such barriers have somewhat limited the applications of nanoparticles in cementitious materials.

Biological approaches offer an alternative to the conventional synthesis of nanoparticles. During biosynthesis, microorganisms (e.g., fungi and bacteria) take target metal ions from the environment and convert them into metal or metal oxide NPs (called bio-NPs hereafter) (Li et al., 2011; Hulkoti and Taranath, 2014; Tiquia-Arashiro and Rodrigues, 2016). Such processes eliminate or reduce the use of expensive and potentially toxic chemicals, a benefit that has significantly promoted research in the field of NP biosynthesis (Li et al., 2011; Faramarzi and Sadighi, 2013). Biological synthesis of NPs also eliminates high energy-consuming processes (e.g., grinding of ore, reacting with strong acid, and treating with steam). A bio-based approach is even more favorable considering the potential to carry out such biosynthesis under environments of varying temperature, pH and pressure, salt concentration, acidity and alkalinity, either by using extremophiles (i.e., microorganisms that survive under extreme environmental conditions) or through genetic modification (Stabnikov et al., 2015; Beeler and Singh, 2016; Tiquia-Arashiro and Rodrigues, 2016). As specific examples, genetic modification has been shown to control *E. coli*'s capability for producing $CaCO_3$ of tailored morphology and mechanical properties (Liang et al., 2018; Heveran et al., 2019) and its tolerance to harsh environment (e.g., high NaCl concentration) (Eslami et al., 2016).

While bio-based nanotechnologies have been applied to a number of fields, such as nanomedicine, environmental remediation, and energy generation (Li et al., 2011; Tiquia-Arashiro and Rodrigues, 2016), their applications in the field of construction is relatively new. Although other biotechnologies have been applied in construction (Pacheco-Torgal and Labrincha, 2013; Ivanov et al., 2015; Stabnikov et al., 2015), these technology's *nanoscale* aspects, a scale that exhibits great potential for future civil engineering materials (Pacheco-Torgal and Jalali, 2011), has not been reviewed in detail.

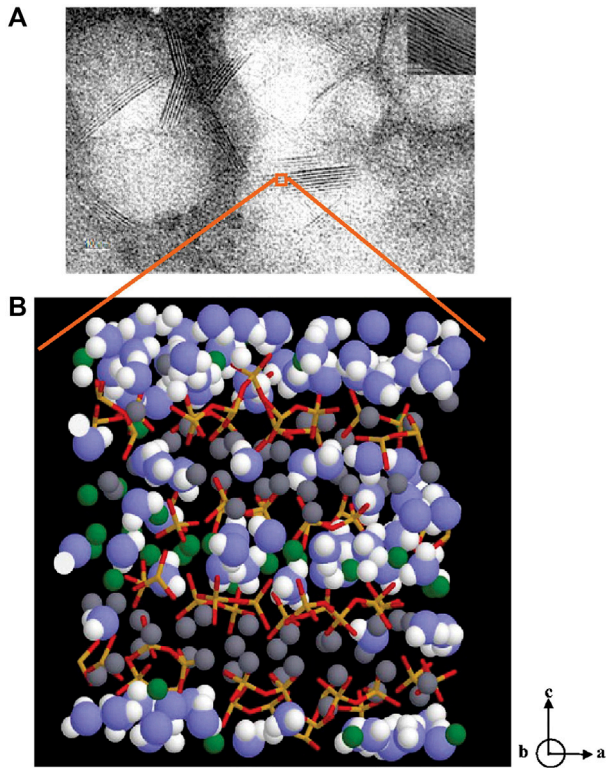

FIGURE 1 | (A) TEM image of clusters of C-S-H, the inset is a TEM image of tobermorite **(B)** the molecular model of C-S-H: the blue and white spheres are oxygen and hydrogen atoms of water molecules, respectively; the green and gray spheres are inter and intra-layer calcium ions, respectively; yellow and red sticks are silicon and oxygen atoms in silica tetrahedra (Pellenq et al., 2009).

This work summarizes for the first time the progress, promise, and potential of a new field—*nanoscale construction biotechnology*. First, we review nanoscale construction technology and biotechnology and identify links that bridge gaps between the two. Specifically, we focus on improving the performance of cementitious materials and the synergistic benefits related to environmental remediation capability. We begin with a current summary of NPs used to enhance engineering performance of cementitious materials, then examine the feasibility of bio-NP production (mainly *via* bacteria) for the same purpose and summarize possible approaches for such applications. Next, we focus on environmental remediation by cementitious materials or microorganisms alone, followed by a review of several ways to apply microorganisms (mainly bacteria, occasionally fungi and

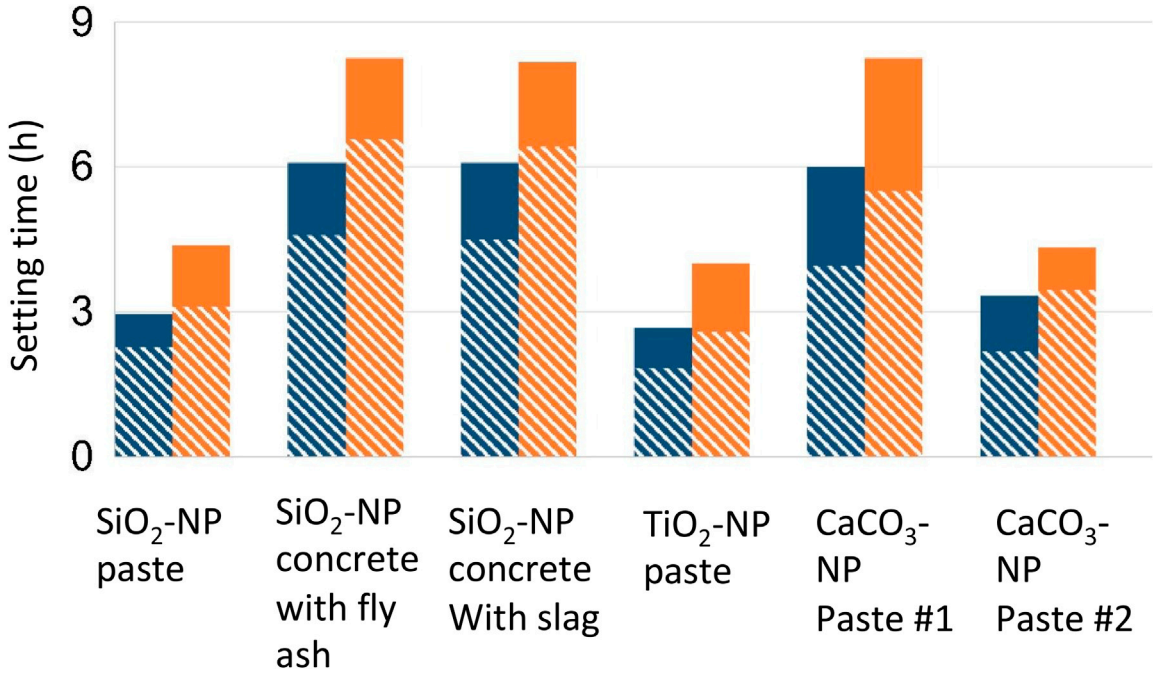

FIGURE 2 | Initial (blue color) and final (yellow color) setting of cement products prepared with or without NPs in different cementitious mixtures, adapted from Reches, (2018). While solid represent control mixtures, the line-filled part represents seeded mixtures.

algae) to cementitious materials for enhanced remediation capability. Finally, the significance and future development of the field of nanoscale construction biotechnology are discussed in light of opportunities and challenges that civil engineers will face in the 21st century.

2 ENGINEERING PERFORMANCE

2.1 Nanotechnology in Cementitious Materials

Because of the ubiquity of cement paste and concrete, the study of the nanostructure of cementitious materials has attracted great interest. Among multiple phases of hydration products (*eg*, ettringite, monosulfate and calcium hydroxide) that are formed during portland cement hydration, calcium silicate hydrate (C-S-H) is the main phase in hydrated portland cements. A typical nanoscale TEM image of C-S-H clusters and its molecular structure are shown in **Figure 1** (Pellenq et al., 2009). The C-S-H structure consists of calcium (green and gray spheres in **Figure 1**) layers sandwiched with chains composed of Si-O tetrahedra (yellow and red spheres), in addition to water molecules (blue and white spheres).

Nanoparticles (NPs, <100 nm) are highly efficient at tailoring the properties of cementitious materials at both early and late ages, even at low concentrations (<1%) (Reches, 2018; Mohajerani et al., 2019). In general, these effects are attributed to three mechanisms: 1) increased nucleation sites due to the NPs' high surface area that facilitates formation of C-S-H; 2) formation of C-S-H *via* pozzolanic reaction of some silica-containing nanoparticles; and 3) densification of cementitious materials *via* the filler effect (Reches, 2018).

Increased nucleation sites substantially accelerate the setting time of C_3S, the primary mineral in portland cement. The seminal work by Thomas (Thomas et al., 2009) demonstrated that C-S-H NP acts as nuclei for further growth of C-S-H, a change that eliminates the induction period of the cement hydration and substantially increases the total heat of hydration in the first 24 h. In addition to product-based seeds (i.e., C-S-H), many different types of NPs also exhibit accelerating effects on the setting of cementitious pastes (**Figure 2**) (Reches, 2018). Such nucleation promotes precipitation of C-S-H/C-A-S-H in alkali-activated fly ash/slag binders (Puligilla et al., 2019). This finding is in line with the concept of heterogeneous nucleation, in which the energy barrier is reduced, due to the presence of external surfaces that facilitate the reaction to proceed. Besides affecting the reaction kinetics, nucleation effects can also tailor the microstructures (Thomas et al., 2009; Puligilla et al., 2018; Puligilla et al., 2019). For example, the promoted nucleation of the C-S-H products in between the cement particles homogenizes the microstructure.

Consistent with the effects on setting time, many types of NPs, such as SiO_2, TiO_2, Fe_2O_3 and ZrO_2, increase the strength of common cementitious materials (**Table 1**) (Khoshakhlagh et al., 2012; Li et al., 2017; Afzali Naniz and Mazloom, 2018; Trejo-Arroyo et al., 2019) and macroporous pervious concrete (Barnhouse and Srubar, 2016). The most substantial effects of NPs on strength occur at early ages (i.e., 1–7 days) (Reches, 2018). The effect is also pronounced when relatively low-reactive mineral admixtures (e.g., fly ash, rice husk ash, and other

TABLE 1 | Example applications of abiotic NPs in cementitious materials and biotic NPs with similar characteristics.

NP Type	Applications of Abiotic NPs in Cementitious Materials					Biotic NPs with Comparable Characteristics			
	Size (nm)	characteristic[a]	% Cement	Property improved/ changed	Ref	Size (nm)	characteristic[a]	Microorganism	Ref
SiO_2	10–20	Colloid	1, 3, 5	Compressive, flexural and splitting strength (up to +30.9); electric resistance	Afzali Naniz and Mazloom (2018)	20–50	Amorphous[b]	*Fusarium oxysporum*	Marikani et al. (2016)
	13	Amorphous	0.3, 0.9	Water penetration (–45%); chloride migration (–28.7%); diffusion coefficient (–31%)	Du et al. (2014)	15 ± 5	Amorphous	*Thermoanaerobacter* sp. BKH1	Show et al. (2015)
	7–25	Amorphous	≤0.75	Strength (+48.8%); water penetration (+43.5%)	Hani et al. (2018)	9.8 ± 0.2	amorphous[b]	*Fusarium oxysporum*	Bansal et al. (2005)
TiO_2	350	Anatase	5, 10	Set (–23%); porosity (–22%@28 d)	Chen et al. (2012b)	66–77	Anatase	*Bacillus subtilis*	Kirthi et al. (2011)
	NA	Anatase	≤3.88 vol%	Flexural strength (+52.7% @3 d, 47.1%@28 d); electric resistivity (–13.6%)	Li et al. (2017)	65	Anatase	*Propionibacterium jensenii*	Babitha and Korrapati (2013)
	15	Anatase	≤1.5	Compressive strength increased up to +18%	Noorvand et al. (2013)	8–35	Anatase	*Lactobacillus*	Jha et al. (2009)
	15 ± 3	NA	Up to 5%	Strength (+58.5%, split tensile strength by +81.3%, and flexural strength by +50%	Nazari and Riahi (2010)	10.2 ± 0.1	Rutile	*Fusarium oxysporum*	Bansal et al. (2005)
	25	Colloid	3, 5	Pore size (–54%); set (–4 h s); strength (+28%)	Zhang et al. (2015)				
Fe_2O_3	60	Particle	Up to 5	Permeability (+44%); electric resistivity (+114%)	Madandoust et al. (2015)	11–99	Hematite	*Shewanella oneidensis*	Bose et al. (2009)
	15 ± 2	Crystalline	≤4.0	Compressive strength (+57%@2 d, +72%@28 d); increase of tensile and flexural strength	Khoshakhlagh et al. (2012)	10–20	Maghemite	*Actinobacteria*	Bharde et al. (2008)
	14	Amorphous	3, 5	Water penetration (–64@ 5%); increased strength; reduced chloride penetration	Joshaghani et al. (2020)	1–2	Ferrihydrite suspension	*Klebsiella oxytoca*	Balasoiu et al. (2010)
CuO	20 ± 3	Powder	1, 2, 3	Electrical resistivity (+167%); decreased chloride permeability and water adsorption	Miyandehi et al. (2016)	79–295	Spherical	*Species of Penicillium*	Honary et al. (2012)
	15 ± 3	Powder	≤4	Chloride permeability (–63%); reduced water adsorption	Khotbehsara et al. (2015)	5–20	Spherical	*Stereum hirsutum*	Cuevas et al. (2015)
	15	Powder	≤5	Permeability (–44%); electric resistivity (+275%)	Madandoust et al. (2015)				
ZrO_2	20	Monoclinic	≤5	Increased strength @ 1%; increased heat capacity	Yuan et al. (2013)	7.3 ± 2.0	Monoclinic	*Fusarium oxysporum*	Bansal et al. (2004)
	15–19	Tetragonal and monoclinic		Compressive strength (+9%)	Trejo-Arroyo et al. (2019)	4.8	NA	*Sargassum wightii*	Kumaresan et al. (2018)
Ag	72.6	~6 nm surface roughness	≤4	Thermal conductivity (+129.7%); porosity (–14.2%); split tensile strength (+189.4%)	Ceran et al. (2019)	10–100	Spherical	*Ureibacillus thermosphaericus*	Juibari et al. (2011)

[a]*Particles unless specified otherwise.*
[b]*Depending on calcination temperature.*

supplementary cementitious materials (SCMs)) are introduced as partial replacement for portland cement. While these mineral admixtures are a key solution to concrete's sustainability (Juenger et al., 2019), the addition of NPs overcomes the slow reaction by accelerating the reaction kinetics.

The permeability of concrete is a key parameter that affects long-term durability. Permeability affects carbonation, sulfate attack, chloride intrusion, and alkali-aggregate reactions (i.e., alkali-silica reaction and alkali-carbonate reaction), among other degradation mechanisms (Mindess, 2019). NPs

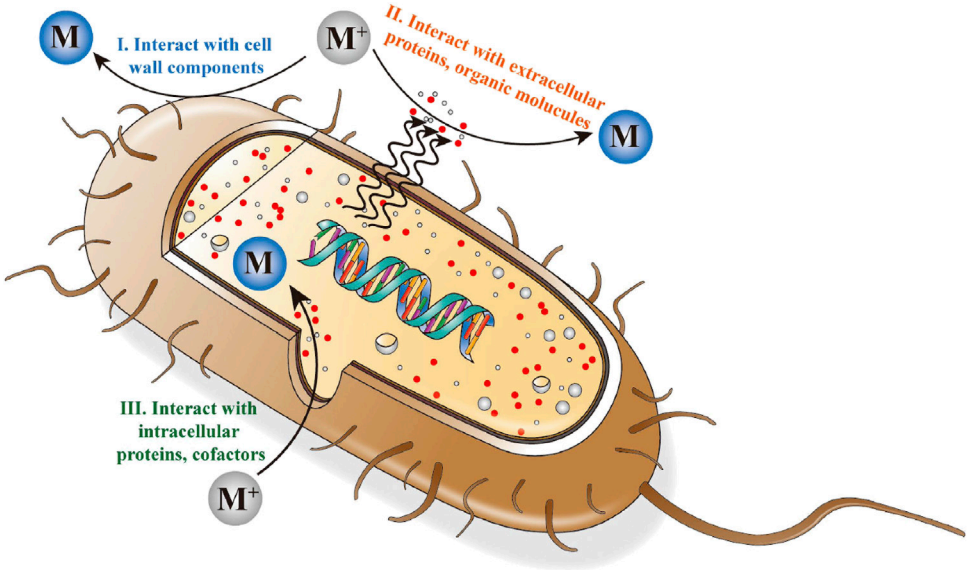

FIGURE 3 | Schematic illustration of bacterial synthesis of NPs (intracellular and extracellular procedures) (Fang et al., 2019).

have shown to decrease the diffusivity to gases in dry conditions and ions in water-saturated conditions (Reches, 2018), likely due to the beneficial nucleation and densification effects previously discussed. The effect of NPs on permeability can be substantial. Depending on the mixture proportions, up to 75% decrease in permeability has been observed with addition of ~1 wt% NPs (Reches, 2018). Relevantly, the reduced permeability (or porosity) is associated with concomitant increase in electrical resistivity and resistance to penetration of chloride and water (see **Table 1**).

2.2 Applications of Bio-NPs in Cementitious Materials

Abiotic NPs are fabricated *via* conventional (mainly physical and chemical) techniques. Although these techniques can produce large quantities of NPs in a short time with well-defined characteristics (e.g., size and shape), their procedures are complicated and cost/energy consuming (Li et al., 2011). These conventional techniques usually employ atomistic and molecular processing in an aqueous condition and commonly use chemicals that are considered toxic to the environment and, especially, human health (Li et al., 2011; Tiquia-Arashiro and Rodrigues, 2016).

Microorganism-based synthesis can serve as a non-toxic and environment-friendly alternative to NP production. A wide range of fungi and bacteria have been exploited for such synthesis (Li et al., 2011; Tiquia-Arashiro and Rodrigues, 2016). During synthesis, the microorganisms either uptake ions intracellularly or adsorb them onto surface structures, thereby resulting in passive NP precipitation or active conversion by enzymes. These processes, in lieu of expensive and oftentimes toxic chemicals, enable an environmentally friendly synthesis route. As a result, many researchers in the field of NP synthesis have turned to bio-synthesis (Li et al., 2011; Faramarzi and Sadighi, 2013). This bio-based approach is even more favorable, considering the potential to genetically engineer microorganisms for desirable characteristics, for example, engineering genetic control over NP morphology or harnessing extremophiles (Tiquia-Arashiro and Rodrigues, 2016) capable of biosynthesis and persistence under the extreme environments that may occur during and after construction.

2.2.1 Synthesis Mechanisms of Bio-NPs

While biosynthesis of NPs involve multiple complex processes, it typically starts by trapping the metal ions to the surface or inside of the cells, followed by conversion of these ions into NPs (Li et al., 2011). During the conversion process, microorganisms act as biocatalysts and alter the ionic concentration of the surrounding environment in a very localized manner, thus supersaturating the solution and facilitating precipitation. Alternatively, the conversion of metal ions can take place either through interaction with intracellular or extracellular proteins and organic molecules or by interacting with the cell wall components, as illustrated in **Figure 3** with bacteria as an example (Fang et al., 2019). As an example, during the biosynthesis of Ag NPs by *Cladosporium cladosporioides* fungi, Ag ions are adsorbed on the cell surface and subsequently converted to silver nuclei through an enzyme-induced reduction reaction. These nuclei grow through further reduction and accumulation (Balaji et al., 2009). More fundamentally, this conversion process is related to the electron shuttling (or redox mediating) enzymes, for example, nitrate reductase (Kalishwaralal et al., 2008).

Similar procedures (i.e., entrapment followed by conversion) are seen in synthesis of metal oxide NPs (Li et al., 2011). In the synthesis of magnetic iron oxide particles by magnetotactic bacteria, including magnetite (Fe_3O_4) and maghemite

(γ-Fe_2O_3), vesicles are first formed and serve as a scaffold for proteins involved in the production of the NPs. These vesicles then assemble into a line along with cytoskeletal filaments, and Fe ions accumulate in the vesicles. This accumulation is aided by membrane transporters (e.g., proteins and siderophores). In the last step, relevant proteins trigger and regulate the nucleation and growth process of the iron oxide NPs. Throughout this process, various proteins contribute to supersaturation of Fe and maintain conditions for reduction and oxidation reactions that induce NP production (Arakaki et al., 2008). An alternative process was observed for synthesis of magnetite with *Shewanella oneidensis* (Perez-Gonzalez et al., 2010). This mechanism initially involves active production of Fe^{2+} by using ferrihydrite as a terminal electron acceptor. Then, a passive process takes place, during which Fe^{2+} and Fe^{3+} accumulate at the negatively charged cell wall and extracellular structures leading to supersaturation and precipitation of NPs.

2.2.2 Direct Addition of Bio-NPs to Cementitious Materials

Bio-NPs exhibit great potential for applications in cementitious materials. As mentioned in **section 2.1**, NPs improve the performance of cementitious materials mainly by enhancing nucleation of the C-S-H product and by acting as a filler to densify the microstructures. Both mechanisms relate to the small particle sizes and large surface area of NPs. It follows that bio-NPs of sufficiently small size and large surface area would improve the performance of cementitious materials in a similar fashion.

In **Table 1**, we summarize biogenic NPs reported in literature that exhibit similar sizes and characteristics to conventional NPs added to cementitious materials to enhance engineering performance. SiO_2 NP additives used in cementitious materials exhibit amorphous features with average sizes of 7–25 nm (Du et al., 2014; Hani et al., 2018; Afzali Naniz and Mazloom, 2018). Similarly, SiO_2 particles produced *via Fusarium oxysporum* and *Thermoanaerobacter* sp. BKH1 bacteria exhibit amorphous features and sizes from 9.8 to 50 nm (Bansal et al., 2005; Show et al., 2015; Marikani et al., 2016). These nanostructural characteristics indicate feasibility of these bio-NPs to serve as additives to improve performance of cementitious materials, unlike the micro-sized particles that exhibit less pronounced effects (Sato and Diallo, 2010). Other common additives to cementitious materials (e.g., TiO_2, Fe_2O_3, CuO, ZrO_2 ang Ag) can also be produced with a variety of microorganisms in comparable sizes and characteristics.

Additionally, the size and morphology of the bio-NPs can be controlled by tuning the biosynthesis parameters. During the *Corynebacterium glutamicum*-mediated synthesis, the particle sizes of Ag NPs could be tuned by varying the media parameters including pH, temperature and $AgNO_3$ concentration (Sneha et al., 2010). Besides the media-related parameters, biological factors also control the synthesis of bio-NPs. For example, The CuO NPs synthesized from *Penicillium citrium, Penicillium waksmanii and Penicillium aurantiogriseum* under the same pH and temperature conditions exhibit different values of polydispersity index (PDI) and average particles, indicating that strain selection has a significant impact on NP morphology (Honary et al., 2012).

Bio-NPs need to be purified after production to avoid any complications to hydration of cementitious materials (Basaran Bundur et al., 2015). Purification typically requires specialized equipment. For example, Ag NPs synthesized from *Escherichia coli* are preliminarily centrifuged and washed several times and then transferred to a dialysis tube to remove high molecular weight molecules, followed by an ultracentrifugation (200,000 rpm at 4°C for 16 h) (Gurunathan et al., 2009). In another example, the biosynthesized Au NPs from *Bacillus cereus* or *Fusarium oxysporum* were purified three times by centrifugation (14,700 rpm, 30 min) using double-distilled water. For comparison, to purify chemically synthesized NPs (again by taking Ag as an example), while centrifugation can be carried out (Guzman et al., 2009), simple filtration and washing can also be conducted (Sun et al., 2003), given that the purification process is relatively straightforward in most chemical synthesis processes (Tan and Cheong, 2013).

In summary, the bio-NPs, upon purification, exhibit great potential to be directly used in cementitious materials, because their size and characteristics are comparable to abiotic counterparts that have been used successfully to enhance the performance of cementitious materials. Additionally, the size and morphology of bio-NPs can be tuned by optimizing the biosynthesis conditions, which offers new pathways to optimizing biosynthesis to produce bio-NPs with the most desirable characteristics.

2.2.3 Addition of Bio-NPs via Surface Treatment of Aggregates

In addition to the direct addition of purified bio-NPs to cementitious materials during mixing, bio-NPs could potentially be precipitated/coated on the surface of aggregates before mixing with cements. A similar strategy has been proposed by Wong (Wong, 2015). Specifically, soil/sand, aggregates (Wang et al., 2017) or some solid industrial wastes (Achal et al., 2013; Cuzman et al., 2015) can be biomineralized and subsequently used as fillers and aggregates in concrete. Besides densifying the aggregates/fillers themselves, such biomineralization benefits the performance for the final concrete materials, especially when the resulting precipitation 1) exhibits preferred nanostructural morphology and 2) occurs on surfaces of fillers/aggregates. The treated fillers/aggregates, when possessing nanostructural morphology, would enhance the engineering performance similar to direct addition. Additionally, the presence of the NPs at the interface between aggregates and cement matrix (i.e., interfacial transition zone or ITZ) promotes localized nucleation of hydration products. Since the ITZ is usually the weakest zone in concrete (Mindess et al., 2003), the application of NP-modified aggregate offers great potential benefits to enhancing engineering performance.

Currently, microorganism-based precipitation on the surface of cementitious materials and aggregates has been studied mainly *via* calcium carbonate ($CaCO_3$) biomineralization (Seifan et al., 2016). Biomineralization by living organisms has also been explored for biosynthesis of NPs (Achal et al., 2015; Salehizadeh et al., 2020), though it, unlike many other studies related to the biosynthesis of NPs, can also produce larger-sized

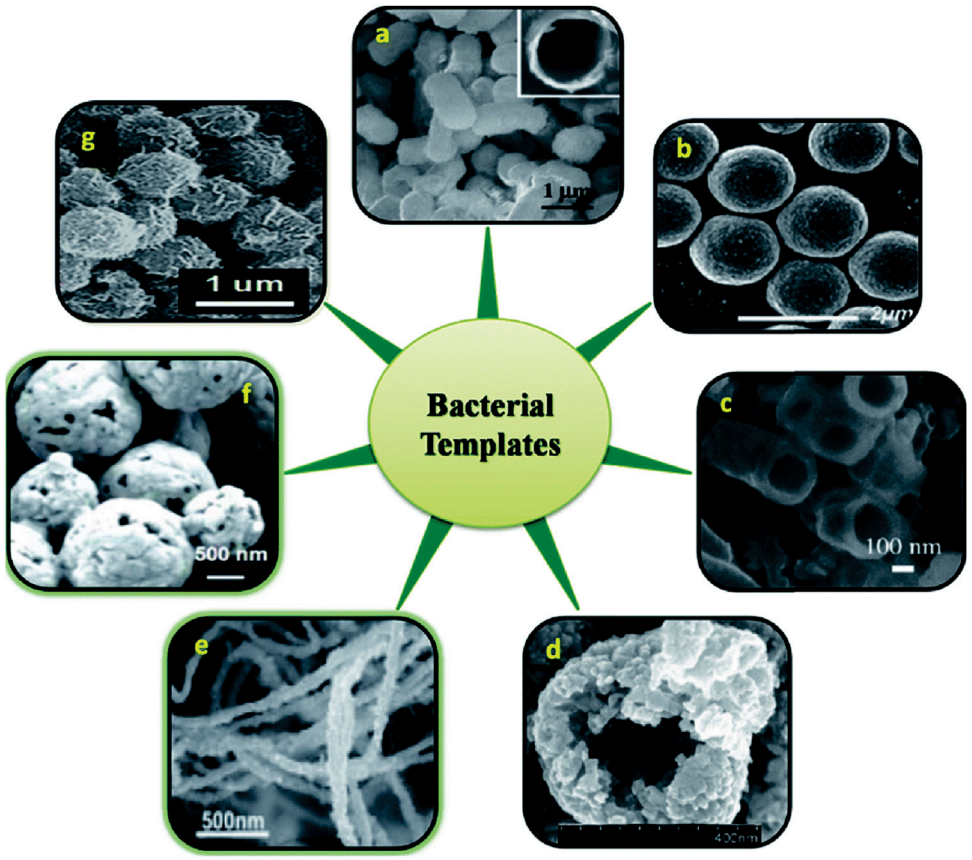

FIGURE 4 | Various nanostructures derived using the entire cell of bacteria *via* extracellular biomineralization. **(A)** FESEM images of ***E****. coli* templated hollow silica microparticles (insert: cross sectional view of calcined particle); **(B)** *S. thermophilus*/ZnO core–shell spheres; **(C)** SEM images of crushed calcined zirconia particles using ***E****. coli* template; **(D)** Co_3O_4-decorated ZnO hollow spheres; **(E)** Au nanostructures synthesized by the reduction of aqueous $HAuCl_4$; **(F)** SEM image of H_2O_2 etched Ag microspheres at a higher magnification using *S. thermophilus* template; **(G)** FE-SEM image of uniform, bacteria-supported, hierarchical Co_3O_4 superstructures produced without changing the spherical shape of the original *micrococcus* template (Selvakumar et al., 2014).

minerals or structural features, including shells and bones. During biomineralization, metal ions are precipitated with ligands (e.g., sulfide, phosphate or organic functional groups) or with carbonates/hydroxides (Newsome et al., 2014; Bhattacharyya et al., 2019).

As a typical type of biomineralization, microbially induced carbonate precipitation (MICP) produces calcium carbonates as NPs that exhibit nanostructural morphology at initial stages of precipitation (Zhang, 2016). This observation suggests that with well-controlled environmental conditions the MICP-treated aggregates exhibit nanostructural feature that could promote the hydration upon mixing with cement pastes. Similar nanostructural morphology is also seen in other types of extracellular biogenic NPs, for example, on bacterial cell walls (**Figure 4**) (Selvakumar et al., 2014) or in biofilms (*i.e.,* a group of microorganisms in which cells stick to each other and also to a surface) (Kalathil et al., 2011).

MICP-produced $CaCO_3$ have been applied in infrastructure usually through binding with cementitious materials. $CaCO_3$ precipitation approaches have been adopted to fill or heal the external cracks to enhance durability (De Muynck et al., 2010). For example, a $CaCO_3$-based bio-cementitious crust on the surface of sand has been developed that exhibits a flexural strength of 35.9 MPa and high water impermeability (Stabnikov et al., 2011). Besides surface treatment, such bio-based precipitation has been reported to form bulk bio-blocks, such as reinforced soil and sand (van Paassen et al., 2010; Gorospe et al., 2013). More recently, microorganism-induced mineralization has been utilized to engineer a living building material through binding and toughening a structural scaffold of sand and gelatin (Heveran et al., 2020).

Besides the above examples of $CaCO_3$ precipitation, more direct evidence and explanation indicate that precipitation can occur on the surface of cementitious materials and aggregates. SEM images reveal that $CaCO_3$ precipitates occur on the surface of microbial-treated sand (Porter et al., 2017) and recycled aggregates (Wang et al., 2017). Based on SEM and micro-CT characterizations of magnesia cement-based blends, microbial-induced formation of nesquehonite and hydromagnesite has been identified on the surface of cementitious materials and has been shown to exhibit healing effects (Ruan et al., 2019). The high cohesion of this precipitation was attributed to the incorporation

of inorganic components and epitaxial growth of the crystals (Wang et al., 2016).

Taken together, the aforementioned studies indicate that microorganism-induced precipitation can produce NPs that exhibit beneficial nanostructural morphologies directly on aggregates surfaces. This potential type of nano-modified aggregates could enhance the engineering performance as common nano-additives and strengthen the ITZ of concrete.

3 ENVIRONMENTAL SUSTAINABILITY

In this section, we examine the feasibility of nanoscale biotechnologies to enhance the capability of cementitious materials to remediate heavy metals (**section 3.1**) and remove air pollutants (**section 3.2**). We then discuss application methods for these biotechnologies (**section 3.3**).

3.1 Heavy Metal Removal

Acceleration of some industrial activities, such as mining and battery production, has induced substantial discharge of heavy metals into the environment (Fu and Wang, 2011). Heavy metals with atomic weights from 63.5 to 200.6 and specific gravity >5.0, can accumulate in living microorganisms rather than being biodegraded. Some common heavy metals of great toxicity include cadmium, mercury, lead, zinc, copper, nickel and chromium. While these heavy metals possess a variety of chemical properties that correspond to multiple mechanisms of toxicity, in general, exposure results in cellular changes resulting in various health issues (Giovanella et al., 2020). For example, mercury causes dysfunction of proteins *via* complexing with the protein's sulfhydryl groups that lead to long-lasting neurological and developmental deficits (Farina et al., 2011); chromium, when accumulated in the food chain especially in the form of Cr(VI), result in severe skin irritation or even lung carcinoma (Khezami and Capart, 2005).

Numerous techniques have been developed to remediate heavy metals, including chemical precipitation, membrane filtration, ion exchange and electrochemical technologies for treating wastewater, groundwater, and soil (Bradl, 2004; Fu and Wang, 2011; Hashim et al., 2011). The most common methods involve chemical precipitation (*via* hydroxide, carbonate and sulfide groups), lime coagulation, ion exchange (e.g., *via* resins), and chemical oxidation or reduction. These methods, however, are ineffective or costly (Suresh Kumar et al., 2015).

Microorganisms, including bacteria and algae, have proven useful candidates for remediation of heavy metals. Biological technologies exhibit high efficiency and low cost for removal of heavy metals from dilute solutions (Suresh Kumar et al., 2015). For example, the adsorption and elution of selected heavy metals were reported to be much higher by algae than by activated carbon and natural zeolites (Doshi et al., 2006). Here, we explore the feasibility of applying bioremediation in cementitious materials.

3.1.1 Immobilization in Cementitious Materials

Portland cement pastes have been shown to be a cost-efficient technique to immobilize heavy metals through three mechanisms: 1) sorption, 2) chemical incorporation (mainly precipitation and co-precipitation) and 3) encapsulation (Paria and Yuet, 2006; Chen et al., 2009). While sorption can be achieved physically *via* attraction to charged surfaces or chemically *via* covalent bonding especially at functional group sites of C-S-H phase, the latter two are more common mechanisms.

Chemical incorporation, mainly the formation of insoluble hydroxides, is a dominant mechanism for solidification and stabilization of heavy metals (Chen et al., 2009). As a result, metals including As(III), Cr(VI), and Hg that do not form hydroxides are not suitable for cement-based solidification. Meanwhile, pH is a critical influencing factor for the solidification of Cd, Cr, Cu, Pb Ni and Zn, because it affects solubility of their hydroxides. Besides hydroxide precipitation, carbonates, sulfates, and silicates of heavy metals are also precipitation strategies for solidifying heavy metals (Chen et al., 2009). Chemical incorporation in cement hydration products can also occur directly, since heavy metals, such as Zn and Pb, incorporate in the C-S-H in the Ca layer, Si chain or in the interlayer space (Guo et al., 2017a).

Heavy metals can be physically encapsulated by the C-S-H phase (Cartledge et al., 1990). Heavy metal wastes can be mixed with cementitious materials during their fresh state. Once materials are hardened, the heavy metals are isolated in a monolithic waste-like form that can exhibit long-term stability. Though physical encapsulation here is the main mechanism, chemical stabilization could also play a role (Guo et al., 2017a).

Geopolymers, as an alternative to ordinary portland cement (Chen et al., 2017b), also exhibit a propensity to adsorb heavy metals. In one study, the removal rate of Zn was shown to be 97.7% by the volcanic tuff based geopolymers but only 78.5% by the raw tuff, corroborating the potential of the geopolymerization techniques to remediate heavy metals (Al-Zboon et al., 2016). The mechanism often relates to the participation of heavy metals (e.g., Zn^{2+}, Cu^{2+}, Cd^{2+}, and Cr^{3+}) to charge-balance aluminates in the geopolymer framework (Rasaki et al., 2019), while other components (e.g., silicates) also react with heavy metals (e.g., Pb) to form Pb_3Si_5 precipitates (Guo et al., 2017a). Additionally, physical encapsulation and adsorption effects are also reported as primary immobilization mechanisms (Guo et al., 2017c; Ji and Pei, 2019).

The surface morphology and porosity of geopolymers affect their efficiency to remove heavy metals. For instance, the NaOH activated metakaolin geopolymers exhibit ~90% removal capacity for Pb^{2+}, Cu^{2+}, Cr^{3+}, and Cd^{2+}, a phenomenon that is attributed to the mesoporous surface of aluminosilicate network (Cheng et al., 2012). A porous geopolymer (~74.6% porosity) made from fly ash and iron ore tailing as the precursor and H_2O_2 as the foaming agent exhibited uptake percentage of Cu^{2+} at 90.7%, a high efficiency that was attributed to its well defined pore size distribution and high total porosity (Duan et al., 2016). Many other studies report that the adsorption of heavy metals (e.g., Pb^{2+}, Cu^{2+}, Sr^{2+}, Co^{2+}, Cs^{+}, Cu^{2+}, Cd^{2+}, Zn^{2+}, and Ni^{2+}) follows the pseudo-second-order model (Rasaki et al., 2019). Fitting to this model, which involves intra-particle diffusion and kinetics parameters (Ho and McKay, 1999), suggests a heterogeneous surface of geopolymers for uptake of heavy metals. Considering the

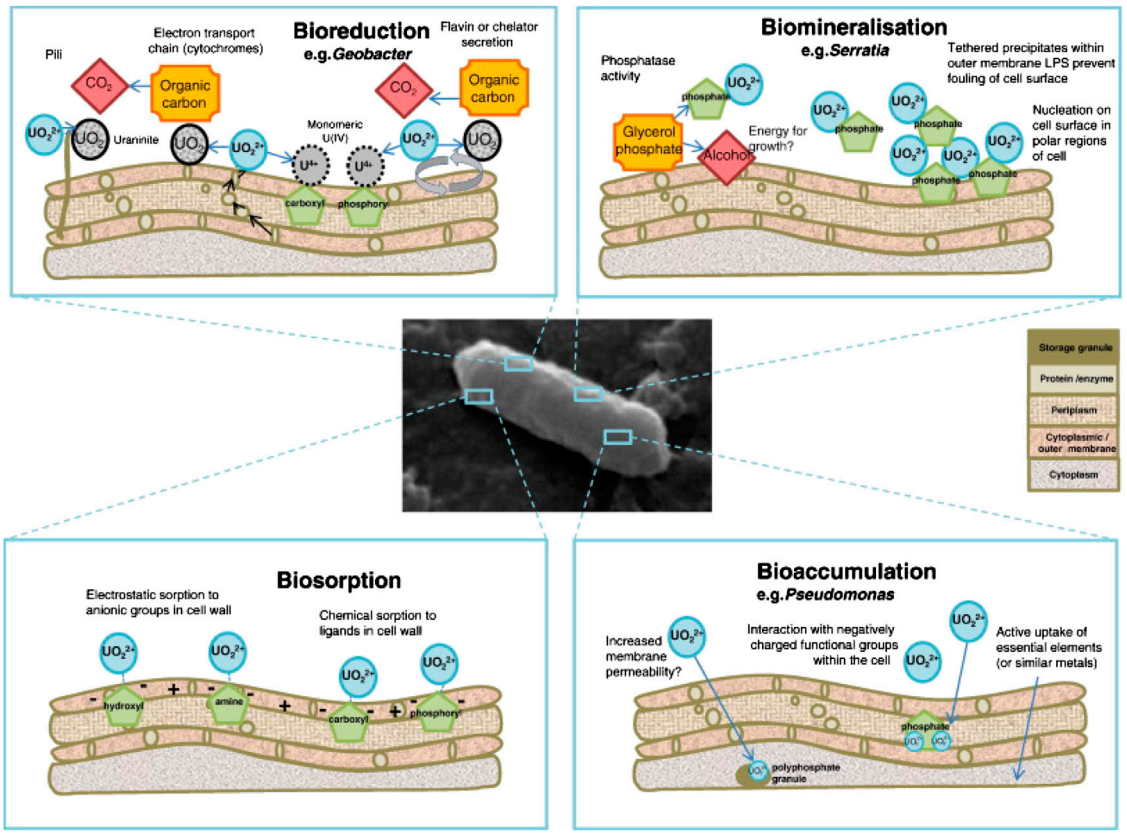

FIGURE 5 | Schematic illustrating the mechanisms of interaction between a microbe and heavy metals (taking uranium as a general example): bioreduction, biomineralization, biosorption, and bioaccumulation (Newsome et al., 2014).

surface is a critical factor for removal capacity, several treatments that enhance the mesoporous nature by introducing chemical additives have shown to significantly increase the removal efficiency for heavy metals (Tang et al., 2015; Ge et al., 2017).

In summary, portland cements immobilize/solidify heavy metals mainly through the hardening process or precipitation (e.g., hydroxide). Furthermore, adsorption by geopolymers generally depends on their microstructural porosity and surface morphology. Both materials exhibit a potential to benefit from additional efficacy of heavy metal remediation enabled by biotechnology, for example *via* biomineralization on surfaces of aggregates or concrete materials, among other ways, as reviewed in detail in **section 3**.

3.1.2 Removal via Microorganisms

Many different types of microorganisms exhibit the capacity to remove heavy metals. A halophilic *Haloferax* strain was found to remove up to 21% of cadmium in a culture solution (Das et al., 2014). The thermophilic *Geobacillus thermodentrificans* cells removed multiple types of heavy metals (e.g., Fe, Cr, Cd, and Pb) *via* biosorption from an industrial effluent (Chatterjee et al., 2010). Mercury ions (Hg^{2+}) from soil were reduced to Hg by the acidophile *Acidithiobacillus ferrooxidans* SUG 2–2 (Takeuchi et al., 2001). Many other acidophiles also exhibit great potency in removal of many types of heavy metals through various mechanisms (Dopson et al., 2003; Wu et al., 2012; Dopson and Holmes, 2014). Like bacteria, algae also exhibit high efficiency for heavy metal removal (Monteiro et al., 2012), even when used as non-living biomass (after acid-, heat- or other treatment of live cells) (Mehta and Gaur, 2005).

Most processes of bioremediation by cells are a resistance mechanism that allows for the survival in presence of heavy metals. These mechanisms are the foundation to develop biotechnologies for civil engineering that involve bioremediation. Using uranium as a general example, the bacterial mechanisms categorized as bioreduction (or biotransformation), biomineralization, biosorption, and bioaccumulation are illustrated in **Figure 5** (Newsome et al., 2014).

Bioreduction involves the conversion of oxidation states of metals, for example, by reducing U(VI) to U(IV) with *Geobacter* through respiration of metal ions as an electron acceptor to gain energy for metabolism (**Figure 5**) (Newsome et al., 2014). Aggregation of such bio-reduced metal ions would lead to the formation of NPs (as reviewed in **section 2.2.1**). For the transformation from Hg(II) to the least toxic form of Hg^0 (Mathema et al., 2011), the mercury resistance genes relate to the key enzymes in the biotransformation process (Barkay et al., 2003). Specifically, the organomercury lyase (MerB) promotes the

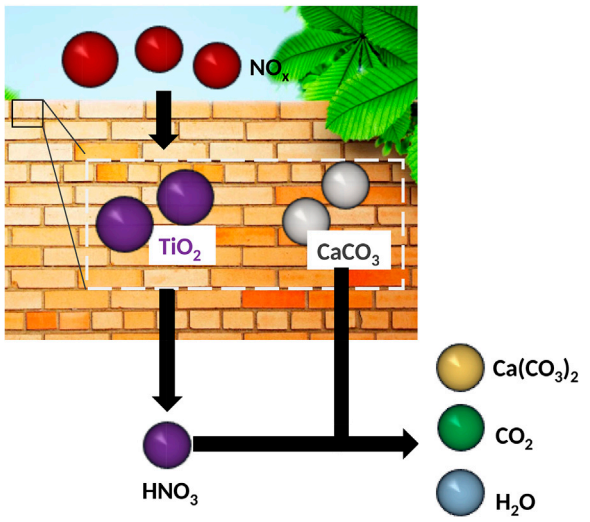

FIGURE 6 | Schematic for neutralization of vehicle pollution (mainly NO_x) *via* utilizing of energy captured from sunlight, adapted from Spasiano et al., (2015).

cleavage of organomercury compounds, and the released Hg^{2+} is reduced to Hg^0 by mercuric reductase (MerA) (Benison et al., 2004).

Biomineralization, commonly seen as MICP in cementitious materials as reviewed in **section 2.2.3**, is also a critical mechanism to remediate heavy metals. To biomineralize uranium, the *Serratia* species convert the organic glycerol phosphate to inorganic phosphate that then precipitates U(VI) to form hydrogen uranyl phosphate (**Figure 5**) (Newsome et al., 2014).

Other resistance mechanisms involve removing heavy metals through biosorption or bioaccumulation. During biosorption, the heavy metals are bound to cell surface through a physio-chemical process, such as electrostatic and chemical sorption (Newsome et al., 2014). This process, however, is not effective in remediation for some metals, such as uranium, due to the high desorption rate. Usually, biosorption is among the first steps before bioreduction and biomineralization take place (Giovanella et al., 2020). To the contrary, bioaccumulation accumulates the heavy metals inside the cell (Chojnacka, 2010). During bioaccumulation, heavy metals are immobilized in cells through formation of metalloproteins, metal-binding peptides and polymers (Diep et al., 2018; Giovanella et al., 2020).

These processes/mechanisms of heavy-metal removal *via* microorganisms impart pathways for environmental remediation to civil engineers. Specifically, all the four mechanisms (*i.e.,* bioreduction, biomineralization, biosorption, and bioaccumulation) could be exploited by directly adding microorganisms into polluted water/suspensions. Biomineralization could be promoted on surfaces of aggregates/fillers or bulk concrete materials in order to remove heavy metals. Bioreduction, biosorption and bioaccumulation can take place in biofilms that could grow on surfaces of cementitious materials. These applications are discussed in detail in **section 3.3**.

3.2 Air-Pollution Removal

3.2.1 Removal via Cementitious Materials

While heavy metal pollution mainly affects water and soil, air pollution is another major issue that has attracted much recent attention from academia and industry. Polluted air was found to be responsible for 6.4 million deaths worldwide in 2015 (Landrigan, 2017). CO_2, NO_x (e.g., nitrogen dioxide), and volatile organic compounds (VOCs) are major sources of pollution in urban regions (Petronella et al., 2017).

Cement paste has been shown to react with atmospheric CO_2 (Šavija and Luković, 2016). Hempcrete, which consists of CH and CSH (i.e., the reaction products also seen in cement pastes), has been shown to sequester up to -16 $kgCO_2e/m^2$ over its lifecycle (Souto-Martinez et al., 2018b; Arehart et al., 2020). While the CO_2-remediation capability of cement pastes is limited (Souto-Martinez et al., 2017; Souto-Martinez et al., 2018a), the remediation by calcium- and/or magnesium-containing minerals (usually present or being added to cements) are expensive. Sequestration is estimated at $50 to $300 per tCO(2) sequestered (Sanna et al., 2014).

The degradation of NO_x has been explored by utilizing catalytic properties of TiO_2 nanoparticles (Spasiano et al., 2015). As shown in **Figure 6**, upon illumination, TiO_2 coated surfaces generate oxygen to oxidize NO_x into nitric acid, which are subsequently neutralized by alkaline phases in the cementitious materials. This mechanism has been applied to treat NO_x polluted air in research studies experimentally (Hüsken et al., 2009; Guo et al., 2017b), *via* modeling (Ballari et al., 2010), and by developing commercial products (Petronella et al., 2017).

The photocatalytic process induced by TiO_2 NPs have also been utilized to remove the toxic VOCs (e.g., ketones, halogenated hydrocarbons and aromatic compounds), leading to formation of benign products (e.g., H_2O vapor and CO_2) (Mo et al., 2009; Chen et al., 2012a; Petronella et al., 2017). An introduction of 1 wt% of TiO_2 nanoparticles into portland cement was found to remove BTEX (benzene, toluene, ethylbenzene and o-xylene) up to 54% (Strini et al., 2005). Besides portland cement, geopolymers, when coated with a thin film of TiO_2 NPs, exhibited degradation capability *via* photocatalytic process (Falah et al., 2016; Chen et al., 2017a).

Even though the applications of bio-based TiO_2 NPs to cementitious have been limited so far, similar characteristics of abiotic TiO_2 NPs with the bio-based NPs indicate such applications are promising. Microorganism produced TiO_2 NPs can be anatase or rutile with particle sizes of ~ 8–77 nm based on selected reports from literature (**Table 1**) (Bansal et al., 2005; Jha et al., 2009; Kirthi et al., 2011; Babitha and Korrapati, 2013). These characteristics are expected to exhibit identical photocatalytic properties and effects on the engineering performance of cement paste and concrete (Chen et al., 2012a).

3.2.2 Removal via Microorganisms

While TiO_2 NPs produced via microorganisms (**Table 1**) can be applied to cementitious materials in the same manner as discussed in **section 2.2.2**, in this section we aim to review the remediation of air pollution directly by microorganisms. Some microorganisms exhibit great potential to sequester CO_2. For

example, growth of 1.0 kg microalgae is associated with fixation of 1.88 kg CO_2 (Ho et al., 2011), much higher than carbon sequestration by type I cement based concrete over 25 years of exposure (i.e., <30 kg CO_2 per 1 m^3 of concrete column, or <0.0125 kg CO_2 per kg of concrete if we assume a concrete density of 2,400 kg/m^3) (Souto-Martinez et al., 2018a).

To remove CO_2, MICP that converts CO_2 into carbonate minerals has been shown to be an effective method (Anbu et al., 2016). As a safe and environment-friendly technique, carbonic-anhydrase-enzyme mediated MICP catalyzes reversible hydration of CO_2 to formations of bicarbonates and calcite crystals (Liu et al., 2005; Kim et al., 2012). The carbonic anhydrase enzyme when purified deposits 15 times more carbonates than its crude counterpart (i.e., cells washed and resuspended in lysis buffer) (Ramanan et al., 2009).

While the CO_2 remediation *via* carbonic-anhydrase based MICP could be costly (at least under lab scale where the extraction and purification of enzymes is complex), algae-based CO_2 capture seems to be a more cost-efficient method. This CO_2 capturing process is sustained under ambient temperature and daylight, and the resulting algal biomass can be used as biofuel, animal feed, and many other high-value products (Judd et al., 2015). Additionally, the algal photobioreactors can be as simple as a pond system that is robust to changes in CO_2 concentration. Different algae have been reported to fix CO_2 at different rates. While up to 56% of the total CO_2 from a feed gas of 15% CO_2 at a flow rate under 50 ml/min can be fixed by *Chlorella vulgaris* (Li et al., 2013), a fixation efficiency of 10% is seen for a gas containing 10% CO_2 (flow rate not reported) by *Dunaliella tertiolecta* (Sydney et al., 2010). These efficiency values are generally dependent on many factors, including mass transfer of CO_2 from gas to liquid phase, CO_2 loading, biomass concentration and light intensity (Judd et al., 2015).

Microorganism-aided phytoremediation has been studied as one of the bio-approaches to remove air pollution. Endophytic microorganisms that colonize in the plant have shown to accelerate phytoremediation processes efficiently to decrease or remove VOCs and greenhouse gases (Stępniewska and Kuźniar, 2013). The bacterium *Burkholderia cepacia* L.S.2.4, a natural endophyte of yellow lupine, was genetically modified (commonly carried out to improve microorganisms' target performance, such as the control of $CaCO_3$ precipitation cited in the introduction section) by introducing a pTOM toluene-degradation plasmid of *Burkholderia cepacian* G4 and exhibited strong degradation capability for toluene (Barac et al., 2004). Some methanotropic bacteria (e.g., *Methylocella palustris* and *Methylocapsa acidiphila*) found in *Sphagnum* moss tissues were found to oxidize methane to carbon oxide that is then used by the moss plant during photosynthesis (Raghoebarsing et al., 2005; Stępniewska and Kuźniar, 2013). Such a cycle by oxidizing methane and utilizing carbon dioxide reduced the emission of these gases by up to 50% from peatlands (Kip et al., 2012).

More relevant to the removal of N_xO gases by TiO_2 as reviewed in **section 3.2.1** above, several bacteria have been found to exhibit N_2O-reducing capability (Hallin et al., 2018). The *Bacillus vireti* with the N_2O reductase acts as the potential sink for N_2O with the efficiency depending on the nitrate concentrations in the culture medium (Mania et al., 2016). While exploration in biochemistry and genetics of N_2O respiration has made great progress (e.g., the discovery of the multicopper enzyme that catalyzes the transformation of N_2O), further such mechanistic understanding at molecular level is needed before we can tailor the microorganisms for more efficient mitigation of N_2O emissions (Zumft and Kroneck, 2006).

3.3 Applications of Nanoscale Biotechnology in Cementitious Materials

Currently, while very few applications of microorganisms have been reported to enhance the heavy metal removal in civil engineering, the reported cases as discussed above suggest great potential of bioremediation using civil engineering materials. Methods of application can be categorized into three types: 1) direct application of microorganisms in polluted water/suspensions; 2) surface treatment of cementitious materials and/or aggregates *via* biomineralization; and 3) surface treatment *via* formation of a biofilm. While biomineralization (2nd method) could directly relate to the nanoscale aspect, the direct application (1st method) and formation of biofilm (3rd method) could associate with formation of NPs and thus can also be regarded as "nanoscale" biotechnology.

Microorganisms have been directly mixed with polluted water or suspension and found to exhibit high efficiency for heavy metal removal (e.g., Fe, Zn, Cr) in soil, constructed wetland, and unclear waste disposal cells (Alquier et al., 2014; Singh et al., 2015; Bano et al., 2018; Wang et al., 2020). Below we focus on the two surface treatments that are more directly relevant to cementitious materials.

3.3.1 Surface Treatment of Cementitious Materials and Aggregates via Biomineralization

Surface precipitation on cementitious materials and aggregates can be achieved by biomineralization, as reviewed in **section 2.2.3**. Biomineralization has also been shown to remediate heavy metals (Anbu et al., 2016; Kumari et al., 2016). For example, the strain *Kocuria flava* CR1, an isolate from a mining area in China, removed up to 97% of copper through formation of carbonates (Achal et al., 2011). Biomineralization was seen to remove 99.95% of Cd at 2 g/L in 48 h in a culture media (Kang et al., 2014). Radionuclides (e.g., U, Sr, Np, and Cs) have also been removed through biomineralization of calcium carbonates and coprecipitation of radionuclide carbonates (Newsome et al., 2014).

With the capability to remove heavy metals, as well as to induce nanostructural surface precipitates (see **section 2.2.3**), the biomineralization process potentially brings additional functionality of heavy-metal removal to cementitious materials. More specifically, there are two possible approaches: 1) to promote biomineralization of heavy metals on the surface of concrete; and 2) to biomineralize aggregates prior to mixing with cementitious binders. The direct biomineralization or coating on the surface of concrete aided by microorganisms (De Muynck et al., 2008; Wang et al., 2016; Wong et al., 2020) potentially

equips the concrete surfaces with the functionality of bioremediation. Alternatively, the aggregates or even recycled cementitious aggregates can be used to remove heavy metals in polluted media through biomineralization in a similar fashion to $CaCO_3$ precipitation in soil and sand and on aggregate surfaces (Achal et al., 2013; Cuzman et al., 2015; Wang et al., 2017). Once precipitated as NPs on the aggregate surfaces, heavy metal pollutants can be encapsulated in the cementitious matrix as reviewed in **section 3.1.1**. Furthermore, nanostructural morphology on the aggregate surface could further enhance the engineering performance of concrete materials, as discussed in **section 2.2.3**. Such a pathway would not only allow bioremediation of heavy metals but also convert contaminated materials into high-performance concrete materials. Though more studies are needed to develop such multi-functional concrete with enhanced bioremediation capability and engineering performance, currently available information indicates this area of research and applications is promising.

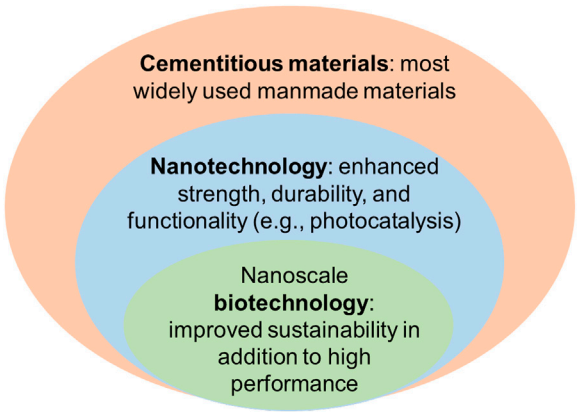

FIGURE 7 | Schematic illustrating that nanoscale biotechnology leverages the advantages of two maturing fields—nanotechnology and biotechnology—and has applications in the design of high-performance, sustainable construction materials.

3.3.2 Surface Treatment via Formation of Beneficial Biofilms

A biofilm is a group of microorganisms, including bacteria, fungi and protists, that commonly grow on living or non-living surfaces (Flemming and Wingender, 2010). In addition to the cells, biofilms are composed of a matrix of extracellular polysaccharides (EPS), proteins, and DNA, as well as absorbed nutrients, metabolites, ions/minerals, and some detritus from the surrounding environment.

Besides promoting precipitation through MICP (Decho, 2010) and protecting Ca-bearing materials by the precipitation of calcium oxalate at their surface (e.g., by lichen (Ariño et al., 1997)), biofilms exhibit remediation capability for heavy metals. For example, a sulphate-reducing bacterial biofilm was found to remediate a copper-contaminated medium through formation of copper sulfide (White and Gadd, 2000); natural films of sulfate-reducing bacteria of the *Desulfobacteriaceae* family were seen to concentrate Zn ions and promote precipitation of sphalerite (ZnS) particles of 2–5 nm (Labrenz et al., 2000). Other heavy metals (e.g., Cd, Ni, Co. Pd) can also be remediated (Singh et al., 2006). Such bioremediation process usually involves an immobilization of contaminants by microbial transformation that leads to detoxification and precipitation, sorption to cells or matrix, and biomineralization (Barkay and Schaefer, 2001). This remediation capability likely relates to biofilms' high resistance to heavy metals (e.g., up to 600 times higher resistance for *Pseudomonas eruginosa* based biofilm than free-swimming cells (Teitzel and Parsek, 2003)), together with their wide chemical, physical, and structural diversity (Pal and Paul, 2008).

Apart from remediating heavy metals (usually accompanied by formation of NPs), biofilms can be applied on concrete surfaces. While biofilms have been more widely applied to protect the metal surfaces from corrosion (Zuo, 2007), several applications to concrete have been reported (Soleimani et al., 2013a; Soleimani et al., 2013b; Soleimani et al., 2013c). An *E. coli* DH5α biofilm can successfully cover mortar samples, continue to grow (almost doubling the thickness) despite application of sulfuric acid down to pH of 3, and reduce leaching of Ca^{2+} by 23–47% compared to samples without the biofilms (Soleimani et al., 2013a). This biofilm-covered mortar, when soaked in a culturing media with the undesirable sulfur-oxidizing bacteria (SOB) that induce the formation of sulfuric acid, exhibits a competing effect with growth of the SOB (Soleimani et al., 2016). Biofilms also help improve the durability through sealing the underlying microcracks and lowering the diffusion rates of chloride (Chlayon et al., 2018). In summary, the application of biofilms that are capable of both heavy metal bioremediation and formation of a barrier on concrete surface is a promising tool to tailor concrete materials with capability of bioremediation and high durability.

4 RESEARCH SIGNIFICANCE AND FUTURE DEVELOPMENTS

4.1 Significance: Opportunities and Challenges

This review highlights innovations in a new field of nanoscale construction biotechnology and applications in the design of resilient and sustainable civil engineering materials to benefit the construction industry. Nanotechnology has been shown to substantially improve the strength and durability of cementitious materials (see **Table 1**) (Sobolev et al., 2006; Rashad, 2013a; Rashad, 2013b; Reches, 2018; Mindess, 2019), while new biotechnologies offer an ideal solution to design environmentally friendly nano-additives by minimizing environmental and economic costs (Li et al., 2011; Tiquia-Arashiro and Rodrigues, 2016). Among biotechnology's great environmental benefits to civil engineering materials as discussed in **section 3.1 and 3.2**, water treatment is one main application. As one example, yeast- and lactose-assisted bioremediation has successfully cleaned a large area (2–3 ha) of chlorine-contaminated area (town of Salem, New Hampshire) with an expenditure of just US $ 300,000 by saving an estimated US $ 2

million in remediation by conventional pump-and-treat approach (Schaffner, 2004). By taking the advantages of both nanotechnology and biotechnology, the engineering performance and environmental benefits of cementitious materials can be substantially improved (see **Figure 7**).

4.2 Opportunity: Enhancing Environmental Tolerance and Performance via Genetic Engineering

Recent advances in synthetic biology can further enhance the environmental tolerance and bioproduction of microorganisms. Synthetic biology is an engineering approach to biology that aims to construct new biological systems (e.g., living organisms) to have novel—or enhanced—abilities or useful purposes (e.g., material production, sense-and-respond functionality). Some of the methods used by synthetic biologists include DNA manipulation technologies, as well as omits approaches (i.e., genomics, transcriptomics, proxemics, and metabonomics).

The ability of microorganisms to survive (when necessary) while producing NPs and removing heavy metals largely depend on their adaptation to relevant environmental conditions. Under the extreme conditions in the cementitious materials (e.g., high ionic concentration, and high alkalinity), microorganisms' survival and capability in NP production and metal removal could be of critical importance. To elucidate the genetic underpinnings of microorganism biosynthesis and persistence, omits approaches have been adopted to examine genomes, transcriptases, and proteomes (Giovanella et al., 2020) and their governance rules on microorganism behavior. For example, genome sequencing is often conducted on extremophiles that exhibit a strong adaptation to harsh pH, temperature, pressure, salinity and others. In doing so, genes relevant to the versatile environmental adaptability are revealed (Giovanella et al., 2020).

With this understanding, genetic modification can be achieved by utilizing recombinant DNA technology and selective pressure for rational design and directed evolution. While rational design involves construction of a single strain that possesses desirable metabolic characteristics or proteins from different organisms to allow specific reactions using recombinant DNA technology (Ang et al., 2005), directed evolution engineers the organism for improved characteristics through mutagenesis and environmental pressure based on Darwinian principles of mutation and selection (Hibbert and Dalby, 2005).

Based on this genetic engineering, genetically engineered microorganisms can be produced that exhibit boosted biosynthesis or efficiency in heavy metal removal. Heterologous biosynthesis pathways can also be engineered into non-native producer organisms (Kumar et al., 2013). For example, the size, shape and mechanical properties of biogenic $CaCO_3$ precipitates can be tailored *via* genetically engineered *E. coli* strains (Liang et al., 2018; Heveran et al., 2019). Similarly, the abilities of sulfur-oxidizing and sulfate-reducing microorganisms have been engineered to increase extraction and capture of metals (Dopson and Johnson, 2012).

In addition to improvement in biosynthesis and heavy-metal removal, enhanced survivability of microorganisms can be achieved *via* genetic modification. For example, a new strain of *E. coli* was engineered to express a hypersaline azoreductase gene originally from *Halomonas elongata* allowing it to tolerate higher NaCl concentrations (Eslami et al., 2016). In another instance, *Pichia pastoris* expressed the laccase gene from *Thermus* thermophiles inducing greater tolerance to high temperature (~90°C) (Liu et al., 2015). More relevant to the high alkaline environment in concrete materials, mutations to the *Sporosarcina pasteurii* (a strain capable of MICP) genome were induced *via* ultraviolet irradiation, and the mutants were capable of biomineralization under pH of 11–12 (Achal et al., 2009b). Such improved biosynthesis and tolerance to the harsh environments exhibits potential to enhance microorganism's resilience for NP synthesis and removal of heavy metals.

In short, with the advent of new, rapid throughput DNA sequencing techniques, data analysis, and recombinant DNA technology, the fundamental understanding and modification of genes at a molecular level provide great opportunities to impart boosted functionalities to microorganisms that are of specific interest to civil engineers (e.g., biosynthesis of NPs and heavy metal remediation).

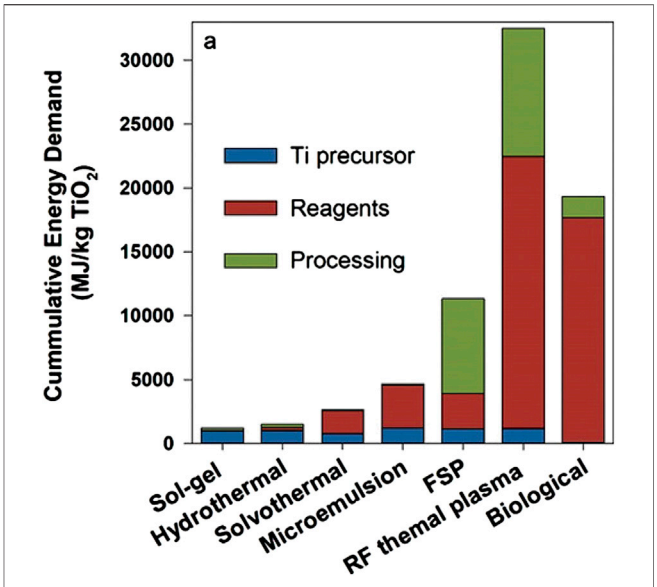

FIGURE 8 | Cumulative energy demand (MJ/kg TiO_2) of different conventional methods vs. the biological counterpart (Wu et al., 2019). FSP = flame spray pyrolysis; FR = radio frequency.

4.3 Challenge: Ensuring the Energy- and Cost-Efficiency of Biotechnology

Improved sustainability related to biological vs. physical or chemical synthesis has been claimed in almost all relevant studies (Li et al., 2011; Hulkoti and Taranath, 2014; Tiquia-Arashiro and Rodrigues, 2016; Iravani and Varma, 2020). The primary argument relates to the potential elimination of expensive and sometimes toxic solvents and by replacing energy intensive processes with biological ones. Improved

sustainability, however, is not always guaranteed. For example, the biological process for producing TiO_2 NPs demands cumulative energy only lower than the RF thermal plasma method but higher than all the other conventional methods, as shown in **Figure 8** (Wu et al., 2019). As an example of potentially lower energy consumption, parameter optimization for biosynthesis of magnetite NPs (e.g., reducing the amount of sodium hydroxide and replacing iron sources) offers a six-fold reduction in environmental impacts (Sadhukhan et al., 2017). Furthermore, a systematic comparison between the biosynthesis of NPs and their conventional counterparts is rarely reported (Sadhukhan et al., 2017). Even for conventional synthesis, life cycle assessments using standardized methodologies that quantify environmental impacts face a number of challenges, especially at the industrial scale (Charitidis et al., 2014). These challenges are partially due to different equipment and methods required between lab and industrial scales (Hetherington et al., 2014). Therefore, in addition to research that leverages the advancements in nanotechnology and biotechnology, systematic quantification of environmental and economic impacts is essential prior to full-scale production and widespread application.

In addition to energy consumption associated with biotechnology, cost is an important consideration. The majority of biotechnology cost is claimed to come from the nutrients used to grow microorganisms (Achal et al., 2015). In the case of biocementation *via* MICP, yeast extract, meat extract, glucose, peptone and salts are commonly added to the nutrient media. The cost of these nutrients is estimated to be around $250 per kilogram, which could be used to produce 5.4E6 unit urease (i.e., enzyme that could hydrolyze 5.4E6 micromoles of urea in 1 min) (Achal et al., 2015). Fortunately, some nutrient-rich industrial effluents, such as lactose mother liquor (Achal et al., 2009a) and corn steep liquor (Achal et al., 2010; Fahmi et al., 2018), could serve as replacements and end with comparable or even enhanced precipitation of carbonates. In a similar fashion of using wastes, pumpkin peel is used as a carbon and energy source for fungi to produce Cu/Zn NPs (Noman et al., 2019). Additionally, careful selection of microorganism species offers additional benefits, for example, by using cyanobacteria to promote MICP *via* photosynthesis that does not require as much exogenous nutrient addition (Kamennaya et al., 2012). Future research in this area is of great importance to advance applications of biotechnology in civil engineering at scale.

5 CONCLUSION

In this review, we summarize the promise and potential of a new field of *nanoscale construction biotechnology*. By combining the advantages of nanotechnology with advances in biotechnology, this new field offers multiple opportunities to revolutionize the field of construction.

As a green alternative to the conventional nanotechnology, biologically produced NPs can exhibit comparable characteristics to those that have been proven to enhance the performance of cementitious materials. While direct addition of bio-NPs is proven feasible, surface treatment of NPs on the surfaces of aggregates prior to mixing with cementitious binders is an alternate, yet unexplored, strategy to enhance concrete performance.

While nanotechnological enhancements of materials can reduce economic and environmental costs, the application microorganisms potentially equip cementitious materials with additional functionality to remove heavy metals (e.g., Hg, U, Cr) from water and soil and clean pollutants from the air. Three possible approaches to achieve this multifunctionality have been reviewed: 1) direct application of microorganisms, 2) surface treatment in cementitious (and other) materials *via* biomineralization, and 3) formation of active biofilm surfaces. Together, these opportunities afford civil engineers a materials-centric approach to water treatment and recover rare earth elements.

This review also summarizes the challenges and opportunities of nanoscale biotechnology and proposes a roadmap of research for civil engineers of the 21st century. There exist great opportunities to enhance the environmental tolerance and performance of biotechnological systems, thanks in large part to the rapid development of genetic engineering. While concerns are present with regards to the biotechnology's energy- and cost-efficiency, corresponding opportunities exist in parallel, as evidenced by initial proofs of concept that have been successfully reported. By taking advantage of both nanotechnology and advances in biotechnology, critical aspects of resilience and sustainability could be addressed within (and beyond) the modern civil engineering discipline.

AUTHOR CONTRIBUTIONS

WS conceived of the study and provided writing and editing. XC conducted the study and wrote the first draft of the manuscript. MC contributed to the study and provided editing and revision of the manuscript.

FUNDING

The work depicted was sponsored by the Advanced Research Projects Agency-Energy (Award Number: DE-AR0001145) and the Defense Advanced Research Projects Agency (Agreement HR0011-17-2-0039). Publication of this article was funded by the University of Colorado Boulder Libraries Open Access Fund

ACKNOWLEDGMENTS

The content does not necessarily reflect the position or the policy of the Government, and no official endorsement should be inferred.

REFERENCES

Achal, V., Mukherjee, A., Basu, P. C., and Reddy, M. S. (2009a). Lactose mother liquor as an alternative nutrient source for microbial concrete production by Sporosarcina pasteurii. *J. Ind. Microbiol. Biotechnol.* 36, 433–438. doi:10.1007/s10295-008-0514-7

Achal, V., Mukherjee, A., Basu, P. C., and Reddy, M. S. (2009b). Strain improvement of Sporosarcina pasteurii for enhanced urease and calcite production. *J. Ind. Microbiol. Biotechnol.* 36, 981–988. doi:10.1007/s10295-009-0578-z

Achal, V., Pan, X., Lee, D. J., Kumari, D., and Zhang, D. (2013). Remediation of Cr(VI) from chromium slag by biocementation. *Chemosphere*. 93, 1352–1358. doi:10.1016/j.chemosphere.2013.08.008

Achal, V., Mukherjee, A., Kumari, D., and Zhang, Q. (2015). Biomineralization for sustainable construction–a review of processes and applications. *Earth Sci. Rev.* 148, 1–17. doi:10.1016/j.earscirev.2015.05.008

Achal, V., Mukherjee, A., and Reddy, M. S. (2010). Original research: biocalcification by Sporosarcina pasteurii using corn steep liquor as the nutrient source. *Ind. Biotechnol.* 6, 170–174. doi:10.1089/ind.2010.6.170

Achal, V., Pan, X., and Zhang, D. (2011). Remediation of copper-contaminated soil by Kocuria flava CR1, based on microbially induced calcite precipitation. *Ecol. Eng.* 37, 1601–1605. doi:10.1016/j.ecoleng.2011.06.008

Afzali Naniz, O., and Mazloom, M. (2018). Effects of colloidal nano-silica on fresh and hardened properties of self-compacting lightweight concrete. *J. Build. Eng.* 20, 400–410. doi:10.1016/j.jobe.2018.08.014

Al-Zboon, K. K., Al-Smadi, B. M., and Al-Khawaldh, S. (2016). Natural volcanic tuff-based geopolymer for Zn removal: adsorption isotherm, kinetic, and thermodynamic study. *Water, Air, Soil Pollut.* 227, 248. doi:10.1007/s11270-016-2937-5

Alquier, M., Kassim, C., Bertron, A., Sablayrolles, C., Rafrafi, Y., Albrecht, A., et al. (2014). Halomonas desiderata as a bacterial model to predict the possible biological nitrate reduction in concrete cells of nuclear waste disposals. *J. Environ. Manag.* 132, 32–41. doi:10.1016/j.jenvman.2013.10.013

Anbu, P., Kang, C. H., Shin, Y. J., and So, J. S. (2016). Formations of calcium carbonate minerals by bacteria and its multiple applications. *SpringerPlus*. 5, 250. doi:10.1186/s40064-016-1869-2

Ang, E. L., Zhao, H., and Obbard, J. P. (2005). Recent advances in the bioremediation of persistent organic pollutants via biomolecular engineering. *Enzym. Microb. Technol.* 37, 487–496. doi:10.1016/j.enzmictec.2004.07.024

Arakaki, A., Nakazawa, H., Nemoto, M., Mori, T., and Matsunaga, T. (2008). Formation of magnetite by bacteria and its application. *J. R. Soc. Interface*. 5, 977–999. doi:10.1098/rsif.2008.0170

Arehart, J. H., Nelson, W. S., and Srubar, W. V. (2020). On the theoretical carbon storage and carbon sequestration potential of hempcrete. *J. Clean. Prod.* 266, 121846. doi:10.1016/j.jclepro.2020.121846

Ariño, X., Gomez-Bolea, A., and Saiz-Jimenez, C. (1997). Lichens on ancient mortars. *Int. Biodeter. Bioder.* 40, 217–224. doi:10.1016/S0964-8305(97)00036-X

Babitha, S., and Korrapati, P. S. (2013). Biosynthesis of titanium dioxide nanoparticles using a probiotic from coal fly ash effluent. *Mater. Res. Bull.* 48, 4738–4742. doi:10.1016/j.materresbull.2013.08.016

Balaji, D. S., Basavaraja, S., Deshpande, R., Mahesh, D. B., Prabhakar, B. K., and Venkataraman, A. (2009). Extracellular biosynthesis of functionalized silver nanoparticles by strains of Cladosporium cladosporioides fungus. *Colloids Surf. B. Biointerfaces*. 68, 88–92. doi:10.1016/j.colsurfb.2008.09.022

Balasoiu, M., Ischenko, L. A., Stolyar, S. V., Iskhakov, R. S., Raikher, Y. L., Kuklin, A. I., et al. (2010). Structural investigation of biogenic ferrihydrite nanoparticles dispersion. *Optoelectron Adv. Mat.* 4, 2136–2139.

Ballari, M. M., Hunger, M., Hüsken, G., and Brouwers, H. J. H. (2010). NOx photocatalytic degradation employing concrete pavement containing titanium dioxide. *Appl. Catal. B Environ.* 95, 245–254. doi:10.1016/j.apcatb.2010.01.002

Bano, A., Hussain, J., Akbar, A., Mehmood, K., Anwar, M., Hasni, M. S., et al. (2018). Biosorption of heavy metals by obligate halophilic fungi. *Chemosphere*. 199, 218–222. doi:10.1016/j.chemosphere.2018.02.043

Bansal, V., Rautaray, D., Ahmad, A., and Sastry, M. (2004). Biosynthesis of zirconia nanoparticles using the fungus Fusarium oxysporum. *J. Mater. Chem.* 14, 3303–3305. doi:10.1039/B407904C

Bansal, V., Rautaray, D., Bharde, A., Ahire, K., Sanyal, A., Ahmad, A., et al. (2005). Fungus-mediated biosynthesis of silica and titania particles. *J. Mater. Chem.* 15, 2583–2589. 10.1039/b503008k

Barac, T., Taghavi, S., Borremans, B., Provoost, A., Oeyen, L., Colpaert, J. V., et al. (2004). Engineered endophytic bacteria improve phytoremediation of water-soluble, volatile, organic pollutants. *Nat. Biotechnol.* 22, 583–588. doi:10.1038/nbt960

Barkay, T., Miller, S. M., and Summers, A. O. (2003). Bacterial mercury resistance from atoms to ecosystems. *FEMS Microbiol. Rev.* 27, 355–384. doi:10.1016/S0168-6445(03)00046-9

Barkay, T., and Schaefer, J. (2001). Metal and radionuclide bioremediation: issues, considerations and potentials. *Curr. Opin. Microbiol.* 4, 318–323. doi:10.1016/s1369-5274(00)00210-1

Barnhouse, P. W., and Srubar, W. V. (2016). Material characterization and hydraulic conductivity modeling of macroporous recycled-aggregate pervious concrete. *Conster. Build. Mater.* 110, 89–97. doi:10.1016/j.conbuildmat.2016.02.014

Basaran Bundur, Z., Kirisits, M. J., and Ferron, R. D. (2015). Biomineralized cement-based materials: impact of inoculating vegetative bacterial cells on hydration and strength. *Cement Concr. Res.* 67, 237–245. doi:10.1016/j.cemconres.2014.10.002

Beeler, E., and Singh, O. V. (2016). Extremophiles as sources of inorganic bio-nanoparticles. *World J. Microbiol. Biotechnol.* 32, 156. doi:10.1007/s11274-016-2111-7

Benison, G. C., Di Lello, P., Shokes, J. E., Cosper, N. J., Scott, R. A., Legault, P., et al. (2004). A stable mercury-containing complex of the organomercurial lyase MerB: catalysis, product release, and direct transfer to MerA. *Biochemistry*. 43, 8333–8345. doi:10.1021/bi049662h

Bharde, A. A., Parikh, R. Y., Baidakova, M., Jouen, S., Hannoyer, B., Enoki, T., et al. (2008). Bacteria-mediated precursor-dependent biosynthesis of superparamagnetic iron oxide and iron sulfide nanoparticles. *Langmuir*. 24, 5787–5794. doi:10.1021/la704019p

Bhattacharyya, A., Schmidt, M. P., Stavitski, E., Azimzadeh, B., and Martínez, C. E. (2019). Ligands representing important functional groups of natural organic matter facilitate Fe redox transformations and resulting binding environments. *Geochem. Cosmochim. Acta*. 251, 157–175. doi:10.1016/j.gca.2019.02.027

Bose, S., Hochella, M. F., Gorby, Y. A., Kennedy, D. W., Mccready, D. E., Madden, A. S., et al. (2009). Bioreduction of hematite nanoparticles by the dissimilatory iron reducing bacterium Shewanella oneidensis MR-1. *Geochem. Cosmochim. Acta*. 73, 962–976. doi:10.1016/j.gca.2008.11.031

Bradl, H. B. (2004). Adsorption of heavy metal ions on soils and soils constituents. *J. Colloid Interface Sci.* 277, 1–18. doi:10.1016/j.jcis.2004.04.005

Cartledge, F. K., Butler, L. G., Chalasani, D., Eaton, H. C., Frey, F. P., Herrera, E., et al. (1990). Immobilization mechanisms in solidification/stabilization of cadmium and lead salts using portland cement fixing agents. *Environ. Sci. Tech.* 24, 867–873. doi:10.1021/es00076a012

Ceran, Ö. B., Şimşek, B., Doruk, S., Uygunoğlu, T., and Şara, O. N. (2019). Effects of dispersed and powdered silver nanoparticles on the mechanical, thermal, electrical and durability properties of cementitious composites. *Conster. Build. Mater.* 222, 152–167. doi:10.1016/j.conbuildmat.2019.06.138

Charitidis, C. A., Georgiou, P., Koklioti, M. A., Trompeta, A.-F., and Markakis, V. (2014). Manufacturing nanomaterials: from research to industry. *Manuf. Rev.* 1, 11. doi:10.1051/mfreview/2014009

Chatterjee, S. K., Bhattacharjee, I., and Chandra, G. (2010). Biosorption of heavy metals from industrial waste water by Geobacillus thermodenitrificans. *J. Hazard Mater.* 175, 117–125. doi:10.1016/j.jhazmat.2009.09.136

Chen, H., Nanayakkara, C. E., and Grassian, V. H. (2012a). Titanium dioxide photocatalysis in atmospheric chemistry. *Chem. Rev.* 112, 5919–5948. doi:10.1021/cr3002092

Chen, J., Kou, S.-C., and Poon, C.-S. (2012b). Hydration and properties of nano-TiO2 blended cement composites. *Cement Concr. Compos.* 34, 642–649. doi:10.1016/j.cemconcomp.2012.02.009

Chen, L., Zheng, K., and Liu, Y. (2017a). Geopolymer-supported photocatalytic TiO2 film: preparation and characterization. *Conster. Build. Mater.* 151, 63–70. doi:10.1016/j.conbuildmat.2017.06.097

Chen, Q. Y., Tyrer, M., Hills, C. D., Yang, X. M., and Carey, P. (2009). Immobilisation of heavy metal in cement-based solidification/stabilisation: a review. *Waste Manag.* 29, 390–403. doi:10.1016/j.wasman.2008.01.019

Chen, X., Sutrisno, A., Zhu, L., and Struble, L. J. (2017b). Setting and nanostructural evolution of metakaolin geopolymer. *J. Am. Ceram. Soc.* 100, 2285–2295. doi:10.1111/jace.14641

Cheng, T. W., Lee, M. L., Ko, M. S., Ueng, T. H., and Yang, S. F. (2012). The heavy metal adsorption characteristics on metakaolin-based geopolymer. *Appl. Clay Sci.* 56, 90–96. doi:10.1016/j.clay.2011.11.027

Chlayon, T., Iwanami, M., and Chijiwa, N. (2018). Combined protective action of barnacles and biofilm on concrete surface in intertidal areas. *Conster. Build. Mater.* 179, 477–487. doi:10.1016/j.conbuildmat.2018.05.223

Chojnacka, K. (2010). Biosorption and bioaccumulation--the prospects for practical applications. *Environ. Int.* 36, 299–307. doi:10.1016/j.envint.2009.12.001

Colvin, V. L. (2003). The potential environmental impact of engineered nanomaterials. *Nat. Biotechnol.* 21, 1166–1170. doi:10.1038/nbt875

Cuevas, R., Durán, N., Diez, M. C., Tortella, G. R., and Rubilar, O. (2015). Extracellular biosynthesis of copper and copper oxide nanoparticles by *Stereum hirsutum*, a native white-rot fungus from Chilean forests. *J. Nanomater.* 2015, 789089. doi:10.1155/2015/789089

Cuzman, O. A., Rescic, S., Richter, K., Wittig, L., and Tiano, P. (2015). Sporosarcina pasteurii use in extreme alkaline conditions for recycling solid industrial wastes. *J. Biotechnol.* 214, 49–56. doi:10.1016/j.jbiotec.2015.09.011

Das, D., Salgaonkar, B. B., Mani, K., and Braganca, J. M. (2014). Cadmium resistance in extremely halophilic archaeon Haloferax strain BBK2. *Chemosphere.* 112, 385–392. doi:10.1016/j.chemosphere.2014.04.058

De Muynck, W., De Belie, N., and Verstraete, W. (2010). Microbial carbonate precipitation in construction materials: a review. *Ecol. Eng.* 36, 118–136. doi:10.1061/(ASCE)MT.1943-5533.0003141

De Muynck, W., Debrouwer, D., De Belie, N., and Verstraete, W. (2008). Bacterial carbonate precipitation improves the durability of cementitious materials. *Cement Concr. Res.* 38, 1005–1014. doi:10.1016/j.cemconres.2008.03.005

Decho, A. W. (2010). Overview of biopolymer-induced mineralization: what goes on in biofilms? *Ecol. Eng.* 36, 137–144. doi:10.1016/j.ecoleng.2009.01.003

Dejong, J. T., Soga, K., Banwart, S. A., Whalley, W. R., Ginn, T. R., Nelson, D. C., et al. (2011). Soil engineering *in vivo*: harnessing natural biogeochemical systems for sustainable, multi-functional engineering solutions. *J. R. Soc. Interface.* 8, 1–15. doi:10.1098/rsif.2010.0270

Diep, P., Mahadevan, R., and Yakunin, A. F. (2018). Heavy metal removal by bioaccumulation using genetically engineered microorganisms. *Front. Bioeng. Biotech.* 6, 157. 10.3389/fbioe.2018.00157

Dopson, M., Baker-Austin, C., Koppineedi, P. R., and Bond, P. L. (2003). Growth in sulfitic mineral environments: metal resistance mechanisms in acidophilic micro-organisms. *Microbiology (Reading, Engl).* 149, 1959–1970. doi:10.1099/mic.0.26296-0

Dopson, M., and Holmes, D. S. (2014). Metal resistance in acidophilic microorganisms and its significance for biotechnologies. *Appl. Microbiol. Biotechnol.* 98, 8133–8144. doi:10.1007/s00253-014-5982-2

Dopson, M., and Johnson, D. B. (2012). Biodiversity, metabolism and applications of acidophilic sulfur-metabolizing microorganisms. *Environ. Microbiol.* 14, 2620–2631. doi:10.1111/j.1462-2920.2012.02749.x

Doshi, H., Ray, A., Kothari, I. L., and Gami, B. (2006). Spectroscopic and scanning electron microscopy studies of bioaccumulation of pollutants by algae. *Curr. Microbiol.* 53, 148–157. doi:10.1007/s00284-005-0401-7

Du, H., Du, S., and Liu, X. (2014). Durability performances of concrete with nano-silica. *Conster. Build. Mater.* 73, 705–712. doi:10.1016/j.conbuildmat.2014.10.014

Duan, P., Yan, C., Zhou, W., and Ren, D. (2016). Development of fly ash and iron ore tailing based porous geopolymer for removal of Cu(II) from wastewater. *Ceram. Int.* 42, 13507–13518. doi:10.1016/j.ceramint.2016.05.143

Eslami, M., Amoozegar, M. A., and Asad, S. (2016). Isolation, cloning and characterization of an azoreductase from the halophilic bacterium Halomonas elongata. *Int. J. Biol. Macromol.* 85, 111–116. doi:10.1016/j.ijbiomac.2015.12.065

Fahmi, A., Katebi, H., Hajialilue Bonab, M., and Samadi Kafil, H. (2018). Microbial sand stabilization using corn steep liquor culture media and industrial calcium reagents in cementation solutions. *Ind. Biotechnol.* 14, 270–275. doi:10.1089/ind.2018.0016

Falah, M., Mackenzie, K. J. D., Knibbe, R., Page, S. J., and Hanna, J. V. (2016). New composites of nanoparticle Cu (I) oxide and titania in a novel inorganic polymer (geopolymer) matrix for destruction of dyes and hazardous organic pollutants. *J. Hazard Mater.* 318, 772–782. doi:10.1016/j.jhazmat.2016.06.016

Fang, X. J., Wang, Y., Wang, Z. G., Jiang, Z. X., and Dong, M. D. (2019). Microorganism assisted synthesized nanoparticles for catalytic applications. *Energies.* 12, 21. doi:10.3390/en12010190

Faramarzi, M. A., and Sadighi, A. (2013). Insights into biogenic and chemical production of inorganic nanomaterials and nanostructures. *Adv. Colloid Interface Sci.* 189–190, 1–20. doi:10.1016/j.cis.2012.12.001

Farina, M., Aschner, M., and Rocha, J. B. (2011). Oxidative stress in MeHg-induced neurotoxicity. *Toxicol. Appl. Pharmacol.* 256, 405–417. doi:10.1016/j.taap.2011.05.001

Flemming, H. C., and Wingender, J. (2010). The biofilm matrix. *Nat. Rev. Microbiol.* 8, 623–633. doi:10.1038/nrmicro2415

Fu, F., and Wang, Q. (2011). Removal of heavy metal ions from wastewaters: a review. *J. Environ. Manag.* 92, 407–418. doi:10.1016/j.jenvman.2010.11.011

Ge, Y., Cui, X., Liao, C., and Li, Z. (2017). Facile fabrication of green geopolymer/alginate hybrid spheres for efficient removal of Cu(II) in water: batch and column studies. *Chem. Eng.* 311, 126–134. doi:10.1016/j.cej.2016.11.079

Giovanella, P., Vieira, G. A. L., Otero, I. V. R., Pellizzer, E. P., Fontes, B. D., and Sette, L. D. (2020). Metal and organic pollutants bioremediation by extremophile microorganisms. *J. Hazard Mater.* 382, 14. doi:10.1016/j.cej.2016.11.079

Gorospe, C. M., Han, S.-H., Kim, S.-G., Park, J.-Y., Kang, C.-H., Jeong, J.-H., et al. (2013). Effects of different calcium salts on calcium carbonate crystal formation by Sporosarcina pasteurii KCTC 3558. *Biotechnol. Bioproc. Eng.* 18, 903–908. doi:10.1007/s12257-013-0030-0

Guo, B., Liu, B., Yang, J., and Zhang, S. (2017a). The mechanisms of heavy metal immobilization by cementitious material treatments and thermal treatments: a review. *J. Environ. Manag.* 193, 410–422. doi:10.1016/j.jenvman.2017.02.026

Guo, M.-Z., Ling, T.-C., and Poon, C. S. (2017b). Photocatalytic NOx degradation of concrete surface layers intermixed and spray-coated with nano-TiO2: influence of experimental factors. *Cement Concr. Compos.* 83, 279–289. doi:10.1016/j.cemconcomp.2017.07.022

Guo, X., Zhang, L., Huang, J., and Shi, H. (2017c). Detoxification and solidification of heavy metal of chromium using fly ash-based geopolymer with chemical agents. *Conster. Build. Mater.* 151, 394–404. doi:10.1016/j.conbuildmat.2017.05.199

Gurunathan, S., Kalishwaralal, K., Vaidyanathan, R., Venkataraman, D., Pandian, S. R., Muniyandi, J., et al. (2009). Biosynthesis, purification and characterization of silver nanoparticles using *Escherichia coli*. *Colloids Surf. B. Biointerfaces.* 74, 328–335. doi:10.1016/j.colsurfb.2009.07.048

Guzman, M., Dille, J., and Stephan, G. (2009). Synthesis of silver nanoparticles by chemical reduction method and their antibacterial activity. *Int. J. Chem. Biomol. Eng.* 2, 104–111. doi:10.7897/2230-8407.041024

Hallin, S., Philippot, L., Löffler, F. E., Sanford, R. A., and Jones, C. M. (2018). Genomics and ecology of novel N2O-reducing microorganisms. *Trends Microbiol.* 26, 43–55. doi:10.1016/j.tim.2017.07.003

Hani, N., Nawawy, O., Ragab, K. S., and Kohail, M. (2018). The effect of different water/binder ratio and nano-silica dosage on the fresh and hardened properties of self-compacting concrete. *Conster. Build. Mater.* 165, 504–513. doi:10.1016/j.conbuildmat.2018.01.045

Hashim, M. A., Mukhopadhyay, S., Sahu, J. N., and Sengupta, B. (2011). Remediation technologies for heavy metal contaminated groundwater. *J. Environ. Manag.* 92, 2355–2388. doi:10.1016/j.jenvman.2011.06.009

Hetherington, A. C., Borrion, A. L., Griffiths, O. G., and Mcmanus, M. C. (2014). Use of LCA as a development tool within early research: challenges and issues across different sectors. *Int. J. Life Cycle Assess.* 19, 130–143. doi:10.1007/s11367-013-0627-8

Heveran, C. M., Liang, L., Nagarajan, A., Hubler, M. H., Gill, R., Cameron, J. C., Cook, S. M., and Srubar, W. V. (2019). Engineered ureolytic microorganisms can tailor the morphology and nanomechanical properties of microbial-precipitated calcium carbonate. *Sci. Rep.* 9, 14721. doi:10.1038/s41598-019-51133-9

Heveran, C. M., Williams, S. L., Qiu, J., Artier, J., Hubler, M. H., Cook, S. M., et al. (2020). Biomineralization and successive regeneration of engineered living building materials. *Matter.* 2, 481–494. doi:10.1002/adma.201605903

Hibbert, E. G., and Dalby, P. A. (2005). Directed evolution strategies for improved enzymatic performance. *Microb. Cell Factories.* 4, 29. doi:10.1186/1475-2859-4-29

Ho, S. H., Chen, C. Y., Lee, D. J., and Chang, J. S. (2011). Perspectives on microalgal CO_2-emission mitigation systems--a review. *Biotechnol. Adv*. 29, 189–198. doi:10.1016/j.biotechadv.2010.11.001

Ho, Y. S., and Mckay, G. (1999). Pseudo-second order model for sorption processes. *Process Biochem*. 34, 451–465. doi:10.1016/S0032-9592(98)00112-5

Honary, S., Barabadi, H., Gharaei-Fathabad, E., and Naghibi, F. (2012). Green synthesis OF copper oxide nanoparticles using penicillium aurantiogriseum, penicillium citrinum and penicillium waksmanii. *Dig. J. Nanomater. Bios*. 7, 999–1005.

Hulkoti, N. I., and Taranath, T. C. (2014). Biosynthesis of nanoparticles using microbes- a review. *Colloids Surf. B. Biointerfaces*. 121, 474–483. doi:10.1016/j.colsurfb.2014.05.027

Hüsken, G., Hunger, M., and Brouwers, H. J. H. (2009). Experimental study of photocatalytic concrete products for air purification. *Build. Environ*. 44, 2463–2474. doi:10.1016/j.buildenv.2009.04.010

Iravani, S., and Varma, R. S. (2020). Bacteria in heavy metal remediation and nanoparticle biosynthesis. *ACS Sustain. Chem. Eng*. 8, 5395–5409. doi:10.1021/acssuschemeng.0c00292

Ivanov, V., Chu, J., and Stabnikov, V. (2015). "Basics of construction microbial biotechnology," in *Biotechnologies and biomimetics for civil engineering*. Editors F. Pacheco Torgal, J.A. Labrincha, M.V. Diamanti, C.P. Yu, and H.K. Lee (Cham, Germany: Springer International Publishing), 21–56.

Jayapalan, A. R., Lee, B. Y., and Kurtis, K. E. (2013). Can nanotechnology be 'green'? Comparing efficacy of nano and microparticles in cementitious materials. *Cement Concr. Compos*. 36, 16–24. doi:10.1016/j.cemconcomp.2012.11.002

Jha, A. K., Prasad, K., and Kulkarni, A. R. (2009). Synthesis of TiO2 nanoparticles using microorganisms. *Colloids Surf. B Biointerfaces*. 71, 226–229. doi:10.1016/j.colsurfb.2009.02.007

Ji, Z., and Pei, Y. (2019). Bibliographic and visualized analysis of geopolymer research and its application in heavy metal immobilization: a review. *J. Environ. Manag*. 231, 256–267. doi:10.1016/j.jenvman.2018.10.041

Joshaghani, A., Balapour, M., Mashhadian, M., and Ozbakkaloglu, T. (2020). Effects of nano-TiO2, nano-Al2O3, and nano-Fe2O3 on rheology, mechanical and durability properties of self-consolidating concrete (SCC): an experimental study. *Conster. Build. Mater*. 245, 118444. doi:10.3390/ma12213608

Judd, S., Van Den Broeke, L. J., Shurair, M., Kuti, Y., and Znad, H. (2015). Algal remediation of CO_2 and nutrient discharges: a review. *Water Res*. 87, 356–366. doi:10.1016/j.watres.2015.08.021

Juenger, M. C. G., Snellings, R., and Bernal, S. A. (2019). Supplementary cementitious materials: new sources, characterization, and performance insights. *Cement Concrete Res*. 122, 257–273. doi:10.1016/j.cemconres.2019.05.008

Juibari, M. M., Abbasalizadeh, S., Jouzani, G. S., and Noruzi, M. (2011). Intensified biosynthesis of silver nanoparticles using a native extremophilic Ureibacillus thermosphaericus strain. *Mater. Lett*. 65, 1014–1017. doi:10.1016/j.matlet.2010.12.056

Kalathil, S., Lee, J., and Cho, M. H. (2011). Electrochemically active biofilm-mediated synthesis of silver nanoparticles in water. *Green Chem*. 13, 1482–1485. doi:10.1039/C1GC15309A

Kalishwaralal, K., Deepak, V., Ramkumarpandian, S., Nellaiah, H., and Sangiliyandi, G. (2008). Extracellular biosynthesis of silver nanoparticles by the culture supernatant of Bacillus licheniformis. *Mater. Lett*. 62, 4411–4413. doi:10.1016/j.matlet.2008.06.051

Kamennaya, N. A., Ajo-Franklin, C. M., Northen, T., and Jansson, C. (2012). Cyanobacteria as biocatalysts for carbonate mineralization. *Minerals*. 2, 338–364. 10.3390/min2040338

Kang, C. H., Han, S. H., Shin, Y., Oh, S. J., and So, J. S. (2014). Bioremediation of Cd by microbially induced calcite precipitation. *Appl. Biochem. Biotechnol*. 172, 2907–2915. doi:10.1007/s12010-014-0737-1

Khezami, L., and Capart, R. (2005). Removal of chromium(VI) from aqueous solution by activated carbons: kinetic and equilibrium studies. *J. Hazard Mater*. 123, 223–231. doi:10.1016/j.jhazmat.2005.04.012

Khoshakhlagh, A., Nazari, A., and Khalaj, G. (2012). Effects of Fe2O3 nanoparticles on water permeability and strength assessments of high strength self-compacting concrete. *J. Mater. Sci. Technol*. 28, 73–82. 10.3389/fpls.2015.01263

Khotbehsara, M. M., Mohseni, E., Yazdi, M. A., Sarker, P., and Ranjbar, M. M. (2015). Effect of nano-CuO and fly ash on the properties of self-compacting mortar. *Conster. Build. Mater*. 94, 758–766. doi:10.1016/j.conbuildmat.2015.07.063

Kim, I. G., Jo, B. H., Kang, D. G., Kim, C. S., Choi, Y. S., and Cha, H. J. (2012). Biomineralization-based conversion of carbon dioxide to calcium carbonate using recombinant carbonic anhydrase. *Chemosphere*. 87, 1091–1096. doi:10.1016/j.chemosphere.2012.02.003

Kip, N., Fritz, C., Langelaan, E. S., Pan, Y., Bodrossy, L., Pancotto, V., et al. (2012). Methanotrophic activity and diversity in different *Sphagnum magellanicum* dominated habitats in the southernmost peat bogs of Patagonia. *Biogeosciences*. 9, 47–55. doi:10.5194/bg-9-47-2012

Kirthi, A. V., Rahuman, A. A., Rajakumar, G., Marimuthu, S., Santhoshkumar, T., Jayaseelan, C., et al. (2011). Biosynthesis of titanium dioxide nanoparticles using bacterium Bacillus subtilis. *Mater. Lett*. 65, 2745–2747. doi:10.1016/j.matlet.2011.05.077

Kumar, S., Dagar, V. K., Khasa, Y. P., and Kuhad, R. C. (2013). "Genetically modified microorganisms (GMOs) for bioremediation," in *Biotechnology for environmental management and resource recovery*. Editors R.C. Kuhad and A. Singh (India, SA: Springer India), 191–218.

Kumaresan, M., Vijai Anand, K., Govindaraju, K., Tamilselvan, S., and Ganesh Kumar, V. (2018). Seaweed Sargassum wightii mediated preparation of zirconia (ZrO. *Microb. Pathog*. 124, 311–315. doi:10.1016/j.micpath.2018.08.060

Kumari, D., Qian, X.-Y., Pan, X., Achal, V., Li, Q., and Gadd, G. M. (2016). "Chapter two - microbially-induced carbonate precipitation for immobilization of toxic metals," in *Advances in applied microbiology*. Editors S. Sariaslani and G.M. Gadd (Cambridge, MA, Academic Press), 79–108.

Labrenz, M., Druschel, G. K., Thomsen-Ebert, T., Gilbert, B., Welch, S. A., Kemner, K. M., et al. (2000). formation of sphalerite (ZnS) deposits in natural biofilms of sulfate-reducing bacteria. *Science*. 290, 1744–1747. doi:10.1126/science.290.5497.1744

Landrigan, P. J. (2017). Air pollution and health. *The Lancet Public Health*. 2, e4–e5. doi:10.1016/S0140-6736(17)32345-0

Li, S., Luo, S., and Guo, R. (2013). Efficiency of CO2 fixation by microalgae in a closed raceway pond. *Bioresour. Technol*. 136, 267–272. doi:10.1016/j.biortech.2013.03.025

Li, X., Xu, H., Chen, Z.-S., and Chen, G. (2011). Biosynthesis of nanoparticles by microorganisms and their applications. *J. Nanomater*. 2011, 270974. doi:10.1155/2011/270974

Li, Z., Han, B., Yu, X., Dong, S., Zhang, L., Dong, X., et al. (2017). Effect of nano-titanium dioxide on mechanical and electrical properties and microstructure of reactive powder concrete. *Mater. Res. Express*. 4, 095008. doi:10.1088/2053-1591/aa87db

Liang, L., Heveran, C., Liu, R., Gill, R. T., Nagarajan, A., Cameron, J., et al. (2018). Rational control of calcium carbonate precipitation by engineered *Escherichia coli*. *ACS Synth. Biol*. 7, 2497–2506. doi:10.1021/acssynbio.8b00194

Liu, H., Cheng, Y., Du, B., Tong, C., Liang, S., Han, S., et al. (2015). Overexpression of a novel thermostable and chloride-tolerant laccase from Thermus thermophilus sg0.5jp17-16 in Pichia pastoris and its application in synthetic dye decolorization. *PloS One*. 10, e0119833. doi:10.1371/journal.pone.0119833

Liu, N., Bond, G. M., Abel, A., Mcpherson, B. J., and Stringer, J. (2005). Biomimetic sequestration of CO2 in carbonate form: role of produced waters and other brines. *Fuel Process. Technol*. 86, 1615–1625. doi:10.17311/sciintl.2015.48.57

Madandoust, R., Mohseni, E., Mousavi, S. Y., and Namnevis, M. (2015). An experimental investigation on the durability of self-compacting mortar containing nano-SiO2, nano-Fe2O3 and nano-CuO. *Conster. Build. Mater*. 86, 44–50. doi:10.1016/j.conbuildmat.2015.03.100

Mania, D., Heylen, K., Van Spanning, R. J., and Frostegård, Å. (2016). Regulation of nitrogen metabolism in the nitrate-ammonifying soil bacterium Bacillus vireti and evidence for its ability to grow using N2 O as electron acceptor. *Environ. Microbiol*. 18, 2937–2950. doi:10.1111/1462-2920.13124

Marikani, D. K., Sangareswari, K., Suganya, P., Ganesan, R., and Rajarathinam, K. (2016). Biobased approach for the synthesis, characterization, optimization and application of silica nanoparticles by fungus Fusarium oxysporum. *Pharm. Biol. Eval*. 2, 223–233.

Mathema, V. B., Thakuri, B. C., and Sillanpää, M. (2011). Bacterial mer operon-mediated detoxification of mercurial compounds: a short review. *Arch. Microbiol*. 193, 837–844. doi:10.1007/s00203-011-0751-4

Mehta, S. K., and Gaur, J. P. (2005). Use of algae for removing heavy metal ions from wastewater: progress and prospects. *Crit. Rev. Biotechnol.* 25, 113–152. doi:10.1080/07388550500248571

Mindess, S. (2019). "6–resistance of concrete to destructive agencies," in *Lea's chemistry of cement and concrete*. Editors P.C. Hewlett and M. Liska. 5th Edn. (Cambridge, MA, Butterworth-Heinemann), 251–283.

Mindess, S., Young, J. F., and Darwin, D. (2003). *Concrete*. 2nd Edn. Upper Saddle River, NJ: Prentice Hall, 372.

Miyandehi, B. M., Feizbakhsh, A., Yazdi, M. A., Liu, Q.-F., Yang, J., and Alipour, P. (2016). Performance and properties of mortar mixed with nano-CuO and rice husk ash. *Cement Concr. Compos.* 74, 225–235. doi:10.1016/j.cemconcomp.2016.10.006

Mo, J., Zhang, Y., Xu, Q., Lamson, J. J., and Zhao, R. (2009). Photocatalytic purification of volatile organic compounds in indoor air: a literature review. *Atmos. Environ.* 43, 2229–2246. doi:10.1016/J.ATMOSENV.2009.01.034

Mohajerani, A., Burnett, L., Smith, J. V., Kurmus, H., Milas, J., Arulrajah, A., et al. (2019). Nanoparticles in construction materials and other applications, and implications of nanoparticle use. *Materials*. 12, 3052.

Monteiro, C. M., Castro, P. M., and Malcata, F. X. (2012). Metal uptake by microalgae: underlying mechanisms and practical applications. *Biotechnol. Prog.* 28, 299–311. doi:10.1002/btpr.1504

Nazari, A., and Riahi, S. (2010). The effect of TiO2 nanoparticles on water permeability and thermal and mechanical properties of high strength self-compacting concrete. *Mater. Sci. Eng.* 528, 756–763. doi:10.1016/j.msea.2010.09.074

Newsome, L., Morris, K., and Lloyd, J. R. (2014). The biogeochemistry and bioremediation of uranium and other priority radionuclides. *Chem. Geol.* 363, 164–184. doi:10.1016/j.chemgeo.2013.10.034

Noman, E., Al-Gheethi, A., Talip, B. A., Mohamed, R., and Kassim, A. H. (2019). Inactivating pathogenic bacteria in greywater by biosynthesized Cu/Zn nanoparticles from secondary metabolite of Aspergillus iizukae; optimization, mechanism and techno economic analysis. *PloS One*. 14, e0221522. doi:10.1371/journal.pone.0221522

Noorvand, H., Abang Ali, A. A., Demirboga, R., Farzadnia, N., and Noorvand, H. (2013). Incorporation of nano TiO2 in black rice husk ash mortars. *Conster. Build. Mater.* 47, 1350–1361. doi:10.1016/j.conbuildmat.2013.06.066

Osterwalder, N., Capello, C., Hungerbühler, K., and Stark, W. J. (2006). Energy consumption during nanoparticle production: how economic is dry synthesis? *J. Nanopart. Res.* 8, 1.

Pacheco-Torgal, F., and Jalali, S. (2011). Nanotechnology: advantages and drawbacks in the field of conster. *Build. Mater. Conster. Build. Mater.* 25, 582–590. doi:10.1016/j.conbuildmat.2010.07.009

Pacheco-Torgal, F., and Labrincha, J. A. (2013). The future of construction materials research and the seventh UN Millennium Development Goal: a few insights. *Conster. Build. Mater.* 40, 729–737. doi:10.1016/J.CONBUILDMAT.2012.11.007

Pal, A., and Paul, A. K. (2008). Microbial extracellular polymeric substances: central elements in heavy metal bioremediation. *Indian J. Microbiol.* 48, 49–64. doi:10.1007/s12088-008-0006-5

Paria, S., and Yuet, P. K. (2006). Solidification–stabilization of organic and inorganic contaminants using portland cement: a literature review. *Environ. Rev.* 14, 217–255. doi:10.1139/A06-004

Pellenq, R. J., Kushima, A., Shahsavari, R., Van Vliet, K. J., Buehler, M. J., Yip, S., et al. (2009). A realistic molecular model of cement hydrates. *Proc. Natl. Acad. Sci. U.S.A.* 106, 16102–16107. doi:10.1073/pnas.0902180106

Perez-Gonzalez, T., Jimenez-Lopez, C., Neal, A. L., Rull-Perez, F., Rodriguez-Navarro, A., Fernandez-Vivas, A., et al. (2010). Magnetite biomineralization induced by Shewanella oneidensis. *Geochem. Cosmochim. Acta*. 74, 967–979. doi:10.1016/j.gca.2009.10.035

Petronella, F., Truppi, A., Ingrosso, C., Placido, T., Striccoli, M., Curri, M. L., et al. (2017). Nanocomposite materials for photocatalytic degradation of pollutants. *Catal. Today*. 281, 85–100. doi:10.1016/j.cattod.2016.05.048

Porter, H., Dhami, N. K., and Mukherjee, A. (2017). Synergistic chemical and microbial cementation for stabilization of aggregates. *Cement Concr. Compos.* 83, 160–170. doi:10.1016/j.cemconcomp.2017.07.015

Puligilla, S., Chen, X., and Mondal, P. (2019). Does synthesized C-S-H seed promote nucleation in alkali activated fly ash-slag geopolymer binder? *Mater. Struct.* 52, 65. doi:10.1617/s11527-019-1368-3

Puligilla, S., Chen, X., and Mondal, P. (2018). Understanding the role of silicate concentration on the early-age reaction kinetics of a calcium containing geopolymeric binder. *Conster. Build. Mater.* 191, 206–215. doi:10.1016/j.conbuildmat.2018.09.184

Raghoebarsing, A. A., Smolders, A. J., Schmid, M. C., Rijpstra, W. I., Wolters-Arts, M., Derksen, J., et al. (2005). Methanotrophic symbionts provide carbon for photosynthesis in peat bogs. *Nature*. 436, 1153–1156. doi:10.1038/nature03802

Ramanan, R., Kannan, K., Sivanesan, S. D., Mudliar, S., Kaur, S., Tripathi, A. K., et al. (2009). Bio-sequestration of carbon dioxide using carbonic anhydrase enzyme purified from Citrobacter freundii. *World J. Microbiol. Biotechnol.* 25, 981–987. doi:10.1007/s11274-009-9975-8

Rasaki, S. A., Bingxue, Z., Guarecuco, R., Thomas, T., and Minghui, Y. (2019). Geopolymer for use in heavy metals adsorption, and advanced oxidative processes: a critical review. *J. Clean. Prod.* 213, 42–58. doi:10.1016/j.jclepro.2018.12.145

Rashad, A. M. (2013b). A synopsis about the effect of nano-Al2O3, nano-Fe2O3, nano-Fe3O4 and nano-clay on some properties of cementitious materials – a short guide for Civil Engineer. *Mater. Des.* 52, 143–157. doi:10.1016/j.matdes.2013.05.035

Rashad, A. M. (2013a). Effects of ZnO2, ZrO2, Cu2O3, CuO, CaCO3, SF, FA, cement and geothermal silica waste nanoparticles on properties of cementitious materials – a short guide for Civil Engineer. *Conster. Build. Mater.* 48, 1120–1133. doi:10.1016/j.conbuildmat.2013.06.083

Reches, Y. (2018). Nanoparticles as concrete additives: review and perspectives. *Conster. Build. Mater.* 175, 483–495. doi:10.1016/j.conbuildmat.2018.04.214

Ruan, S., Qiu, J., Weng, Y., Yang, Y., Yang, E.-H., Chu, J., and Unluer, C. (2019). The use of microbial induced carbonate precipitation in healing cracks within reactive magnesia cement-based blends. *Cement Concrete Res.* 115, 176–188. doi:10.1016/j.cemconres.2018.10.018

Sadhukhan, J., Joshi, N., Shemfe, M., and Lloyd, J. R. (2017). Life cycle assessment of sustainable raw material acquisition for functional magnetite bionanoparticle production. *J. Environ. Manag.* 199, 116–125. doi:10.1016/j.jenvman.2017.05.048

Salehizadeh, H., Yan, N., and Farnood, R. (2020). Recent advances in microbial CO2 fixation and conversion to value-added products. *Chem. Eng. J.* 390, 124584. doi:10.1016/j.cej.2020.124584

Sanna, A., Uibu, M., Caramanna, G., Kuusik, R., and Maroto-Valer, M. M. (2014). A review of mineral carbonation technologies to sequester CO2. *Chem. Soc. Rev.* 43, 8049–8080. doi:10.1039/c4cs00035h

Sato, T., and Diallo, F. (2010). Seeding effect of nano-CaCO3 on the hydration of tricalcium silicate. *Transport. Res. Rec.* 2141, 61–67. 10.3141/2141-11

Šavija, B., and Luković, M. (2016). Carbonation of cement paste: understanding, challenges, and opportunities. *Conster. Build. Mater.* 117, 285–301. doi:10.1016/j.conbuildmat.2016.04.138

Schaffner, R. (2004). Bioremediation offers an effective, ethical, and economical alternative to standard cleanups. *Am. Water Works Assoc. J.* 96, 22. doi:10.1002/j.1551-8833.2004.tb10519.x

Seifan, M., Samani, A. K., and Berenjian, A. (2016). Bioconcrete: next generation of self-healing concrete. *Appl. Microbiol. Biotechnol.* 100, 2591–2602. doi:10.1007/s00253-016-7316-z

Selvakumar, R., Seethalakshmi, N., Thavamani, P., Naidu, R., and Megharaj, M. (2014). Recent advances in the synthesis of inorganic nano/microstructures using microbial biotemplates and their applications. *RSC Adv.* 4, 52156–52169. doi:10.1039/C4RA07903E

Show, S., Tamang, A., Chowdhury, T., Mandal, D., and Chattopadhyay, B. (2015). Bacterial (BKH1) assisted silica nanoparticles from silica rich substrates: a facile and green approach for biotechnological applications. *Colloids Surf. B Biointerfaces*. 126, 245–250. doi:10.1016/j.colsurfb.2014.12.039

Singh, R., Paul, D., and Jain, R. K. (2006). Biofilms: implications in bioremediation. *Trends Microbiol.* 14, 389–397. doi:10.1016/j.tim.2006.07.001

Singh, R., Dong, H., Liu, D., Zhao, L., Marts, A. R., Farquhar, E., et al. (2015). Reduction of hexavalent chromium by the thermophilic methanogen Methanothermobacter thermautotrophicus. *Geochem. Cosmochim. Acta*. 148, 442–456. doi:10.1016/j.gca.2014.10.012

Sneha, K., Sathishkumar, M., Mao, J., Kwak, I. S., and Yun, Y. S. (2010). Corynebacterium glutamicum-mediated crystallization of silver ions through sorption and reduction processes. *Chem.l Eng. J.* 162, 989–996. doi:10.1016/j.cej.2010.07.006

Sobolev, K., Flores, I., Hermosillo, R., and Torres-Martinez, L. M. (2006). "Nanomaterials and nanotechnology for high-performance cement composites," in Proceedings of ACI Session on "Nanotechnology of concrete: recent Developments and future perspectives", Denver, USA, November 7, 2006 [abstract].

Soleimani, S., Ormeci, B., and Isgor, O. B. (2013b). Evaluation of *E. coli* biofilm as a protective barrier against microbiologically influenced deterioration of concrete (MICD) under mesophilic temperatures. *Water Sci. Technol.* 68, 303–310. doi:10.2166/wst.2013.252

Soleimani, S., Ormeci, B., and Isgor, O. B. (2013c). Growth and characterization of *Escherichia coli* DH5α biofilm on concrete surfaces as a protective layer against microbiologically influenced concrete deterioration (MICD). *Appl. Microbiol. Biotechnol.* 97, 1093–1102. doi:10.1007/s00253-012-4379-3

Soleimani, S., Isgor, O. B., and Ormeci, B. (2016). Effectiveness of *E. coli* biofilm on mortar to inhibit biodegradation by biogenic acidification. *J. Mater. Civ. Eng.* 28, 04015167. doi:10.1061/(ASCE)MT.1943-5533.0001440

Soleimani, S., Isgor, O. B., and Ormeci, B. (2013a). Resistance of biofilm-covered mortars to microbiologically influenced deterioration simulated by sulfuric acid exposure. *Cement Concr. Res*, 229–238. doi:10.1016/j.cemconres.2013.06.016

Souto-Martinez, A., Arehart, J. H., and Srubar, W. V. (2018a). Cradle-to-gate CO2e emissions vs. *in situ* CO2 sequestration of structural concrete elements. *Energy Build.* 167, 301–311. doi:10.1016/j.enbuild.2018.02.042

Souto-Martinez, A., Delesky, E. A., Foster, K. E. O., and Srubar, W. V. (2017). A mathematical model for predicting the carbon sequestration potential of ordinary portland cement (OPC) concrete. *Conster. Build. Mater.* 147, 417–427. doi:10.1016/j.conbuildmat.2017.04.133

Souto-Martinez, A., Sutley, E. J., Liel, A. B., and Srubar, W. V. (2018b). "Embodied carbon of wood and reinforced concrete structures under chronic and acute hazards," in *Embodied carbon in buildings: measurement, management, and mitigation*. Editors F. Pomponi, C. De Wolf, and A. Moncaster (Cham, Germany: Springer International Publishing), 77–103.

Spasiano, D., Marotta, R., Malato, S., Fernandez-Ibañez, P., and Di Somma, I. (2015). Solar photocatalysis: materials, reactors, some commercial, and pre-industrialized applications. A comprehensive approach. *Appl. Catal. B Environ.* 170–171, 90–123. doi:10.1016/j.apcatb.2014.12.050

Stabnikov, V., Ivanov, V., and Chu, J. (2015). Construction Biotechnology: a new area of biotechnological research and applications. *World J. Microbiol. Biotechnol.* 31, 1303–1314. doi:10.1007/s11274-015-1881-7

Stabnikov, V., Naeimi, M., Ivanov, V., and Chu, J. (2011). Formation of water-impermeable crust on sand surface using biocement. *Cement Concrete Res.* 41, 1143–1149. doi:10.1016/j.cemconres.2011.06.017

Stępniewska, Z., and Kuźniar, A. (2013). Endophytic microorganisms—promising applications in bioremediation of greenhouse gases. *Appl. Microbiol. Biotechnol.* 97, 9589–9596. doi:10.1007/s00253-013-5235-9

Strini, A., Cassese, S., and Schiavi, L. (2005). Measurement of benzene, toluene, ethylbenzene and o-xylene gas phase photodegradation by titanium dioxide dispersed in cementitious materials using a mixed flow reactor. *Appl. Catal. B Environ.* 61, 90–97. doi:10.1016/j.apcatb.2005.04.009

Sun, L., Zhang, Z., and Dang, H. (2003). A novel method for preparation of silver nanoparticles. *Mater. Lett.* 57, 3874–3879. doi:10.1016/S0167-577X(03)00232-5

Suresh Kumar, K., Dahms, H. U., Won, E. J., Lee, J. S., and Shin, K. H. (2015). Microalgae - a promising tool for heavy metal remediation. *Ecotoxicol. Environ. Saf.* 113, 329–352. doi:10.1016/j.ecoenv.2014.12.019

Sydney, E. B., Sturm, W., De Carvalho, J. C., Thomaz-Soccol, V., Larroche, C., Pandey, A., et al. (2010). Potential carbon dioxide fixation by industrially important microalgae. *Bioresour. Technol.* 101, 5892–5896. doi:10.1016/j.biortech.2010.02.088

Takeuchi, F., Iwahori, K., Kamimura, K., Negishi, A., Maeda, T., and Sugio, T. (2001). Volatilization of mercury under acidic conditions from mercury-polluted soil by a mercury-resistant Acidithiobacillus ferrooxidans SUG 2-2. *Biosci. Biotechnol. Biochem.* 65, 1981–1986. doi:10.1271/bbb.65.1981

Tan, K. S., and Cheong, K. Y. (2013). Advances of Ag, Cu, and Ag–Cu alloy nanoparticles synthesized via chemical reduction route. *J. Nanopart. Res.* 15, 1537. doi:10.1007/s11051-013-1537-1

Tang, Q., Ge, Y.-Y., Wang, K.-T., He, Y., and Cui, X.-M. (2015). Preparation and characterization of porous metakaolin-based inorganic polymer spheres as an adsorbent. *Mater. Des.* 88, 1244–1249. doi:10.1016/j.matdes.2015.09.126

Teitzel, G. M., and Parsek, M. R. (2003). Heavy metal resistance of biofilm and planktonic *Pseudomonas aeruginosa*. *Appl. Environ. Microbiol.* 69, 2313–2320. doi:10.1128/AEM.69.4.2313-2320.2003

Thomas, J. J., Jennings, H. M., and Chen, J. J. (2009). Influence of nucleation seeding on the hydration mechanisms of tricalcium silicate and cement. *J. Phys. Chem. C.* 113, 4327–4334. doi:10.1021/jp809811w

Tiquia-Arashiro, S., and Rodrigues, D. F. (2016). *Extremophiles: applications in nanotechnology*, Cham, Switzerland, Springer International Publishing, 193.

Trejo-Arroyo, D. L., Acosta, K. E., Cruz, J. C., Valenzuela-Muniz, A. M., Vega-Azamar, R. E., and Jimenez, L. F. (2019). Influence of ZrO2 nanoparticles on the microstructural development of cement mortars with limestone aggregates. *App. Sci.-Basel.* 9, 12. doi:10.3390/app9030598

Van Paassen, L. A., Daza, C. M., Staal, M., Sorokin, D. Y., Van Der Zon, W., and Van Loosdrecht, M. C. M. (2010). Potential soil reinforcement by biological denitrification. *Ecol. Eng.* 36, 168–175. doi:10.1016/j.ecoleng.2009.03.026

Wang, J., Ersan, Y. C., Boon, N., and De Belie, N. (2016). Application of microorganisms in concrete: a promising sustainable strategy to improve concrete durability. *Appl. Microbiol. Biotechnol.* 100, 2993–3007. doi:10.1007/s00253-016-7370-6

Wang, J., Vandevyvere, B., Vanhessche, S., Schoon, J., Boon, N., and De Belie, N. (2017). Microbial carbonate precipitation for the improvement of quality of recycled aggregates. *J. Clean. Prod.* 156, 355–366. doi:10.1016/j.jclepro.2017.04.051

Wang, Y., Cai, Z., Sheng, S., Pan, F., Chen, F., and Fu, J. (2020). Comprehensive evaluation of substrate materials for contaminants removal in constructed wetlands. *Sci. Total Environ.* 701, 134736. doi:10.1016/j.scitotenv.2019.134736

White, C., and Gadd, G. M. (2000). Copper accumulation by sulfate-reducing bacterial biofilms. *FEMS Microbiol. Lett.* 183, 313–318. doi:10.1111/j.1574-6968.2000.tb08977.x

Wong, L. S. (2015). Microbial cementation of ureolytic bacteria from the genus Bacillus: a review of the bacterial application on cement-based materials for cleaner production. *J. Clean. Prod.* 93, 5–17. doi:10.1016/j.jclepro.2015.01.019

Wong, L. S., Oweida, A. F. M., Kong, S. Y., Iqbal, D. M., and Regunathan, P. (2020). The surface coating mechanism of polluted concrete by Candida ethanolica induced calcium carbonate mineralization. *Conster. Build. Mater.* 257, 119482. doi:10.1016/j.conbuildmat.2020.119482

Wu, F., Zhou, Z., and Hicks, A. L. (2019). Life cycle impact of titanium dioxide nanoparticle synthesis through physical, chemical, and biological routes. *Environ. Sci. Tech.* 53, 4078–4087. doi:10.1021/acs.est.8b06800

Wu, Y., Li, T., and Yang, L. (2012). Mechanisms of removing pollutants from aqueous solutions by microorganisms and their aggregates: a review. *Bioresour. Technol.* 107, 10–18. doi:10.1016/j.biortech.2011.12.088

Yuan, H., Shi, Y., Xu, Z., Lu, C., Ni, Y., and Lan, X. (2013). Influence of nano-ZrO2 on the mechanical and thermal properties of high temperature cementitious thermal energy storage materials. *Conster. Build. Mater.* 48, 6–10. doi:10.1016/j.conbuildmat.2013.06.088

Zhang, G. (2016). Biomineralization on the wavy substrate: shape transition of nacreous tablets from pyramids of amorphous nanoparticles to dome-capped prisms of single crystals. *Acta Biomater.* 36, 277–285. doi:10.1016/j.actbio.2016.03.018

Zhang, R., Cheng, X., Hou, P., and Ye, Z. (2015). Influences of nano-TiO2 on the properties of cement-based materials: hydration and drying shrinkage. *Conster. Build. Mater.* 81, 35–41. doi:10.1016/J.CONBUILDMAT.2015.02.003

Zumft, W. G., and Kroneck, P. M. (2006). Respiratory transformation of nitrous oxide (N2O) to dinitrogen by bacteria and archaea. *Adv. Microb. Physiol.* 52, 107–227. doi:10.1016/S0065-2911(06)52003-X

Zuo, R. (2007). Biofilms: strategies for metal corrosion inhibition employing microorganisms. *Appl. Microbiol. Biotechnol.* 76, 1245–1253. doi:10.1007/s00253-007-1130-6

Conflict of Interest: The authors declare that the research was conducted in the absence of any commercial or financial relationships that could be construed as a potential conflict of interest.

Advantages of publishing in Frontiers

OPEN ACCESS
Articles are free to read for greatest visibility and readership

FAST PUBLICATION
Around 90 days from submission to decision

HIGH QUALITY PEER-REVIEW
Rigorous, collaborative, and constructive peer-review

TRANSPARENT PEER-REVIEW
Editors and reviewers acknowledged by name on published articles

Frontiers
Avenue du Tribunal-Fédéral 34
1005 Lausanne | Switzerland

Visit us: www.frontiersin.org
Contact us: frontiersin.org/about/contact

REPRODUCIBILITY OF RESEARCH
Support open data and methods to enhance research reproducibility

DIGITAL PUBLISHING
Articles designed for optimal readership across devices

FOLLOW US
@frontiersin

IMPACT METRICS
Advanced article metrics track visibility across digital media

EXTENSIVE PROMOTION
Marketing and promotion of impactful research

LOOP RESEARCH NETWORK
Our network increases your article's readership